

Proceedings of the U.S. Nuclear Regulatory Commission

---

---

# Thirteenth Water Reactor Safety Research Information Meeting

Volume 4

- Integral Systems Tests
- 2D/3D Research
- Separate Effects

Held at  
National Bureau of Standards  
Gaithersburg, Maryland  
October 22-25, 1985

---

---

## U.S. Nuclear Regulatory Commission

Office of Nuclear Regulatory Research

Proceedings prepared by  
Brookhaven National Laboratory



## NOTICE

These proceedings have been authored by a contractor of the United States Government. Neither the United States Government nor any agency thereof, or any of their employees, makes any warranty, expressed or implied, or assumes any legal liability or responsibility for any third party's use, or the results of such use, of any information, apparatus, product or process disclosed in these proceedings, or represents that its use by such third party would not infringe privately owned rights. The views expressed in these proceedings are not necessarily those of the U.S. Nuclear Regulatory Commission.

Available from

Superintendent of Documents  
U.S. Government Printing Office  
P.O. Box 37082  
Washington D.C. 20013-7082

and

National Technical Information Service  
Springfield, VA 22161

Proceedings of the U.S. Nuclear Regulatory Commission

---

# Thirteenth Water Reactor Safety Research Information Meeting

## Volume 4

- Integral Systems Tests
- 2D/3D Research
- Separate Effects

Held at  
National Bureau of Standards  
Gaithersburg, Maryland  
October 22-25, 1985

---

Date Published: February 1986

Compiled by: Allen J. Weiss

**Office of Nuclear Regulatory Research  
U.S. Nuclear Regulatory Commission  
Washington, D.C. 20555**

Proceedings prepared by  
Brookhaven National Laboratory



## ABSTRACT

This six-volume report contains 151 papers out of the 178 that were presented at the Thirteenth Water Reactor Safety Research Information Meeting held at the National Bureau of Standards, Gaithersburg, Maryland, during the week of October 22-25, 1985. The papers are printed in the order of their presentation in each session and describe progress and results of programs in nuclear safety research conducted in this country and abroad. Foreign participation in the meeting included thirty-one different papers presented by researchers from Japan, Canada and eight European countries. The titles of the papers and the names of the authors have been updated and may differ from those that appeared in the final program of the meeting.

PROCEEDINGS OF THE  
THIRTEENTH WATER REACTOR SAFETY RESEARCH  
INFORMATION MEETING

October 22-25, 1985

Published in Six Volumes

**GENERAL INDEX**

VOLUME 1

- Plenary Session
- Risk Analysis/PRA Application
- Severe Accident Sequence Analysis
- Risk Analysis/Dependent Failure Analysis
- Industry Safety Research

VOLUME 2

- Materials Engineering Research/Pressure Vessel Research
- Materials Engineering Research/Piping Research & Fracture Mechanics
- Environmental Effects in Piping
- Surry Steam Generator/Examination and Evaluation
- Materials Engineering Research/Non-Destructive Evaluation

VOLUME 3

- Mechanical and Structural Research
- Seismic Research
- Equipment Qualification
- Nuclear Plant Aging
- Process Control

VOLUME 4

- Integral Systems Tests
- 2D/3D Research
- Separate Effects/Experiments and Analyses

VOLUME 5

- International Code Assessment Program
- Code Assessment and Improvement
- Nuclear Plant Analyzer

VOLUME 6

- Fission Product Release and Transport in Containment
- Containment Systems Research/Containment Loads Analysis
- Severe Accident Source Term

REGISTERED ATTENDEES  
13th WRSR INFORMATION MEETING

Abe, Y.  
Japan Atomic Energy Research Institute  
3000 Trinity Dr. #23  
Los Alamos, NM 87544

Acker, D.  
Centre d'Etudes Nucleaires de Saclay  
DEM/SMTS/RDMS  
GIF S/YVETTE  
FRANCE 91191

Adamantlades, A.  
MITRE Corp.  
1820 Dolly Madison Blvd.  
McLean, Virginia 22102

Adams, R.E.  
Oak Ridge National Laboratory  
P.O. Box Y, Bldg. 9108, MS-2  
Oak Ridge, Tennessee 37831

Agarwal, B.K.  
Poster Wheeler  
#1503, 20W., Clark Street  
Chicago, Illinois 60602

Ahlfeld, C.E.  
E.I. duPont de Nemours-Savannah River Lab.  
Building 773-A/A-235  
Aiken, SC 29808

Ahmad, J.  
Battelle Columbus Laboratory  
505 King Avenue  
Columbus, Ohio 43201

Akimoto, H.  
Japan Atomic Energy Research Institute  
Tokai-mura, Ibaraki-ken  
Japan

Almeida, K.  
University of Maryland  
College Park, Maryland 20740

Amico, P.  
Applied Risk Technology Corp.  
P.O. Box 175  
Columbia, Maryland 21045

Andersen, J.G.  
General Electric  
175 Curtner Avenue  
San Jose, California 95125

Andersen, P.  
DYNATREK, Inc.  
2115 E. Jefferson St.  
Rockville, Maryland 20852

Anderson, J.L.  
EG&G Idaho, Inc.  
P.O. Box 1625  
Idaho Falls, Idaho 83401

Andrews, B.  
Battelle - Pacific Northwest Laboratory  
P.O. Box 999  
Richland, Washington 99336

Anoda, Y.  
Japan Atomic Energy Research Institute  
197 Dale #8  
Idaho Falls, Idaho 83402

Araya, F.  
Japan Institute of Nuclear Safety  
Mita Kokusai Bldg., Mita 1-4-28  
Minato-ku, Tokyo  
Japan

Aro, I.M.  
Finnish Centre for Radiation & Nuc. Safety  
P.O. Box 268  
SF-00101 Helsinki 10. FINLAND

Atkinson, J.D.  
CERL, CEGB  
Kelvin Avenue  
Leatherhead, Surrey KT22 7SE  
United Kingdom

Bailey, G.F.  
UNC Nuclear Industries  
19815 Bazzellton Place  
Gaithersburg, Maryland 20879

Ball, D.G.  
Oak Ridge National Laboratory  
P.O. Box P  
Oak Ridge, Tennessee 37831

Sandyopadhyay, K.K.  
Brookhaven National Laboratory  
Building 129  
Upton, New York 11973

Bari, R.A.  
Brookhaven National Laboratory  
Building 130  
Upton, New York 11973

Bass, B.R.  
Martin Marietta Energy Systems, Inc.  
P.O. Box P  
Oak Ridge, Tennessee 37831

Basselier, J.E.  
Belgonucleaire  
36, Tentersdreef  
Overijse, Belgium 1900  
Belgium

Bell, C.R.  
Los Alamos National Laboratory  
P.O. Box 1663  
Los Alamos, NM 87545

Bennett, J.G.  
Los Alamos National Laboratory  
P.O. Box 1663, MS J576  
Los Alamos, NM 87545

Bergeron, K.D.  
Sandia National Laboratory  
Division 6449  
Albuquerque, New Mexico 87185

Berman, M.  
Sandia National Laboratory  
Division 6427  
Albuquerque, New Mexico 87111

Berry, D.L.  
Sandia National Laboratory  
Division 6447  
Albuquerque, NM 87111

Bezier, P.  
Brookhaven National Laboratory  
Building 129  
Upton, New York 11973

Bingham, B.E.  
Babcock & Wilcox  
3315 Old Forest Road  
Lynchburg, Virginia 24506

Binner, W.  
Austrian Research Center Seibersdorf  
Lenaugasse 10  
Vienna A-1082  
Austria

Bloomfield, W.L.  
GPU Nuclear  
P.O. Box 480  
Middletown, PA 17057

Board, S.J.  
CEGB - Berkeley Nuclear Laboratory  
Berkeley, Gloucestershire, England

Soccio, J.L.  
Brookhaven National Laboratory  
Bldg. 130  
Upton, New York 11973

Boehnert, P.A.  
U.S. Nuclear Regulatory Commission  
Washington, D. C. 20555

Bonzon, L. L.  
Sandia National Laboratory  
Division 6446  
Albuquerque, NM 87185

Borsum, R.B.  
Babcock & Wilcox  
7910 Woodmont Avenue, Suite 220  
Bethesda, MD 20814

Boucher, T.J.  
EG&G Idaho, Inc.  
P.O. Box 1625  
Idaho Falls, Idaho 83402

Boyack, B.E.  
Los Alamos National Laboratory  
P.O. Box 1663  
Los Alamos, NM 87545

Bradley, D.R.  
Sandia National Laboratory  
P.O. Box 5800  
Albuquerque, New Mexico 87185

Bratby, P.A.  
National Nuclear Corporation  
Cambridge Road, Whetstone  
Leicester, LE83LH ENGLAND

Brittain, I.  
United Kingdom Atomic Energy Authority  
AEE Winfrith  
Dorchester, Dorset DT28DN  
United Kingdom

Bruemmer, S.M.  
Battelle - Pacific Northwest Laboratory  
P.O. Box 999  
Richland, Washington 99352

Brust, B.  
Battelle - Pacific Northwest Laboratory  
505 King Avenue  
Columbus, Ohio 43214

Bryan, R. H.  
Oak Ridge National Laboratory  
P.O. Box Y  
Oak Ridge, Tennessee 37831

Budnitz, R.J.  
Future Resources Associates Inc.  
2000 Center Street--Suite 418  
Berkeley, California 94704

Burda, A.J.  
Nuclear Regulatory Commission  
Mail Stop 1130SS  
Washington, D. C. 20555

Burns, N. L.  
Westinghouse Electric Corp.  
P.O. Box 355  
Pittsburgh, Pennsylvania 15230 5230

Butland, A.T.  
United Kingdom Atomic Energy Authority  
AEI Winfrith  
Dorchester, Dorset DT28DH  
United Kingdom

Butler, C.N.  
Baltimore Gas & Electric  
P.O. Box 1475  
Baltimore, Maryland 21203

Butler, J.  
UKAEA Winfrith  
Barn Road Broadstone  
Dorset BH18 8NT

Butler, T.A.  
Los Alamos National Laboratory  
P.O. Box 1663, MS J576  
Los Alamos, NM 87545

Buxbaum, S.R.  
Baltimore Gas & Electric  
P.O. Box 1475  
Baltimore, Maryland 21203

Buxton, L.D.  
Sandia National Laboratory  
Division 6444  
P.O. Box 5800  
Albuquerque, New Mexico 87185

Byrne, S.T.  
Combustion Engineering  
1000 Prospect Hill Road  
Windsor, CT 06095

Cadek, F.F.  
Westinghouse  
P.O. Box 355  
Pittsburgh, Pennsylvania 15230

Cadwallader, L.C.  
Idaho National Engineering Lab/EG&G Idaho  
P.O. Box 1625  
Idaho Falls, Idaho 83415

Campbell, D.J.  
JBF Associates  
1000 Technology Park Center  
Knoxville, Tennessee 37932

Cardinal, J. W.  
Southwest Research Institute  
6220 Culebra Road  
P.O. Drawer 28510  
San Antonio, Texas 78284

Carey, C.  
Tennessee Valley Authority  
400 W. Summit Hill Drive, W100181  
Knoxville, TN 37902

Carroll, D.E.  
Sandia National Laboratory  
Division 6449  
Albuquerque, New Mexico 87185

Carter, H.R.  
Babcock & Wilcox  
1562 Beeson Street  
Alliance, Ohio 44601

Casper, H.F.  
Gesellschaft für Reaktorsicherheit  
5 Köln 1, Schwertnergasse 1  
FRG

Catton, I.  
UCLA  
5731 Boelter Hall  
Los Angeles, California 90024

Cazzoli, E.G.  
Brookhaven National Laboratory  
Building 130  
Upton, New York 11973

Charlton, T.R.  
EG&G Idaho, Inc  
5374 Township Road  
Idaho Falls, Idaho 83401

Chen, J.C.  
Lehigh University  
Department of Chemical Engineering  
Bethlehem, PA 18015

Chen, Y.  
Institute of Nuclear Energy Research  
P.O. Box 3-  
Lung-Yan, Taiwan 325  
Republic of China

Cheng, H-S  
Brookhaven National Laboratory  
Building 130  
Upton, New York 11973

Cheng, T.C.  
EG&G Idaho, Inc.  
P.O. Box 1625  
Idaho Falls, Idaho 83415

Cheverton, R.D.  
Oak Ridge National Laboratory  
P.O. Box Y  
Oak Ridge, Tennessee 37831

Chien, T.  
Argonne National Laboratory  
9700 South Cass Avenue  
Argonne, Illinois 60439

Chiou, J-S.  
Westinghouse  
178 Penn Lear Drive  
Monroeville, Pennsylvania 15146

Choi, Y.S.  
Korea Electric Power Corporation R & D  
52, Cheongdam-Dong, Kangnam-Ku  
Seoul  
Korea

Chopra, G.K.  
Argonne National Laboratory  
9700 S. Cass Avenue  
Argonne, Illinois 60439

Chow, S.K.  
Westinghouse  
178 Penn Lear Drive  
Monroeville, Pennsylvania 15146

Cirilli, J.J.  
Northwest Utilities  
P.O. Box 270  
Hartford, Connecticut 06141-0270

Clark, R.A.  
Battelle-Pacific Northwest Laboratory  
Box 999  
Richland, WA 99352

Cleary, J. M.  
Combustion Engineering  
1000 Prospect Hill Road  
Windsor, CT 06095

Cleveland, J.W.  
SEA Consultants, Inc.  
1625 The Alameda Ste303  
San Jose, California 95126

Cliquet, J.P.  
Brussels University  
AV. F.D. Roosevelt, 50  
Bruxelles 1050  
Belgium

Colagrossi, M.  
ENEA/Rome  
V.V. Brancati 48  
Rome, Italy 00144

Cole, R.K.  
Sandia National Laboratory  
Division 6444  
P.O. Box 5800  
Albuquerque, New Mexico 87185

Condie, K.G.  
EG&G Idaho, Inc.  
P. O. Box 1625  
Idaho Falls, Idaho 83415

Cook, T.L.  
Baltimore Gas & Electric  
P.O. Box 1475  
Room 720, G&E Bldg.  
Baltimore, Maryland 21203

Corwin, W.R.  
Oak Ridge National Laboratory  
Building 4500S, Room D61  
P.O. Box X  
Oak Ridge, TN 37831

Courtsaud, M.  
C.E.A./CENG/STT  
85X -38041 Grenoble CEDEX  
Grenoble, FRANCE

Coward, R.N.  
MPR Associates  
1050 Conn. Avenue, N.W.  
Washington, D. C. 20030

Cowne, S.R.  
Baltimore Gas & Electric  
P.O. Box 1535  
Calvert Cliffs  
Luby Maryland 20657

Cramblitt, K.L.  
Baltimore Gas & Electric  
P.O. Box 1475  
Baltimore, Maryland 21203

Crawford, T.J.  
American Electric Power  
1 Riverside Plaza  
Columbus, Ohio 43215

Creswell, S. L.  
HM Nuclear Installations Inspectorate  
Thames House North  
Millbank  
London SW1P 4QJ, U.K.

Cummings, G.E.  
Lawrence Livermore National Laboratory  
L-198, P.O. Box 808  
Livermore, CA 94526

Dahlgren, D.A.  
Sandia National Laboratory  
Dept. 6440  
P.O. Box 5800  
Albuquerque, NM 87185

Dal, A.  
Shanghai Rekeleau, Eng. of Research Inst.  
Shanghai  
China

Dallman, R.J.  
EG&G Idaho, Inc.  
P.O. Box 1625  
Idaho Falls, Idaho 83415

Damerall, P.  
MPR Associates  
1050 Connecticut Avenue, N.W. 20036

Dankosky, J.D.  
Westinghouse - Bettis  
P.O. Box 79  
West Mifflin, Pennsylvania 15122

Darling, W.R.  
Duke Power Company  
P.O. Box 33189  
Charlotte, NC 28242

Davis, R.E.  
Brookhaven National Laboratory  
Bldg. 703M  
Upton, New York 11973

De, N.K.  
U.S. Nuclear Regulatory Commission  
9451 Lee Highway, #1016  
Fairfax, VA 22031

DeAgostino, E.  
ENEA/Rome  
V.V. Brancati 48  
Rome, Italy 00144

Deem, R.E.  
New York Power Authority  
123 Main Street  
White Plains, New York 10601

Della Loggia, E.  
CEC - DG XII  
Rue De La Loi, 200 5de 7/77  
Brussels B-1049  
BELGIUM

Denning, R.S.  
Battelle - Pacific Northwest Laboratory  
505 King Avenue  
Columbus, Ohio 43201

DeVault, R.H.  
Tennessee Valley Authority  
400 West Summit Hill Drive, W10D2.0  
Knoxville, TN 37902

deWit, R.  
National Bureau of Standards  
Room B113, Materials Building  
Gaithersburg, MD 20899

Dietershagen, H.P.  
Knolls Atomic Power Laboratory  
P.O. Box 1072  
Schenectady, New York 12301

Dingman, S.E.  
Sandia National Laboratory  
P.O. Box 5800  
Division 6415  
Albuquerque, New Mexico 87185

Dluzniewski, E.J.  
GRS Representative in U.S.A.  
GLOUCENGASSE 1  
5000 KOLN I  
West Germany

Dobbe, C.A.  
EG&G Idaho, Inc.  
P.O. Box 1625  
Idaho Falls, Idaho 83415

Doctor, P.G.  
Battelle - Pacific Northwest Laboratory  
Box 999  
Richland, WA 99352

Doctor, S.R.  
Battelle - Pacific Northwest Laboratory  
Battelle Blvd.  
Richland, Washington 99352

Dodd, C.V.  
Oak Ridge National Laboratory  
P.O. Box X  
Oak Ridge, Tennessee 37831

Dougherty, E.M.  
Science Applications International Corp.  
3400 Middlebrook Park C-1  
Knoxville, Tennessee 37923

Duco, J.J.  
CEA/FRANCE  
IPSN/CEN/FAR  
92265 Fontenay aux Roses  
France

Duffey, R.B.  
Electric Power Research Institute  
3412 Millview Avenue  
Palo Alto, California 94303

Eiji, T.  
Japan Institute of Nuclear Safety  
Mita 1-4-2B Minato-ku  
Tokyo 108  
Japan

El-Zeftawy, M.M.  
U.S. Nuclear Regulatory Commission  
11621 Flints Grove  
Gaithersburg, Maryland 20878

Emilio, V.E.  
University of PISA  
Via Diotisalvi, 2  
Pisa, Italy 56100

English, W.F.  
General Electric Company  
175 Curtner Avenue  
San Jose, California 95125

Esnwine, R.C.  
Baltimore Gas & Electric  
P.O. Box 1475  
Baltimore, Maryland 21203

Espefalt, R.G.  
Swedish State Power Board  
Vaellingby, Sweden S-16287

Fabry, A.M.  
SCF-CEN  
270 Boeretang  
2400 Mol  
Belgium

Farber, S.A.  
Radiation Controls, Inc.  
114 Airport Road  
Warren, VT 05674

Farrant, D.R.  
British Nuclear Fuels PLC  
Springfields Work, Salwick, Preston  
Lancashire PR4 0XJ  
U.K.

Fell, J.  
United Kingdom Atomic Energy Authority  
AEF Winfrith  
Dorchester, Dorset DT28DN  
United Kingdom

Fernandez, R.T.  
YAEC  
1671 Worcester Road  
Framingham, MA 01701

Ferris, R.H.  
Battelle - Pacific Northwest Laboratory  
Box 999  
Richland, WA 99352

Fiege, A.W.  
Kernforschungszentrum Karlsruhe GmbH  
P.O. Box 3640  
D-7500 Karlsruhe, FRG 7500

Fields, R.J.  
National Bureau of Standards  
A113/223  
Gaithersburg, Maryland 20855

Figlhuber, D.  
Utility Power Corporation  
Atlanta, Georgia

Filacchione, R.E.  
NUS Corporation  
910 Clopper Road  
Gaithersburg, Maryland 20878

Finley, M.T.  
Baltimore Gas & Electric  
Calvert Cliffs  
Lusby, Maryland 20632

Florino, E.  
Ente Nazionale Energia Elettrica  
V.G.B. Martini 3  
Rome 00100  
ITALY

Flanagan, G.F.  
Oak Ridge National Laboratory  
P.O. Box X  
Building 6025  
Oak Ridge, TN 37831

Fox, J.R.  
Combustion Engineering  
1000 Prospect Hill Road  
Windsor, CT 06095

Freed, D.A.  
MPR Associates  
1050 Connecticut Avenue, N.W. 20036

Freund, G.A.  
Science Applications International Corp.  
P.O. Box 596  
Idaho Falls, Idaho 83402

Friderichs, T.  
MPR Associates  
1050 Connecticut Avenue, N.W. 20036

Fujimoto, H.  
Mitsubishi Atomic Power Industries, Inc.  
No. 4-1, Shibakouen 2-chome, Minato-ku  
Tokyo 105  
Japan

Fujishiro, T.  
Japan Atomic Energy Research Institute  
Tokai-mura, Nakagun, Ibaraki-ken  
Japan

Gabetta, G.  
CISE  
Via Reggio Emilia, 39  
Segrate (MI), Italy 20090



Gallerly, R.T.  
UKAEA, SRD  
Wignshaw Lane, Culcheth  
Warrington, Cheshire  
U.K.

Gaspari, G.  
SIET  
N. Bixio 21 P  
Piacenza, Italy

Gasparini, M.  
ENEA-Disp  
Via Vitaliano Brancati 48  
Rome, Italy 00144

Gast, P.  
Kernforschungszentrum Karlsruhe GmbH  
Postfach 3640  
D-7500 Karlsruhe  
FRG 7500

George, P.R.  
CEGB-PMT  
Booths Hall  
Knutsford, Cheshire WA17  
ENGLAND

Ghosh, S.  
Central Electricity Generating Board  
Boothshall, Chelsford Road  
Knutsford, Cheshire, England  
UK

Gieseke, J.A.  
Battelle - Columbus Laboratories  
505 King Avenue  
Columbus, Ohio 43201

Gilman, J.D.  
Electric Power Research Institute  
P.O. Box 10412  
Palo Alto, California 95120

Ginsberg, T.  
Brookhaven National Laboratory  
Building 820  
Upton, New York 11973

Girrens, S.P.  
Los Alamos National Laboratory  
P.O. Box 1663  
Los Alamos, NM 87545

Gitnick, B.J.  
ENSA, Inc.  
15825 Shady Grove Road  
Rockville, Maryland 20850

Gloudeems, J. R.  
Babcock & Wilcox  
Old Forrest Road  
Lynchburg, Virginia 24501

Gold, N.  
Hanford Engineering Development Laboratory  
P.O. Box 1970  
Richland, WA 99301

Gonzales, E.G.  
Consejo De Seguridad Nuclear  
Sor Angela de la Cruz  
Madrid, Spain 28020

Goodwin, E.F.  
Stone & Webster  
P.O. Box 5200  
Cherry Hill, NJ 08034

Gordon, B.M.  
General Electric Company  
175 Curtner Avenue, MC 785  
San Jose, California 95125

Grant, S.F.  
Carolina Power & Light Co.  
P.O. Box 1551  
Raleigh, North Carolina 27602

Greenblatt, M.  
Materials Engineering Associates  
9700 B Palmer Highway  
Lanham, Maryland 20706

Greene, G.A.  
Brookhaven National Laboratory  
Building 820  
Upton, New York 11973

Griffith, P.  
Massachusetts Inst. of Technology  
77 Massachusetts Avenue  
Cambridge, Massachusetts 02139

Grotenhuis, M.  
U.S. Nuclear Regulatory Commission  
7920 Norfolk Avenue  
Bethesda, Maryland 20014

Guppy, J.G.  
Brookhaven National Laboratory  
Building 130  
Upton, New York 11973

Hall, R.E.  
Brookhaven National Laboratory  
Bldg. 130  
Upton, New York 11973

Hampel, G.  
Battelle-Institut e.V.  
Am Roemerhof 35  
6000 Frankfurt 90  
Germany

Hawley, J. T.  
MPR Associates  
1050 Connecticut Ave., N.W.  
Washington, D. C. 20036

Hawthorne, J.R.  
Materials Engineering Associates  
9700 B Palmer Highway  
Lanham, Maryland 20706

Hazzan, M.J.  
Stone & Webster  
3 Executive Campus  
Cherry Hill, NJ 08034

Heck, C. L.  
Westinghouse Electric Corp.  
P.O. Box 355  
Pittsburgh, Pennsylvania 15230

Hepper, P.J.  
Central Electricity Generating Board  
Berkeley Nuclear Lab  
Berkeley, England

Herter, K.H.  
MFA-Stuttgart/W. Germany  
505 King Avenue  
Columbus, Ohio 43201

Hewitt, G. F.  
AERE Harwell  
Oxfordshire OX11 0RA  
United Kingdom

Hidinger, D.E.  
Knolls Atomic Power Laboratory  
P.O. Box 1072  
Schenectady, New York 12301

Hill, P.K.  
Pennsylvania Power & Light Co.  
2N 9th Street  
Allentown, Pennsylvania 18101

Hill, R.C.  
EG&G Idaho, Inc.  
P.O. Box 1625  
Idaho Falls, Idaho 83415

Hiser, Jr., A. L.  
Materials Engineering Associates  
9700-B George Palmer Highway  
Lanham, Maryland 20801

Hitchcock, J.T.  
Sandia National Laboratories  
P.O. Box 5800  
Albuquerque, NM 87185

Hodge, S.A.  
Oak Ridge National Laboratory  
P.O. Box Y  
Building 9104-1  
Oak Ridge, Tennessee 37831

Hofmann, K.R.  
GRS (Gesellschaft fuer Reaktorsicherheit)  
Schwertnergaasse 1  
5000 Koeln 1  
West Germany

Hofmayer, C.H.  
Brookhaven National Laboratory  
Building 129  
Upton, New York 11973

Hollan, S.E.  
Baltimore Gas & Electric  
CCNPP  
Lusby, Maryland 20657

Holler, P.J.  
Fraunhofer-Institut fuer zerstorungsfreie  
Universitat, Gebaude 37  
D-6600 Saarbrucken 11  
West Germany

Holsan, G.S.  
Lawrence Livermore National Laboratory  
P.O. Box 808  
Livermore, CA 94550

Holmstrom, H. L.  
Technical Research Centre of Finland (VTT)  
P.O. Box 169, SF-00181 Helsinki, Finland

Holtzclaw, K.W.  
General Electric  
175 Curtner Avenue, M/C 682  
San Jose, California 95125

Hoppe, R.G.  
Westinghouse - Bettis  
P.O. Box 79  
West Mifflin, Pennsylvania 15122

Hosemann, P.J.  
Kernforschungszentrum Karlsruhe GmbH  
Postfach 3640  
D-7500 Karlsruhe  
Federal Republic of Germany

House, R.K.  
Intermountain Technologies Inc.  
P.O. Box 1604  
Idaho Falls, Idaho 83403-1604

Hsia, D.Y.  
Atomic Energy Council of P. Republic of China  
67 Lane 144 Keelung Road Sec. 4  
Taipei, Taiwan  
Rep. of China

Hsu, T.W.  
Virginia Power  
P.O. Box 26666  
Richmond, Virginia 23113

Hsu, Y-Y.  
University of Maryland  
College Park, Maryland 20742

Hu, T.K.  
Bechtel Power Corporation  
15740 Shady Grove Road  
Gaithersburg, Maryland 20878

Hull, A.P.  
Brookhaven National Laboratory  
Building 535A  
Upton, New York 11973

Hutton, P.H.  
Battelle - Pacific Northwest Laboratory  
Box 999  
Richland, Washington 99352

Hwang, H.H.  
Brookhaven National Laboratory  
Building 129  
Upton, New York 11973

Hyman, C.R.  
Oak Ridge National Laboratory  
P.O. Box Y  
Building 9104-1  
Oak Ridge, TN 37831

Iguchi, T.  
Japan Atomic Energy Research Institute  
Tokai-mura  
Ibaraki-ken  
Japan 319-11

Imai, T.  
JEPIC  
1726 M Street, N.W., S. 503  
Washington, D. C. 20036

Irby, R.G.  
Tennessee Valley Authority  
400 West Summit Hill Drive, W10D205  
Knoxville, TN 37902

Irwin, G.R.  
University of Maryland  
College Park, Maryland 20742

Ishigomi, T.  
Japan Atomic Energy Research Institute  
Naka-Ibaraki 319-11  
Japan

Ishii, H.  
Argonne National Laboratory  
9700 South Cass Avenue  
Argonne, Illinois 60439

Iskander, S.K.  
USNRC/ORNL/MPA  
MPA, Pfaffenwaldring 32  
7000 Stuttgart 80  
FRG (West Germany)

Iwamura, T.  
Japan Atomic Energy Research Institute  
Tokai-mura Naka-gun  
Ibaraki-ken, Japan 319-11

Izquierdo, J.M.  
Consejo Seguridad Nuclear  
Sor Angela de la Cruz 3  
Madrid, Spain

Jacobs, F.J.  
EG&G Idaho, Inc.  
P.O. Box 1625  
Idaho Falls, Idaho 83415

Janassen, L.G.  
Netherlands Energy Research Foundation  
Westerduinweg 3, P.O. Box 1  
Petten 1755 ZG  
The Netherlands

Jeanmougin, N.M.  
Energy Technology Engineering Center  
P.O. Box 1449  
Canoga Park, California 91304

Jegu, J.A.  
FRAMATOME  
Tour Fiat Cedex 16  
Paris La Defense 92084  
FRANCE

Jenks, R.  
Los Alamos National Laboratory  
P.O. Box 1663  
Los Alamos, New Mexico 87545

Jo, J.H.  
Brookhaven National Laboratory  
Building 130  
Upton, New York 11973

Johnsen, G.W.  
EG&G Idaho, Inc.  
P.O. Box 1625  
Idaho Falls, Idaho 83415

Jones, D.  
AEC SA  
Private Bag X256  
Pretoria, Transvaal 0001  
South Africa

Jun, H.R.  
KAERI/DaeJeon  
DaeJeon, Korea

Kaira, S.P.  
Electric Power Research Institute  
3412 Hillview Avenue  
Palo Alto, California 94303

Kam, F.S.  
Oak Ridge National Laboratory  
P.O. Box X, Bldg. 3001  
Oak Ridge, Tennessee 37831

Kannberg, L.D.  
Battelle - Pacific Northwest Laboratory  
P.O. Box 999  
Richland, Washington 99352

Kanninen, M.F.  
Southwest Research Institute  
6220 Culebra Road (P.O. Drawer 28510)  
San Antonio, TX 78284

Kanzleiter, T.F.  
Battelle-Institut e.V.  
Am Roemerhof 35  
D-6000 Frankfurt, FR Germany D-6000  
FRG

Kao, L.  
MIT  
80 Wadsworth Street, Apt. 3A  
Cambridge, MA 02142

Karwat, H.  
Techn. Univ. Munich-FRG  
Forschungsgelaende  
D8046 Garching  
Bavaria 8046  
FRG

Kashima, K.  
Central Res. Inst. of Elec. Power Inst.  
11-1, Iwato Kita 2-Chome  
Komae-Shi, Tokyo 201  
Japan

Kasprzak, S.  
Rensselaer Polytechnic Institute  
NES Bldg., Tibbits Avenue  
Troy, New York 12180-3590

Kato, W.Y.  
Brookhaven National Laboratory  
Building 197C  
Upton, New York 11973

Kawaji, M.  
Japan Atomic Energy Research Institute  
2-4, Shirane, Shirakata, Naka-gun, Ibaraki-ken  
Japan

Kawasaki, M.  
NIPPON Energy Incorporated  
1-16-5 Mishishinbashi  
Minato-ku, Tokyo 105  
Japan

Kayser, W.V.  
Exxon Nuclear Company, Inc.  
P.O. Box 130  
Richland, Washington 99352

Kazimi, M.S.  
MIT  
77 Mass Avenue  
Cambridge, MA 02139

Kelly, J.E.  
Sandia National Laboratory  
Division 6425  
P.O. Box 5800  
Albuquerque, New Mexico 87185

Khatib-Rahbar, M.  
Brookhaven National Laboratory  
Building 130  
Upton, New York 11973

Kikuta, M.  
Mitsubishi Atomic Power Industries, Inc.  
No. 4-1, Shibakouen 2-chome, Minato-ku  
Tokyo 105  
Japan

Kim, J.  
Korea Power Eng. Co.  
3785-D Logans Ferry Road  
Pittsburgh, PA 15239

Kimmins, A.D.  
ORNL/Nuclear Safety Journal  
P.O. Box Y - Bldg. 9201-3, M/S-5  
Oak Ridge, TN 37831

Kiyoshi, K.  
Japan Atomic Energy Research Institute  
Tokai-mura  
Ibaraki-ken  
Japan 319-11

Klansnitzer, E.H.  
KWN  
Hammerbacher Street  
Erlangen, FRG

Kleinols, F.W.  
NUCLEDYNE Engineering Corporation  
728 W. Michigan Avenue  
Jackson, Michigan 49201

Klorig, W.N.  
Aptech Eng. Services  
101 1/2 S. Union Street  
Alexandria, VA 22314

Kmetyk, L.N.  
Sandia National Laboratory  
Division 5444  
P.O. Box 5800  
Albuquerque, New Mexico 87185

Knight, T.D.  
Los Alamos National Laboratory  
P.O. Box 1663  
Los Alamos, New Mexico 87545

Knipe, A.D.  
UKAEA (EG & G Idaho, Inc.)  
Building TSA  
P.O. Box 1625  
Idaho Falls, Idaho 83415

Koch, D.A.  
Gilbert/Commonwealth  
P.O. Box 1498  
Reading, PA 19603

Logan, V.  
Battelle - Pacific Northwest Laboratory  
305 King Avenue  
Columbus, Ohio 43201

Koizumi, Y.  
Japan Atomic Energy Research Institute  
Tokai-mura, Naka-gun  
Ibaraki-ken, Japan 319-11

Koski, S.J.  
TVO Power Company  
SF-27160 Olkiluoto  
FINLAND

Kot, C.A.  
Argonne National Laboratory  
9700 S. Cass Avenue  
Building 335  
Argonne, Illinois 60439

Koziol, J.J.  
Combustion Engineering Inc.  
1000 Prospect Hill Road  
Windsor, CT 06095-0500

Kress, T.S.  
Oak Ridge National Laboratory  
102 Daniel Lane  
Oak Ridge, TN 37830

Kumamaru, H.  
Japan Atomic Energy Research Institute  
1-4, Shirane, Shirakata, Naka-gun, Ibaraki  
Japan

Kupperman, D.S.  
Argonne National Laboratory  
9700 S. Cass Avenue  
Building 212  
Argonne, Illinois 60439

Kurts, R.J.  
Battelle - Pacific Northwest Laboratory  
P.O. Box 999  
Richland, WA 99352

Kussmaul, K.F.  
MPA Stuttgart  
32 Pfaffenwaldring  
Stuttgart, FRG 07000

Laats, T.  
EG&G Idaho, Inc.  
P.O. Box 1625  
Idaho Falls, Idaho 83415

Laguardia, T.S.  
TLG Engineering, Inc.  
640 Federal Road  
Brookfield, CT 06804

Lain, P.J.  
Westinghouse Electric Power Systems  
P.O. Box 355  
Pittsburgh, PA 15230

Lang, R.E.  
U.S. Department of Energy  
9800 S. Cass Avenue  
Argonne, Illinois 60439

Lareau, J.P.  
Combustion Engineering  
1000 Prospect Hill Road  
Windsor, CT 06095

Larson, T.K.  
EG&G Idaho, Inc.  
P.O. Box 1625  
Idaho Falls, Idaho 83415

Lee, C.T.  
Ontario Hydro  
700 University Avenue, (H9)  
Toronto, Ontario M5G 1X6  
Canada

Lee, G.  
KAERI  
Holiday Inn  
Seoul, Korea

Lau, J.H.  
Ontario Hydro  
700 University Avenue, (H9)  
Toronto, Ontario M5G 1X6  
Canada

Lee, N.  
Westinghouse  
Monroeville Nuclear Center  
Monroeville, PA 15146

Leven, D. W.  
Gesellschaft für Reaktorsicherheit  
Schwertnergasse  
Koin, FRG

Lewe, C.K.  
MUS Corporation  
910 Clopper Road  
Gaithersburgh, Maryland 20878

Liesch, K.  
Gesellschaft fuer Reaktorsicherheit  
Bernheimerstr. 4  
Munchen, W. Germany

Lindeman, E.D.  
McGraw Hill  
1120 Vermont Avenue, N.W.  
Washington, D. C. 20005

Lippincott, E.P.  
Westinghouse  
P.O. Box 355  
Pittsburgh, PA 15230

Lloyd, G. J.  
United Kingdom Atomic Energy Authority  
Risley, Cheshire WA36AT  
England

Loewenstein, W.S.  
Electric Power Research Institute  
3412 Millview Avenue  
P.O. Box 10412  
Palo Alto, CA 94303

Loss, F.V.  
Materials Engineering Associates  
9700-B George Palmer Highway  
Lanham, Maryland 20706

Lowe, A.L.  
Babcock & Wilcox  
2708 Evergreen Road  
Lynchburg, VA 24503

Majumdar, D.  
U.S. Department of Energy  
785 DOE Place  
Idaho Falls, Idaho 83402

Malinauskas, A.P.  
Oak Ridge National Laboratory  
P.O. Box X  
Building 4500S, Rm. AL74  
Oak Ridge, TN 37831

Mallen, A.N.  
Brookhaven National Laboratory  
Building 130  
Upton, New York 11973

Malliakos, A.  
Combustion Engineering, Inc.  
1000 Prospect Hill Rt.  
Windsor, CT 06095

Mancuso, V.  
ENEA-Rome  
Dipartimento Reattori Termici  
Roma, Italia 00060

Mandl, R.M.  
Kraftwerk Union Aktiengesellschaft  
Hammerbacherstr. 12+14  
8520 Erlangen  
West Germany

Martinell, J.S.  
EG&G Idaho, Inc.  
Foote Drive  
Idaho Falls, Idaho 83401

Marx, K.D.  
Sandia National Laboratory  
P.O. Box 969  
Livermore, California 94550

Maskewitz, B.F.  
Oak Ridge National Laboratory  
P.O. Box X  
Oak Ridge, Tennessee 37831

Masuda, F.  
Tohiba  
9-3-104, 5-chome, Isogo  
Yokohama, Japan

Matsumoto, K.  
Japan Atomic Energy Research Institute  
43220 Wyoming N.E. Apt. 5  
Albuquerque, NM 87111

Mattson, J.S.  
Swedish Nuclear Power Inspectorate  
Box 27106  
S-102 52 Stockholm  
Sweden

McCabe, D.E.  
Materials Engineering Associates, Inc.  
9700B Palmer Highway  
Lanham, Maryland 20706

McElroy, W.N.  
Hanford Engineering Development Laboratory  
P.O. Box 1970  
Richland, Washington 99352

McGarry, E.D.  
National Bureau of Standards  
Gaithersburg, Maryland 20855

McLean, J.  
Robert L. Cloud Associates  
20 Main Street  
Cotuit, Massachusetts 02635

McMillan, R.N.  
UKAEA, SRD  
Wigshaw Lane, Culcheth  
Warrington, England

McPherson, L.D.  
U.S. Department of Energy  
6636 Kirby Court  
Falls Church, VA 22043

Mebich, C.  
SIET  
Via Nino Bixio 27  
Piacenza 29100  
Italy

Mercier, O. M.  
Swiss Federal Institute for Reactor Res.  
Wuerenlingen, Switzerland 5430

Meyer, P.E.  
Westinghouse  
P.O. Box 355  
Pittsburgh, PA 15230

Micaelli, J.  
CEA/CENG/STT  
85X-38041 Grenoble Cedex  
Grenoble  
FRANCE

Milella, P.P.  
ENEA  
Via V. Brancati 48  
Roma, Italy 00144

Miller, C.D.  
CBI Industries  
1501 N. Division St.  
Naperville, IL 60544

Miller, R.L.  
UNC Nuclear Industries  
P.O. Box 490 J1  
Richland, Washington 99352

Mitake, S.  
EG&G Idaho/JAERI  
P.O. Box 1625  
Idaho Falls, Idaho 83415

Modro, S.H.  
FZS-Austria  
c/o EG&G Idaho, Inc.  
P.O. Box 1625  
Idaho Falls, Idaho 83415

Moody, J.H.  
YAECCO  
1671 Worcester Road  
Framingham, MA 01701

Mukherjee, S.  
Ontario Hydro Research  
800 Kipling Avenue  
Toronto, Ontario M8Z 5S4

Muramoto, T.  
Chubu Electric Power Co., Inc.  
900 17th St., N.W., Suite 714  
Washington, D. C. 20006

Murao, Y.  
Japan Atomic Energy Research Institute  
Tokai-mura, Ibaraki-ken, Japan 319-11

Murase, M.  
Hitachi, Ltd.  
1168 Moriyama-cho  
Hitachi, Ibaraki 316  
Japan

Naff, S.A.  
EG&G Idaho, Inc.  
Esperstr 19  
8525 Uttenreuth, W. Germany

Nair, P.K.  
Southwest Research Institute  
P.O. Drawer 28510  
6720 Culebra Road  
San Antonio, TX 78284

Nakagawa, S.  
Kansai Electric Power  
1100 17th St., N.W.  
Washington, D. C. 20036

Nakajima, H.  
Century Research Center Corporation  
2,3-chome, Hon-cho, Nihonbashi, Chuo-ku  
Tokyo 103  
JAPAN

Nakajima, H.  
Japan Atomic Energy Research Institute  
Tokai-mura, Ibaraki-ken, Japan 319-11

Nanstad, R.K.  
Oak Ridge National Laboratory  
Bldg. 4500-S, Mail Stop D-61  
P.O. Box X  
Oak Ridge, TN 37831

Nelson, E.M.  
Knolls Atomic Power Laboratory  
P.O. Box 1072  
Schuylkill, New York 12301

Nelson, L.S.  
Sandia National Laboratory  
P.O. Box 5800  
Albuquerque, New Mexico 87185

Nelson, R. A.  
Los Alamos National Laboratory  
MS-K553  
Los Alamos, NM 87545

Neuvonen, A.  
Imatran Voima Oy  
P.O. Box 138  
Helsinki, Finland

Neymotin, L.  
Brookhaven National Laboratory  
Bldg. 130  
Upton, New York 11973

Ni, H.S.  
Atomic Energy Council of Republic of China  
67 Lane 144 Kailung Road Sec. 4  
Taipei, Taiwan  
Rep. of China

Niemczyk, S.J.  
Gull Associates  
1545 18th St., N.W.  
Washington, D. C. 20036

Nithianandan, C.K.  
Babcock & Wilcox  
1313 Old Forest Road  
Lynchburg, VA 24506

North, P.  
LOFT - TAN 402  
P.O. Box 1625  
Idaho Falls, Idaho 83415

O'Neill, L.A.  
Stone & Webster  
50 Summer Street  
Boston, MA 02146

Oddo, J.M.  
Stone & Webster Eng. Corp.  
P.O. Box 2325  
Boston, MA 02107

Ogata, Y.  
Mitsubishi Heavy Industries, Ltd.  
4-1 Shibakoen 2-Chome  
Minato Ku, Tokyo 105 JAPAN

Ohno, T.  
Nuclear Power Engineering Test Center  
No. 2 Akiyama Bldg., 6-2,3-chome  
Toranomon Minato  
Tokyo, Japan

Ohnuki, A.  
Japan Atomic Energy Research Institute  
Tokai-mura  
Ibaraki-ken, Japan 319-11

Ohtsubo, A.  
Nuclear Power Engineering Test Center  
1-4-28, Mita, Minato-ku  
Tokyo 108, Japan

Okada, S.  
Japan Atomic Energy Research Institute  
1233 Watanuki-machi, Takasaki, Gunma-ken JAPAN

Okano, Y.  
EG&G Idaho  
1361 S. Woodruff  
Idaho Falls, Idaho 83401

Oldfield, G.V.  
Washington Public Power Supply System  
P.O. Box 968  
Richland, WA 99352

Olsen, C.S.  
EG&G Idaho, Inc.  
P.O. Box 1625  
Idaho Falls, Idaho 83415

Omar, A. M.  
Atomic Energy Control Board  
270 Albert Street  
Ottawa, Ontario K1P5S9, Canada

Onesto, A.T.  
ETEC/Rockwell  
P.O. Box 1449  
Canoga Park, CA 91304

Ott, L.J.  
Oak Ridge National Laboratory  
P.O. Box Y  
Building 9104-1  
Oak Ridge, TN 37831

Pan, J.  
The University of Michigan  
Ann Arbor, Michigan 48109

Parce, M.V.  
Babcock & Wilcox  
206 Shadwell Drive  
Lynchburg, VA 24503

Parish, H. G.  
Atomic Energy Corp. of South Africa  
Private Box X256  
Pretoria 0001  
South Africa

Pearson, K.G.  
United Kingdom Atomic Energy Authority  
AEE Winfrith  
Dorchester, Dorset DT28DH  
United Kingdom

Fence, J.H.  
Baltimore Gas & Electric  
P.O. Box 1475  
Baltimore, Maryland 21203

Perkins, K.  
Brookhaven National Laboratory  
Bldg. 130  
Upton, New York 11973

Peterson, A.C.  
Sandia National Laboratories  
P.O. Box 5800  
Albuquerque, NM 87185

Petrangeli, G.  
ENEA/Disp  
Via Vitaliano Brancati, 48  
Rome, Italy 00144

Philippacopoulos, A.J.  
Brookhaven National Laboratory  
Building 129  
Upton, New York 11973

Piccolo, P.L.  
Brookhaven National Laboratory  
Building 830  
Upton, New York 11973

Pilch, M.  
Sandia National Laboratory  
Division 6425  
P.O. Box 5800  
Albuquerque, New Mexico 87185

Pino, G.  
ENEA/Disp  
Via Vitaliano Brancati, 48  
Rome, Italy 00144

Podowski, M. Z.  
Rensselaer Polytechnic Institute  
NRS Bldg., Tibbits Avenue  
Troy, New York 12810-3590

Posakony, G.J.  
Battelle - Pacific Northwest Laboratory  
P.O. Box 999  
Richland, WA 99352

Potter, C.  
HM Nuclear Installations Inspectorate  
Thames House North  
Millbank  
London SW1P 4QJ, U.K.

Powers, D.A.  
Sandia National Laboratory  
P.O. Box 5800  
Albuquerque, New Mexico 87185

Prelewicz, D.A.  
ENSA, Inc.  
15825 Shady Grove Road, Suite 170  
Rockville, Maryland 20850

Pugh, C.E.  
Oak Ridge National Laboratory  
P.O. Box Y  
Oak Ridge, Tennessee 37831

Pugh, M. C.  
UKAEA  
Wigshaw Lane  
Culcheth, Cheshire  
W43ANE, England

Rahn, F.  
Electric Power Research Institute  
P.O. Box 10412  
Palo Alto, California 94301

Rainey, P.  
Rolls Royce Associates  
P.O. Box 31  
Raynesway  
Derby, England

Reich, M.  
Brookhaven National Laboratory  
Bldg. 129  
Upton, New York 11973

Reimann, M.  
Kernforschungszentrum Karlsruhe GmbH  
Postfach 3640  
Karlsruhe, W. Germany D-7500

Renner, H.  
NUS Corporation  
910 Clopper Road  
Gaithersburg, Maryland 20878

Reocreux, M. L.  
CEA/France  
CEN Fontenay aux Roses BP n° 6  
Fontenay aux Roses, France 92265

Reuland, W.B.  
Electric Power Research Institute  
P.O. Box 10412  
Palo Alto, California 94304

Reynen, J.  
EEC  
2100 M SW NW  
Washington, D. C. 20037

Rhoads, J.E.  
Washington Public Power Supply System  
3000 George Washington Way  
Richland, Washington 99352

Rib, L.N.  
LNR Associates  
8605 Griesby Court  
Potomac, Maryland 20854

Robinson, D.  
IIT Res. Institute  
10 W. 35th  
Chicago, Illinois 60616

Robinson, G.E.  
Penn State University  
1101 Oak Ridge Avenue  
State College  
PA 16801

Roh, E.R.  
Korea Electric Power Corporation R & D  
52, Cheongdam-Dong, Kangnam-Ku  
Seoul  
Korea

Rohatgi, U.S.  
Brookhaven National Laboratory  
Building 130  
Upton, New York 11973

Rohde, J.  
Gesellschaft für Reaktorsicherheit (GRS)  
Schwertnergasse 1  
5000 Köln 1  
FRG  
West Germany

Romano, A.J.  
Brookhaven National Laboratory  
Building 197C  
Upton, New York 11973

Ross, C.P.  
DuPont  
10024-203 Stedwick Road  
Gaithersburg, Maryland 20879

Rouhani, S.Z.  
EG&G Idaho, Inc.  
P.O. Box 1625  
Idaho Falls, Idaho 83415

Rupprecht, S.D.  
Westinghouse  
P.O. Box 355  
Pittsburgh, PA 15146

Saluja, J.K.  
Viking Energy Corp.  
121 N. Highland Avenue  
Suite 203  
Pittsburgh, PA 15206

Samanta, P.K.  
Brookhaven National Laboratory  
Bldg. 130  
Upton, New York 11973

Sandervag, O.S.  
Studsvik Energiteknik AB  
S-61182  
Nyköping, Sweden

Satoshi, M.  
Hitachi, Ltd.  
Hitachi, Ibaraki 316  
Japan

Scarborough, T.G.  
U.S. Nuclear Regulatory Commission  
Washington, D. C. 20555

Schelling, F.J.  
Sandia National Laboratory  
Division 6449  
Albuquerque, New Mexico 87185

Schikarski, W.O.  
Kernforschungszentrum Karlsruhe GmbH  
P.O. Box 36 40  
Karlsruhe, Baden-Wuerttemberg D-7500  
FRG

Schleifer, F.  
GRS (Gesellschaft für Reaktorsicherheit)  
Schwertnergasse 1  
Köln (Cologne) 1 5000  
FRG

Schlotthauer, U.C.  
FRAMATOME  
Tour Fiat Cedex 16  
Paris La Defense 92084  
FRANCE

Schmidt, E.R.  
NUS  
910 Clopper Road  
Gaithersburg, Maryland 20874

Schmitt, A.F.  
Commissariat A L'Energie Atomique  
CEN-FAR-8Pu-692260  
Fontenay-Aux-Roses  
France

Schnurstein, R.E.  
ETEC  
P.O. Box 1449  
Canoga Park, California 91304

Schoech, W.  
Kernforschungszentrum Karlsruhe GmbH  
Weberstr. 5  
Karlsruhe, FRG 7500

Schrock, V.E.  
University of California, Berkeley  
Berkeley, California 94720

Schwarzer, W.J.  
Kerntechnischer Ausschuss (KTA)  
c/o GRS mbH, Schwertnergasse 1  
5000 Koeln  
F.R. of Germany

Schweitzer, G.J.  
Sargent & Lundy Engineers  
55 E. Monroe Street  
MC/31V30  
Chicago, Illinois 60603

Scott, P.M.  
UK Atomic Energy  
Aere  
Harwell, Oxon OX11 0RA, U.K.

Seihiro, I.  
Nippon Atomic Industry Group Co.  
4-1, Ukishima-cho, Kawasaki-ku  
Kawasaki, Kanagawa 210  
Japan

Sestak, P.F.  
Stone & Webster Eng. Corp.  
3 Executive Campus  
Cherry Hill, New Jersey

Seth, S.S.  
MITRE Corp.  
1820 Dolley Madison  
McLean, VA 22102

Sgalambro, G.  
ENEA/Disp  
Via V. Brancati, 48  
Roma, Italy 00144

Shaoh, W.J.  
Argonne National Labor. . .y  
Bldg. 212  
Argonne, Illinois 60439

Shah, N.R.  
Babcock & Wilcox  
Lynchburg, Virginia 24502

Sharma, R.S.  
American Electric Power  
One Riverside Plaza  
Columbus, Ohio 43215

Sharp, D.A.  
Savannah River Laboratory, E.I. duPont  
Aiken, SC 29801

Sherman, M.  
Sandia National Laboratory  
P.O. Box 5800  
Albuquerque, NM 87185

Sherry, R.R.  
NUS  
910 Clopper Road  
Gaithersburg, Maryland 20878

Shigero, K.  
Tokyo Electric Power Co.  
No. 1-3-1-choe Hchisaiwai-cho  
Chiyodako/Tokyo 100  
Japan

Shimeck, D.J.  
Westinghouse Electric Corp.  
P.O. Box 355  
Pittsburgh, PA 15146

Shipsky, W.E.  
Westinghouse Electric Corp.  
Expomart  
Monroeville, PA

Shiralkar, B.S.  
General Electric  
175 Curtner Avenue  
San Jose, California 95125

Shoji, T.  
Res. Instr. for Strength and Fracture of...  
Aramaki Aoba Sendai/980, Japan  
SENDAI, MIYAGI  
JAPAN

Shunro, N.  
Tokoteestack Co. Ltd.  
21-10 6Chome Sagamidai  
Sagamihara, Kanagawa  
Japan

Sigal, G.S.  
Burns & Roe  
800 Kinderkamack Road  
Oradell, New Jersey 07649

Simonen, F.A.  
Battelle - Pacific Northwest Laboratory  
P.O. Box 999  
Richland, WA 99352

Slaughter, G.M.  
Oak Ridge National Laboratory  
Oak Ridge, Tennessee 37831

Slegers, L.  
KW  
605 Uffenbach  
Berlinerstr. W. Germany

Slovik, G.C.  
Brookhaven National Laboratory  
Building 130  
Upton, New York 11973

Smith, D.L.  
Wyle Laboratories  
1841 Hillside Avenue  
Norco, California 91760

Snyder, A.W.  
Sandia National Laboratory  
P.O. Box 5800  
Albuquerque, NM 87185

Soda, K.  
Japan Atomic Energy Research Institute  
Tokaimura  
Nakagun, Ibarakiken 319-11  
Japan

Somers, W.S.  
Dept. of Energy-Idaho Operations Office  
785 DOE Place  
Idaho Falls, Idaho 83402

Soong, D.Y.  
Bechtel Power Corp.  
Gaithersburg, Maryland 20877

Sozer, A.  
Oak Ridge National Laboratory  
P.O. Box Y, Building 9104-1  
Oak Ridge, TN 37831

Spatz, R.  
Institut fur Verfahrenstechnik  
Universitat Hannover  
Callinstr. 36  
Hannover D-3000

Spencer, S.W.  
Argonne National Laboratory  
Argonne, Illinois 60439

Squarer, D.  
Westinghouse  
P.O. Box 355  
Pittsburgh, PA 15230

St. John, K.E.  
Yankee Atomic Electric Company  
1671 Worcester Road  
Framingham, Massachusetts 01701

Stadtke, H.  
EURATOM - Joint Research Centre, Ispra  
I-21020 Ispra (Varese), Italy  
Ispra, ITALY

Stallmann, F.W.  
Oak Ridge National Laboratory  
P.O. Box X  
Building 3001  
Oak Ridge, Tennessee 37831

Stepnewski, D.D.  
Westinghouse, Hanford Co.  
P.O. Box 1970  
Richland, Washington 99352

Strawson, D.  
MPR Associates  
1050 Connecticut Avenue, N.W. 20036

Stubbe, E.J.  
Tractionel/Belgium  
31 Rue De La Science  
Brussels, Belgium 1040  
Belgium

Sullivan, H.L.  
Los Alamos National Laboratory  
Mail Stop K552  
Los Alamos, New Mexico 87545

Suo-Anttila, A.J.  
Sandia National Laboratory  
Division 6425  
P.O. Box 5800  
Albuquerque, New Mexico 87185

Sutherland, W.A.  
General Electric Co.  
173 Curtner Avenue  
Mail Code 186  
San Jose, California 95125

Swan, D.I.  
Rolls Royce & Associates, Ltd.  
P.O. Box 31  
Derby  
De2 8BJ, U.K.

Syouichi, S.  
Japan Institute of Nuclear Safety  
Mita Kokusai, Bldg. 4-28  
Minato-ku, Tokyo, Japan 108

Tajbakhsh, A.  
Westinghouse Electric Co.  
Northern Pike  
Monroeville, PA 15146

Takeda, M.  
SHIMIZU Construction Co., Ltd.  
13-16, Mita 3-choe, Minato-ku  
Tokyo 108  
JAPAN

Tang, H.  
Electric Power Research Institute  
3412 Hillview Avenue  
P.O. Box 10412  
Palo Alto, CA 94303

Tasaka, K.  
Japan Atomic Energy Research Institute  
2-4, Shirane, Shirakata, Naka-gun, Ibaraki-ken  
Japan

Taylor, J.H.  
Brookhaven National Laboratory  
Building 130  
Upton, New York 11973

Taylor, L.G.  
National Nuclear Corp.  
Bbothe Hall  
Chelford Road  
Knutsford, England

Tazawa, K.  
Japan NUS Co., Ltd.  
7-1 Nishi-shinjuku 2-chome shinjuku  
Tokyo, Japan

Thiess, P.E.  
American Env. Central Systems Inc.  
P.O. Box 1189  
Washington, D. C. 20013

Thomas, A.F.  
Rolls Royce & Associates  
P.O. Box 31 Raynesway  
Derby, U.K. DE2

Thomas, G.R.  
Electric Power Research Institute  
P.O. Box 10412  
Palo Alto, California 94306

Thorne, L.R.  
Sandia National Laboratory  
P.O. Box 969  
Livermore, California 94550

Tieszen, S. R.  
Sandia National Laboratory  
P.O. Box 5800  
Albuquerque, New Mexico 87185

Tkach, R.J.  
PSEG  
P.O. Box 370  
80 Park Plaza  
Newark, New Jersey 07101

Toman, G.J.  
Franklin Research  
20th & Race Streets  
Philadelphia, Pennsylvania 19103

Tong, L.S.  
Tong and Associates, Inc.  
9733 Lookout Place  
Gaithersburg, Maryland 20879

Torronen, K.J.  
Technical Research Centre of Finland  
Metals Lab.  
Metallistienkuja 6  
SF-02150 Espoo  
Finland

Toshiyuki, Y.  
Japan Atomic Energy Research Institute  
100 Sanford Lane  
Oak Ridge, Tennessee 37830

Trammell, H.E.  
Oak Ridge National Laboratory  
P.O. Box Y  
Oak Ridge, Tennessee 37831

Tsai, C-K.  
Westinghouse Electric Corp.  
P.O. Box 353  
Pittsburgh, Pennsylvania 15230

Tsai, S-S.  
Westinghouse Electric Corp.  
P.O. Box 355  
Pittsburgh, Pennsylvania 15230

Tsai, Z.  
Institute of Nuclear Energy Research  
P.O. Box 3-6  
Lung-tan, Taiwan 325  
Taiwan, Republic of China

Tunon-Sanjur, L.J.  
Westinghouse  
100 Penn Center  
Wilkins Twp., Pennsylvania 15239

Turland, S.D.  
UKAEA Culham Laboratory  
Culham Laboratory, Abingdon  
Oxon, England OX 143DB  
England

Ueda, S.  
Japan Atomic Energy Research Institute  
Tokai-mura, Ibaraki-ken  
Japan

Unger, H.E.  
University Stuttgart  
Pfaffenwaldring 31  
Stuttgart-80, W. Germany D-7000

Utton, D.S.  
National Nuclear Corporation  
Cambridge Road, Whetstone  
Leicester, LE83LH ENGLAND

Van Kuijk, R.M.  
KEMA  
Utrechtseweg 310  
Arnhem, The Netherlands

Varrin, R.  
MPR Associates  
1050 Connecticut Avenue, N.W.  
Washington, D. C. 20036

Vasudevan, N.  
Babcock & Wilcox  
P.O. Box 1360  
Old Forest Road  
Lynchburg, VA 24503

Versteegh, A.M.  
Netherlands Energy Research Foundation  
Westerduinweg 1, P.O. Box 1  
Petten 1755 ZG  
The Netherlands

Vesely, W.E.  
Sattelle - Columbus Laboratories  
505 King Avenue  
Columbus, Ohio 43201

Vinjamuri, K.  
EG&G Idaho, Inc.  
P.O. Box 1625  
Idaho Falls, Idaho 83415

Vogel, R.C.  
Electric Power Research Institute  
3412 Hillview Avenue  
Palo Alto, California 94303

von Riesenmann, W. A.  
Sandia National Laboratory  
Division 6642  
Albuquerque, New Mexico 87185

Vorees, J.  
Arizona Nuclear Power Project  
P.O. Box 52034, MS 4082  
Phoenix, Arizona 85072-2034

Walker, L.I.  
Westinghouse  
Pittsburgh, PA 15542

Wang, W.Y.  
Stone & Webster Eng.  
P.O. Box 5200, 3, Executive Campus  
Cherry Hill, NJ 08054

Ward, D.T.  
Baltimore Gas & Electric  
P.O. Box 1475  
Baltimore, Maryland 21203

Ward, G.N.  
Exxon Nuclear  
2101 Horn Rapids Road  
Richland, Washington 99352

Ware, A.G.  
EG&G Idaho, Inc.  
P.O. Box 1625  
Idaho Falls, Idaho 83415

Watkins, J.C.  
EG&G, Idaho  
P.O. Box 1625  
Idaho Falls, Idaho 83415

Webb, S.W.  
Sandia National Laboratory  
Division 6444  
P.O. Box 5800  
Albuquerque, New Mexico 87185

Weber, C.F.  
Oak Ridge National Laboratory  
P.O. Box X  
Bldg. 6025  
Oak Ridge, TN 37831

Weber, G.  
Gesellschaft für Reaktorsicherheit  
Forschungsgelände  
D-8046  
Garching, Germany

Weeks, J.R.  
Brookhaven National Laboratory  
Building 703  
Upton, New York 11973

Weiss, A. J.  
Brookhaven National Laboratory  
Building 197-C  
Upton, New York 11973

Weiss, P. A.  
Kraftwerk Union R 515  
Hammerbacherstrasse 12+14  
Erlangen 8520, FRG

Welch, E.C.  
EG&G, Idaho  
P.O. Box 1625  
Idaho Falls, Idaho 83415

Wells, J.E.  
Lawrence Livermore National Laboratory  
740 Hanover Street  
Livermore, California 94550

Wessel, E.T.  
Consultant to ORNL  
3570 Meadowgate Drive  
Murrysville, Pennsylvania 15668

Wheatley, P.D.  
EG&G Idaho, Inc.  
P.O. Box 1625  
Idaho Falls, Idaho 83415

Whipple, R.C.  
Combustion Engineering  
1000 Prospect Hill Road  
Windsor, CT 06095

White, J.R.  
J.R. White Consulting  
2100 Belmont Avenue  
Idaho Falls, Idaho 83401

Whitehead, T.J.  
Science Applications International Corp.  
101 S. Park Avenue  
Idaho Falls, Idaho 83407

Wilkowski, G.M.  
 Battelle Columbus Laboratory  
 505 King Avenue  
 Columbus, Ohio 43201

Williams, K.A.  
 Science Applications International Corp.  
 Suite 1200  
 Albuquerque, New Mexico 87102

Vinegardner, W.K.  
 Battelle - Pacific Northwest Laboratory  
 P.O. Box 999  
 Richland, Washington 99352

Winkler, F. J.  
 Kraftwerk Union Aktiengesellschaft  
 Hammerbacherstrasse 12+14  
 P.O. Box 1220  
 D-8520 Erlangen, FRG

Winslow, S.G.  
 Oak Ridge National Laboratory  
 P.O. Box X  
 Oak Ridge, TN 37831

Wolf, J.R.  
 EG&G Idaho, Inc.  
 P.O. Box 1625  
 Idaho Falls, Idaho 83401

Wolf, L.  
 Projekt HDR-Sicherheitsprogramm  
 Kernforschungszentrum Karlsruhe GMBH  
 Postfach 3640,7600

Woodruff, S.B.  
 Los Alamos National Laboratory  
 Q-9/MS K553  
 Los Alamos, New Mexico 87544

Wolfert, K.  
 Gesellschaft für Reaktorsicherheit  
 Forschungsgelände  
 D-8046 Garching, Germany

Wong, C.C.  
 Sandia National Laboratory  
 P.O. Box 5800  
 Albuquerque, NM 87185

Worner, J.  
 König & Heunisch  
 Gerhart Hauptmann str. 12  
 6100 Darmstadt, W. Germany

Wos, S.  
 Westinghouse - Bettis  
 P.O. Box 79  
 West Mifflin, Pennsylvania 15122

Wright, D.A.  
 Baltimore Gas & Electric  
 9612 Quarry Bridge Ct.  
 Columbia, Maryland 21046

Wu, D.  
 Suzhou Nuclear Power Research Institute  
 Jinmen Road  
 Suzhou, Jiangsu Province  
 Peoples Rep. of China

Wulff, W.  
 Brookhaven National Laboratory  
 Building 130  
 Upton, New York 11973

Yagawa, G.  
 University of Tokyo  
 Hongo, Bunkyo-ku  
 Tokyo 113  
 Japan

Yang, C.  
 Nuclear Industry Ministry of PRC  
 Beijing, China

Yarsmy, E.M.  
 International Atomic Energy Agency  
 Wagrammerstrasse 5  
 Vienna, A-1400 Austria

Ybarrondo, L.J.  
 SCIENTECH, Inc.  
 P.O. Box 1406  
 Idaho Falls, Idaho 83403-1406

Young, M.Y.  
 Westinghouse  
 P.O. Box 355  
 Pittsburgh, Pennsylvania 15230

Young, S.L.  
 UKAEA/SRD  
 Wigshaw Lane  
 Culcheth, Cheshire  
 U.K.

Zbárek, J.  
 Czechoslovakian Embassy  
 3900 Linnean Avenue  
 Washington, D.C. 20008

Zhong, W.  
 National Nuclear Safety Administration  
 54 Sanlihe Road  
 Beijing  
 Peoples Republic of China

Zinnari, R.  
 Ansaldo Divisione Impianti/Italy  
 Via G. D'Annunzio, 113  
 Genova 16100  
 Italy



PROCEEDINGS OF THE  
THIRTEENTH WATER REACTOR SAFETY RESEARCH  
INFORMATION MEETING

October 22-25, 1985

TABLE OF CONTENTS - VOLUME 4

	<u>Page</u>
ABSTRACT. . . . .	111
GENERAL INDEX . . . . .	v
REGISTERED ATTENDEES. . . . .	vii

INTEGRAL SYSTEMS TESTS

Chairman: W. D. Beckner (NRC)

FIST Analysis . . . . . W. A. Sutherland (GE)	1
OTIS Test Results . . . . . J. R. Gloudemans (B&W)	31
University of Maryland Test Facility Results. . . . . Z. Wang et al. (U. of Md.)	47
MIST Facility Status. . . . . H. R. Carter (B&W)	83
Highlights of the OECD LOFT Experiment Program. . . . . J. Birchley (UKAEA/EG&G) and P. North (EG&G)	101

INTEGRAL SYSTEMS TESTS

Chairman: D. E. Solberg (NRC)

Introduction. . . . . D. E. Solberg (NRC)	107
Semiscale Secondary Transient Investigations: Results from Semiscale MOD-2C Feedwater and Steam Line Break Tests . . . . . T. J. Boucher (EG&G)	111
Semiscale Liquid Hold-Up Investigations: A Comparison of Results from Small Break LOCA Tests Performed in the Semiscale MOD-2A and MOD-2C Facilities. . . . . G. G. Loomis (EG&G)	131
The Results of the ROSA-IV LSTF Small-Break LOCA Experiments. . . . . K. Tasaka et al. (JAERI)	157

INTEGRAL SYSTEMS TESTS  
(Cont'd)

	<u>Page</u>
PKL Reflood Tests Including End-of-Blowdown . . . . .	173
R. M. Mandl, B. Brand and H. Watzinger (KWU)	
Integral Systems Test (ISI) Program Facility Scaling and Integration . . . . .	197
T. K. Larson (EG&G)	
Continuing Integral Testing Capability-Scaling Study Approach and Preliminary Results. . . . .	237
K. G. Condie et al. (EG&G) and G. E. McCreery (UCSB)	

2D/3D RESEARCH  
Chairman: G. S. Rhee (NRC)

Results of CCTF Tests . . . . .	289
Y. Murao et al. (JAERI)	
Results of SCTF Reflood Tests . . . . .	315
T. Iwamura et al. (JAERI)	
Status of the German UPTF Program . . . . .	331
K. R. Hofmann (GRS)	
TRAC Analyses for CCTF and SCTF Tests and UPTF Design/Operation . . . .	351
J. W. Spore et al. (LANL)	

SEPARATE EFFECTS/EXPERIMENTS AND ANALYSES  
Chairman: N. Zuber (NRC)

Heat Transfer, Carryover and Fall Back in Nuclear Steam Generators During Transients. . . . .	371
L-Y Liao, A. Parlos and P. Griffith (MIT)	
Steam Generator Module Description. . . . .	393
C. Y. Paik and P. Griffith (MIT)	
Critical Flow Through a Small Break on a Large Pipe with Stratified Flow. . . . .	397
V. E. Schrock et al. (UCB)	
Critical Flow Through IGSCC in Pipes. . . . .	417
V. E. Schrock, S. T. Revankar and S. Y. Lee (UCB)	
A Final Report on Thermal Mixing for PTS Analyses . . . . .	431
T. G. Theofanous (Purdue Univ.)	

SEPARATE EFFECTS/EXPERIMENTS AND ANALYSES  
(Cont'd)

Page

Steam Explosions: Energy Conversion Efficiencies of Steam Explosions from Two Major Accidents in the Pulp and Paper Industry. . . . .	443
T. M. Grace (Inst. of Paper Chem.), R. R. Robinson (IIT Research Inst.) and J. Hopenfeld (NRC)	

FIST ANALYSIS  
Wm. A. Sutherland  
General Electric Company

ABSTRACT

The Full Integral Simulation Test (FIST) Program is a three pronged approach to the development of best-estimate analysis capability for BWR systems. An experimental program in the FIST single bundle BWR system simulator facility extends the LOCA data base and adds operational transients data. An analytical method development program with the BWR-TRAC computer code extends the modeling of BWR specific components and major interfacing systems, and improves numerical techniques to reduce computer running time. A method qualification program tests TRAC-B against experiments run in the FIST facility and extends the results to reactor system applications. With the completion and integration of these three activities, the best-estimate analysis capability objective has been achieved.

INTRODUCTION

The FIST facility is an integral system capable of full power steady state operation, as well as real time LOCA and operational transients. The facility design incorporates BWR system features important to thermal-hydraulic performance. It is a full height simulation of the reactor vessel and internals, with scaled regional volumes, and includes all major interfacing systems and automatic control system trip signals. This provides full scale values for thermodynamic state, fluid conditions, and heat transfer performance. Since each BWR fuel bundle is individually channeled (i.e., there is no cross flow in the core region), the thermal-hydraulic conditions within the core are accurately represented by a single bundle.

Large and small break LOCA tests, steam line break LOCA tests, and power transient simulations have been completed, as well as measurement of the natural circulation flow characteristics. The test results have been compiled, and comparisons made to show trends in different types of events<sup>(1)</sup>. Tests of greatest interest have been evaluated in detail to identify, understand, and model the controlling physical phenomena. These analysis provided guidance for development of BWR system features and components in TRAC-B.

A BWR-TRAC version with the component and phenomena models developed under the program was used to analyze the FIST facility response in three LOCA tests and an operation transient test<sup>(2)(3)</sup>. Particular attention to system definition and application modeling is given to the lower plenum region, two-phase level tracking within all regions, vessel stored heat, flow path loss coefficients, and break geometry. The pre-test analyses of the large break and small break LOCA tests are found to represent the observed controlling thermal-hydraulic phenomena very well. The analyses of a break originating inside the shroud (i.e., LPLI line) and a turbine trip transient with delayed rod run-in compare equally well with the system performance measured in the tests. Careful system definition leads to the TRAC-B large break analysis correctly handling lower plenum flow split performance, and the resulting prediction of core flow and liquid inventory leads to representative thermal performance in the bundle. Detailed system modeling for vessel stored heat and break geometry contribute to good agreement with system response measured in the small break and operational transient tests as well.

#### EXPERIMENTAL INVESTIGATION - FIST

The FIST facility, Figure 1, is a full height representation of a BWR/6-218 standard plant, and is designed to simulate BWR system thermal-hydraulic response, in real time, over the full range of reactor conditions. The core region is a full size electrically heated bundle capable of full power, as well as decay or transient power. Kinetic

feedback effects are simulated by programmed bundle power that matches the core average rod surface heat flux with that determined from BWR analysis. Scaling the facility to one full size bundle for the core region leads to a scaling ratio of 1/624 for the regional volumes, flows, and internal components. The eight major regions, region interfaces, and internal component characteristics are closely matched, with few scaling compromises.

As for the BWR, FIST has two external recirculation loops, each with a centrifugal pump driving a jet pump that circulates flow from the downcomer through the core. The drive pump inertia is sized so that FIST has the same flow coastdown characteristics following a pump trip. One recirculation loop is used for the pipe break simulation to achieve the correct interaction between the break flow and the recirculation flow, while the other loop continues in flow coastdown. Prototypical steam-water separator and dryer components are used to redirect the liquid in the two-phase flow back to the downcomer. Prototypical tie-plates and rod spacers are used in the bundle region. The bundle is installed in a standard zircaloy channel, providing the correct heat transfer characteristics between the bundle and bypass regions.

Five valves are installed along the steamline for simulating the safety relief valve (S/RV) group functions. S/RV opening and closing setpoints, operational logic, and the automatic depressurization system function (ADS) are included. The pressure control valve regulates steam flow from the system to maintain a constant system pressure. A heated feedwater system enables the FIST facility to achieve steady-state operation at full power with correct initial conditions. FIST is also equipped with BWR water level instrumentation to provide level signals for real time simulation of key control events in a transient (e.g., MSIV closure, ADS activation, HFCS initiation, recirculation pump trip, etc.). High Pressure Core Spray (HPCS) and Low Pressure Core Spray

(LPCS) injection into the upper plenum region are provided, as well as the three Low Pressure Coolant Injections (LPCI) into the bypass region. Each of these injection pumps is sized to provide correct pressure/flow characteristic.

The FIST thermal-hydraulic conditions are full scale with the BWR system. The same thermodynamic state point is achieved by establishing the same specific energy and specific volume in both systems, and within each major region in the systems. In terms of measurable quantities, FIST has the same system pressure and the scaled amount of steam, saturated liquid, and subcooled liquid. The change and rate of change of state points is then the same by maintaining scaled boundary flows. With local mass flows scaled proportionally by the number of bundles, the same hydrodynamic condition is achieved by scaling the flow cross section so that the velocity across interfaces is full scale. With similar geometric flow loss characteristics, the pressure field in FIST is then also full scale. Heat transfer performance in regions of interest, the bundle region in particular, is representative in full scale with full scale geometric and prototype components, full scale power input, and these full scale thermal-hydraulic conditions.

The system response tests with the FIST facility address both loss-of-coolant transients and power transients. Initial operating conditions are established at 1000 psi, full power, steady state conditions. In the case of LOCA tests, a valve is opened to simulate a pipe break. The parameters varied between tests are the break type, (e.g., recirculation suction line, steam line, or injection line), various combinations of control system malfunctions (e.g., stuck open SRV, or without rod run-in), and the system types (e.g., BWR/6 and BWR/4). One test simulates a turbine trip test at the Peach Bottom plant, and a number of tests simulate steam line isolation with various operator actions. A third test category evaluates natural circulation performance characteristics with various downcomer level driving heads, with system make-up by HPCS injection into the upper plenum region vs. feedwater injection into the downcomer region, and under transient depressurization conditions.

## ANALYTICAL REPRESENTATION - TRAC-B

The TRAC engineering computer code, initially formulated for PWR system analysis by LANL, is developed for BWR system analysis by INEL. In a co-operative effort with INEL under the joint NRC/EPRI/GE BWR Refill-Reflood and subsequent BWR FIST programs, TRAC-B has become a very effective and flexible tool for analysis of BWR systems. An analytical model developed and verified for the individually channeled fuel bundles in a BWR, includes heat transfer across the channel wall as well as the small, but important, "leakage" flow between the bypass and bundle regions. Similarly, there are models developed for the jet pumps and steam-water separators. These BWR unique component models can "pass through" three dimensional vessel nodes as needed for system definition modeling. There are also specific analytical models for the control system characteristics (i.e., the pressure control, level control, etc.), the neutron kinetics feedback to reactor power, and balance of plant systems (i.e., turbine, feedwater heaters, etc.).

Need for a number of new models had been identified for two-phase phenomena present in a BWR system. The analysis is tied back to empirical observation by the constitutive relationships at the two-phase interface. One of the early TRAC-B improvements developed consistent flow regimes for interfacial shear and interfacial heat transfer relationships. Another major improvement is the development of a phase separation model to determine, within each node, the location of the two-phase "level", (i.e., the interface between a high void fraction vapor continuous mixture and a lower void fraction liquid continuous mixture). Since determination of the fluid state crossing a region boundary is a necessary part of evaluating the change of mass and energy within the region, the phase separation model obviates the need for very costly fine mesh noding techniques to track the two-phase interface. A new model also addresses the two-phase flow situation of a core spray system injecting into the upper plenum region. In this situation subcooled liquid is sprayed radially inward from the circumference of the cylindrical upper plenum region. The model



determines the distribution of liquid drops across the top of the core when spraying into a vapor filled plenum, and alternately the turbulent mixing when spraying into a liquid continuous two-phase mixture. To extend TRAC-B capability to include containment systems, the formulation and constitutive relationships now include provision for non-condensable gas (i.e., air) in the system. With both the containment system and the reactor system included in the analysis, the boundary condition (e.g., back pressure, etc.) on the vessel during blowdown are determined explicitly, and the analysis can be carried to the equilibrium condition in which air flows back into the reactor vessel. To extend TRAC-B capability in non-LOCA applications, a non-homogeneous boron transport is modeled to track the stratification and mixing of the boron solution injected into the recirculating water.

In addition to model development and improvement addressed to BWR system characteristics, BWR unique components, and phenomena, a significant focus has been given to improving the cost effectiveness of TRAC-B for engineering analyses. These models provide simplification and flexibility for BWR system definition modeling (e.g., using a jet pump component instead of a multi-node representation, or the phase-separation model instead of fine mesh noding) that results in improved analytical efficiency. There is also significant improvement in numerical analysis techniques that substantially reduce computation costs. "Water packing" in two-phase system analysis can occur when a region fills, changing from a compliant to an incompressible fluid, and requiring very small timesteps. Improvement in the detection logic eliminated "water packing" as a problem. Also, a major improvement in computation time results from the two-step fast numerics technique, developed for both one dimensional and three dimensional regions which greatly increase time step size in all nodes while maintaining acceptable computational accuracy. Figure 2 illustrates an example in which, with this improvement, the time step limit has been increased by a factor of 100, with no deterioration of accuracy, and the run time is improved by a factor of 32.

## QUALIFICATION - TRAC-B

The development and assessment of each component or phenomena model incorporated TRAC-B is founded on a wide range of experimental results. These are separate effects tests, such as jet pump flow test, film boiling heat transfer tests, etc. To demonstrate the adequacy of the TRAC-B engineering computer code incorporating these models, an independent qualification program has been carried out. This qualification compares results from integrated system analysis with the BWR system performance measured in simulation tests carried out in the FIST facility.

A one ring vessel model is used for FIST analysis, with two sections to represent the region inside the core shroud and the downcomer. The vessel is divided into axial levels, or nodes, to provide 1) geometric definition the principal regions in the system (e.g., lower plenum), 2) correspondence between the vessel node centers and measurement locations so that direct comparison can be made between prediction and measurement, 3) flow modeling detail (e.g., jet pump exit), and 4) nodalization consistency (e.g., to locate vessel cell elevations at the correct component junction locations). The bundle is modeled with a "CHAN" component. The nodes in the bundle coincide with the spacer and the tieplate locations, and are further subdivided to align the node centers with the measurement tap locations. The spacer and tieplate flow areas are used when checking for possible CCFL at these locations, and to calculate the effect of local flow acceleration on the bundle void distribution. The 64 rods are divided into 4 radial groups according to power peaking, and have a chopped cosine axial power distribution. Eight radial nodes are used within each rod, one of which corresponds to the actual thermocouple location. Through careful selection of material properties, heat capacity and thermal diffusivity match closely with the actual heater. Other component models used in the system definition represent the steam separator, jet pumps and tail pipes, guide tube, and recirculation loops and pumps. Additional components are used for the connecting pipes such as the ECC systems.

Vessel wall stored heat is modeled with double sided "heat slab" components between the principal regions and the environment, augmented by "lumped heat capacity slabs" to model heavy section flanges. Heat loss to the environment is based on an outside surface heat transfer coefficient determined from system characterization heat loss tests. System characterization tests at full power steady state conditions are used to quantify the as-built flow loss coefficients throughout the system, and calibration tests are used to verify measurement locations, regional volumes, recirculation pump inertia, injection pump pressure/flow characteristics, etc.

Particular attention is given in setting up TRAC-B system definition modeling in the jet pump exit region, the vessel stored heat, and the break location geometry. In cases where the two-phase level in the lower plenum falls to the jet pump exit plane, flow modeling detail is needed to capture the exit uncover and calculation of the subsequent split of steam flow between the jet pump and core region. The level tracking model, which determines two-phase level location within a vessel cell, is used throughout, particularly in the jet pump exit region. The thermal capacity of the vessel wall and heavy flanges attenuate system pressure response by absorbing energy from the fluid during pressurization following an isolation and adding energy to the fluid during depressurization. Care in heat slab modeling detailed is needed to capture this effect, particularly in analyzing small system such as the FIST facility.

#### Large Break LOCA Test

The large break LOCA test simulated a 2.23 ft<sup>2</sup> double ended break in one recirculation pipe, with the additional failure of two of the three Low Pressure Coolant Injection (LPCI) pumps. The facility is initially operating at full power steady state conditions. The transient is initiated by opening the break and tripping power to the recirculation pumps (i.e., to simulate the simultaneous loss of off-site

power). Feedwater flow is shut off, bundle power is controlled to simulate the power decay transient following a scram, and the recirculation pumps coastdown. System pressure is maintained by the pressure regulator system until the falling water level in the downcomer reaches the break location and steam escaping through the break depressurizes the system. The high pressure ECC system begins to refill the vessel when initiated at 27 seconds, augmented by the low pressure ECC systems when system pressure falls below the shut-off head of these pumps.

System response following break initiation is characterized by a sudden reversal of the broken loop jet pump flow and the corresponding decrease in core inlet flow. System pressure is maintained by the pressure control system for about eight seconds, core power decreases, and core flow decreases to natural circulation rates. TRAC-B predicts the system thermal-hydraulic response during this period very well. The downcomer level decreases, due to inventory loss, until the break is uncovered and the increased steam flow depressurizes the system. The level uncover time and initial depressurization rate are well predicted. The calculated pressure after about 40 seconds is slightly lower than measured, which is attributed to an under prediction of liquid drop entrainment in the steam flow up the jet pumps and out the break. The lower plenum remains essentially full during the first part of the transient, and is then partially voided by flashing caused by system depressurization. The resulting lower plenum two-phase level is well predicted with TRAC-B, which leads to correctly calculating the proportion of the mass flow discharged to the downcomer or to the bundle. As a result the bundle inventory, shown in Figure 3, is well predicted throughout the inventory loss and system refill sequence. The oscillations in the later part of the calculation are due to shortcomings in "water packing" detection logic in an early version of the code used for this analysis. Liquid inventory in the bundle is depleted at 40 to 50 seconds and the refill by the ECC system shows a positive effect by about 100 seconds.

With system thermal-hydraulic characteristics satisfactorily modeled the bundle inventory and inlet flow are well predicted, and the bundle thermal response is also well predicted. Figure 4 shows the calculated average rod surface temperature at the bundle mid-plane compared with individual measurements at that elevation. The temperature remains essentially at saturation throughout the power decay and natural circulation period, including the depressurization following break uncover. There is an increase of flow into the bundle from the lower plenum due to initial flashing, and a subsequent return to the bundle draining mode that results in a mid-plane dryout at 40 seconds. The average measured rod heat up, about 50°F above saturation, is on the same order as calculated by TRAC-B. ECCS injection into the upper plenum region is predicted, and observed, to attenuate the rod heat-up. One thermocouple indicates a peak temperature of about 700°F. The remaining measurements, similar to the calculated average, show little or no heat up. The individual rod temperatures exhibit a variability in local rod surface rewet, apparently from non-uniform planar fluid conditions in the bundle, until the bundle is reflooded with a liquid inventory about the same as when dryout occurred. The analysis satisfactorily predicts the bundle dryout. Although the bundle heat transfer model is not expected to predict individual rod rewet behavior, the reflood inventory response in the bundle adequately bounds the quenching period and the calculated temperature represents an average response based on planar average fluid conditions.

#### Small Break LOCA Test

The small break LOCA test simulates a 0.05 ft<sup>2</sup> break in the suction side of one recirculation pump, with the additional failure of the High Pressure Core Spray (HPCS) system. The facility is initially operated at full power steady state conditions. The transient is initiated by opening the break and tripping power to the recirculation pumps (i.e., to simulate the simultaneous loss of off-site power). The recirculation

pumps coastdown, feedwater flow is shut off, and bundle power is controlled to simulate the power decay transient following a scram. System pressure is maintained by the pressure regulator system until the falling water level in the downcomer reaches the Level-1 set point, closing the Main Steamline Isolation Valve (MSIV) and initiating the Automatic Depressurization System (ADS). The water level continues to fall until the ADS delay time, set for 120 seconds, opens the Safety Relief Valve (SRV) to depressurize the system. The low pressure ECC systems begin to refill the vessel when system pressure falls below the shut-off head at these pumps.

System response following the break initiation is very similar to a recirculation pump trip operating transient. Pressure is maintained by the pressure control system, core power decreases to decay power level, and the core flow decreases to natural circulation rates. In the small break case the downcomer level continues to decrease due to inventory loss through the break. As expected, TRAC-B adequately predicts the system thermal-hydraulic response during this period, which lasts about three minutes.

The downcomer level is calculated to reach the Level 1 trip point at 60 seconds, which closes the MSIV and starts the 120 second time delay for the ADS system. The measured Level 1 trip is  $73\frac{1}{2}$  seconds; this difference is attributed to a 20% over prediction of subcooled critical flow through the break during this period. The calculated system pressurization following the main steam line isolation is slightly greater than measured, which may be due to heat slab modeling in the analysis or may be due to a suspected incomplete isolation of the steam line in the test. After the specified 120 second delay, the ADS system is activated, depressurizing the system. The difference between calculated time and measured time for ADS activation corresponds to the difference in times for reaching Level 1. The satisfactory prediction of the pressure response following ADS, which is dependent on predicting the critical steam flow through the SRVs as well as the energy input to the fluid from the core and vessel walls, leads to satisfactory prediction of ECCS injection time.

The downcomer inventory shows good correspondence. The difference in the rate of decrease is due to the prediction of higher subcooled critical flow discussed above. It is seen that the level is calculated to reach the top of the jet pumps at 130 seconds and is measured at 165 seconds. The downcomer inventory comparison shows satisfactory agreement during the post lower plenum flashing period (flow surge up the jet pumps) and post ECC injection period (liquid spill over from the jet pumps).

The bypass remains essentially full during the first 100 seconds of the transient. When the downcomer level falls below the top of the core region, the bypass inventory has a corresponding decrease. The subsequent bypass inventory draining and refill is well predicted. The lower plenum remains essentially full during the first 180 seconds of the transient, and is then partially voided due to flashing caused by system depressurization. The resulting lower plenum mass inventory is well predicted, as is the distribution of mass discharged to the downcomer and to the bundle. The bundle inventory, shown in Figure 5, is well predicted throughout the entire inventory loss and system refill sequence. The slight offset during the 80 to 180 second period is again due to the downcomer inventory difference discussed above. ECCS injection occurs when system pressure decreases below the pump shut-off head. The start of injections by the two ECC systems in the test are indicated by the first and second arrows, and in the calculation by the second and third arrows. The oscillations in the predicted trace is due to a limitation in the "water packing" detection logic in this early code version.

With system thermal-hydraulic characteristics satisfactorily modeled, the bundle inventory and inlet flow are well predicted, and the resulting bundle thermal response is also well predicted. Figure 6 shows the calculated rod surface temperature at the bundle mid-plane compared with the average of the seven measured temperatures at that elevation. The temperature remains at saturation throughout the power

decay and natural circulation period, including the depressurization following ADS activation. There is an increase of flow into the bundle from the lower plenum due to flashing following ADS, and subsequent return to the bundle draining mode that results in a mid-plane dryout at 270 seconds. ECCS injection into the bypass and upper plenum regions is predicted, and observed, to attenuate the planar average rod heat-up shortly after initiation. The individual rod temperatures, exhibit a variability in local rod surface rewet during the period from ECCS initiation until the bundle is reflooded with a liquid inventory about the same as when dryout occurred (i.e., at 270 seconds). The analysis satisfactorily predicts the bundle dryout and heatup and, although not expected to predict individual rod rewet behavior, the reflood inventory response in the bundle adequately bounds the quenching period.

#### Injection Line LOCA Test

The injection line LOCA test simulates an LPCI line break, which discharges inventory out of the system from the bypass region. One LPCS and the two remaining LPCI systems are operational, and the HPCS is assumed to be unavailable. Following the jet pump flow coastdown, the water level inside the shroud falls and uncovers the break. This leads to system depressurization and flashing prior to the ADS actuation. The top of the core uncovers shortly after the ADS, and some rod heatup is observed. The cladding temperature increase is limited by ECCS cooling. The measured peak cladding temperature is 650°F. Steam generation caused by ADS induced fluid flashing leads to CCFL at the side entry orifice, the upper tie plate, and the top of the jet pumps. The core is completely reflooded by the ECCS injection.

The pressure history may be divided into three distinct phases. In the first phase (0-30 seconds) following the break initiation the system pressure is maintained at a nearly constant value by the pressure control system. In this phase the core power decreases to decay power level and the core flow decreases to natural circulation level. Fluid



levels, both inside and outside the shroud, initially decrease as a result of the combined effects of core void decrease due to power decay, liquid discharge through the broken LPCI line, and continuing steam line flow after stopping of the feedwater make-up. The downcomer water level is calculated to reach Level 1 trip point at 15 seconds, about 2 seconds earlier than observed in the test. The difference is attributed to a slightly higher calculated subcooled break flow rate. At this point the MSIV is closed and the trip signal starts a 105 second time delay before ADS initiation. The end of the first phase is marked by the bypass water level falling to the break elevation. Throughout this phase the calculated system response compares well with that measured in the test.

The second phase begins with the uncovering of the LPCI line break elevation and the break flow changing from all liquid to two-phase. The calculated time to this uncovering is 30 seconds versus the measured value of 31 seconds. With additional steam leaving, the system begins to depressurize. The calculated pressure follows the data trend, but is somewhat lower. During this period, the two phase level is in the vicinity of the break and, in the test, there is liquid entrainment into the break. This Bernoulli-type entrainment (see Reference 4 for discussion of this phenomenon and its implication on system pressure) is not included in the two-phase critical flow phenomena model, leading to a calculated depressurization rate greater than in the test. The pressure falls to a value where flashing is initiated in various single phase regions of the system, such as the downcomer, the lower plenum, and the guide tube and bypass. Due to the faster calculated depressurization rate, the calculated time to flashing is 53 seconds, 10 seconds earlier than in the test. The flashing generates additional steam in the system which attenuates the depressurization rate, and the analysis matches this observed effect.

The third phase is marked by actuation of the ADS, and a more rapid system depressurization. ECCS injection begins when the system pressure falls below the pump shut off head. The satisfactory prediction of the pressure response following ADS, which is dependent on predicting the critical flow through the SRVs and the break, as well as energy input to the fluid from the core and the vessel walls, leads to satisfactory prediction of the ECCS injection times.

A comparison of the calculated LPCI line integrated break flow with the measured total mass flow out of the break shows the initial subcooled break flow to be calculated slightly high. In the long term the break flow comparison is satisfactory, and the ADS flow compares well also. The regional liquid inventory comparisons show the calculated regional inventories in agreement with the measurements. Pre-ADS flashing in the system redistributes regional masses and further redistribution occurs due to increased flashing after the ADS actuation. Liquid inventory comparisons for the downcomer, lower plenum, bundle, bypass, and upper plenum show that TRAC-B correctly calculates the system mass and mass distribution, including refilling of the bundle and the bypass by the ECC system.

Lower plenum two phase level formation occurs in the test shortly after the ADS, but remains above the jet pump exit plane until about 200 seconds. During this period there is CCFL at the side entry orifice (SEO). At about 170 seconds both the calculated and measured SEO flow (as indicated in the test by the SEO pressure drop) exhibit a brief transition to cocurrent upflow. With the lower plenum level near the core inlet, there is substantial entrainment occurring in the test that transports liquid into the bundle. This entrainment, which is under-predicted in the code, effects the initiation time of rod heat up in the lower part of the bundle. ECCS injection increases the static head in the bundle, increasing the flow up the jet pumps, and causing the lower plenum level to drop to the jet pump exist at about 225 seconds. The TRAC-B analysis predicts this level transient satisfactorily.

Rod heat up occurs as the bundle inventory, Figure 7, is depleted. Figure 8 compares the calculated and measured rod temperatures at the mid-plane axial location in the bundle. With entrainment from the lower plenum to the bundle underpredicted, an earlier heat up initiation time (10 to 20 seconds) is calculated in the lower two-thirds of the bundle. However, the calculated heat up rates are quite similar to the data. The predicted PCT of 700°F occurs at the bundle mid-plane and is 50°F above the data. Top quench of different rods at different times by the LPCS are observed. TRAC calculates a planar average fluid condition at the bundle nodes and does not capture these individual rod rewets. However, all the rods are rewetted as the bundle reflood is complete in both the calculation and the test at about 300 seconds.

#### Isolation Transient Test

The isolation transient test is a FIST facility simulation of one of the turbine trip tests (TT-3) in the Peach Bottom-2 BWR power plant. The FIST test is initiated by closing the turbine stop valve followed by opening of the turbine bypass valve. Boundary conditions include simulation of kinetic feedback by a programmed initial core power increase and subsequent power decay, recirculation pump trip, and feedwater injection into the downcomer. The feedwater flow follows a specified transient, decreasing to zero at 16 seconds, and the bypass valve is closed at 28 seconds. The total test duration is 62 seconds. System pressure, initially 991 psia, increases to 1050 psia following turbine stop valve closure, and then decreases as steam leaves the system through the turbine bypass valve. Sustained depressurization produces flashing and level swell in various regions of the system. After turbine bypass valve closure the system pressurizes slowly for the remainder of the test. As expected, the bundle remains full throughout the test without heat up.

A TRAC-B analysis of this test was undertaken to assess the code capability for predicting the complex thermal-hydraulic system response observed in the test, (e.g., pressure history, level swell, regional

flows, and bundle void). TRAC-B analysis of the reactor test itself is reported in Reference 5. The steamline is nodalized in more detail for this analysis to model the dynamics of pressure wave propagation, and for accurately calculating critical steam flow through the turbine stop and bypass valves. The measured core power and feedwater flow are boundary conditions, as well as the turbine stop valve and bypass valve areas which are specified as functions of time, derived from the measured valve stem positions. Also, the recirculation pump trip at 3.5 seconds into the transient and loop isolation at 23.5 seconds are boundary conditions for both the test and the analysis.

The initial conditions established in the steady state calculation show close correspondence with measurements. Closure of the turbine stop valve generates a compression wave that propagates towards the vessel and produces a rapid increase of the system pressure; the turbine bypass valve begins to open and vent steam out of the system. The system pressure peaks and begins to decrease. The pressure history, Figure 9 shows that the analysis predicts this response very well, and the calculated peak pressure is within 5 psia of the measurement.

The system depressurization rate in the intermediate period (5 to 28 seconds), is due to the combined effects of critical flow of steam with liquid entrainment through the bypass valve, energy addition to the vessel fluid from core power and from the hot vessel walls, and fluid addition to the vessel by the feedwater system. The higher calculated depressurization rate is due to underpredicting liquid entrainment into the steamline from the high two-phase level in the downcomer. The system depressurization initiates flashing in the downcomer, lower plenum, bypass, and guide tube regions, redistributing the regional mass inventories. Because the calculated pressure is lower, flashing occurs 2 to 5 seconds earlier than observed. The higher calculated depressurization rate then leads to greater flashing, somewhat higher regional voids, and more level swell than in the test.

The bypass valve is closed at 28.1 seconds and the system is then in a "bottled up" mode, pressure begins to increase, and the voids collapse. Because of somewhat higher regional voids in the calculation, the interfacial heat transfer area, and the corresponding interfacial condensation rates, are also higher, and the calculated pressurization rate is consequently lower. The downcomer two-phase level comparison is shown in Figure 10. The initial level decrease corresponds to void collapse inside the shroud, which results from the early system pressurization and core power decay. The downcomer level begins to increase when the feedwater flow is ramped up at 4 seconds. At 15 seconds into the test the system pressure decreases to a low enough value to initiate flashing in the downcomer. The corresponding calculated time to downcomer flashing is 14.7 seconds. The two-phase level then rises rapidly, reaching the elevation of the steam line at 26 seconds in the test, and 24 seconds in the calculation. Between  $10 < t < 15$  seconds, the downcomer two-phase level is quite close to the steamline, causing liquid entrainment into the flow to the turbine bypass valve via the steam line. The faster calculated depressurization in this period is the result of underpredicting this entrainment, (i.e., overpredicting the volumetric flow through the turbine bypass valve). After the turbine bypass valve closure the system begins to repressurize and the downcomer two-phase level decreases as voids collapse in the system. The calculation reproduces this portion of the level transient very well. Since the calculated repressurization is slower the level decrease somewhat more slowly in the late transient.

The analysis indicates good overall correspondence of the system thermal-hydraulic responses with data. The system pressure response is in good agreement with measurement. The system pressure is slightly underpredicted in the depressurization phase due to underprediction of liquid entrainment through the steam line. The calculated long term repressurization rate is slower due to the higher interfacial condensation induced by the higher system voids calculated in the depressurization phase. The calculated downcomer two-phase level, jet pump and core inlet flows, and the bundle pressure drop comparisons show satisfactory agreement.

## Qualification Summary

The TRAC-B analysis quantifies the important BWR thermal-hydraulic phenomena. System pressure response and bulk flashing, and the corresponding void distribution and two-phase level, are well predicted. Counter-current flow limiting (CCFL) is predicted and observed at key areas, such as the bundle inlet and outlet, and two-phase levels are found in various vessel regions. The TRAC/data comparison is quite good overall.

## APPLICATION TO BWR SYSTEMS

TRAC-B application to a BWR system follows the same approach to system definition input modeling as used in the analyses of the FIST facility. The principal thermal-hydraulic characteristics difference between the two systems is the absence of a significant amount of vessel stored heat in a BWR system and the presence of parallel channel flow during system refill. It has also been found that, for some transients, the FIST facility has counter current flow limiting (CCFL) at some junctions where the BWR system does not. These differences all lead to a more effective refill/reflood process in a BWR system than observed in FIST.

Evaluation of the effect of these differences is made by examining each parameter individually. An assessment of the overscaled stored heat in FIST is made by using the small break LOCA test analysis, and modifying the heat slab modeling to represent vessel and internal structure of the reference BWR<sup>(6)</sup>. As expected, with this change in the system definition model, the depressurization following ADS is somewhat faster than FIST, both measured and predicted. As shown in Figure 11, the pressure at which LPCS and LPCI start to inject is reached earlier, and the refill/reflood takes place sooner, Figure 12. The TRAC-B analysis of the BWR-LIKE FIST (i.e., the response that would have occurred if the FIST stored heat was not over scaled) is a lower average mid-plane temperature, as shown in Figure 13.

To assess the single channel effect, the FIST bundle is modeled with three separate channels of 4 rods, 25 rods, and 35 rods. With the system definition modified, the parallel channel phenomena permits some cocurrent upflow, as well as the predominant counter current flow. There is some redistribution of inventory calculated, as shown in Figure 14, and a slightly earlier dryout time, Figure 15.

The pre-test analyses of the tests in the FIST facility were carried out with particular attention paid to system definition input modeling. The subsequent post-test comparisons demonstrate that TRAC-B thermal-hydraulic models capture the controlling phenomena and predict system response very well. The system definition modeling leads to correct handling of level/inventory performance, and the bundle and core inventory model capture bundle heat-up and quench very well.

The completed TRAC-B, incorporating BWR system component models, improved thermal-hydraulic phenomena models, and improved numerical methods, and qualified with the series of FIST system response tests, is used for "best-estimate" benchmark analysis of BWR system. A typical application has been completed for a BWR/4 type system response to the large break LOCA design basis accident. The system model includes a multi-region core and includes peak power, as well as average and low power bundles. Figure 16 shows the peak power bundle temperature response through the blowdown and refill/reflood period.

#### SUMMARY

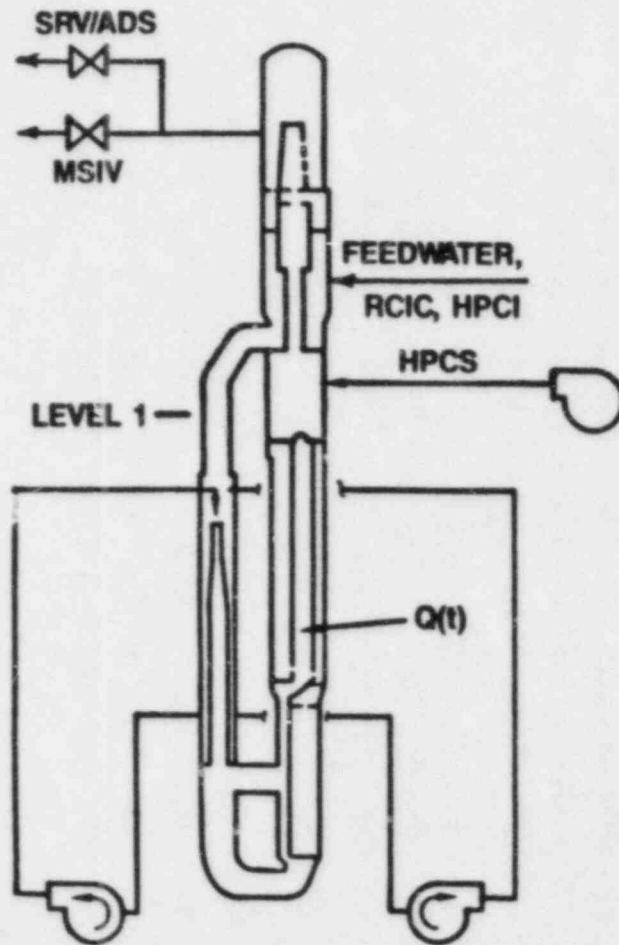
In summary, the data base is extended to a wide range of system response situations, and analysis of these results provided guidance for many model improvements. The method development program provides improved TRAC-B analysis capability as well as system definition and modeling flexibility and improved running time. Qualification against LOCA and operational transient test demonstrates BWR-TRAC capability to handle these transients. Application for reactor system analysis evaluates the main FIST vs. BWR scaling effects, and shows a "best-estimate" benchmark analysis for a reference BWR system.

## REFERENCES

1. Wm. A. Sutherland, and W. S. Hwang, "BWR FIST Test and Analysis", Proceedings of the USNRC 12th Water Reactor Safety Research Information Meeting (NUREG/CP-0058, Vol. 1), October 22-26, 1984, Gaithersburg, Maryland.
2. Wm. A. Sutherland and Md. Alamgir, "BWR Full Integral Simulation Test FIST - Pretest Predictions with TRACB02", Proceedings of the USNRC 11th Water Reactor Safety Research Information Meeting (NUREG/CP-0048, Vol. 1), October 24-28, 1983, Gaithersburg, Maryland.
3. Md. Alamgir and Wm. A. Sutherland, "FIST Small Break Accident Analysis with BWR TRAC02 - Pretest Predictions", Proceedings of an ANS Topical Meeting on Anticipated and Abnormal Plant Transients in Light Water Reactors, September 26-29, 1983, Jackson, Wyoming.
4. Md. Alamgir, "BWR Refill-Reflood Program Task 4.8 - TRAC-BWR Model Qualification BWR Safety Analysis Final Report", NUREC/CP-2571, EPRI NP-2377, GEAP-28049, July, 1983.
5. Md. Alamgir and Wm. A. Sutherland, "Peach Bottom Transient Analysis with BWR TRACB02", Proceedings of an ANS Topical Meeting on Anticipated and Abnormal Plant Transients in Lighth Water Reactors, September 26-29, 1983, Jackson, Wyoming.
6. Md. Alamgir and Wm. A. Sutherland, "Using TRAC to Apply Integral Test Experience to Reactor System Analysis", Transactions of ANS, Vol 46, June 3-7, 1984, New Orleans, Louisiana.



FIGURE 1

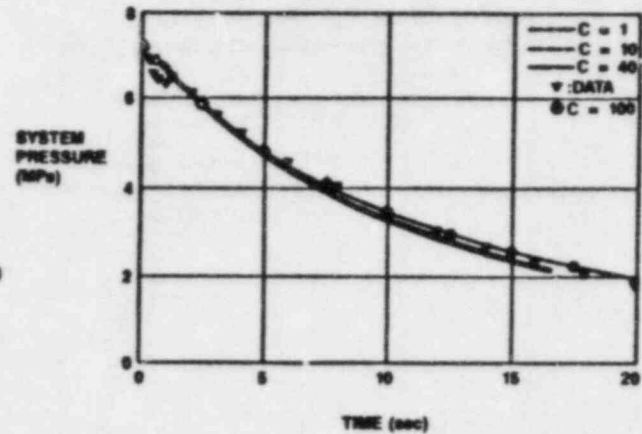
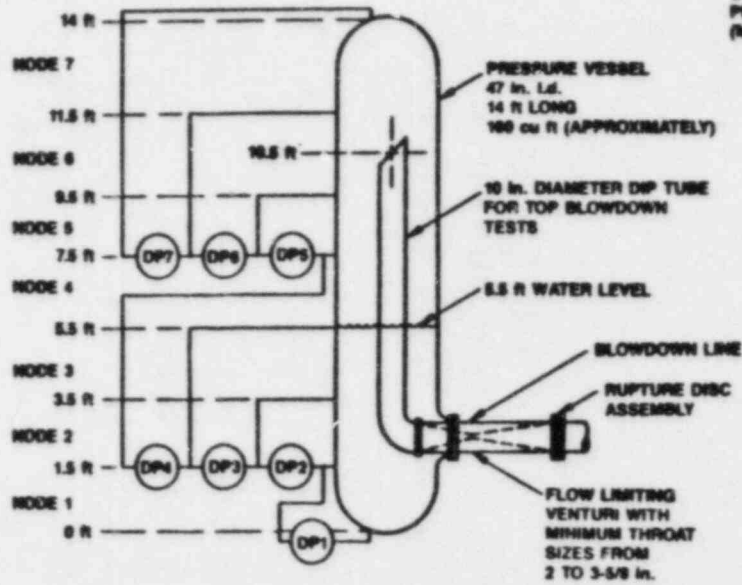


## FULL INTEGRAL SYSTEM TEST FACILITY

- Full Height
- Regional Volumes Proportional to Core Size
- BWR Components:
  - Jet Pump
  - Steam Separator/Dryer
  - Channeled Fuel Bundle
- Reactor Control System:
  - Feedwater/Level
  - Steam Flow/Pressure
  - Recirculation Flow
  - Power
  - Safety System Activation
- ECC Systems:
  - High Pressure Core Spray
  - Low Pressure Core Spray
  - Low Pressure Coolant Injection

FIGURE 2

## ASSESSMENT OF PREDICTOR-CORRECTOR METHOD PSTF TEST 5801-15



<u>ΔT/COURANT LIMIT</u>
STEAM BLOWDOWN
1
10
40
100

<u>REDUCTION IN RUN TIMES</u>
1
7
21
32

FIGURE 3

### LARGE BREAK LOCA Bundle Inventory

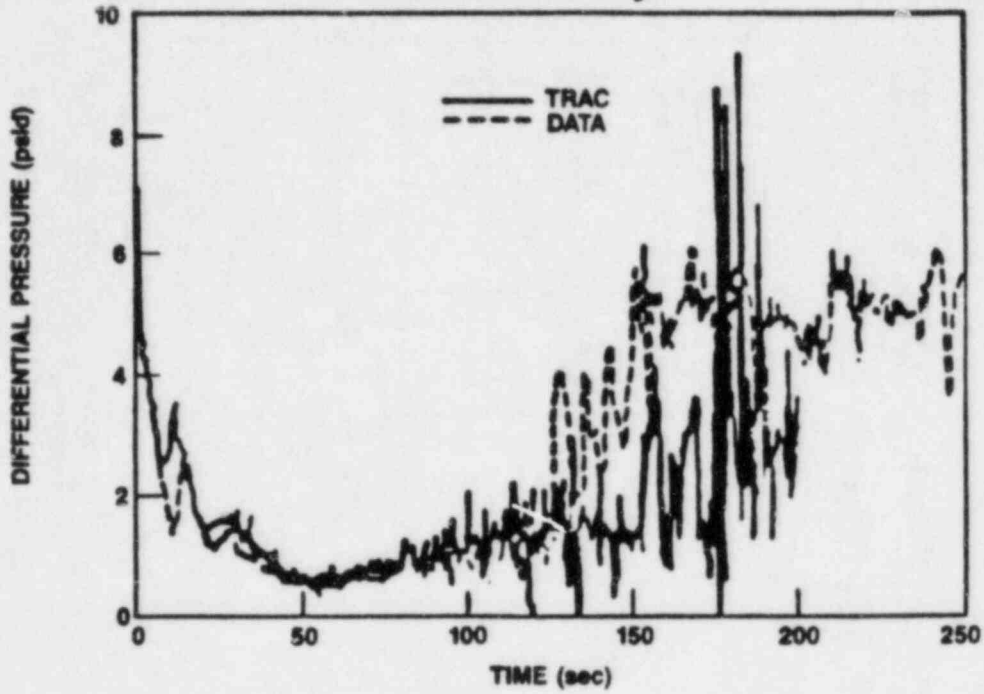


FIGURE 4

### LARGE BREAK LOCA Bundle Mid-Plane Temperature

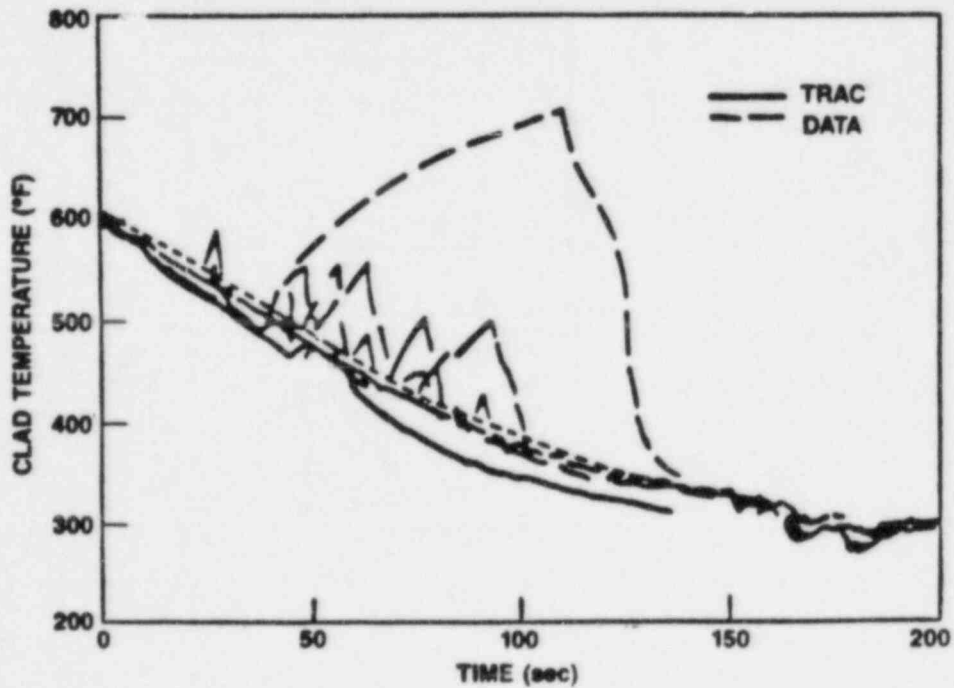


FIGURE 5

### SMALL BREAK LOCA Bundle Inventory

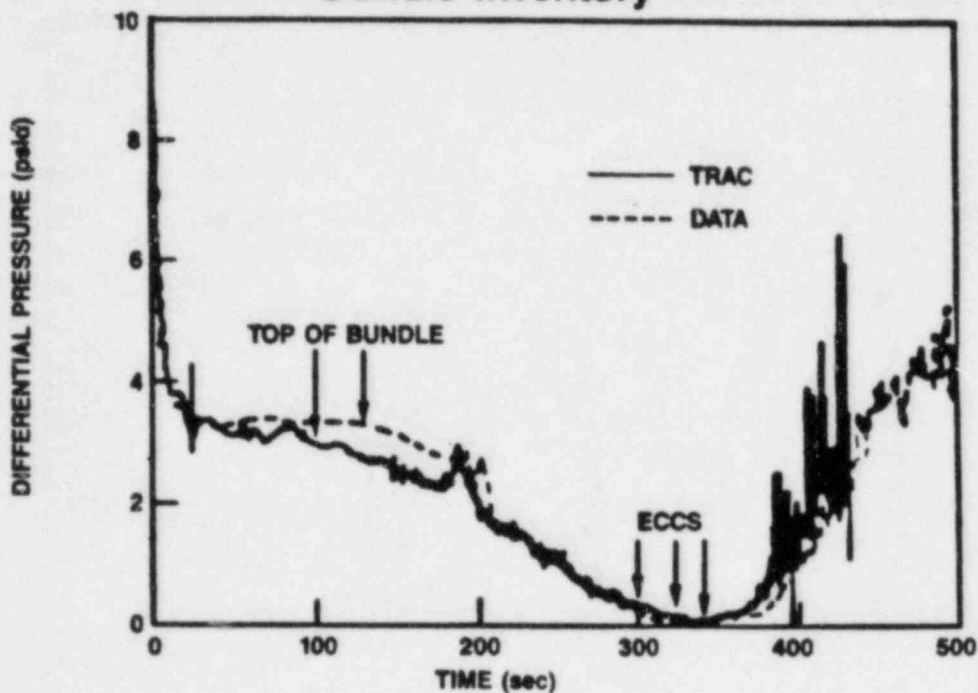


FIGURE 6

### SMALL BREAK LOCA Bundle Mid-Plane Temperature

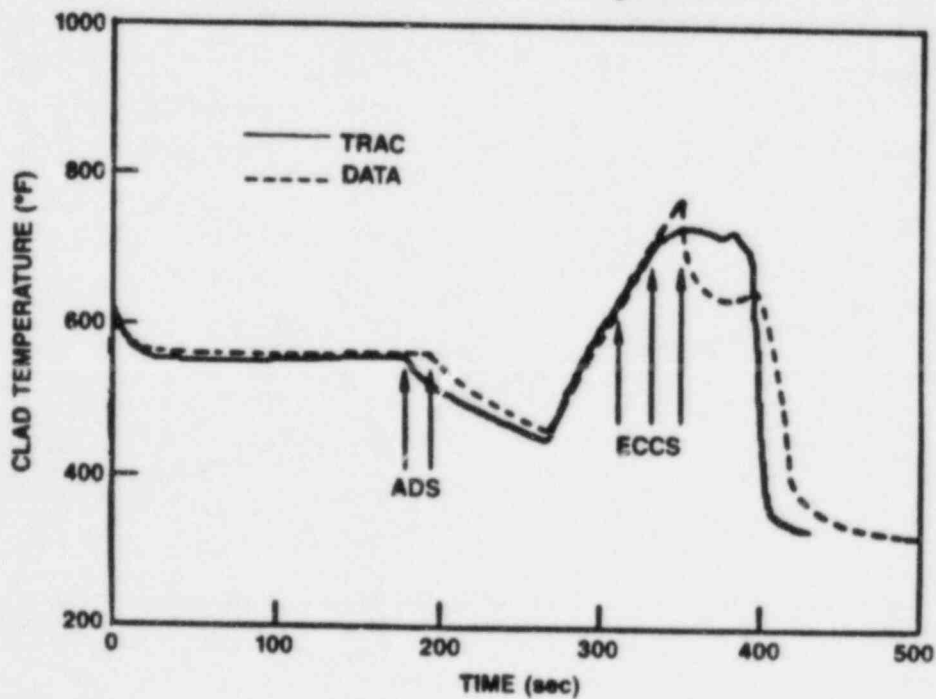


FIGURE 7

### INJECTION LINE LOCA Bundle Inventory

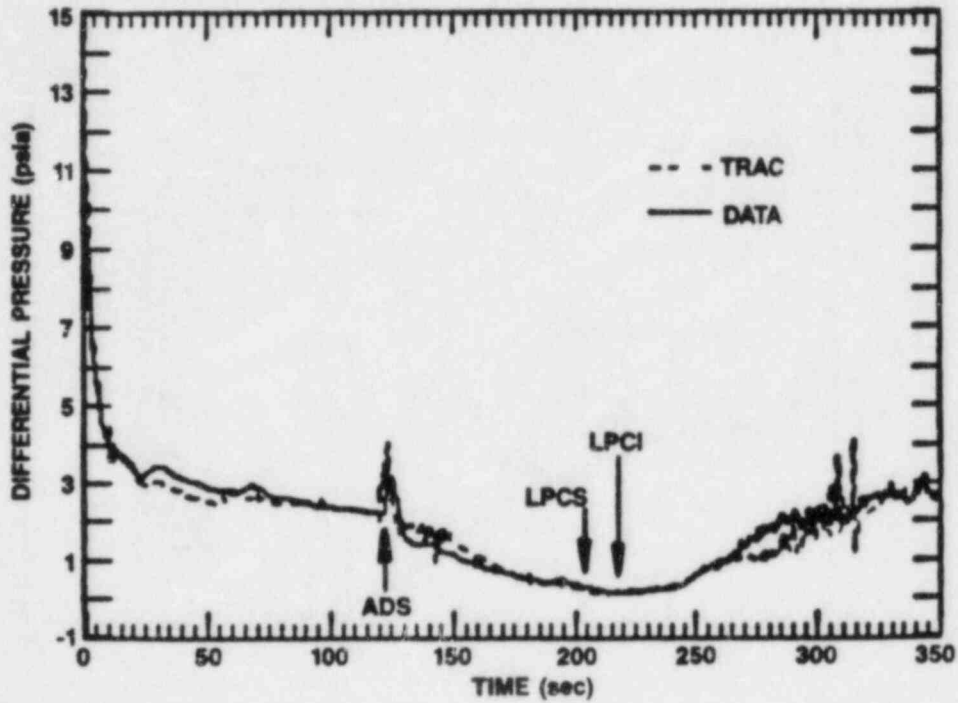


FIGURE 8

### INJECTION LINE LOCA Bundle Mid-Plane Temperature

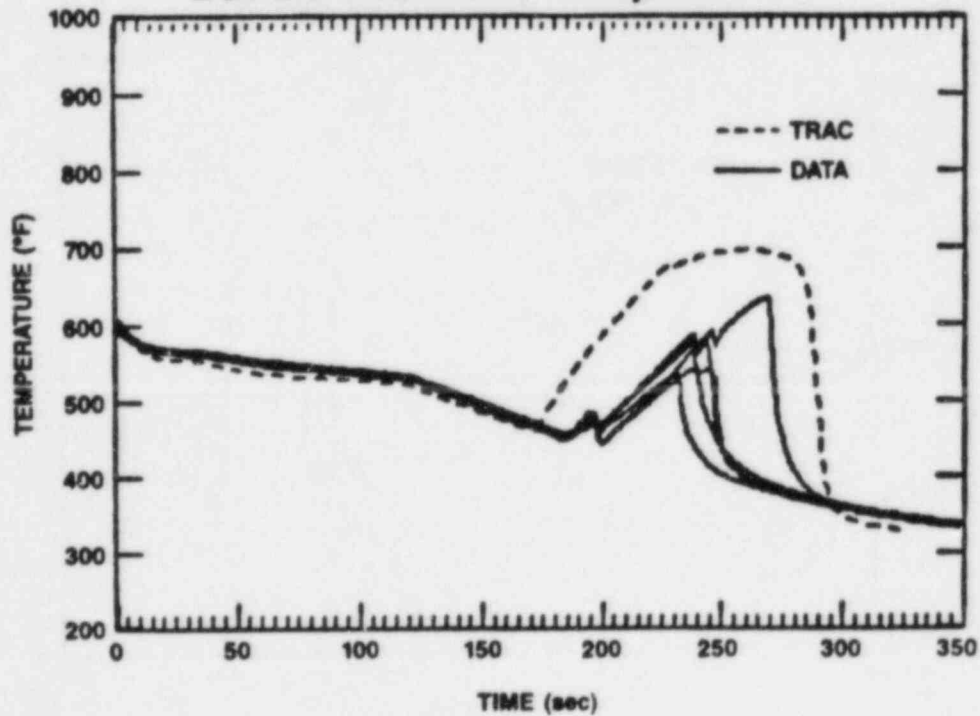


FIGURE 9

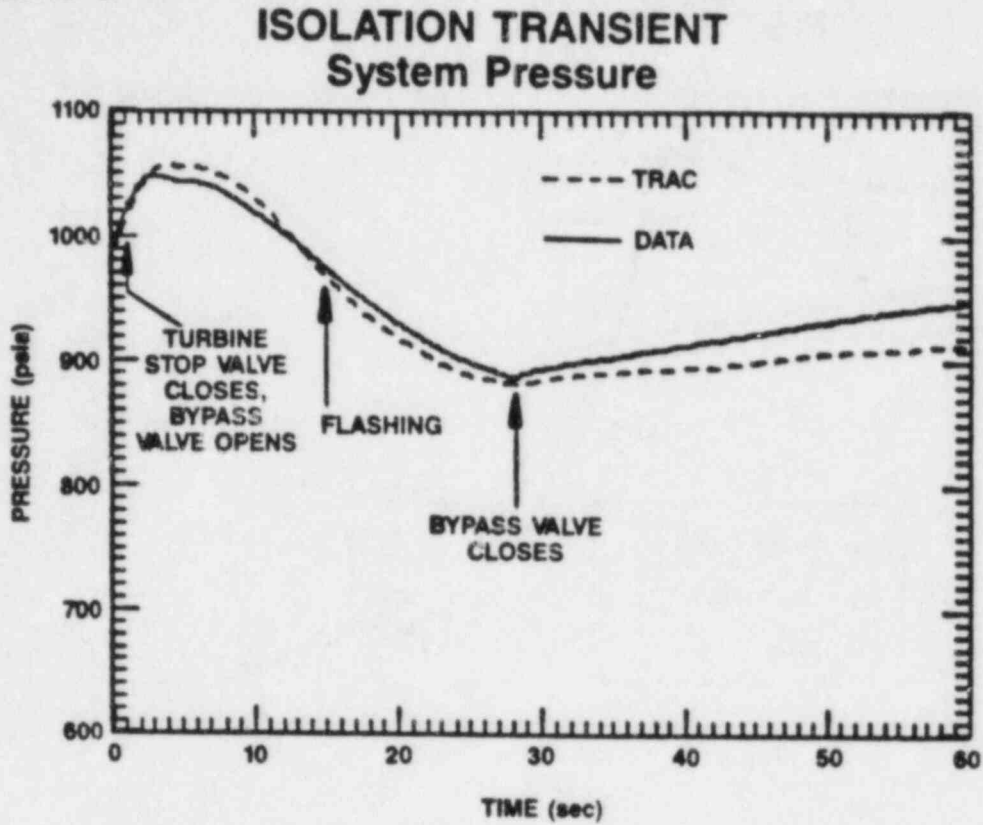


FIGURE 10

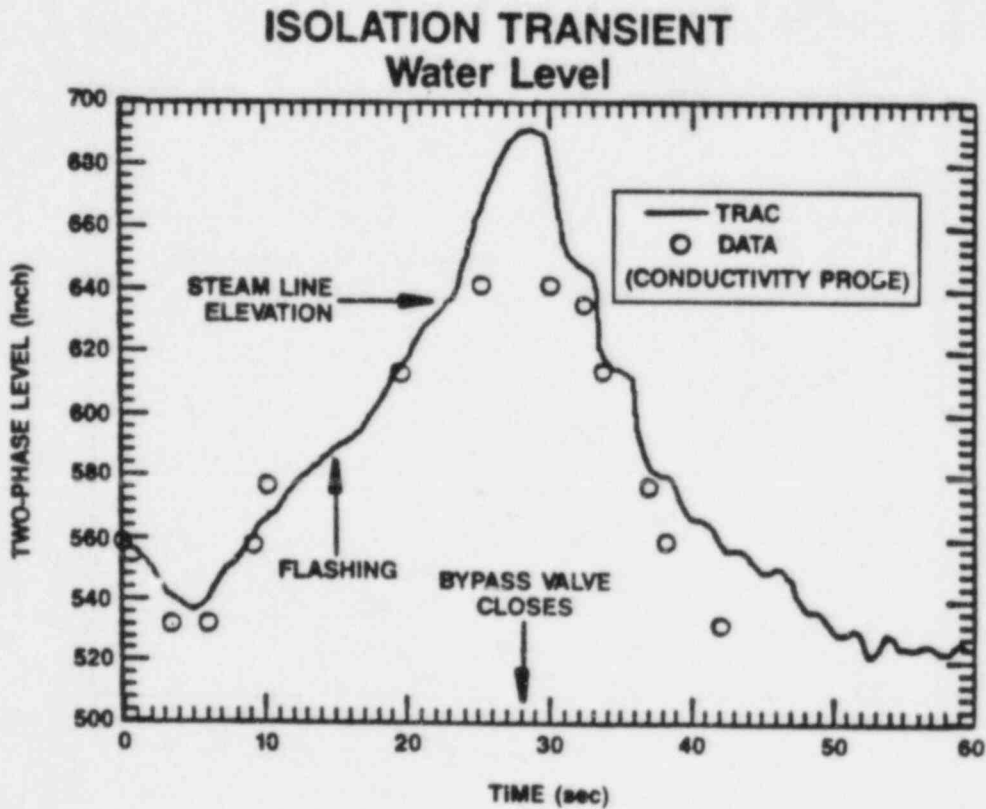


FIGURE 11

### FIST STORED HEAT EFFECT System Pressure

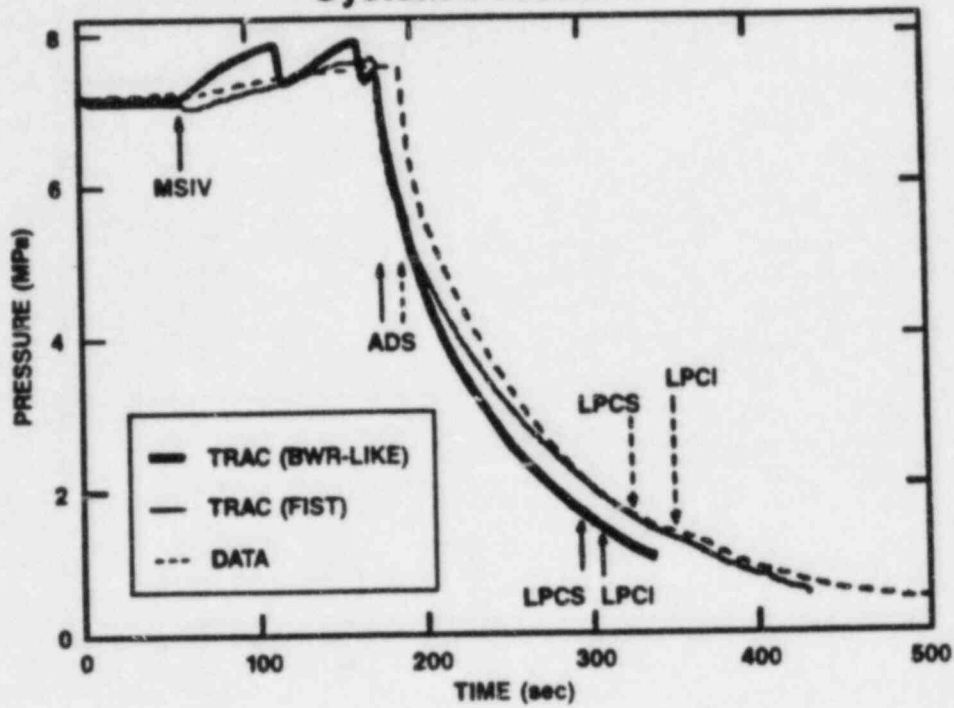


FIGURE 12

### FIST STORED HEAT EFFECT Bundle Inventory

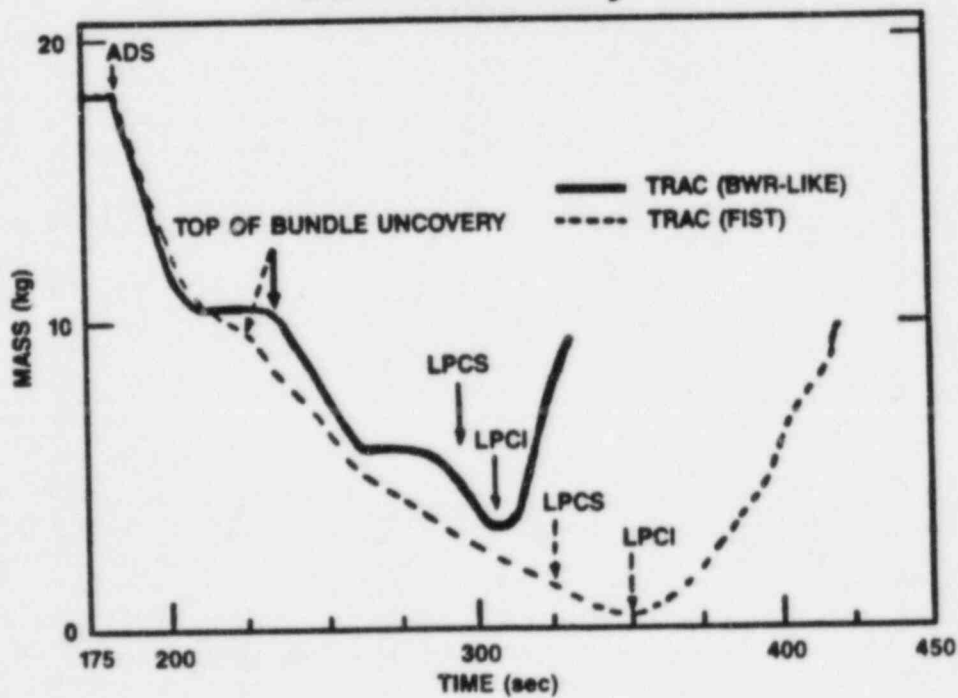


FIGURE 13

**FIST STORED HEAT EFFECT  
Bundle Mid-Plane Temperature**

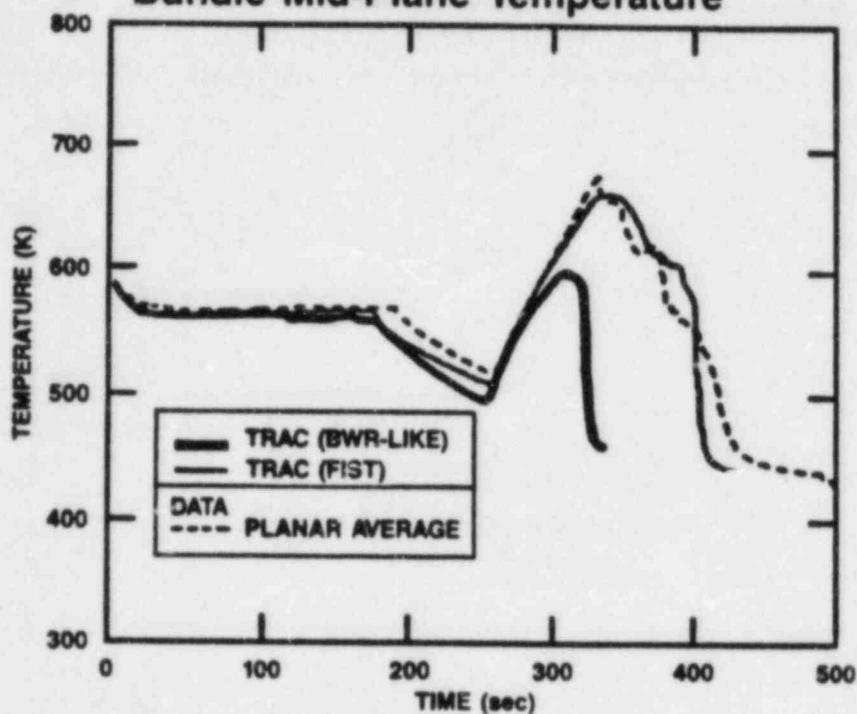


FIGURE 14

**FIST PARALLEL CHANNEL EFFECT  
Bundle Inventory**

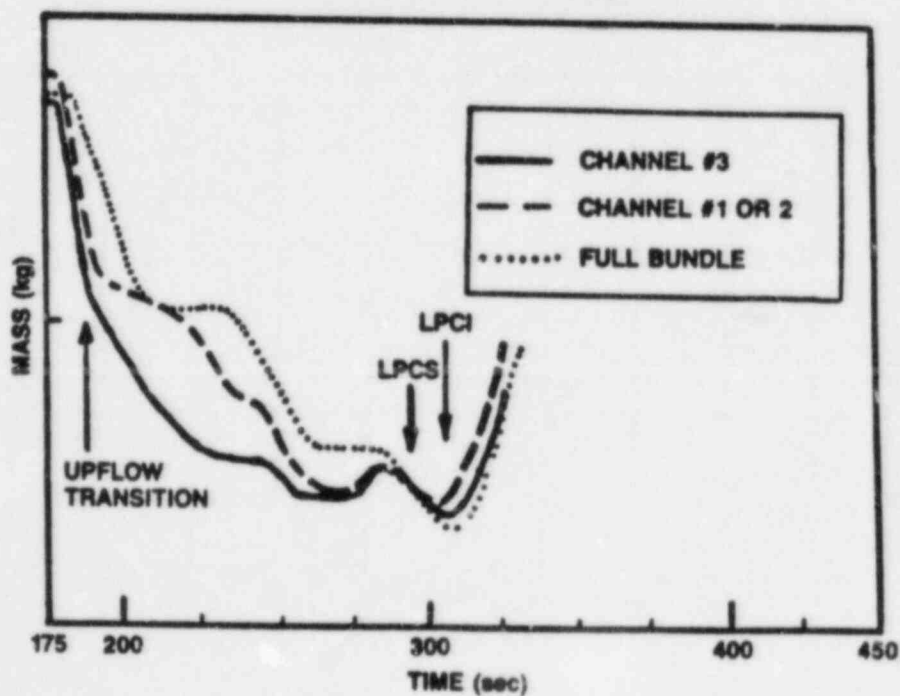




FIGURE 15

### FIST PARALLEL CHANNEL EFFECT Bundle Peak Temperature

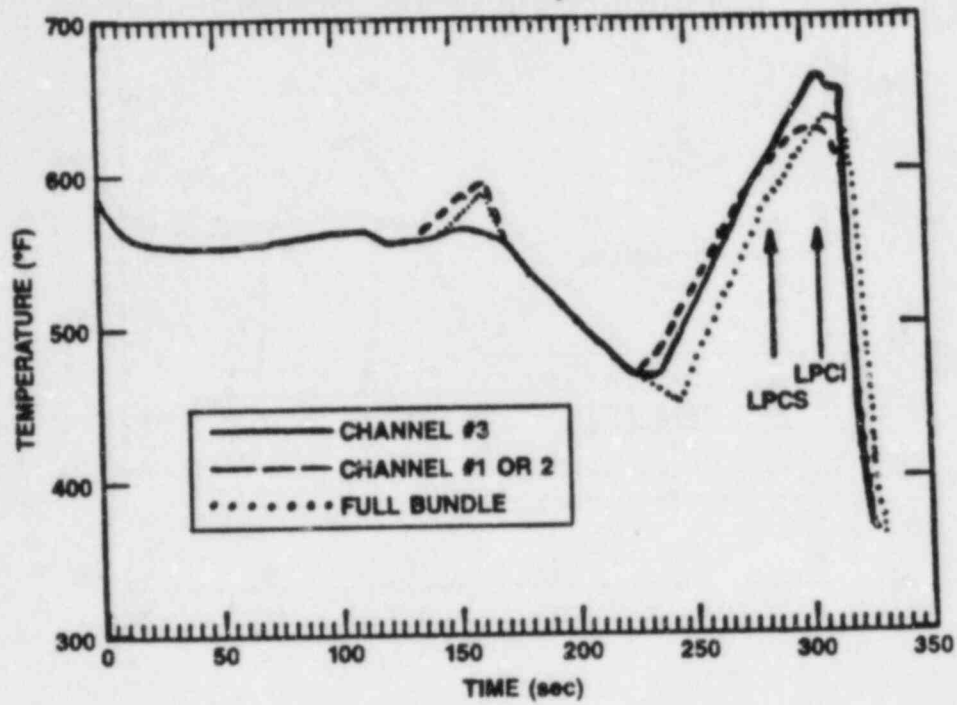
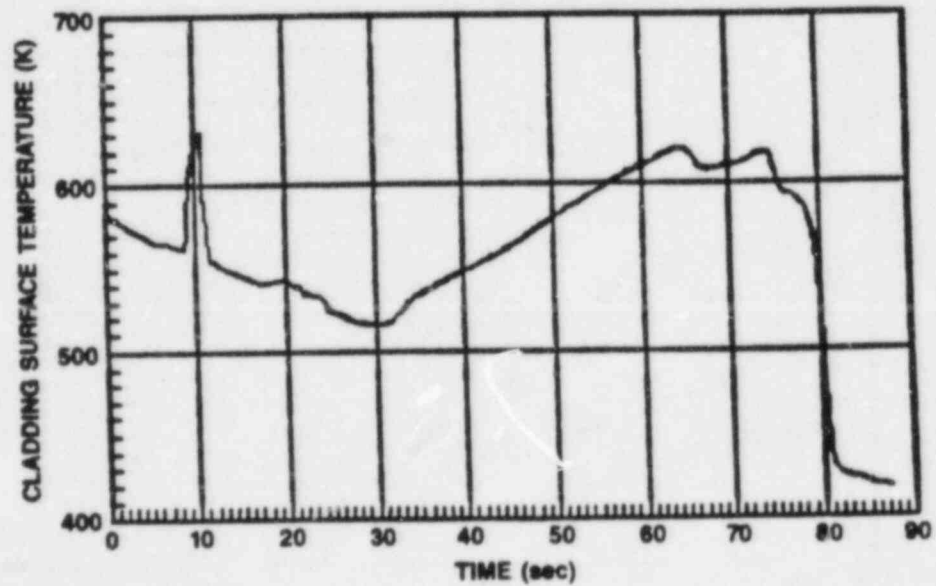


FIGURE 16

### BWR SYSTEM PERFORMANCE Large Break LOCA



## OTIS TEST RESULTS

J. R. Gloudemans  
Nuclear Power Division  
The Babcock & Wilcox Company  
Lynchburg, VA

### ABSTRACT

OTIS (Once Through Integral System) was a 1 x 1 full-elevation model of a domestic, raised-loop B&W plant. Five types of tests were performed: benchmark, single-variable, cool-down, operator-controlled, and guard heater effects. These tests generated a broad base of integral system data. The importance of the boiler-condenser mode (BCM) and event timing were apparent. The single-variable tests encountered a wide range of system interactions. Various depressurization mechanisms and trends, combinations of BCMs, and refill responses were observed.

### INTRODUCTION

OTIS (Once Through Integral System) testing was performed to generate integral-system data with which to benchmark system codes.<sup>1,2</sup> OTIS was sponsored by the Nuclear Regulatory Commission, the B&W Owners Group, the Electric Power Research Institute, and Babcock & Wilcox. The tests were performed in the 1 x 1 (one HL, SG, and CL) loop at Alliance, Ohio; this test facility was also used for the earlier GERDA tests.<sup>3</sup> The key features of the test facility included: full elevation, power-to-volume scaling generally but with an oversized HL to obtain plant-similar two-phase behavior, and hydraulic resistances sized to obtain full-scale pressure drops with power-scaled flow rates. Full scale pressures and fluid temperatures were used. Consistent with the emphasis on SBLOCA testing, the test facility was designed and fabricated for negligible leakage and minimal heat losses. Several hardware changes were made between GERDA and OTIS testing. These included: guard heating of the pressurizer surge line and reactor vessel upper head, in addition to the hot leg guard heating of GERDA; installation of a flow restriction in the RV upper plenum to accentuate the flow stagnation in this region; relocation of the cold leg flow-metering orifice toward the steam generator outlet, primarily to extend the range of conditions of useful flow measurements by moving the orifice toward a region less likely to void; and installation of leak fluid temperature indications.

The OTIS tests extended the GERDA data base. The 113 GERDA tests ranged from separate-effects examinations of SG heat transfer to composite transients. OTIS simulated the boundary system characteristics of domestic rather than German plants of the raised-loop B&W design. With the exception of the single GERDA-OTIS benchmark test, the OTIS tests simulated integral-system transients. The fifteen OTIS tests were of five types: benchmark, single-variable, cooldown, operator-controlled, and guard heating effects. Preliminary OTIS results were presented at last year's meeting,<sup>4</sup> therefore this presentation will concentrate on inter-test comparisons and interpretations. The results of the seven

single-variable tests will be discussed in detail, following a summary of the other test categories.

#### BENCHMARK

The OTIS-GERDA benchmark test used the steady-state Boiler Condenser Mode (BCM) for comparison. "BCM" denotes primary-to-secondary heat transfer by the condensation of primary vapor within the SG. Two types of BCM have been observed, AFW BCM and Pool BCM. "AFW BCM" denotes the condensation of primary vapor within the SG by the introduction of subcooled auxiliary feedwater (AFW), but with the primary and secondary levels not overlapping. The levels do overlap in "Pool BCM," and condensation occurs both within the pool region and in the region cooled by AFW. System conditions during Pool BCM are shown in Figure 1.

The benchmark test indicated that the performance of OTIS paralleled that of GERDA. The BCM was again shown to be an effective method of primary system heat removal. Periodic cold leg (CL) condensation events were observed, under the conditions of no leak, no high pressure injection (HPI), and low-elevation AFW injection. The transfer from low-elevation to high-elevation AFW injection stabilized the system conditions. These results are indicated in Figure 2.

Figure 2 is a pressure-time trace throughout the OTIS Benchmark Test. The upper and lower curves are the primary and secondary system pressures; the major test phases are also indicated on the figure. After the core power increase to 3.5% of scaled full power, the primary-to-secondary pressure difference gradually declined. This was caused by the periodic variations in loop conditions which generated successive pressurizer (PZR) insurges and outsurges. The attendant mixing gradually cooled the PZR liquid, causing the PZR to gain inventory; the SG condensing length increased correspondingly thus, for a fixed rate of heat transfer, the primary-to-secondary pressure difference (and primary pressure) decreased accordingly. The predominant pressure difference was roughly 100 psi. This corresponded to a primary-to-secondary temperature difference of 12F, or approximately 4F per percent of scaled full power.

Later in the benchmark test, the boundary system controls were varied beyond those used in GERDA. The reactor vessel vent valve was manually opened, then the AFW control was transferred from automatic to manual, both with no discernible effect. Subsequently the AFW injection elevation was changed from low to high in the SG. This elevation change caused the SG secondary pool, which had been highly subcooled, to heat toward the secondary saturation temperature. The primary condensate returning from the SG to the reactor vessel (RV) downcomer via the CL was no longer able to condense the primary vapor in the RV region, thus the condensation events ceased and the primary conditions stabilized. Similarly, had HPI been used in these pseudo-steady state tests, the periodic condensation events would not have occurred.

#### HPI-PORV COOLING

A single HPI-PORV (Bleed and Feed) Cooling test was performed. To accentuate the effects of this mode of cooling, no leak was simulated and the SG was isolated upon test initiation. As the test progressed, the relatively stagnant hot leg U-bend (HLUB) fluid reached saturation and the primary system pressure stabilized. Also, as loop flow diminished and then began to oscillate, the primary system fluid conditions became increasingly variable both with time and

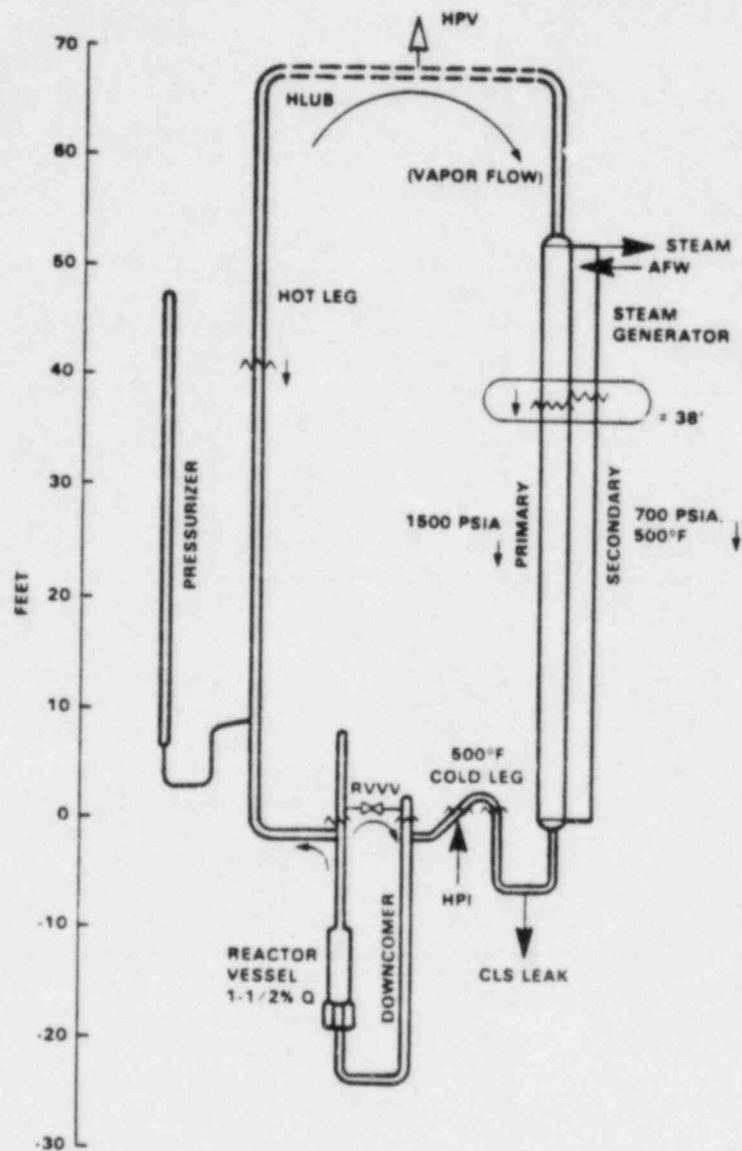
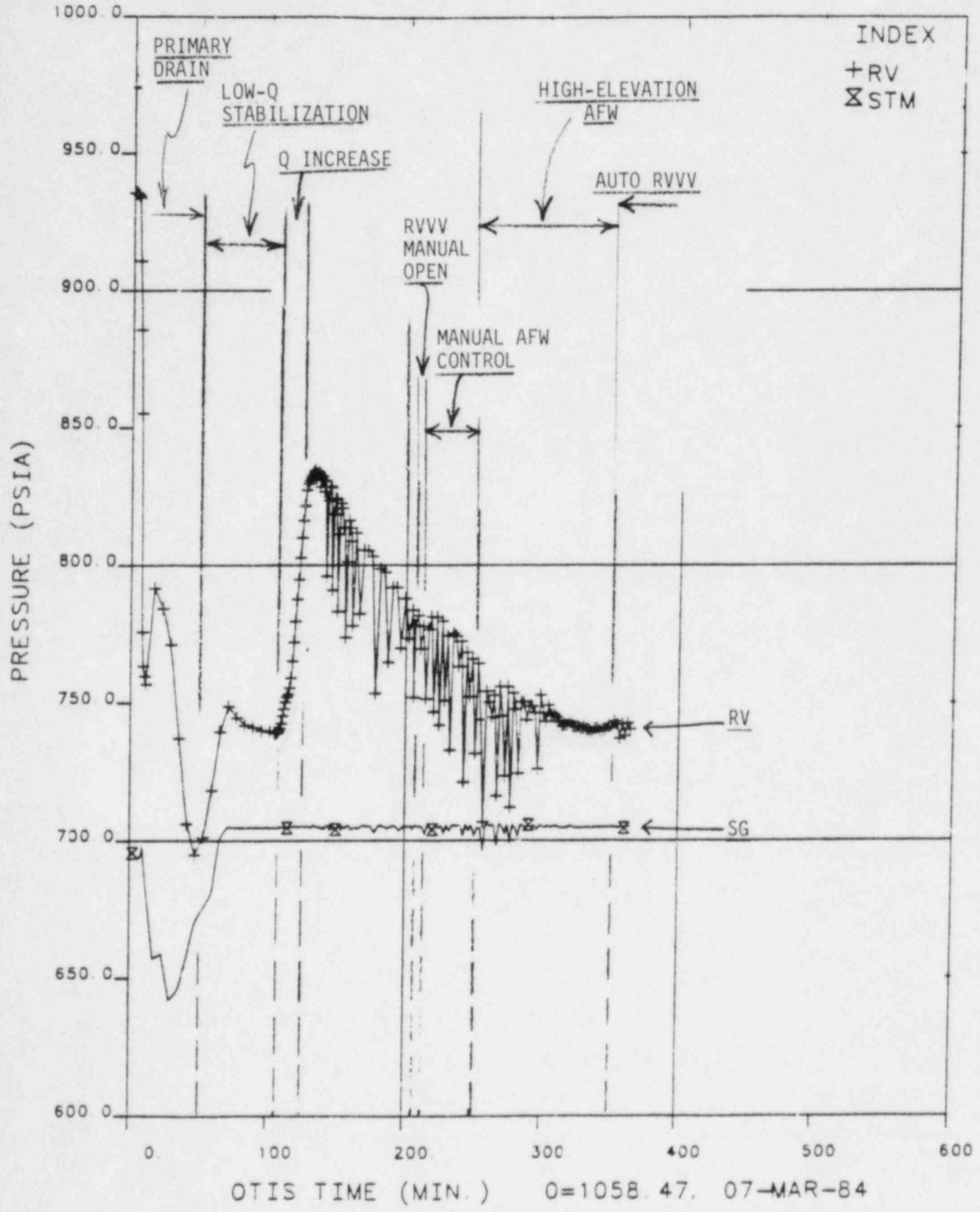


FIGURE 1 - Boiler - Condenser Mode (BCM)

OTIS layout showing fluid conditions during Pool BCM.

Figure 2. GERDA-OTIS Benchmark

Pressure Vs. Time Showing Test Evolutions



with elevation. Variations notwithstanding, the core-exit fluid cooled at a roughly constant rate, 60F/h, throughout the transient. The core-region fluid temperatures are shown in Figure 3.

The primary and secondary saturation temperatures are also plotted on Figure 3. The abrupt increase in primary saturation temperature at the initiation of the transient corresponded to the initial primary pressure rise to the PORV actuation pressure. The fluid in the RV head saturated and subsequently superheated. But the core-exit fluid reached saturation only briefly, within a few minutes of PORV actuation, then remained subcooled for the duration of the cooldown. Examining the core-exit and SG secondary fluid temperatures shown in Figure 3, it is evident that they track together as the loop flow rate diminished. Also, the primary fluid temperatures became increasingly variable as the test progressed. Finally, the cooldown of the core-region fluid was remarkably constant.

#### NATURAL CIRCULATION COOLDOWN

Two natural circulation cooldowns were performed. RV head voiding and its effects were of particular interest. No venting was performed in the first test; in the second test the RV Upper Head (RVUH) vent was actuated after the head had voided. In both tests, the head-region fluid did void as the primary system was depressurized below its saturation conditions. Even though the RV quickly voided down to the reactor vessel vent valve (RVVV) elevation and void generation continued as the primary system was further depressurized, the loop flow continued uninterrupted and the cooldown was maintained. When the RVUH vent was used, the head void was rapidly eliminated, and the head was refilled and cooled. The loop conditions in these tests with and without venting were quite similar, however, and they were maintained within the specified pressure-temperature envelope throughout both tests.

Levels versus time without venting are shown in Figure 4. The RV level decrease with voiding is clearly evident just beyond six hours. There was a corresponding increase in PZR level, reflecting the displacement of the RV head liquid. The RV collapsed liquid level dropped to approximately 0.6 ft, the elevation of the RVVV, which is more than two feet above the elevation of the HL nozzle. The subsequent vapor generation was discharged through the RVVV and condensed in the upper downcomer, permitting natural circulation to continue unimpeded.

#### OPERATOR-CONTROLLED TRANSIENTS

Two of the fifteen OTIS tests were controlled by a plant-trained operator.<sup>5</sup> These tests represented a significant departure from the other tests in which operator actions were minimized to enhance the analysis and modeling of the results. The HPI characteristics were varied between the two tests. Both tests used the nominal break configuration, namely a (scaled) 10-cm<sup>2</sup> cold leg suction (CLS) break. The leak was isolated at 30 min, and AFW was simulated to be unavailable until 1 h. The operator exercised similar control of the tests, even though the HPI characteristics were quite dissimilar between the tests. The operator actuated the PORV to control primary system pressure. When AFW became available, the operator throttled the AFW flow rate to gradually depressurize the primary through the BCM. Both test transients were completed relatively rapidly--the loop was refilled within approximately 15 minutes after AFW became available.

Figure 3. Core-Region Fluid Temperatures, HPI-PORV Cooling

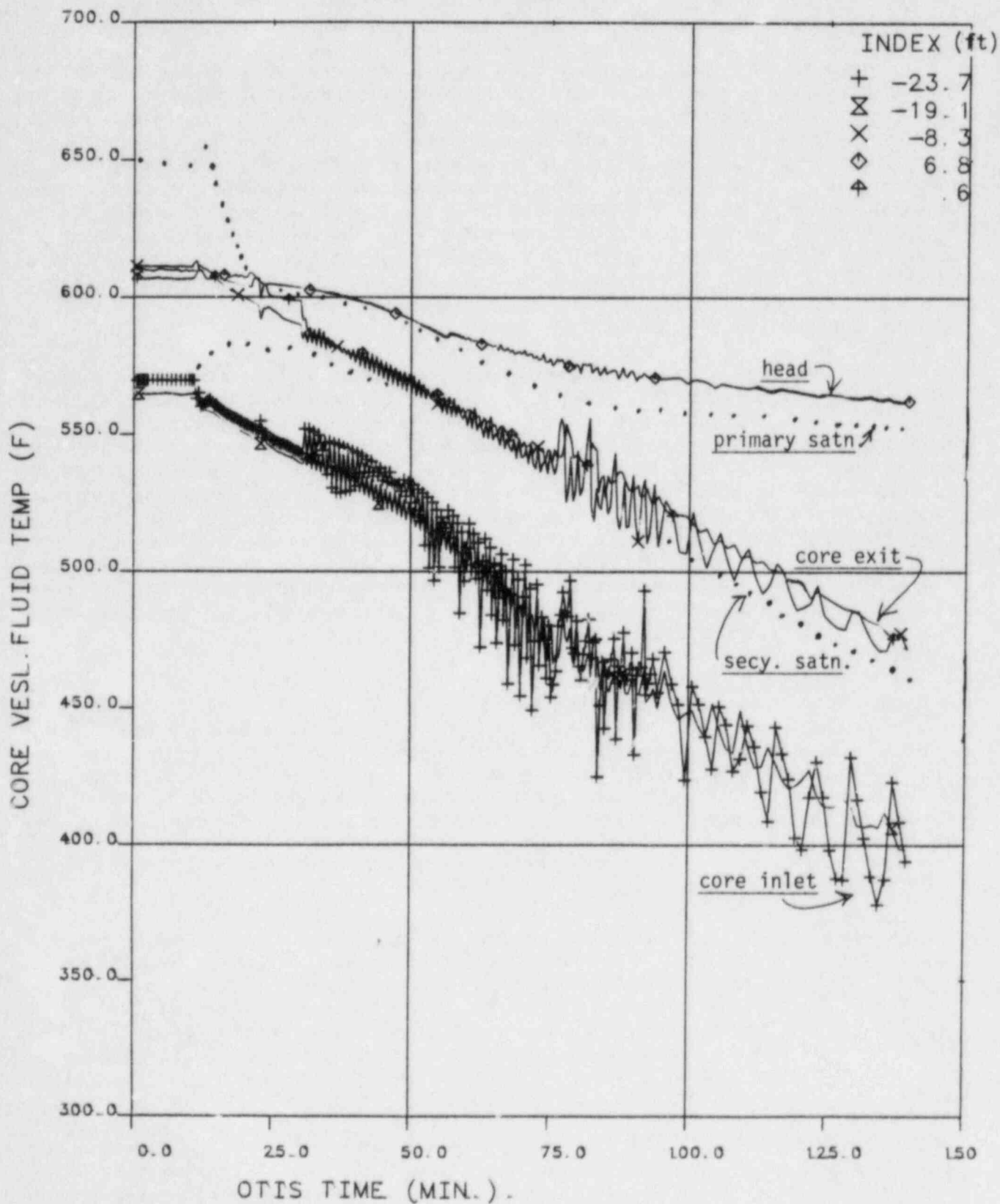
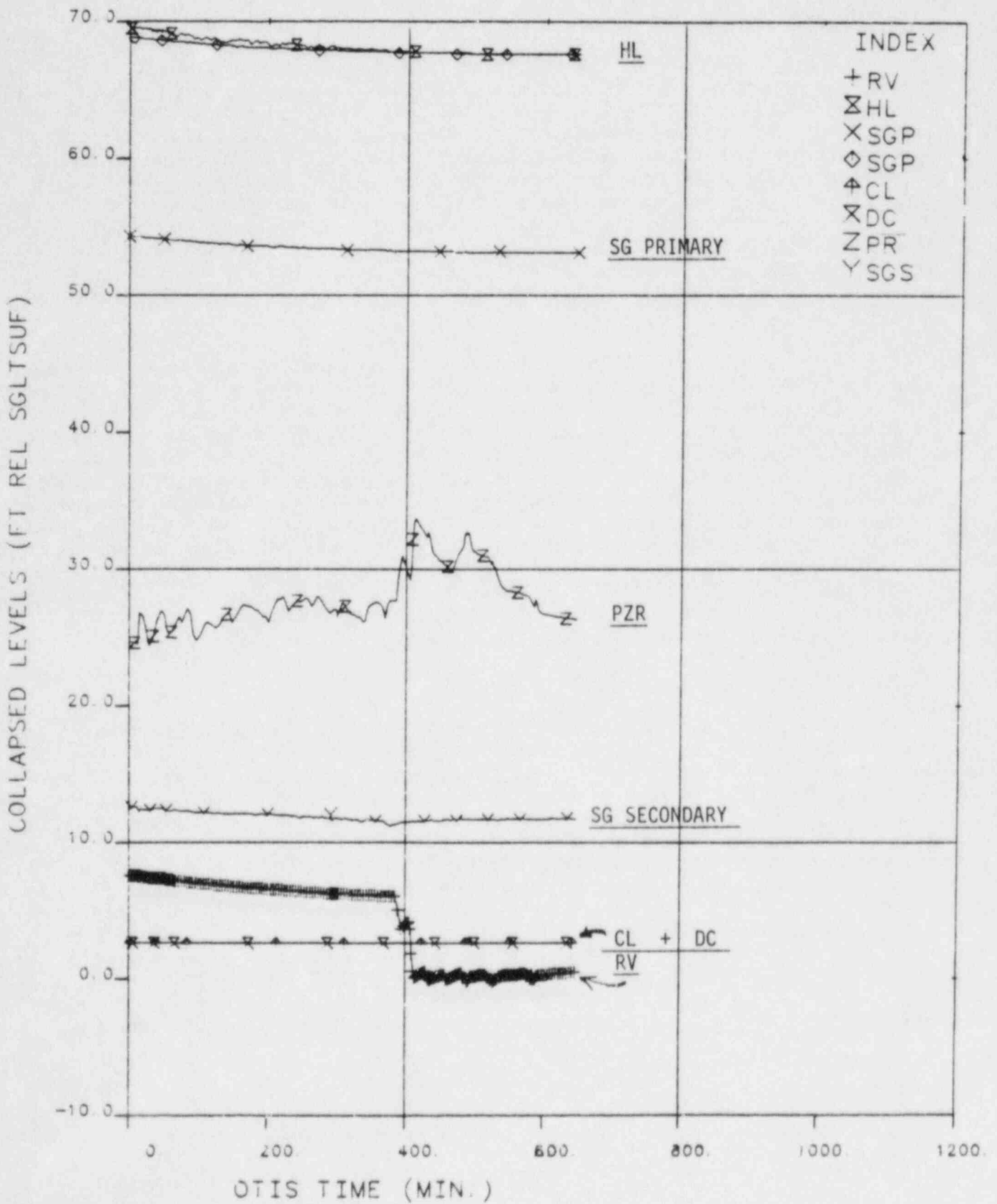


FIGURE 4 - Liquid Levels, Natural Circulation Cooldown (without venting)





## GUARD HEATER EFFECTS

The OTIS HL, RVUH, PZR, and surgeline were guard heated. The influences of guard heating were observed during the original OTIS testing, particularly with a larger break size. The larger-than-nominal break obtained a lower primary pressure and saturation temperature. There was an increased difference between the temperature at which the guard heater controls had been adjusted and the predominant loop fluid and metal temperatures. Two tests were added to the original OTIS test matrix to examine the effects of guard heating. Both were based on, and referenced to, the larger-than-nominal (15-cm<sup>2</sup>) break test. In the first test, the PZR was isolated at break initiation to eliminate the effects of its guard heaters and stored energy. The PZR was also isolated in the second test; in addition, all the guard heaters were deenergized upon test initiation.

The early transient events were virtually identical among the three tests with and without guard heaters and the PZR. These early events included the initial depressurization to saturation, intermittent and then interrupted loop flow, the BCM, and the beginning of refill. This portion of the transients lasted approximately one-half hour. Guard heating was observed to sustain the HLUB metal temperatures and thus to accentuate the primary system repressurization during refill. Without guard heating, loop refill was somewhat more rapid because of the dissipation of a portion of the upper-elevation fluid and metal energy. The method of RVVV control was also observed to influence refill; if the valve had been allowed to actuate automatically, it may have closed during the latter stages of refill and hastened the completion of refill. Of special significance, the HLUB metal remained somewhat warmer than the adjacent fluid, during a ten-hour transient without guard heating.

## SINGLE-VARIABLE TESTS

The fifth and final type of OTIS tests were the so-called "single-variable" tests. Each of these tests were based on the Nominal Test, singly varying the more significant boundary conditions. The Nominal Test used a 10-cm<sup>2</sup> CLS break, full-capacity and high-head HPI, a 38-ft SG secondary level, and an unisolated leak. The variations of the remaining six single-variable tests are shown in Table 1. These variations were: larger break size (15 versus 10 cm<sup>2</sup>), half-capacity HPI, reduced SG level (after refill of the SG secondary), break location (CL discharge versus suction), low versus high HPI shutoff head, and break isolation. These seven single-variable tests will be compared from initiation through refill and cooldown.

TABLE 1 SINGLE-VARIABLE TESTS

<u>Number</u>	<u>Test Description</u>	<u>Setting</u>	<u>Nominal</u>
1	Nominal	(Nominal)	-
2	Leak Size (Scaled cm <sup>2</sup> )	15	10
3	HPI Capacity	1/2	Full
4	SG Level (Feet)	10	38
5	Leak Location	CLD	CLS
6	HPI Characteristics	Low Head	High Head
7	Leak Isolation	Isolated	Unisolated

## Initial Conditions

Each test was begun by opening the designated break after initialization in sustained steady state. The initial conditions as well as the initial depressurization to loop saturation were virtually identical among the tests. The initial conditions of each of the single-variable tests were sufficiently similar to be represented by a single set of conditions. These included:

### PRIMARY

Core Power, %	4.17 (1% = 21.4 kw)
Pressure, psia	2200
T <sub>hot</sub> , F	609
T <sub>cold</sub> , F	571
Flow Rate, %	5.5 (1% = 0.259 lbm/s)
PZR Level, ft	19

### SECONDARY

Pressure, psia	1200
Level, ft	5.8
Feed & steam flow rates, %	2.25 (1% = 0.0265 lbm/s)
Saturation at 1200 psia, F	567
Max. steam temp., F	585
AFW temperature, F	115

The heat transfer rates defined by these initial conditions have been compared for consistency. The core power agreed with the heat transferred from the primary system, to ambient and to the SG, to within 0.1% of scaled full power. Similarly, the heat transferred to the SG primary agreed with that transferred from the SG, to ambient and to the feed-steam stream, again to within 0.1% of scaled full power. These differences in heat transfer rates, albeit small, reflected the uncertainties in both the estimates of the losses to ambient and the measurements of flow rates. The total difference in heat transfer rates was less than 6% of the initial core power level.

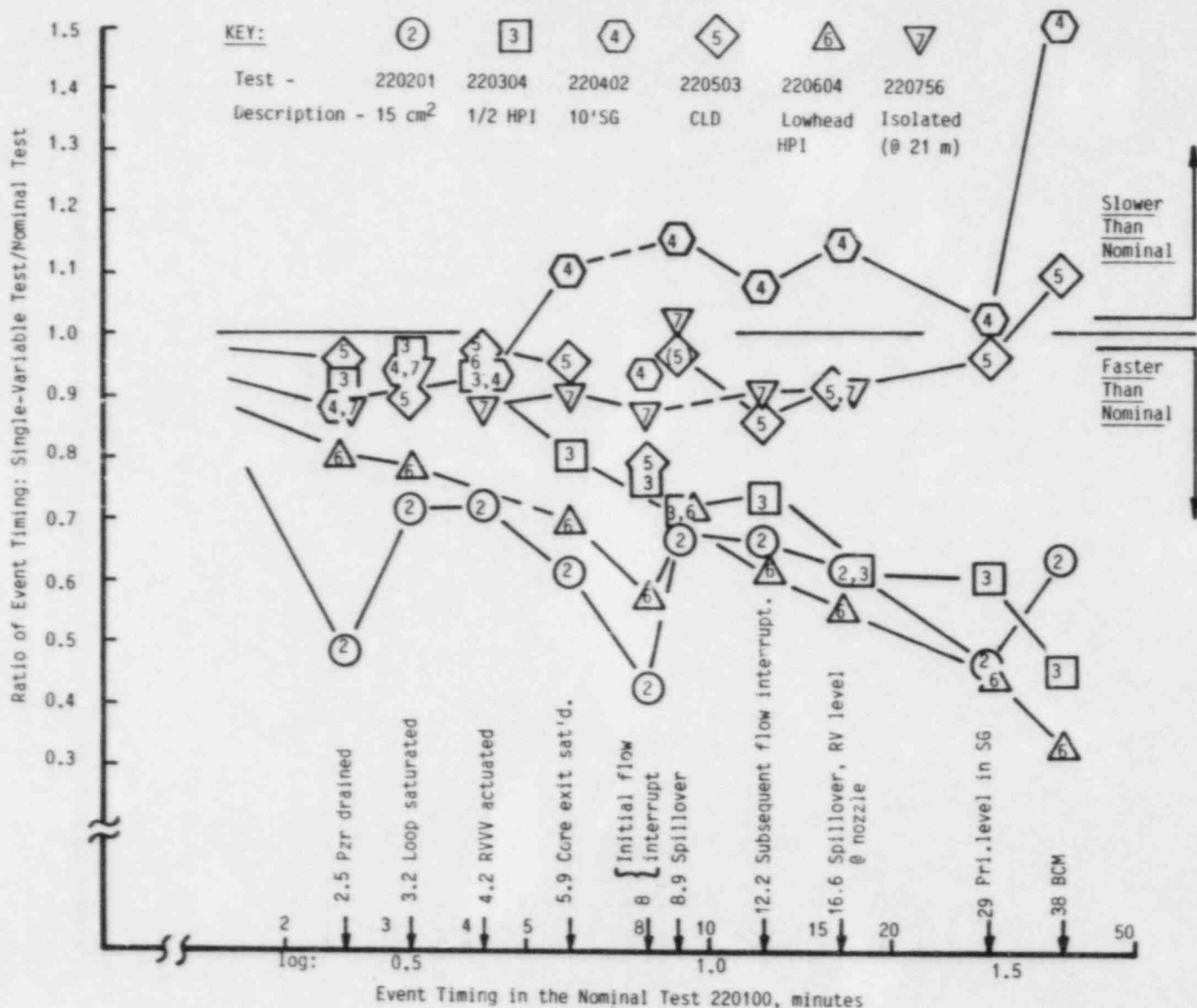
### Event Timing

The timing of the initial events in each of the single-variable tests is compared in Figure 5. The ordinate is the ratio of event times in each off-nominal test, to the event time in the Nominal Test. The abscissa shows the more-significant early events and their timing in the Nominal Transient. For example, the earliest event was PZR draining which occurred at 2.5 min in the Nominal Test. All the points corresponding to this event have ordinates of unity or less, indicating that PZR draining in the off-nominal tests occurred at the same time or earlier than in the Nominal Test. The time ratio for Test 2 is below 0.5, indicating that the PZR drained more than twice as fast as nominal (and in just over one minute) with the larger break size.

The time-versus-event plots of Figure 5 may be examined for trends. The transients generally began with near-nominal timing, but certain transients evolved more rapidly. More-rapid transients occurred in Tests 2, 3, and 6

FIGURE 5

Event Timing (Earlier Events)  
Single-Variable Tests Vs. Nominal Test



which used, respectively, a larger break size, reduced HPI capacity, and a low HPI shutoff head. These faster transients were each associated with an increased imbalance between HPI and break flow, caused by either an increased break size or by a decreased injection rate (at the relatively high initial primary system pressures). The timing of the Test 4 transient (with a reduced SG level) was near nominal until the BCM, which was much delayed. This is attributable not only to the lowered SG secondary pool height, but also to irregularities of the model feed control system. The measured feed rates can be used to benchmark this data.

## Pressure

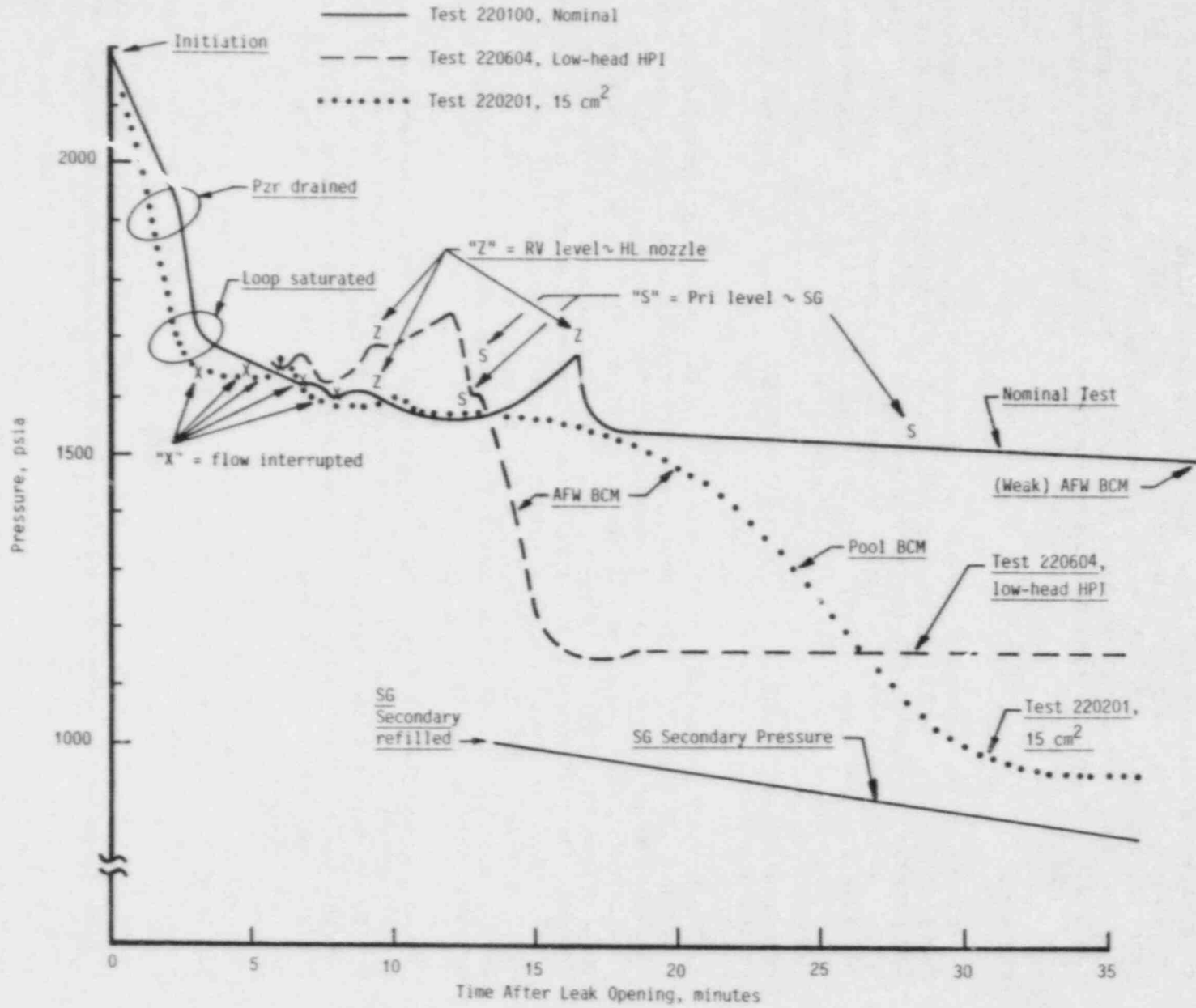
Primary system pressure was one of the more significant system indicators. Early in the transients, following the initial depressurization to saturation, the pressure in each of the tests ranged from 1600 to 1680 psia. This apparently narrow pressure range was remarkable because of the imposed inter-test variations. For example, there was virtually no HPI available during the early portions of the low-head HPI test, Test 6. HPI-leak cooling is the major method of heat removal remaining during periods of interrupted primary flow, therefore repressurization would seem likely without HPI. Figure 6 displays the early pressure trends.

The primary pressures for the Nominal, larger-break, and low-head HPI tests are shown in Figure 6. The pressures were the same initially, and remained similar through the initial depressurization to saturation and the subsequent flow interruptions (which are indicated on Figure 6). In the Nominal Test, the primary system gradually repressurized following flow interruption, then abruptly depressurized to roughly the initial saturation value when the RV collapsed liquid level descended to the elevation of the HL nozzle (this occurred at 16 min, as also shown on Figure 6). The primary level descended into the SG beyond 29 min, but AFW was inactive and the primary pressure continued to decrease only gradually.

The increased break flow of the larger-break test caused the early events to occur more rapidly than nominal. The primary level reached the elevation of the SG in only thirteen minutes; the period of interrupted flow was similarly shortened, thus there was virtually no primary repressurization. The primary pressure was reduced by primary-to-secondary heat transfer through both AFW BCM and Pool BCM.

There was little HPI-leak cooling in Test 6 (with low-head HPI), therefore the rate of primary repressurization following flow interruption was relatively high. But, without HPI, the rate of primary inventory loss was similarly enhanced. The primary level reached the SG elevations while AFW was still being used to refill the SG secondary. The AFW BCM rapidly reduced primary pressure to within 200 psi of the secondary pressure, and to within the pressure range of the low-head HPI pumps; the augmented HPI flow rate then reduced the rate of primary inventory loss. Had the primary level not reached the SG while AFW remained active, the continued rapid reduction of primary inventory would have quickly obtained primary-to-secondary heat transfer and primary pressure reduction through Pool BCM. In this case, the maximum primary pressure with low-head HPI would have been relatively high. Had it caused PORV actuation, the consequent enhancement of the rate of primary inventory loss would have further hastened the attainment of Pool BCM depressurization. Thus, the inherent

FIGURE 6 - Primary Pressure



integral-system interactions countered the imposed boundary system variations. With low-head HPI, the relatively early and robust AFW BCM interrupted the ongoing primary system repressurization. In this manner, the early primary system pressures were quite similar among the single-variable tests.

#### BCM And Timing

The preceding discussion of pressure trends has indicated the importance of BCM heat transfer and of the timing of the early events. These observations were highlighted in the guard heater effects test with the PZR isolated and the guard heaters in operation. As has been previously discussed, this test was based on the larger (15-cm<sup>2</sup>) break size. The primary and secondary pressures are shown in Figure 7. The behavior of primary pressure was customary through the initial blowdown, flow interruptions, and the uncovering of the HL nozzle.

The primary level reached the elevation of the SG upper tubesheet at 12 min (after leak actuation). At this time the refill of the SG secondary was just nearing completion. AFW was active, but the AFW flow rate was being reduced in anticipation of constant level control. These circumstances obtained a brief but pronounced depressurization of the primary system through AFW BCM. The depressurization reduced the primary system pressure roughly half way from the starting pressure to the SG secondary pressure. Following the termination of AFW, the primary depressurized only gradually through lingering SG heat transfer. At 24 min the primary level in the SG reached the elevation of the secondary pool, triggering Pool BCM and the second phase of primary depressurization. The primary pressure was then reduced almost to that of the SG secondary. But the equilibrium pressure, at which the HPI capacity equaled the leak flow rate, was well below the current primary and secondary pressures. The primary level remained below the elevation of the SG secondary pool and the primary remained coupled to the secondary through a sustained Pool BCM. The results of this test are thus especially useful for code benchmarking. Both AFW BCM and Pool BCM were evident and distinct, and occurred within a half hour of test initiation.

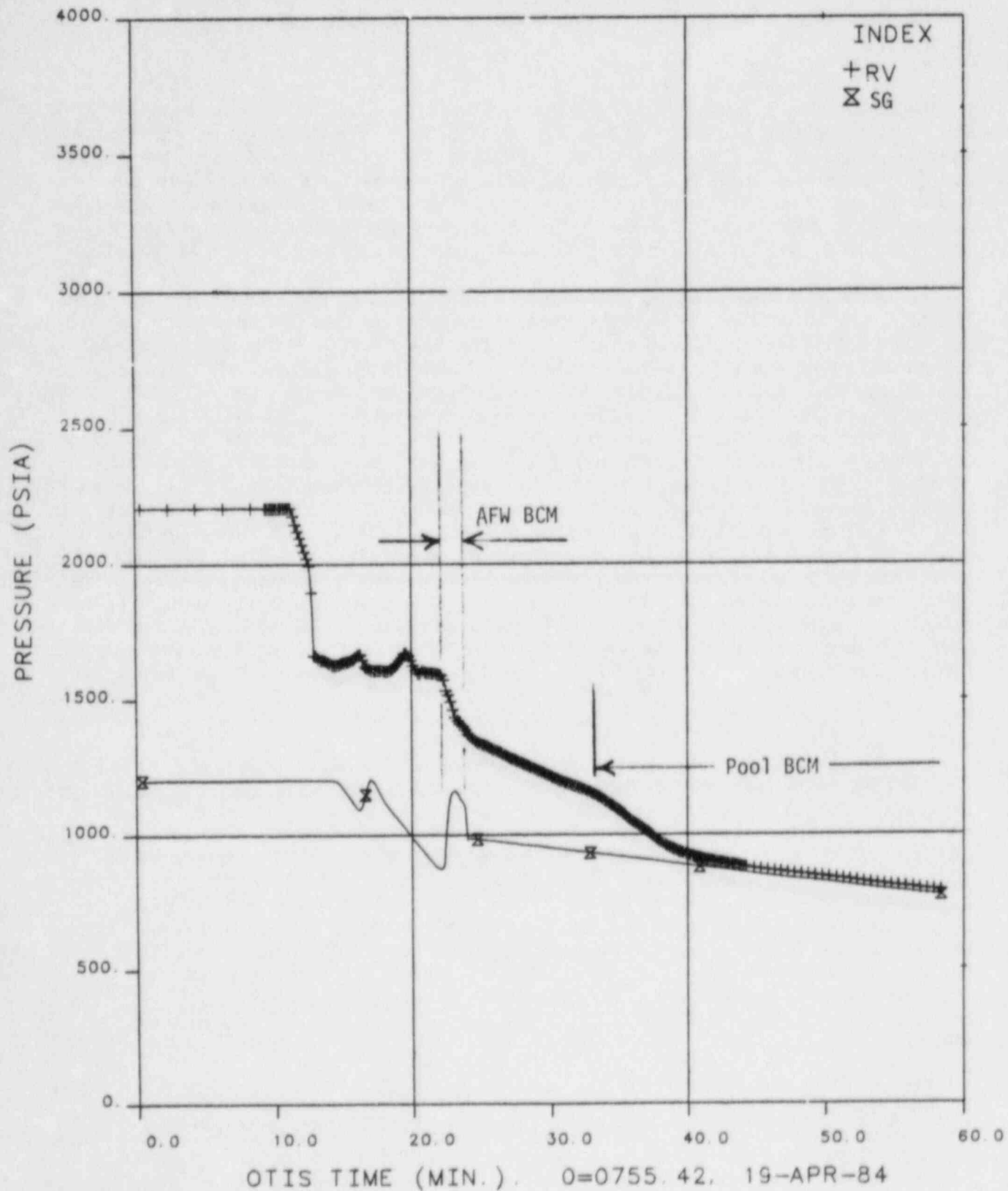
#### Refill

The timing of the single-variable transients generally converged during the completion of loop (HL) refill. The isolated-leak test was an exception; following the closure of the leak, refill was achieved quite rapidly and at a relatively high primary system pressure. In the remaining single-variable tests, the primary system gradually repressurized as refill progressed. The loop conditions tended toward equilibrium and the rate of refill diminished. Refill was not achieved during the test using half-capacity HPI. In the other tests, HL refill was completed only after the HL vent had been opened. Event timing generally converged following vent actuation. Natural circulation began with a few minutes after the completion of HL refill. In each of the tests, core cooling was maintained throughout the transients.

#### SUMMARY

Each of the Single-Variable tests was initialized almost identically. Test initiation and the initial transient were similar among the tests. The initial heat balances were consistent within 0.2% of scaled full power. The major post-SBLOCA events were observed, including the depressurization to saturation, intermittent flow, flow interruption with repressurization, BCM, refill, and

FIGURE 7 - Depressurization By AFW BCM and Pool BCM  
 PRIMARY AND SECONDARY PRESSURE VERSUS TIME



post-refill circulation and cooldown. The transients varied in response to the imposed boundary system variations. The OTIS tests obtained challenging and self-consistent integral system data with which to benchmark system codes.<sup>6,7</sup>

#### LEGAL NOTICE

This report was prepared by the Babcock & Wilcox Company as an account of work sponsored by the Nuclear Regulatory Commission (NRC), the Electric Power Research Institute (Institute), the Babcock & Wilcox Company (B&W), and the B&W Owners' Group. No person acting on behalf of the NRC, the Institute, members of the Institute, B&W, or the B&W Owners' Group:

- 1) makes any warranty, express or implied, with respect to the use of any information, apparatus, method, or process disclosed in this report or that such use may not infringe privately-owned rights; or
- 2) assumes any liabilities with respect to the use of, or for damages resulting from the use of any information, apparatus, method, or process disclosed in this report.

#### REFERENCES

1. C. D. Morgan, "MIST Scaling and Design Considerations," Proceedings of the International Nuclear Power Plant Thermal Hydraulics and Operations Topical Meeting, Taipei, Taiwan, Republic of China, October 22-24, 1984; pp. B3-1 - B3-11.
2. C. D. Morgan, "The OTIS/MIST Test Program," First Meeting of the International Thermal Hydraulic Code Assessment and Applications Program, Silver Springs, Maryland, April 23-26, 1985.
3. H. R. Carter, "Integral System Test Program," Ninth Annual Operating and Maintenance Experience Conference, Lynchburg, Virginia, 1983.
4. H. R. Carter and J. R. Gloude-mans, "An Experimental Study of the Post-Small Break Loss-of-Coolant Accident Phenomena In a Scaled Babcock & Wilcox System," Proceedings of the Twelfth Water Reactor Safety Research Information Meeting, Gaithersburg, Maryland, October 22-26, 1984; Vol. 1, pp. 113-135.
5. D. P. Birmingham, R. L. Black, and G. C. Rush, "An Experimental Study of the Application of Abnormal Transient Operating Guidelines (ATOG) to the Babcock & Wilcox Nuclear Steam Supply System During a Small Break Loss-of-Coolant Accident," 23rd ASME/AICHE/ANS National Heat Transfer Conference, Denver, August 6-9, 1985.
6. R. K. Fujita and T. D. Knight, "TRAC-PF1/MOD1 Support Calculations for the MIST/OTIS Program," Proceedings of the Twelfth Water Reactor Safety Research Information Meeting, Gaithersburg, Maryland, October 22-26, 1984; Vol. 1, pp. 153-173.
7. M. T. Childerson and R. K. Fujita, "TRAC-PF1 Code Verification with Data from the OTIS Test Facility," (to be presented at the 1985 ASME Winter Annual Meeting).



UNIVERSITY OF MARYLAND TEST FACILITY RESULTS  
University of Maryland, College Park, MD 20742

Z. Wang  
W.K. Lin  
C.J. Munno

M. Popp  
D.W. Sallet  
F.J. Munno

M. Di Marzo  
M. Massoud  
Y.Y. Hsu

The UMCP 2x4 Loop construction was completed in this summer. The test facility is a 1/500-scale by volume of the B&W power plant (lowered loop), with scaled pressure vessel, OTSG-type steam generators (2), pressurizer. The pressure vessel is provided with annulus downcomer and flapper-type vent valves. The power is provided by 15 electrical heater rods.

Since late spring, many tests were performed. But in this report, main emphases were placed at natural circulation tests and SB LOCA depressurization tests. Also reported were tests results for heat loss and for hydraulic characterization, as well as modeling of Reactor Vessel Vent Valves.

The main point to be conveyed is that for the depressurization phase we can scale low pressure test to high pressure condition through pressure ratio  $p/p_0$  as function of coolant inventory ratio.

## I. INTRODUCTION

The UMCP 2x4 Loop test facility is a simulation of the B&W lowered loop power plant. The volume is scaled 500:1. The height is reduced by a factor of about 4 and the flow areas are proportionally enlarged. The layout and design details were reported in last WSRS Information Meeting (1984) and can be found in Ref. 1.

The current objectives of UMCP Loop are to investigate:

- U-bend phase separation
- RVVV (Reactor Vessel Vent Valve) effect
- Interaction between primary and secondary thermal hydraulics.

The main missions of the UMCP Loop, as we visualize, are four folds:

- To obtain data for modeling B&W plant
- To provide data for code assessment
- To provide data to assess the sensitivity of MIST atypicalities
- To develop a methodology to model the high pressure (2200 psia) plant system by a low pressure (300 psia) test system.

Since the completion of the UMCP Loop in late spring, many tests have been conducted (Table 1). However, the bulk of attentions were directed to the pressure-scaling for SBLOCA and to obtain data of natural circulation. In this report, although the results of characterization tests as well as some pertinent analysis are also reported, the main part will be devoted to Natural Circulation test results and SBLOCA depressurization test results.

## II. NATURAL CIRCULATION LOOP CHARACTERISTICS

In order to determine the UMCP single-phase characteristics, several steady-state tests were performed. The loop characteristics include;

- hot leg mass flow rate versus secondary side mass flow rate and inlet subcooling,
- heat exchanger overall heat transfer coefficient versus hot leg mass flow rate,
- system thermal length versus hot leg mass flow rate,
- system flow resistance versus hot leg mass flow rate.

The time to achieve steady-state was estimated from:

$$t = \frac{(W_{s s} c_s + UA/2) \rho c_p V}{W_{s s} c_s UA} \quad (1)$$

The actual time, however, was allowed to well exceed that given by Equation (1) to ensure attainment of steady-state condition.

Shown in Figure 1 is the inferred hot leg mass flow rate versus secondary side mass flow rate. The solid line represents curve fit to the data. The hot leg mass flow rate was not measured directly due to the lack of any primary side flow measuring device.

The overall heat transfer coefficient is calculated, for the counter current heat exchangers, by using the heat reject rate and measured primary and secondary sides temperatures. Its variation with hot leg flow rate is depicted in Figure 2. It is interesting to note the near linear relationship between  $UA$  and  $W_{HL}$ . In fact, in single-phase natural circulation, the overall heat transfer coefficient shows a strong dependency on the primary side flow rate and is rather independent of that of the secondary side.

System thermal length, as shown in Figure 3, is calculated theoretically using the experimental data. The equation used to calculate  $L_{Th}$ , is derived from a heat balance in the heat exchanger and is as follows;

$$(L_{Th})_{HX} = \left( \frac{T_{pi} - T}{T_{pi} - T_{po}} \right) \left( 1 + \frac{1 - \text{Exp}(b-a)}{a-b} \right) L_{HX} \quad (2)$$

where  $a$ ,  $b$ , and  $T$  in Equation (2) are given by

$$a = \frac{UA}{W_{s s} c_s} \quad (3)$$

$$b = \frac{UA}{W_{HL} c_{HL}} \quad (4)$$

and

$$T = \frac{aT_{so} - bT_{pi}}{a-b} \quad (5)$$

respectively. The rest of variables are defined in the nomenclature. Having  $(L_{Th})_{HX}$ , the system thermal length can be calculated from;

$$l_{Th} = L_{HX} - (L_{Th})_{HX} - (L_{Th})_c - Z_{HX} \quad (6)$$

where in Equation (6),  $(L_{Th})_{HX}$  is measured from the heat exchanger upper tube sheet,  $(L_{Th})_c$  is measured from core inlet plane, and  $Z_{HX}$  is the distance between the heat exchanger lower tube sheet and core inlet plane, respectively.

Notice that an increase in hot leg mass flow rate, which in turn stems from an increase in the secondary side mass flow rate (Figure 1), reduces the system thermal length or equivalently the buoyancy head. The reason is due to the fact that increased mass flow rate reduces the temperature differences alongside the heat exchanger which tends to flatten the temperature profile. This in turn brings the thermal center of the heat exchanger closer to the geometrical center.

Having the thermal length, system flow resistance,  $\hat{R}_1 = R_{1loop} + 4 R_v$  is calculated from;

$$\hat{R}_1 = \frac{2\beta\rho^2 g l_{Th} q_1}{(W_{HL})_1^3 c_p} \quad (7)$$

Notice that Equation (7) is derived on the assumption that flow resistance is constant and does not depend upon the flow rate, the same assumption is made for the system thermal length. The calculated  $\hat{R}$  is depicted in Figure 4.

To check the accuracy of the calculational quantities, the heat exchanger mid point temperature is measured and predicted with that calculated from;

$$T_s(z) = T_{so} - \frac{b}{a} (T_{pi} - T) \{1 - \text{Exp}(b-a) \left(\frac{z}{L_{HX}}\right)\} \quad (8)$$

where  $a$ ,  $b$ , and  $T$  in Equation (8) are given by Equations (3) through (5), respectively.

### III. SMALL BREAK LOCA PRELIMINARY RESULTS

#### III. 1 Background

The small Break LOCA events are controlled by a multitude of parameters. The sequence of the various phenomenology is rather complex and can vary greatly for various situations.

In order to proceed in the study of the small break phenomena in an orderly fashion sequence of events proposed in the SBLOCA nominal case TRAC Run 300,000 is considered.

Three major check points were identified by looking at the behavior of the various parameters in the TRAC simulation (See Figures 5 and 6).

- a) the pressurizer empties at the same time the hot leg experiences flashing
- b) the HPI flow equals the break flow
- c) the BC mode is established in both steam generators.  
(Boiling Condensation Mode)

In accordance with this scenario, three transients are identified:

- a) rapid depressurization transient (time zero to 190 seconds)
- b) flow equalization transient (from 190 seconds to 3000 seconds)
- c) two phase flow transient (from 3000 seconds to 4500 seconds)

A brief description of each transient is given in the following;

#### III. 2 Rapid Depressurization Transient

In this transient the loop is subcooled and the void is present only in the pressurizer. Flashing in the hot leg will occur as the pressurizer empties and these two events will determine the end of this first transient. A simplistic model was proposed to scale the events and the various boundary conditions (eg.: decay power, break size, etc....). Experimental data were collected and will be presented and discussed later on.

#### III. 3 Flow Equalization Transient

The flashing in the hot leg and the complete drainage of the pressurizer are the two coincident events that will initiate this second transient. The HPI pump will start to inject coolant at this initial time with a constant flow rate as prescribed by the nominal case. Interruption and resumption of natural circulation will be observed in this transient and BC mode will occur in one of the steam generators. The flow equalization between the HPI and the break will determine the end of this transient.

### III. 4 Two-phase Flow Transient

In this last phase (governed by conservation of mass considerations), the phenomenology of the previous transient is observed while stable BC mode will be established in the other steam generator; at that time the small break event will be considered concluded.

### III. 5 Scaling Principles for the Rapid Depressurization Transient

The problem of adequately scaling the various parameter at low pressure was addressed with a highly simplified model, based on the first law of thermodynamics applied on the pressurizer. The results of the analytical computations were reported in a recent paper [2] and are also presented in Figures 7 and 8. From the model we deduced that adequate representation of the pressure decay should be obtained by referring it to the void generation. The results of this important statement are presented in Figure 9. The principle of using the void fraction as a time scale parameter is a major ingredient of the pressure scaling and the results of quite different experiments correlated along such a principle are rather interesting, as it will be shown in the following:

The initial pressure for the various rapid depressurization tests was fixed at 1.5 MPa and the pressurizer liquid inventory was scaled by volume (1:500) to the prototype inventory (50% of full). The final pressure of this transient was evaluated by considering the pressure ratio illustrated in Figure 7. Hence the final pressure was estimated at 1.38 MPa. The initial core temperature was determined as the saturation temperature at such pressure (195 C). The break size was obtained by considering the simple flow through an orifice described as

$$Q = 0.61 A \sqrt{2p/\rho_w} \quad (9)$$

where the volumetric flow rate was scaled by volume and the initial pressure is used. The hole diameter obtained in this fashion is equal to  $D = 2.55 \times 10^{-2}$  m (0.10 inches). The actual diameters of the break used are 1/4, 1/8, 1/16 of an inch. The decay power is approximated with a constant power level through the three minutes of the transient. The scaling of the decay power is based on single-phase natural circulation.

$$\dot{W}_{MODEL} = (4.4 \times 10^3 \frac{\phi_{PROTOTYPE}}{\phi_{MODEL}})^{-1} \dot{W}_{PROTOTYPE} \quad (10)$$

where  $\phi = (\rho c / 2\beta g)$

Figure 10 shows the prototype power versus the model power (in percent). Table 2 summarizes the test procedures.

### III. 6 Test Data and Discussion

The various information collected by the data acquisition system allows to describe the major events during the rapid depressurization transient. In particular, the pressurizer water inventory (namely the system void) and the system pressure are the most important data. The pressurizer water inventory versus time is presented in Figure 11. Three different break sizes are used ( $1/4''$ ,  $1/8''$  and  $1/16''$ ). The calculated value is for a break size of 0.10 inch. The time elapsed from the break initiation is about 200 seconds well in agreement with the TRAC calculation. Figure 12 illustrates the pressure ratio decay as a function of time for various power levels. It is found that best agreement with the calculated values is obtained for a decay power of about 2.3% of full power. This percent of full power should be compared with the value deduced from the ANS decay power curve. Which indicates that values in the range of 3% are expected. The most important result of this first round of experiment is obtained by comparing the pressure ratio of the various events with the liquid fraction. Figure 13 shows that for very different events the experimental results are collapsed to a single generalized behavior. Note that the depressurization with a  $1/16''$  break last about ten minutes while the same event with  $1/4''$  break occurs in about 40 seconds. This information allows us to conclude that time can be replaced by liquid volume fraction in the scaling of the event. This conclusion will be the basis for the time stretching that will have to be performed in the following phases of the small break event. Figures 14 and 15 typify the behavior of pressure and pressurizer level for the flow equalization transient. These two figures are qualitative in nature and are included to give a first glance of the future set of experiments to be performed at the UMCP facility.

#### IV HEAT LOSS TEST

To measure the amount of heat loss through insulated system, cork patch is used. They are attached to the wall (inside the insulation) at different locations. Assuming negligible heat loss through the wall of secondary side of S.G., cork patches are located at three locations of one hot leg and those of one cold leg, and two on the vessel (See Figure 16). By measuring the temperature difference across cork and the conductivity of cork at that average temperature (See Figure 17), the amount of heat being transferred to the environment is estimated. (Thickness of cork = 0.005m).

After several tests, it is found the estimated total heat loss is only about 0.5% of total input power, of which 0.24% is in two hot legs, 0.23% is in four cold legs and 0.03% is in vessel. It indicates that three inches thick of fiberglass heavy density insulation works very well.

#### V HEAT BALANCE TEST

This test is done by comparing the input power in core and power taken out from steam generator when system is at steady state. Input power data is taken directly from power calibration curve, while the power removed from steam generator is calculated by measuring the secondary flow rate and temperature difference in the secondary side of S.G.

Figure 18 shows the trend of deviation in heat balance versus % of core power. It indicates that deviation is reasonable (within  $\pm 7\%$ ) as core power goes up above 70%. But it is not good at low power range (below 70%). The reason for this discrepancy in low power range is due to the fact that some mismatches are found in the present power module system when operating at low power range. Effort is being made to rectify this situation.

## V.1 REACTOR VESSEL CHARACTERIZATION

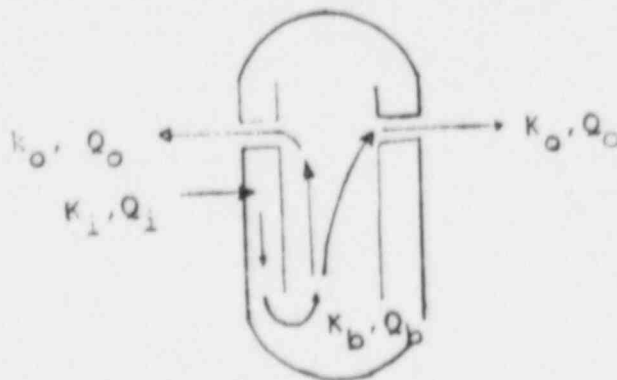
In order to determine the internal flow resistance structure of the vessel, a number of flow configurations are implemented and the pressure drops are measured for the various cases. A summary of the different configurations versus resistances ( $K_V$ ) for the various configuration is presented in Table 3.

Three loss coefficients were defined  $k_i$ ,  $k_o$ ,  $k_b$  so that

$$K_V Q^2 = k_i Q_i^2 + k_o Q_o^2 + k_b Q_b^2 \quad (11)$$

where:

- $K_{\text{vessel}}$  : total loss coefficient of the vessel
- $Q_{\text{tot}}$  : total flowrate
- $k_i$  : loss coefficient due to the inlet stream
- $Q_i$  : flowrate from the inlet into the vessel, is affected by the symmetrical or unsymmetrical configuration, where symmetrical case is defined the flowrate in each of the 2 cold legs or 2 hot legs are the same for example, the symmetrical cases:
  - 4 inlets:  $Q_i = Q_{\text{tot}}/4$
  - 2 inlets:  $Q_i = Q_{\text{tot}}/2$
  - 1 inlet:  $Q_i = Q_{\text{tot}}$
- $k_o$  : loss coefficient due to the outlet stream
- $Q_o$  : flowrate in the two outlets, for convenient, one may set this two outlets the same flowrate by control valves for example, if 2 outlets  $Q_o = Q_{\text{tot}}/2$   
1 outlet  $Q_o = Q_{\text{tot}}$
- $k_b$  : loss coefficient due to the flow processes in the vessel
- $Q_b$  : flowrate in the vessel, for steady-state  $Q_b = Q_{\text{tot}}$



Minor Losses in the Vessel



In this case,  $k_p$  can be generally divided into another two values according to their directions,  $k_v$  (loss coefficient of the vertical flow) and  $k_o$  (loss coefficient of the cross flow), where vertical flow can be imagined as the flow stream takes 45 degree direction, and cross flow can be imagined as the flow stream takes 135 degree direction. Furthermore, from the macroscopic view, will be the average of the  $k_v$  and  $k_o$  depend on how many stream there are, Figure 19 show these three cases:

The discrepancies between the analytical prediction of the model and the experimental data are listed in the last column of Table 4. In conclusion, the model seems to predict the vessel resistance reasonably well.

## VII RVVV SCALING ANALYSIS

For the UMCP 2x4 loop prototypical flapper valves were chosen, as shown in Figure 20. The use of flapper valves in conjunction with the annular downcomer insures that prototypical phenomena can be observed in the model. According to Ref. 3 the RVVV s will be partially open under certain subcooled natural circulation conditions. The scaling requirements for a steady single phase flow follow from the simplified energy equations

$$\text{Core-HL-SG-DC: } \Delta p = \frac{\rho Q_{HL}^2}{2} K_{HL}^* - \frac{\dot{q}\beta g \Delta z_{bc}}{Q_{HL} c_p} \quad (12)$$

$$\text{DC-Core: } \Delta p = \frac{q\beta g \Delta z_{ca}}{Q_c c_p} - \frac{\rho Q_c^2}{2} K_c^* \quad (13)$$

$$\text{RVVV path: } \Delta p = \frac{(Q_{VV}/4)^2}{2} \frac{K_{VV}}{A_{VV}^2} = \frac{Q_{VV}^2}{32} K_{VV}^* \quad (14)$$

Here  $K^* = \sum K_i / A_i^2$ ;  $i$  = number of loop component involved. Inserting Equation (14) into (12) and (13) yields two equations which are written in dimensionless form. Four dimensionless parameters are obtained:

$$\Pi_1 = \left(\frac{Q_{VV}}{Q_{HL}}\right)^2 \frac{K_{VV}^*}{K_{HL}^*} \quad (15)$$

$$\Pi_2 = \frac{\dot{q}\beta g \Delta z_{bc}}{\rho Q_{HL}^3 c_p K_{HL}^*} \quad (16)$$

$$\Pi_3 = \left(\frac{Q_{VV}}{Q_c}\right)^2 \frac{K_{VV}^*}{K_c^*} \quad (17)$$

$$\Pi_4 = \frac{\dot{q} \beta g \Delta z_{ca}}{\rho Q_c^2 c_p K_c^*} \quad (18)$$

The resulting scaling requirements for a true time simulation ( $\delta = Q_M/Q_P = V_M/V_P$ ) are:

$$\frac{(K_{VV}^*)_M}{(K_{VV}^*)_P} = \frac{(K_{HL}^*)_M}{(K_{HL}^*)_P} \quad (19)$$

$$\frac{(\Delta z_{bc})_M}{(\Delta z_{bc})_P} = \frac{\dot{q}_P}{\dot{q}_M} \delta^3 \frac{\beta_{P^c PM}^0}{\beta_{M^c PP}^0} \frac{(K_{HL}^*)_M}{(K_{HL}^*)_P} \quad (20)$$

$$\frac{(K_{VV}^*)_M}{(K_{VV}^*)_P} = \frac{(K_c^*)_M}{(K_c^*)_P} \quad (21)$$

$$\frac{(\Delta z_{ca})_M}{(\Delta z_{ca})_P} = \frac{\dot{q}_M}{\dot{q}_P} \delta^3 \frac{\beta_{P^c PM}^0}{\beta_{M^c PP}^0} \frac{(K_c^*)_M}{(K_c^*)_P} \quad (22)$$

If it is assumed that the model geometry has been chosen, then there are 4 requirements and 6 variables, namely  $K_{VV}^*$ ,  $K_{HL}^*$ ,  $K_c^*$ ,  $\Delta z_{bc}$ ,  $\Delta z_{ca}$  and  $q$ . Two of the variables can be chosen, the others will be fixed due to the scaling requirements. The value for the pressure differential in the model,  $\Delta p_M$  should be picked such that the flapper valve will function properly. This choice of  $p_M$  will fix all  $K^*$  values. Now either one of the two  $\Delta z$ 's can be chosen in the model design. Then all variables are fixed, including the scaled power  $\dot{q}$ . Example: for the UMCP 2x4 Loop (300 psi); pick  $\Delta p_M/\Delta p_P = 1/2$ ; then the ratio of loss factors for the RVVV is:

$$K_{VVM}/K_{VVP} = 10.$$

Separate hydraulic tests will be run on the model RVVV's to characterize the flapper valve and find the optimum setting point.

## VIII SUMMARY AND CONCLUSIONS

Several tests were performed at the UMCP facility in the areas of:

- a) Natural circulation performances,
- b) system heat loss characterization,
- c) heat balance closure and
- d) reactor vessel flow resistance.

These tests contribute to present a more detailed and precise description of the UMCP Loop.

The study of the small break LOCA is the focus of this report and information characterizing the rapid depressurization transient were provided. The most significant result is the effectiveness of the pressure versus void representation that allows to collapse the data in a remarkable way. The criteria of preservation of the void fraction and the consequence time scaling criteria seems to find experimental confirmation in this early part of the small break LOCA event.

A brief discussion on the scaling of the RVVV is presented in the final portion of the paper.

## REFERENCES

1. Sallet, D.W., Hsu, Y.Y., Pertmer, G.A., et. al., "Final Design Report for the UMCP 2x4 B&W Simulation Loop", The University of Maryland, August, 1984.
2. Hsu, Y.Y., et. al., "Facility Description and Scaling Principles of the UMCP 2x4 Lop", The University of Maryland College Park, Presented in Specialists Meeting on Small Break LOCA Analyses in LWRs, Pisa, Italy, June, 1985.
3. Gloudemans, J.R., "Simulation of Reactor Vessel Vent Valves", to be published, 1985.

## Nomenclature

A; area  
c; specific heat @ constant pressure  
g; gravitational acceleration  
K; pressure loss coefficient  
L; length  
p; pressure  
q; power  
Q; volumetric flow rate  
R; flow resistance  
t; time  
T; temperature  
U; overall heat transfer coefficient  
V; volume  
W; mass flow rate  
Z; height

## Greek

$\rho$ ; density  
 $\beta$ ; volumetric expansion coefficient  
 $\Pi$ ; dimensionless ratio  
 $\phi$ ; property parameter

## Subscripts

C; core  
HX; heat exchanger  
M; model  
p; prototype,  
primary side  
pi; primary side inlet  
po; primary side outlet  
S; secondary side  
so; secondary outlet  
Th; thermal  
v; vessel  
vv; vent valve

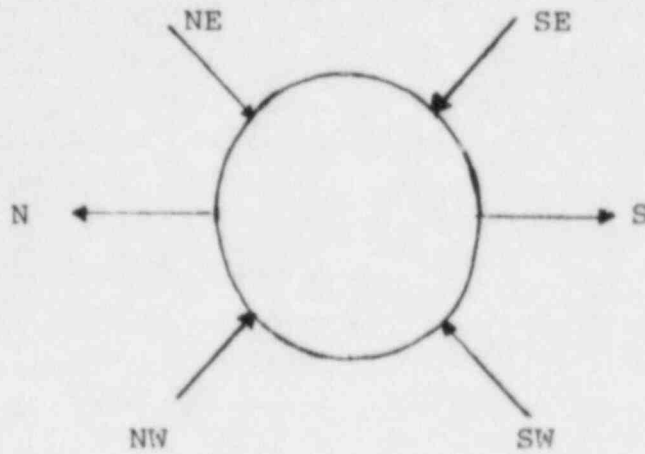
Table 1 List of Completed Tests.

Shake-down Tests  
Hydraulic Characterization Tests  
Heat Transfer Characterization Tests  
Preliminary Natural Circulation Tests  
Preliminary Blow-down Tests  
Preliminary High-Point Venting & Flow Resumption Tests  
Preliminary SB-LOCA Simulating Nominal Base Case Run

Table 2. Small Break LOCA Test Procedure  
(Rapid depressurization transient)


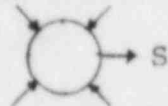
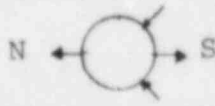
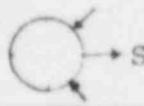

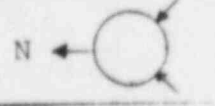
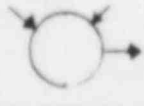
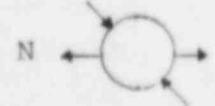

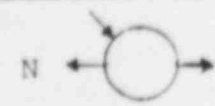

1. Set up the software and controls on the D.A.S.
2. Fill up system (primary, secondary). Then drain the primary until the pressurizer level is at 50% of full.
3. Keep all boundary valves closed on the primary except the pressurizer vent valve. Turn on the feedwater pump and the cooling tower fan. Leave the steam lines open.
4. Turn on the power in the pressurizer and bring the water to boil (atmospheric conditions).
5. Let the water boil for 15 minutes then close the pressurizer vent valve.
6. Turn on the core power and keep the power level such that the core bulk temperature stays 50°F below the pressurizer bulk temperature.
7. Turn on the secondary and/or the auxiliary feedwater to promote natural circulation and obtain a fairly uniform temperature in the primary.
8. When the pressurizer bulk temperature reaches 395°F and the core bulk temperature is 380°F, start collecting the data and after one minute open the break.
9. Cut the pressurizer power and set the core power to a specified decay power level.
10. The rapid depressurization event is terminated when the pressurizer is empty. Continue to collect data for about three minutes thereafter and then stop. Save the data and plot the results.

Table 3. Test Matrix



Test No.	N hot leg	S hot leg	NE cold leg	SE cold leg	NW cold leg	SW cold leg
1	X	X	X	X	X	X
2		X	X	X	X	X
3	X	X		X		X
4		X		X		X
5	X	X	X	X		
6	X			X		X
7		X	X	X		
8	X	X	X			X
9		X	X			X
10	X	X	X			
11		X	X			

Table 4. K value in different configurations

Test No.	Configuration	K (inch H <sub>2</sub> O/ftm <sup>2</sup> X 10 <sup>6</sup> ) experiment	K (inch H <sub>2</sub> O/ftm <sup>2</sup> X 10 <sup>6</sup> ) calculate	error
1		190 (N=S)	193	2%
2		510	530 Δ=0.07	3%
3		N=210 S=250	N=195 S=245	7% 2%
4		580	575	0.85%
5		250 (N=S)	220	12%
6		500	525	5%
7		580	576	0.6%
8		250 (N=S)	220	12%
9		580	576 Δ=0.07	0.6%
10		N=280 S=300	N=350 S=300	25% 0%
11		640	630	1%



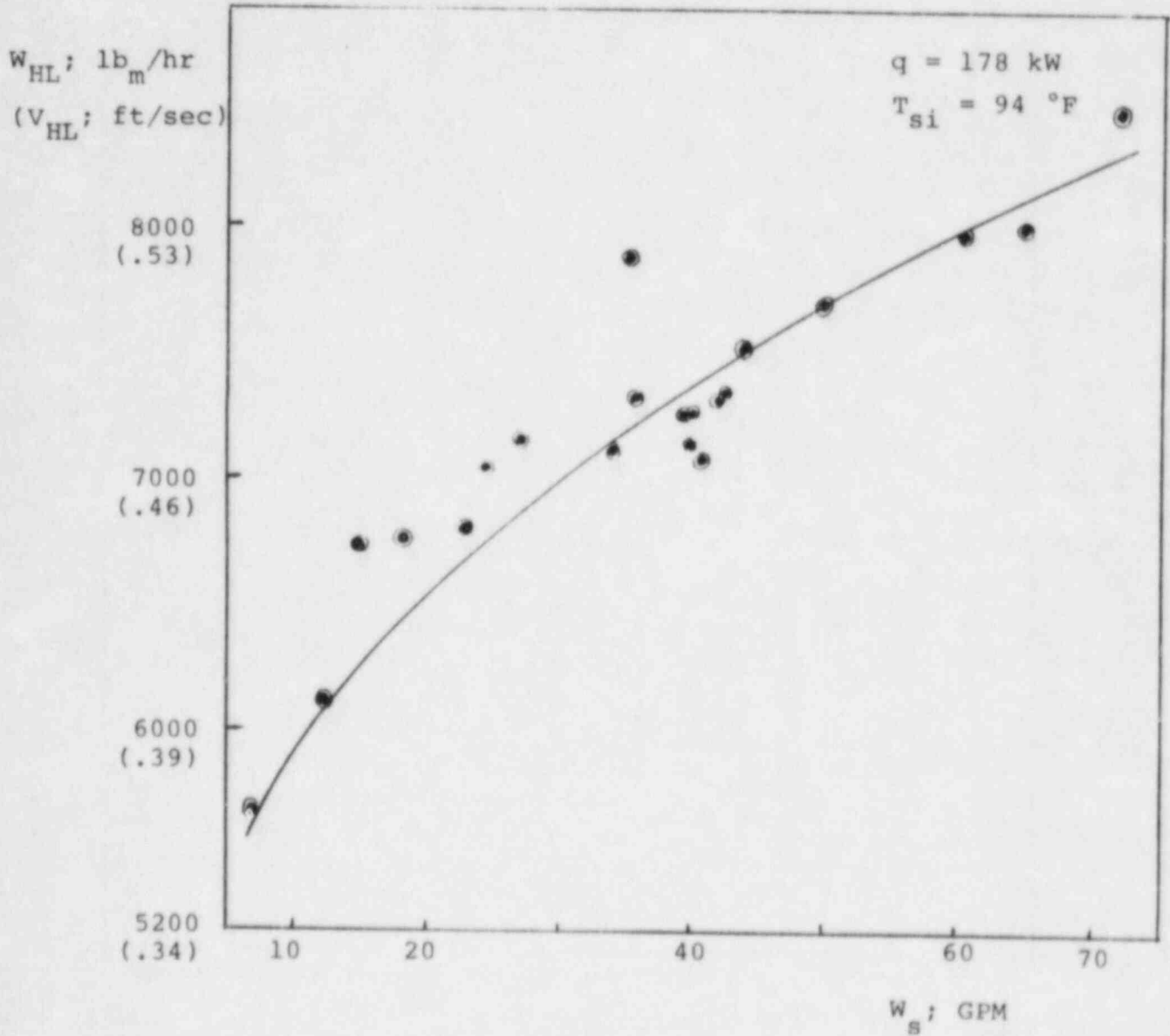


Fig 1. Hot Leg Flow Rate Versus Secondary Side Flow Rate Under Steady-State, Single-Phase Condition.

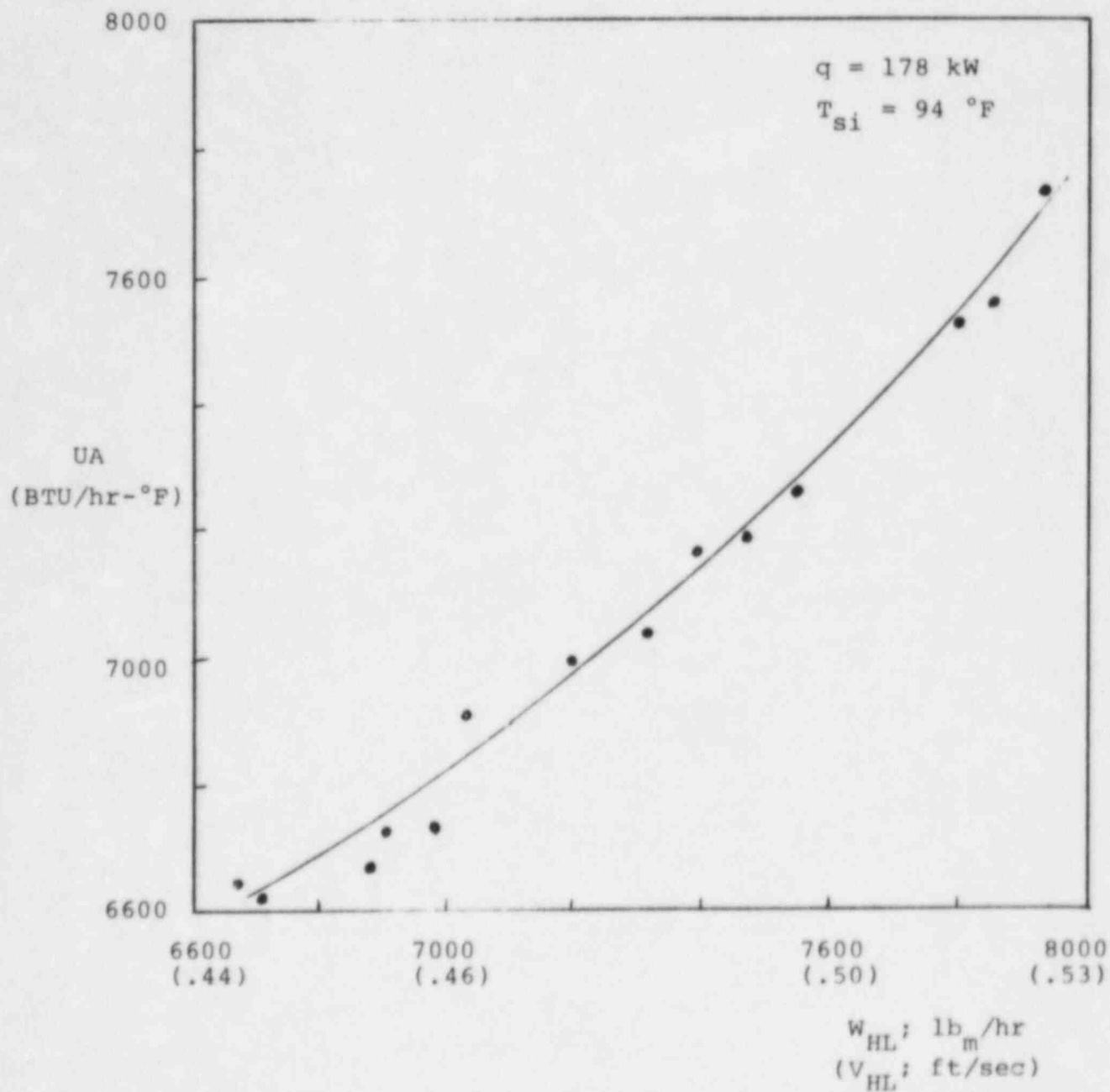


Fig 2. Heat Exchanger Overall Heat Transfer Coefficient Versus Hot Leg Flow Rate Under Steady-State, Single-Phase Condition.

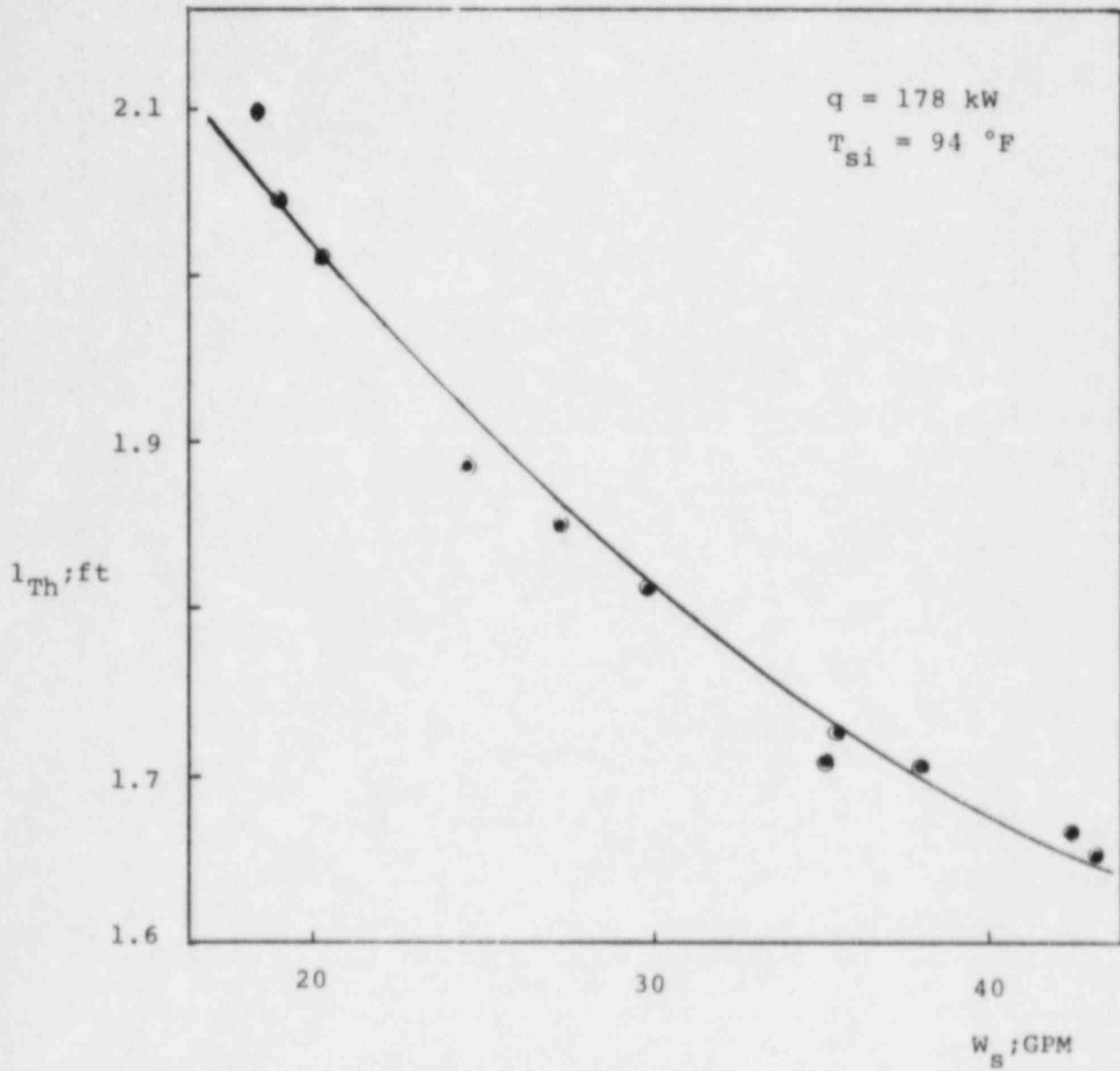


Fig 3. Primary System Thermal Length Versus Secondary Side Flow Rate, Under Steady-State, Signe-Phase Condition.

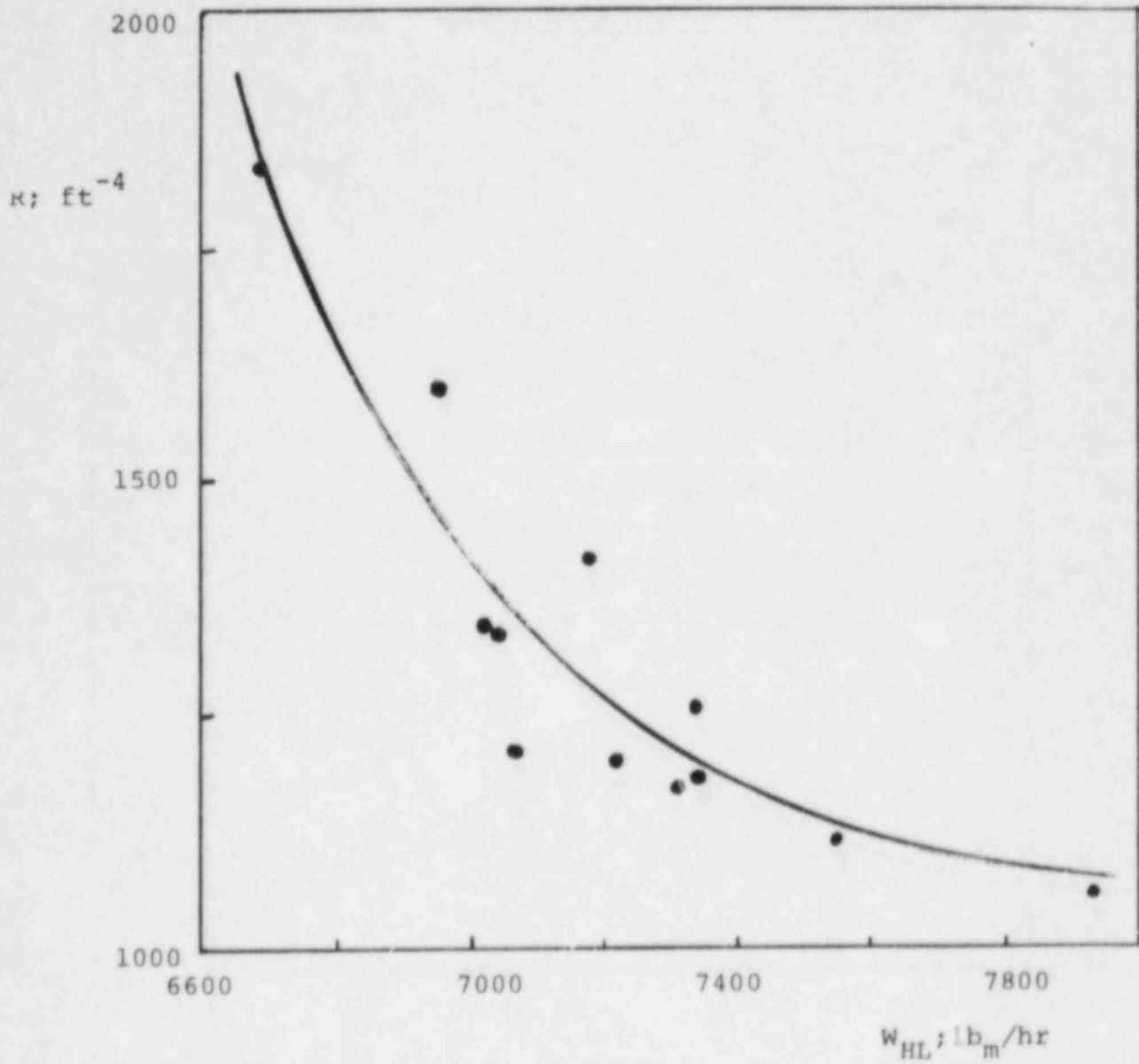


Fig 4. Loop Flow Resistance Versus Primary Side Flow Rate Under Steady-State, Single-Phase Condition.

FIGURE 5. WATER LEVEL TRANSIENT OF SBLOCA NOMINAL CASE  
TRAC RUN 300,000

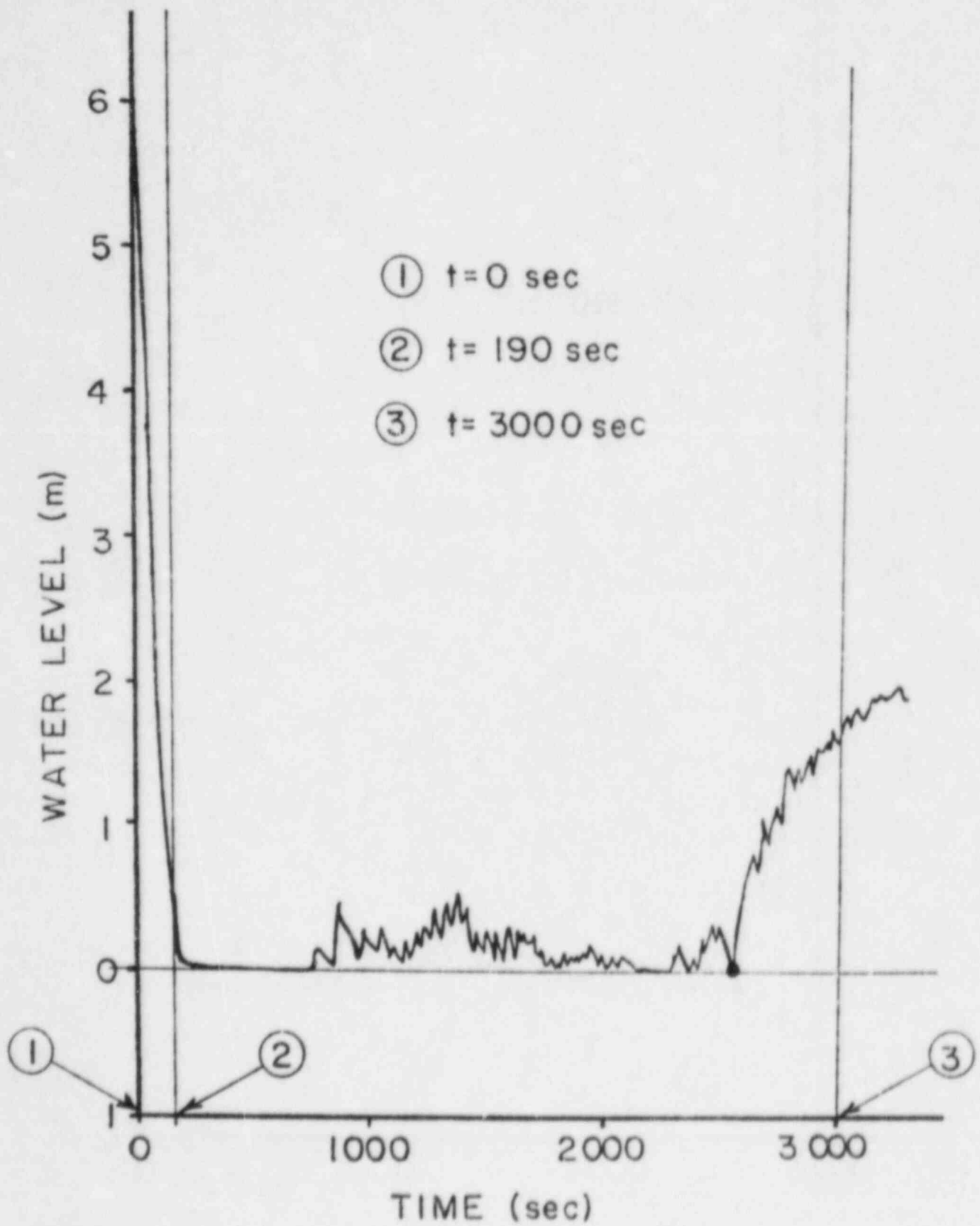


FIGURE 6. PRESSURE TRANSIENT OF SBLOCA NOMINAL CASE  
TRAC RUN 300,000

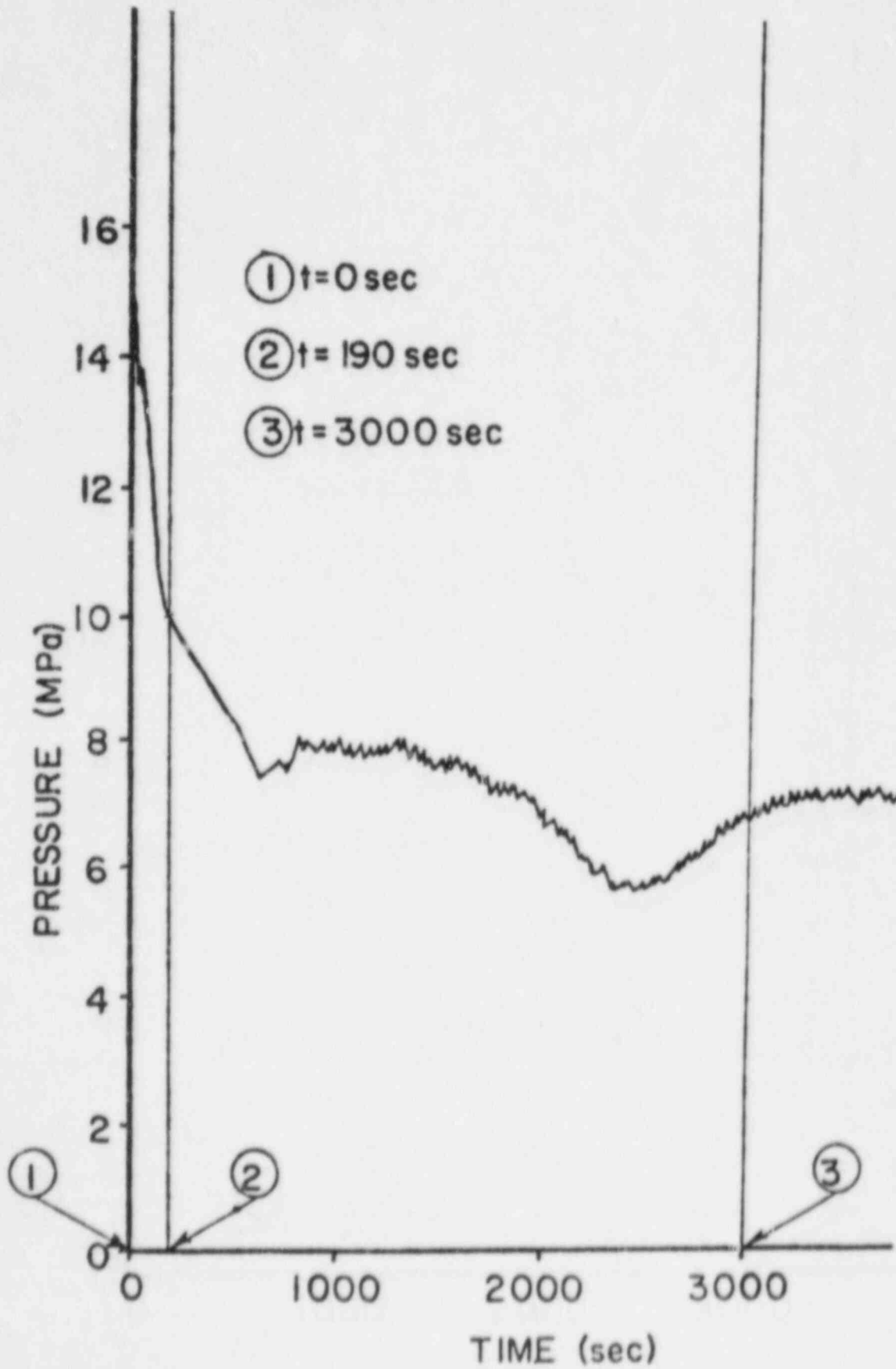


Fig 7. Corresponding Pressure Ratio for Model and Prototype during Depressurization Period

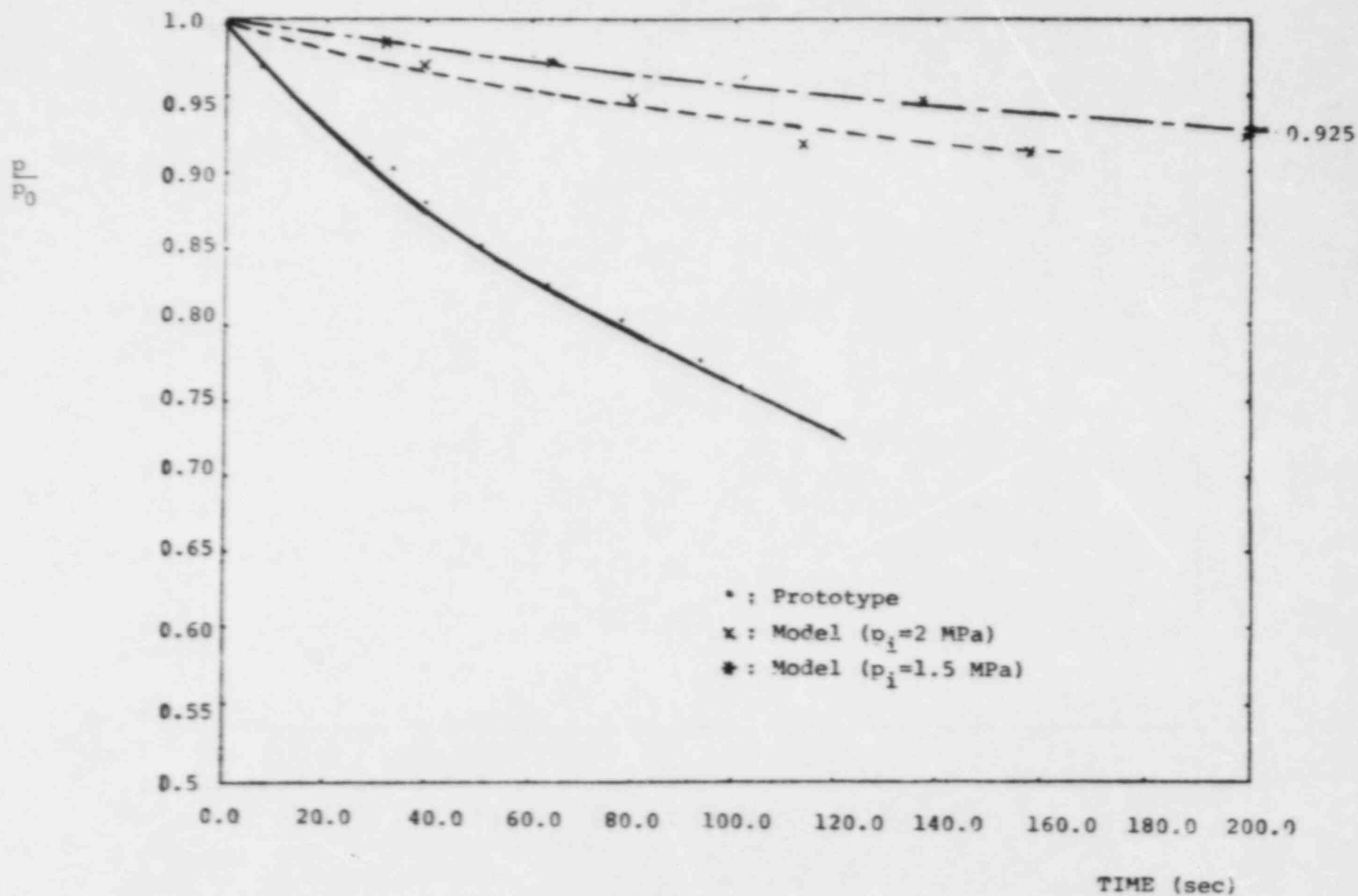


Fig 8. Matching of Liquid Fraction Ratio in Pressurizer  
for Model and Prototype  
(Presented at the S LOCA Specialist Meeting, Pisa, Italy (1985))

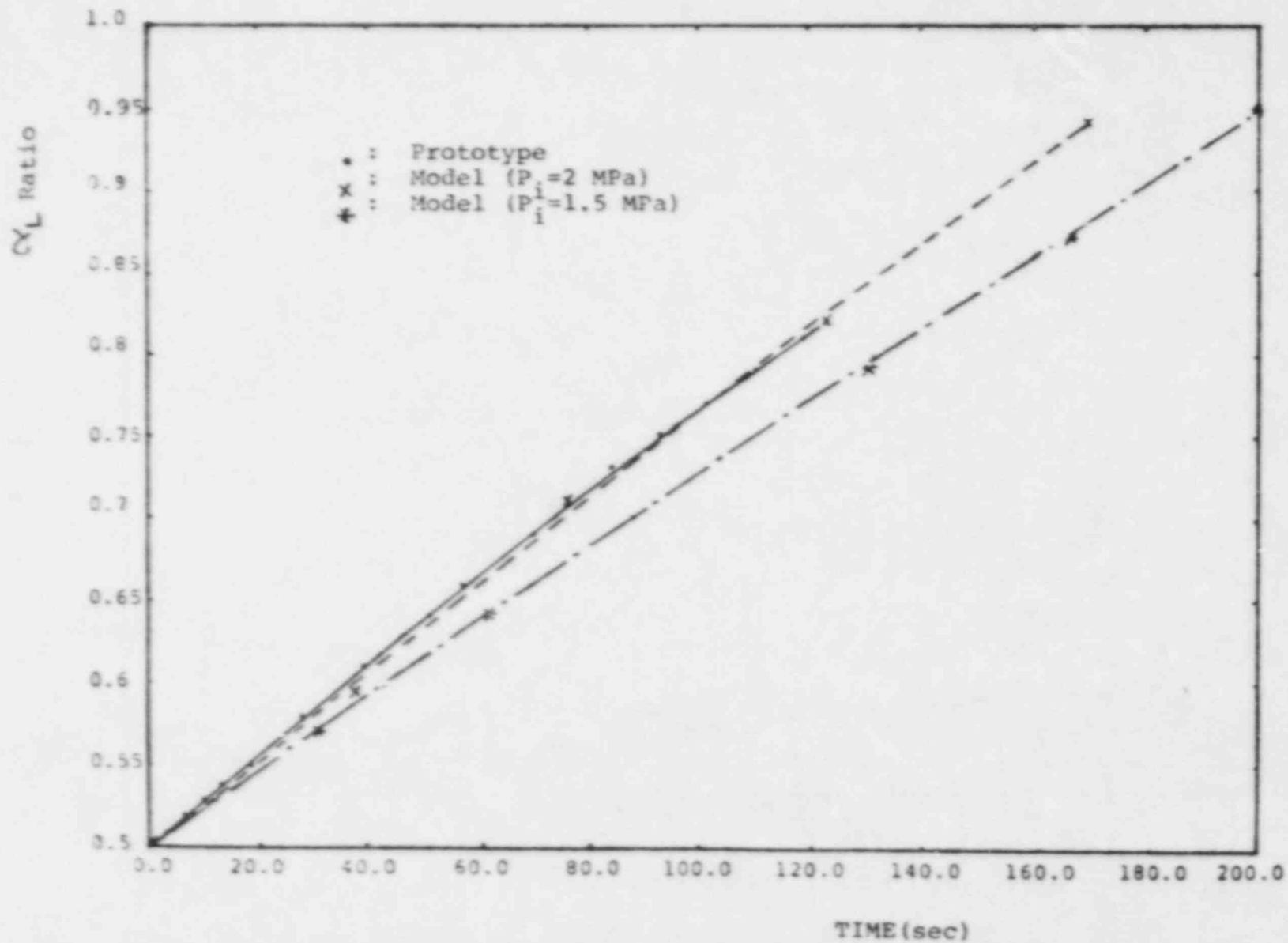




FIG 9. PRESSURE RATIO VS. VOID RATIO

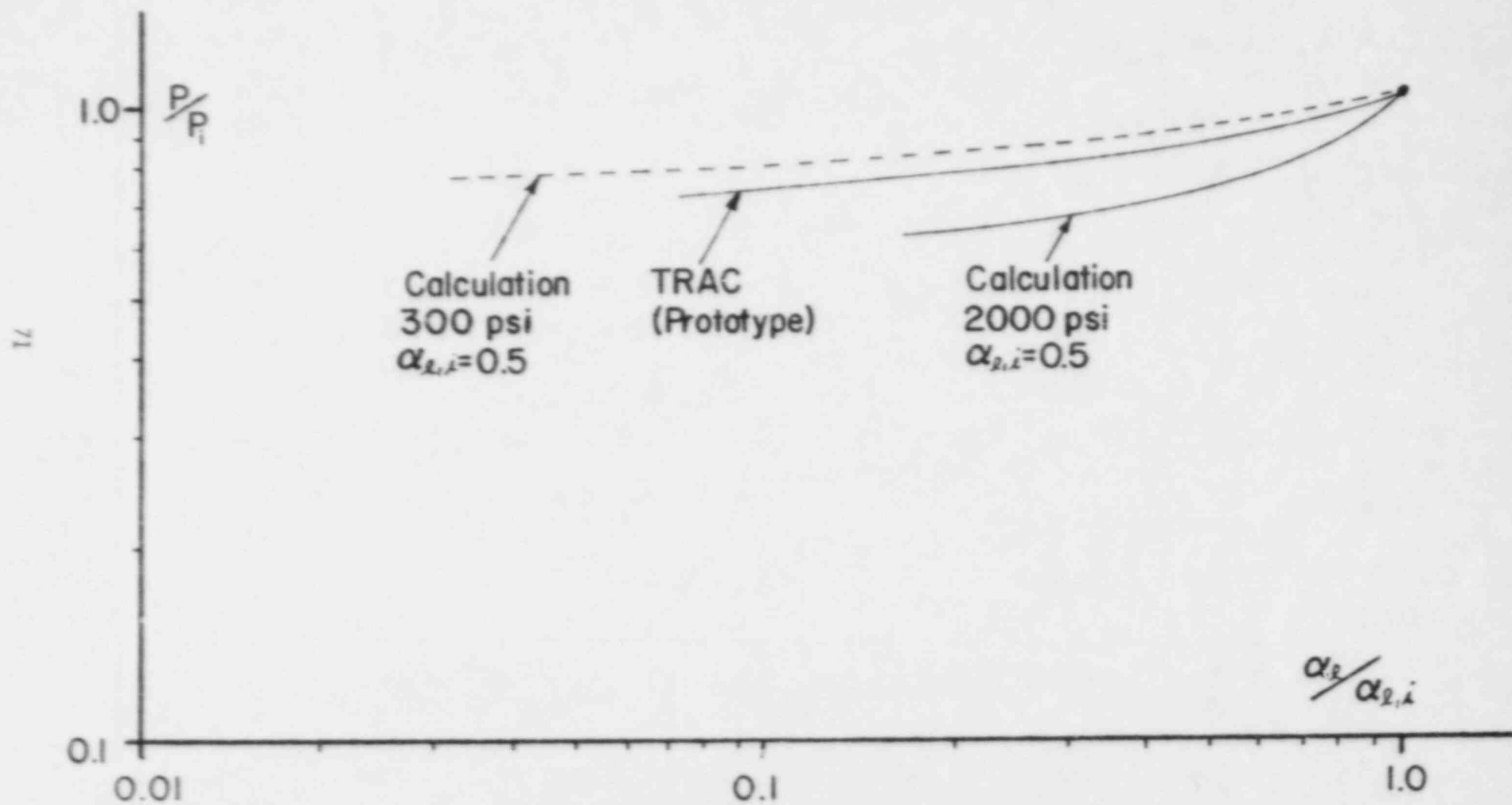


Fig 10. Decay Power of Prototype Vs. Model

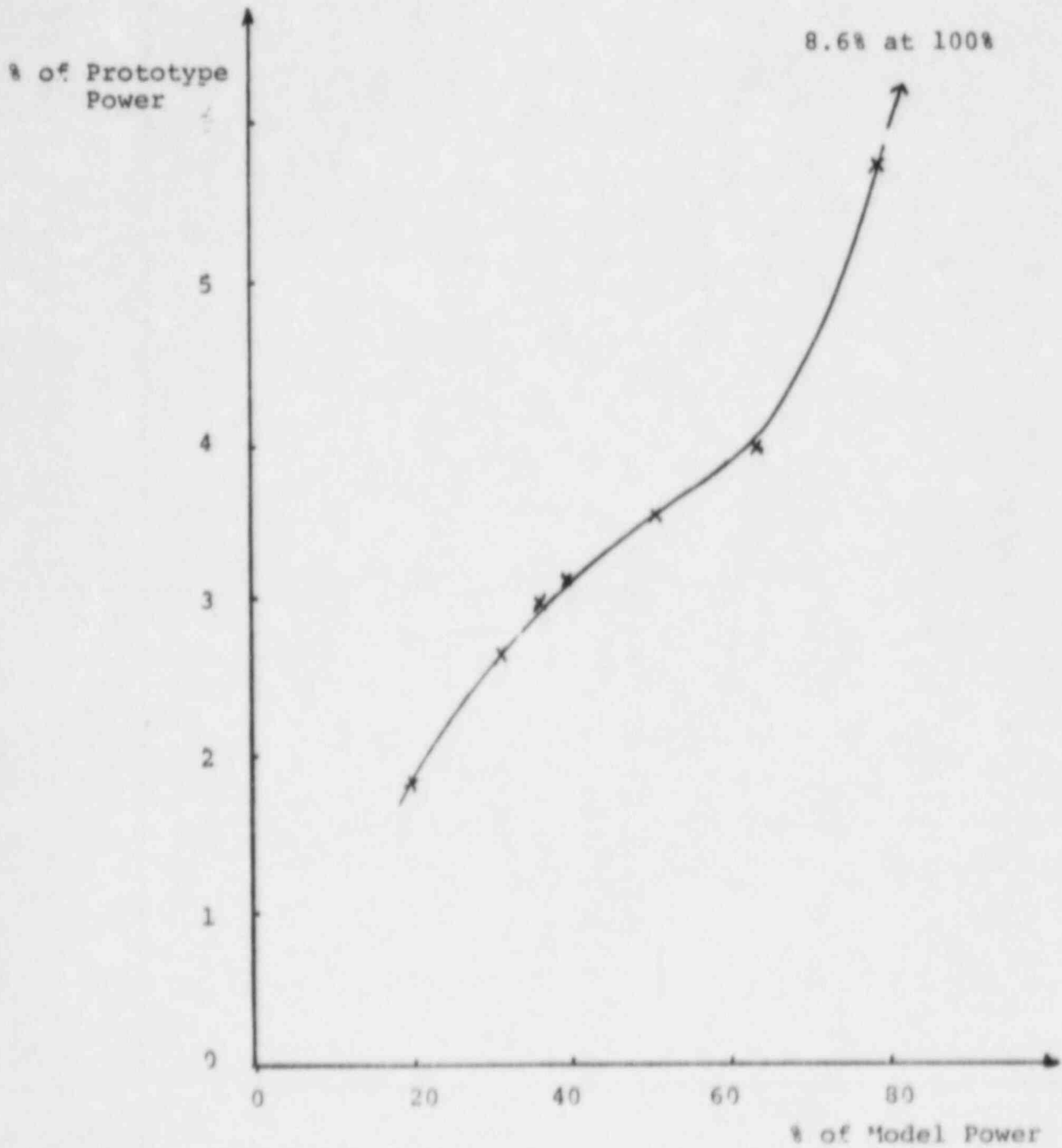


FIG 11. PRESSURIZER LIQUID INVENTORY VS. TIME  
FOR VARIOUS BREAK SIZES

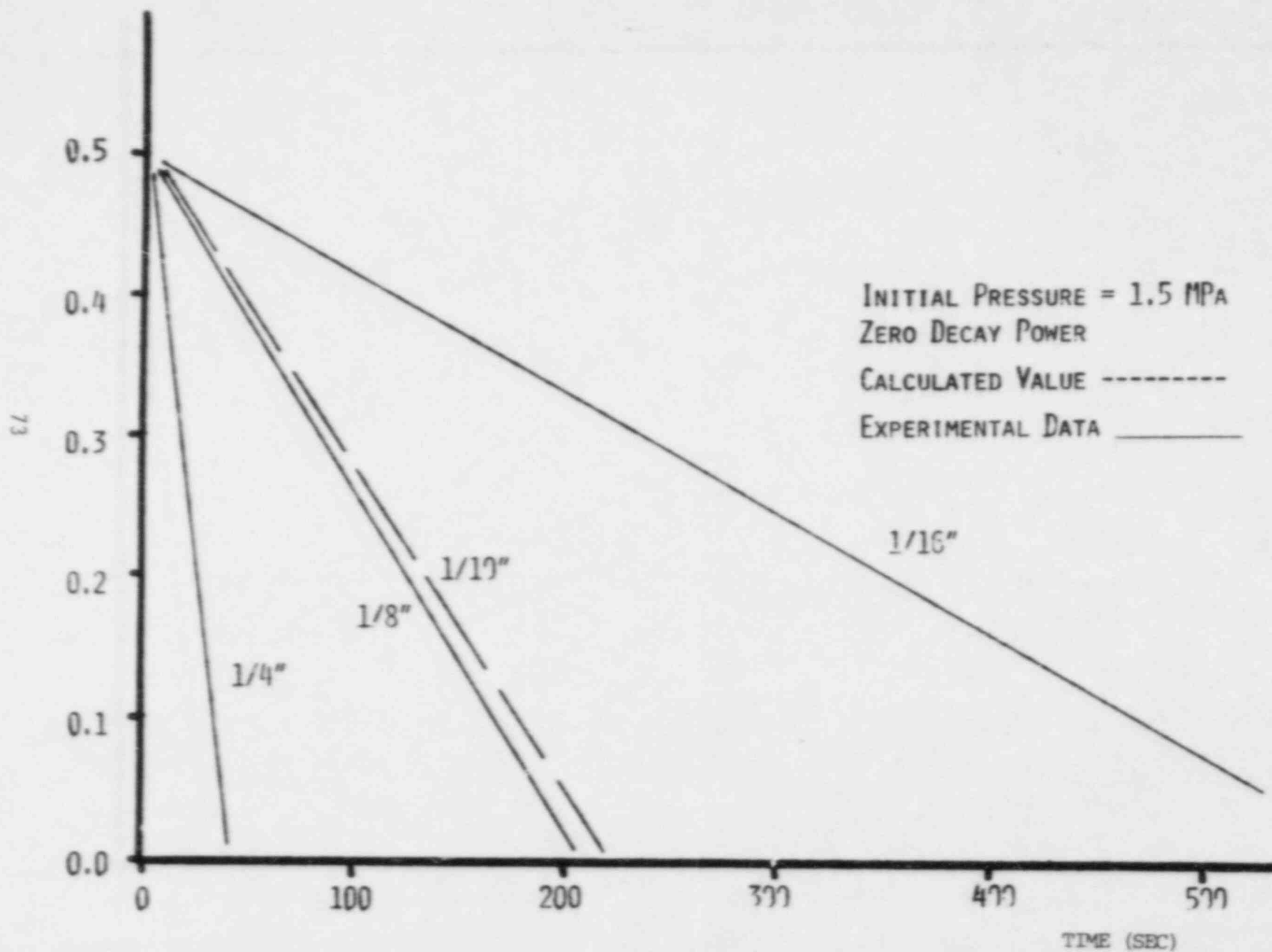


FIG 12. PRESSURE RATIO VS. TIME

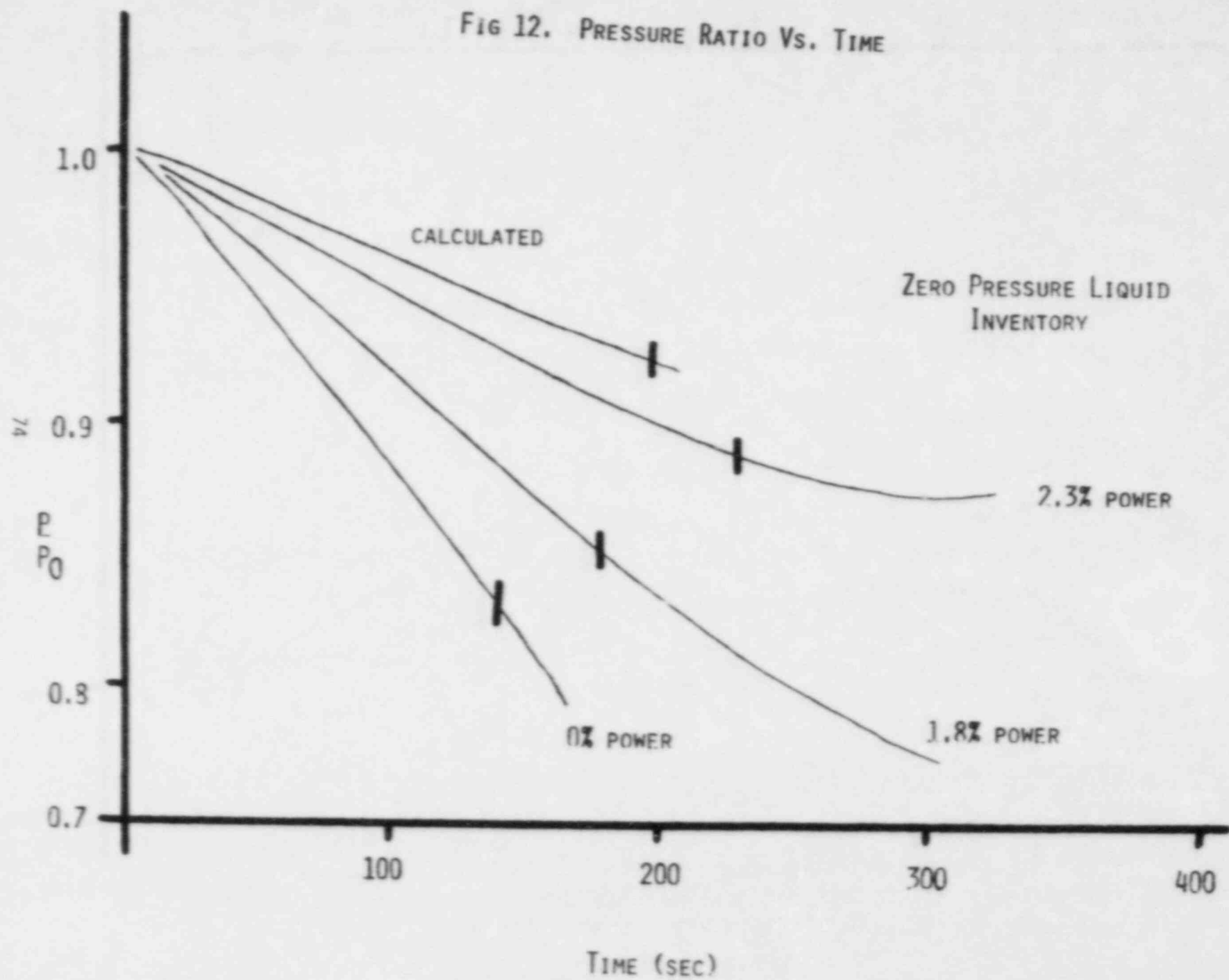


FIG 13. PRESSURE RATIO Vs. VOID

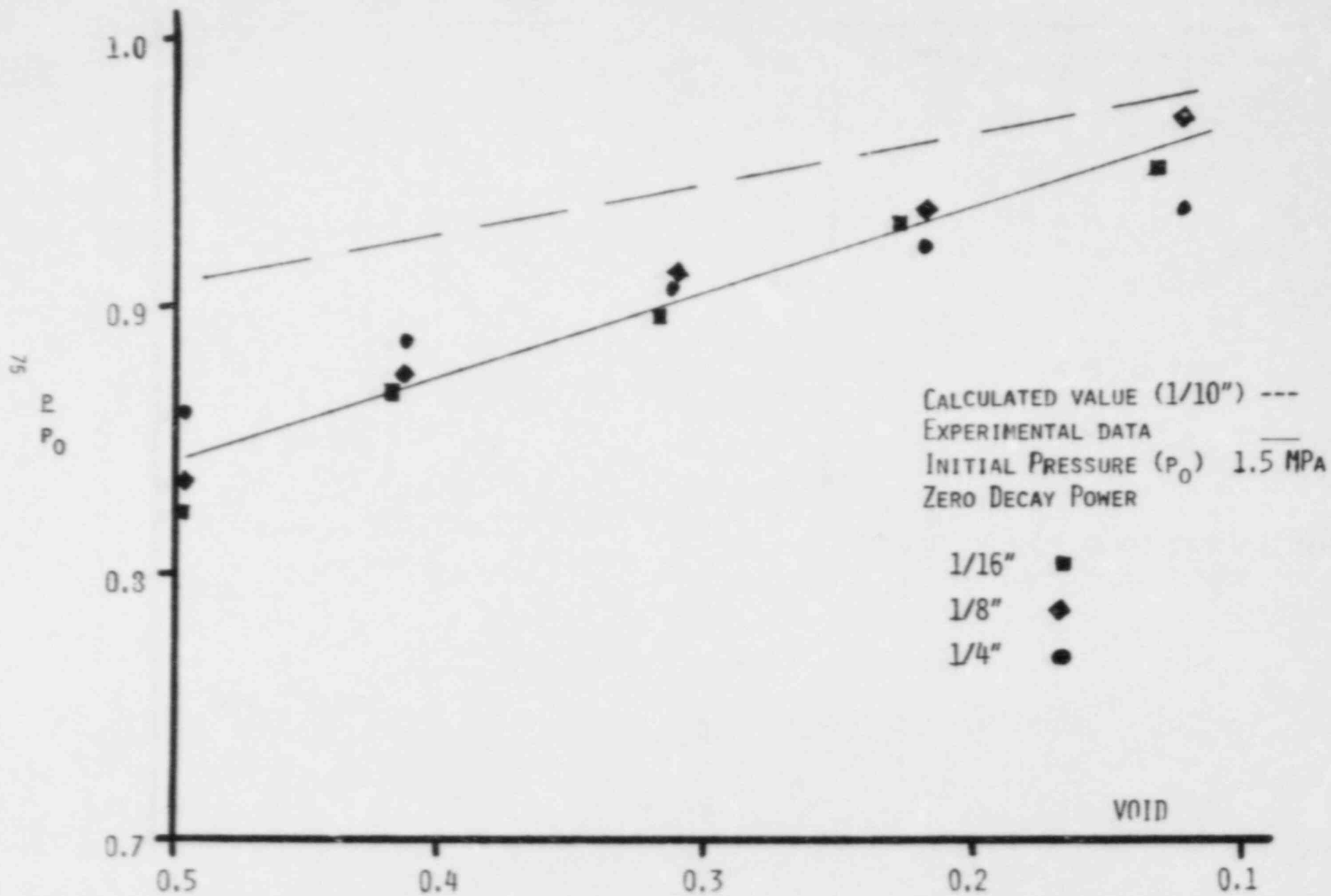


FIG-14. PRESSURIZER LIQUID INVENTORY TREND COMPARISON

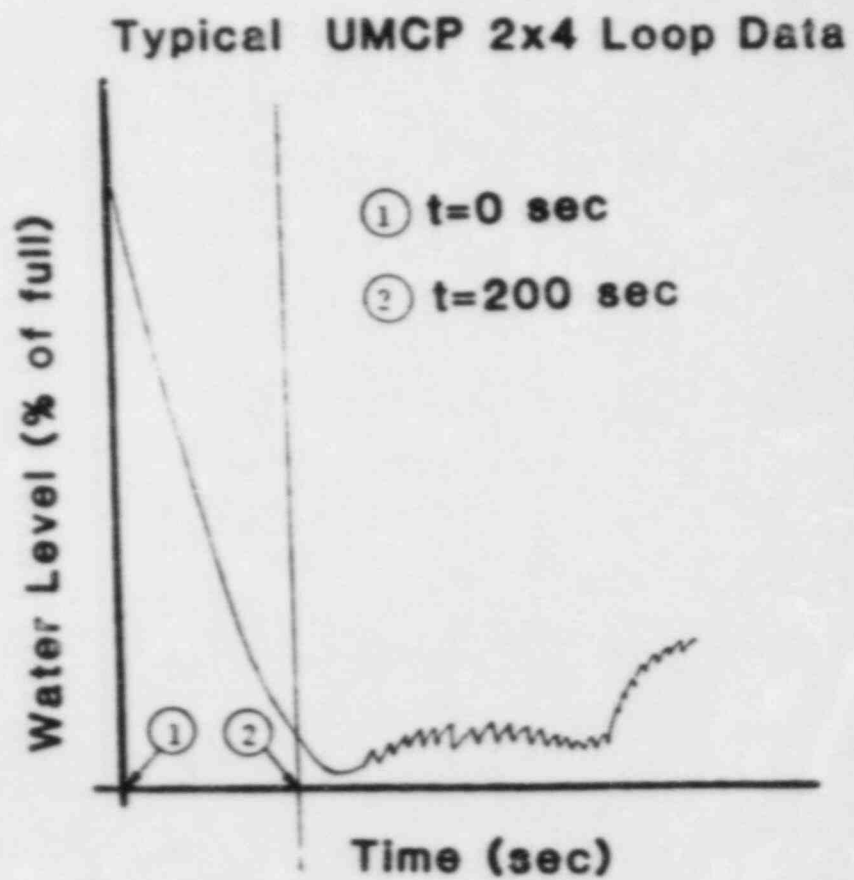
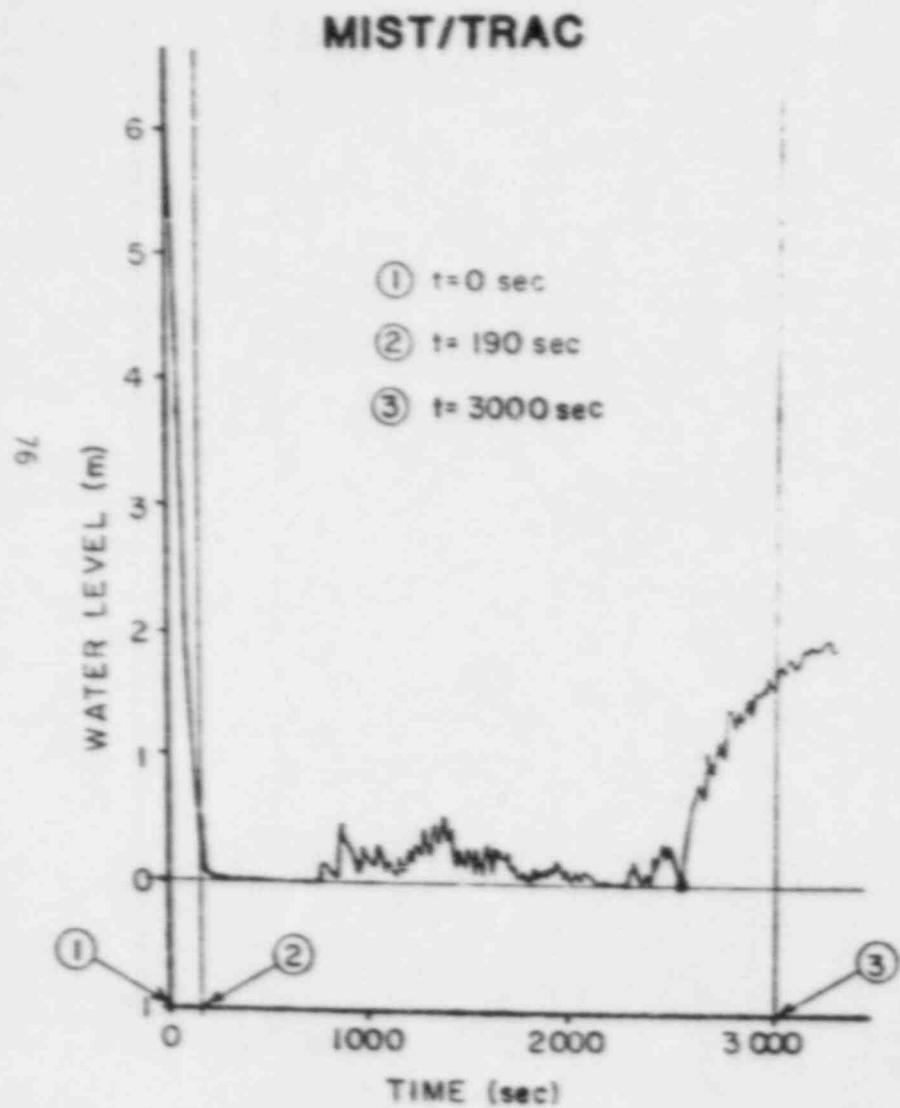


FIG 15. SYSTEM PRESSURE TREND COMPARISON

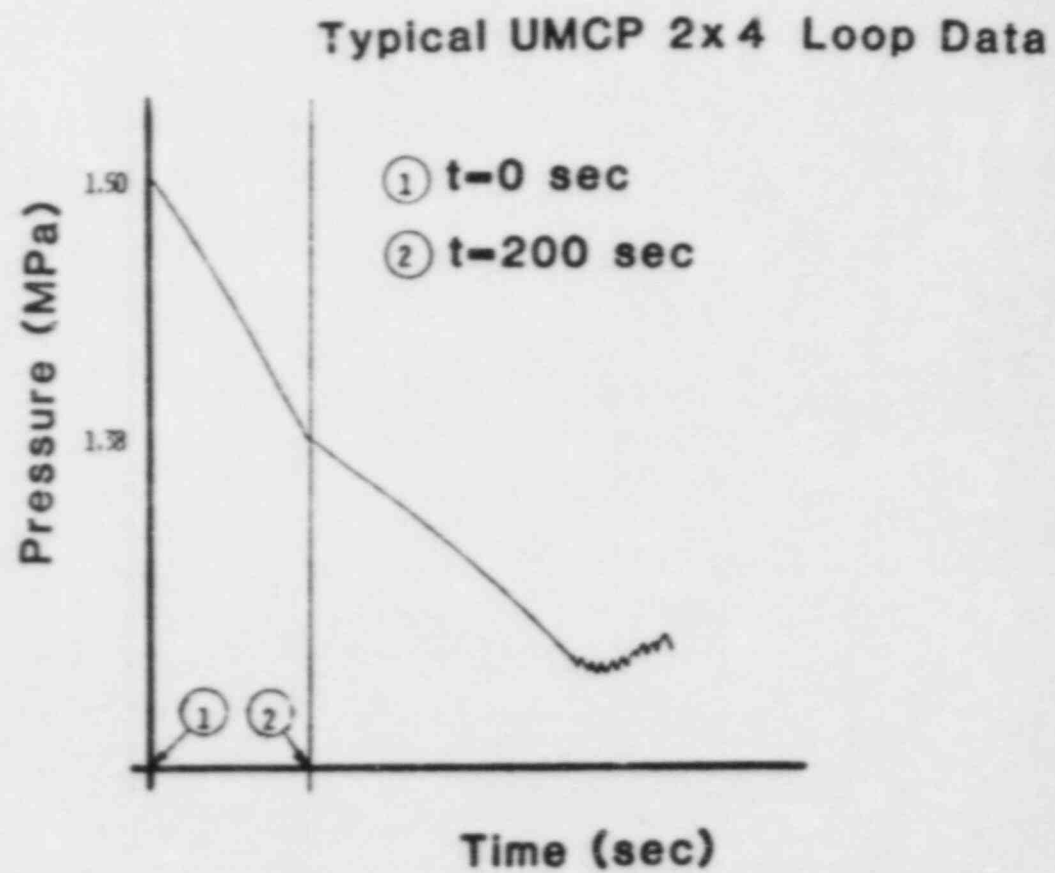
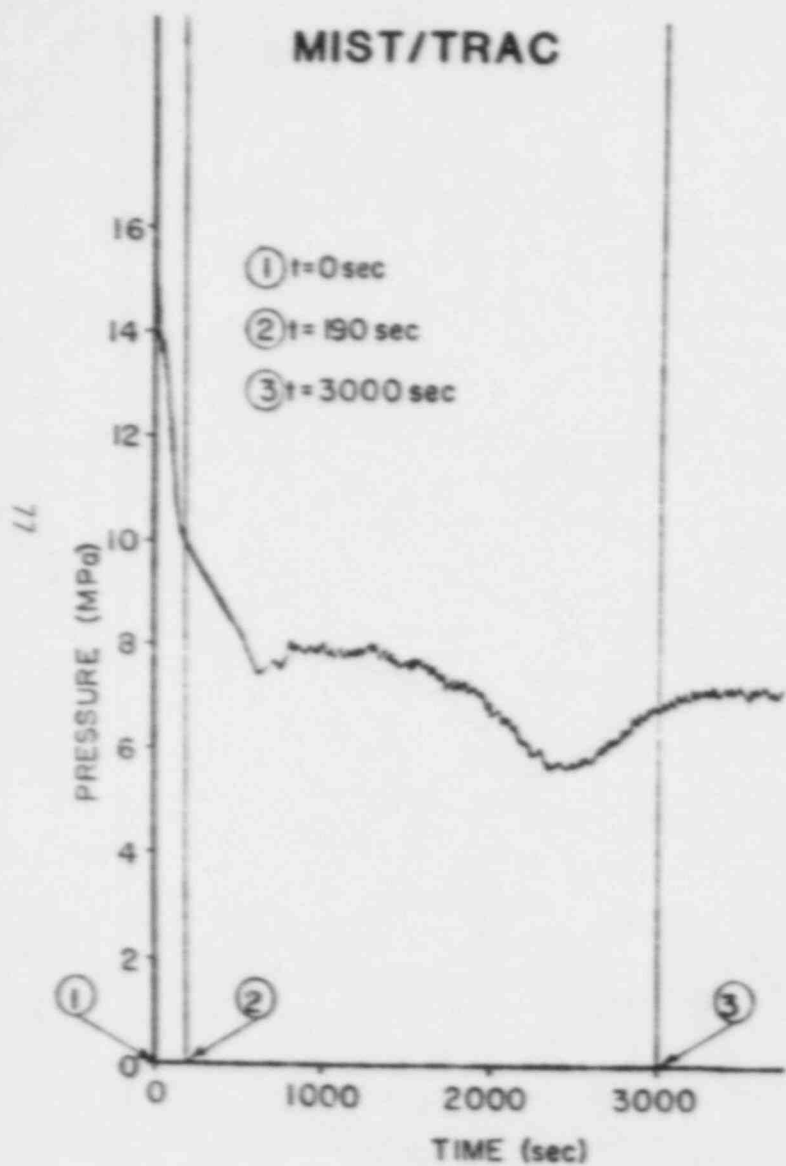


Fig 16. Locations of Cork Patch

x: shows the position of  
Cork Patch

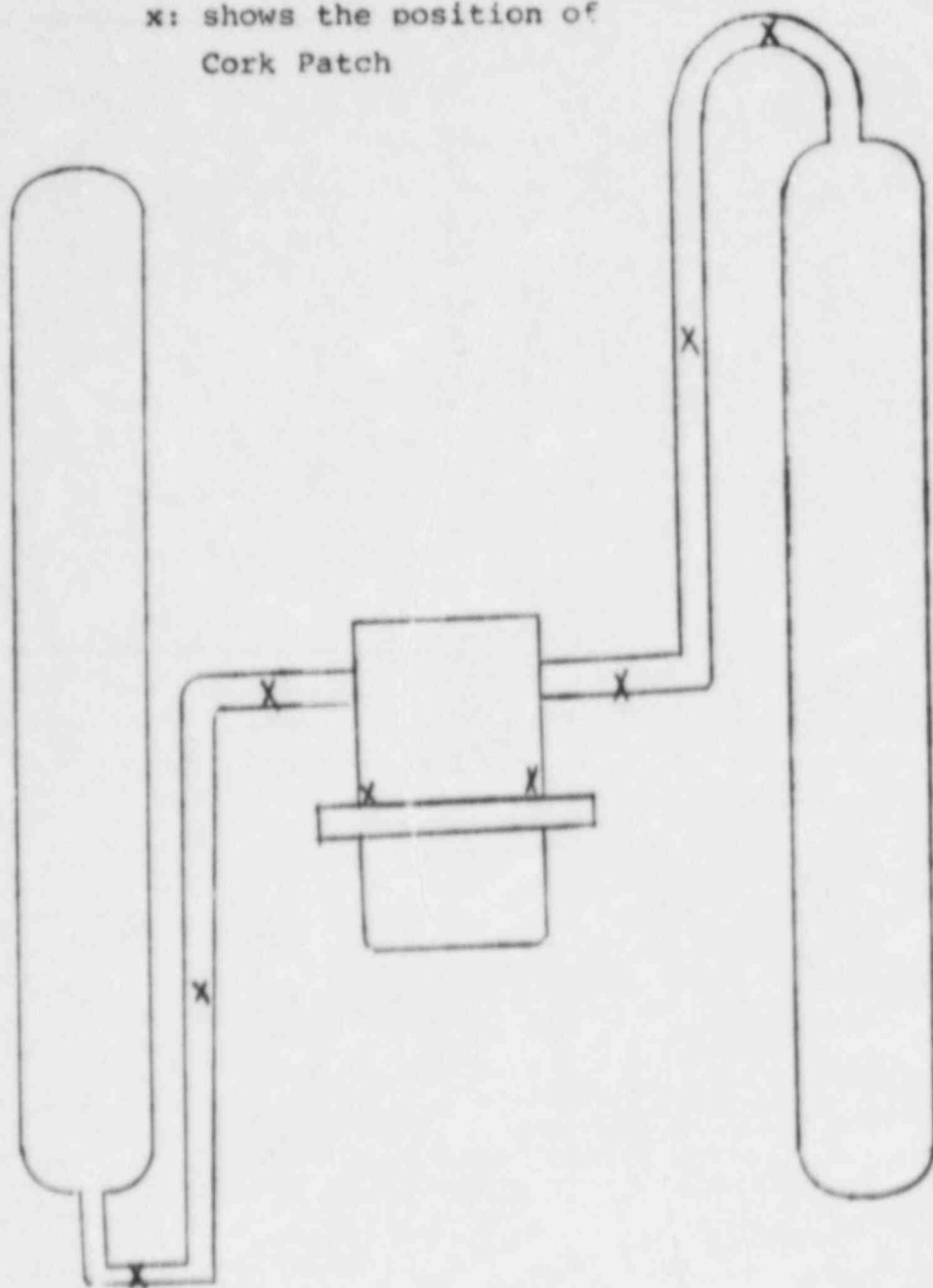




Fig 17. Conductivity of Cork

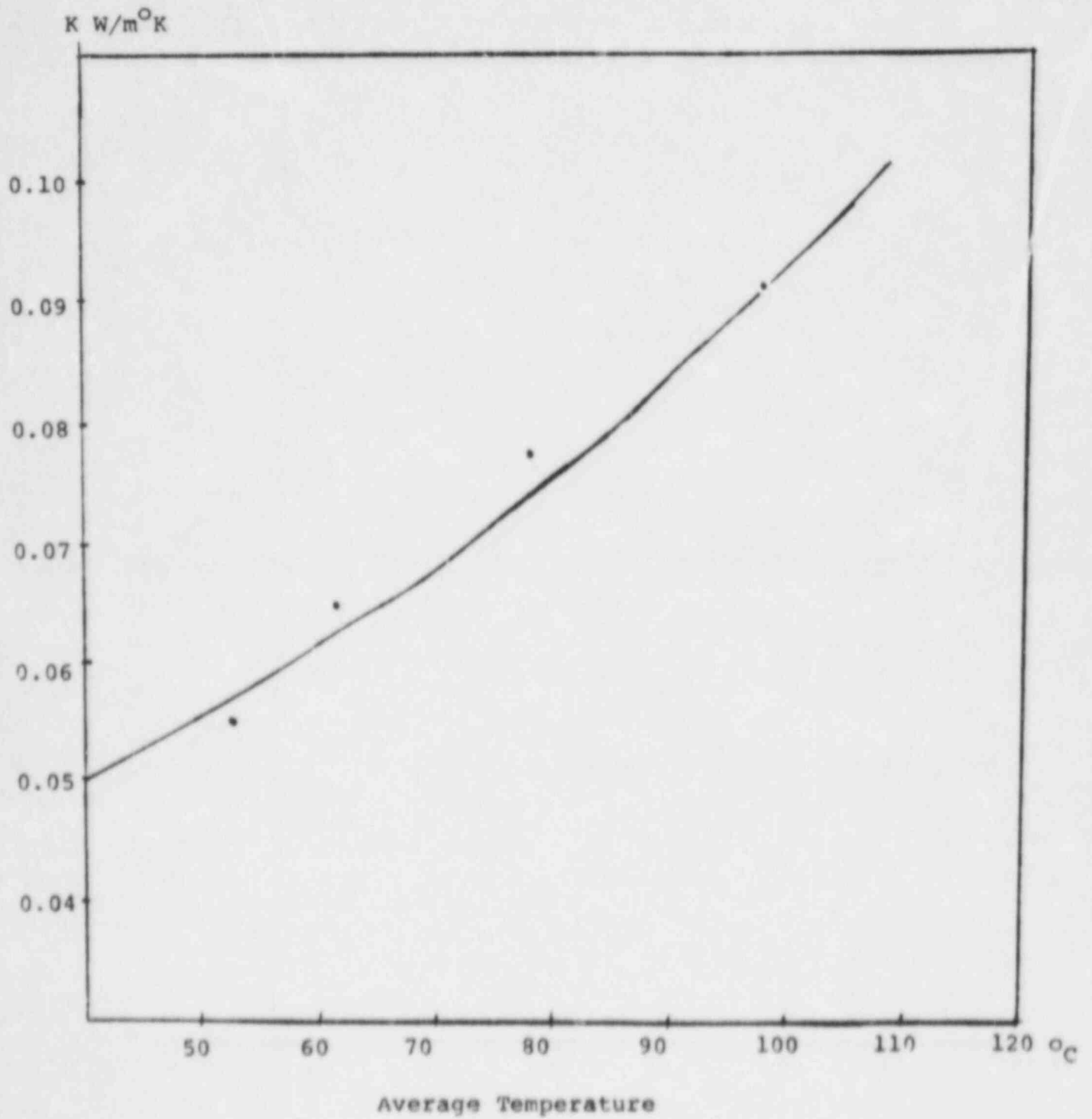
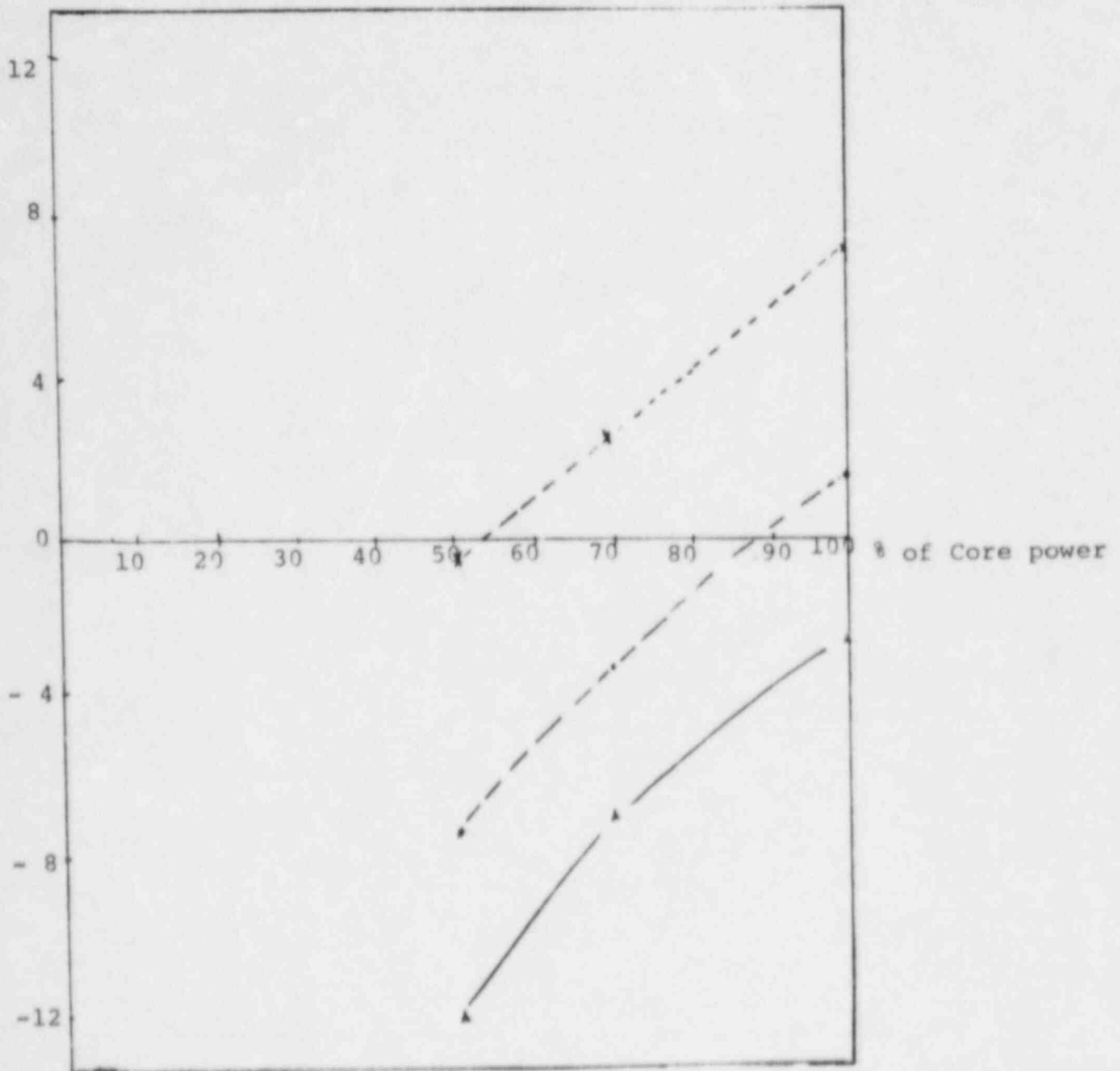
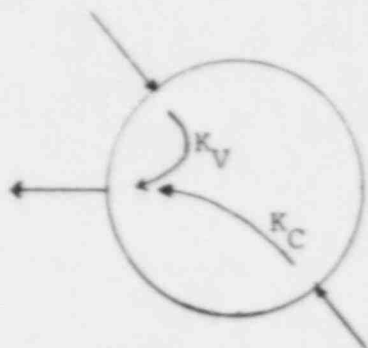


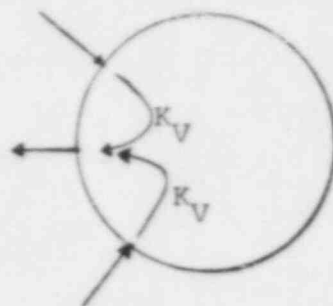
Figure 18. Trend of deviation in heat balance versus % of core power

$$\% \text{ of deviation in heat balance} = \frac{\text{power core} - \text{power out}}{\text{power core}}$$

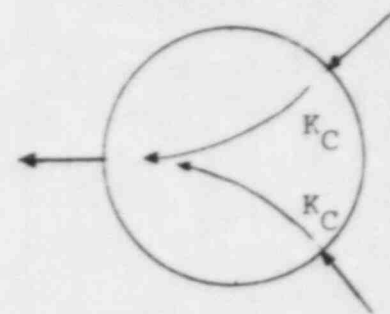




$$\text{I. } K_b = \frac{1}{2} (K_V + K_C)$$



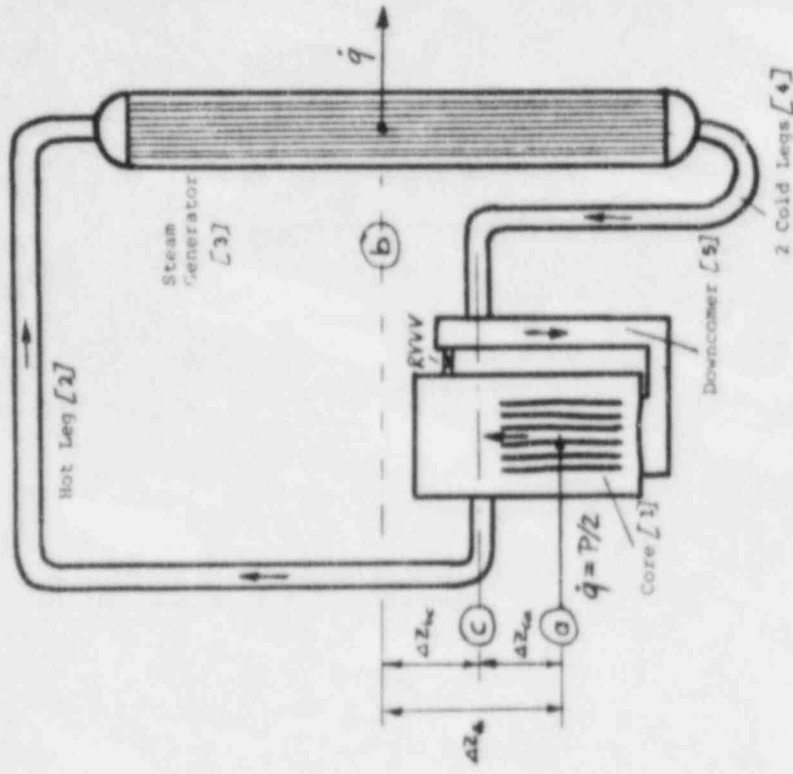
$$\text{II. } K_b = K_V$$



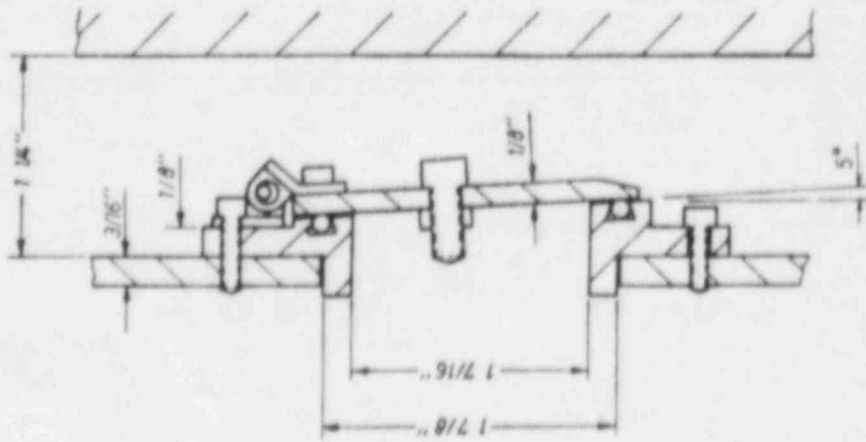
$$\text{III. } K_b = K_C$$

Figure 19. different  $K_b$  for different configurations

Fig. 20 Design of RVVV in the Loop



Simplified Schematic of B&W 2x4 Loop.  
 (Note: Only one half of the primary loop is shown for analysis).



REACTOR VESSEL VENT VALVE (RVVV) DESIGN DRAWING. (NOT TO SCALE).

## MIST FACILITY STATUS

By H. R. Carter

The Babcock & Wilcox Company  
Research and Development Division  
Alliance Research Center  
1562 Beeson Street  
Alliance, Ohio 44601

### Abstract

The Multiloop Integral System Test (MIST) is part of a multiphase, four-year program that started in 1983 to address small break loss-of-coolant accidents (SBLOCAs) specific to Babcock & Wilcox-designed plants. MIST is sponsored by the Nuclear Regulatory Commission, Babcock & Wilcox (B&W) Owners Group, Electric Power Research Institute, and B&W. The unique features of the B&W design, specifically the hot-leg U-bends and steam generators, prevented the use of existing integral system data or existing integral system facilities to address the thermal/hydraulic SBLOCA questions. MIST and two other supporting facilities [1] were specifically designed and constructed for this program, and an existing facility -- the Once-Through Integral System (OTIS) [2 - 9] -- was also used. Data from MIST and the other facilities will be used to benchmark the adequacy of system codes, such as RELAP-5 and TRAC, for predicting abnormal plant transients. The status of MIST scaling and design, instrumentation, and testing is described in this paper.

### Introduction

MIST is a scaled, 2-by-4 (two hot legs and four cold legs) model of a Babcock & Wilcox, lowered-loop, nuclear steam supply system (NSSS). It is designed to operate at typical plant pressure and temperature. Experimental data obtained from this facility during post-small-break, loss-of-coolant accident (SBLOCA) testing are used for computer code benchmarking.

The reactor coolant system of MIST is scaled according to the following criteria, listed in order of descending priority: elevation, post-SBLOCA flow phenomena, component volume, and irrecoverable pressure drop. MIST consists of: two, 19-tube, once-through steam generators; reactor; pressurizer; two hot legs; and four cold legs. A scaled reactor coolant pump is present in each of the cold legs.

Other loop components in MIST include: a closed, secondary system; four simulated reactor vessel vent valves; pressurizer pilot-operated relief valve (PORV); hot-leg and reactor vessel upper-head vents; high-pressure injection; core flood system; and critical flow orifices for scaled leak simulation. Guard heaters, used in conjunction with passive insulation to reduce model heat loss, are included on the steam generator and all primary coolant components. The system is also capable of noncondensable gas addition at selected loop sites.

Approximately 850 instruments are present in MIST and interfaced to a computer-controlled, high-speed, data acquisition system. MIST instrumentation consists of measurements of temperature, pressure, and differential pressure. Fluid level and phase indications are provided by optical viewports, gamma densitometers, conductivity probes, and differential pressures. Mass flow measurements in the circulation loop are made using venturis and cooled thermocouples and at the system boundaries using Coriols flowmeters and weigh scales.

The MIST Test Program is divided into three parts: debug, characterization, and transient tests. The test program started with debug in September 1985. Testing will continue with three months of debug, three months of characterization, and six months of post-SBLOCA transients.

#### MIST Design

MIST is a scaled, full-pressure, experimental facility arranged to represent the B&W lowered-loop plant design. Like the plant, MIST is a 2-by-4 arrangement with two hot legs and four cold legs, as shown in Figure 1. MIST is designed for prototypical fluid conditions, with emphasis on leak-tightness and minimization of heat loss.

Scaling of MIST followed the approach and priorities used for OTIS; that is, elevation, post-SBLOCA phenomenon, component and piping volumes, and irrecoverable pressure losses. MIST is full elevation throughout. The only elevations compromised are: the top of the pressurizer; the top plenum of the reactor vessel; the inlet and outlet of the steam generator's plenums; and several, incidental, stagnant, fluid zones. Key interfaces are maintained -- these include: the hot-leg, U-bend spillover; upper and lower tubesheets of the steam generator (secondary faces); cold-leg low point; pump discharge; cold- and hot-leg nozzles; core (throughout); and points of ECCS (emergency core cooling system) injection.

Two-phase behavior during voiding of the hot-leg U-bend and flow interruption is sufficiently prototypical; that is, both the plant and the model will experience phase separation early in the post-SBLOCA transient. Hot-leg pipes in MIST are large enough to admit bubbly flow.

Fluid volume is 40% larger than power-to-volume scaling would dictate; the hot legs, cold legs, and upper downcomer are oversized. This atypicality is imposed by the previously described two-phase characteristics and by considering component irrecoverable pressure losses. The excess volume of the hot leg slows the rate of level decrease for power-scaled draining and similarly retards the rate of level increase for power-scaled injection. Although the excess volume of loop fluid delays system heatup and cooldown, this effect is minor compared to the long-term impact on system energy of leak versus high pressure injection (HPI) cooling. The concentration of excess volume in the piping runs decreases fluid velocities in the hot and cold legs and therefore lengthens the transit time of loop fluid.

Irrecoverable pressure drops are well preserved.

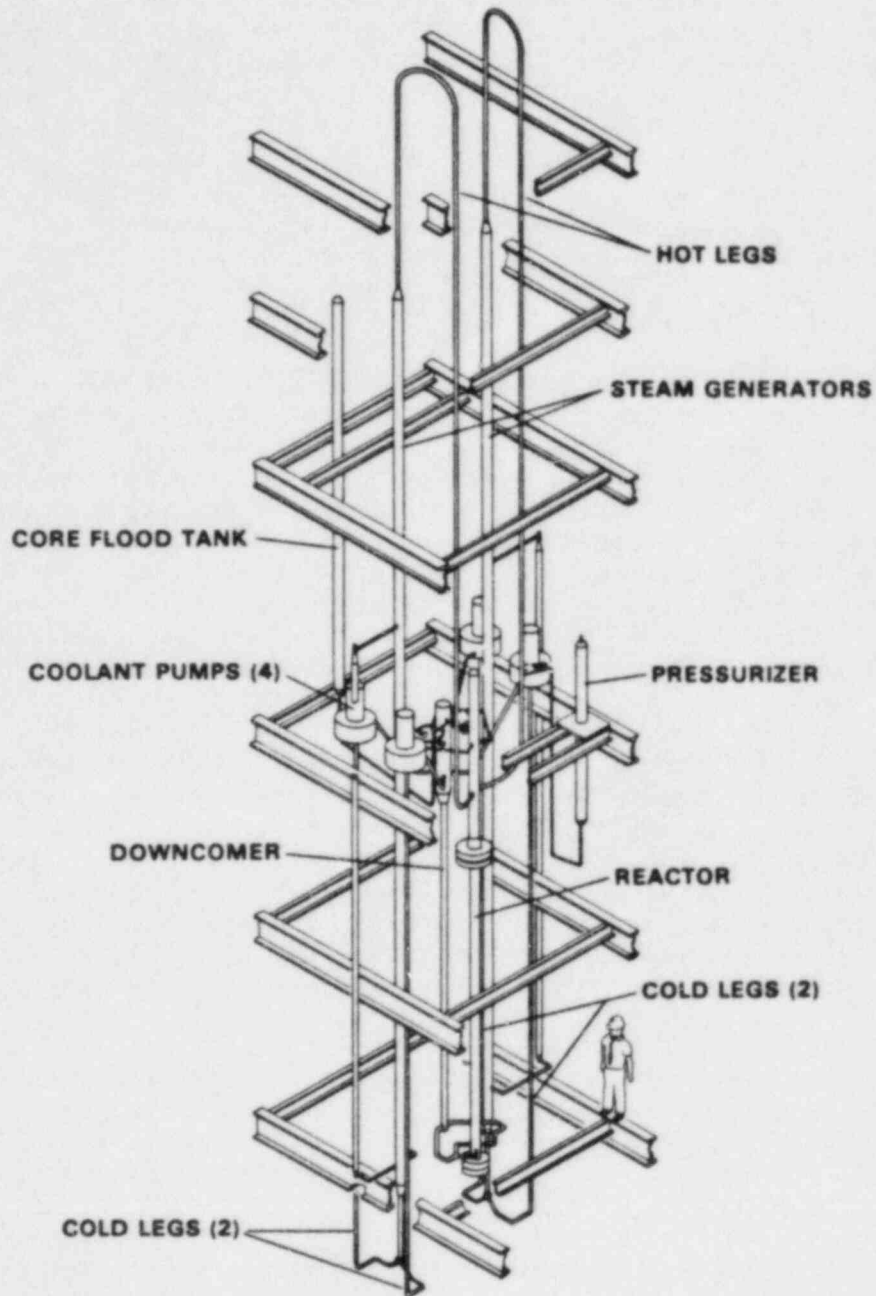


Figure 1. Reactor coolant system -- Multiloop Integral System Test (MIST).

## Components

The MIST core and steam generators are full-length subsections of their plant counterparts. As shown on Figure 2, the core consists of a 7-by-7 array of 45, full-length, 0.430-inch-diameter heater rods and four in-core guide tubes. Plant-typical, fuel pin pitch and grid geometry are used. The simulated rods are capable of full-scale power output but will be limited to approximately 10% scaled power for the planned MIST testing. (Plant/MIST power = 817.) A fixed, axial, heat flux profile (peak-to-average flux ratio = 1.25) and a flat, radial, heat flux profile are used.

The steam generators, shown in Figure 3, each contain 19 full-length tubes. The tubing diameter (5/8-inch OD), material, and tube bundle's triangular pitch (7/8 inch, tube centerline to centerline) are prototypical. The geometry of the tube support plate (TSP) is similar to the plant and provides equivalent characteristics of irrecoverable pressure loss.

The hot legs use 2.5-inch, schedule-80 piping (2.32 inch ID). This diameter admits bubbly flow and approximates irrecoverable pressure loss of a plant hot leg. With the schedule-80 piping, the metal-to-fluid ratio in MIST is only 20% greater than that of the plant. The horizontal runs in the hot leg, as noted in Figure 1, are approximately 1 foot long to accommodate the gamma densitometers. The hot-leg U-bend maintains pipe diameter, and a 1.61-foot bend radius is used to conform to the model system layout. The elevation of the hot U-bend spillover is prototypical. Phase separation at the U-bend is predicted to occur at approximately 18% of full power versus 8% in the plant. Beyond the U-bend, the hot-leg piping in the model extends 12 feet (versus 1.5 feet in the plant) to span the height of the plant steam generator's inlet plenum.

The four cold legs preserve elevation throughout. Two-inch, schedule-80 piping (1.939-inch ID) is used primarily to match irrecoverable pressure drop. This piping size also preserves cold-leg Froude number, which governs the mixing of HPI and reactor vessel vent valve (RVVV) fluid streams. The cold-leg horizontal piping runs are shortened, but the slope of the plant cold-leg discharge piping is approximately maintained. HPI is injected into the sloping pipes at the appropriate elevation, and the diameter of the model HPI nozzle is selected to preserve the ratio of fluid momentum between the cold leg and HPI.

A model reactor coolant pump is mounted in each cold leg. Suction and discharge orientations are prototypical. The pumps deliver single-phase scaled flows at plant typical heads, allow for simulated pump bumps by matching the plant pump spinup and coastdown times, and permit operation under single- and two-phase conditions. However, the pumps do not preserve specific speed or the two-phase degradation characteristics of the plant pumps.

The MIST reactor vessel employs an external annular downcomer, as shown in Figure 1. Cold-leg coupling is restricted by using fins in the downcomer annulus to form quadrants, as noted in Figure 4. The annular gap is 1.4 inches; the gap at each fin is 0.4 inches. Each downcomer quadrant is connected to a separate RVVV simulation and cold leg. The two nozzles on the core flood tank are connected at the interface between two downcomer quadrants.



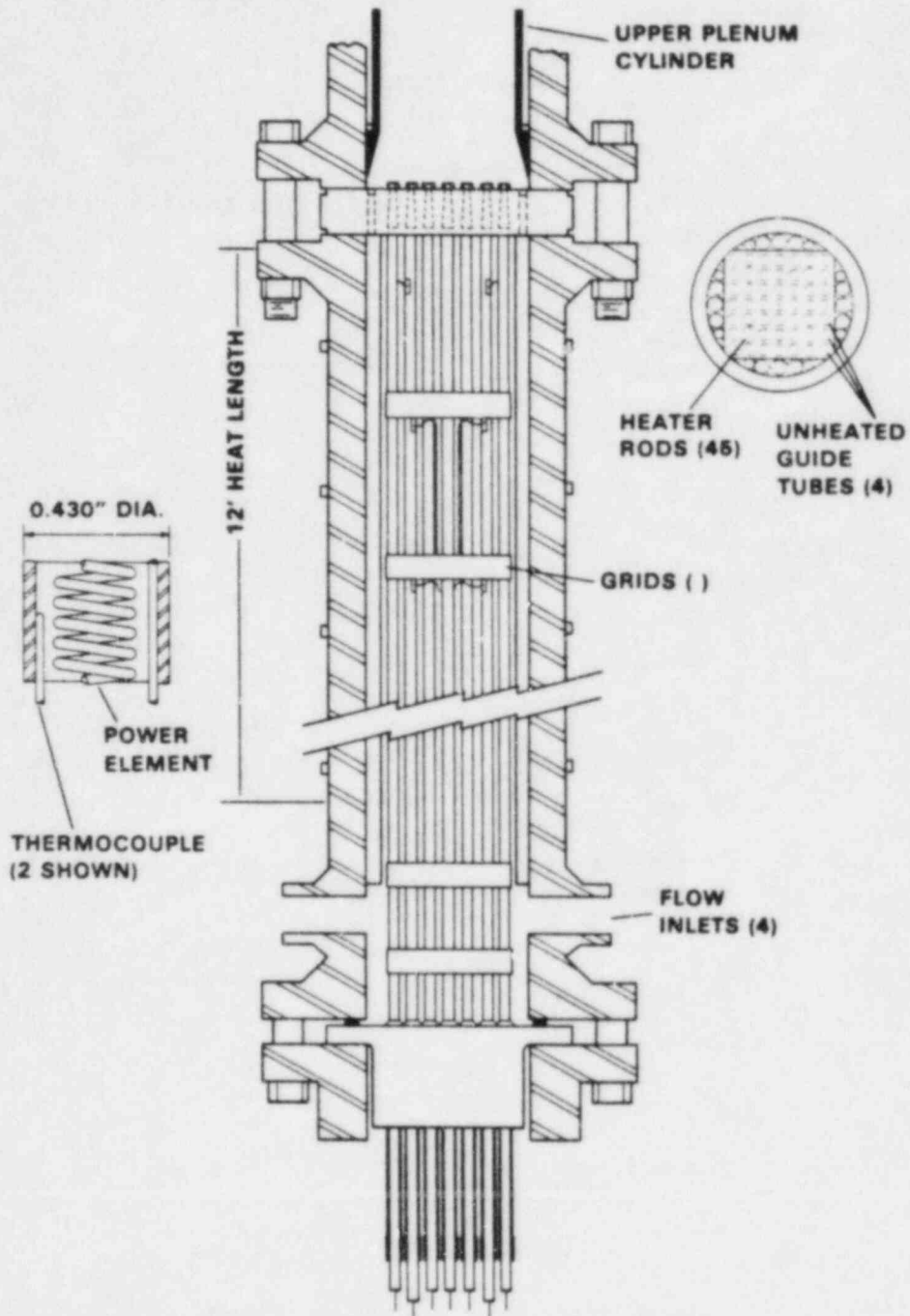


Figure 2. Mist core arrangement.

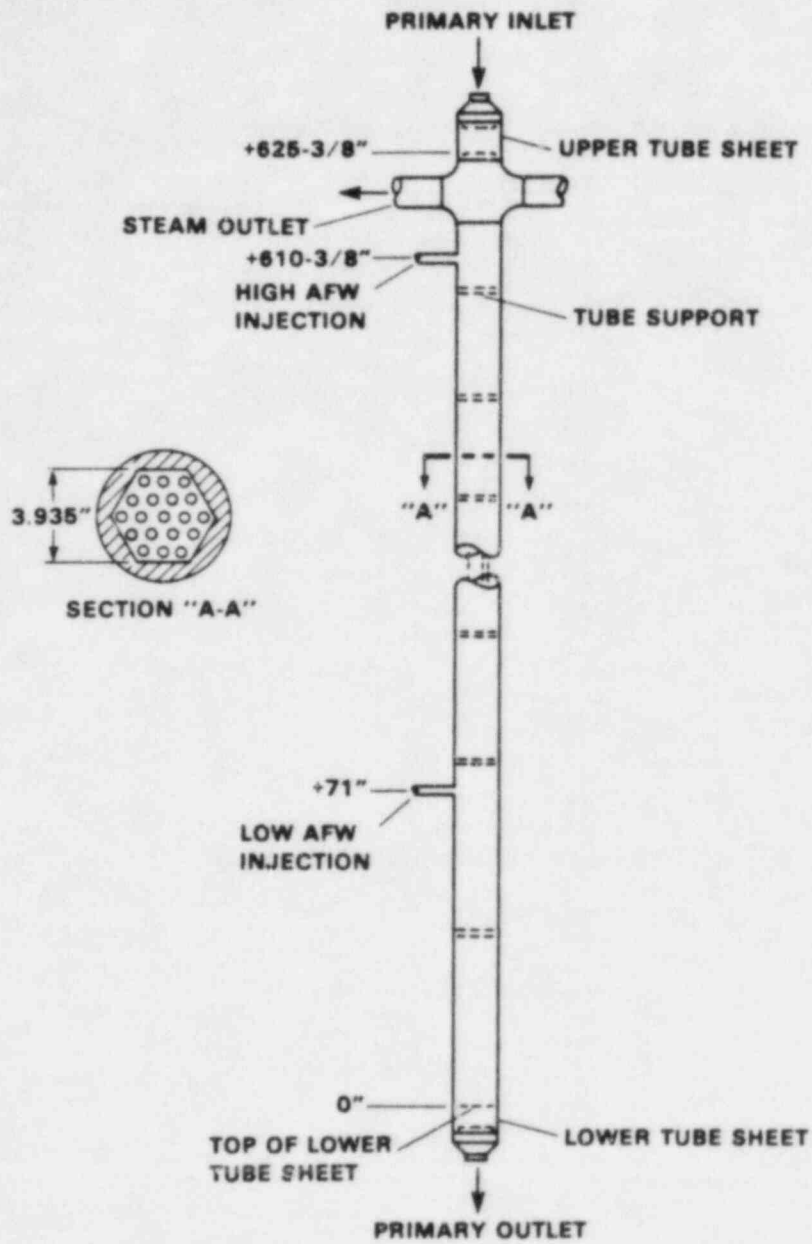


Figure 3. Nineteen-tube, once-through steam generator.

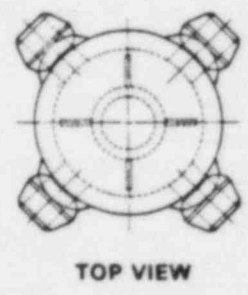
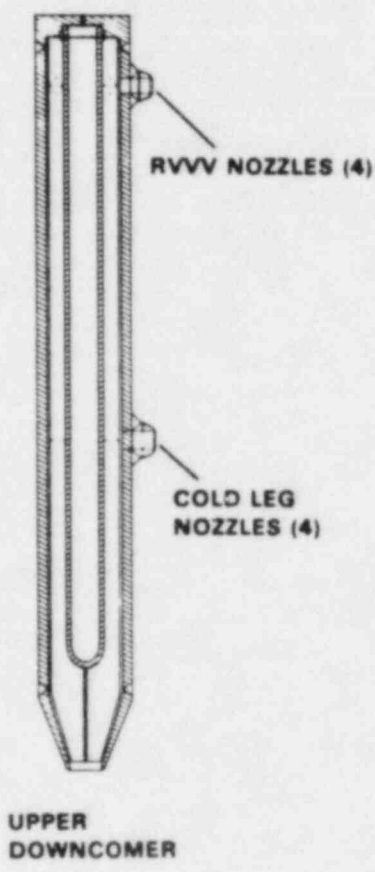


Figure 4. Upper downcomer arrangement.

The geometry of the model downcomer is annular down to the elevation of the top of the core. Just above the top of the core, the downcomer is gradually re-configured to form a single pipe for the remaining elevation. The lower downcomer region obtains roughly power-scaled fluid volume over the elevation of the core. Four model RVVVs are used to simulate eight plant valves [10]. The MIST RVVVs can be controlled individually or in unison. Individual controllers provide automatic actuation of the valves on the upper plenum to downcomer-quadrant pressure differences. The MIST RVVVs thus provide the head-flow response of the plant valves. But partially open operation is not possible in MIST; therefore, detailed valve dynamics of the plant flapper valves are absent.

The MIST pressurizer is power-to-volume scaled and contains heaters and spray. The lower pressurizer elevations are prototypical, as are those of the surge line. The model pressurizer height is reduced from that of the plant to increase the diameter. This lessens atypical fluid stratification and the likelihood of spray impinging the vessel wall.

One core flood tank is used in MIST. This tank is power-to-volume scaled to represent two plant tanks. The model tank is installed vertically, with the bottom of the tank at the prototypical elevation. The injection line from the tank to the nozzle on the downcomer is sized to preserve plant-typical irrecoverable losses, and the nozzle is sized to maintain the plant ratio of core-flood-injected fluid momentum to the downcomer fluid momentum.

#### Boundary Systems

The MIST boundary systems are sized to power-scale the plant boundary conditions. HPI and auxiliary feedwater (AFW) head-flow characteristics are based on composite plant characteristics. Scaled model vents are included in each hot leg, the pressurizer, and reactor vessel upper head. Leaks are located in the cold-leg suction and discharge piping and the upper and lower elevations of the "B" steam generator (for tube rupture simulation). The desired vent and leak flows are obtained using power-scaled restrictors.

#### Heat Losses and Guard Heaters

MIST is designed to minimize heat losses from the reactor coolant system. Fin effects (instrument penetrations through the insulation) are minimized by using 1/4-inch penetrations for most of the instrumentation. Heat losses due to conduction through component supports are minimized by designing the supports to reduce the cross-sectioned area and placing ceramic blocks between load-bearing surfaces. The reactor coolant system piping and vessel are covered with passive insulation, active insulation (or guard heaters), and an outer-sealed jacket (to prevent chimney effects). The insulation arrangement is illustrated on Figure 5. The guard heaters are divided into 42 zones, and each are controlled by a zonal temperature difference and pipe metal temperature. This provides a differential temperature control as a function of temperature. Detailed finite-difference analysis of the insulation system showed that heat loss was strongly dependent on metal temperature and weakly related to fluid state. The control temperature difference required to minimize heat losses will be experimentally determined at several loop temperatures.

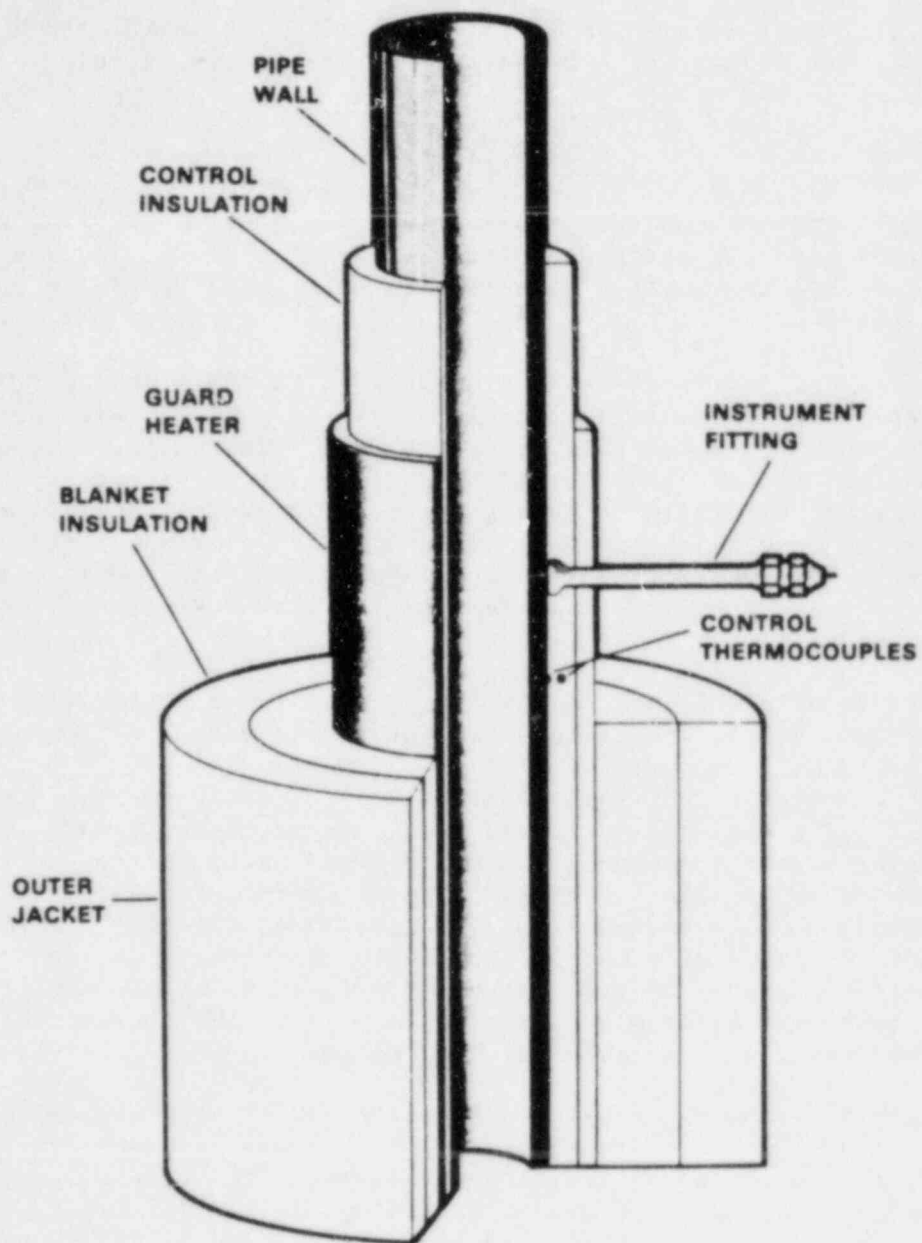


Figure 5. MIST insulation arrangement.

However, the guard heaters are not used to compensate for all heat losses in the loop. Large local losses occurring, for example, at the gamma densitometers and viewports, are not compensated. Analysis results indicate that component metal temperatures could be elevated by nearly 100°F in a steam-filled component. The increased metal temperature would not challenge the integrity of the pressure boundary, but it would result in an atypically large component of metal-stored energy.

The total MIST heat loss at 650°F is estimated to be 14 KW or 0.4% of scaled full power. The heat losses are attributable to the previously discussed uncompensated heat losses.

### Instrumentation

The selection and placement of the MIST instrumentation was made with input from experimenters and code analysts. This process considered the use of the instrumentation for code benchmarking, indication of thermal/hydraulic phenomena, and system closure.

Approximately 850 instruments are present in MIST and interfaced to a computer-controlled, high-speed, data acquisition system. MIST instrumentation consists of measurements of temperature, pressure, and differential pressure. Fluid level and phase indications are provided by optical viewports, conductivity probes [8], differential pressures, and gamma densitometers. Mass flow measurements at the system boundaries are made using Coriols flowmeters and weigh scales. Mass flow rate measurements in the loop are performed with venturis or turbines. Tables 1 and 2 provide a summary of the MIST instrumentation by component and instrument type.

The largest grouping of instrumentation is in the two steam generators. Roughly 250, or 30%, of the instruments are located in these two components.

The steam generator instrumentation provides for measurement of fluid temperature, metal and differential temperature, total guard heater power, differential pressure, gauge pressure, and conductivity (for void determination). The allocation of instruments to the steam generators resulted from the judgment that observations of AFW wetting effects and steam generator heat transfer are of major importance. Several other micro- and multidimensional phenomena are also of considerable interest: noncondensable gas coating of primary tubes, intermittent radial advancement of condensation fronts in the region of the AFW nozzle, and boiler-condenser heat transfer in the region of the secondary pool.

The core and RVVV instrumentation measures fluid temperature, metal and differential temperature, total guard heater and core power, conductivity (for void determination), and gauge and differential pressures. The core instrument distribution is intended to concentrate on the recording of axially varying parameters. A flat, radial, heat flux profile is used in the core, and radial maldistribution of inlet flow is expected to result in only minor variations in enthalpy.

Table 1

## MIST INSTRUMENTATION BY COMPONENT

<u>Component</u>	<u>Number of Instruments</u>
Cold Legs	164
Core Flood	7
Hot Legs	121
Pressurizer	25
Primary Boundary Systems	72
Reactor Vessel and Core	169
Steam Generators	249
Steam Generator Feedwater and Steam Circuit	<u>44</u>
TOTAL	851

Table 2

## MIST INSTRUMENTATION BY MEASUREMENT TYPE

<u>Measurement Type</u>	<u>Number of Instruments</u>
Conductivity Probes	36
Cooled Thermocouple	12
Differential Pressure	133
Differential Temperature	42
Fluid Temperature	381
Gamma Densitometer	12
Limit Switches	79
Mass Flow	9
Metal Temperature	69
Miscellaneous	17
Power	48
Pressure	9
Volumetric Flow	<u>4</u>
TOTAL	851

Therefore, extensively distributing radial instrumentation was deemed less important, so the majority of the in-core temperature instrumentation is located in a single, interior flow channel. Possible radial variations at the core outlet are recorded, but with a limited number of instruments. The core instrument allocation provides data regarding core heat input, inlet and exit fluid properties, and fluid gradients within the reactor vessel. In addition, it is possible to calculate collapsed levels and regional void fractions from the measurements. Vent valve mass flow rates are also calculated based on single-phase conditions existing at the vent valve.

Downcomer instruments measure fluid temperature, metal and differential temperature, total guard heater power, and differential pressures.

Forty fluid thermocouples are concentrated in the upper downcomer, detailing mixing information for the RVVV, core flood and cold-leg streams. Six additional fluid thermocouples are uniformly spaced in the lower downcomer to indicate the extent of mixing as the fluid leaves the upper downcomer. Downcomer flow measurement is obtained using a venturi and cooled thermocouple probe.

Cold-leg instrumentation provides measurements of fluid temperature, metal and differential temperature, total guard heater power, and differential pressure. Gamma densitometers are also part of the system. Loop flow measurements are included in the cold legs using venturis and cooled thermocouples located in the suction piping of each cold leg. For tests requiring full (100%) forced flow, turbines are used in place of the venturis. In addition, measurements at the reactor coolant pump are included for power, speed, and head rise.

Special instrument groupings, thermocouple rakes, and gamma densitometers, are included in the cold legs upstream and downstream of the HPI injection points to indicate thermal stratification, density, and void fraction near the junction of the cold legs and downcomer.

Hot-leg instrumentation measures fluid temperature, metal and differential temperature, total guard heater power, and differential pressure. Void measurements using gamma densitometers and conductivity probes are also made. In addition, viewports provide visual data to assess the local flow regime.

Hot-leg instrument density provides detailed information regarding fluid temperature gradients, local void fractions, and overall collapsed level. A conductivity probe, combined with local differential pressures in the U-bend region, provides additional information regarding loop refill and spillover. Gamma densitometers in hot-leg horizontals downstream of the reactor vessel's outlet nozzle and viewports in the 29-foot elevation and at the U-bend high points will improve understanding of fluid state and flow conditions in these regions. A fifth and sixth viewport in one of the hot-leg horizontals just upstream of the densitometer and one in the upturn downstream of the densitometer will provide information about developed or developing flow regimes upstream of vertical hot-leg piping.



The boundary systems, which include HPI, leaks, vents, and gas addition, are instrumented with fluid thermocouples, gauge, absolute and differential pressure transmitters, mass flowmeters, and weigh scales. These instruments provide the measurements needed to perform mass and energy closure for the facility.

### Test Program

The MIST test program will be performed in three parts: debug, characterization, and transient tests.

The debug tests are performed to demonstrate the operability of MIST hardware, controls, instrumentation, and data acquisition system.

The characterization tests generally follow the debug tests and examine the behavior of individual systems and explore limited integral system interactions. These tests include in-place instrument and guard heater calibrations, control system evaluation, and RVVV-DC interactions.

The MIST transient tests are defined for the generation of integral system data for code benchmarking. The transient test series is divided into seven groups: mapping, boundary systems, leak-HPI configuration, feed and bleed, steam generator tube rupture, noncondensable gas (NCG) and venting, and RCP operation. A total of 46 transient tests are planned. Currently, 42 of the tests are defined, as noted in the following descriptions and in Table 3. The remaining four tests are reserved for later definition and performance.

The 10 mapping tests examine the initial post-SBLOCA transient interactions. In these tests, the primary system inventory is carefully controlled and slowly varied to provide careful examination of the normally rapid and overlapping post-SBLOCA events.

The seven boundary system tests examine the adequacy and impact of the major boundary system simulations of MIST; namely, the RVVVs, guard heating, and level controls of the steam generators. These tests are the first to be conducted after mapping to ensure that the boundary system simulations are understood and that the proper simulation has been selected before most of the transient tests are performed. One test, with a plant-versed operator, is also scheduled early to permit revision of the subsequent tests if required. The base test conditions for the group include: a scaled, 10-cm<sup>2</sup>, cold-leg discharge leak; full HPI and AFW available; no NCG; RCPs not available; automatic RVVV actuation on differential pressure; automatic guard heater control; constant steam generator level control (after refill); and symmetric steam generator cooldown. The intertest variations included in the boundary system test series are RVVVs manually closed, RVVVs manually opened, no guard heating, band control of the secondary steam generator level, asymmetric steam generator cooldown, and use of abnormal transient operating guidelines (ATOG).

Leak sizes, locations, and HPI capacity are varied in the leak-HPI group. Two tests are planned with changes in leak size. Leak sizes of 5 and 50 cm<sup>2</sup> are planned for the cold-leg discharge location. Other tests with varied leak location are planned -- one with a cold-leg suction and a second with a PORV leak

Table 3

## TRANSIENT TESTS

Test Group	Number of Tests	Description
Mapping	10	Examine post-SBLOCA transient with primary inventory controlled
Boundary System	7	Examine MIST boundary system simulations and their effects (RVVVs, guard heating, SG controls) on post-SBLOCA interactions
Leak-HPI	6	Determine the changes of the integral system response caused by varied break size, break location, and HPI capacity
Feed and Bleed	3	Observe feed and bleed (HPI-PORV cooling) phenomena
Steam Generator Tube Rupture	5	Simulate SGTR transients and examine integral system interactions
Noncondensable Gas and Venting	5	Observe NCC effects and the impact of primary system venting
Reactor Coolant Pumps	6	Introduce pump operation into the SBLOCA transient to observe their impact on post-SBLOCA interactions

location. The remaining two tests are a break isolation and a reduced-HPI-capacity test. The isolated-break test repeats the boundary system test using the baseline conditions previously described but with the leak isolation at interruption of natural circulation. The reduced-HPI-capacity test uses the evaluation model HPI rather than full HPI.

The feed and bleed cooling tests examine HPI-PORV cooling. Three tests are planned; a fourth test with RCP operation is included in the RCP operation tests. The three tests of this group do not simulate the RCPs. In each test, a complete loss of feedwater is simulated and no leaks are used. The feed and bleed test uses full HPI, which is activated when the PORV lifts. No venting is to be performed during the test transient.

The steam generator tube rupture (SGTR) tests study system interactions resulting from single and multiple leaks in steam generator tubes. Five tests are defined, with simulated breaks of 10 tubes at the top and bottom of the steam generator, a single tube leak at the top of the steam generator, a steam line break superimposed on a rupture of 10 tubes, and a 10-tube rupture followed by isolation of the affected steam generator.

Five noncondensable gas (NCG) and venting tests are defined. These tests examine the impact of hot-leg and reactor vessel vents and NCGs on the post-SBLOCA interactions. One test is defined to determine the maximum amount of NCG that can be tolerated before encountering a facility limit, such as primary pressure. This amount of NCG will be used in three subsequent tests without any vents, with hot-leg vents, and with reactor vessel vents, respectively. One test will be performed without NCG but with hot-leg vents in use.

The reactor coolant pump (RCP) group includes six tests that will be performed after the primary loop is reconfigured to install the turbines for 100%-scaled flow measurement. One test is a repeat of a boundary system test to assess the effects of loop reconfiguration. Two additional tests are repeats of the feed and bleed and SGTR tests but with the RCPs operating. Two of the tests examine the effect of a continuously running pump and a pump stop with minimum loop inventory on a post-SBLOCA transient. The remaining test is performed at the direction of a plant-versed operator.

#### Schedule

The MIST project started in June 1983 with preparation of the facility specification. Construction of MIST hardware began in September 1983 and was completed in September 1985. Table 4 shows the planned and actual completion dates for the contract-defined milestones.

Facility debug was initiated in September 1985 and will continue through December 1985. Three months of characterization testing and six months of transient testing will follow the completion of debug.

#### Legal Notice

This report was prepared by the Babcock & Wilcox Company (B&W) as an account of work sponsored by the Nuclear Regulatory Commission (NRC), the Electric Power Research Institute (EPRI), B&W, and the B&W Owners Group. No person acting on behalf of the NRC, EPRI, members of EPRI, B&W, or the B&W Owners Group:

- Makes any warranty, express or implied, with respect to the use of any information, apparatus, method, or process disclosed in this report or that such use may not infringe privately owned rights; or
- Assumes any liabilities with respect to the use of, or for damages resulting from the use of any information, apparatus, method, or process disclosed in this report.

Table 4

## MIST CONTRACT MILESTONES AND DATES

<u>Milestone</u>	<u>Planned</u>	<u>Actual</u>
1. Program Management Group (PMG) Limited Release for MIST Construction	9/83	9/83
2. PMG Approval of Facility Specification	10/83	2/84
3. Issue Design & Construction Quality Assurance Plan	12/83	12/83
4. Complete Building Modification	4/84	2/84
5. Start OTIS Reconfiguration	7/84	7/84
6. Complete Building Utilities	8/84	9/84
7. First Data Acquisition System (DAS) Computer Installed	8/84	9/84
8. PMG Decision on Leak Quality	10/84	1/85
9. Complete Draft Design Verification Report	10/84	11/84
10. New Steam Generator Installed	11/84	10/84
11. Loop Automatic Control System Available	11/84	12/84
12. Receive Hot-Leg Densitometers	1/85	1/85
13. Receive Cold-Leg Densitometers	4/85	5/85
14. Reactor Coolant Pump (Casings) Installed	5/85	5/85
15. Primary and Secondary Loop Code Hydro	6/85	6/85
16. DAS Software Operational	7/85	8/85
17. Start of Facility Debug	9/85	9/85
18. Start of Transient Testing	3/86	
19. Issue Draft Final Analysis Report	2/87	

References

1. Coordination of Support Projects for the B&W Integral System Test Program, edited by J. P. Sursock and M. W. Young, NUREG-1163, to be published.
2. H. R. Carter, "Integral System Test Program," Babcock & Wilcox Operating Experience Seminar, Lynchburg, Virginia, 1983.

3. H. R. Carter and J. R. Gloude-mans, "An Experimental Study of the Post-Small Break Loss-of-Coolant Accident Phenomena in a Scaled Babcock & Wilcox System," NUREG/CP-0058, Proceedings of the U. S. Nuclear Regulatory Commission, Twelfth Water Reactor Safety Research Information Meeting, October 1984, Vol. 1, pp. 113-135.
4. E. H. Davidson and R. L. Black, "Research Relating to Reactor Vessel Head Vent Exemption: Core Cooling by Natural Circulation and Feed/Bleed in the Presence of Noncondensibles," NUREG/CP-0058, Proceedings of the U. S. Nuclear Regulatory Commission, Twelfth Water Reactor Safety Research Information Meeting, October 1984, Vol. 1, pp. 136-152.
5. R. K. Fujita and T. D. Knight, "TRAC-FF1/MOD1 Support Calculations for the MIST/OTIS Program," NUREG/CP-0058, Proceedings of the U. S. Nuclear Regulatory Commission, Twelfth Water Reactor Safety Research Information Meeting, October 1984, Vol. 1, pp. 153-173.
6. D. P. Birmingham, R. L. Black, and G. C. Rush, "An Experimental Study of the Application of Abnormal Transient Operating Guidelines (ATOG) to the Babcock & Wilcox Nuclear Steam Supply System During a Small Break Loss-of-Coolant Accident," ASME/AIChE/ANS National Heat Transfer Conference, Denver, Col., August 6 - 9, 1985.
7. M. T. Childerson and R. K. Fujita, "TRAC-PF1 Code Verification with Data from the OTIS Test Facility," (Paper to be presented at the 106th ASME Winter Annual Meeting), November 1985.
8. Y. A. Hassan and G. C. Rush, "A New Technique for Estimation of Void Fraction from Conductivity Probe Signals in a Small Break Loss of Coolant Accident Test Facility," (Paper to be presented at the 106th ASME Winter Annual Meeting), November 1985.
9. J. R. Gloude-mans, "OTIS Test Results," (Paper to be presented at the Thirteenth Water Reactor Safety Research Information Meeting), October 1985.
10. J. R. Gloude-mans, "Simulation of Reactor Vessel Vent Valves," (Paper to be presented at the 106th ASME Winter Annual Meeting), November 1985.

## Highlights of the OECD LOFT Experiment Program

J. Birchley UKAEA/EG&G Idaho, Inc.  
P. North, EG&G Idaho, Inc.

A group of countries (a), each of which is a member of the Organization for Economic Cooperation and Development (OECD), formed and sponsored the OECD LOFT Project under the auspices of the OECD Nuclear Energy Agency (NEA). The purpose of the Project was to undertake research intended to improve the understanding and predictability of transient behavior and to enhance the reliability, availability, economics and safety of pressurized water reactors. The specific objectives of the OECD LOFT experiment program were formulated to meet the needs of the participating countries. The resultant experiment program was defined on the basis of consensus among the participants and comprised a total of six thermal-hydraulic experiments and two fission product release and transport experiments.

The Loss of Fluid Test (LOFT) facility, in which the experiment program was conducted, is a nuclear integral test facility at the Idaho National Engineering Laboratory, operated by EG&G Idaho Inc. for the U. S. Department of Energy. The LOFT pressurized water reactor (PWR) incorporated the major functional components of a commercial PWR, was capable of operation under nominal PWR operating conditions and a wide range of off-normal and accident conditions, and was unique in providing nuclear heat generation within an integral test facility.

The objectives and conduct of the six thermal hydraulic experiments addressed a number of issues of current concern to the various member nations. The issues and major findings of the thermal-hydraulic experiments are summarized as follows.

Pump operation for small hot leg breaks. Two experiments were conducted to determine the effects of pump operation on factors such as primary system coolant inventory and core cooling during a small hot leg break transient. These experiments, LP-SB-1 and LP-SB-2, had identical 3-inch equivalent hot leg breaks, but whereas the first terminated pump operation early in the transient, the second provided pump operation for an extended period. Flow stratification in the hot leg and consequent break uncover occurred with pumps on as well as with pumps off. Neither experiment exhibited core uncover and, in contrast to the case of a small cold leg break, system mass depletion was not sensitive to pump operation.

Plant recovery from highly voided conditions. One experiment was conducted to examine aspects of plant recovery from high void conditions in the primary system. The experiment, LP-SB-3, simulated a small cold

(a) Current Project membership comprises: Austria, Finland, Italy, Japan, Spain, Sweden, Switzerland, United Kingdom, U.S.A. (EPRI, USDOE and USNRC as individual participants), and West Germany.

leg break without HPIS or auxiliary feedwater, resulting in a highly voided primary system and core uncover at a pressure above the accumulator setpoint. Secondary feed and bleed was found to be effective in reestablishing good primary to secondary heat transfer, providing depressurization to the accumulator setpoint and consequent recovery of the core.

A second experiment was conducted to examine behavior related to plant recovery from high void conditions in the secondary system. Experiment LP-FW-1 simulated a total loss of feedwater, with consequent voiding of and degraded heat transfer in the steam generator. Primary system feed and bleed, by means of latching open the PORV and injection from the HPIS, was effective in allowing the primary mass inventory to be maintained while providing energy removal.

Response to large break design basis LOCA and ECCS effectiveness with licensing assumptions employed by different countries. The focus of this work relates to evaluation of best estimate codes and evaluation of licensing conservatisms. Experiments LP-02-6 and LP-LB-1 showed core rewet during blowdown to be highly sensitive to the rate of pump coastdown following trip. Cooling and quenching of the core was achieved in each experiment and even with very pessimistic assumptions concerning ECCS failures and pump behavior. New insights were obtained into post-CHF heat transfer at high pressures and into the role of nitrogen purge from the accumulators during reflood.

The objectives of the two fission product experiments addressed the magnitude and physical and chemical character of the radionuclide source term for accidents resulting in fuel damage. The LOFT system configuration for these experiments included modified test fuel modules to facilitate the release of fission products and aerosols, and specially designed fission product instrumentation.

Experiment LP-FP-1 was conducted to determine the release of volatile fission products from the fuel-cladding gap in the event of cladding rupture and to examine the transport and deposition of the fission products in a vapor dominated transport medium. Leaching of additional fission products by water following reflood was also a major interest as were the transport and deposition of the fission products within a liquid filled primary system. The bulk of the noble gases (Xe, Kr) were found to be transported out of the coolant system. Most of the volatile fission products detected (Cs, I, Te, Ba, Sr) were retained in the coolant system. Significant leaching of fission products occurred, particularly Te, by the reflood water.

Experiment LP-FP-2 represented a V-sequence accident from initiation of a LPIS pipe break through the early stages of severe core damage. The primary objective of the experiment was to provide data on the release of fission products through the early stages of severe core damage and on their transport in an environment where aerosols, formed from control rods and core structural materials, could provide a major transport mechanism.

In the experiment, temperatures in excess of 2100K were sustained for at least 4.5 minutes. There was evidence of extensive metal-water reaction in the test fuel bundle, control rod failure, and major core relocation. Fission products detected shortly following the experiment, include isotopes of Xe, Kr, Cs, I, Te, Rb, Ba, and Sr. Post-test data will be acquired by examination of aerosol collection filters, primary system metal surfaces, and liquid and vapor grab samples. Analysis of the gamma spectroscopy data is continuing. The data thus obtained will be of particular benefit in assessing the current understanding of the processes controlling fission product release, and the predictive capability of state-of-the-art computer models.

The International OECD LOFT Experiment Program has benefited greatly from the active and expert participation by the Project members, and has been successfully completed with the achievement of the major immediate objectives. The details of the experiment specifications and the resultant data are proprietary to the sponsors. The bulk of the experiment documentation and data has been issued to the participating countries, and is available to organizations within those countries through the respective OECD LOFT Project Program Review Group member. A list of the various Review Group members and their respective organizations is presented in Appendix I.



APPENDIX I

OECD LOFT PROGRAM REVIEW GROUP

Mr. Jesse Fell, Deputy Director Water Reactor Programme  
UKAEA  
Atomic Energy Establishment  
Mail Stop166/A32  
Winfrith  
Dorchester Dorset  
DT2 8DH  
UNITED KINGDOM

Mr. D. F. Giessing  
U. S. Department of Energy  
Office of Nuclear Power Systems  
MS B-107  
Washington, D.C. 20545

Prof. E. F. Hicken  
Manager, Processes Division  
Gesellschaft für Reaktorsicherheit mbH  
Forschungsgelände  
D-8046 Garching  
FEDERAL REPUBLIC OF GERMANY

Mr. Heikke Holmstrom  
Technical Research Center of Finland (VTT)  
Nuclear Engineering Laboratory  
POB 169  
SF-00181  
Helsinki 18  
FINLAND

Mr. P. D. Jenkins  
GDCD  
Central Electricity Generating Board  
Barnett Way  
Barnwood  
Gloucester  
GL4 7RS  
UNITED KINGDOM

Mr. O. M. Mercier  
Eidgenössisches Institut für Reaktorforschung  
CH-5303 Würenlingen  
SWITZERLAND

Mr. M. Merilo  
EPRI  
P. O. Box 10412  
Palo Alto, CA 94304

S. M. Modro  
Osterreichisches  
Forschungszentrum Seibersdorf Gesellschaft mbH  
c/o EG&G Idaho, Inc.  
P. O. Box 1625  
Idaho Falls, ID 83415  
USA

Dr. Giorgio Palazzi  
Ente Nazionale Energie Alternative  
CRE Cassaccia  
S. P. Anguillarese km 1 + 300  
C. P. No. 2400  
I-00100 Rome  
ITALY

Mr. Jose Puga  
ENUSA  
c/Santiago Rusinol, 12  
E-28040 Madrid  
SPAIN

Mr. O. Sandervaag  
Studsvik Energiteknik AB  
S-61182 Nykoping  
SWEDEN

Dr. Brian Sheron  
Office of Nuclear Reactor Regulation  
U. S. Nuclear Regulatory Commission  
Washington, D.C. 20555

Dr. Robert Van Houten  
U.S. Nuclear Regulatory Commission  
Washington, D.C. 20555

Dr. Kanji Tasaka  
Japan Atomic Energy Research Institute  
Tokai-mura, Naka-gun  
Ibaraki-ken 219-11  
JAPAN

Japanese Industries Group  
c/o Mitsubishi Corporation  
Power and Electrical Systems  
Attention: Mr. T. Hada, Manager  
Nuclear Power Systems, Team A  
6-3, 2-Chome Marunouchi  
Chiyoba-Ku, Tokyo 100  
JAPAN

## INTRODUCTION

Donald E. Solberg  
U.S. Nuclear Regulatory Commission

In my presentation at last year's Water Reactor Safety Research Information Meeting, I summarized the history of testing in Semiscale from 1974 through 1984 and provided references for the Quick-Look Reports that were available for all of these tests. One purpose of my current presentation is to update that list for testing during 1985, which consisted of two test series. The first series consisted of two steam line breaks (Tests S-FS-1 and S-FS-2) and three feedwater line breaks (Tests S-FS-6, S-FS-7, and S-FS-11). The second test series consisted of two tests, S-FS-1 and S-FS-2, which essentially duplicated tests S-UT-6 and S-UT-8, which were conducted in a somewhat different Semiscale system design in 1981; these are small-break LOCAs in which core liquid level depression and core heatup have been observed. Results from both of these test series will be described in the next two papers.

When unexpected phenomena occur, as was the case with the core heatup during the S-UT-8 test, it is helpful to our understanding of the likely response in a large reactor to have both a wide range of highly reliable data to aid in our assessment of the individual experiment responses, as well as additional experiments conducted with important design differences, such as scaling, to assess the effects of this design differences on system response. Thus we are most fortunate to have a test series performed on ROSA-IV under similar conditions to Semiscale tests S-UT-6 and S-UT-8, and the recent reruns, S-LH-1 and S-LH-2. These tests should form a solid experimental baseline for code assessment. These ROSA-IV experiments will be described in the third paper this afternoon.

The fourth paper this afternoon presents results from reflood experiments in the PKL facility in the Federal Republic of Germany.

In the Semiscale program, we take very seriously our role in system code assessment. We have tried to structure our reporting to be of the greatest possible use to those who would use the data for code assessment. This includes complete definition of the system design and measurement locations for code modeling, discussion of important transient phenomenological relationships, and finally, an evaluation of uncertainties. Since the codes are used extensively in setting up and assessing the experimental results, these efforts are logically the first step in code assessment. The purpose of the fifth paper this afternoon, which has unfortunately been withdrawn, was to provide information on the experience gained from application of the International Code Assessment Program approach to experimental data evaluation for one Semiscale test series. Although this work is ongoing, the results will not be presented here. I refer you to Gary Wilson's paper tomorrow afternoon for further information on uncertainty evaluation and its application.

During 1986, four small-break LOCA experiments will be performed in Semiscale. In this test, the high pressure ECCS will be disabled and plant recovery capabilities of various operator actions will be evaluated. Among these actions will be restart of the primary coolant pumps in voided loops. Following these tests, Semiscale will be shutdown with no currently scheduled restart. We have yet to decide whether to keep it in a test-ready condition or to allow the system to degraded and be scavenged, as needed. FIST, the BWR integral test facility, is currently being kept intact at GE's San Jose site. The MIST facility, the principal integral test facility for B&W plant designs, will start testing shortly and continue through 1986, or perhaps into 1987. Following MIST shutdown, NRC will no longer have major integral test facilities in the U.S. in which to perform experiments. Foreign facilities, such as ROSA-IV and Bethsy, will perhaps continue to operate and provide us with useful data. However, these sources of experimental data do not completely satisfy our data needs, e.g., when important safety issues arise requiring rapid action by the NRC staff, for example, as a result of a serious transient in an operating reactor. Experience has shown that as these regulatory issues arise, a combined analytical and experimental approach provides input to the staff that enables regulatory decision making with acceptable confidence. Experience also shows that at least one transient of major safety significance occurs in an operating reactor each year that requires extensive staff evaluation, e.g., the Davis-Besse loss-of-feedwater transient on June 9, 1985. Parametric assessments performed by the staff to evaluate implications of these transients and appropriate regulatory actions often require analyses with best-estimate codes into response conditions for which little or no directly applicable code assessment has been performed. An available, rapid responding experimental capability is needed in these cases. In addition, advanced LWR concepts, e.g., the GE GESSAR plant, the Westinghouse SP-90 plant, and more advanced small plants under investigation for EPRI may also require independent evaluation by the NRC staff which could require improved analysis methods or experimental support. Thus we have concluded that for the NRC staff to make timely decisions in the future on plant design and operational issues using a sound technical basis such that unnecessary controversy and debate do not result, and such that excessive delays in providing needed results does not cause power reductions, plant shutdowns, or delays in licensing which would be costly to the public, it is necessary to maintain both analytical and experimental thermal hydraulic expertise.

In recent years, the NRC research budget has been shrinking. Ideally this could be accommodated with minimal effect on the scope and quality of the research being performed. One approach to achieve this objective is by consolidation of staffs now being funded at multiple locations. This approach is not being planned by NRC for both analytical and experimental research, insofar as practical. Two options currently being considered for maintaining integral system experimental capability are construction of new facilities and moving existing facilities to the consolidated site.

To assure ourselves that any new future facilities are the most cost-effective means for NRC to resolve these undefined future issues, we have initiated a scaling study to determine if there are technical or cost advantages to

integral facility designs, different from those in current general use. We have, for example, noted with interest the University of Maryland's facility design and we will examine carefully its capabilities and shortcomings when compared with results from more standard facilities, such as MIST. To assure NRC that this scaling study, being performed by EG&G Idaho, is well founded, we have asked outside experts to evaluate the basis of the study part way through its development. A group of experts reviewed and discussed the EG&G results at meetings on October 10-11, 1985. This meeting provided valuable input to the study. The final two papers today will discuss scaling evaluations of experimental facilities. The first will discuss the relationship among the available U.S. facilities modeling B&W reactors, i.e., MIST, University of Maryland, and an EPRI-sponsored facility at SRI. The final paper will provide some of the scaling study results applicable to future facility designs.

Table 1

## 1985 SEMISCALE TEST REPORTS

<u>TEST NUMBER</u>	<u>EXPERIMENTAL OPERATING SPECIFICATION</u>	<u>QUICK-LOOK REPORT</u>
S-FS SERIES	EGG-SEMI-6625	- - -
S-FS-1	EGG-SEMI-6783	EGG-SEMI-6858
S-FS-2	EGG-SEMI-6761	EGG-SEMI-6827
S-FS-6	EGG-SEMI-6871	EGG-SEMI-7022
S-FS-7	EGG-SEMI-6871	- - -
S-FS-11	EGG-SEMI-6909	- - -
S-LH-1 and S-LH-2	EGG-SEMI-6813	EGG-SEMI-6884

SEMISCALE SECONDARY TRANSIENT INVESTIGATIONS:  
RESULTS FROM SEMISCALE MOD-2C FEEDWATER AND STEAM LINE BREAK TESTS

T. J. Boucher

Idaho National Engineering Laboratory

ABSTRACT

A series of experiments was conducted in a scaled model of a pressurized water reactor (Semiscale MOD-2C) to investigate the system response to steam generator main steam line and bottom main feedwater line breaks. The two main steam line break tests simulated double-ended offset shears upstream and downstream of the flow restrictor. The three bottom main feedwater line break tests simulated 100% (percentage of feedwater distribution box outlet flow area), 50%, and 14.3% breaks downstream of the check valve. From the experimental results, the characteristic system responses for these secondary transients have been examined. Experimental results are compared to Final Safety Analysis Report code calculation assumptions regarding separator performance during steam line breaks and primary-to-secondary heat transfer degradation with loss of mass during feedwater line breaks. Finally, the results are discussed with respect to current safety concerns regarding pressurized thermal shock and primary overpressurization phenomena.

INTRODUCTION

This paper presents a discussion of the results from steam generator main steam line and bottom main feedwater line break experiments<sup>1</sup> performed in the Semiscale MOD-2C facility. Tests S-FS-1<sup>2,3</sup> and S-FS-2<sup>4,5</sup> simulated double-ended offset shears of the main steam line (downstream and upstream respectively) flow restrictor with compounding factors. Tests S-FS-6<sup>6,7</sup>, S-FS-7<sup>6,8</sup> and S-FS-11<sup>9,10</sup> simulated 100%, 14.3% and 50%<sup>a</sup> respectively, breaks downstream of the main feedwater line check valve with compounding factors. The Semiscale MOD-2C system consists of the MOD-2B system with a new Type III single loop steam generator which allows increased instrumentation while providing a more prototypical simulation of a full scale steam generator.

The background for these tests is discussed in brief below. A large number of assumptions and simplifications are employed when performing secondary side transient calculations. Main steam line break calculations performed for pressurized water reactor (PWR) Final Safety Analysis Reports (FSARs) have predicted primary fluid overcooling, raising concerns regarding possible pressurized thermal shock (PTS) occurrences. Bottom feedwater line break calculations, performed for the Combustion Engineering (C-E) System 80 FSAR,<sup>11</sup> have predicted peak primary system pressures in excess of 110% of the system design pressure. These calculations employed a large number of assumptions and simplifications. The foremost assumptions for main steam line break calculations were regarding transient separator performance which were

a. Percentage of the bottom feed steam generator feedwater distribution box outlet flow area.

considered to be conservative. The most important assumption regarding feedwater line break calculations concerned the degradation of primary-to-secondary heat transfer with secondary inventory and was considered by C-E to be highly conservative. Although the FSAR calculations are believed to be conservative, the degree of conservatism remains unanswered. Quantification of the degree of conservatism requires performing best estimate calculations utilizing a computer code which has been assessed for this type of event. To provide data to help answer these concerns, the steam line and feedwater line break tests were performed with conditions consistent with, or scaled from, those used for Westinghouse and C-E System 80 FSAR calculations.

All of the experiments performed consisted of an initial phase during which only automatic actions were assumed to occur followed by phases during which operator initiated plant recovery actions were simulated. For all of the tests the timing of the initial phase was set at 600 s as a minimum, and Main Steam Isolation Valve (MSIV) closure as a maximum. The initial phase of Tests S-FS-1 and S-FS-2 were essentially identical with the exception of the steam line break flow areas. The initial phase of Tests S-FS-6, S-FS-7 and S-FS-11 were also essentially identical with the exception of the bottom feedwater line break flow areas.

Discussions in this paper will be limited to the initial phase of the tests. A brief description of the Semiscale MOD-2C facility will be presented first. This will be followed by a discussion of the main steam line break test conduct and test results, followed by a discussion of the bottom main feedwater line break test conduct and results. Finally, conclusions derived from these test results are discussed.

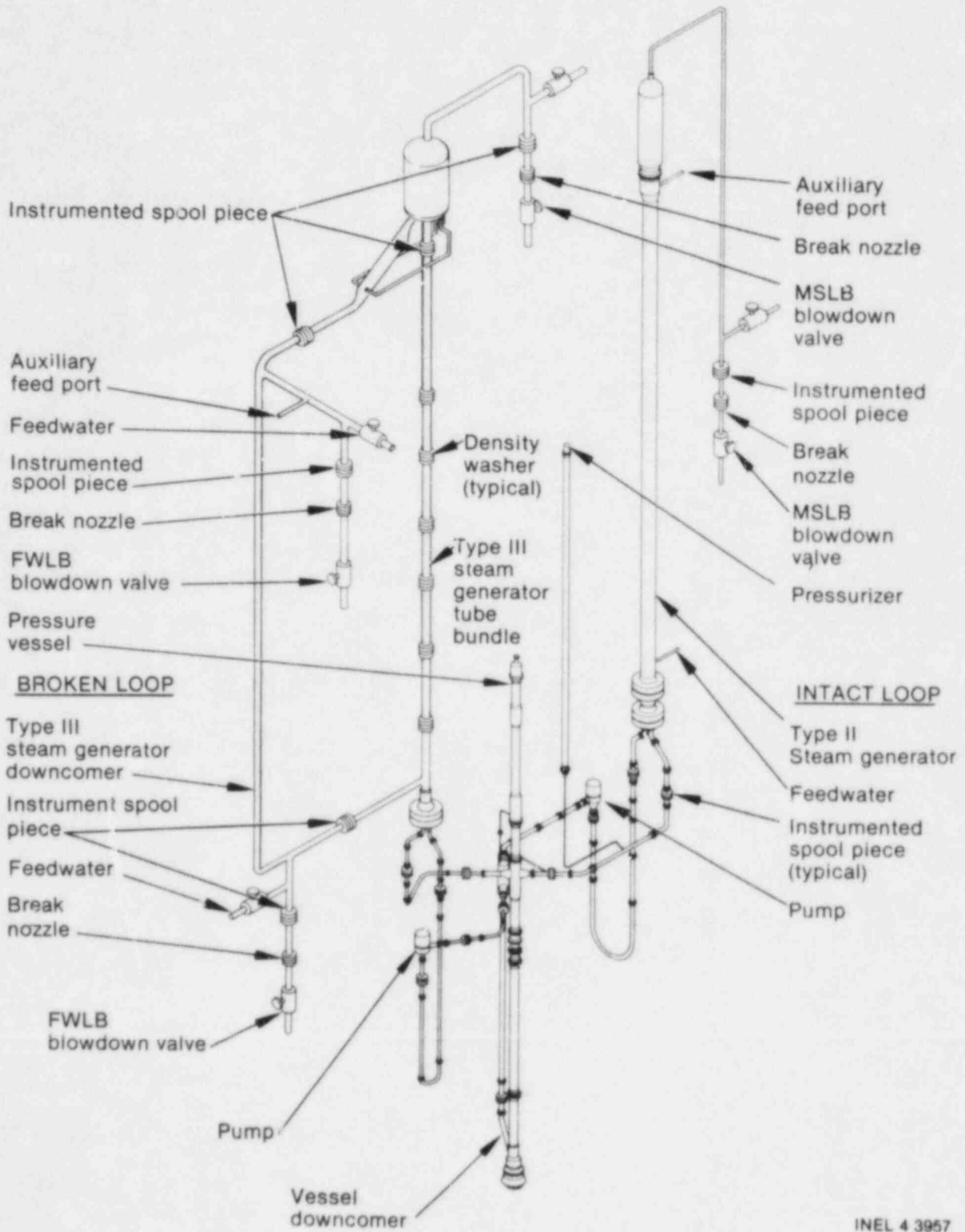
#### FACILITY DESCRIPTION

The facility configuration required for the Feedwater and Steam Line Break (FS) Test Series is the Semiscale MOD-2C system which is illustrated in Figure 1. The system is scaled from a reference four-loop PWR system based on the core power ratio,  $2(\text{MW})/3411(\text{MW})$ .<sup>12</sup> Component elevations, dynamic pressure heads, and liquid distribution were maintained as similar as practical. The two-loop test configuration consisted of the vessel with a 25-rod electrically heated core and external downcomer, tube-and-shell steam generators and associated loop piping with circulation pumps. The affected loop (in which the steam line break occurs) is scaled to represent one loop of a four-loop PWR and the unaffected loop represents three loops of a four-loop PWR. The MOD-2C system consists of the MOD-2B system with several modifications. A new "Type III" broken loop steam generator, new main steam line and feedwater line break assemblies, break effluent catch tanks, and refined steam generator control systems have been incorporated into the system for this test series.

The Type III broken loop steam generator design incorporates a downcomer that is outside the tube bundle and riser sections (Figure 2). In this manner, component mass inventory and fluid property (including density/void fraction) information may be obtained. The design also includes a steam dome with separator equipment expected to provide steam exit qualities of at least 90% during full-power, steady-state operations.

Component flow areas, volumes, lengths, and pressure drops have been sized to simulate a Westinghouse Model 51 steam generator. To increase the





INEL 4 3957

Figure 1. The Semiscale MOD-2C facility as configured for the FS test series.

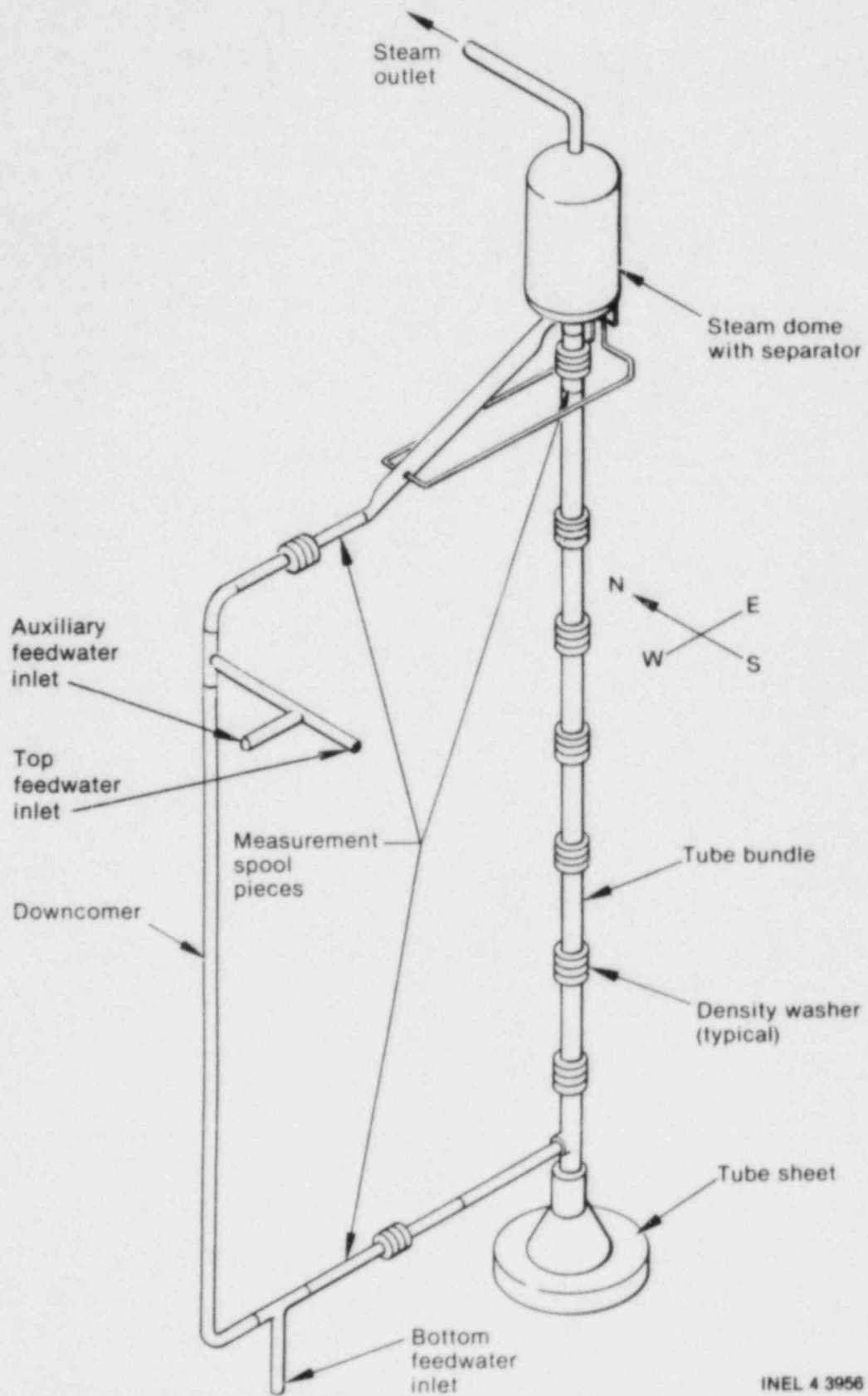


Figure 2. The Semiscale Type III steam generator configuration.

reliability and longevity of the Type III steam generator temperature thermocouples, U-tubes with a 0.165-cm (0.065-in.) wall thickness were used. Design calculations indicate very little difference in either heat transfer or flooding characteristics for the 0.165-cm (0.065-in.) wall thickness as opposed to the 0.124-cm (0.049-in.) wall thickness used in Westinghouse Model 51 steam generator U-tubes. The Type III steam generator U-tubes are configured with a "square" pitch similar to a Model 51 steam generator and simulate a long and a short tube in the prototype. Tube heights were selected to maintain symmetry with the intact loop steam generator.

The downcomer flow area and volume were sized to obtain approximately the correct liquid volume and velocity while producing approximately the correct frictional pressure drop. Either top or bottom feedwater injection can be accommodated with the new downcomer design.

The steam/dome separator was designed to simulate the behavior of the corresponding component in a Westinghouse Model 51 steam generator. Similar to the Westinghouse Model 51 steam generator component, separation of the liquid from the steam occurs in three stages. The two-phase mixture exiting the riser section is deflected into the steam dome wall where some of the liquid is separated from the mixture, flows down the wall, and is transferred to the downcomer through a connecting line. The remaining mixture continues up through the dome to the secondary separator, with some gravity-separated liquid falling back down to the bottom of the dome and mixing with the liquid separated by the deflector at the first stage ("primary" separator). The "secondary" separator, or third stage of separation, accepts the remaining two-phase mixture and imparts a centripetal motion to it. The resulting separated liquid then flows down through connecting lines to the downcomer. This final stage of separation is expected to produce steam dome exit qualities of at least 90% for full-power conditions.

#### STEAM LINE BREAK TEST CONDUCT

Tests S-FS-1 and S-FS-2 simulated transients initiated by a double-ended offset shear of a steam generator main steam line (downstream and upstream respectively) of the flow restrictor. Simulation of the communication resulting from failure of the check valve in the affected main steam line was realized by allowing the intact loop steam generator to blow down until main steam isolation valve (MSIV) closure. Initial conditions represented normal "hot standby" operation of the ZION Unit 1 plant<sup>13</sup> (a Westinghouse four-loop PWR), a postulated worst case scenario for this type of transient. Effects of reactivity feedback on nuclear power were not simulated. Hence, a constant power level of 1-1/2% was simulated.

Many of the assumptions made for Final Safety Analysis Report (FSAR) steam line break calculations were used for Tests S-FS-1 and S-FS-2. The safety injection signal (SIS) was assumed to be generated by a low steam line pressure signal from the affected steam generator. Loss of Off-site Power (LOP), causing primary coolant pump trips (with a 2 s delay to simulate the transformer decay time) and delaying safety injection and auxiliary feedwater availability for 25 s, was assumed to occur at SIS. Degraded safety injection flows were assumed such that only one train of

high pressure injection system (HPIS) and one train of charging were available. The performance of an automatic faulted secondary detection system was simulated such that auxiliary feedwater was supplied to only the unaffected steam generator. Main feedwater isolation and MSIV closure were assumed to occur at SIS with 1 and 4 s, respectively, valve closure times.

Compensation for environmental heat loss was provided through heat addition with trace heaters on the exterior of the pressure boundary and through augmentation of the core power. To allow maximum depressurization of the pressurizer, the pressurizer external heater was not powered for these tests. The total power provided by the five remaining external heater banks was 44.0 kW. Since this was below the system environmental heat loss, an additional 15 kW of core power augmentation was required to offset the heat loss.

### STEAM LINE BREAK TEST RESULTS

The occurrence of a double-ended offset shear of a steam generator main steam line produces severe effects on the steam generator secondaries. The steam line break initiated the transients at 0 s. Compounded by failure of the affected loop steam line check valve, the unaffected as well as affected loop steam generator experienced loss of inventory. For the break upstream of the flow restrictor (S-FS-2), the flow from the affected loop steam generator represented flow limited only by the steam generator exit piping flow area; whereas, the flow from the unaffected loop steam generator represented flow limited by the affected steam line flow restrictor. For the break downstream of the flow restrictor (S-FS-1), the flow from the affected loop steam generator represented flow limited by the affected steam line flow restrictor. At the same time the flow from the unaffected loop steam generator represented flow from three steam generators (with the flow from each limited by its respective flow restrictor). Secondary fluid originally at 6.76 MPa (980 psia) flowed from the steam generators through the break flow nozzles and into the catch tanks. The affected loop secondary emptied much faster during S-FS-2 due to the much larger break area for the break upstream of the flow restrictor. This produced the faster affected loop secondary depressurization shown in Figure 3 and resulted in a much earlier SIS. The break flow from the unaffected loop secondary was much slower in S-FS-2 due to the smaller break area for one versus three flow restrictors. This caused the slower unaffected loop secondary depressurization shown in the figure.

The flow from the Type III affected loop steam generator was mostly steam for both tests with only slight two-phase flow evident early in the transients, (Figure 4). During the initial part of the blowdowns, the high mass flow rates in the affected loop steam generator and the rapid depressurization, caused a high initial flow from downcomer to riser, followed by flow reversal in the separator drain lines, and degraded the performance of the steam separator. This allowed the two-phase mixture to exit the steam dome until the flows reduced to within the range of the steam separator capabilities. The minimum measured break void fraction was 92% for test S-FS-2 and 96% for Test S-FS-1. Hence, almost perfect separation was maintained by the Type III affected loop steam generator during the tests.

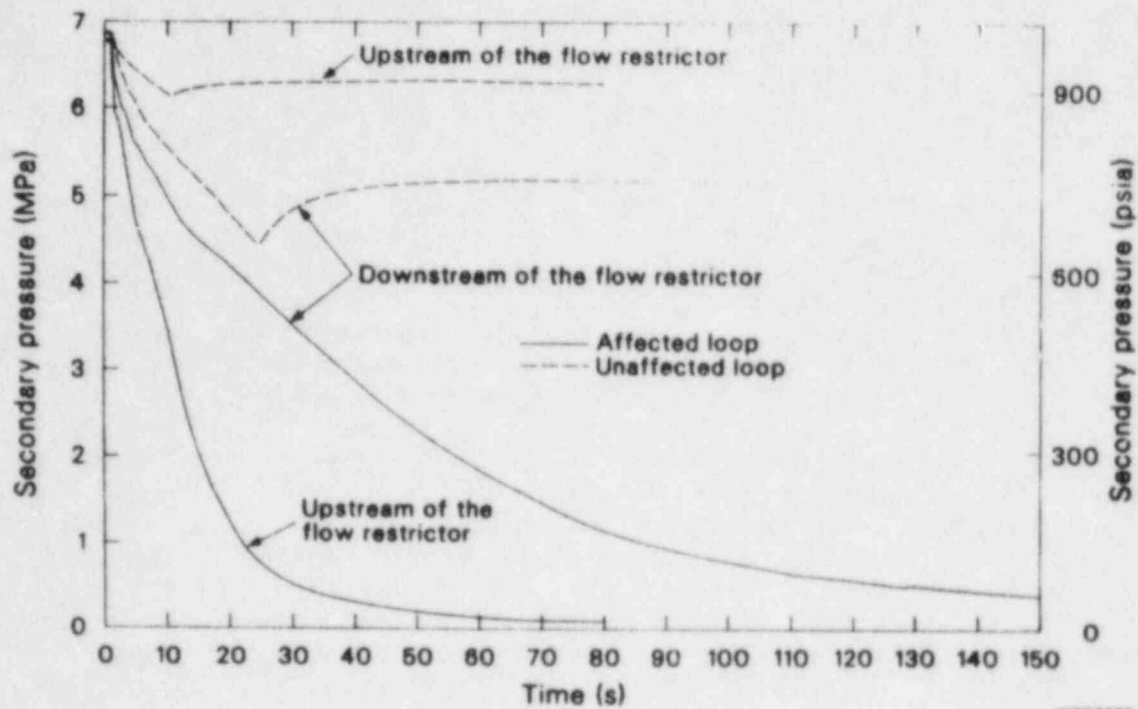


Figure 3. Affected and unaffected loop secondary pressures for Tests S-FS-1 and S-FS-2.

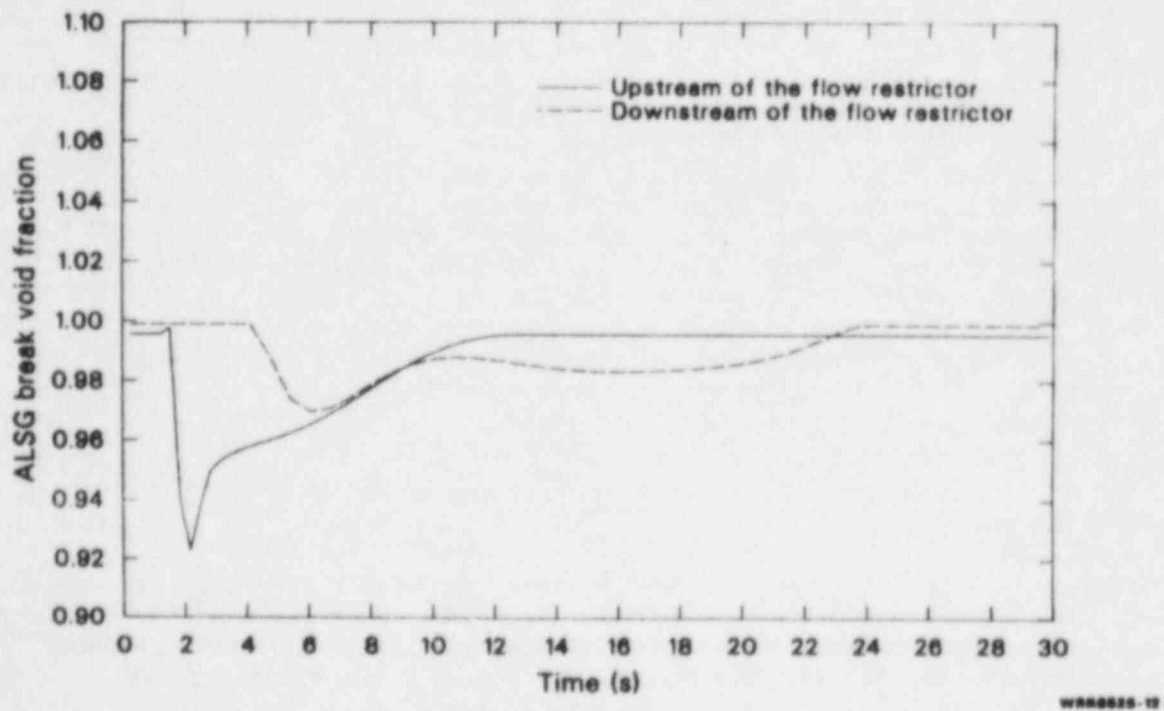


Figure 4. Type III steam generator break void fraction for Tests S-FS-1 and S-FS-2.

The low affected loop steam generator pressure trip setpoint of 4.14 MPa (600 psia) was reached at about 7.5 s during S-FS-2 and about 21 s during S-FS-1. This initiated the SI and MSIV closure signals and the LOP. The depressurization of the unaffected loop steam generator was halted when the MSIV fully closed at about 11 s during S-FS-2 and about 27 s during S-FS-1. The unaffected loop steam generator mass loss for S-FS-2 was approximately 3-1/2% of the initial mass whereas approximately 36% of the initial mass was lost in S-FS-1. Following MSIV closure, the unaffected loop steam generator experienced a slight repressurization due to energy addition from the primary fluid system in the absence of secondary feeding and steaming. The affected loop steam generator continued to depressurize until the generator was essentially empty at about 50 s during S-FS-2 and about 110 s during S-FS-1.

The pump coastdowns resulting from LOP limited the primary-to-secondary heat transfer during both tests. The primary-to-secondary heat transfer from the affected and unaffected loop steam generators increased until the primary coolant pump coastdowns and MSIV closures occurred at about 11 s during S-FS-2 and about 25 s during S-FS-1, as shown in Figure 5. The heat transfer then decreased with the decreasing loop flows, with final reduction occurring when the pumps were turned off at 52 s during S-FS-2 and 67 s during S-FS-1. The slight rise in heat transfer starting at about 45 s for the affected loop steam generator during S-FS-1 is attributed to the increasing primary-to-secondary temperature difference due to the secondary depressurization. The increasing temperature difference in conjunction with the relatively flat nature of the loop flow coastdown curve over this portion of the test produced the net increase in heat transfer.

The primary-to-secondary heat transfer was obviously limited by several mechanisms since the total energy transferred was at least an order of magnitude smaller than the energy removal potential provided by the break flows. Calculation of the local secondary side convective heat transfer coefficients from temperature triplet data indicates that the secondary convection increased over a brief period and then remained essentially constant before degrading to zero. An example of this is shown in Figure 6. During the period of constant secondary convective heat transfer coefficients, the primary-to-secondary heat transfer continued to increase. Over this same time period the primary-to-secondary temperature difference continued to increase. This indicates that the heat transfer was limited by the conduction through the tube walls rather than the secondary convective heat transfer. The process appears to have been conduction limited prior to the LOP, and primary fluid convection limited during the loop flow reduction, with some secondary convection limiting observed during S-FS-2.

The increased primary-to-secondary heat transfer during both tests cooled the primary fluid causing primary fluid shrinkage and primary depressurization, as shown in Figure 7. Whereas the pressurizer inventory was only reduced by about 30% during S-FS-2, the pressurizer emptied at about 17 s during S-FS-1 resulting in an increased depressurization rate that can be seen in Figure 7. The cooling of the primary fluid continued until about 15 s during S-FS-2 and 69 s during S-FS-1, as shown in Figure 8. The minimum cold leg temperatures reached were about 554 K

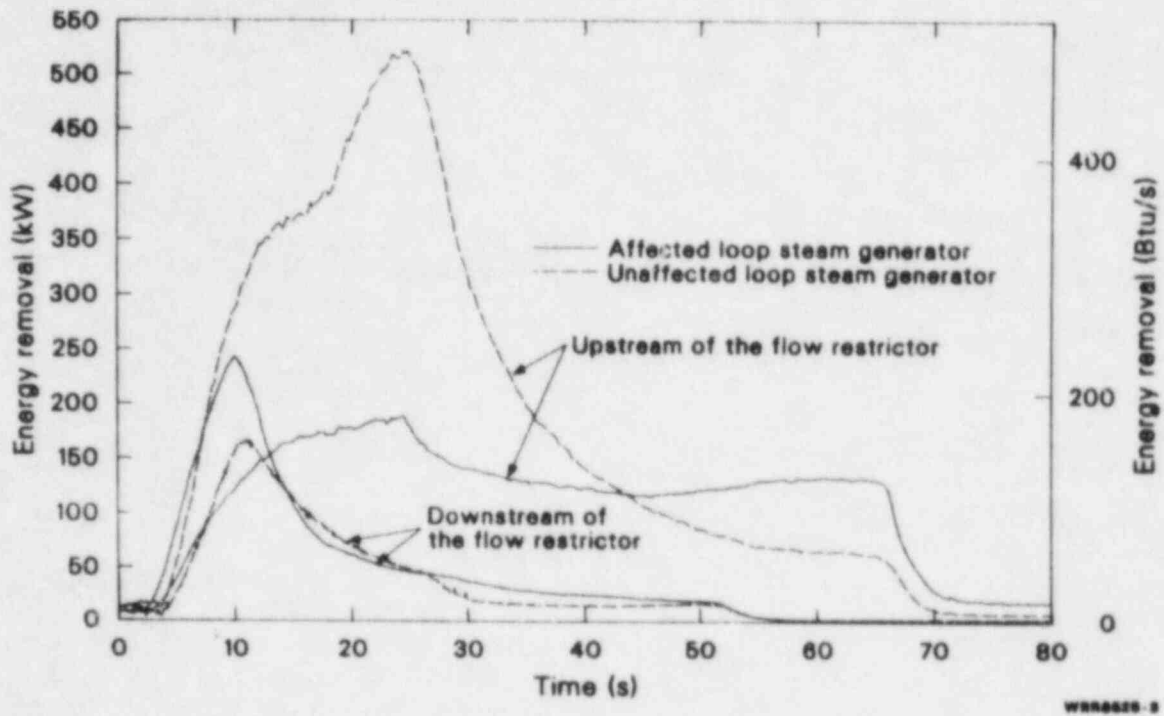


Figure 5. Affected and unaffected loop steam generator overall primary-to-secondary heat transfer for Tests S-FS-1 and S-FS-2.

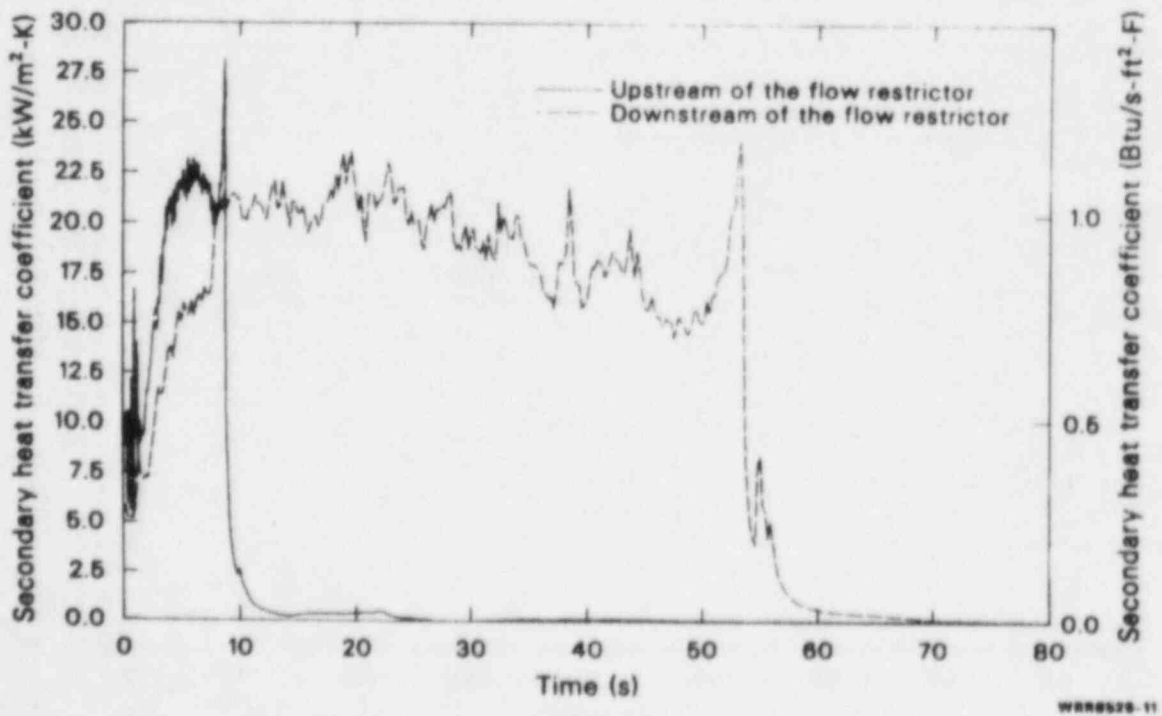


Figure 6. Secondary convective heat transfer coefficient at the 404 cm (159 in.) elevation for Tests S-FS-1 and S-FS-2.

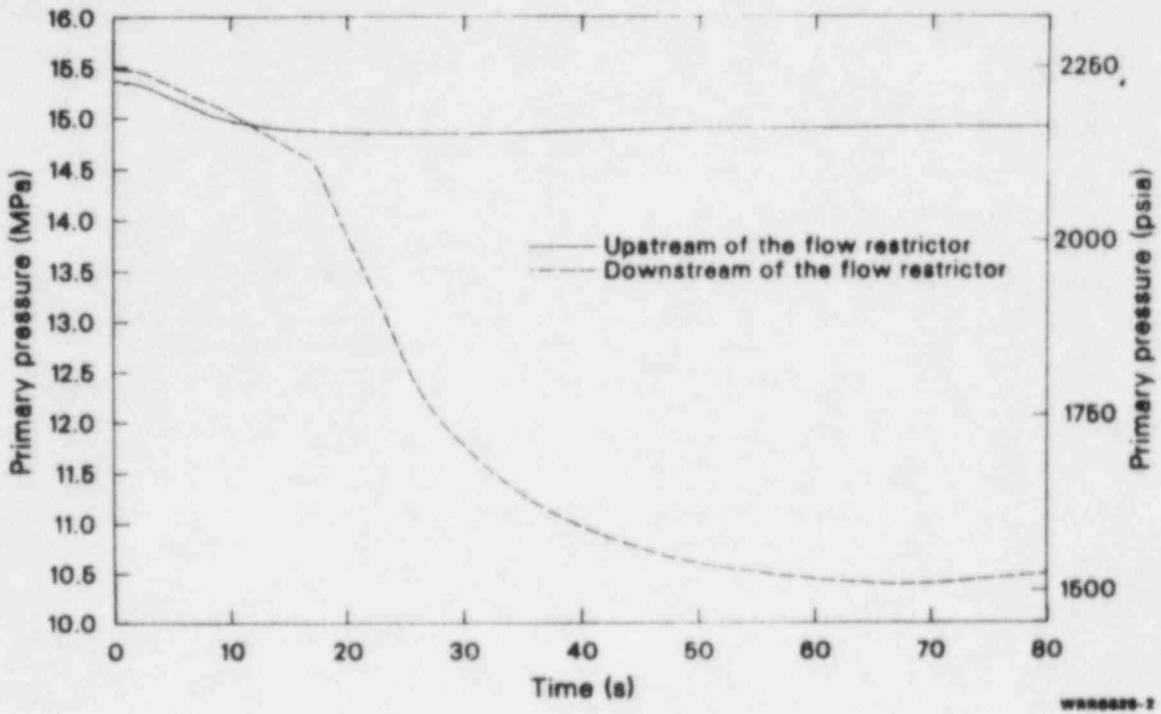


Figure 7. Primary pressure for Tests S-FS-1 and S-FS-2.

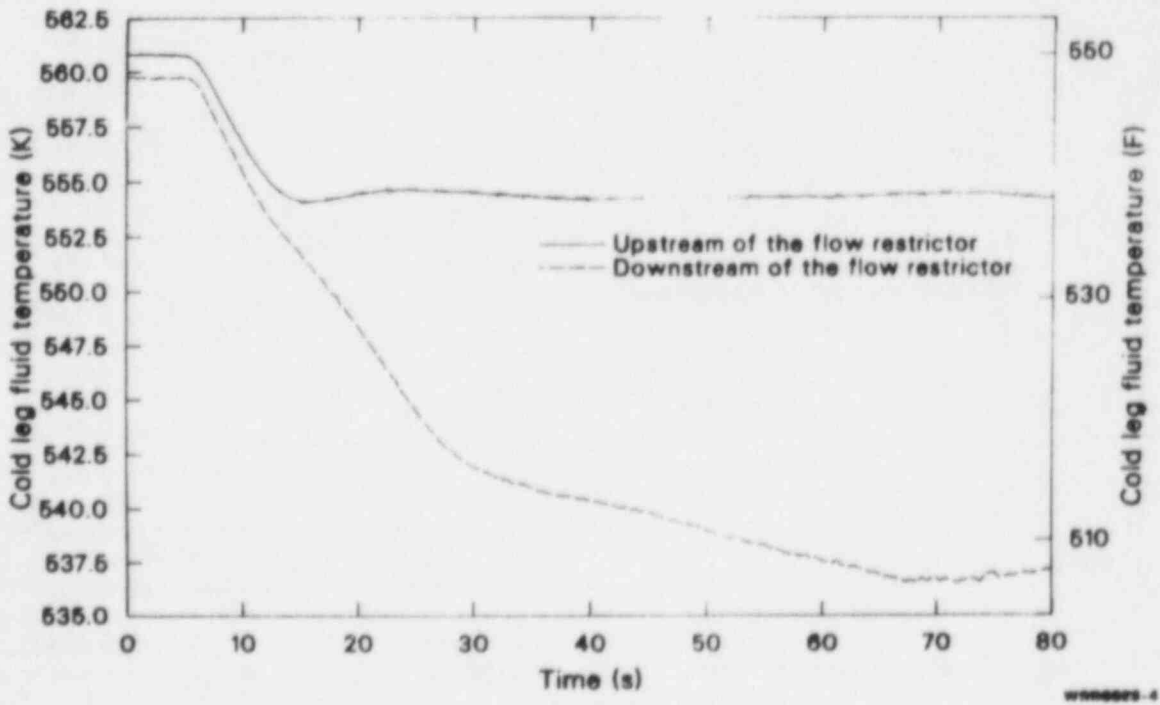


Figure 8. Cold leg temperature for Tests S-FS-1 and S-FS-2.



(538°F) during S-FS-2 and about 536 K (506°F) during S-FS-1. These temperatures were well above the pressurized thermal shock (PTS) minimum temperature limit of 450 K (350°F).

Test S-FS-1 (break downstream of the flow restrictor) was a much more severe transient as judged by primary system overcooling. The results from the tests indicate that a severe potential for PTS occurrence does not exist for these events in Semiscale. However, the reduction in heat transfer resulting from LOP induced loop flow reductions limited the overcooling to some degree. Further analysis without the LOP assumption and perhaps for smaller break sizes (due to the indicated trend in overcooling versus break size) is warranted. The high void fractions observed for the break flows indicated that FSAR assumptions of perfect separation are only mildly conservative for the Semiscale Type III affected loop steam generator. The data obtained should be adequate for code assessment of these tests.

#### FEEDWATER LINE BREAK TEST CONDUCT

Tests S-FS-6, S-FS-11 and S-FS-7 simulated transients initiated by a 100%, 50% and 14.3% break, respectively, in a steam generator bottom main feedwater line downstream of the check valve. With the exception of primary pressure, the initial conditions for the tests represented the full power conditions used for the Combustion Engineering (C-E) System 80 FSAK<sup>11</sup> Appendix 15B calculations. The initial primary pressure represented the normal full power operating pressure of the C-E System 80 reference plant.

Many of the assumptions made for C-E System 80 FSAR calculations were used for these tests. To simulate inoperability of the main feedwater system due to the break, main feedwater flow to both steam generators was discontinued at break initiation. Simulation of the communication between steam generators resulting from failure of the check valve in the affected steam generator main steam line was realized by utilizing the "crossover" line connecting the intact and broken loop steam generator steam lines. Reactor trip was assumed to occur due to a high pressurizer pressure signal. To simulate the delays associated with transducer response times and rod drop time, the core power decay was delayed until 3.2 s after the reactor trip signal was generated. The intact and broken loop steam generator steady-state steam flow control valves were held at their steady-state position until reactor trip. They were then closed over a 4 s interval to simulate the closure of the turbine stop valves. LOP was assumed to occur at reactor trip causing primary coolant pump trips (with a 2 s delay for transformer decay) and delaying HPIS and auxiliary feedwater availability for the 25 s required to get the pumps up to speed. Low affected steam generator pressure was assumed to generate the safety injection signal (SIS) which in turn induced HPIS and auxiliary feedwater initiation (but not before 25 s after LOP) and MSIV closure (with a 4 s valve closure time). MSIV closure was simulated by closing a valve in the "crossover" line. Identification of the affected steam generator was assumed to occur at MSIV closure, but not before 600 s into the transient. The auxiliary feedwater to that steam generator was then halted. No credit was taken for the charging system. Therefore, as was done in the C-E FSAR calculations, the charging portion of the safety injection (charging and

high pressure injection system) flow was not simulated. Degraded HPIS flow was assumed such that only one train of high pressure injection was available.

Compensation for environmental heat loss was provided through heat addition with trace heaters on the exterior of the pressure boundary and through augmentation of the core power. To preserve the pressurization of the pressurizer, the pressurizer external heater was powered at 3.0 kW for these tests. The total power provided by the five remaining external heater banks was 44.0 kW. Since this was below the system environmental heat loss, an additional 22 kW of core power augmentation was required to offset the heat loss.

#### FEEDWATER LINE BREAK TEST RESULTS

The occurrence of a break in a steam generator bottom feedwater line downstream of the check valve produces severe effects on the steam generator secondary. The bottom feedwater line break initiated the transient at 0 s. Secondary fluid originally at 6.26 MPa (908 psia) flowed from the affected loop steam generator through the break flow nozzle and into the catch tank. The unaffected loop steam generator also experienced a reduction in inventory under the influence of the continued steam flow prior to closure of the normal main steam flow control valves (turbine stop valve simulators) at SCRAM. This effect was compounded by the loss of all main feedwater at transient initiation. Further compounded by the failure of the affected loop steam line check valve, the unaffected and affected loop steam generators remain coupled, with transfer of inventory from the unaffected loop to the affected loop steam generator and out the break, until MSIV closure. As shown in Figure 9 the loss of mass from the secondaries initially produced essentially no change in pressure. The pressures held fairly steady as vapor generation in the secondaries, due to the primary-to-secondary heat transfer, continued.

The affected loop steam generator liquid inventory was depleted at about 13 s in S-FS-6, about 17 s in S-FS-11, and about 45 s in S-FS-7, as shown in Figure 10 (the mass is normalized to the initial value). Depletion of the liquid inventory caused a rapid reduction in the affected loop steam generator primary-to-secondary heat transfer (Figure 11). The normalized heat transfer versus normalized liquid mass (normalized to initial values) for the three tests are shown in Figure 12. For the 100% and 50% break test (S-FS-6 and S-FS-11), the heat transfer remained at 100% until the liquid mass reached about 5 to 10%. The heat transfer then reduced to about 90% over the next 5% reduction in liquid mass. This was followed by a rapid reduction to 0% heat transfer at 0% liquid inventory for S-FS-6 and 2% liquid inventory for S-FS-11. For the 14.3% break test (S-FS-7), the heat transfer remained at 100% until the liquid mass reached about 20%. The heat transfer then reduced gradually to 90% over the next 10% reduction in liquid mass. This was followed by a more rapid reduction to 80% heat transfer at 6% inventory, and finally, a rapid reduction to 0% heat transfer at 4% liquid inventory. Although a slight break size dependency is indicated by these results, the basic trend is very similar. The heat transfer remains at nearly 100% until the liquid inventory is nearly depleted. This is followed by a rapid reduction to 0% heat transfer with little further reduction in mass. This indicates that the assumption made for the C-E FSAR Appendix 15B calculations regarding the reduction of

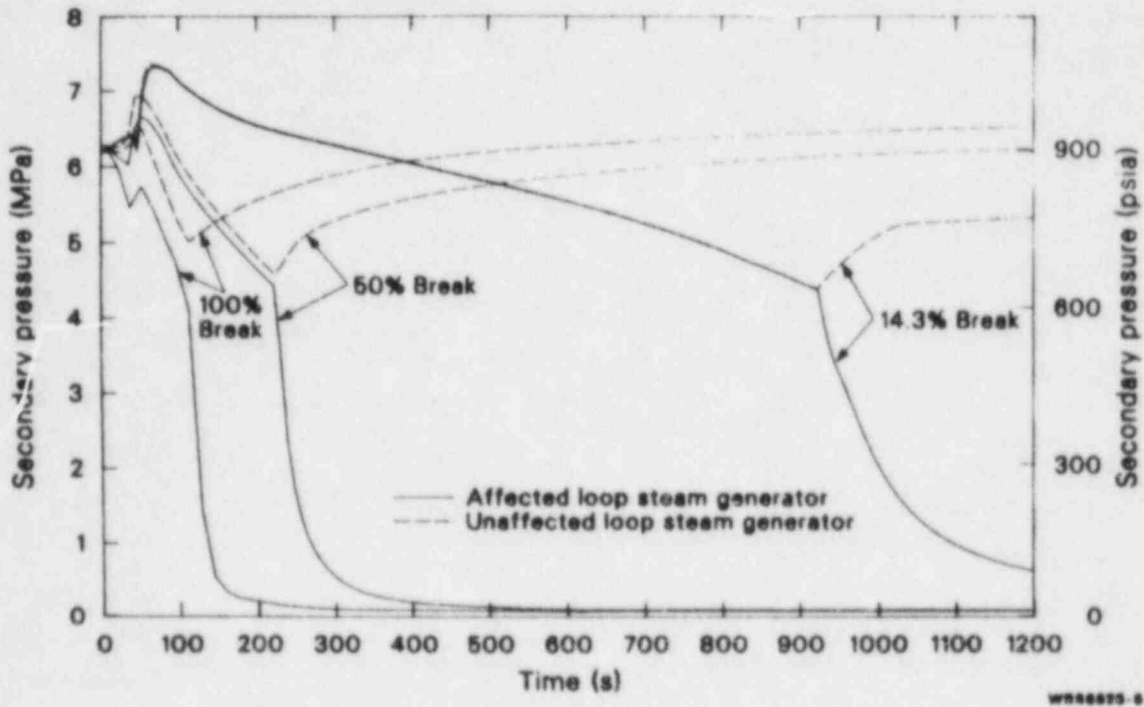


Figure 9. Affected and unaffected loop secondary pressures for Tests S-FS-6, S-FS-11 and S-FS-7.

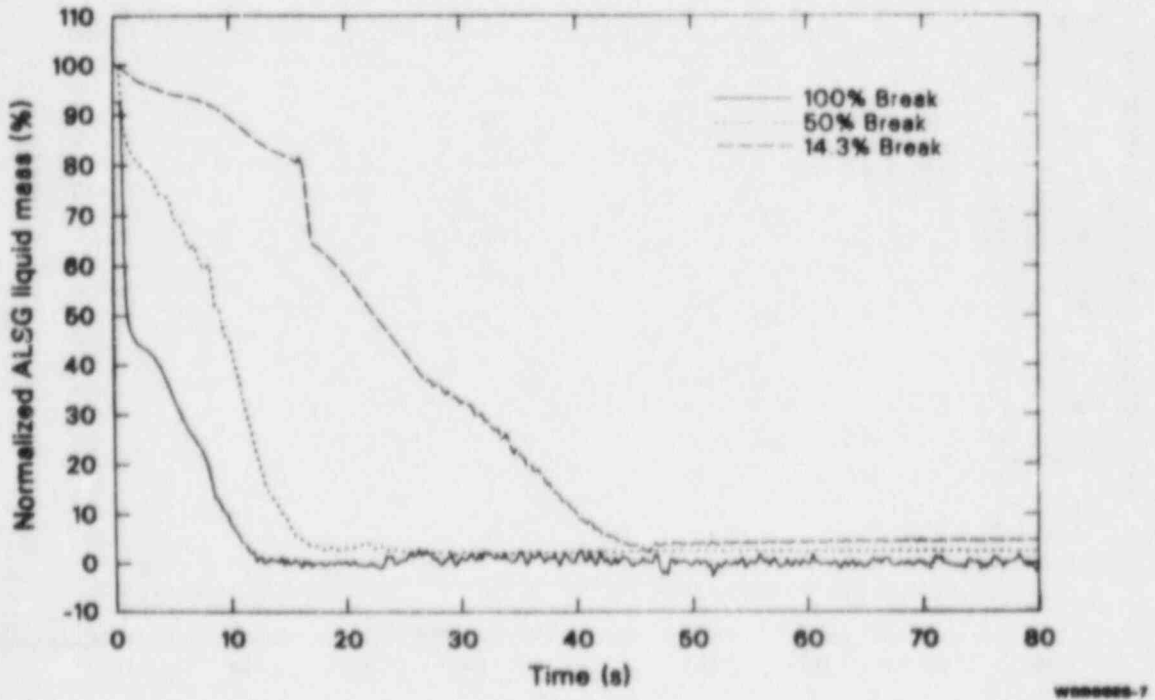


Figure 10. Affected loop steam generator normalized liquid mass for Tests S-FS-6, S-FS-11 and S-FS-7.

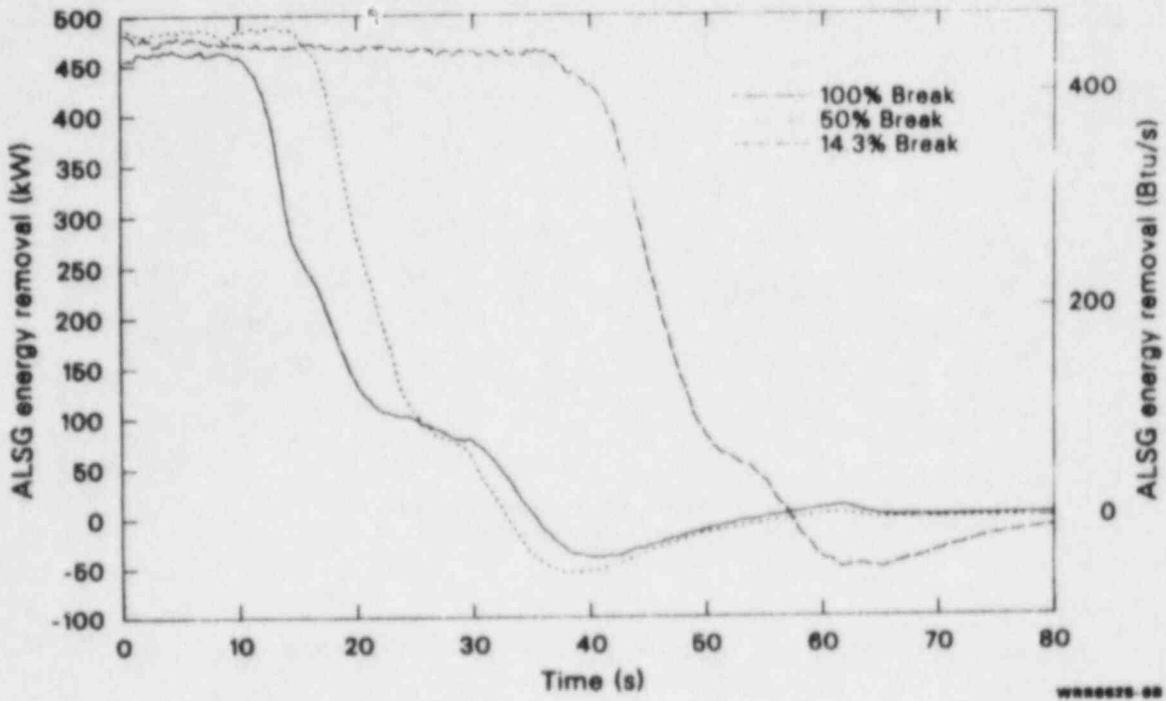


Figure 11. Affected loop steam generator overall primary-to-secondary heat transfer for Tests S-SF-6, S-FS-11 and S-FS-7.

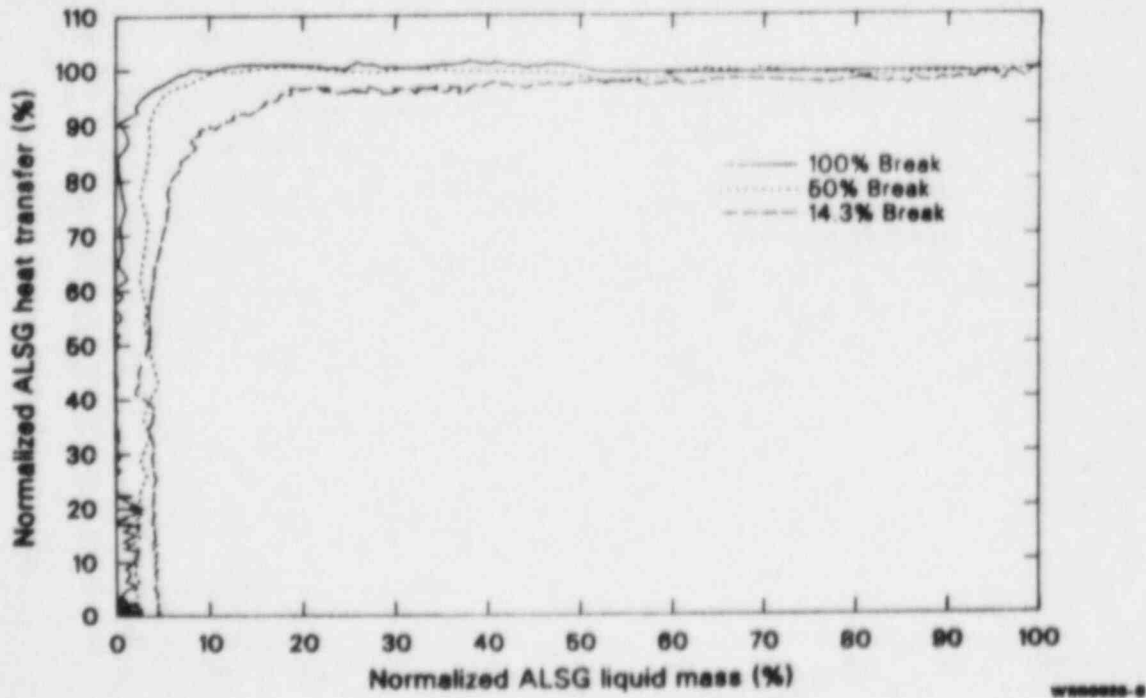


Figure 12. Affected loop steam generator normalized heat transfer versus normalized liquid mass for Tests S-FS-6, S-FS-11 and S-FS-7.

heat transfer with liquid inventory (i.e., 100% heat transfer until the liquid inventory is depleted followed by a step change reduction in the heat transfer to 0%) is not conservative for the Semiscale Type III steam generator.

After the loss of liquid inventory the vapor generation in the affected loop steam generator was stopped. The continued loss of inventory via the break and the main steam line produced a reduction in the affected loop steam generator secondary pressure for all three tests. As the flow out of the affected loop main steam line decreased, the flow between the secondaries via the crossover line increased. The increased loss of inventory from the unaffected loop steam generator increased the primary-to-secondary heat transfer during S-FS-6, as shown in Figure 13, and initiated a slow depressurization of the unaffected loop secondary. During S-FS-11 and S-FS-7, the increased crossover line flow was limited by the affected loop secondary pressure response to the break flow and was not large enough to significantly affect the unaffected loop steam generator primary-to-secondary heat transfer. The high pressurizer pressure reactor and turbine trip (SCRAM) setpoint of 15.86 MPa (2300 psia) was reached at about 23 s during S-FS-6, about 24 s during S-FS-11, and about 4 s during S-FS-7. The normal main steam flow control valves began to close due to the SCRAM signal and were fully closed about 2 s later. During, and following, the closure of the steam flow control valves the secondaries experienced a period of repressurization as the energy addition to the secondaries from the primary exceeded the energy removed via the break. This continued until the break energy removal exceeded the energy addition to the secondaries from the primary. The secondaries then entered a period of gradual depressurization under the influence of the break energy removal. The affected loop steam generator secondary pressure reached the low pressure setpoint of 4.47 MPa (648 psia) at about 101 s during S-FS-6, about 215 s during S-FS-11, and about 920 s during S-FS-7. This initiated the SI and MSIV closure signals. The depressurization of the unaffected loop steam generator was halted when the MSIV fully closed about 3 s later. Following MSIV closure, the unaffected loop steam generator experienced a slight repressurization due to energy addition from the primary fluid system in the absence of secondary feeding and steaming. The affected loop steam generator continued to depressurize until the generator was essentially empty at about 150 s during S-FS-6, about 350 s during S-FS-11, and about 1400 s during S-FS-7. The mass remaining in the unaffected loop steam generator following MSIV closure was about 47%, 35%, and 11% of the initial mass for the 100%, 50% and 14.3% break tests, respectively.

The reduction in primary-to-secondary heat transfer during the tests heated the primary fluid. This caused the primary fluid to expand and pressurized the primary. The pressurization of the primary continued until about 1 s after the core power decay was initiated. As shown in Figure 14, the peak primary pressure for all three tests occurred in the loop cold leg just prior to SCRAM. The double spikes in the system pressure for Tests S-FS-11 and S-FS-7 were due to the pressurizer safety relief valve (SRV) cycling at about 16.2 MPa (2350 psia). Although the pressure got very close to the SRV setpoint during S-FS-6, the valve did not cycle.

The peak primary pressures for Tests S-FS-6, S-FS-11, and S-FS-7 were 16.37 MPa (2374 psia), 16.41 MPa (2380 psia), and 16.42 MPa (2381 psia),

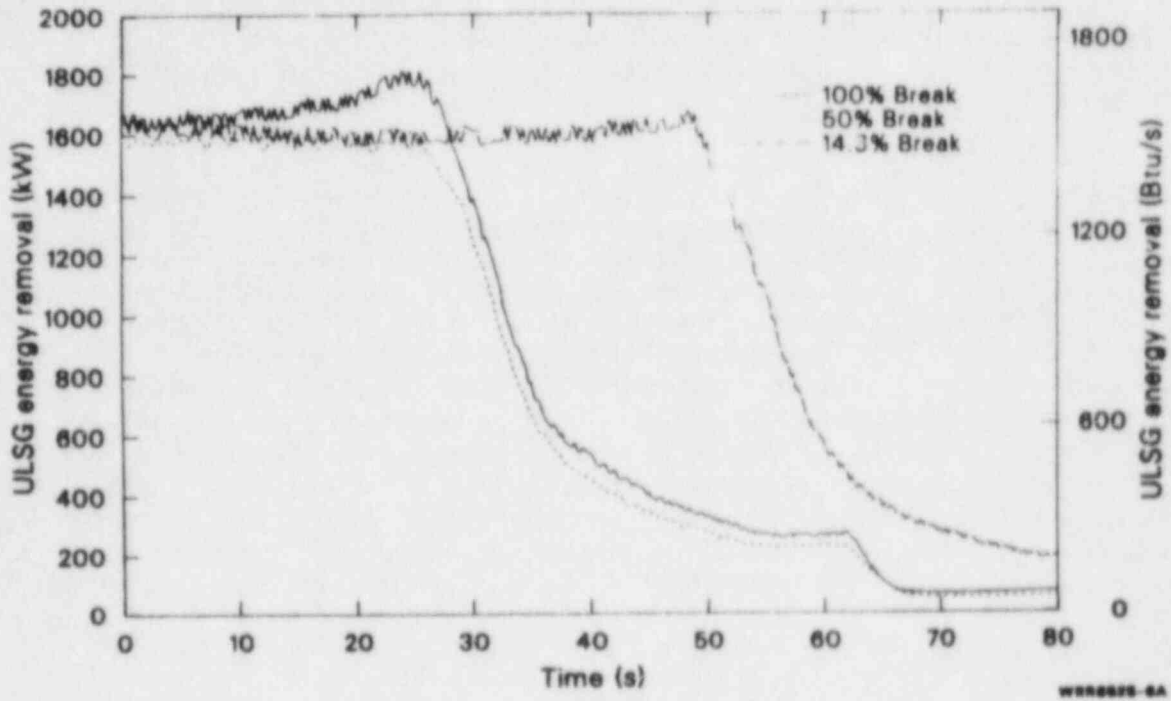


Figure 13. Unaffected loop steam generator overall primary-to-secondary heat transfer for Tests S-FS-6, S-FS-11 and S-FS-7.

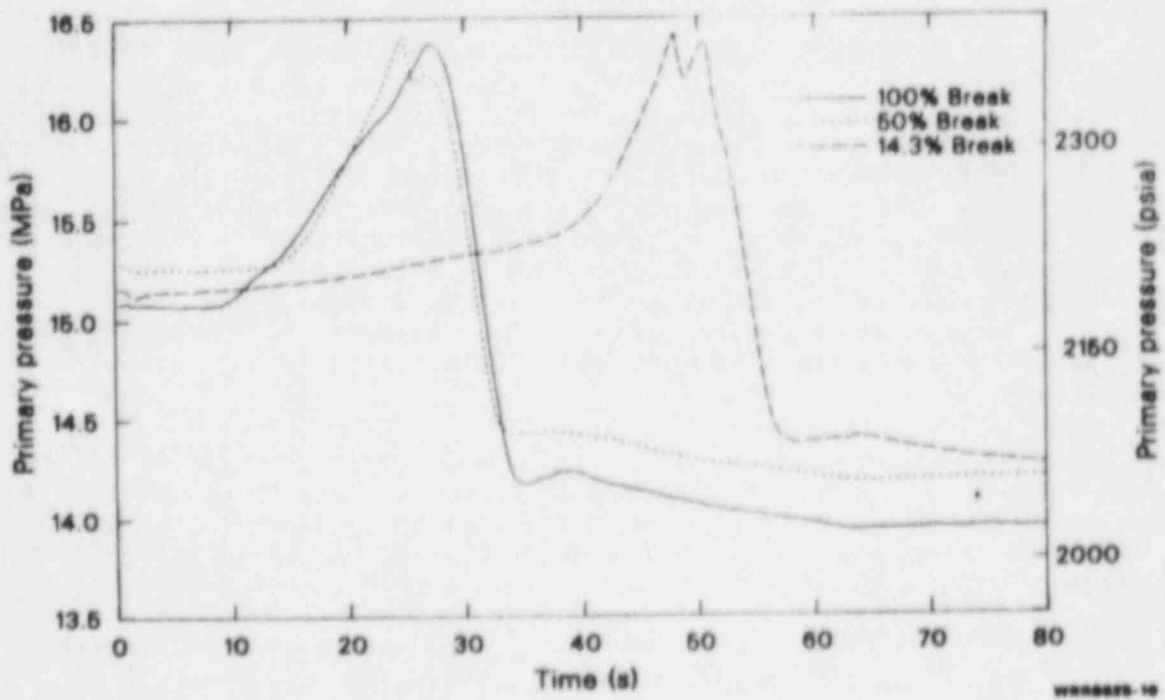


Figure 14. Peak primary system pressure for Tests S-FS-6, S-FS-11 and S-FS-7.

respectively. These pressures represent differences of about 0.51 MPa (74 psid), 0.55 MPa (80 psid) and 0.56 MPa (81 psid) between the high pressure trip setpoint and the peak system pressure. Using the fact that the full flow pump heads are about the same for the C-E System 80 plant and Semiscale and that the loss of the Type III steam generator heat sink represents only half the loss associated with a C-E System 80 steam generator, the predicted differences between the high pressure trip setpoint and the peak system pressure for a C-E System 80 plant are about 1.01 MPa (146 psid), 1.17 MPa (170 psid), and 1.20 MPa (174 psid), respectively. Based on this simplistic analysis and the C-E high pressure trip setpoint of 17.06 MPa (2475 psia), the peak system pressures predicted for the C-E System 80 plant are 18.07 MPa (2621 psia), 18.23 MPa (2645 psia), and 18.26 MPa (2649 psia) for a 100%, 50% and 14.3%, respectively, bottom feedwater line break. These pressures correspond to 104.8%, 105.8% and 106.0% of the system design pressure, all of which are below the 110% of design pressure high pressure limit. The less severe pressurization and more gradual pressure rise during S-FS-6 was due to the greater cooling provided by the larger crossover line flow. The increased unaffected loop steam generator primary-to-secondary heat transfer which occurred during S-FS-6 reduced the net energy removal deficit as shown in Figure 15. The total loss of the affected loop heat sink is evident in the primary energy balance for Tests S-FS-11 and S-FS-7, while it is not for Test S-FS-6.

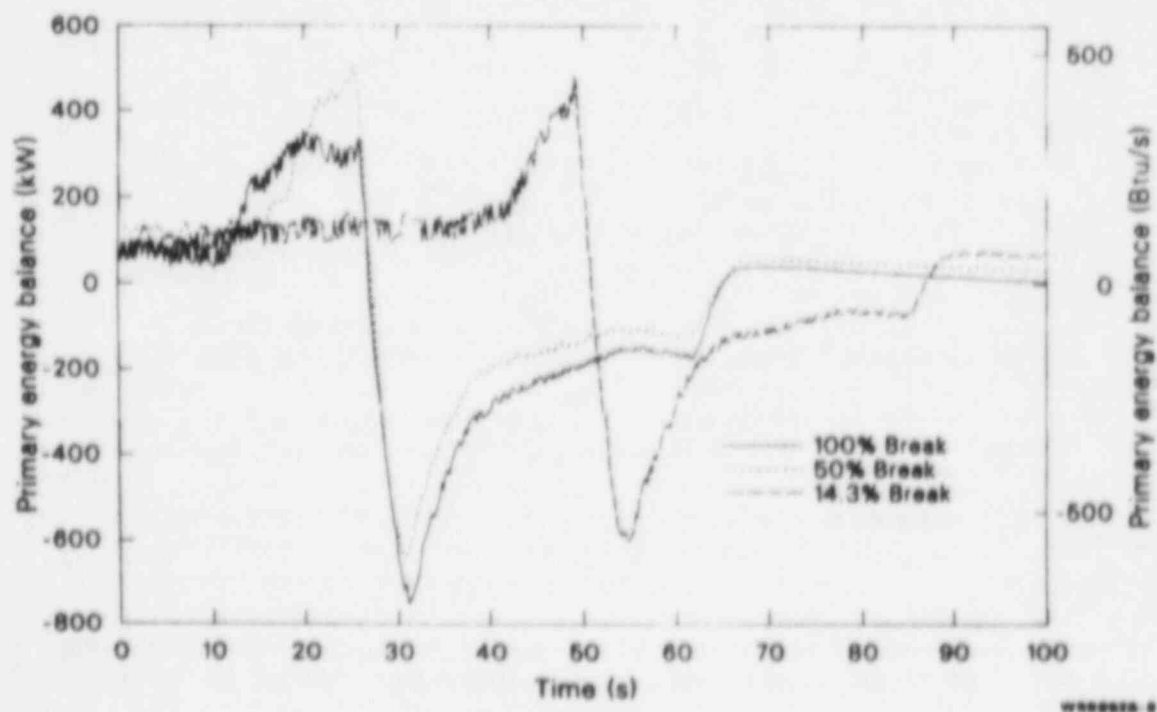


Figure 15. Primary system energy balance for Tests S-FS-6, S-FS-11 and S-FS-7.

All three tests produced approximately the same primary system pressurization. Some slight sensitivity of the normalized heat transfer versus normalized liquid mass to break size was observed. However, the basic response indicates that the C-E FSAR assumption is not conservative for the Semiscale Type III steam generator. A simplistic analysis of the results indicates that although pressurization of the primary system is substantial, pressures in excess of 110% of the system design pressure are not predicted for these events in Semiscale. However, the increased unaffected loop steam generator heat transfer (resulting from the steam line check valve failure induced intersecondary steam flow) limited the pressurization during the 100% break test to some extent. Further analysis without the steam line check valve failure assumption is warranted. While for small breaks the large mass loss from the unaffected loop secondary resulting from this assumption raises some concerns, the extended time required to lose this mass is prohibitive. Operator identification and manual MSIV closure would be quite likely prior to reaching the low secondary pressure setpoint (this took over 15 minutes for the 14.3% break test). The data obtained should be adequate for code assessment of these tests.

#### CONCLUSIONS

Based on the results of the two steam line break tests the following conclusions have been drawn:

- FSAR assumptions of perfect separator performance are only mildly conservative for the Semiscale Type III steam generator.
- The minimum fluid temperatures reached do not indicate a potential for PTS occurrence during these events in Semiscale.
- A double-ended offset shear downstream of the flow restrictor produces much greater cooling of the primary than one upstream of the flow restrictor, when failure of the steam line check valve occurs.
- Further analysis for smaller break sizes is warranted in light of the indicated trend in overcooling versus break size.
- LOP at SIS assumptions decrease the amount of primary cooling. Further analysis without the LOP assumption are warranted.

The data obtained from these main steam line and bottom main feedwater line break tests should be adequate for code assessment of these tests. Having assessed the code for these tests, higher confidence best-estimate steam line and bottom feedwater line break transient calculations may be obtained. These may then be used to determine the degree of conservatism inherent in current FSAR calculations for these kinds of transients.

Based on the results of the three feedwater line break tests the following conclusions have been drawn:

- The C-E FSAR assumption of 100% heat transfer until the liquid inventory is depleted followed by a step change reduction in the heat transfer to 0% is not conservative for the Semiscale



Type III steam generator. Some slight sensitivity to break size was observed but the basic response was the same for all three tests.

- A simplistic analysis of test results indicates that although substantial pressurization occurs during all three tests, pressures in excess of 110% of the system design pressure are not predicted for these events, in Semiscale.
- The peak primary pressure is essentially insensitive to the break size, in Semiscale.
- Substantial mass loss from the unaffected loop secondary can occur for small breaks, due to the failed steam line check valve. However, the extended time required to lose this mass is prohibitive and operator intervention should preclude this.
- Flow between the secondaries (past the failed steam line check valve) partially corrected for the loss of the affected loop heat sink during the 100% break test, and limited the pressurization to some extent. Further analysis without the steam line check valve failure assumption is warranted.

#### REFERENCES

1. T. J. Boucher and J. R. Wolf, Experiment Operating Specification for Semiscale MOD-2C Feedwater and Steam Line Break Experiment Series, EGG-SEMI-6625, May 1984.
2. T. J. Boucher and W. A. Owca, Appendix S-FS-1 of the Experiment Operating Specification for the Semiscale MOD-2C Feedwater and Steam Line Break Experiment Series, EGG-SEMI-6783, January 1985.
3. W. A. Owca and T. H. Chen, Quick Look Report for Semiscale MOD-2C Test S-FS-1, EGG-SEMI-6858, May 1985.
4. T. J. Boucher, Appendix S-FS-2 of the Experiment Operating Specification for the Semiscale MOD-2C Feedwater and Steam Line Break Experiment Series, EGG-SEMI-6761, December 1984.
5. T. J. Boucher and T. H. Chen, Quick Look Report for Semiscale MOD-2C Test S-FS-2, EGG-SEMI-6827, March 1985.
6. T. J. Boucher and W. A. Owca, Appendix S-FS-6 and S-FS-7 of the Experiment Operating Specification for the Semiscale MOD-2C Feedwater and Steam Line Break Experiment Series, EGG-SEMI-6871, May 1985.
7. T. J. Boucher and D. G. Hall, Quick Look Report for Semiscale MOD-2C Test S-SF-6, EGG-SEMI-7022, September 1985.
8. D. G. Hall, Quick Look Report for Semiscale MOD-2C Test S-FS-7, to be published in October 1985.

9. T. J. Boucher and W. A. Owca, Appendix S-FS-11 of the Experiment Operating Specification for the Semiscale MOD-2C Feedwater and Steam Line Break Experiment Series, EGG-SEMI-6909, June 1985.
10. M. P. Plessinger, Quick Look Report for Semiscale MOD-2C Test S-FS-11, to be published in November 1985.
11. CESSAR-80, Final Safety Analysis Report, Appendix 158, Combustion Engineering Company.
12. T. K. Larsen, J. L. Anderson, D. J. Shimeck, Scaling Criteria and Assessment of Semiscale MOD-3 Scaling for Small Break Loss-of-Coolant Transient, EGG-SEMI-5121, March 1980.
13. Zion Nuclear Plant, Final Safety Analysis Report, Commonwealth Edison Company.

SEMISCALE LIQUID HOLD-UP INVESTIGATIONS:  
A COMPARISON OF RESULTS FROM SMALL BREAK  
LOCA TESTS PERFORMED IN THE SEMISCALE MOD-2A  
AND MOD-2C FACILITIES

G. G. Loomis, Idaho National Engineering Laboratory

ABSTRACT

Results are compared from small break loss-of-coolant accident (SBLOCA) experiments performed in two different versions of the Semiscale facility. These experiments were designed to investigate the effect of downcomer to upperhead core bypass flow on transient severity. The first set of experiments, S-UT-6 and S-UT-8 with 4% and 1.1% bypass flows respectively, were performed in the Mod-2A facility. The second set of experiments, S-LH-1 and S-LH-2 with 0.9% and 3% bypass flows, were performed in the Mod-2C facility. The effect of the net head of fluid in the steam generator primary tubes (liquid hold-up) on the transient severity is examined as well as the general mechanism of core level depression. Both Semiscale Mods are volume-scaled representatives of a four-loop pressurized water reactor (PWR), which simulates most of the major features of a PWR. All experiments were performed at high temperature and pressure (595 K hot leg fluid temperature; 15.6 MPa pressure).

INTRODUCTION

A series of small break loss-of-coolant accident (SBLOCA) experiments were performed in two different versions of the Semiscale Facility. Tests S-LH-1 and S-LH-2 were performed in the Mod-2C facility while S-UT-6 and S-UT-8 were performed in the older Mod-2A facility. All four experiments were 5% SBLOCA<sup>a</sup> simulations with various allowed downcomer to upper head core bypass flow. Both Semiscale Mods are volume-scaled representations of a PWR plant consisting of a pressure vessel with external downcomer and simulated reactor internals, an "intact loop" with a shell-and-inverted U-tube active steam generator, pressurizer, and pump, and a "broken-loop" including an active pump, active steam generator, and associated piping which allows break simulations. For both Mods the volume was approximately 1/1705 of a PWR, while elevation was generally scaled on a 1:1 basis.

By way of historical background, Tests S-UT-6 and S-UT-8, performed in the Semiscale Mod-2A facility, exhibited a possible strong relationship between downcomer to upper head core bypass flow and accident severity.<sup>1,2</sup> Test S-UT-6 had a 4.0% bypass flow<sup>b</sup> while S-UT-8 had a 1.1% bypass flow.

---

a. A 200% break equals a double-ended offset shear of the main coolant piping in one loop of a four-loop PWR. Small pipe breaks are assumed to be centerline tears or cracks in the main coolant piping.

b. Core bypass flow refers to the pretransient percent of total core flow that flows from the downcomer inlet annulus to the vessel upper head thus bypassing the core.

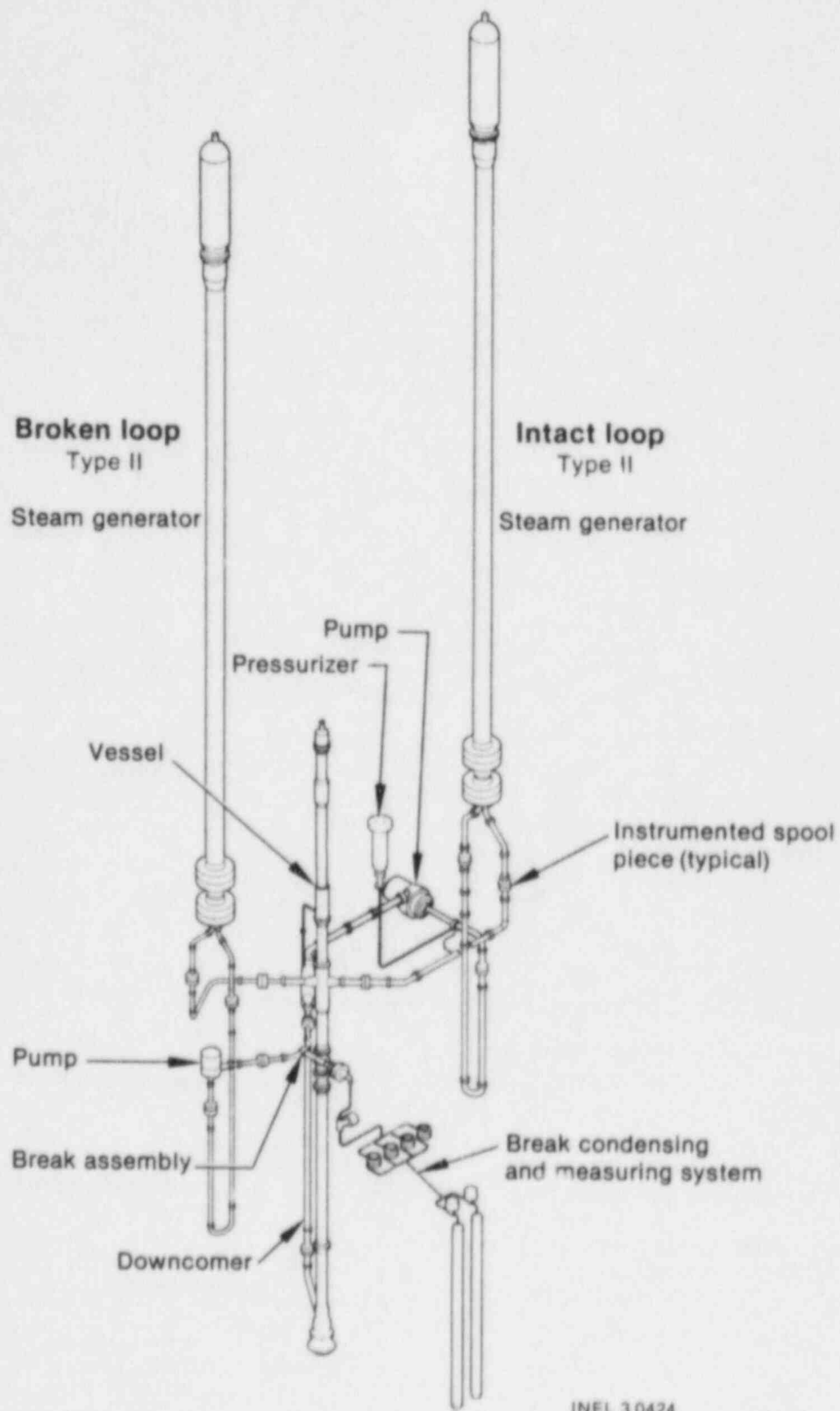
During S-UT-8 the vessel collapsed liquid level was depressed to the bottom of the core resulting in core heat-up while during S-UT-6 the vessel collapsed liquid level was depressed only to 220 cm above the core bottom with no core heat-up. Both experiments had essentially identical initial and boundary conditions. However, other system hardware changes in addition to the core bypass flow resistance were made between the two experiments that could have affected the difference in core level depression. (These changes in hardware were made between S-UT-6 and S-UT-8 to provide a test bed in S-UT-8 for a vendor vessel liquid level probe.) Thus, the comparison between S-UT-6 and S-UT-8 to assess the effect of core bypass flow resistance on SBLOCA severity was not clear. In addition, since S-UT-8 was designed as only a test bed for a vendor liquid level system, emphasis was not placed on measurement of certain boundary conditions and other parameters. Therefore, to provide a clean comparison to examine the effect of downcomer to upper head core bypass flow, and to provide a state-of-the-art simulation with the instrumentation focused on SBLOCA phenomena, S-UT-6 and S-UT-8 experiments were approximately duplicated in the new Mod-2C system.

Tests S-LH-1 and S-LH-2 were identical with the exception of the core bypass flow resistance (Test S-LH-1 had a 0.9% bypass flow and Test S-LH-2 had a 3.0% bypass flow). The Mod-2C facility is a state-of-the-art facility designed specifically for SBLOCA experiments (the Mod-2A facility was an intermediate step in the transition from large break facilities to small break facilities). Special improvements in the Mod-2C facility include comprehensive heat loss make-up techniques and better scaled steam generators.

This paper first discusses the similarities and differences between the Mod-2A and Mod-2C facilities. Next, an experimental overview is presented, followed by a discussion of the S-UT-6/S-UT-8 phenomena and a comparison and description of S-LH-1/S-LH-2 phenomena. Finally, the results of the two experimental tests are contrasted followed by conclusions derived from the comparison.

#### FACILITY COMPARISON

Both the Mod-2A and Mod-2C facilities simulate the major features of a four-loop PWR as shown in Figures 1 and 2 respectively. Both systems are two loop systems for which one loop simulates three unaffected loops of a four-loop PWR undergoing a SBLOCA and the other loop simulates the loop when the break occurs. For both systems, the major scaling from a PWR was a modified volume power scaling with a scaling factor of 1/1705. Geometric similarity, component layout, relative elevations, and hydraulic resistances of the various components have been preserved from the full scale system. The 5% centerline cold leg break in both systems was simulated by opening a rapid-opening valve downstream of the orifice that was fixed to a Tee assembly off the broken loop cold leg piping. The transients in either system were initiated from high pressure/high temperature conditions (15.6 MPa pressure; 595 K hot leg fluid temperature; 37 K core differential temperature). Details of system hardware are described in detail in Reference 3 for the Mod-2A facility and in Reference 4 for the Mod-2C facility.



INEL 3 0424

Figure 1. Semiscale Mod-2A system configuration.

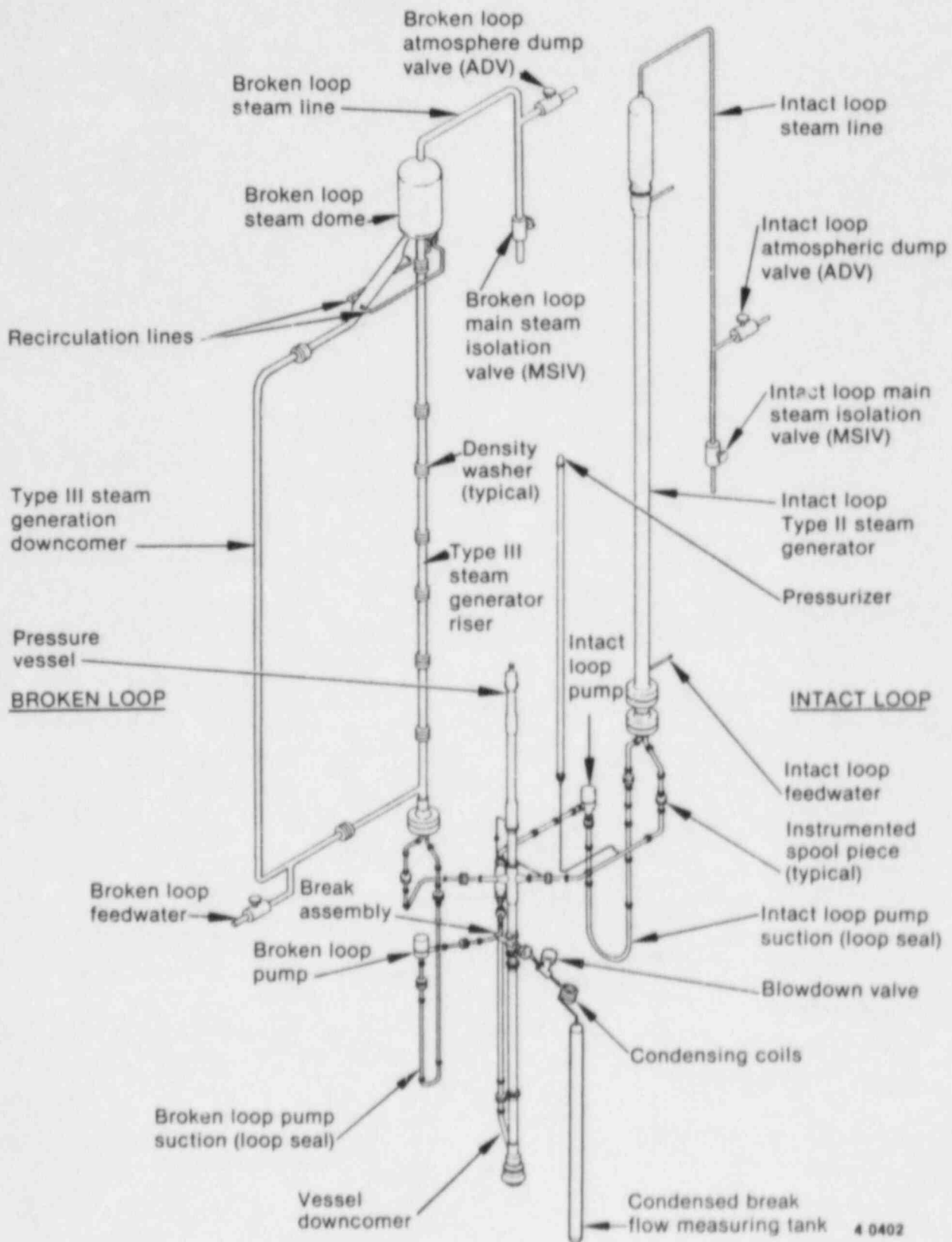


Figure 2. Semiscale Mod-2C system configuration.

The major differences between the two systems are itemized in Table 1. Table 1 also includes major differences between the version of the Mod-2A system used for S-UT-6 and the version used for S-UT-8. Basically S-UT-6 and S-LH-2 were considered the high core bypass flow cases with 4% and 3% core bypass, and S-UT-8 and S-LH-1 with 1.1% and 0.9% core bypass are considered the low core bypass flow cases. These bypass flows cover the range of bypass flows expected for a large PWR (0.4% to 5%). Table 1 shows that no modifications except for the bypass flow were made between S-LH-1 and S-LH-2. However, for S-UT-6 and S-UT-8 major changes were affected especially in the vessel upper head. S-UT-8 was a special test designed only as a test bed for a vendor liquid level measuring device which prompted the changes listed in Table 1 between S-UT-6 and S-UT-8.

The vessel upper head (shown in Figure 3) for S-UT-8 included support columns; however, the instrument ports located below the support plate, were unplugged resulting in a considerably faster drain during blowdown of the vessel upper head for S-UT-8 (see Figure 4). For S-LH-1 and S-LH-2 the instrument ports were plugged and the upper head drain during blowdown for S-LH-2 (with the higher bypass flow) was twice as fast as for S-LH-1 (see Figure 5). The importance of upper head drain on transient severity is included in a discussion of the results later.

#### EXPERIMENTAL OVERVIEW

Overall, the same phenomena was observed in all four 5% SBLOCA experiments as described in Reference 5. Only the severity of the core liquid level depression and system mass distribution varied during the four experiments. All experiments showed a primary depressurization with a significant mass inventory reduction. As fluid leaves the system via the break, a complicated general top down voiding of system components occurs, resulting in fluid being trapped in the pump suction of both loops and the vessel. Steam created in the core pushes against these fluid plugs causing a simultaneous manometric depression of the core liquid level and the pump suction liquid level. Once the intact loop suction cleared of fluid<sup>a</sup> the overall manometric balance was partially relieved (because a steam path existed from the core to the break) and the vessel was refilled from the downcomer. During both S-LH-1 and S-UT-8 (with low bypass flow) the vessel level was depressed below the level corresponding to the bottom of the pump suction, resulting in core rod heat-ups. However, for both S-UT-6 and S-LH-2, the core level was depressed only to the level of the suctions, resulting in no core rod heat-up. Regardless of bypass flow, clearing of the suctions was followed by a second core liquid depletion supported by boiling from core decay heat accompanied by core heat-up in all cases. Accumulator injection mitigated the second core rod heat-up for all cases. A detailed discussion of the results from the subject experiments follows. Reference 5 contains further details of the fluid mass distribution and pressure response during 5% SBLOCA's.

---

a. Reference 5 describes the intact loop suction clearing first (180 s) followed by the broken loop suction at 280 s because of the 9 to 1 hydraulic resistance split between broken loop and intact loop. Break flow is preferentially supplied by the less resistive intact loop.

TABLE 1. MAJOR DIFFERENCES BETWEEN MOD-2A (S-UT-6; S-UT-8) AND MOD-2C (S-LH-1; S-LH-2)

Parameter	S-UT-6	S-UT-8	S-LH-1	S-LH-2
Vessel upper head structures	Support column open to flow with instruments in-place; no holes in guide tube	Guide tube has 8 holes below support plate; support columns plugged however, instrument ports allowed draining during (S-UT-8 drained faster than S-UT-6 as a result)	Guide tube has 8 holes below support plate; support columns plugged (no flow allowed)	Same as S-LH-1
Core bypass flow	4.0% simulated with a valve	1.1% simulated with a valve	0.9% simulated with an orifice	3.0% simulated with line only
Core heat loss make-up	Band heaters on loop; nothing on vessel	Band heaters on loop; some vessel heat tape available	Heater tape on loop and vessel	Same as S-LH-1
Primary pump	IL-low speed pump (Lawrence) BL-high speed vertical	IL-low speed pump (Lawrence) BL-high speed vertical	IL-high speed vertical BL-high speed vertical	Same as S-LH-1
Steam generator	IL-Type II BL-Type II	IL-Type II BL-Type II	IL-Type II BL-Type III	Same as S-LH-1
Loop piping	10.16 cm Steam generator inlet 7.62 cm pump suction	6.35 cm melt 6.35 cm pump suction	Same as S-UT-8	Same as S-UT-8
Vessel core	3.66 m; 25 rod electrically heated core; 2 MW full power	Same as S-UT-6	New core but same design as S-UT-6	Same as S-LH-1



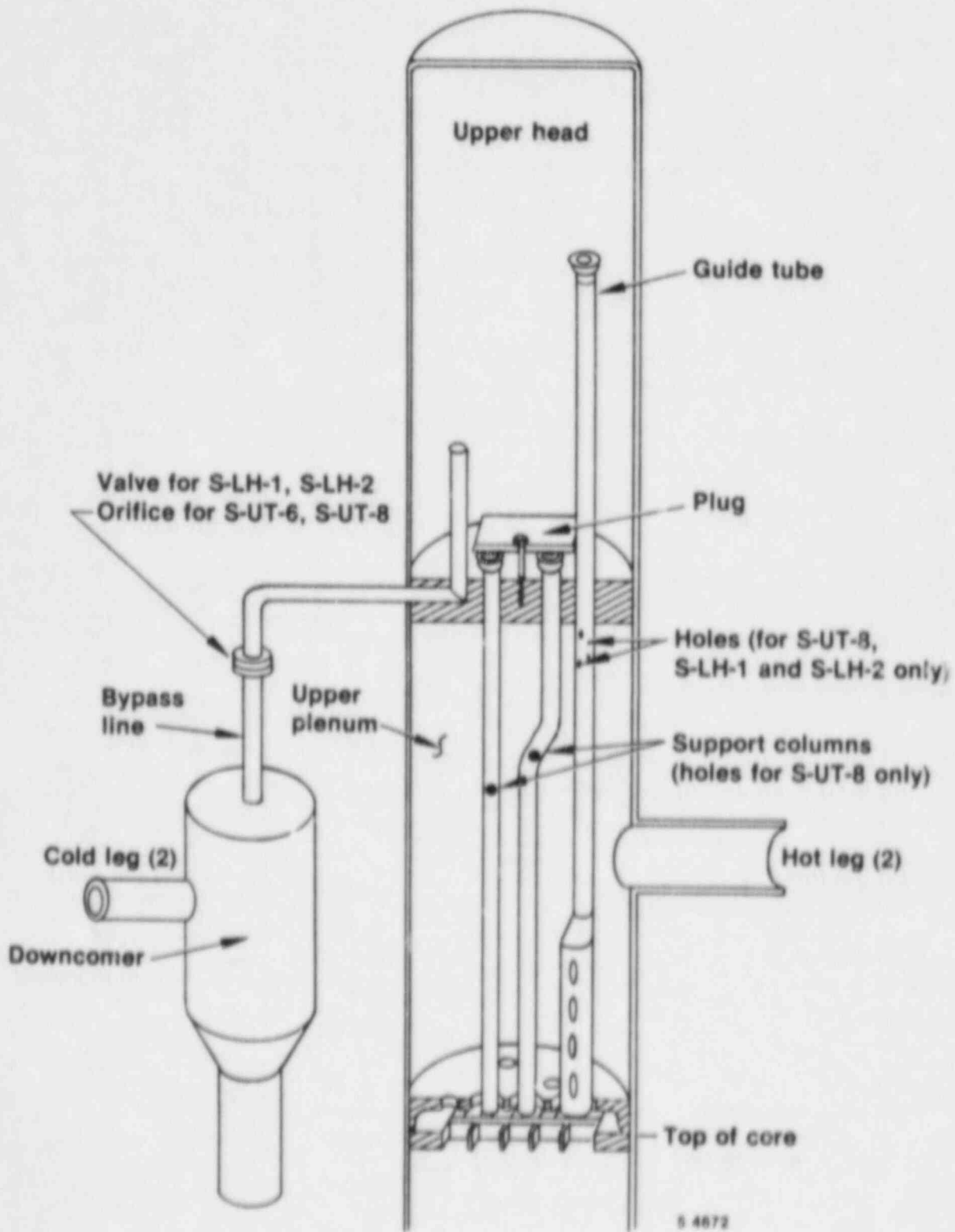


Figure 3. Vessel upper head configuration for Semiscale SBLOCA experiments.

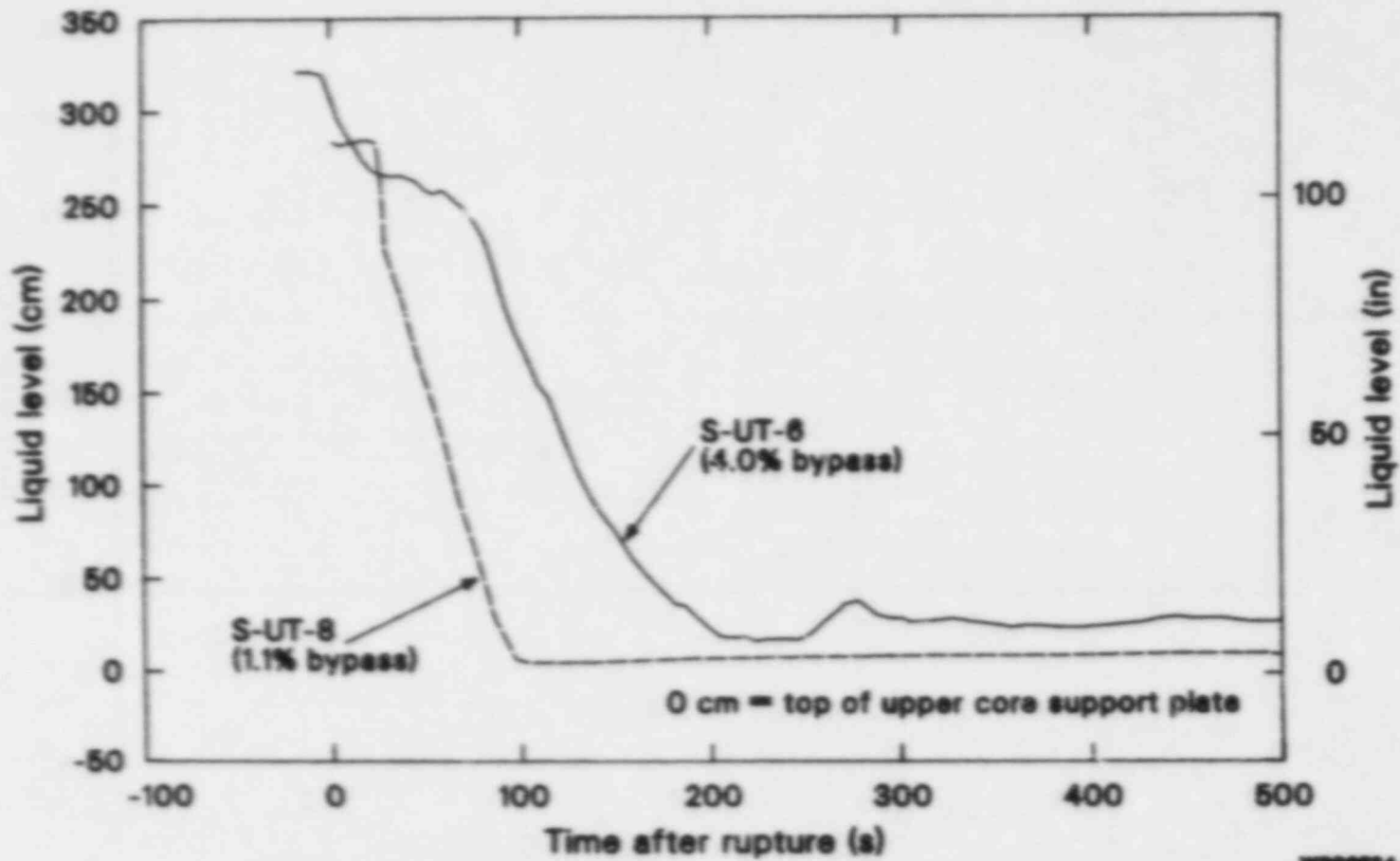


Figure 4. Vessel upper head collapsed liquid level for Semiscale Mod-2A Experiments S-UT-6 and S-UT-8.

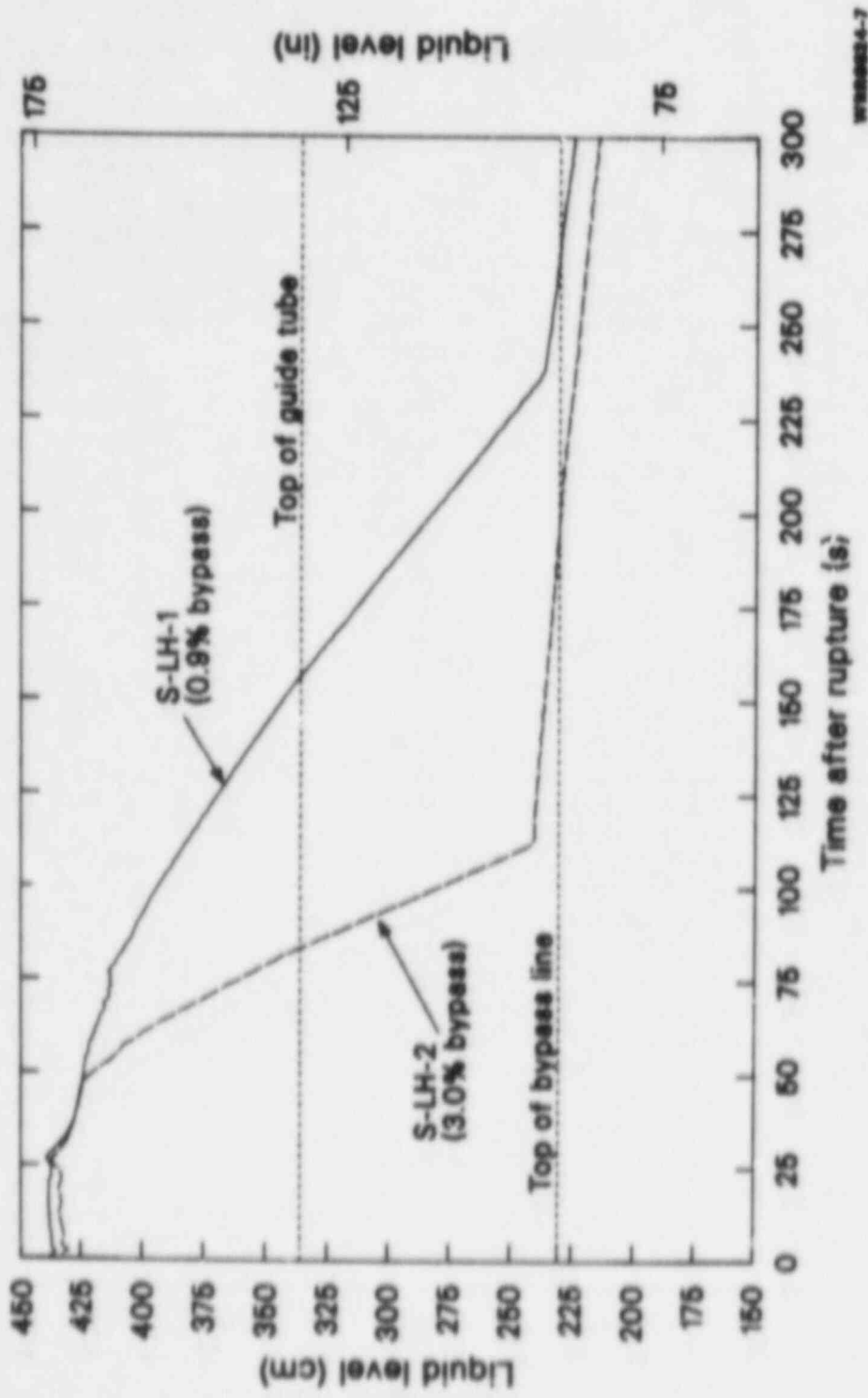


Figure 5. Vessel upper head collapsed liquid level, or Semicale Mod-2C Experiments S-LH-1 and S-LH-2.

## RESULTS FROM S-UT-6/S-UT-8

Comparison of S-UT-6 and S-UT-8 results show an enhanced (core liquid level depression for the lower bypass flow (see Figure 6). S-UT-8, with 1.1% of core bypass, shows a minimum core liquid level near the bottom of the heated length and S-UT-6, with 4.0% core bypass flow, shows a minimum core liquid level near the level associated with the pump suctions. As a result of the manometric core level depression, core rod heat-ups occurred during S-UT-8 but not S-UT-6 as shown on Figure 7. Figure 7 also shows core rod heat-ups associated with the boil-off for both experiments, and the core heater rod quench associated with accumulator injection. Therefore, examining only Figures 6 and 7, the effect of bypass flow is clear: high bypass flow allows more steam relief causing a minimal manometric core liquid level depression. However, many hardware and operational differences between the two experiments precluded a clear comparison. Most important among these differences was the higher upper head drain rate for S-UT-8 (see Figure 4) because of unplugged instrument ports in the support columns (during S-UT-8, the upper head should have drained at about half the rate of S-UT-6 because of a lower bypass line hydraulic resistance). Secondly, the intact loop steam generator condensation potential (primary to secondary temperature difference) was greater for S-UT-8, which has been related to the more severe core liquid level depression in References 1 and 2.

## RESULTS FROM S-LH-1 AND S-LH-2

The relative core liquid level response and core thermal response for S-LH-1 and S-LH-2 are identical to S-UT-6 and S-UT-8. Figure 8 compares the core liquid level for S-LH-1 and S-LH-2, showing a more severe liquid level depression during the manometric balance period for the lower bypass flow case (S-LH-1). Again as with S-UT-6 and S-UT-8, the lower bypass flow had core rod heat-ups during the manometric core liquid level depression and the high bypass flow did not. However, both experiments exhibited core rod heat-ups during the core boil-off period as shown in Figure 9. The primary pressure response varies slightly between S-LH-1 and S-LH-2 starting at about 350 s as shown on Figure 10. This has been attributed to clearing of the broken loop pump suction seal in S-LH-1 but not S-LH-2. With the increased bypass flow and the intact loop seal cleared, the manometric balance in the loop did not require clearing of the broken loop suction. As a result, the overall steam relief on S-LH-2 was not as great as S-LH-1 (where the broken loop seal was cleared) and the primary depressurization rate was diminished. This resulted in a delay in achieving the accumulator pressure set points (4.2 MPa) which resulted in a similar minimum core liquid level for S-LH-2 as S-LH-1 at the time of accumulator injection as shown on Figure 8. In terms of overall severity, the results of S-LH-1 and S-LH-2 show no real effect on transient severity due to a variation in bypass flow. The only real effect is a more severe core level depression during the manometric balance period.

## DISCUSSION OF RESULTS

Considering the two data bases discussed above, the only valid comparison to examine the effect of bypass flow on transient severity is to use S-LH-1 and S-LH-2 data where only the bypass flow was changed. Hardware and

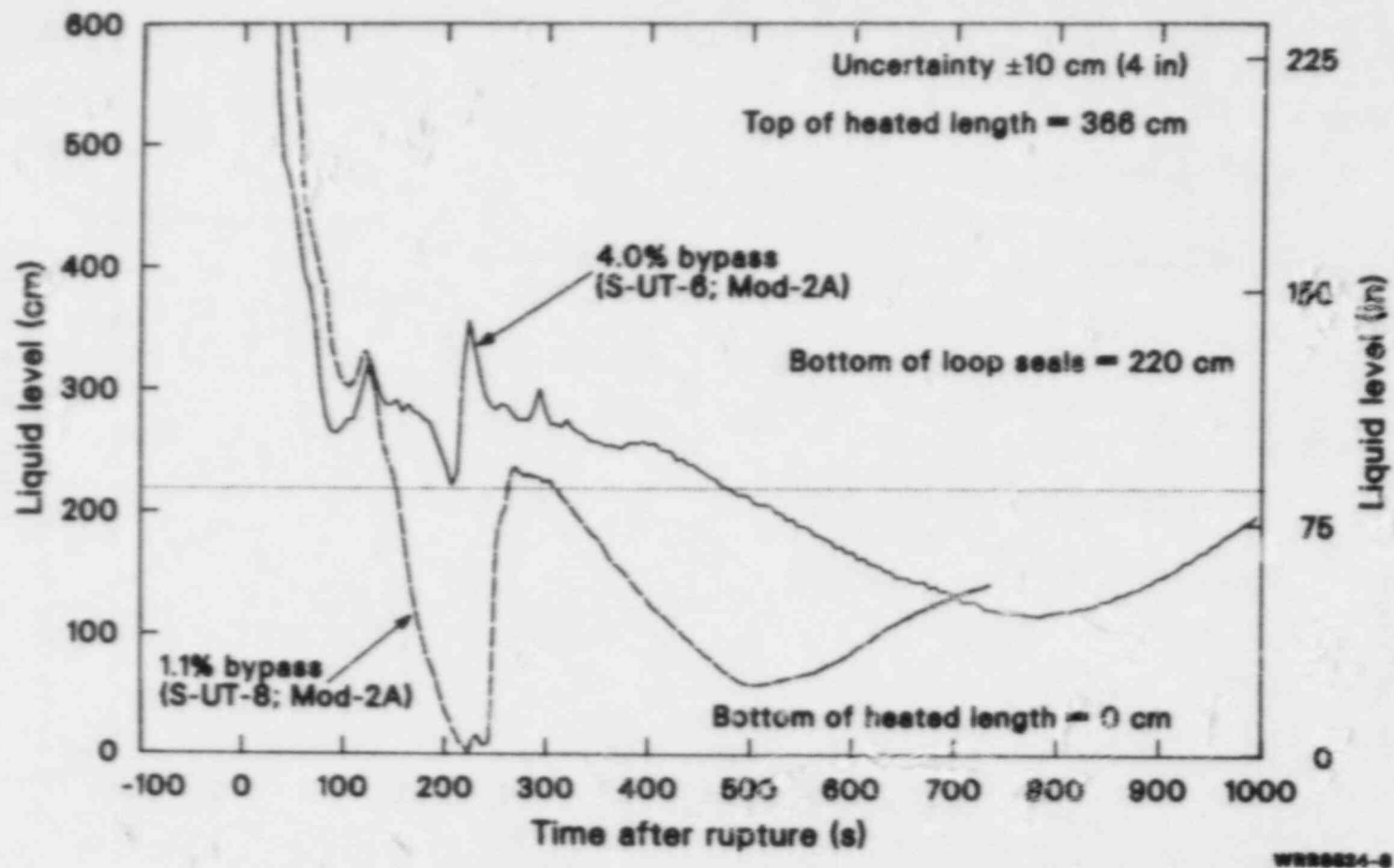


Figure 6. Vessel collapsed liquid level for Semiscale Mod-2A Experiments S-UT-6 and S-UT-8.

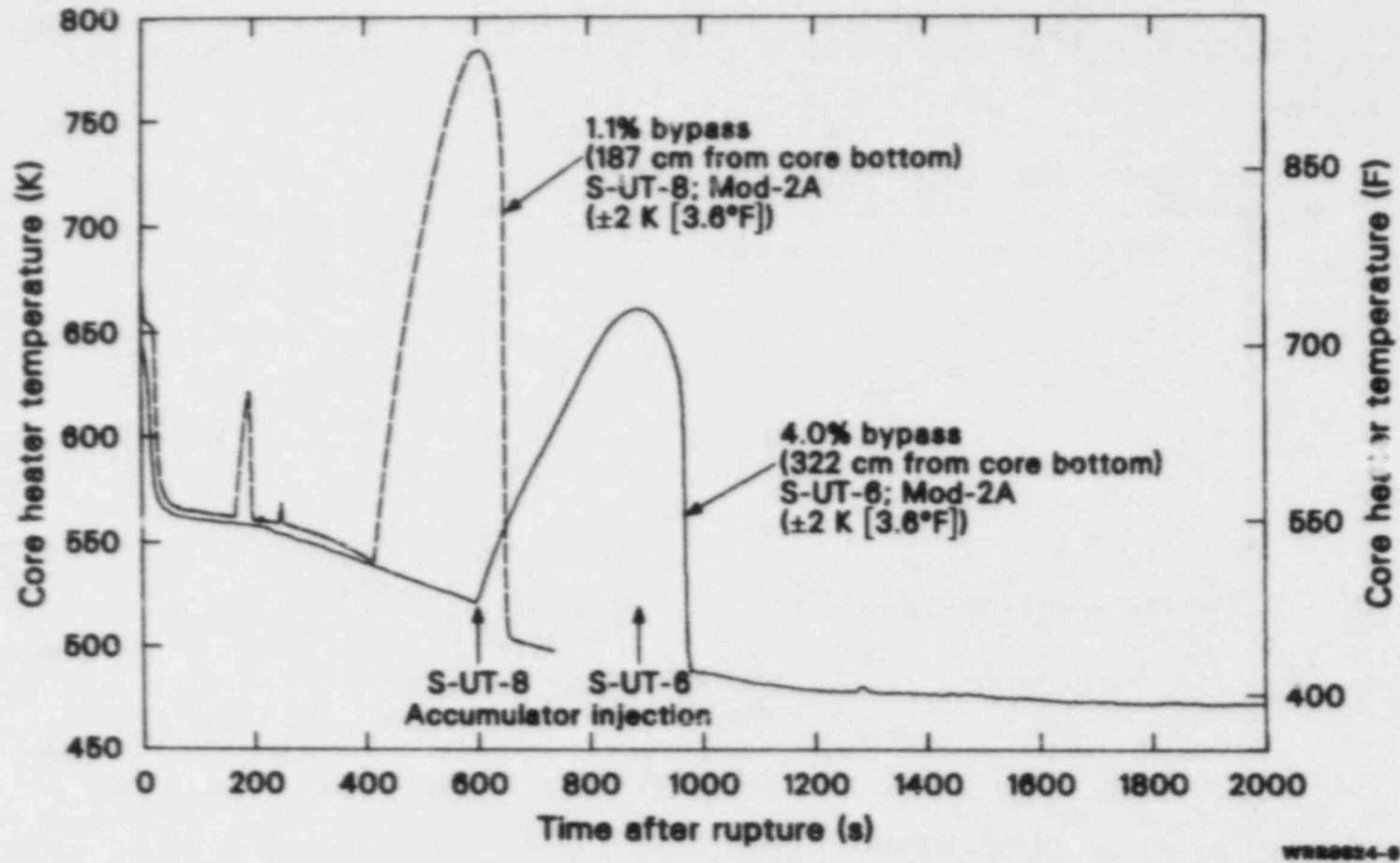


Figure 7. Core heater rod temperature response for Semiscale Mod-2A Experiments S-UT-6 and S-UT-8.

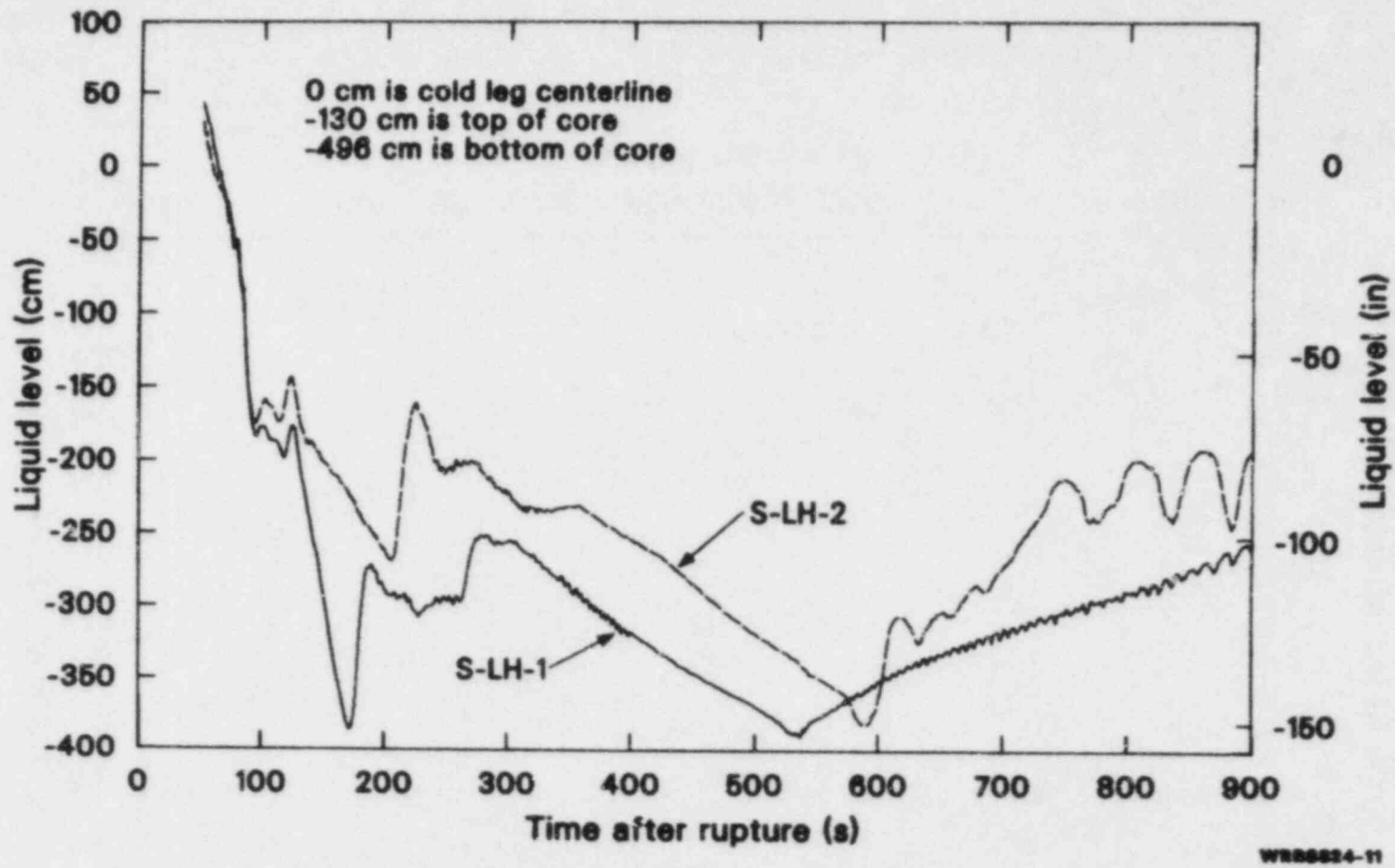


Figure 8. Vessel collapsed liquid level for Semiscale Mod-2C Experiments S-LH-1 and S-LH-2.

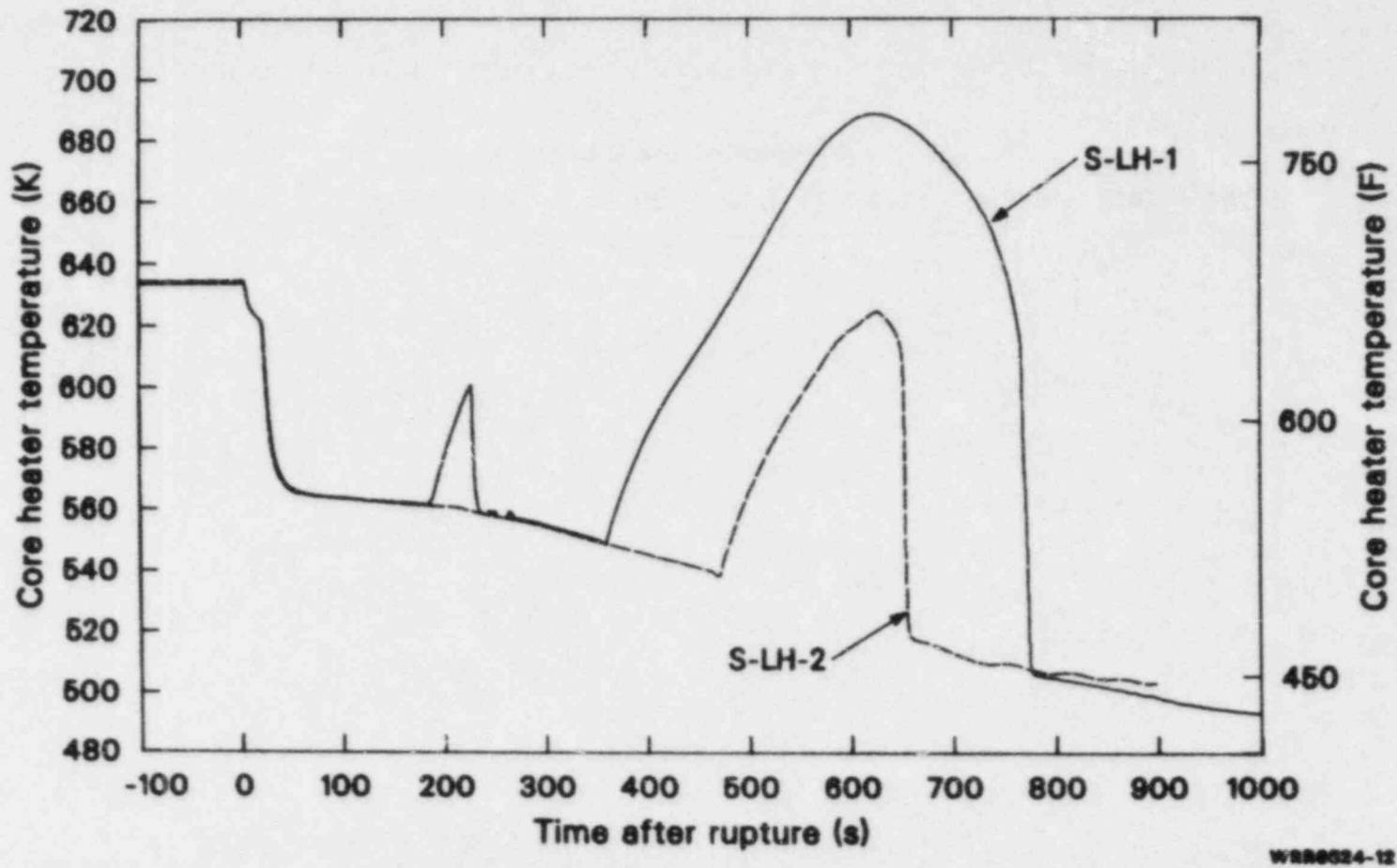


Figure 9. Core heater rod temperature response for Semiscale Mod-2C Experiments S-LH-1 and S-LH-2.



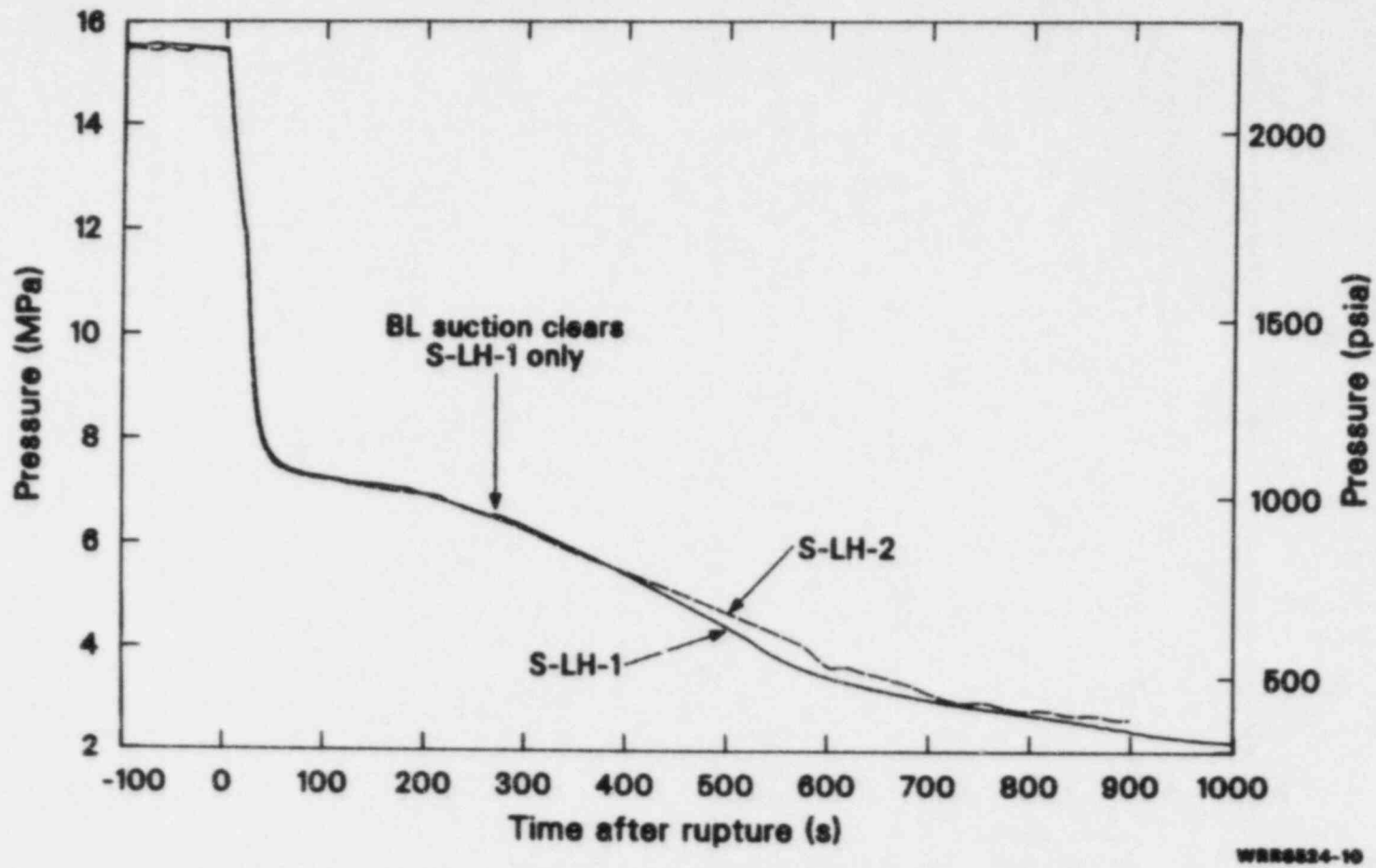


Figure 10. Primary pressure for Semiscale Mod-2C Experiments S-LH-1 and S-LH-2.

operational differences between S-UT-6 and S-UT-8 precluded a valid comparison on the effect of bypass flow. Even though the bypass flow was reduced, for S-UT-8 compared to S-UT-6, the faster drain of the upper head during S-UT-8 (because of upper head structure differences) provided earlier core steam relief to the break. This would cause the core level depression to be less severe for S-UT-8. However, during the time of primary U-tube drain during S-UT-8, a higher condensation potential due to operational differences in the intact loop steam generator (See Figure 11) caused an increase in the density of the fluid in the primary U-tubes. The increased density for S-UT-8 but not for S-UT-6 caused the measured collapsed level to increase about 3 m on both the upflow and downflow side of the tubes during S-UT-8 as shown on Figure 12. This increase in steam generator primary tube level did not occur on S-UT-6 (Figure 13) nor on S-LH-1 as shown on Figure 14. In fact with similar condensation potential for S-LH-1 and S-UT-6, the increase in primary tube level following the decrease in the effect of the primary circulating pumps was only about 0.5 m.

The higher condensation potential and increased primary tube level for Test S-UT-8 contributed to a higher net head across the steam generator primary tubes (see Figure 15), which contributed to the increased core liquid level depression shown on Figure 6. Previous studies on S-UT-6 and S-UT-8 suggest this net head in only intact loop steam generator primary tubes accounted for the depression in core liquid level below the suction. However, analysis of S-LH-1 and S-LH-2<sup>5</sup> has shown that the fluid heads throughout the loop contributed to the core liquid level depression below the level associated with the suctions, including upper head and both broken<sup>a</sup> and intact loop primary tube heads, as well as pump suction heads.

S-LH-1 exhibited the core liquid level depression below the level associated with the bottom of the suctions similar to S-UT-8 even though the net head in both the intact and broken loop steam generator primary U-tubes is the same regardless of bypass flow (see Figures 16 and 17 respectively for the net head in the intact loop and broken loop primary U-tubes).<sup>b</sup> Therefore, the higher core liquid level depression for S-LH-1 as compared to S-LH-2 was caused by the combination of net heads as dictated by the amount of allowed steam bypass flow. During S-LH-1 the upper head had sufficient fluid (see Figure 5) to cover the top of the bypass line during the manometric core depression, (which started at about 120 s on Figure 8). For S-LH-2 during the same manometric depression the upper head bypass line was clear of liquid allowing steam relief and thus relieving the overall head balance. Therefore, for S-LH-1 with a lower bypass flow, the drain of upper head fluid was slow enough to preclude using the bypass line for steam relief thus causing

---

a. The broken loop steam generator primary tube liquid level was not available for S-UT-8 analysis.

b. The net head is simply evidence of reflux in the primary tubes. Figure 14 shows a developing head difference at about 130 s as the upflow side head is higher than the downflow side head. Reflux occurs when steam created in the core travels to the steam generator where it is condensed and the condensed fluid then runs back to the core counter-current to the steam flow.

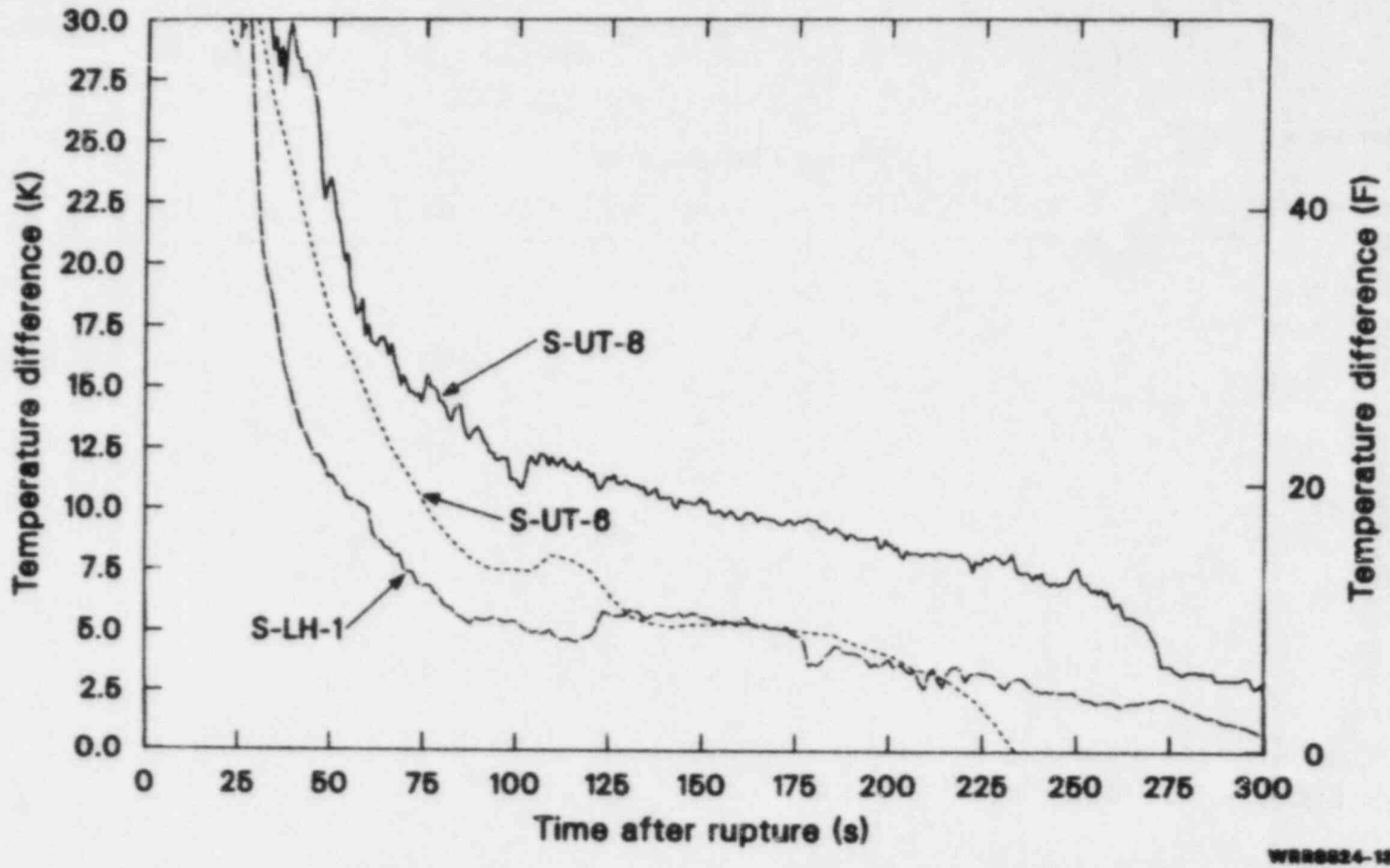


Figure 11. Intact loop primary to secondary fluid temperature difference for Semiscale Experiments S-LH-1, S-UT-6, and S-UT-8.

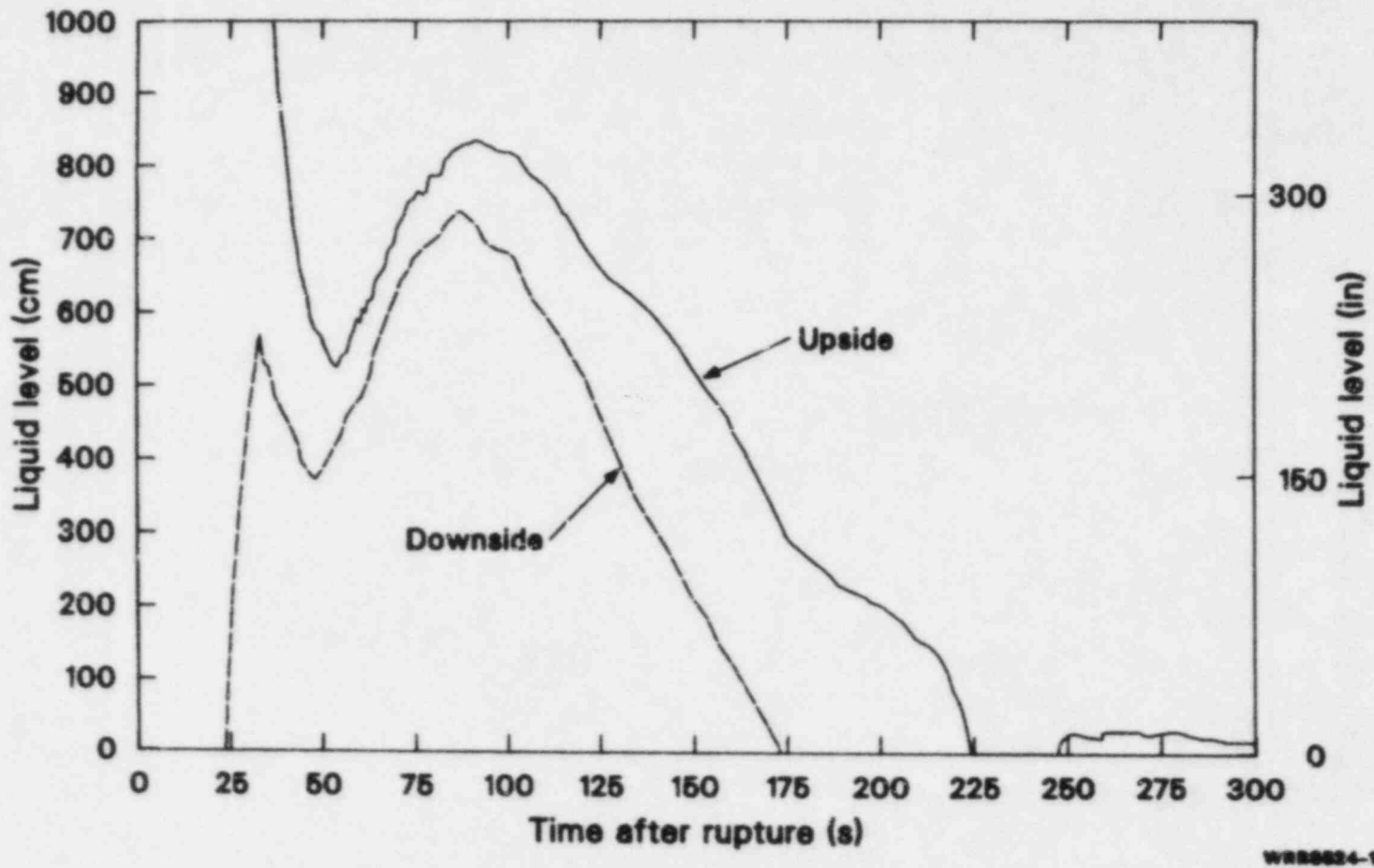


Figure 12. Intact loop steam generator primary U-tube liquid level for Semiscale Experiment S-UT-8.

WR8824-17

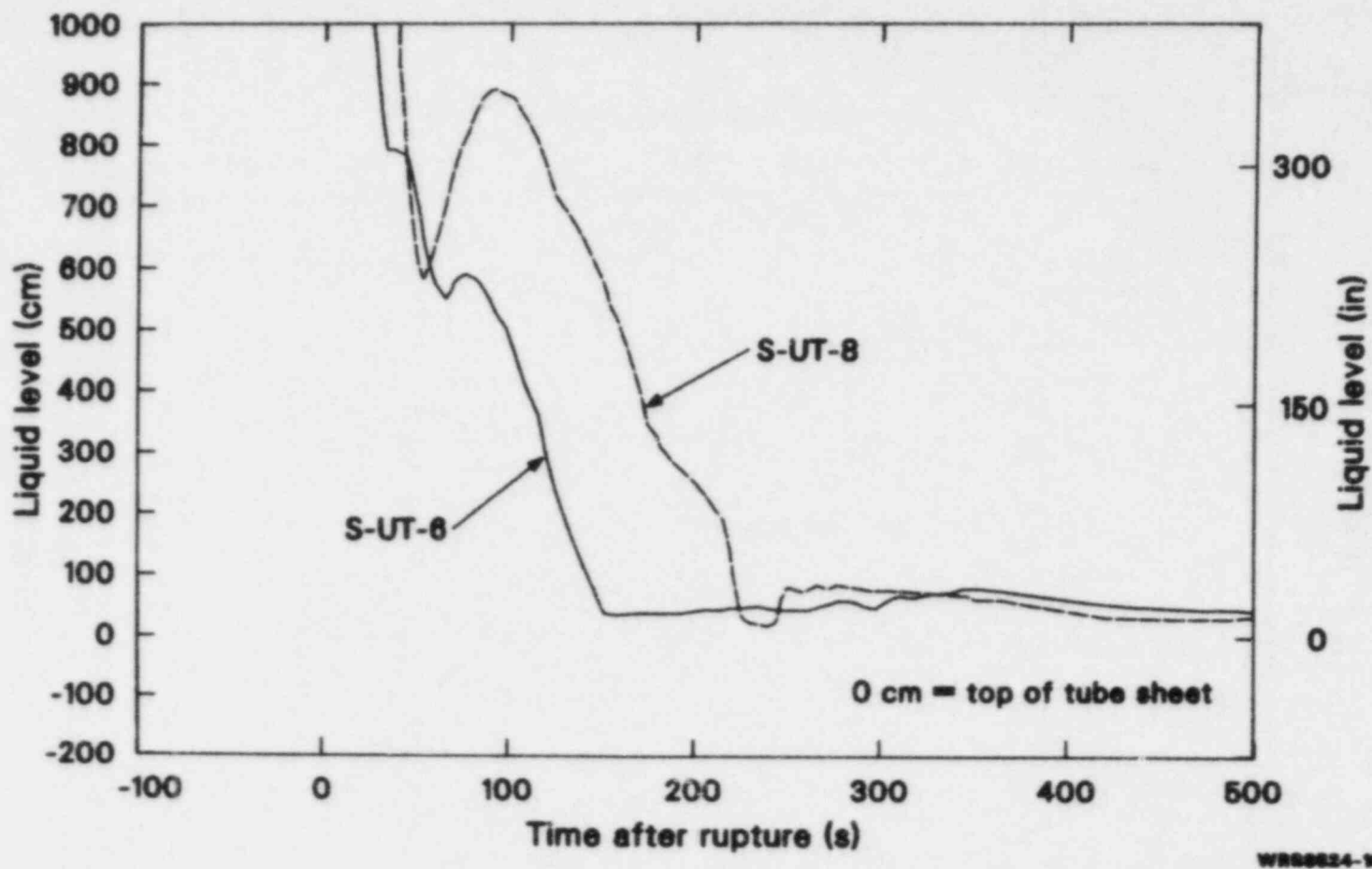


Figure 13. Intact loop steam generator primary U-tube upflow side liquid levels for Semiscale Experiments S-UT-6 and S-UT-8.

WR8824-18

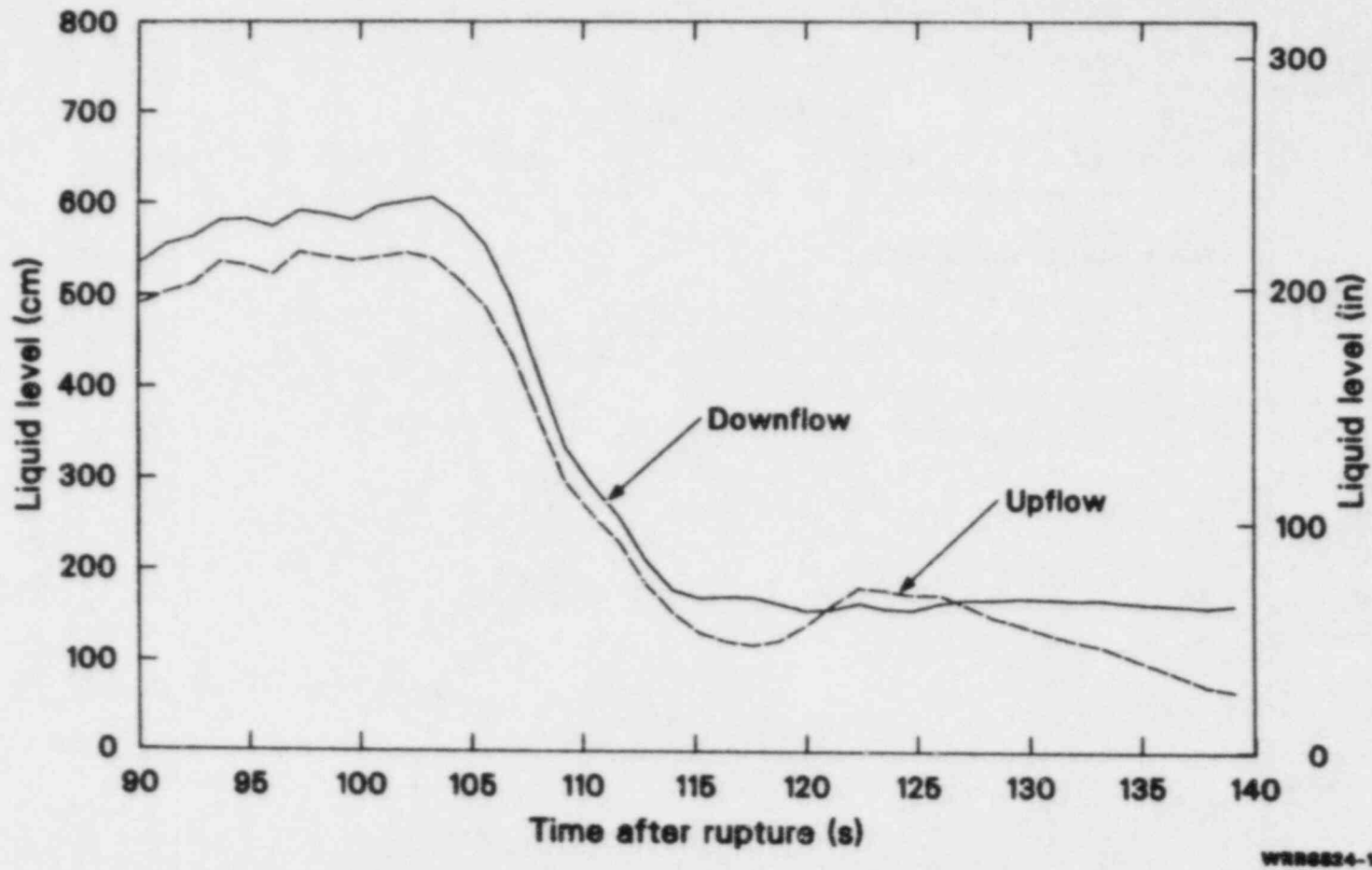


Figure 14. Intact loop steam generator primary U-tube liquid levels for Semiscale Experiments S-LH-2 and S-LH-2.

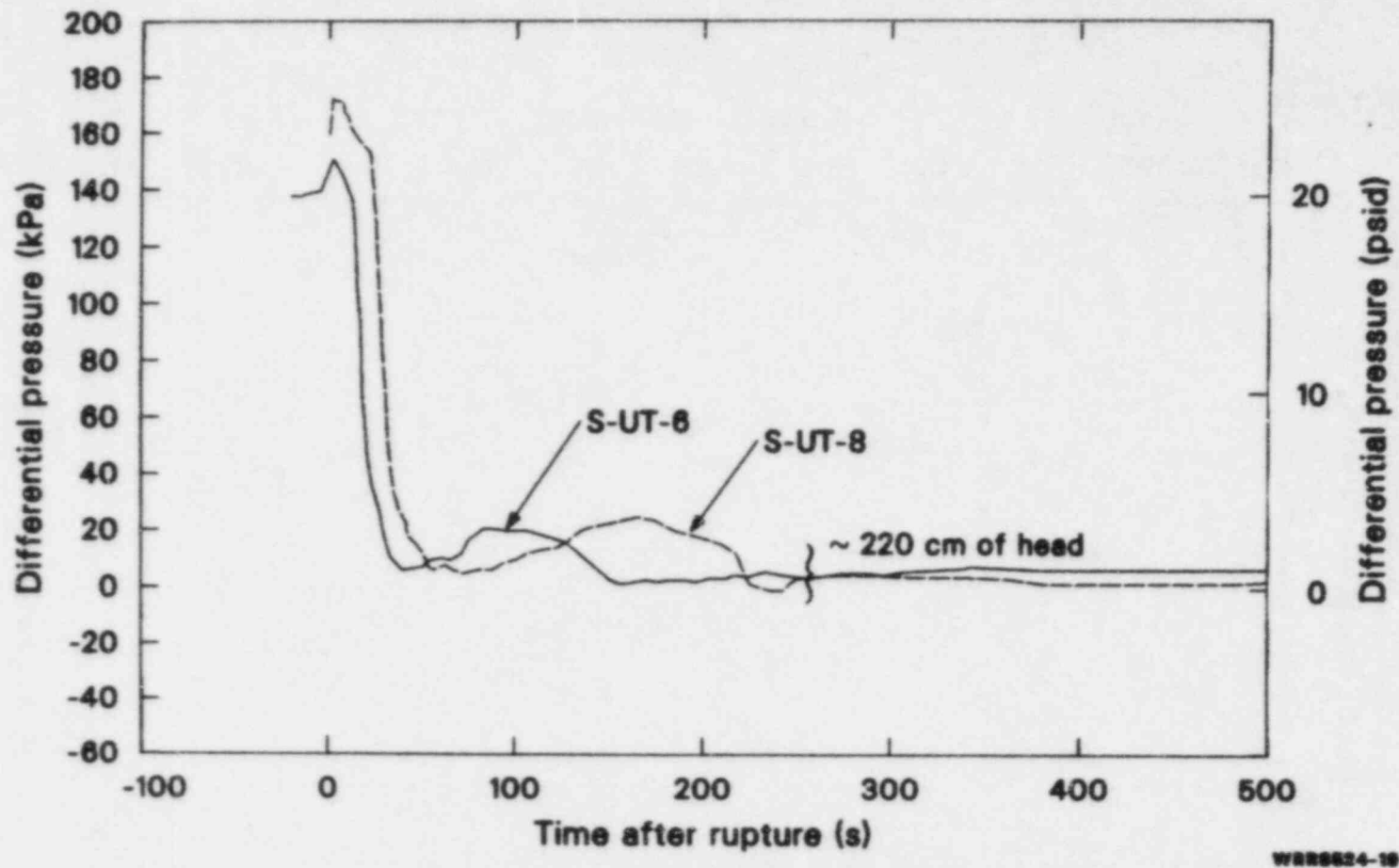


Figure 15. Intact loop steam generator primary side inlet to outlet differential pressure for Semiscale Experiments S-UT-6 and S-UT-8.

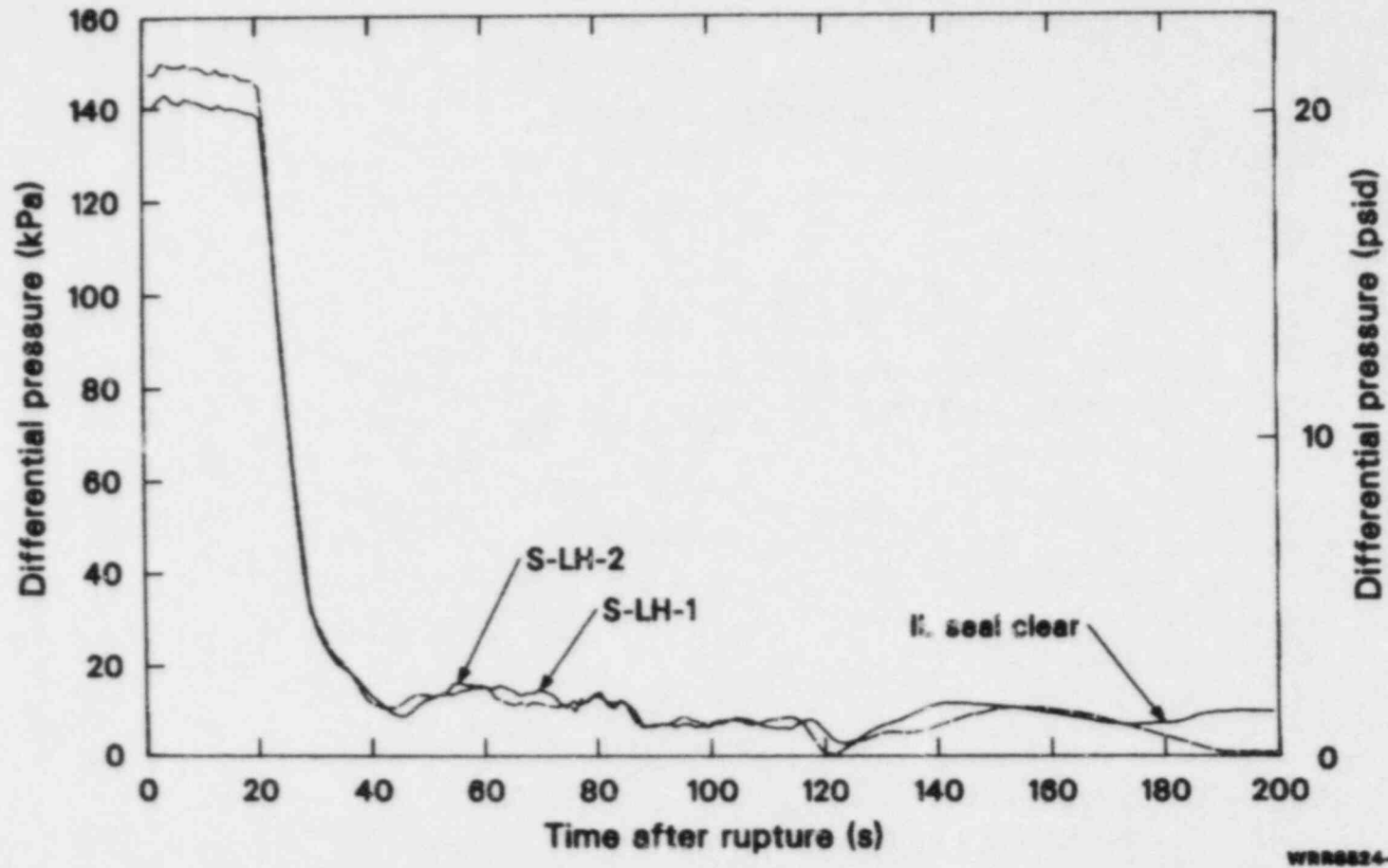


Figure 16. Intact loop steam generator primary side inlet to outlet differential pressure for Semiscale Experiments S-LH-1 and S-LH-2.

WR8824-10



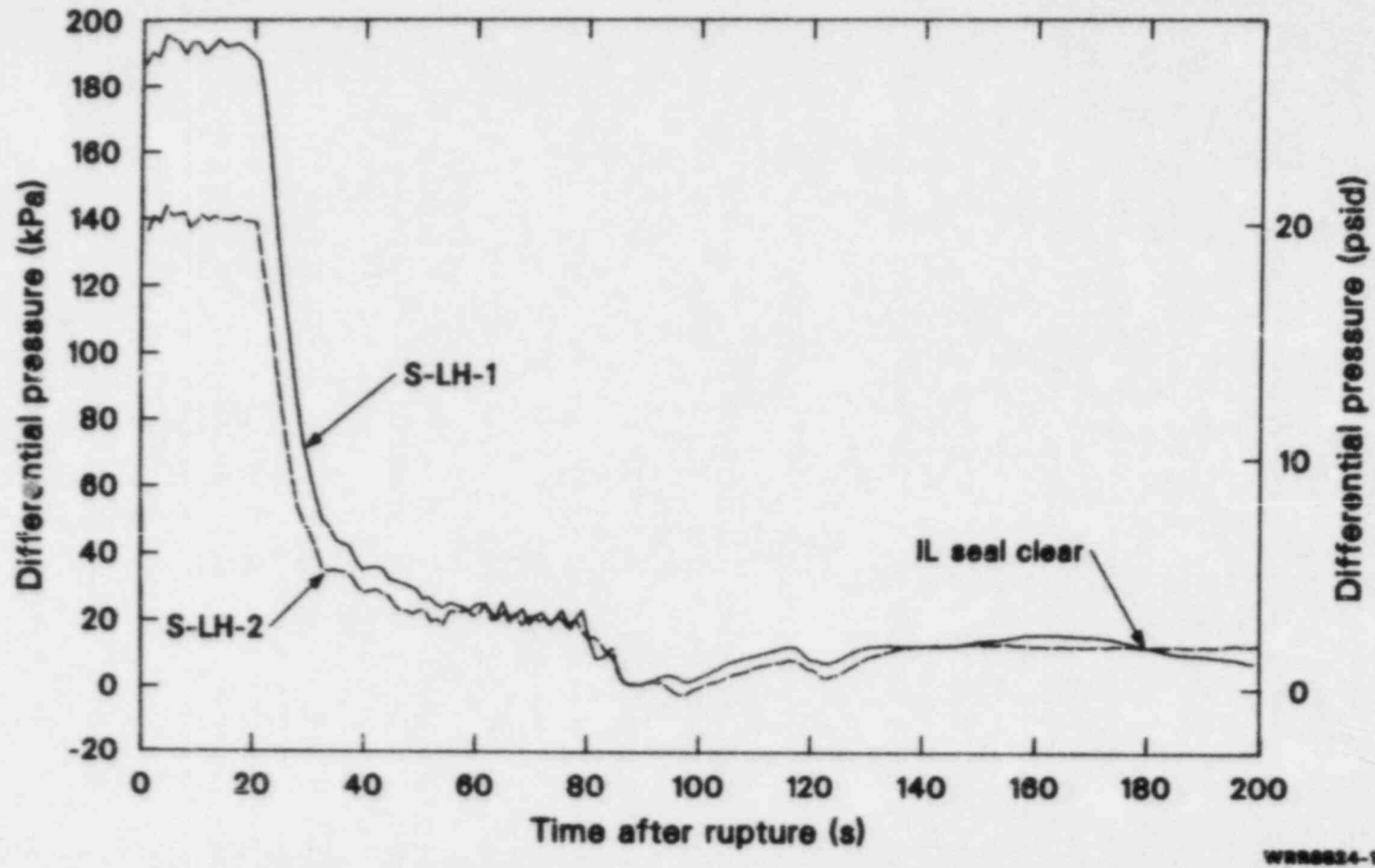


Figure 17. Broken loop steam generator primary side inlet to outlet differential pressure for Semiscale Experiments S-LH-1 and S-LH-2.

the overall head balance to affect a greater core liquid level depression than S-LH-2 where the bypass line was cleared for steam relief. During S-UT-8, with an atypically high upper head drain rate compared to S-UT-6 (see Figure 4), the bypass line was cleared for steam relief; however the condensation potential difference (see Figure 11) overshadowed any steam relief and caused the fluid heads in the loop to balance such that the core liquid level was depressed below the level associated with the suction.

In summary, comparison of S-UT-6 and S-UT-8 to assess the effect of bypass flow is invalid, even though the overall trend is correct. A different condensation potential, caused by operational differences, and atypically different upper head drain rate, caused by hardware differences, precluded a valid comparison. During S-LH-1 and S-LH-2 a clear comparison for the effect of bypass flow on transient severity was possible. The increase bypass flow for S-LH-2 caused a faster drain of the upper head fluid resulting in a steam relief path during the manometric depression. Since the net head in the steam generator primary U-tubes was identical for the two cases (S-LH-1 and S-LH-2), fluid heads in these components did not alone cause the increased core level depression observed in S-LH-1, rather the amount of fluid in the upper head and the availability of a steam relief path caused the differences.

#### CONCLUSIONS

The amount of initial allowed bypass flow affects the transient severity during the manometric balance period associated with pump seal clearing; however, on an overall basis, transient severity is relatively unaffected by bypass flow. With higher bypass flow, the increased steam relief path through the bypass line to the break precludes clearing of the broken loop suction which causes a slower depressurization rate to the accumulator set point pressure. As a result, the core fluid boil-off occurred for a longer time (from a higher initial core liquid level) resulting in a similar minimum core liquid level at the time of accumulator injection.

Tests S-LH-1 and S-LH-2 provide a clear comparison on the effect of bypass flow on transient severity in the Semiscale system. Tests S-UT-6 and S-UT-8 contained too many hardware and operational differences to provide a clear comparison. The upper head structures allowed a too high rate of upper head drain for S-UT-8 compared to S-UT-6. In addition, a higher condensation potential in the intact loop steam generator caused a higher net head of fluid for S-UT-8 than S-UT-6 (liquid hold-up) that contributed to a more severe core level depression. Therefore, in comparing S-UT-8 and S-UT-6 data, the trend for a larger core liquid level depression for lower bypass flow was correct, but, for the wrong reasons. Comparison of S-LH-1 and S-LH-2 results show that with an increased bypass flow, the fluid drain rate of the upper head is enhanced causing an earlier opening of a steam relief path via the bypass line for steam flow to the break. This open relief path precludes the extensive core liquid level depression seen for the lower bypass flow case by relieving the overall fluid head balance. The only evidence of liquid hold-up during S-LH-1 and S-LH-2 was an increase in upflow side primary U-tube level associated with the establishment of reflux in each loop. The core level depression difference occurred even though the amount of liquid hold-up

(reflux) was the same for S-LH-1 and S-LH-2. Therefore, the steam relief alone for the higher bypass flow case caused the difference in core liquid level depression observed between S-LH-1 and S-LH-2.

#### REFERENCES

1. M. T. Leonard, J. L. Perryman, and G. W. Johnson, "The Influence Of Liquid Hold-up In Steam Generator U-tubes On Small Break Severity," ASME, reprint 83-WA-NE-2.
2. M. T. Leonard, Vessel Coolant Mass Depletion During a Small Break LOCA, EGG-SEMI-6010, September 1982.
3. W. W. Tingle, Experiment Operating Specification for Semiscale Mod-2A 5.0% SBLOCA Experiment S-UT-8, EGG-SEMI-5696, December 1981.
4. G. G. Loomis, Experiment Operating Specification for Semiscale Mod 2C 5% Small Break Loss-of-Coolant Experiment S-LH-1, EGG-SEMI-6813, February 1985.
5. G. G. Loomis and J. E. Streit, Results of Semiscale Mod-2C 5% SBLOCA Experiments S-LH-1 and S-LH-2, NUREG, November 1985.

## The Results of the ROSA-IV LSTF Small-Break LOCA Experiments

K. Tasaka, M. Kawaji, M. Osakabe and Y. Koizumi  
Japan Atomic Energy Research Institute  
Tokai-mura, Ibaraki, Japan

### Abstract

The test results are reported on three small-break LOCA experiments recently conducted at the Large Scale Test Facility (LSTF) of the ROSA-IV program. In all of these tests, a break was located horizontally at the side of the cold leg piping (207 mm in diameter). The break sizes tested were equal to 10.0 %, 5.0 % and 2.5 % of the scaled (1/48) flow area of the reference PWR's cold leg.

In both the 10 % and 5 % break tests, HPIS was activated early in the transient and the rest of ECCS operated satisfactorily to prevent the major uncovering of the core. However, partial and temporary core dryout was observed early in the 5 % break test, because of the core liquid level depression due to liquid holdup in the SG U-tubes. In the 2.5 % break test, major core uncovering occurred due to boiloff, because of the assumption that HPIS remains inoperative for 1200 s after break.

### 1. Introduction

The Japan Atomic Energy Research Institute is conducting Rig-of-Safety Assessment Number 4 (ROSA-IV) Program to investigate the thermal-hydraulic behavior of a Westinghouse (W)-type four loop pressurized water reactor (PWR) during small break loss-of-coolant accidents (SBLOCAs) and operational transients. Integral tests of the reference PWR plant behavior using the Large Scale Test Facility (LSTF) are at the heart of this program. [1-4]

This paper describes the test facility, the test conditions and procedures and the results of a series of three cold leg break tests with break size corresponding to 10 %, 5 % and 2.5 % break in a reference PWR.

The tests are conducted to investigate the effect of break size on the response of a plant in case of a cold leg break, and to provide experimental data for improvement and verification of advanced reactor analysis codes.

A recent topic of interest is the early core dryout due to primary coolant holdup in the steam generator U-tubes as observed in such tests as

Semiscale S-UT-8[5]. Although a series of tests are planned in the future to investigate this phenomenon in detail, the present series of tests give precursory information on the plant behavior with a fixed bypass flow area between the core upper head and downcomer.

## 2. Experimental facility

The LSTF is a 1/48 volumetrically scaled model of a W-type 3423 MWt four loop PWR. The LSTF has the same major component elevations as the reference PWR to simulate natural circulation and large loop pipes (hot and cold legs of 207 mm in diameter) to simulate two phase flow regimes and phenomena. The LSTF equipment can be controlled in the same way as that of the reference PWR to simulate long term reference PWR operational transients. Furthermore, the LSTF is designed to be operated at the same high pressures and temperatures as the reference PWR.

Figure 1 and Table 1 show the structure and major dimensions of the LSTF, respectively. The four primary loops of the reference PWR are represented by two equal-volume loops. The overall facility scaling factor is 1/48. The hot and cold legs were sized to conserve the volume scaling and the ratio of the length to the square root of pipe diameter, i.e.,  $L/\sqrt{D}$  for the reference PWR. Thus, the flow regime transitions in the primary loops will be simulated [6]. (Detailed LSTF system description is presented in Reference [7].) In the present series of tests, the break point was located in the B-loop (loop without a pressurizer) cold leg between the reactor coolant pump and the reactor pressure vessel. The break orientation was horizontal in all cases.

## 3. Test Conditions

The major initial conditions of the LSTF cold leg break tests are almost identical as shown in Table 2. To set up the steady state conditions, the following design compromises of the LSTF were examined. The test procedures were also designed to minimize their effect on the test.

The most important design scaling compromise is the 10 MW maximum core power limitation (14 % of the scaled reference PWR rated power). The low LSTF rated power affects the steady state operation and early

Table 1  
Major Dimensions of LSTF

		LSTF	PWR	PWR/LSTF
Pressure	(MPa)	16	16	1
Temperature	(K)	598	598	1
No. of fuel pins		1064	50952	48
Core height	(m)	3.66	3.66	1
Fluid volume V	(m <sup>3</sup> )	7.23	347	48
Core power P	(MW)	10	3423(t)	342
P/V	(MW/m <sup>3</sup> )	1.4	9.9	7.1
Core inlet flow	(ton/s)	0.0488	16.7	342
Downcomer gap	(m)	0.060	0.260	4.33
Hot leg D	(m)	0.207	0.737	3.56
L	(m)	3.69	6.99	1.89
$L/\sqrt{D}$	(m <sup>1/2</sup> )	8.15	8.15	1.0
$\frac{\pi}{4} D^2 L$	(m <sup>3</sup> )	0.124	2.98	24.0
No. of loops		2	4	2
No. of tubes in steam generator		141	3382	24
Length of steam generator tube (average)	(m)	20.2		

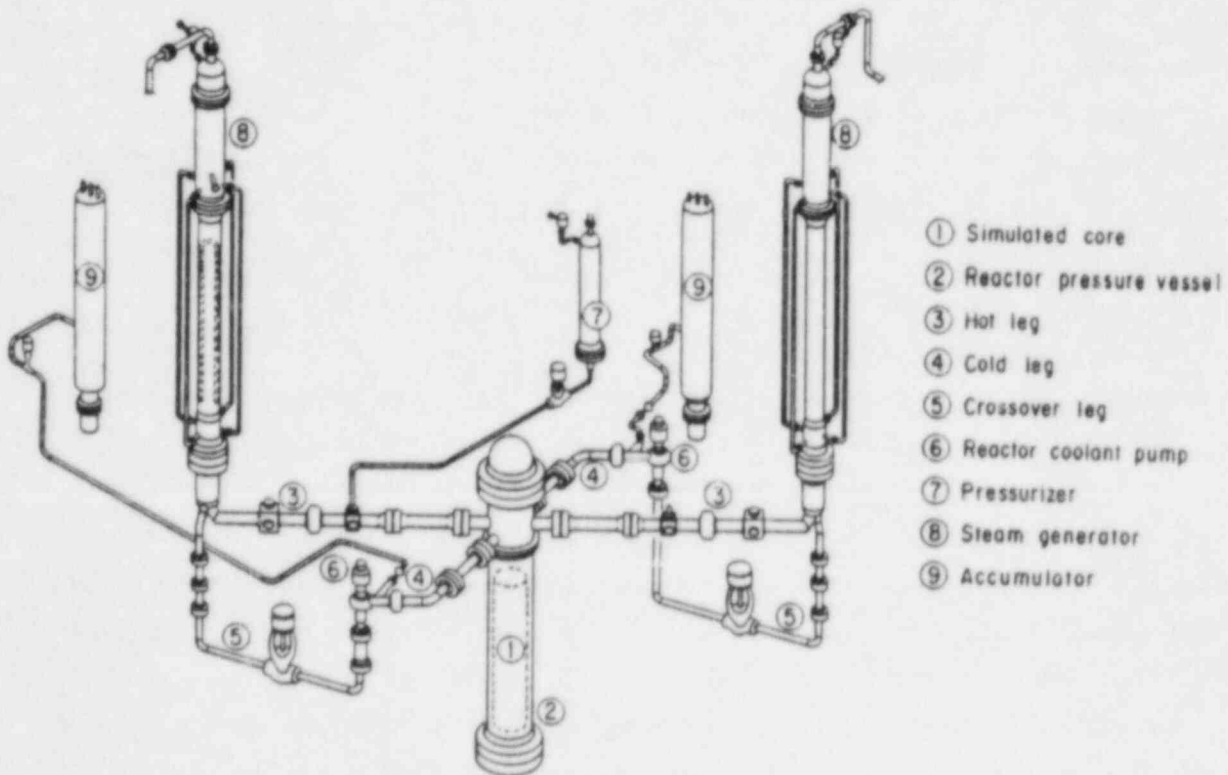


Fig.1 General View of LSTF

transient behavior.

The steady-state condition is restricted to a core mass flow rate that is 14 % of the scaled value to simulate the reference PWR temperature distribution in the loop. The desired primary coolant flow rate can be established either by running the primary coolant pumps at normal speed with the flow control valves (FCVs) in the cross-over legs only partially open or by reducing the pump speed with the FCVs fully open. The former was used in the 10 % test and the latter in 5 % and 2.5 % tests. In both cases, the primary loop flow rate was increased at the time of break to improve the similarity of the LSTF to the reference PWR by either fully opening the FCVs or increasing the pump speed [8].

The primary to secondary heat transfer must also be maintained at 10 MW, i.e., 14 % of the scaled value. Since the LSTF steam generators (SGs) are geometrically scaled to the reference PWR, the 14 % primary to secondary heat transfer rate is established by raising the secondary temperature such that the primary pressure and temperature are representative of the reference PWR. Major operational setpoints including ECCS actuation logic for the three tests are shown in Fig. 2. As the break occurs at time zero, the primary system begins to depressurize quickly. At a pressurizer pressure of 12.97 MPa, reactor scrams. The loss-of-offsite power concurrent with the reactor scram is assumed and the primary coolant pumps are tripped to begin coastdown and the core power begins to decrease along the decay curve. The steam generator feedwater is terminated and the auxiliary feedwater is supplied with a 28 s delay after scram.

At a pressurizer pressure of 12.27 MPa, a safety injection signal is sent that trips ECCS to be actuated at respective pressure setpoints. The ECCS conditions are summarized in Table 3. In the LSTF, a high pressure charging system is included in the ECCS. ECCS pump flow rates, i.e., high pressure injection system (HPIS) and low pressure injection system (LPIS), simulate one of two pump's capacity for each system in the reference PWR. ECCS injection initiation time delays were programmed to be the same as the reference PWR. For the 2.5 % test, HPIS actuation (including a charging system) was programmed to occur 1200 s after break, in order to bring about a major core dryout and heatup.

As shown in Fig.3, the core power decay curve used in the 10 % test is that of ANS standard, however, a revised curve which takes into account

Table 2  
Initial Conditions in Cold Leg Small Break Tests

Run No.		AT-SB-02	SB-CL-05	SB-CL-01
break area	mm	10	5	2.5
core power	MW	10.0	10.1	10.0
primary pressure	MPa	15.5	15.6	15.5
pressurizer liquid level	m	2.23	2.64	2.64
Hot leg (A/B) fluid temp.	K	598/598	599/599	599/599
Cold leg (A/B) fluid temp.	K	564/564	565/564	565/564
Core flowrate	kg/s	50.6	49.3	48.9
secondary pressure (A/B)	MPa	7.35/7.38	7.27/7.41	7.35/7.39
SG secondary liquid level (A/B)	m	10.2/10.1	10.3/10.3	10.2/10.3
SG steam flowrate (A/B)	kg/s	2.66/2.73	2.63/2.73	2.78/2.70
SG feedwater flowrate (A/B)	kg/s	2.94/3.02	2.71/2.76	2.71/2.85
SG feedwater temp.	K	496	495	496

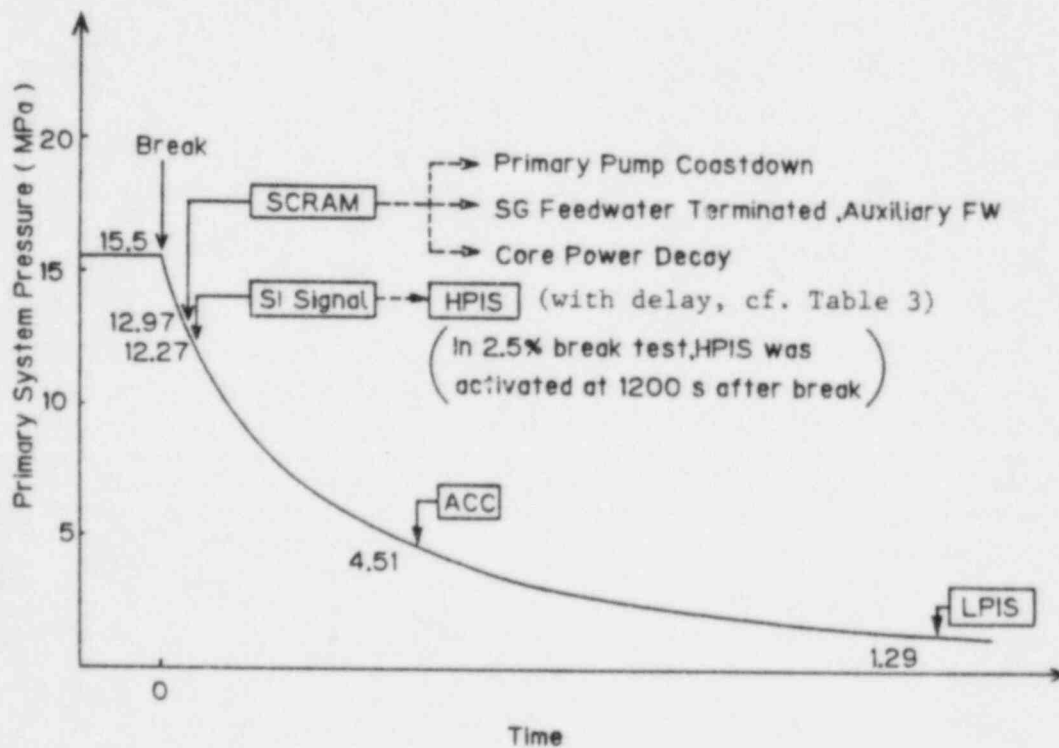


Fig.2 Operational and ECCS Control Logic



Table 3

## ECCS Actuation Conditions

Test	10%	5%	2.5%
High pressure charging system			
Pump shut-off head	18.1 MPa	+	+
Delay time from SI signal	12 s	+	1200s from break
Flowrate	single failure assumed	+	+
Fluid temperature	310 K	+	+
Injection location(ratio)	CLA, CLB (3:1)	+	+
High pressure injection system			
Pump shut-off head	10.7 MPa	+	+
Delay time from SI signal	17 s	+	1200s from break
Flowrate	single failure assumed	+	+
Fluid temperature	310 K	-	+
Injection location(ratio)	CLA, CLB (3:1)	+	+
Low pressure injection system			
Pump shut-off head	1.29 MPa	+	+
Delay time from SI signal	17 s	+	-
Flowrate	single failure assumed	+	+
Fluid temperature	310 K	+	+
Injection location(ratio)	CLA, CLB (3:1)	+	+
ACC system			
Pressure Setpoint	4.51 MPa	+	+
Water temperature	320 K	+	+
Injection location(ratio)	CLA, CLB (3:1)	+	+

the contribution from the delayed neutron fission in the 5 % and 2.5 % tests.

#### 4. Test Results

The sequence and timing of major events observed in the three tests are summarized in Table 4, and the primary and secondary pressures are shown in Fig.4 and 5 respectively. As the break occurs, the primary system depressurizes rapidly in all cases, reactor scrams and a safety injection signal is sent out at respective pressure setpoints. The primary pumps begin coastdown (Fig.6) and the primary flow rate decreases. HPIS (including a charging system) is turned on following the receipt of an SI signal in 10 % and 5 % tests.

At scram, the secondary system is isolated as a result of turbine trip. The secondary pressure increases up to the relief valve (RV) opening pressure and cycles between the RV opening/closing pressures. The secondary pressure begins to gradually decrease below the RV setpoints, when the primary pressure drops below the secondary pressure.

The rate of depressurization in the primary system is strongly dependent on the break size and thus, the break flow rate. In 10 % break, the primary pressure decreases at the fastest rate and consequently, HPIS, AIS and LPIS are actuated preventing the uncovering of the core. The collapsed liquid level in the core and fuel rod temperature at the core midplane are shown in Fig.7 and 8, respectively. There is a sharp decrease in the core liquid level and quick recovery early in the 10 % and 5 % tests. Temporary core liquid level depression is also observed in the 2.5 % test, however, it is not as pronounced as in the other two tests. Instead, major core uncovering is observed in the 2.5 % test preceding the AIS actuation. Despite the depression in the collapsed liquid level in the core, fuel rod temperature excursion anywhere in the core was observed only in 2.5 % and 5 % tests. The core was apparently covered with the two-phase mixture even during the collapsed liquid level depression in 10 % test. For 2.5 % and 5 % tests, a close relationship between the core liquid level depression and fuel rod temperature excursion is noted as shown in Fig.9 and 10.

In 2.5 % test, the loss of primary coolant was the slowest among the three tests, however, failure of HPIS to operate for 1200 s after break

Table 4

Chronology of Events (Time in seconds)

Test	10%	5%	2.5%
break initiation	0	0	0
reactor scram	5	11	16
main steam valve close	8	14	19
main feedwater trip	8	14	19
RCP coastdown initiation	11	16	21
core power decay initiation	13	45	50
HPIS injection initiation	23	30	1200
core uncover initiation	-	133	570
ACC injection initiation	192	417	835
core power trip	-	-	886
LPIS injection initiation	377	2203	1446

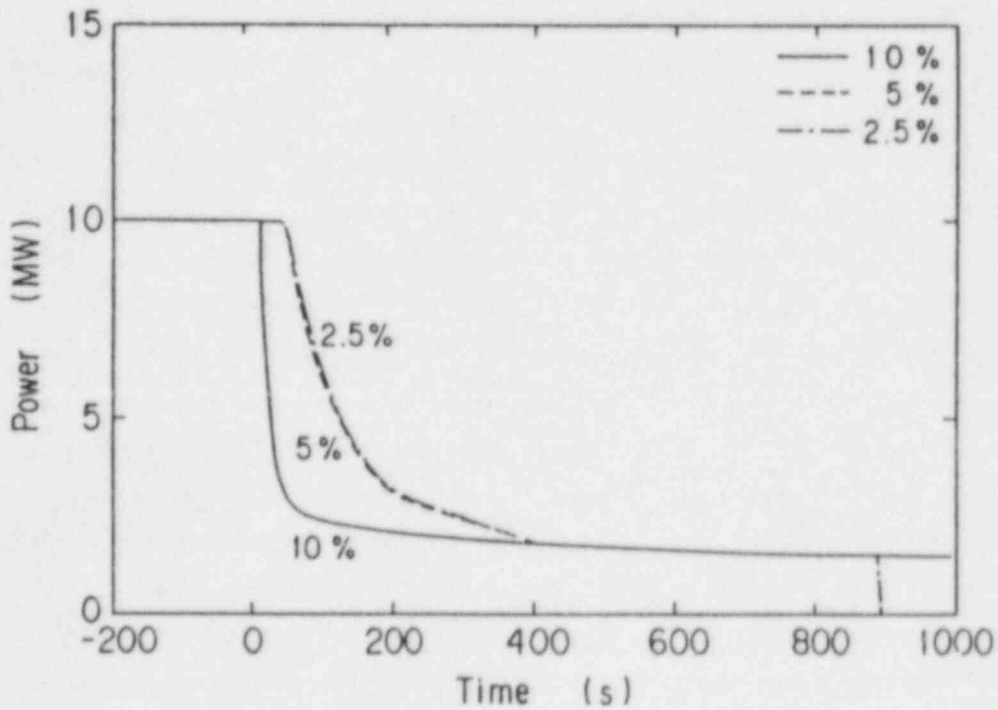


Fig.3 Core Power Decay in Cold Leg Break Tests

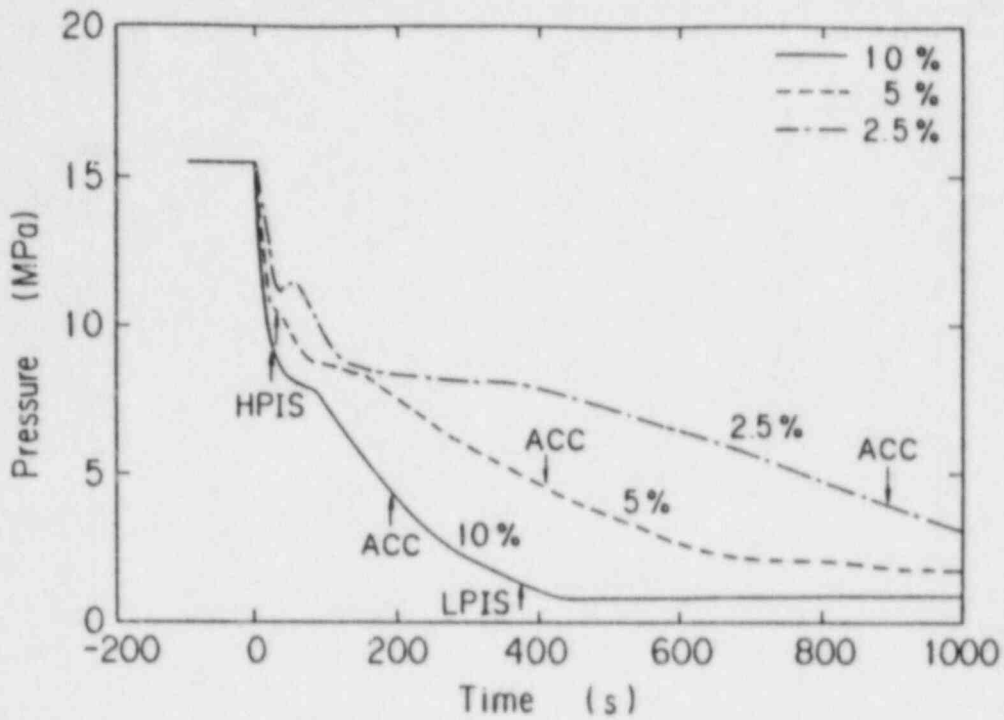


Fig. 4 Comparison of Primary Pressure Transients

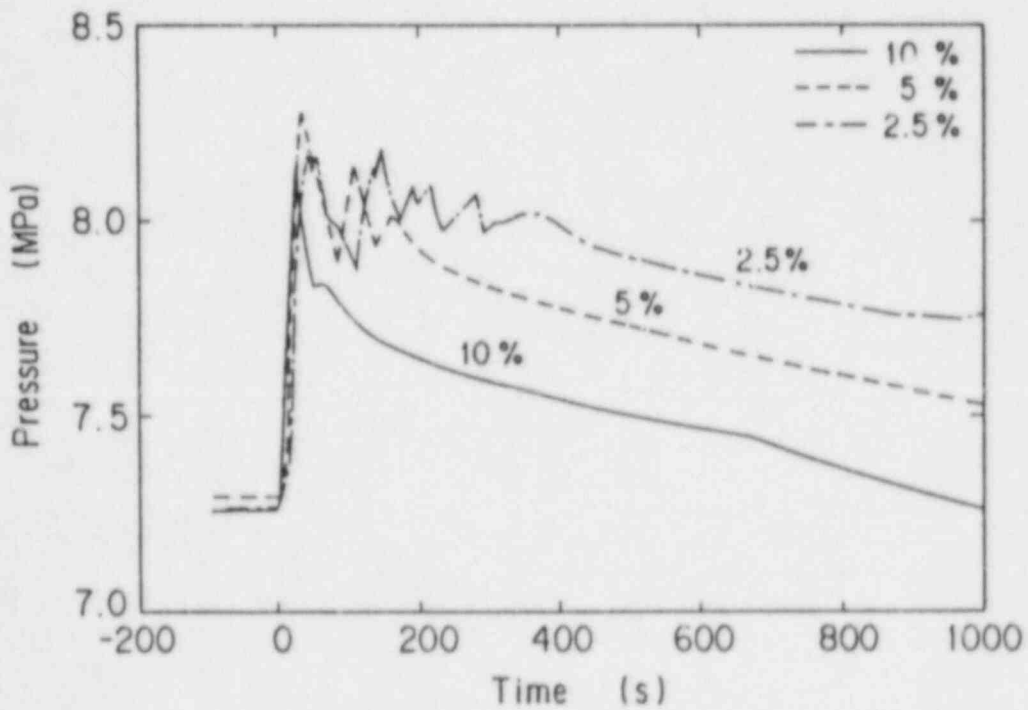


Fig. 5 Comparison of Secondary Pressure Transients

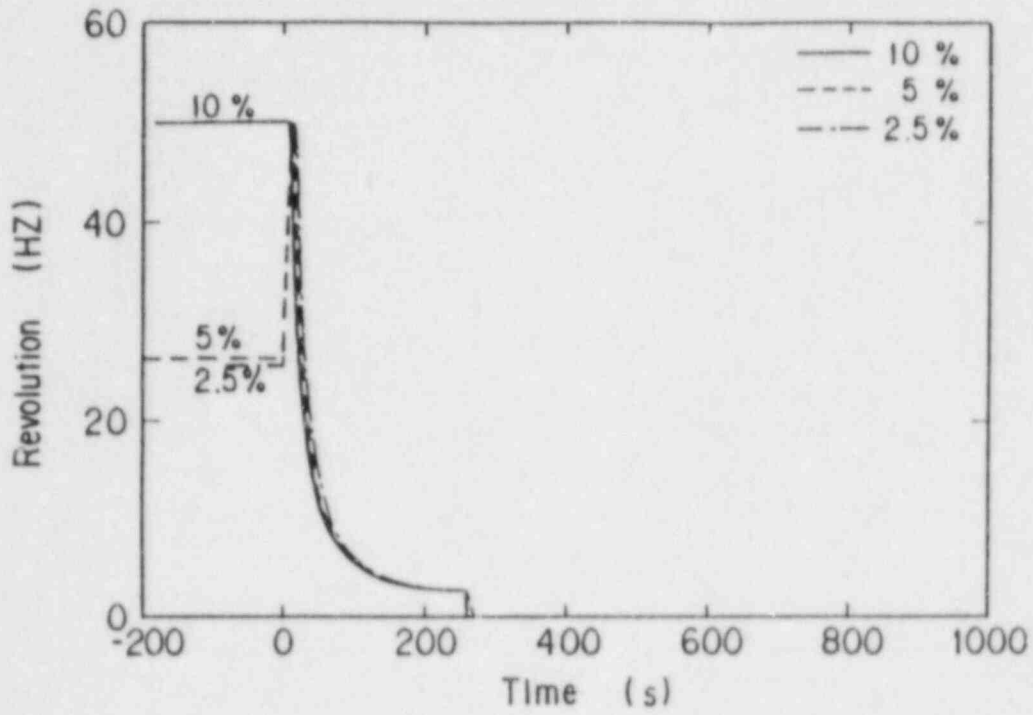


Fig.6 Reactor Coolant Pump Coastdown

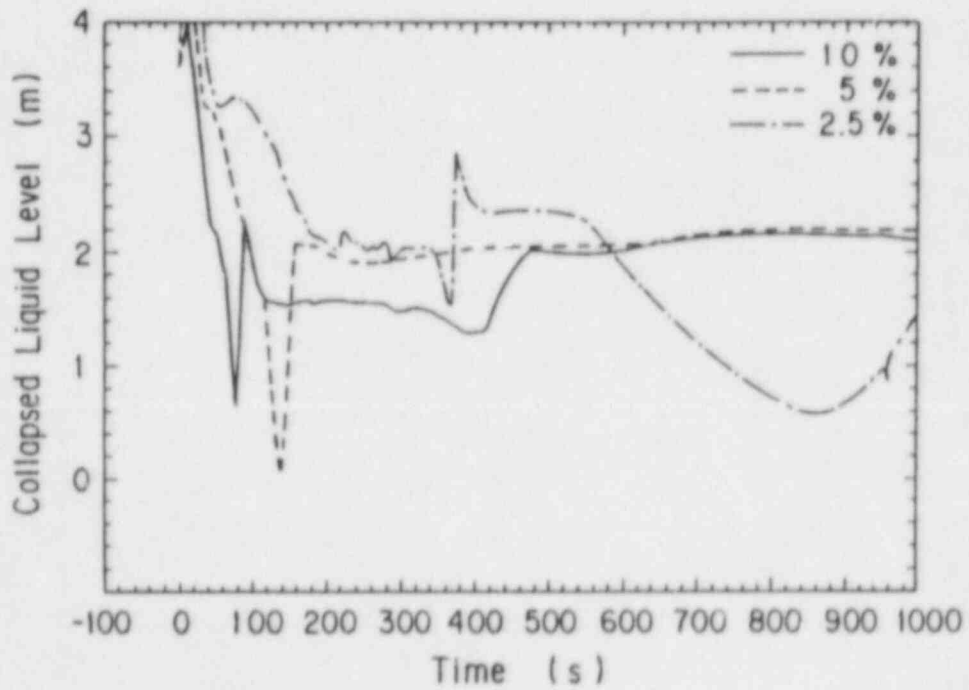


Fig.7 Comparison of Collapsed Liquid Level in Core

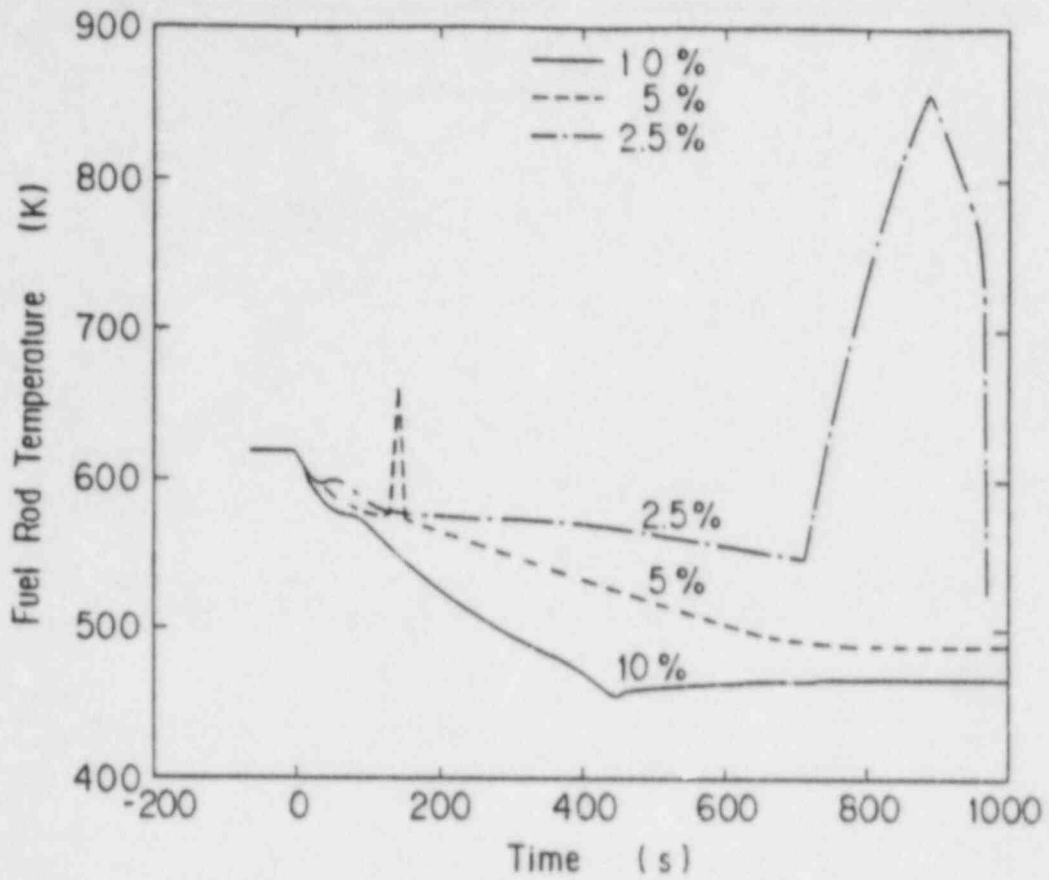


Fig.8 Fuel Rod Temperature Transient at Core Midplane

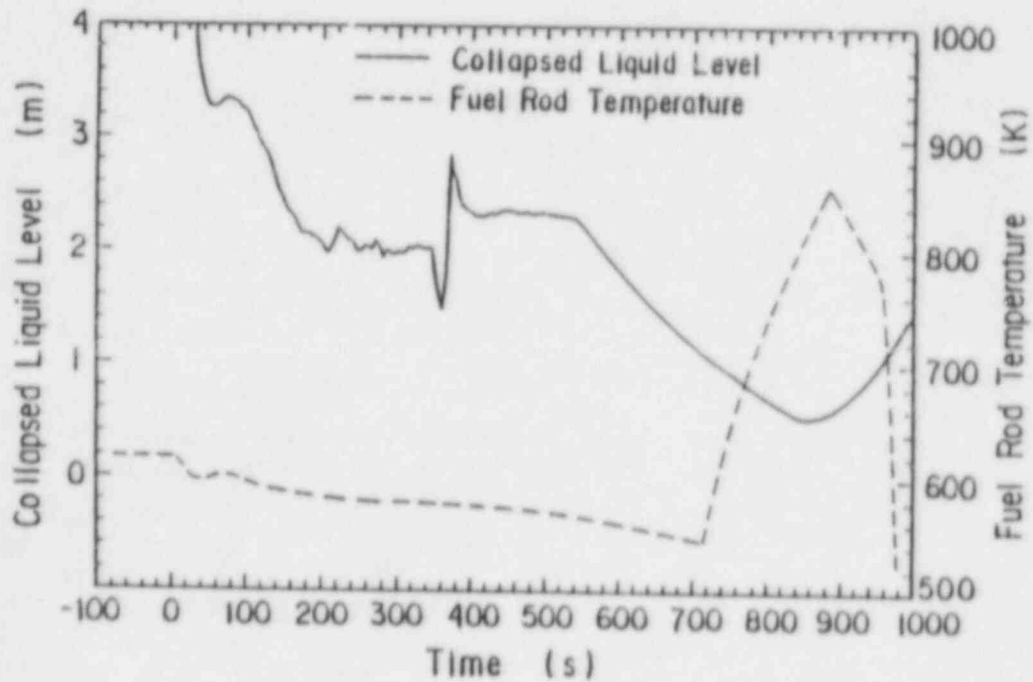


Fig.9 Major Core Dryout and Heatup in 2.5 % Break Test

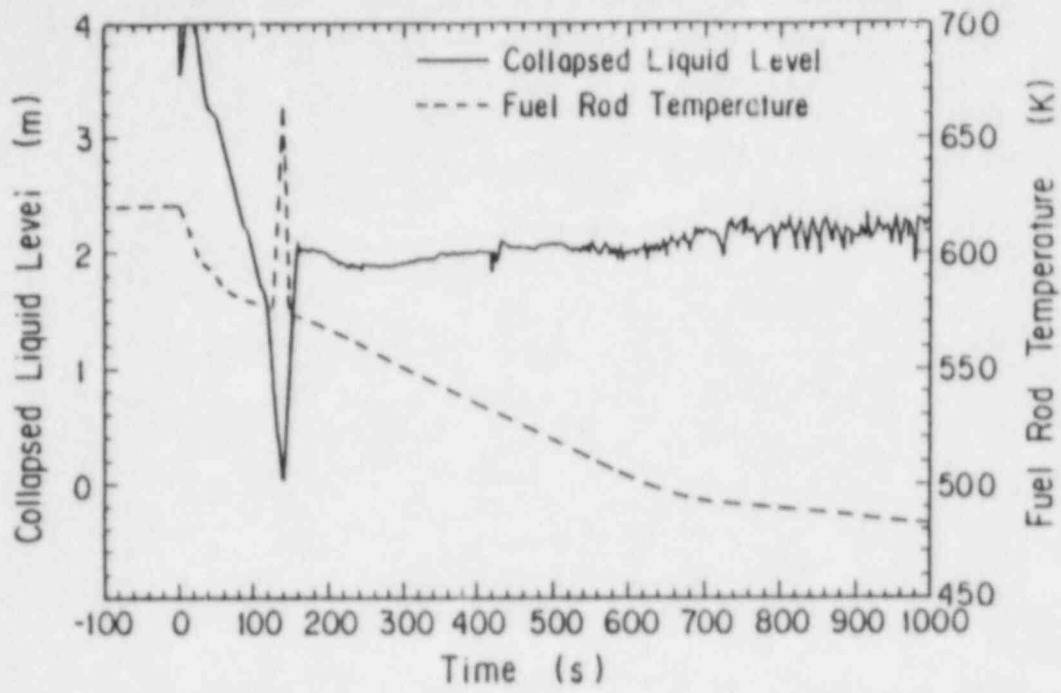


Fig.10 Early Core Dryout and Heatup in 5 % Break Test

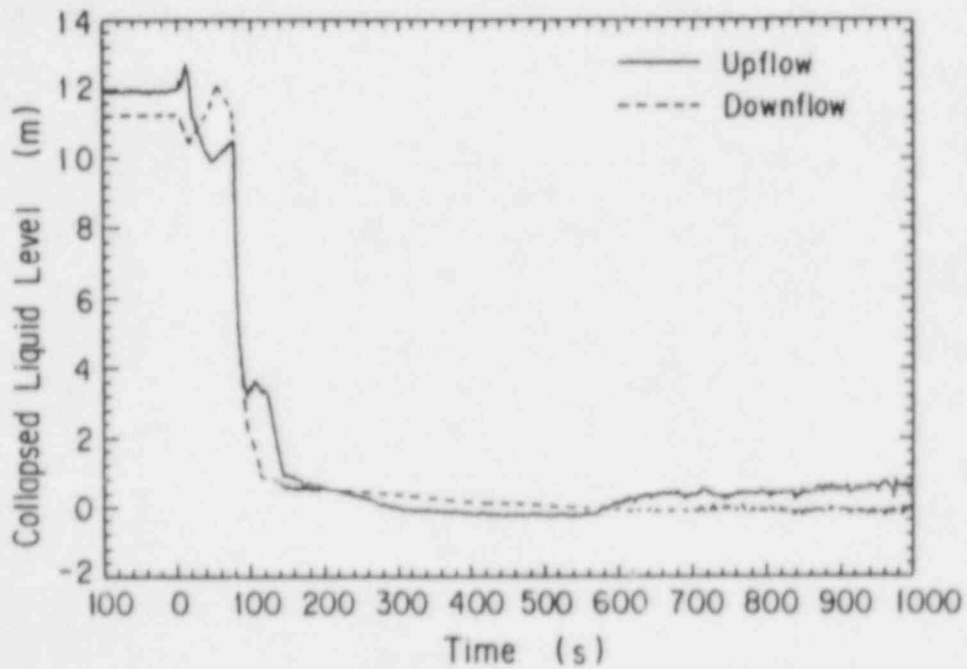


Fig.11 Liquid Holdup in Upflow Leg of Steam Generator U-tube (Intact Loop)

lead to significant depletion of primary coolant inventory especially in the core. Without replenishment, the coolant in the core was boiled off and about a half of the core was uncovered and fuel rods experienced rapid heatup well before the accumulator water was injected into the primary loop.

On the other hand, early but short core liquid level depression and core heatup were observed in 5 % test, despite HPIS actuation. Examination of the coolant distribution in the primary loop indicates prolonged liquid holdup in the upflow leg of the SG U-tubes when the core liquid level depression and initiation of core uncover (133 s) take place as shown in Fig.11. This liquid holdup was observed in all six U-tubes (perloop) instrumented with a differential pressure transducer.

As illustrated in Fig.12, the liquid holdup in the upflow leg of the SG U-tubes presents extra static head which must be counterbalanced by depression in the core liquid level below the bottom of the loop seal. This manometric effect has been observed previously in the Semiscale tests such as S-UT-8[5] and is known to be dependent on the core bypass flow between the core upper head and downcomer. The effect of bypass flow area will be investigated in detail in future LSTF experiments.

## 5. Concluding Remarks

Three cold leg small break LOCA simulation tests have been successfully conducted at the Large Scale Test Facility of the ROSA-IV program. The break areas correspond to 10 %, 5 % and 2.5 % of the scaled (1/48) flow area of the reference PWR's cold leg.

The test results show that the ECCS is effective in preventing the major uncover of the core but the manometric effect due to liquid holdup in the SG U-tubes can cause core liquid level depression early in the transient, and even lead to temporary and partial core dryout in the 5 % break test.



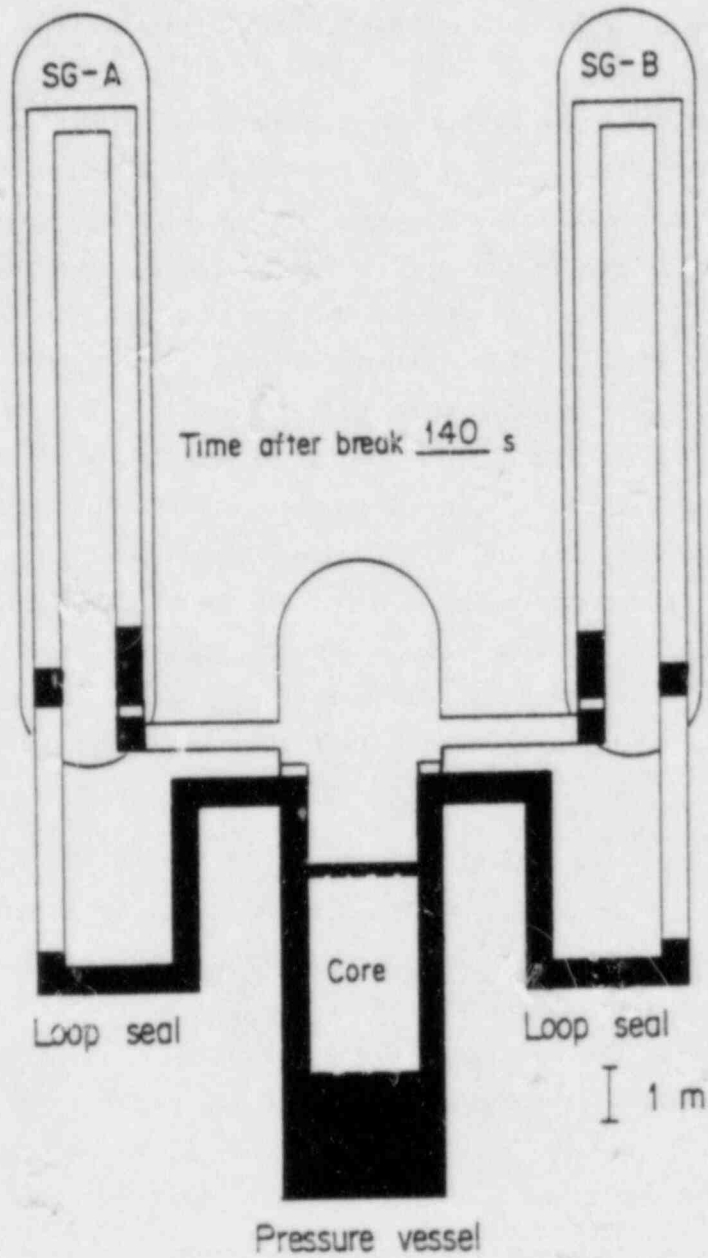


Fig.12 Primary Coolant Distribution during Early Core Uncover in 5 % Break Test

## REFERENCES

1. Koizumi Y. and Tasaka K., "ROSA-IV : Large Scale Test Facility for PWR SBLOCA Integral Simulation Test,"  
Proc. of the Specialists Meeting on Small Break LOCA  
Analysis in LWRs, Pisa, Italy, June 23-27, 1985, Vol.1.
2. Tanaka M. et al., "A 10 % Cold Leg Break Test at ROSA-IV Large Scale Test Facility,"  
Proc. of the Specialists Meeting on Small Break LOCA  
Analysis in LWRs, Pisa, Italy, June 23-27, 1985, Vol.1.
3. Tasaka K. et al., "The ROSA-IV Program TMI-2 Type Scenario Experiments : A Multifaceted Investigation,"  
Proc. of the Specialists Meeting on Small Break LOCA  
Analysis in LWRs, Pisa, Italy, June 23-27, 1985, Vol.1.
4. Kukita, Y. et al., "Simulation of PWR Turbine Trip Transient in ROSA-IV Large Scale Test Facility,"  
Journal of Nuclear Science and Technology, Vol.22, No.8, pp.678 680, August 1985.
5. Leonard, M.T., "Vessel Coolant Mass Depletion during a Small Break LOCA," EGG-SEMI-6010, Sept. 1982.
6. Zuber N., "Problems in Modeling of Small Break LOCA," NUREG-0724, October, 1980.
7. ROSA-IV Group, "ROSA-IV Large Scale Test Facility (LSTF) System Description," JAERI-M 84-237, 1985.
8. Kukita Y. et al., "ROSA-IV Program Large Scale Test Facility (LSTF) Pretest Analysis : Simulation Capability in SBLOCA Tests," Proceedings of 1985 Annual Meeting of Atomic Energy Society of Japan, D36, Tokyo, 1985.

## PKL REFLOOD TESTS INCLUDING END-OF-BLOWDOWN

R. M. Mandl, B. Brand, H. Watzinger

Kraftwerk Union AG, Erlangen

### ABSTRACT

In order to simulate the latter stage of large break LOCA (Loss of Coolant Accident) more realistically it is necessary to relax some of the conservative assumptions applied up till now. More representative boundary conditions are achieved by preceding refill/reflood with End-of-Blowdown (EOB).

The appropriate tests were carried out in the PKL (Primärkreisläufe) test facility. The results, confirming TRAC (Transient Reactor Analysis Code) calculations show that the EOB phase has an influence on the course of a large break LOCA. Residual water as well as the accumulator-injected water effect good core cooling, lead to early rewetting and energy transport out of the core thus speeding up core reflooding. Temperature increase in the refill and reflood phases was limited to 40 K. Quench rates and time of complete core reflood depended on the amount of injected water. Good agreement was found between counterpart PKL and CCTF tests. All tests show the large safety margins of current PWR designs.

### INTRODUCTION

Licensing procedures as well as design basis criteria call for proof of core coolability during postulated loss of coolant accidents (LOCA). To this purpose complex computer codes capable of predicting the thermohydraulic core behaviour have been developed. These codes have to be verified by their correctly predicting the course of a LOCA simulated in test facilities. These facilities, called System Test Facilities must in turn, be capable of simulating, normally on a reduced scale, the behaviour of a PWR under LOCA conditions.

From technical point of view (e. g. fuel rod simulation) it is difficult and expensive to build a test facility capable of simulating the full pressure and power of a PWR and at the same time having sufficiently large dimensions to correctly model phenomena which occur in the refill and reflood phase of a large-break LOCA. The time (at the end of blowdown) of pressure equalization with containment - about 4 bar - appeared to be a natural dividing line between the predominantly homogeneous flow during blowdown and the refill/reflood characterized by a pronounced separation of the liquid and vapour phases of the coolant. The acceptance of this dividing line enabled the simulation of blowdown and refill/reflood in two kinds of test facilities. Full pressure, full-power scaled test facilities with 25 - 70 fuel rod simulators modelled successfully the blowdown conditions whereas test facilities with low pressure capabilities, decay power smaller than ten percent and scaled with 300 - 2000 fuel rods, simulated

the low pressure refill/reflood phase. Conservative assumptions were applied where uncertainties were encountered - one of them being that at the beginning of refill (4 bar) the primary side was devoid of water and filled with stagnant steam.

This and conservatively predicted clad temperatures constituted the initial conditions for all previous refill/reflood tests. No credit was taken for the presence of either blowdown residual water or for ECC water already injected in the latter phase of blowdown by accumulators ( $p < 26$  bar). To bridge the gap in modelling blowdown and refill/reflood phase the Primärkreisläufe (PKL) test facility, Fig. 1, designed for 40 bar, was adapted to simulate refill/reflood preceded by End-of-Blowdown (EOB) thereby creating more realistic boundary conditions.

This presentation describes the logical basis for and way of performing these tests. Results confirming the influence of EOB are presented.

## PKL II TEST OBJECTIVES

In order to simulate the latter stage of large break LOCA more realistically it is necessary to relax some of the conservative assumptions applied up till now. More representative boundary conditions are achieved by preceding refill/reflood with End-of-Blowdown, particularly by considering the cooling effect of accumulator water. This water, injected in the latter phase of blowdown and largely ignored in the conservative analysis, assists in early cooling of fuel rods especially in core of large-size cold leg breaks. Calculations made using the American TRAC PF 1 Code, developed for Best-Estimate analysis, showed for the case of a KWU PWR (combined injection), that taking into account the cooling effect of the accumulator water not only reduces the maximum fuel rod temperatures by several hundred degrees K but also prevents the usually expected second temperature peak during the refill and reflood phase Fig. 2.

The main objective of the PKL IIB test series was to perform refill/reflood experiments under Best-Estimate (BE) conditions and initiated by EOB. The influence of EOB on tests carried out with licensing type of conditions (Evaluation Model, EM) was also investigated. Several tests with a break in the hot leg were performed. The test matrix, Fig. 3, reflects the three classes of experiments mentioned above.

## TEST FACILITY

The PKL (Primärkreisläufe) test facility in which the EOB tests were carried out represents a typical KWU 1300 MWe four loop PWR on a scale of 1 : 145. It was designed to simulate the behaviour of the entire primary system during the refill and reflood phase of LOCA. In view of the importance of the driving gravity forces during reflood all elevations correspond to actual reactor dimensions (1:1).

The test facility is designed for a maximum pressure of 40 bar. In Fig. 1 the PKL test facility is shown as modified for EOB tests. The test bundle simulating the core consists of 314 electrically heated rods. These are

subdivided into 3 independently heated zones. 25 heater rods are instrumented with over 150 thermocouples.

The three loops (one of them of double capacity simulating two loops) contain steam generators with original-size tubes. Their secondary sides are also volume-scaled and are filled during the test with water at 55 bar and its corresponding saturation temperature in order to simulate the energy transfer to the primary side and the resulting pressure drop.

In addition to the scaled components PKL is equipped with a separator (mass flow rate downstream of break) and three conditioning-water tanks which inject water into the system during the conditioning phase (26 bar <math>p < 40 \text{ bar}</math>).

The facility is instrumented with over 600 measuring points. Apart from the conventional measurements of temperature, pressure and single-phase mass flow, two-phase flow instrumentation also exists. The test data are recorded at sampling frequencies of 25 Hz (pressure, diff. pressure, mass flow) and 5 Hz (temperature).

#### TEST PROCEDURE

The so called 'Conditioning Phase' (Fig. 4) is started at 40 bar with stagnant-steam filled system by opening the break and injecting hot water into the pipes to the left and right of the break as well as into the upper plenum for cold leg break or into downcomer for hot leg break. The objective is to achieve, on reaching 26 bar

- pressure gradient
- core mass flow rate
- fluid density distribution
- clad temperature
- containment backpressure

similar to what these would be in a PWR after experiencing a complete blow-down starting at 160 bar. The prevailing conditions at 26 bar were precalculated by system codes TRAC and DRUFAN.

#### RESULTS

The conditioning procedure consisting of injecting water into various points in the system to control the pressure gradient and to effect correct mass flow direction and distribution is practicable and was successfully carried out. The rate of change of pressure during EOB was identical to that predicted by TRAC calculations, with the absolute values differing only slightly, Fig.5. For cold leg breaks maximum velocity indicated in the downcomer was of the order of 70 m/s which compares favourably with the predicted value of 80 m/s. There is no velocity measurement available in the core but correct velocity in the downcomer allows the assumption of correct velocity in the core as the mass distribution at these high velocities will be more or less homogeneous.

Test Run IIB-7 represented a double-ended guillotine break in the cold leg with BE initial and boundary conditions, combined injection, power scaled according to DIN 25463, injection rates representing 7/8 of nominally available capacity.

The initial temperature for the conditioning phase (40 bar) was taken from TRAC GPWR calculations. The temperature envelope is shown in Fig. 6 in comparison with the temperature envelope for IIB-2. The latter was a test similar to IIB-7 but based on Evaluation Model (EM), i. e. high initial temperatures (660°C), reduced availability of ECC and higher decay power (DIN 25463 + 26). In both tests - in BE as well as in the EM type - during the EOB phase (26.0 - 4.0 bar) a sizeable number of TC's are quenched: 15 % in IIB-7 (BE) and 10 % in IIB-2 (EM). This confirms the fact that presence of water in the core ( $x < 1.0$ ), particularly at elevated pressures, produces a considerable cooling effect in the unwetted region, leading to faster quenching. The ensuing differences in temperature histories in those two tests can be attributed mainly to the larger amount of coolant injected in the test IIB-7. The maximum temperature increase was limited to 40 K in both cases. Fig. 7 shows the BE test PKL IIB-7 compared to its counterpart CCTF Run 80 and the EM test PKL IIB-2 is compared to its counterpart CCTF Run 79 in Fig. 8. In spite of slight differences in the initial values (more adverse conditions in the CCTF tests) the similarities are striking.

In the case of combined injection the temperature increase and the quench rate are mainly influenced by the penetration of subcooled water from the upper plenum into the core. Although strong heterogeneous penetration of subcooled water through the upper tie plate is observed in PKL, the process is somehow self-limiting: when a large amount of water penetrates into the core the steam which it forms has only limited cross-sectional area for "escape" into the upper plenum and it eventually stops more water from penetrating. In the case of CCTF, due to its more pronounced 3-D characteristics, it is feasible that in the same situation once water starts penetrating the upper tie plate, the flow of water into the core is sustained for longer periods of time than in PKL, thus providing better cooling. The PKL IIB test matrix also included one test (IIB-5) with cold leg injection only but otherwise with the same conditioning procedures and EM conditions as used in tests with combined ECCs. The injection rates were what we believed to be typical of reactor type with cold leg injection only. Fig. 9 shows the temperature envelope for the above test. Here, too, 4 % of heater rod TCs are quenched in the EOB phase. Although the quench rates are somewhat slower than those in the combined injection tests the large amount of water injected during refill phase helps to limit the temperature increase to 40 K.

We conclude that for both combined and cold leg injection only (BE as well as EM) quenching of some heater rods does take place during the blowdown phase i. e. prior to initiation of refill and reflood.

Of the three hot leg break tests the IIB-3 is most worth mentioning. In this test only 2 out of 8 nominally functioning accumulators and 3 of 8 pumps were in operation (all on the hot side). EM-simulated decay power (DIN 25463 + 26) and maximum initial heater rod temperature of 600°C (TRAC BE-prediction is 380°C) constituted extreme conditions.

Despite these adverse conditions the results are of the same order of magnitude as the cold leg break, EM type tests:

Temperature increase of not more than 50 K and maximum quench rates of the order of 350 seconds, Fig. 10 This clearly demonstrates the safety margins in current PWR ECC designs.

Of special interest in the PKL IIB was the behaviour of subcooled water on the upper tie plate. This region was instrumented with three mini-turbines located 10 mm above the upper tie plate flow holes and with a number of TCs

placed just below the flow holes in core subchannels.

The exact locations are shown in Fig. 11. It is evident that the turbine and TC signals can be correlated, Fig. 12.

Regions below the upper tie plate in which TCs indicate subcooling, region 1 and 4 in Fig. 13, also coincide axially with those rods which exhibit the fastest quench rate. On the other hand regions 2 and 3 where only little or no subcooled water penetrates coincide axially with regions of slower quench rate. It is surprising to observe so pronounced heterogeneous behaviour within such a relatively small area.

Another interesting phenomenon, namely periodic oscillation in hot legs, upper plenum, core and downcomer could be best observed in test IIB-3. Due to the absence of cold leg injection there are only two active elements which force the oscillations: namely steam generation in the core and condensation in upper plenum. The third, steam generation in the riser section of steam generators, is only weakly represented as water inventory is not sufficient to significantly fill the steam generators.

The oscillations - of about 12 s period - are shown in Fig. 14.

Quenching of heater rods produces a pressure increase in the core - the water in the core below the quench front and lower plenum is pushed into the downcomer, the water accumulated in the upper plenum is pushed up into the hot legs. At this point in time there is no water at the quench front and thus no steam generation in core to sustain the pressure. The water from the hot legs and that from the injection points (hutzen) flows back into the now steam filled upper plenum bringing about condensation and a pressure drop of 0.3 - 0.5 bar, see uppermost curve, Fig. 14. Consequently water is "sucked" into the core from the downcomer (some water probably enters the core through the upper tie plate), overtakes the quench front and leads to fresh steam generation and a repetition of the described cycle.

The collapsed liquid level measurements (or rather the interpretation of a  $\Delta p$ -measurement as collapsed liquid level) in the upper plenum and hot legs are always out of phase by  $\pi$  radians thus satisfying the law of conservation of mass. However, there are several "spikes" in the downcomer and core readings (e. g. at  $t \approx 98$  s) indicating an increase of mass inventory in both at a time when there is an increase of water level in the upper plenum. However, the emptying of the hot legs cannot alone account for such a sudden filling of the upper plenum, core and downcomer at the same time. In our opinion these simultaneous spikes come about through flashing in the lower plenum as a result of the sudden decrease in system pressure. The flashing two phase flow mixture is momentarily pushed into both core and downcomer thus increasing the  $\Delta p$  readings partly by its weight and partly by pressure loss. As the pressure stabilizes (sustained by flashing) the thrown-up water falls back into the lower plenum and in both core and downcomer the spikes disappear.

In tests with combined injection the same mechanism is at work - only here there are two more active elements forcing the oscillations, namely condensation at the cold leg injection points and steam generation in the riser of the steam generators. The frequency of oscillations becomes higher and more random, the condensation in upper plenum causes pressure spikes of up to 1 bar, Fig. 15. The more water penetrates into the steam generators the more steam is generated which partly flows towards the cold leg and partly pushes water back through the hot legs into the upper plenum and eventually into the

core giving rise to the now well known hot leg oscillations. The strongly oscillating water levels in the core, upper plenum and hot legs, although difficult to describe by analytical methods, tend to enhance the reflooding process in the core. The phenomenon of steam binding was not observed in any of the PKL IIB tests.

#### CONCLUSIONS

Nine refill/reflood tests preceded by End-of-Blowdown were performed in the PKL IIB test series. Conditioning procedures designed to create the correct dynamic conditions in the primary system on reaching 26 bar proved practicable and were successfully carried out.

A considerable number of heater rod TCs quenched during the EOB phase in both BE and EM tests - the energy removed from the core during EOB was not negligible.

Temperature increase in the refill and reflood phases was limited to 40 K, quench rates and time of complete core reflood depended on the amount of injected water.

Temperature envelopes are very similar for PKL and CCTF counterpart tests showing no significant scaling differences.

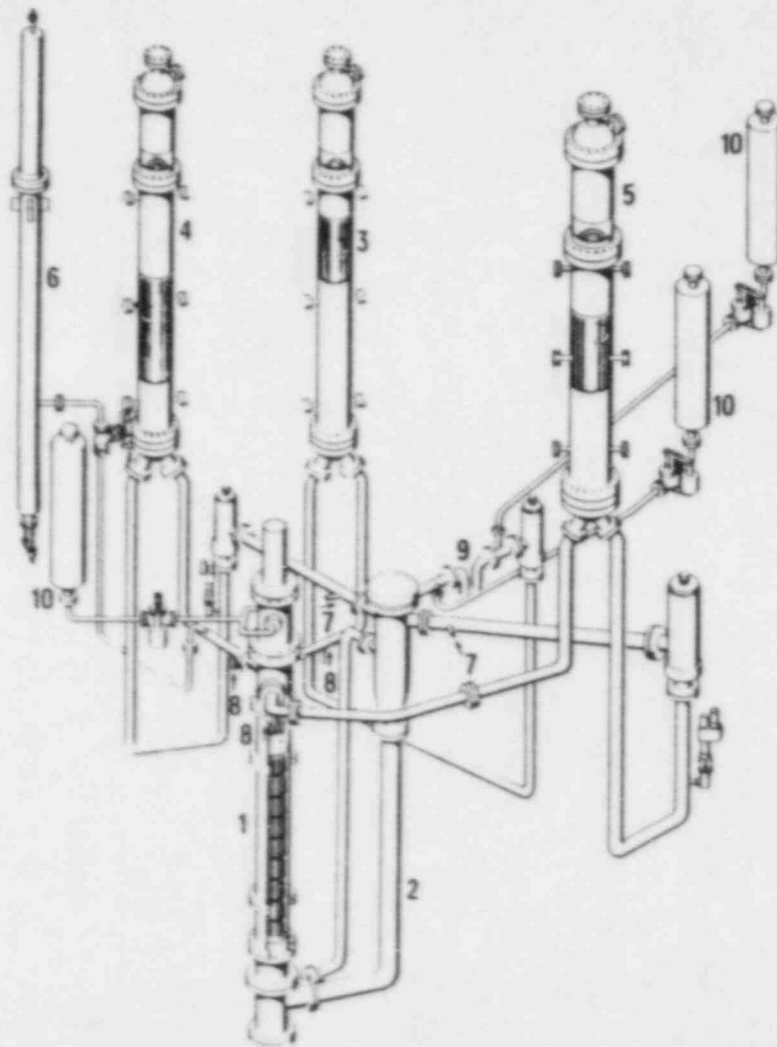
A dependence exists between regions of water penetrating through the upper tie plate and quench rates of heater rods directly below.

The mechanism of oscillations in the hot legs, upper plenum, core and downcomer was experimentally confirmed.

A hot-leg-break test with a minimum of hot leg injection and no cold leg injection shows only a small increase in heater rod temperatures and relatively short quench times.

All tests, particularly the hot-leg-break test described above show the large safety margins of current PWR designs.





**Reactor: 1300 MWe Standard**

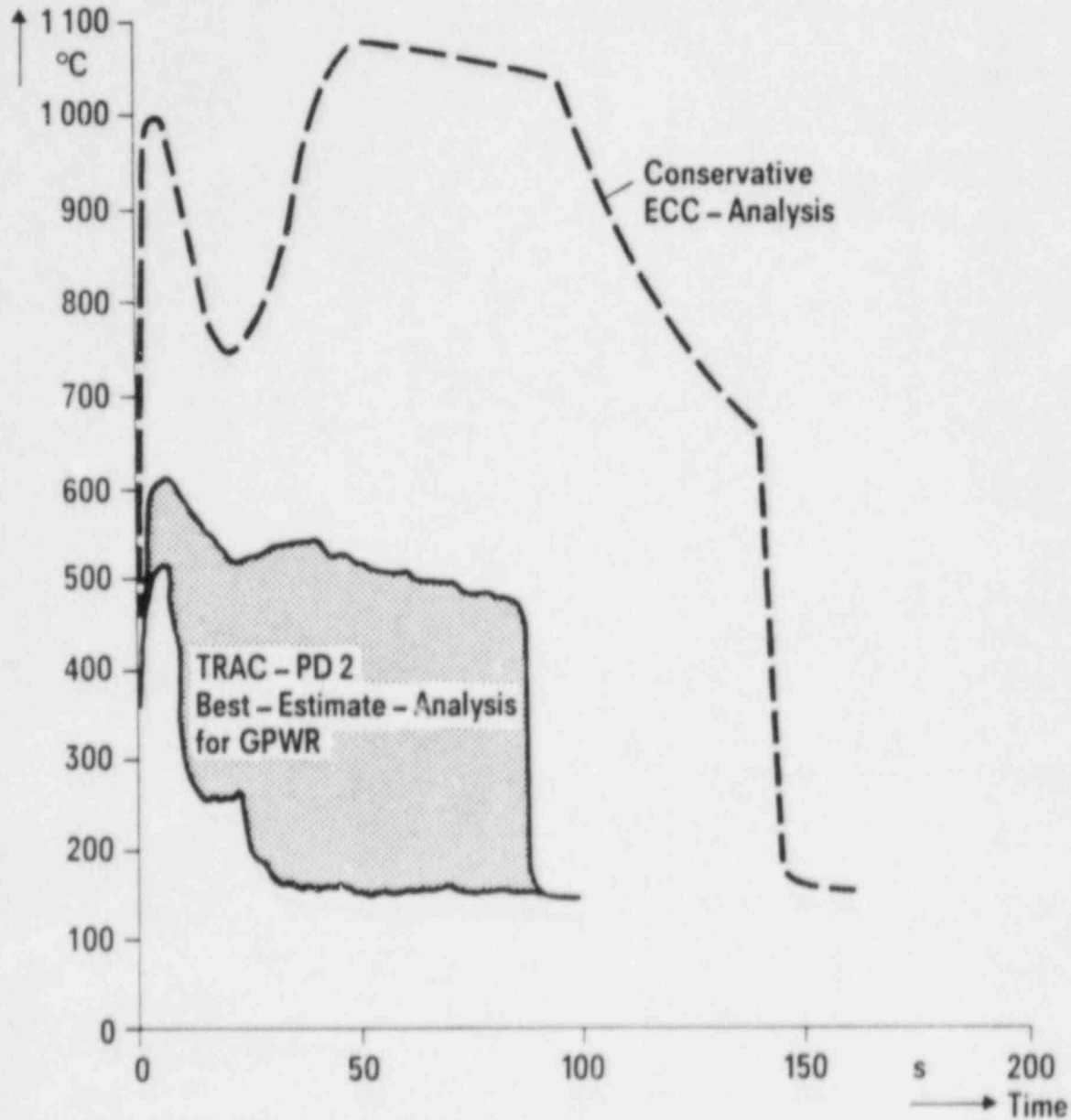
Elevation scaling: 1:1

Volume and power scaling: 1:145

- 1 Pressure vessel
- 2 Downcomer
- 3 Steam generator 1 (broken loop)
- 4 Steam generator 2 (intact loop)
- 5 Steam generator 3 (double loop)
- 6 Pressurizer
- 7 Cold leg ECC injection
- 8 Hot leg ECC injection
- 9 Cold leg break
- 10 Conditioning-water storage tank

*Fig. 1* PKL II Test Facility

Peak Cladding Temperature



1300 MW - PWR, 200% Cold Leg Break

Peak Cladding Temperatures with  
Conservative and Best - Estimate Analysis

Fig. 2

E811412 e

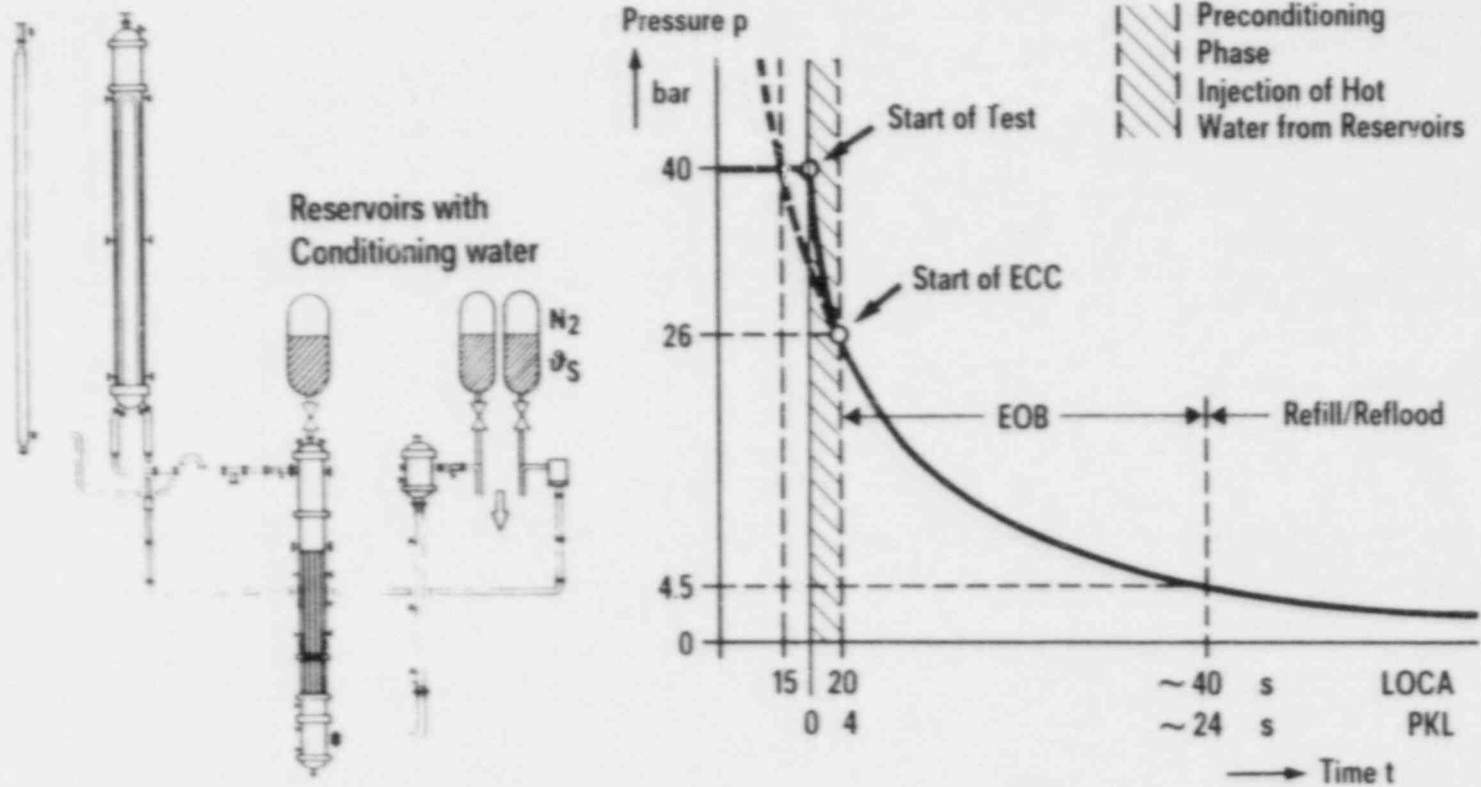
Test No	Break		Coolant Injection* A = Accumulators P = Pumps		Max. Initial Temperature °C	Comments
	Location	Site	Cold leg	Hot leg		
1	Cold leg	200%	3/8 A 3/8 P	4/8 A 4/8 P	500	BE EOB - Baseline Test
7	Cold leg	200%	3/8 A 3/8 P	4/8 A 4/8 P	500	BE Alternative Conditioning
6	Cold leg	100%	3/8 A 3/8 P	4/8 A 4/8 P	625	BE Pre-calculated init. temp. of 380, increased to 625 °C
2	Cold leg	200%	2/8 A 3/8 P	3/8 A 3/8 P	660	EM
8	Cold leg	200%	- 3/8 P	3/8 A 3/8 P	650	EM No cold leg accumulator
5	Cold leg	200%	3/4 A 3/4 P	- -	650	EM Cold leg inject. only
4	Hot leg	200%	- 3/8 P	3/8 A 3/8 P	380	TRAC calculations oriented
4.1	Hot leg	200%	- 3/8 P	2/8 A 3/8 P	600	Reduced ECC availability
3	Hot leg	200%	-	2/8 A 3/8 P	600	Hot leg injection only

\* 1/8 = nominal injection into one leg (of 8)

BE = Best estimate conditions  
EM = Evaluation model

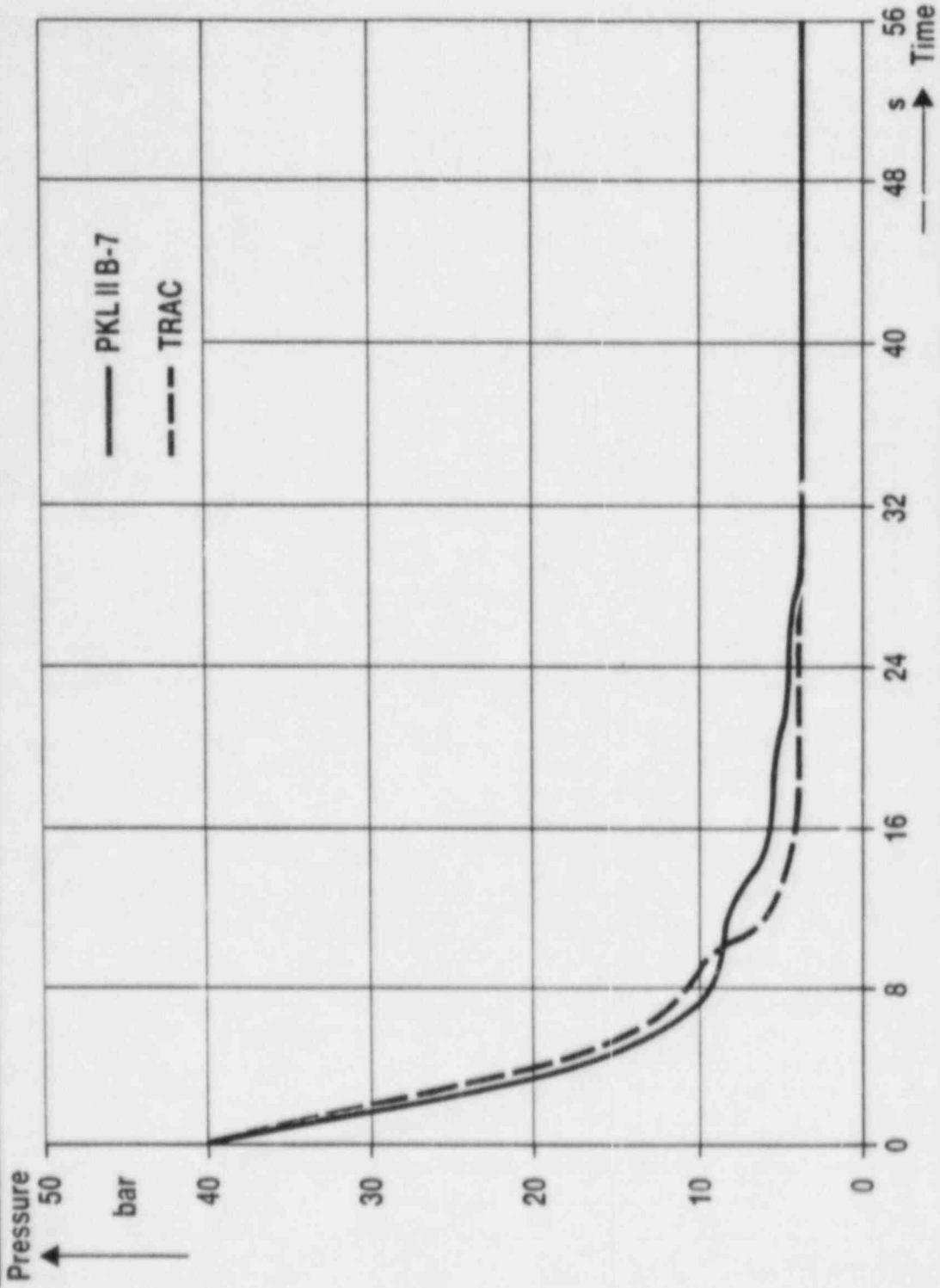
Test Matrix: PKL II B

Fig. 3



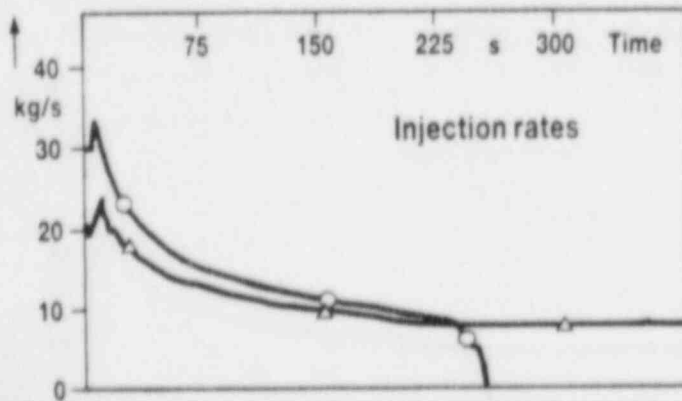
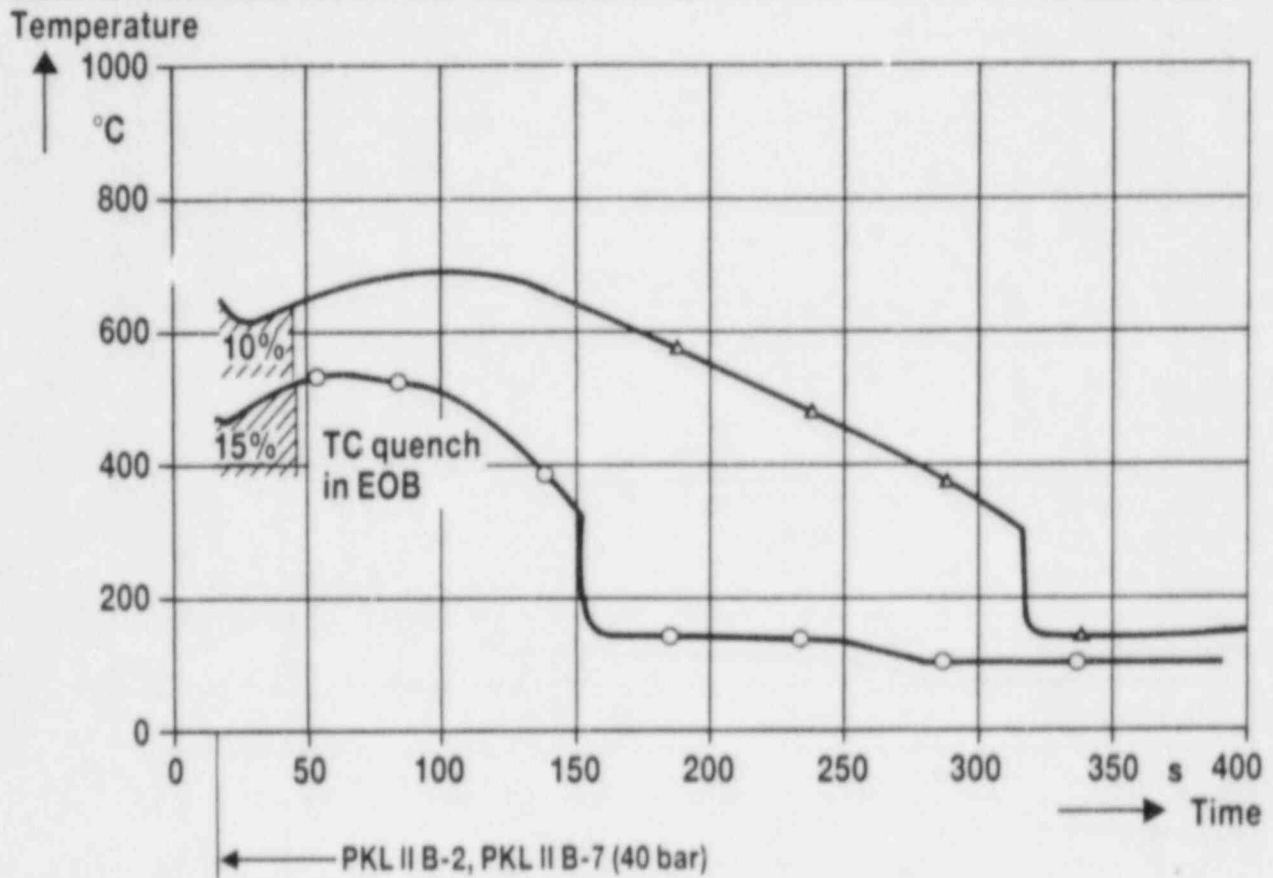
PKL II - Test Procedure for End of Blowdown Tests

Fig. 4



EBS 1432 e

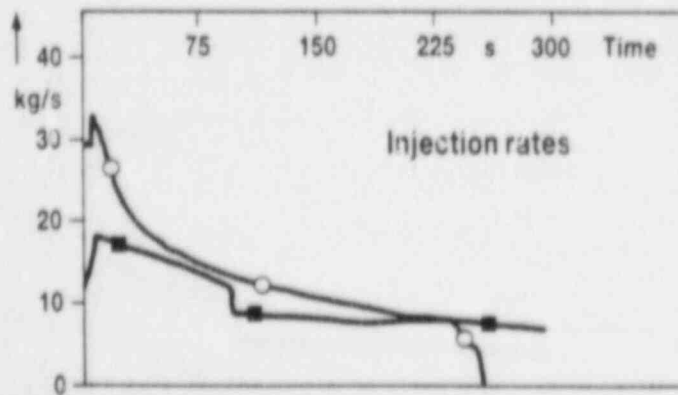
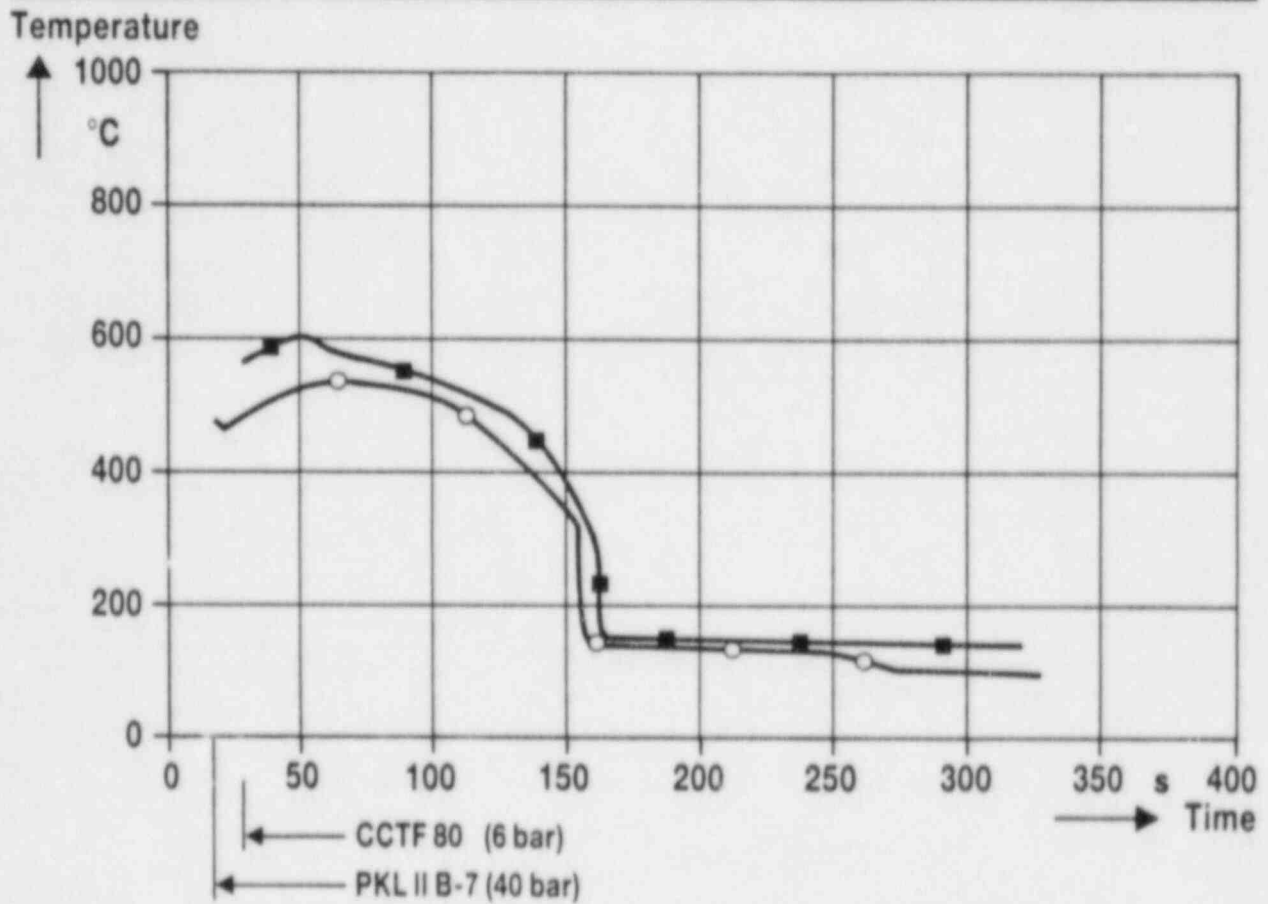
Fig 5 Pressure in Core vs. Time  
PKL IIB-7



	Test no.	Injection, Power	Max. initial temperat.
△	PKL IIB-2	EM	660°C
○	PKL IIB-7	BE	500°C

Temperature Envelope vs. Time  
PKL II B-2, B-7; Combined Injection

Fig. 6

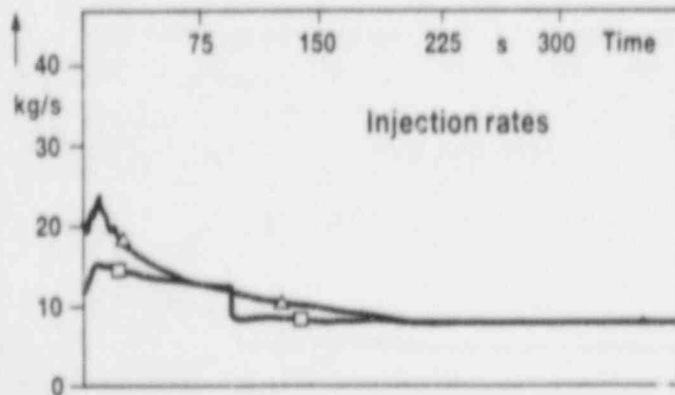
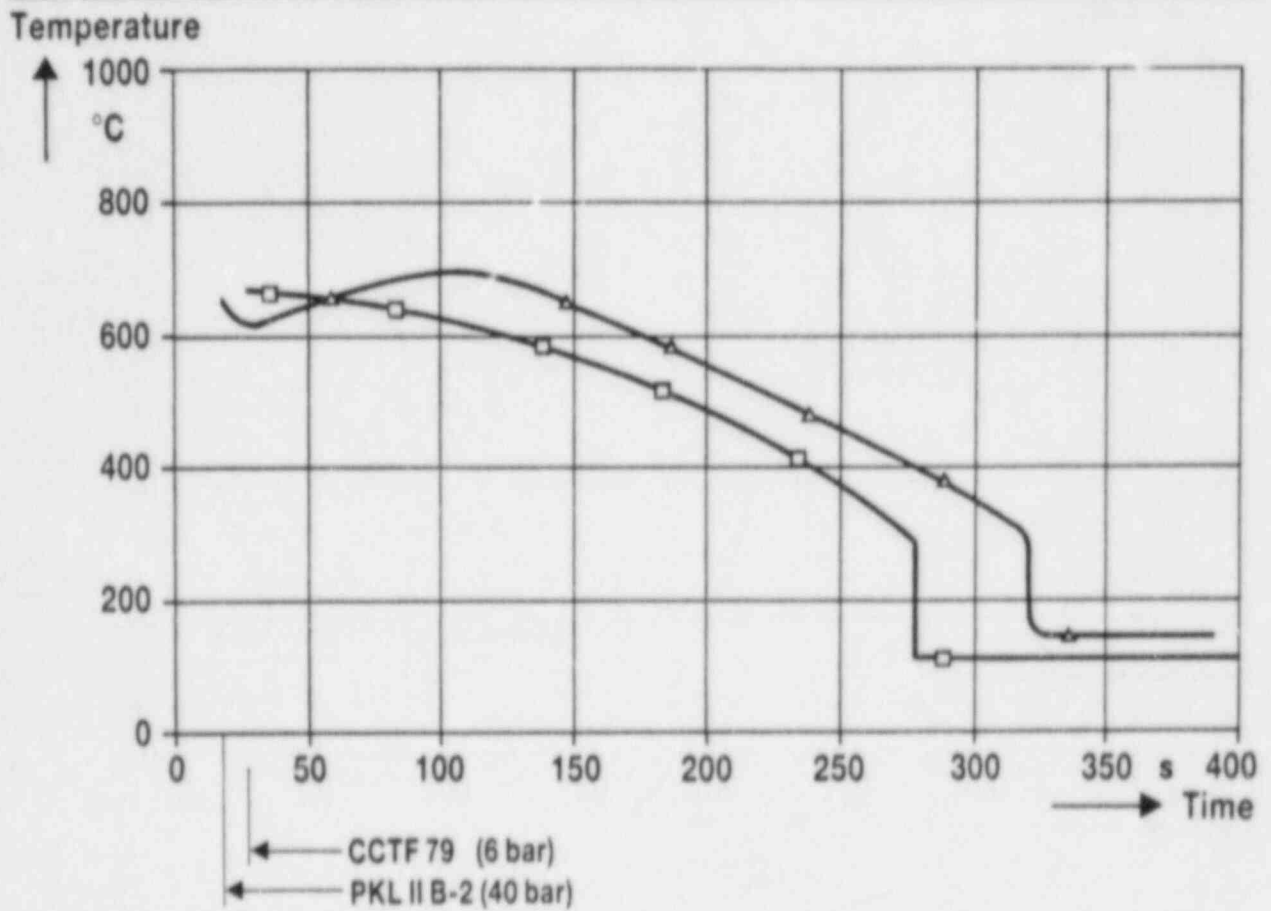


	Testno.	Injection, Power	Max. initial temperat.
○	PKL II B-7	BE	500°C
■	CCTF 80	BE	560°C

Temperature Envelope vs. Time  
Comparison PKL II B-7 vs. CCTF RUN 80; Combined Injection

Fig. 7

E 85 1436 e

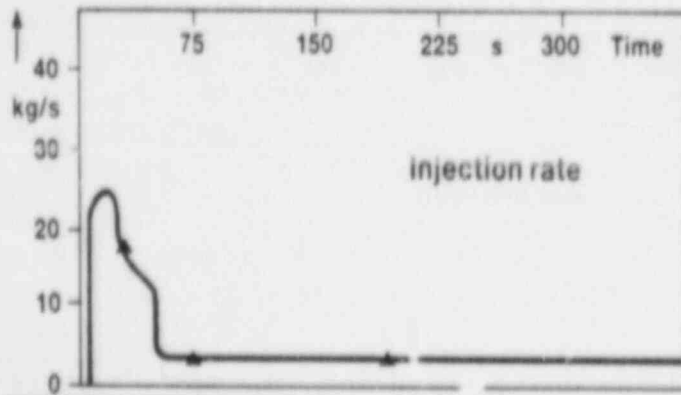
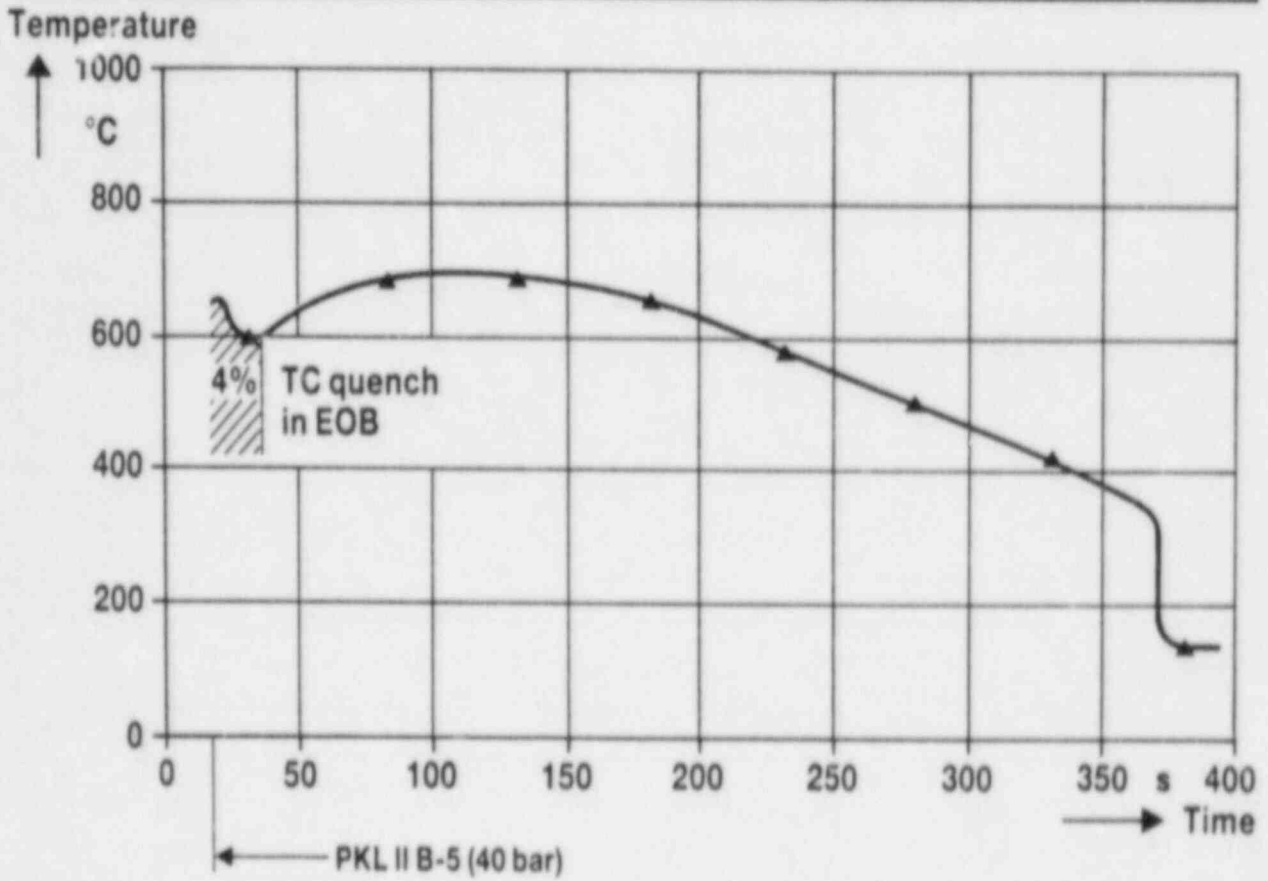


	Test no.	Injection, Power	Max. initial temperat.
△	PKL II B-2	EM	660°C
□	CCTF 79	EM	680°C

Temperature Envelope vs. Time  
Comparison PKL II B-2 vs. CCTF 79; Combined Injection

Fig. 8



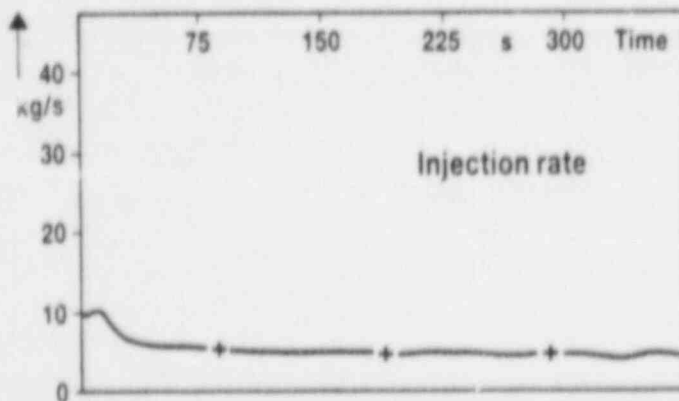
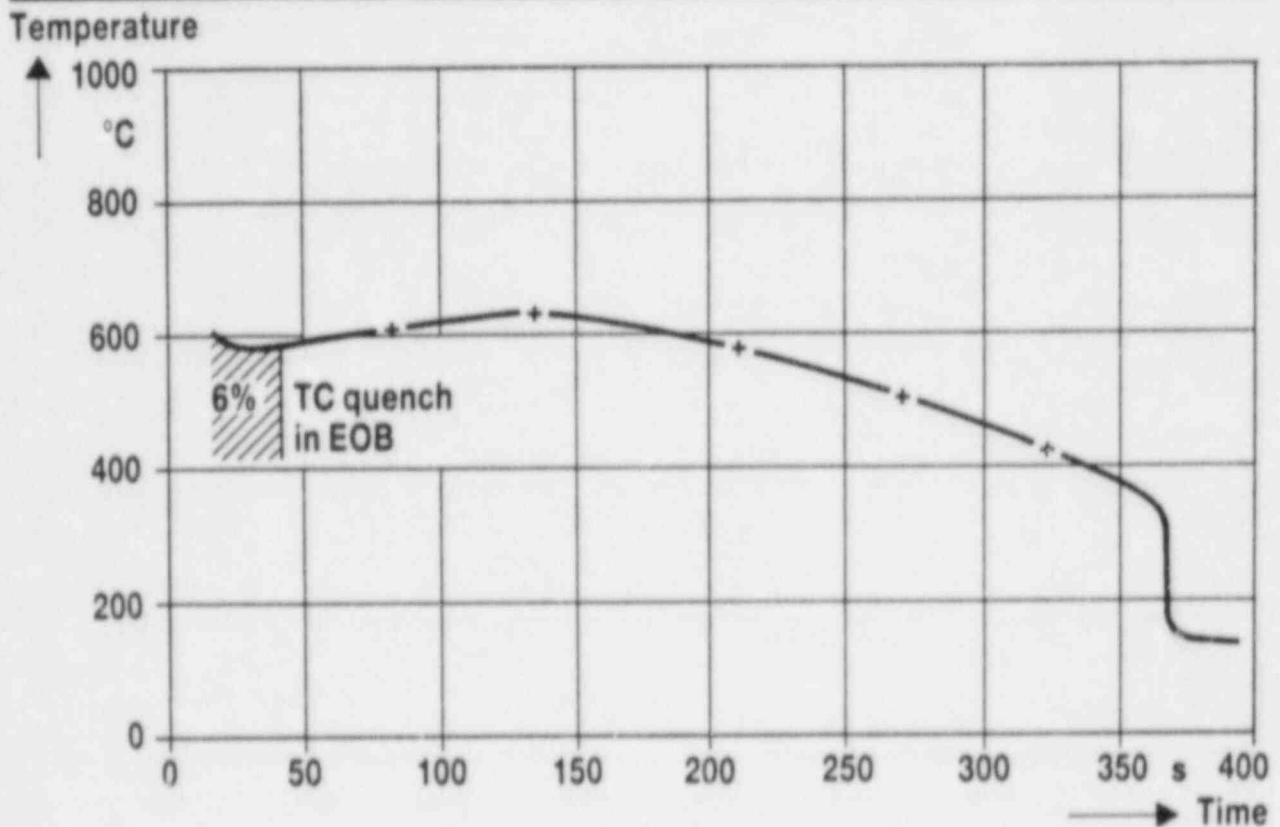


	Test no.	Injection, Power	Max. initial temperat.
▲	PKL II B-5	EM	660 °C

Temperature Envelope vs. Time  
PKL II B-5; Cold Leg Injection Only

Fig. 9

E 85 1433 e

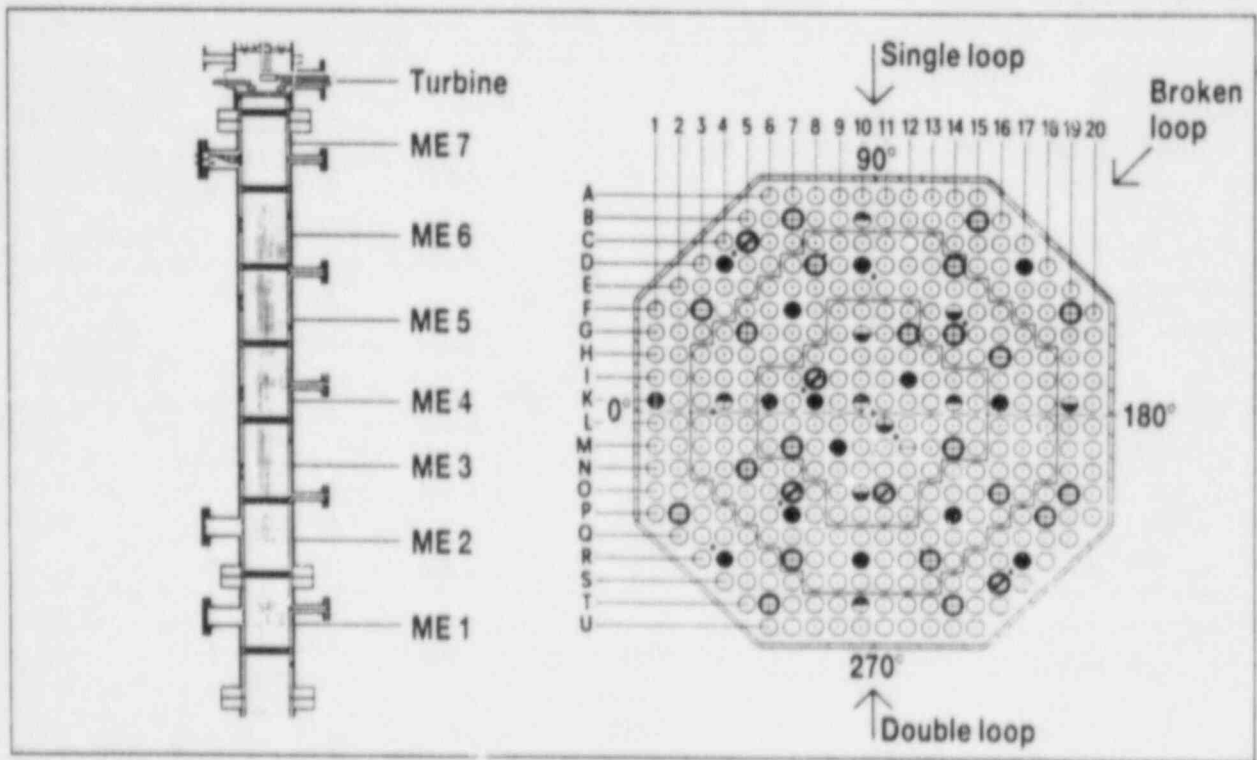
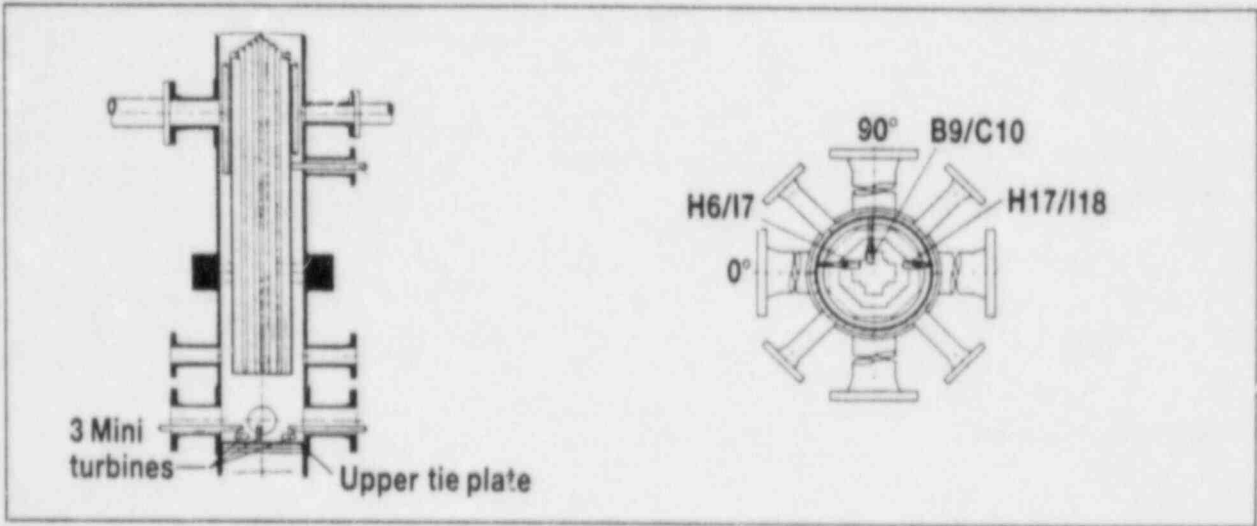


	Test no.	Injection, Power	Max. initial temperat.
+	PKL II B-3	2/8 Acc. 3/8 Pumps DIN 25463 +2σ	600 °C

Temperature Envelope vs. Time  
PKL II B-3; Hot Leg Injection Only

Fig. 10

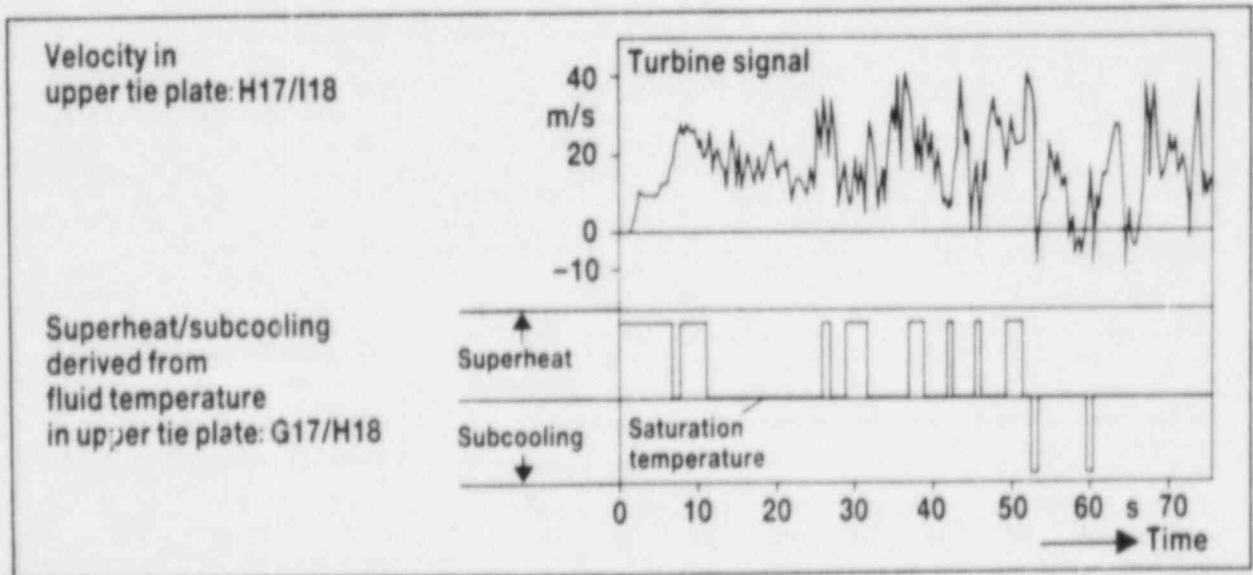
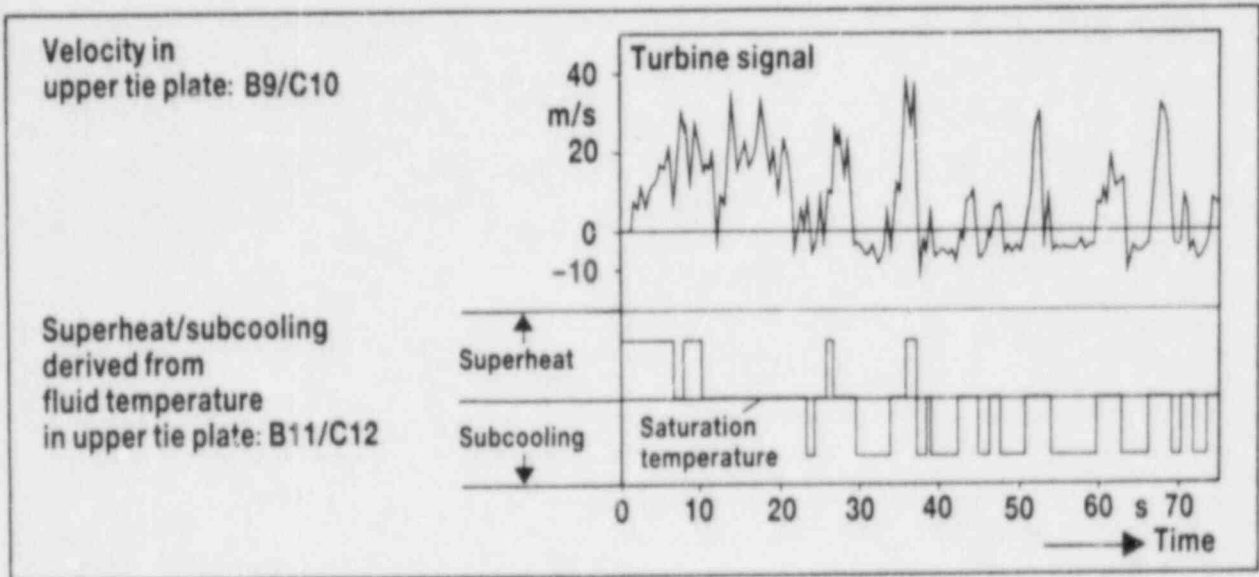
E 85 1435 e



**Turbine Measurement above Upper Tie Plate and Temperature Measurement in Core**

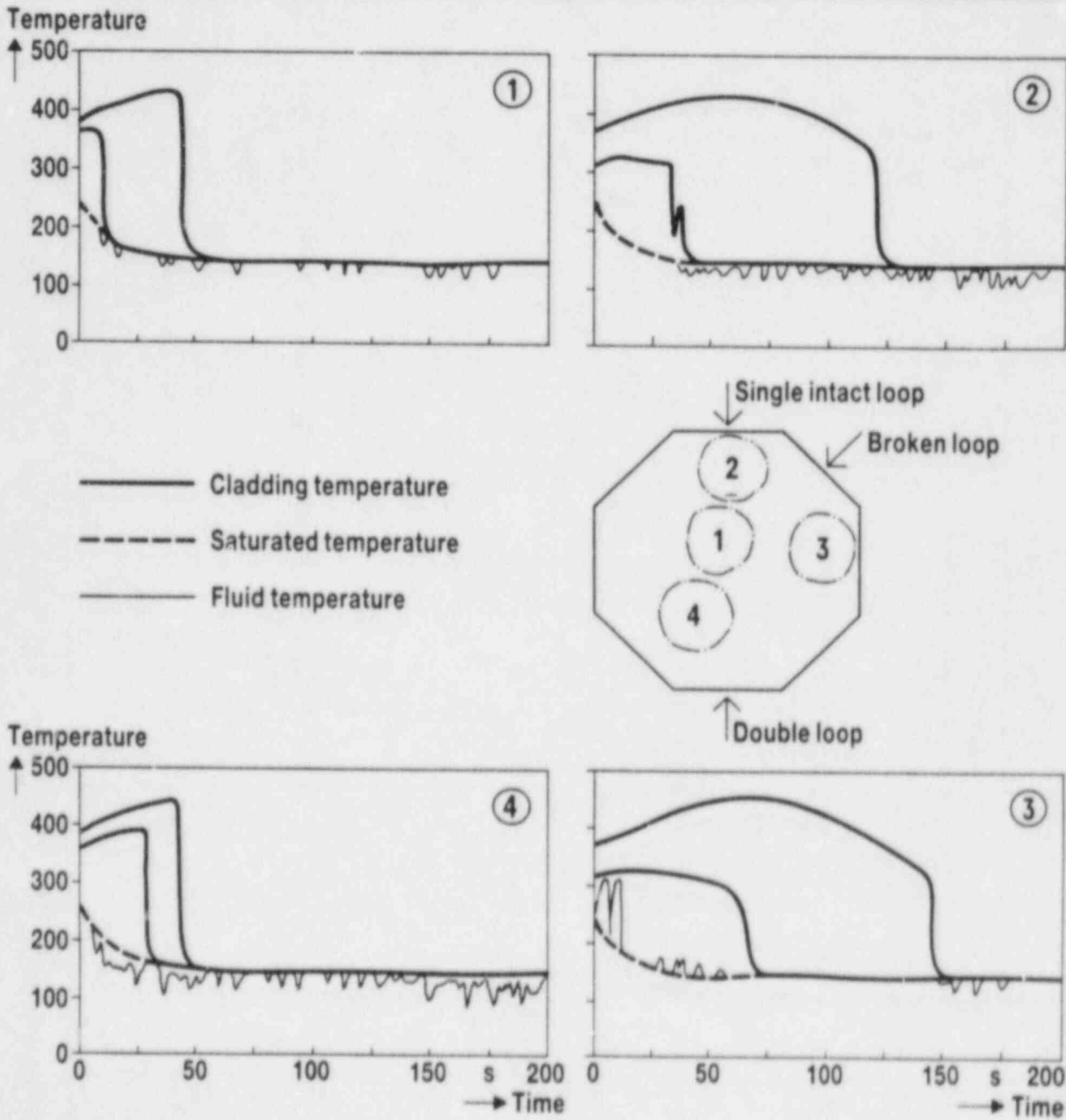
*Fig. 11*

E 85 1426 e



PKL II B-4: Correlation of Turbine Signal with Fluid Temperature in Upper Tie Plate

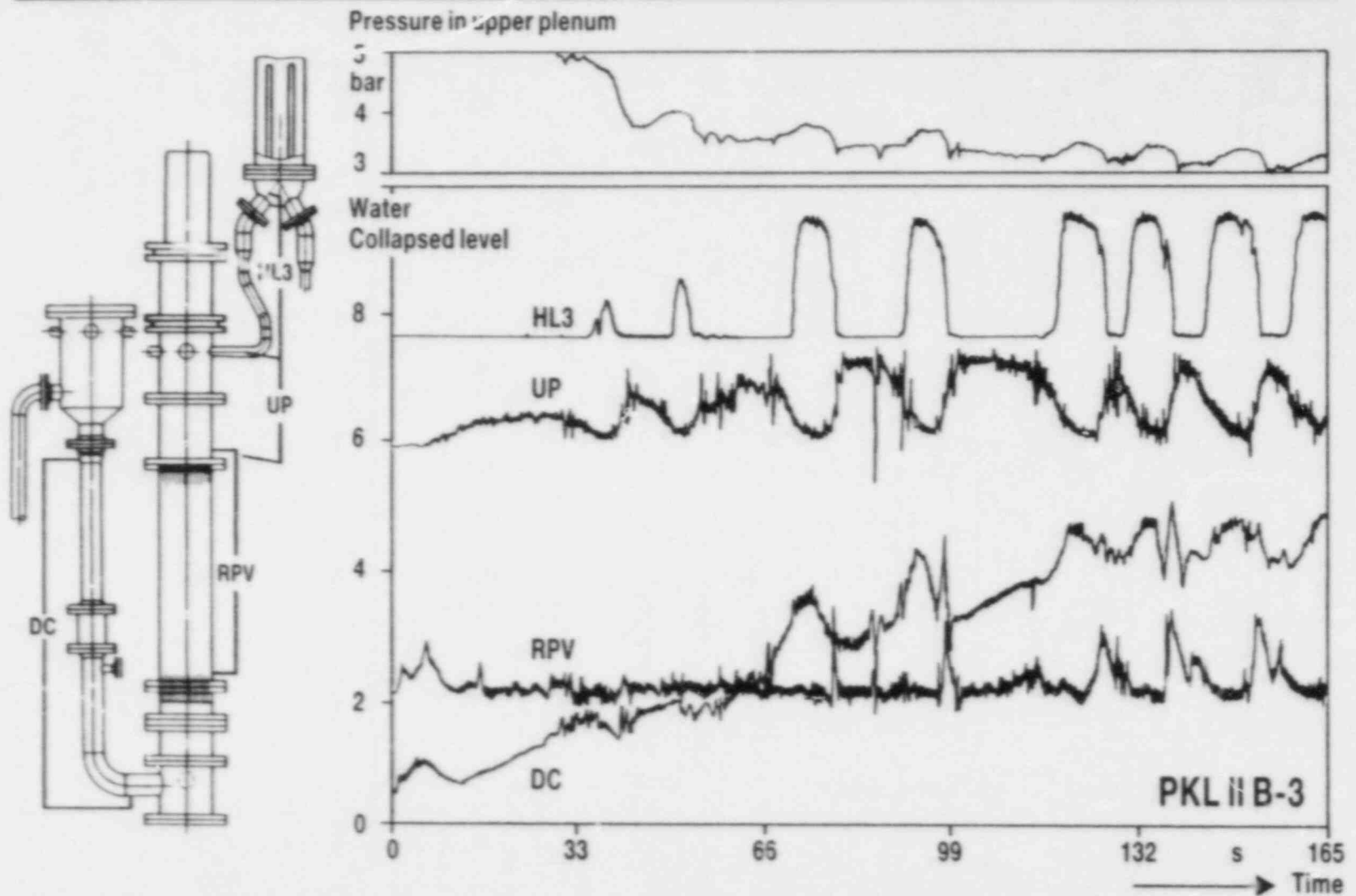
Fig. 12



PKL II B-4: Heterogeneous Distribution of Subcooled Water in Core; Quench Rates

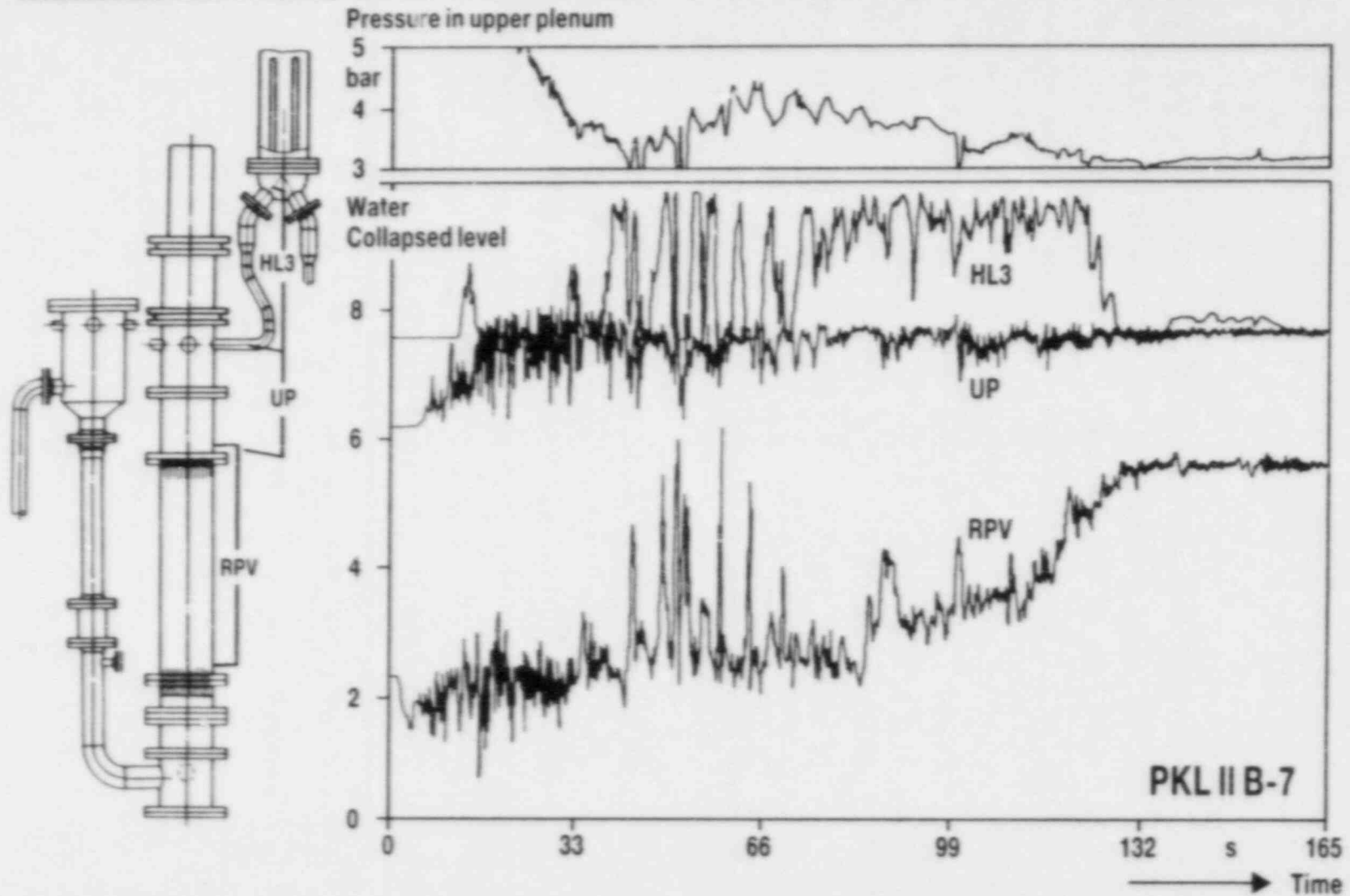
Fig. 13

E851427 e



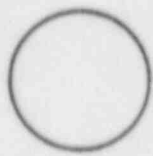
Water Collapsed Level in RPV, Upper Plenum (UP), Downcomer (DC) and Hot Leg 3 (HL3); Absolute Pressure in Upper Plenum

Fig. 14

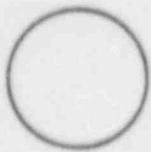


Water Collapsed Level in RPV, Upper Plenum (UP) and Hot Leg 3 (HL3), Absolute Pressure in Upper Plenum

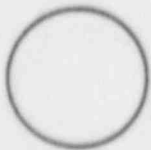
Fig. 15



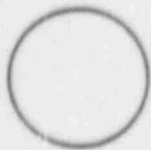
Realistic initial and boundary conditions during refill/reflood are achieved by preceding these tests with End-of-Blowdown.



A number of heater rod thermocouples quench during EOB phase in both BE and EM tests – presence of water in the core ( $x < 1.0$ ) particularly at elevated pressures produces a considerable cooling effect in the unwetted region leading to faster quenching.



Temperature increase during refill/reflood was limited to 40 K; quench rate and time of complete core reflood depend on the amount of injected water.



Temperature envelopes are very similar for PKL and CCTF counterpart test showing no significant scaling differences.

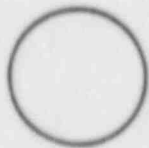
---

## Conclusions

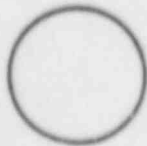
Fig. 16

E 85 1438 e

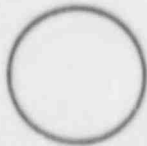




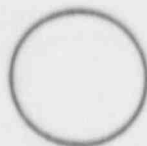
A dependence exists between regions of water penetrating through the upper tie plate and quench rates of heater rods directly below.



The mechanism of oscillations in the hot legs, upper plenum, core and downcomer is experimentally confirmed.



A hot-leg-break test with a minimum of hot leg injection and no cold leg injection shows only a small increase in heater rod temperatures.



All tests, particularly the hot-leg-break test described above, show the large safety margins of current PWR designs.

---

## Conclusions (cont.)

*Fig. 17*

INTEGRAL SYSTEMS TEST (IST) PROGRAM  
FACILITY SCALING AND INTEGRATION

T. K. Larson  
Idaho National Engineering Laboratory  
EG&G Idaho, Inc.

ABSTRACT

The Integral Systems Test (IST) Program was initiated in 1982 by government and industry to help provide information needed to help resolve issues raised by the accident at the Three Mile Island nuclear power station. Three different integral test facilities, each of which is scaled to a Babcock & Wilcox (B&W) design nuclear steam supply system, will ultimately be contributing data to meet the objectives of the program. Each of the facilities was designed using different scaling methodology and has different operating capabilities such as maximum operating pressure and core power. The overall scaling of each facility is examined in this report and local scaling analyses are conducted to demonstrate potential similarities and dissimilarities in facility response relative to expected plant responses. It is shown how local thermal-hydraulic phenomena in each facility can be compared to each other or to expected plant behavior through the scaling relationships. Finally, it is shown how the global response of each facility can be related for a specific small break loss of coolant transient through the concept of an equilibrium plot. Potential complications that may arise as a consequence of the facility scaling or facility limitations are enumerated. This work was performed under the joint auspices of the Electric Power Research Institute and the U.S. Nuclear Regulatory Commission.

## NOMENCLATURE

A	area ratio
$A_b$	break area
a	flow area
$a_s$	solid surface area
$C_p$	specific heat
f	fraction of vapor generated that passes through vent valves
$G^*$	critical mass flux
h	thermal center difference
$\Delta h$	enthalpy difference
$h_{fg}$	latent heat of vaporization
J	superficial velocity
K	loss coefficient
L	length ratio
l	length
M	mass
m	mass flow rate
N	number of rods or tubes
$N_{pCH}$	phase change number $[Q \Delta\rho / (\rho_f a u \rho_g h_{fg})]$
$N_{SUB}$	subcooling number $[\Delta h_{SUB} \Delta\rho / (h_{fg} \rho_g)]$
P	pressure
Q	power
$Q'''$	volumetric heat generation rate
$R'$	hydraulic resistance
$\Delta T$	temperature difference
t	time

u velocity  
V volume

Greek

$\alpha$  void fraction  
 $\beta$  thermal expansion coefficient  
 $\delta$  scale factor  
 $\Delta$  difference  
 $\rho$  density  
 $1\phi$  single phase  
 $2\phi$  two phase  
 $\Psi_1$  property group 1

Subscripts

f (or l) liquid  
g vapor  
HPI high pressure injection  
1 component 1  
o reference section  
R ratio of model to reference system  
s solid  
sub subcooling  
SRI SRI-2 facility  
UMCP University of Maryland facility

## INTRODUCTION

The Integral Systems Test (IST) program is a jointly funded research program initiated by government and industry to help provide information needed to address issues raised by the accident at the Three Mile Island (TMI) nuclear power station. Joint funding is provided to the program by the United States Nuclear Regulatory Commission (NRC), the Babcock and Wilcox (B&W) Company, the Babcock and Wilcox plant owners group organization, and the Electric Power Research Institute (EPRI) as documented in Reference 1. Research in this program is a combined experimental-analytical effort geared toward the study of B&W type nuclear steam supply system behavior during off-normal operating circumstances. Major emphasis is placed on the experimental approach through use of small-scale, nonnuclear, integral thermal-hydraulic test facilities to simulate postulated NSSS off-normal operating conditions. The major program objective is to provide experimental data for use in assessing analytical techniques used in calculating full size B&W type NSSS response.

The Multiloop Integral System Test (MIST) facility<sup>2</sup> is the central integral facility supported under the auspices of the IST program. This facility is being designed and constructed by B&W at the Alliance Research Center in Alliance, Ohio. Two other integral systems are being designed and constructed under funding sources separate from the IST program. These include SRI-2<sup>3</sup>-funded by EPRI and being built by SRI International at their Menlo Park, Ca. facilities and the University of Maryland facility<sup>4</sup> funded by NRC and being built by the University of Maryland at their College Park campus. All three of these facilities are considered to be integral in the sense that they contain most of the components germane to the primary side of a Babcock and Wilcox reactor system. While it is generally agreed that the SRI-2 and UMCP systems do not have the same degree of simulation potential as the MIST system, both will produce data that should compliment MIST results and support the IST program in general.

Each of the three integral facilities mentioned above was conceived, designed, and is being constructed under different set of constraints and assumptions. Such constraints and assumptions include funding limitations, design basis assumptions such as thermal-hydraulic scaling criteria and overall desires with respect to facility capability, facility testing methods and schedules, etc. As a result, each facility is different in terms of hardware geometric parameters as dictated by the scaling criteria utilized in its design and physical constraints introduced by conscious choice, construction material limits, support system limitation, or personnel safety codes.

In spite of differences in design and scaling approach and facility operational limitations in the systems described above, there is an obvious desire and need to investigate what the interrelationships between the facilities are and how facility results will be complimentary. Such an investigation is necessary so that a unified global approach to resolution of the issues forming the basis for the IST program can be effected.

The purpose of this paper is to document work done to investigate the interrelationships between the three facilities in the IST Program and

suggest a methodology for relating the three facilities and the data they produce to each other and to a plant. To meet this purpose, the following is contained in this report: First, summary descriptions of the three systems are given and scaling philosophy, methodology, and principles applied are described. Next, facility limitations and atypicalities are addressed and evaluations of certain physical phenomena are given in light of the scaling rational used for each facility. Finally, methodologies for comparison of local phenomena and global facility behavior are suggested and discussed.

## FACILITY DESCRIPTION AND SCALING

Each of the thermal-hydraulic test facilities mentioned above is intended to be used to simulate transients or off-normal conditions that may occur in a Babcock and Wilcox designed NSSS. Each facility contains most of the components germane to a B&W lowered loop<sup>a</sup> 177-FA plant. The 177-FA plant is a 2 x 4 (two hot legs and four cold legs) loop NSSS design containing a once through steam generator (OTSG) in each loop, a coolant pump in each cold leg, and a vessel containing 177 fuel assemblies producing a total of about 2700 MWt of energy. As such, each of the scaled facilities has a vessel connected by a 2 x 4 loop arrangement to OTSG simulators.

### Facility Descriptions

Brief descriptions of the MIST, UMCP, and SRI-2 facilities are given below. Additional details can be found in References 2, 3, and 4, respectively.

MIST Facility--The MIST facility consists of a vessel with an external pipe downcomer, a pressurizer, two hot legs, two 19-tube OTSG simulators, four cold legs, and four coolant circulating pumps. The vessel contains a 49 rod core simulator consisting of 45 electrically heated rods and four guide tube simulators. Four external vent valves connect the vessel upper plenum to the top of the downcomer and serve to simulate the internal vent valves used in the B&W reactor vessel. By volume, the MIST facility is ~1/817 the size of the reference 177-FA plant. In terms of component elevations and vertical heights, the MIST facility is nearly full height with respect to the reference plant. With the exception of core power (limited to 10% of scaled core power i.e., ~330 kW) the MIST facility can operate at plant typical conditions, i.e., pressure of 15.5 MPa and temperature of 590 K.

The major objective of the MIST facility and the experiments to be conducted in it are "to provide a sufficient data base from a 2 x 4 geometry system for use in computer code assessment."

UMCP Facility--The UMCP facility consists of a vessel with an internal downcomer, a pressurizer, two hot legs, two 28-tube OTSG simulators, and four cold legs. The UMCP does not have coolant circulating pumps. The vessel contains 16 electrical heater rods to provide for a maximum of 203 kW heat addition into the loop. Eight hinged vent valves are contained internally in the vessel to simulate the full scale reactor vessel vent valves. By volume, the UMCP facility is about 1/500 of the volume of a 177-FA plant. Unlike the MIST facility, the UMCP system is not full height. The UMCP hardware is capable of operating at a maximum pressure of 2.07 MPa.

---

a. In the lowered loop plant design, the elevation of the midpoint of the tubes in the steam generator is approximately the same as the elevation of the reactor vessel nozzles.

The stated objectives of the loop are to study small break loss-of-coolant behavior and phenomena associated with natural circulation in a B&W design plant.

SRI-2 Facility--The facility consists of a vessel with internal downcomer, a pressurizer, two hot legs, two 48-tube counter flow heat exchangers modified to simulate OTSG, four cold legs and four coolant circulating pumps. Eighteen heater rods in the vessel will supply up to 88 kW of energy to the fluid. Four internal hinged vent valves are included in the vessel design. By volume, the SRI-2 facility is about 1/1300 the volume of a full size NSSS. Like the UMCP system, SRI-2 is not full height. The SRI system is capable of operating at a maximum pressure of 0.79 MPa.

Stated objectives for the SRI-2 project and facility are; (a) to support the IST program by providing data for code assessment and providing information to help assess compromises in the MIST facility; (b) provide a facility with an alternate scaling approach relative to the UMCP and MIST facilities, and (c) provide a flexible, low operational cost instrument in which any unanticipated phenomena observed in MIST can be studied.

Each of the test facilities described above incorporates various auxiliary support systems and instrumentation. These systems include high pressure injection simulation, leak flow measurement, steam generator feed injection/control systems, data acquisition, etc.

### Scaling

From the above descriptions, it would seem that the three facilities are all quite similar in that each has a 2 x 4 arrangement, a vessel of some sort, simulation of two OTSG, support systems, etc, etc. However, a detailed examination of the thermal-hydraulic scaling philosophy used to design and build each system is necessary to illustrate the significant differences that actually exist and compromises that are introduced by the scaling philosophies and system constraints.

As previously mentioned, each facility contributing to the IST Program was designed and built according to somewhat different scaling criteria. To determine the extent to which these facilities compliment each other scaling philosophy and scaling criteria application for each facility must be examined. In this section, general methods of thermal-hydraulic scaling are briefly described and then the scaling method used for each facility and the results of this scaling method application are given.

General Scaling Methods--For the most part, integral thermal-hydraulic test facilities have been constructed according to a set of criteria known in the industry as "volume scaling" or "modified volume scaling."<sup>5-8</sup> Recently, Ishii and coworkers<sup>9,10</sup> have presented a set of criteria referred to hereafter as Ishii scaling. Kiang<sup>11</sup> has shown that volume scaling criteria are actually a subset of the more general Ishii criteria. Since each of the facilities contributing to the IST program was designed



using the basis of one or the other of these criteria, it is appropriate to describe the foundations of and the criteria prescribed by these techniques.

Scaling relationships are derived by considering a generalized set of conservation equations (mass, momentum, and energy) and an equation of state, selecting a set of kinematic and geometric scale factors, and then transforming the equations from the model domain to the prototype (full size) domain. Scale factors that represent scaling criteria are derived by requiring the transformed equations to be identical to the equation in the model domain. If in this transformation process one requires equivalency of time, operating conditions (pressure, temperature) and working fluid in both domains then the resulting geometric and kinematic scale factors require that the model be full height with the volume of each component maintained in a set ratio to that in the prototype and that the volumetric heat generation rate in the model be the same as that in the prototype. The criteria that result are known as the volume scaling laws and are shown in Table 1. Note that these laws as given assume that model and prototype operating conditions are the same and that the same fluid is used so that fluid properties (pressure, temperature, density, thermal expansion coefficient, etc), enthalpy changes, etc. are equivalent.

Scaling criteria have been developed by Ishii<sup>9</sup> for the design of small scale thermal-hydraulic facilities used for the conduct of natural circulation experiments. Ishii, used the procedure described above (nondimensionalizing a set of conservation equations) and makes the assumption that the scaled facility will operate at typical reactor operating conditions, thereby inducing considerable simplifications to the scaling criteria and the scale equations. It suffices here to state that the premise for single-phase flow is that similarity is achieved if the Richardson, friction, modified Stanton, Biot, and heat source numbers are satisfied in addition to geometrical similarity groups for length and flow area and dynamic similarity (friction number divided by flow area squared). For two-phase flow relative to the plant (assumed to be the reference), if the phase change and subcooling number are matched, then the core exit quality density ratio product is matched and under natural circulation conditions, the drift flux number (or void-quality) relation in the system is approximately correct given that the friction and orifice number requirements are matched in each system component. The Froude number then defines the velocity scale. Reference length and area scales can be selected so that scaled system resistance requirements can be met. If effect then, a length scale is selected so that

$$L_{1,R} = \frac{\lambda_1/\lambda_0|_{\text{model}}}{\lambda_1/\lambda_0|_{\text{plant}}} = 1 \quad (1)$$

and an area scale is selected such that

$$A_{1,R} = \frac{a_1/a_0|_{\text{model}}}{a_1/a_0|_{\text{plant}}} = 1 \quad (2)$$

TABLE 1. VOLUME SCALING CRITERIA

Primary Relations	Secondary Relations
$Q_R''' = 1$	$a_{s,R} = \delta$
$k_R = 1$	$N_R = \delta$
$a_R = \delta$	$\dot{m}_R = \delta$
$V_R = \delta$	$R_R' = \delta^{-2}$
$t_R = 1$	$Q_R = \delta$

TABLE 2. GENERALIZED NATURAL CIRCULATION SCALING CRITERIA PROPOSED BY ISHII

Primary Relations	Single-Phase	Two-Phase
$Q_R'''$	$\rho_{SR} C_{PS,R} U_{OR} \Delta T_{OR} k_{OR}^{-1}$	$\left(\frac{\rho_g h_{fg}}{\Delta p}\right)_R \rho_{f,R} k_{OR}^{-1/2}$
$k_R$	Must be selected	Must be selected
$a_R$	Must be selected	Must be selected
$V_R$	$a_R k_R$	$z_R k_R$
$t_R$	$(\beta_R \Delta T_{OR})^{-1/2} \sqrt{k_{OR}}$	$\sqrt{k_{OR}}$
$U_{OR}$	$\sqrt{\beta_R \Delta T_{OR}} \sqrt{k_{OR}}$	$\sqrt{k_{OR}}$
$\Delta T_{OR}$	$\left(\frac{Q}{\rho c_p}\right)_R^{2/3} \left[\frac{\Sigma(K_1/a_1^2)}{2Bgh}\right]_R^{1/3}$	--
$\Delta h_{SUB}$	--	$\left(\frac{\rho_g h_{fg}}{\Delta p}\right)_R$
<u>Secondary Relations</u>		
$a_{s,R}$	$\left(\frac{\rho_s C_{ps}}{\rho_f C_{pf}}\right)_R \sqrt{\beta_R \Delta T_{OR}} a_R k_{OR}$	$a_R k_{OR}$
$N_R$	$a_R$	$a_R$
$\dot{m}_R$	$\rho_R a_R \sqrt{k_R}$	$\rho_R a_R \sqrt{k_R}$
$R_R'$	$a_R^{-2}$	$a_R^{-2}$
$Q_R$	$\rho_{SR} C_{PS,R} \sqrt{\beta_R} (\Delta T_{OR})^{1.5} a_R \sqrt{k_{OR}}$	$\left(\frac{\rho_g h_{fg}}{\Delta p}\right)_R \rho_{f,R} a_R \sqrt{k_{OR}}$

If the assumption of equal operating conditions is removed from Ishii's analysis the generalized scaling relations for single-phase and two-phase flow are as shown in Table 2. Note that if facility operation is not at typical plant conditions (pressure and other fluid conditions) the single- and two-phase scaling relations may not be the same. Also note that if  $\lambda_{OR} < 1$  the time scale is less than unity. This implies that

events will occur faster in the model relative to the reference.

MIST Scaling--The MIST facility was designed according to volume scaling criteria. An early consideration in the design of the system was to utilize an existing volume scaled, 19-tube model OTSG that had been used in previous experimental programs. The desire to use this existing OTSG then effectively defines the volume scale factor for the system. The scale factor  $\delta$  was defined as the ratio of number of full size tubes in the model OTSG divided by the number of tubes in the plant OTSG. For a typical 177-FA plant with 15531 tubes then

$$\delta = 19/15531 = 1/817$$

With the scale factor thus defined, volume scaling criteria prescribe the following relationships between the plant and the scaled facility designed for plant typical pressure-temperature operation:

$$a_R = V_R = a_{SR} = N_R = \dot{m}_R = Q_R = \delta = (817)^{-1} \quad (3a)$$

$$\lambda_R = t_R = 1 \quad (3b)$$

$$R'_R = \delta^{-2} = (817)^2 \quad (3c)$$

Close examination of these equations shows conflicting requirements. For example Equation (3a) requires that  $d_R$  for piping sections equal  $\sqrt{\delta}$  whereas Equations (3b) and (3c) require  $d_R$  to be  $\delta^{2/5}$ . While Equations (3) provide the fundamental basis for the scaling of the MIST facility, numerous compromises and secondary scaling relationships (secondary meaning not explicitly stated by Equations (3) have been invoked in attempts to preserve two-phase flow criteria. In general, effort was made to preserve the power ratio, the flow rate ratio, the volume ratio for each component, the N ratio (core and steam generators), the hydraulic resistance ratio, and full height was maintained in most components. Horizontal piping lengths have been shortened to help maintain component volume ratios and piping diameters are somewhat oversized relative to the Equation (3a) in order to satisfy Equation (3c). Table 3 shows a comparison of actual MIST parameters versus ideal parameters as obtained by rote application of Equations (3). Reference plant values are shown for comparison. The table results suggest that the facility is generally well scaled. The volume distortions introduced by the conflicting requirements

TABLE 3. MIST ACTUAL VERSUS IDEAL PARAMETER COMPARISON

Parameter	Plant	MIST Actual	MIST Ideal	$\Delta$ (Actual/Ideal)
Operating Pressure (MPa)	15.02	15.02	15.02	1
Primary Volume (m <sup>3</sup> )	313.5	0.57	0.38	1.5
Core Power MW(t)	2700	0.33	3.3	0.1
Total Hydraulic Resistance (m <sup>-4</sup> )	7.53	49.53E5	50.28E5	0.98
Hot Leg Temperature (K)	591.1	591.1	591.1	1
Vessel Downcomer				
Volume (m <sup>3</sup> )	28.31	0.057	0.035	1.6
Flow area (m <sup>2</sup> )	3.2	0.0043	0.0039	1.1
Length (m)	7.87	7.08	7.87	0.9
Core Region				
Volume (m <sup>3</sup> )	22.08	0.0227	0.027	0.84
Flow area (m <sup>2</sup> )	4.57	0.0061	0.0056	1.1
Number rods	36816	45	45	1
Rod diameter (cm)	1.091	1.091	1.091	1
Pitch (cm)	1.443	1.443	1.443	1.0
Rod length (m)	3.66	3.66	3.66	1.0
H.T. area (m <sup>2</sup> )	4620	5.65	5.65	1.0
Hot Leg (1 of 2)				
Volume (m <sup>3</sup> )	13.476	0.0524	0.0165	3.17
Flow area (m <sup>2</sup> )	0.657	0.00273	0.0008	3.4
Length (m)	21.1	19.5	21.1	0.92
Steam Generator (1 of 2)				
Tube volume (m <sup>3</sup> )	41.1	0.0484	0.0503	0.96
Tube flow area (m <sup>2</sup> )	2.387	2.926E-3	2.922E-3	1.0
Tube ID (cm)	1.4	1.4	1.4	1.0
Tube length (m)	15.88	15.88	15.88	1.0
Number tubes	15531	19	19	1.0
H.T. Area (m <sup>2</sup> )	12299.2	15.05	15.05	1.0
Cold Leg Suction (1 of 4)				
Volume (m <sup>3</sup> )	4.84	0.023	5.926E-3	3.9
Flow area (m <sup>2</sup> )	0.397	1.9E-3	4.86E-4	3.9
Length (m)	12.19	11.125	12.19	0.91
Cold Leg Discharge (1 of 4)				
Volume (m <sup>3</sup> )	2.63	3.596E-3	3.22E-3	1.1
Flow Area (m <sup>2</sup> )	0.397	1.9E-3	4.86E-4	3.9
Length (m)	6.7	1.89	6.7	0.28

mentioned above are clearly evident in the hot leg and cold leg suction regions. Note that the overall loop resistance is well scaled as a result of the oversized hot and cold legs.

SRI-2 Scaling--The SRI-2 system was designed according to the criteria derived by Ishii (see General Scaling Methods Section) i.e., Equations (1) and (2). An early consideration in the design of the facility was limited funding available for construction. In part because of this limitation, a maximum operating pressure of 0.689 MPa was selected. Also, a maximum power of 88 kW was available for the SRI-2 facility. In the final design, a length scale and an area scale of 1/4 and 1/324 was selected, respectively. In order to estimate how various parameters scale relative to a plant, it is necessary to pick a reference pressure in the plant so that the equations in Table 2 can be applied. For the purposes here the reference pressure was assumed to be 6.894 MPa.<sup>a</sup> Table 4 shows a comparison of plant and SRI-2 actual and ideal parameters.

With a power of 88 kW available and selecting a plant under single-phase natural circulation conditions at 5% power, it can be shown that  $\Delta T_{\text{OR}} = 0.77$ . Inserting property ratios and length and area scales

given for single-phase flow

$$U_R = 0.56 \sqrt{\ell_R} = 0.28$$

$$Q'''_R = 0.42 \ell_R^{1/2} = 0.84$$

$$V_R = 1/1296$$

$$t_R = 1.758 \sqrt{\ell_R} = 0.88$$

$$Q_R = 0.42 a_R \sqrt{\ell_R} = 1/1542$$

(4)

and likewise for two-phase flow

$$U_R = \sqrt{\ell_R} = 0.5$$

$$Q''_R = 0.132 \ell_R^{1/2} = 0.26$$

$$t_R = \sqrt{\ell_R} = 0.5$$

$$Q_R = 0.132 a_R \sqrt{\ell_R} = 1/4909$$

Note that there is a discontinuity in how all of these parameters scale between single- and two-phase flow. For example, with 88 kW of core power, the SRI-2 system has the capacity simulate 5% decay heat in

---

a. It will be shown later that while this assumption is appropriate for steady-state simulations at constant pressure, it is not appropriate for transient simulations.

TABLE 4. SRI-2 ACTUAL VERSUS IDEAL PARAMETERS COMPARISON

Parameter	Plant	SRI-2 Actual	SRI-2 Ideal	$\Delta$ (Actual/Ideal)
Operating pressure (MPa)	15.017	0.6894	--	--
Primary volume (m <sup>3</sup> )	313.5	0.198	0.24	0.82
Core power (MWt)	2700	0.088	--	--
Total hydraulic resistance (m <sup>-4</sup> )	9.2	9.95E-5	8.82E-5	1.13
Hot leg temperature (K)	591.1	437.2	--	--
Vessel Downcomer				
Volume (m <sup>3</sup> )	28.31	0.0217	0.219	1.0
Flow area (m <sup>2</sup> )	3.198	0.0112	0.009	1.14
Length (m)	7.87	1.788	1.968	0.91
Number vent valves	8	4	--	--
Vent valve area (m <sup>2</sup> )	0.794	2.452E-3	2.453E-3	1.0
Core Region				
Volume (m <sup>3</sup> )	22.08	0.0185	0.017	1.66
Flow area (m <sup>2</sup> )	4.57	0.0269	0.014	1.9
Number rods	36816	18	114	0.158
Rod diameter (cm)	1.091	1.588	1.091	1.45
Pitch (cm)	1.443	3.81	1.443	2.64
Rod length (m)	3.66	0.8128	0.91	0.89
H.T. area (m <sup>2</sup> )	4620	0.73	3.56	0.2
Hot Leg (1 of 2)				
Volume (m <sup>3</sup> )	13.476	0.0128	0.0104	1.23
Flow area (m <sup>2</sup> )	0.657	0.0022	0.00203	1.08
Length (m)	21.1	5.92	5.28	1.12
Steam Generator (1 of 2)				
Tube volume (m <sup>3</sup> )	41.1	0.0322	0.0317	1.0
Tube flow area (m <sup>2</sup> )	2.387	7.548E-3	7.368E-3	1.02
Tube I.D. (cm)	1.415	1.415	1.415	1.0
Tube length (m)	15.88	4.267	3.97	1.08
Number tubes	15531	48	48	1.0
H.T. Area (m <sup>2</sup> )	12299.2	10.21	9.49	1.08
Cold Leg Suction (1 of 4)				
Volume (m <sup>3</sup> )	4.84	3.52E-3	3.736E-3	0.94
Flow area (m <sup>2</sup> )	0.397	1.313E-3	1.226E-3	1.07
Length (m)	12.19	2.667	3.048	0.875
Cold Leg Discharge (1 of 4)				
Volume (m <sup>3</sup> )	2.63	2.196E-3	2.032E-3	1.08
Flow Area (m <sup>2</sup> )	0.397	1.313E-3	1.226E-3	1.07
Length (m)	6.7	1.676	1.676	1.0

single-phase natural circulation or 16% decay heat in two-phase natural circulation. This discontinuity implies that during integral transient simulations during which system fluid conditions degrade from 1  $\phi$  to 2  $\phi$ , the power will have to be changed so that a plant typical scaled energy input will be maintained.

The data shown on Table 4 indicate with the exception of the core that the SRI-2 system was geometrically scaled to adhere very closely to Equations (1) and (2). The actual core was designed to simply provide energy addition at the proper thermal center location and is atypical from a rigorous scaling viewpoint.

UMCP Scaling--The UMCP system was designed to a volume scale of  $\sim 1/500$ .<sup>4</sup> An early constraint on the facility design was the maximum laboratory space (mainly height) available for hardware and funding constraints. In part, because of these limitations and for safety considerations, the facility is not full height and has a maximum pressure capability of 2 MPa. The effect, laboratory space for the UMCP facility limited maximum height floop components to about 6.1 m. This limitation on height and consideration for excessive pressure drops in a full height facility with a volume scaled diameter led to the selection of a vertical length scale of 1/4.4. An arbitrary flow area scale of 1/112 was selected to maintain the volume scale near 1/500. Although never stated in Reference 4, the length scale, arbitrary area scale, and low pressure limitation suggest that the facility should scale according to the criteria given in Table 2. In Reference 4 it was assumed that the flows scale as the volume ratio since the facility was stated to be volume scaled. With 20J kW of power available then it was suggested that the UMCP facility could simulate plant natural circulation at 18.8% power. However, if the facility scaling is examined with the same technique as used in the previous section, different conclusions are reached. Table 5 gives a summary of actual and ideal scaled parameters for the UMCP facility.

With 200 kW of core power available and selecting a plant operating at 5% power natural circulation conditions, it can be shown that  $\Delta T_{OR} = 0.53$ . For single-phase flow then

$$U_R = 0.54 \sqrt{\ell_R} = 0.26$$

$$Q''' = 0.29 \ell_R^{1/2} = 0.608$$

$$\bar{V}_R = 1/493$$

$$t_R = 1.85 \sqrt{\ell_R} = 0.883$$

$$Q_R = 0.29 a_R \sqrt{\ell_R} = 1/810$$

and for the two-phase flow

$$U_R = \sqrt{\ell_R} = 0.48$$

TABLE 5. UMCP ACTUAL VERSUS IDEAL PARAMETERS

Parameter	Plant	UMCP Actual	UMCP Ideal	$\Delta$ (Actual/Ideal)
Operating pressure (MPa)	15.017	2.07	--	--
Primary volume (m <sup>3</sup> )	313.51	0.6	0.627	0.96
Core power (MWt)	2700	0.2	--	--
Total hydraulic resistance (m <sup>-4</sup> )	9.2	5.09E-4	1.1E-5	0.44
Hot leg temperature (K)	591.1	477.8	--	--
Vessel Downcomer				
Volume (m <sup>3</sup> )	28.31	0.045	0.057	0.8
Flow area (m <sup>2</sup> )	3.198	0.045	0.029	1.56
Length (m)	7.87	1.03	1.789	0.58
Number vent valves	8	8	--	--
Vent valve area (m <sup>2</sup> )	0.794	8.37E-3	7.093E-3	1.18
Core Region				
Volume (m <sup>3</sup> )	22.08	0.293	0.197	1.48
Flow area (m <sup>2</sup> )	4.57	0.124	0.041	3.05
Number rods	36816	15	329	0.046
Rod diameter (cm)	1.09	2.54	1.09	2.3
Pitch (cm)	1.443	8.9	1.443	6.16
Rod length (m)	3.66	0.61	0.83	0.73
H.T. area (m <sup>2</sup> )	4620	0.729	9.37	0.07
Hot Leg (1 of 2)				
Volume (m <sup>3</sup> )	13.476	0.031	0.0273	1.13
Flow area (m <sup>2</sup> )	0.657	6.392E-3	5.866E-3	1.09
Length (m)	21.1	4.828	4.795	1.0
Steam Generator (1 of 2)				
Tube volume (m <sup>3</sup> )	41.1	0.077	0.083	0.92
Tube flow area (m <sup>2</sup> )	2.387	0.0198	0.021	0.93
Tube ID (cm)	1.4	2.997	1.4	2.14
Tube length (m)	15.88	3.905	3.886	1.0
Number tubes	15531	28	139	0.2
H.T. Area (m <sup>2</sup> )	12299.2	10.9	24.958	0.44
Cold Leg Suction (1 of 4)				
Volume (m <sup>3</sup> )	4.84	1.217E-2	9.821E-3	1.24
Flow area (m <sup>2</sup> )	0.397	0.0048	3.545E-3	1.34
Length (m)	12.19	2.566	2.77	0.93
Cold Leg Discharge (1 of 4)				
Volume (m <sup>3</sup> )	2.63	8.494E-3	5.337E-3	1.59
Flow Area (m <sup>2</sup> )	0.397	4.765E-3	3.545E-3	1.34
Length (m)	6.7	1.804	1.523	1.19



$$Q''' = 0.344 \bar{\rho}_R^{1/2} = 0.72$$

$$t_R = \sqrt{\rho_R} = 0.48$$

$$Q_R = 0.344 a_R \sqrt{\rho_R} = 1/683$$

As was the case with the examination of SRI-2, note that there are discontinuities in how the velocity, power, and time scale in 1  $\phi$  and 2  $\phi$  flow.

Review of the values in Table 5 indicate that neither the core or steam generators is scaled correctly in the UMCP facility. As was for the SRI-2 facility, the core is viewed simply as a heat source. The steam generator is distorted mainly due to the expense of constructing a steam generator with the scaled number of tubes (139). Also note that the loop hydraulic resistance (as designed) is roughly a factor of two low. The facility does have the provisions for addition of orifice plates in the loops should it be necessary to rectify this distortion.

#### LOCAL SCALING EVALUATION OF FACILITY LIMITATIONS

In the previous section, the hardware and scaling philosophy used in the design of the IST facilities was addressed. Aside from the fact that each facility was designed to somewhat different criteria and constraints and, therefore, are different geometrically, the most significant difference among the three are the operating conditions which can be attained. The most obvious operating condition difference is, of course, pressure although there are other limitations such as core power, loop fluid temperature, etc. Also, there are geometric differences such as pipe diameter that have the potential to influence local phenomena such as flow regime transition, flooding, mixing, critical flow, etc. Each of the facilities under consideration was designed to investigate natural circulation phenomena during a SBLOCA. As such the maximum core power limitations discussed above are not significant since reference plant core power will be at decay heat levels (<5%) during the time of interest. The appropriate scaling of this decay heat will however be quite important especially for the low pressure facilities.

The significance of several of the effects mentioned above are examined in this section. First, the implications of operation at reduced pressures and the potential influence of the property ratio multipliers on the scaling relations are addressed. Power and subcooling scaling are examined. Finally, flow regime transitions, high pressure injection (HPI) mixing, critical flow scaling, and break area sizing are discussed.

#### Implications of Operation at Nontypical Pressures

As noted earlier, the scaling relations presented in Table 2 contain fluid property group ratio multipliers. At plant typical pressures the property group ratios are unity and if  $\rho_R = 1$ , the scaling relations in Table 1 result. At reduced pressure relative to the plant ( $P_R \neq 1$ ), several points should be noted. First, the property group multipliers for

the single-phase regime are not the same as the groups for the two-phase regime. Second, it is apparent that the single-phase property group ratios are not necessarily numerically equal to the two-phase property group ratios. Third, if pressure is changing with time, it is obvious that the property group ratios could be a function of time. These observations imply that there are discontinuities between the single-phase and two-phase scale relations for power, velocity, temperature difference (or subcooling), and time. For steady-state experiments conducted at constant pressure, this is not a problem since the property ratios will be a constant--though a different constant for different pressures. For transient experiments where pressure is changing, changes in the property ratios will be a complicating factor since model pressure will not be known a priori and thus it will be difficult to correctly input power and subcooling boundary conditions. Consider also that reference power and subcooling are time dependent quantities. Subcooling in particular will depend on steam generator control and operation, high pressure injection mixing characteristics, rate of depressurization, etc. With these considerations in mind, the following question can be posed:

1. What must happen so that the property group ratios ( $\psi_{i,R}$ ) are approximately constant?
2. How might important reference variables such as the phase change ( $N_{PCH}$ ) and subcooling ( $N_{SUB}$ ) numbers change with time for a given transient?
3. If  $\psi_{i,R}$  can be "forced" to be approximately constant, what should model power and subcooling be for a given transient?

In order to provide insight to the above questions, the following procedure has been used. First, a TRAC calculation<sup>12</sup> for a small break loss-of-coolant accident in a B&W design plant was reviewed to obtain reference time dependent values for pressure, the phase change number ( $N_{PCH}$ ), and the subcooling number ( $N_{SUB}$ ).<sup>a</sup> It was then hypothesized that if the model system was forced to follow the same normalized pressure transient as the reference then the property ratio groups would be approximately constant, i.e., if

$$\frac{P(t)}{P_0} \Big|_R \approx 1 \rightarrow \psi_{i,R} \sim \text{CONSTANT}$$

Model power and subcooling were then calculated by requiring  $N_{SUB}|_R = 1$  and  $N_{PCH}|_R = 1$ .

The TRAC calculation mentioned above used boundary conditions based on conditions planned for the so-called nominal transient to be conducted in

---

a. The phase change and subcooling numbers are important dimensionless groups that define how core power and core inlet subcooling should be scaled.

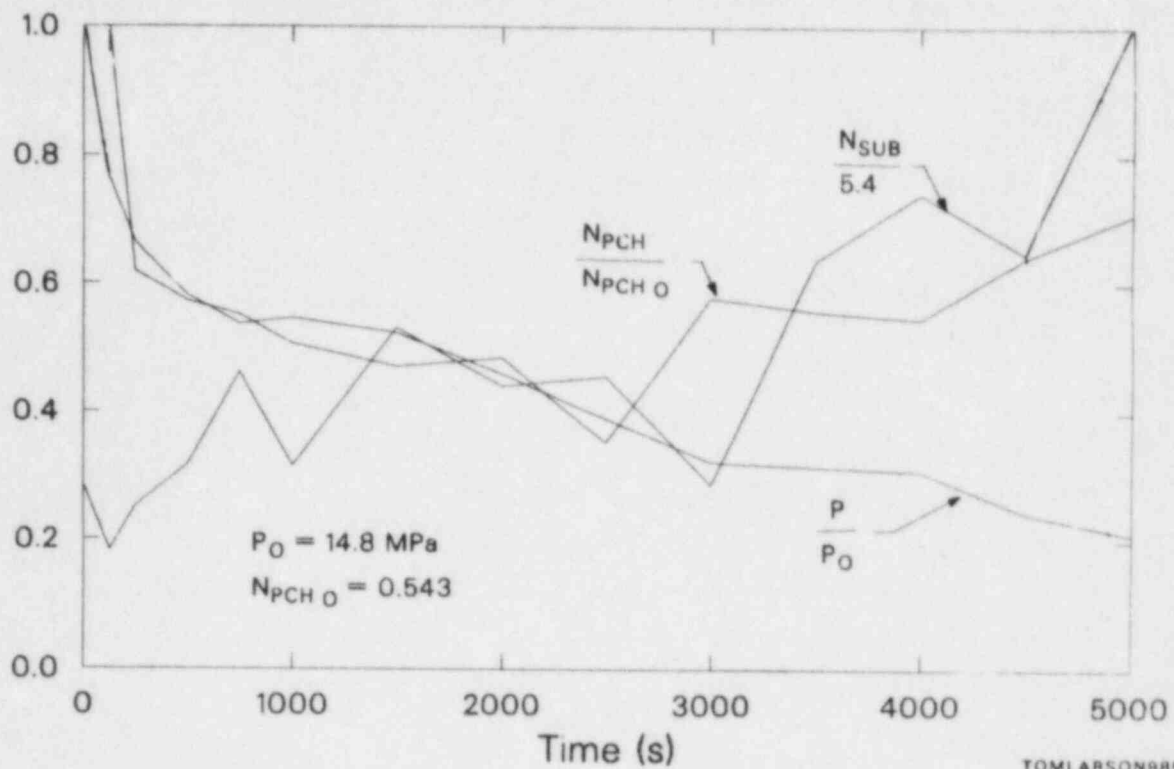
the MIST<sup>5</sup> facility (Test 310000). The transient is a SBLOCA with a scaled 10 cm<sup>2</sup> break in the pump discharge piping. Full HPI capability was utilized and steam generator auxiliary feedwater control was such that constant secondary level (~32 ft) was maintained after the initiation of the transient. Figure 1 shows the calculated normalized pressure transient and the phase change and subcooling number variation with time. The subcooling number is based on the fluid temperature in the cold leg containing the break. This temperature was noted to be almost identical to the core inlet fluid temperature. The phase change number was calculated based on a reference velocity at 5% power (~0.61 m/s). An important point to note is that neither  $N_{SUB}$  or  $N_{PCH}$  are constants with time although  $N_{PCH}$  only changes by 30% whereas  $N_{SUB}$  changes by more than a factor of 3. The calculation was terminated at 5000 s as refill of the hot legs was commencing. Generally, after about 2500 s, the HPI flow was equivalent to or slightly larger than the leak flow rate. For reference, the hot leg started to void between 200 and 250 s and the system was considered two-phase after this point in time.

### Property Ratio Multipliers

To examine the validity of the hypothesis that if  $P(t)/P_0|_R = 1$  then  $\psi_{i,R} \sim \text{constant}$ , the results from Figure 1 were used to construct the pressure transients shown in Figure 2 for the UMCP and SRI systems. Recognize that the choice of the reference conditions and the given length scales makes the single-phase time scale approximately unity (real time) and the two-phase time scale is  $\sim 1/2$  (i.e., equal to the square root of the length ratio) for both facilities. Hence, as indicated on the figure, after the initiation of two-phase, events will occur twice as fast as in the reference and it is desired that the model normalized pressure will be equal to that in the plant at a time equal to  $\sim 1/2$  the plant time referenced to the time where the plant becomes two-phase.

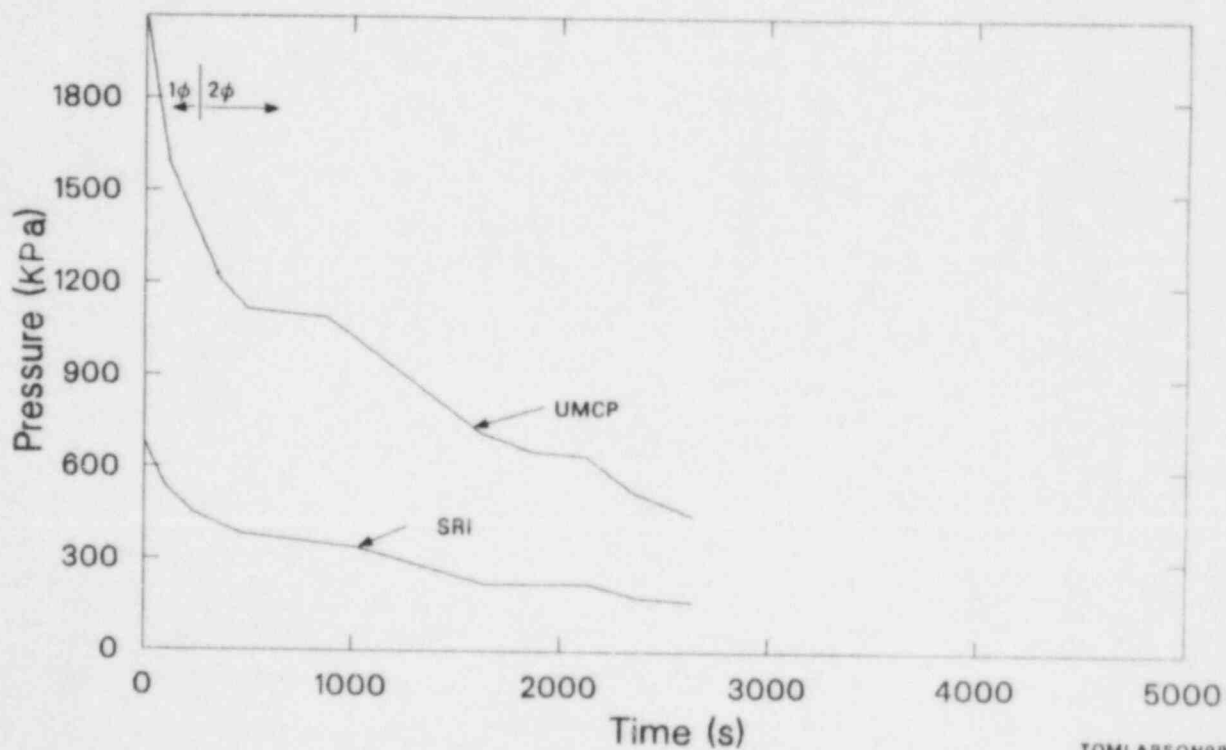
Figures 3 and 4 show the results of calculation of property group ratios for the scale equations shown in Table 2 with the assumption that  $P(t)/P_0|_R = 1$ . The top three curves in each figure are the void, power, and subcooling scale multipliers, respectively. The bottom curve is the quality scale and is a property group that figures significantly into the calculation of superficial velocities and hence flooding and flow regime transition phenomena. It is readily seen that the scale equation multipliers are nearly constant although there is a 20% change in the  $\Delta\rho/\rho_0|_R$  group. The fact that the scale equation multipliers are nearly constant for the assumed circumstances is encouraging since it means that if the break can be appropriately and reliably sized to cause the model normalized pressure to follow that expected in the reference transient, scaling of the power will be straightforward. Scaling of the subcooling will be more difficult, however, even though the property multiplier is approximately constant because of the manner in which  $N_{SUB}$  may change as shown in Figure 1.

A reasonable question at this juncture is "What happens to the property ratio multipliers if the assumed  $P(t)/P_0|_R = 1$  for the full pressure transient is not followed or if it is assumed that the model



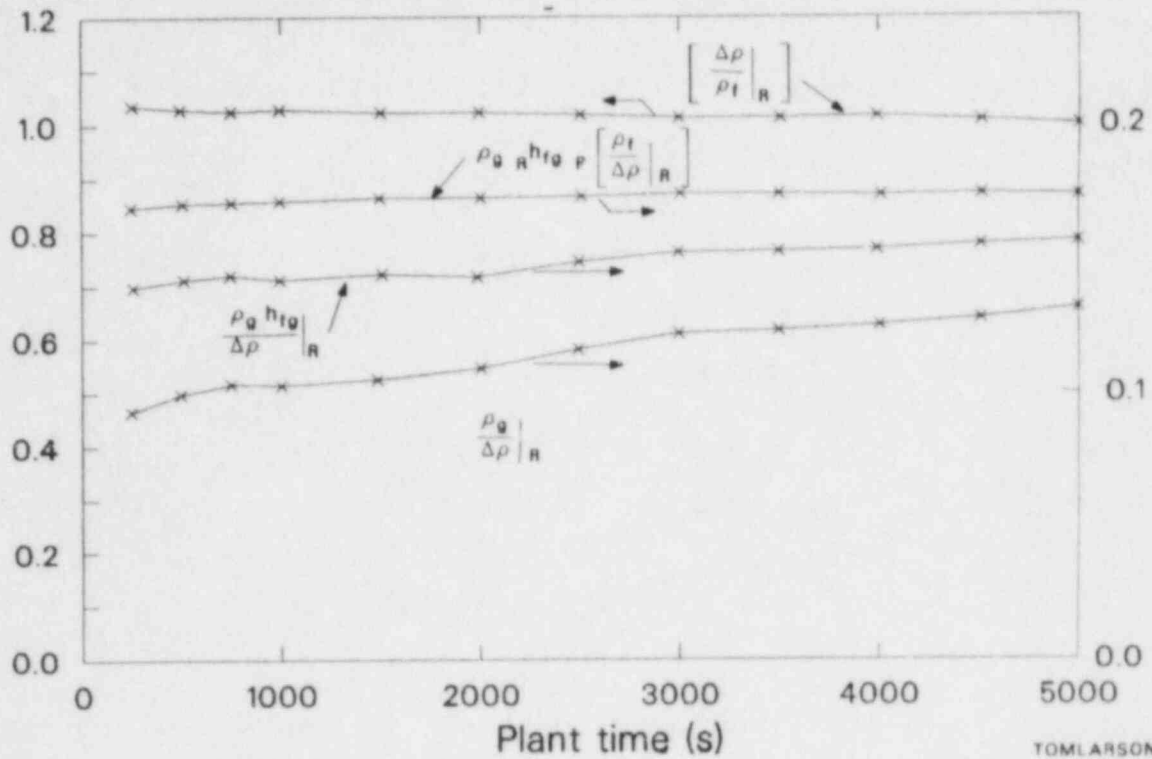
TOMLARSON985-50

Figure 1. Pressure,  $N_{pCH}$ , and  $N_{SUB}$  from TRAC Calculation for Plant.



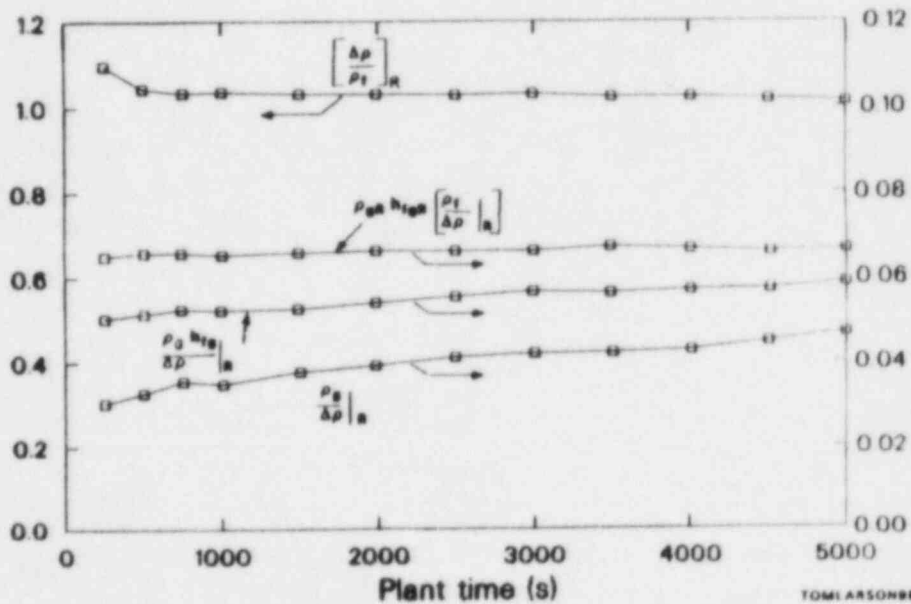
TOMLARSON985-14

Figure 2. Pressure Transient in UMCP and SRI Based on Plant Calculation Normalized Pressure Transient.



TOMLARSON985-22

Figure 3. Scale Equation Multipliers for UMCP Assuming Simulation of  $P/P_0$  from Full Pressure Transient in Plant.



TOMLARSON985-18

Figure 4. Scale Equation Multipliers for SRI Assuming Simulation of  $P/P_0$  for Full Pressure Transient in Plant Calculation.

transient is to simulate the plant transient starting at the initiation of two-phase?" Figure 5 shows two different pressure transients for each facility and the reference plant transient pressure response starting from the initiation of two-phase in the plant. In other words, it is assumed that only the two-phase portion of the plant transient will be simulated. The upper curve for each facility is the pressure required so that

$$\frac{P(t)}{P_{0,2\phi}|_R} = 1 \text{ and the lower curve}$$

is the pressure required to force the property group  $\rho_g/\Delta\rho|_R$  to be constant. Figure 6 demonstrates typical results for the behavior of the property group ratios under either of the pressure curve assumptions. It is seen that a 20-30% variation has been introduced in both the power and subcooling property group ratios. Although this variation is not overly significant, it is obviously more desirable to maintain a constant if at all possible.

The above discussion suggests that if the initial maximum model pressure is assumed to represent initial pressure conditions in the reference, then the minimum pressure to which the facility is depressurized should be chosen to match the expected minimum  $P/P_0$  in the reference. The property ratio multipliers should then remain reasonably constant in time if  $P(t)/P_0|_R$  is close to unity.

#### Power Scaling

As stated before, maintaining the phase change number equal to that in the reference is an important aspect of the similarity criteria. In the section discussing the general scaling of existing low pressure facilities, it was assumed that power would scale by a constant factor taken to be the property group  $\rho_g h_{fg} \rho_f / \Delta\rho$  value at maximum model pressure divided by the same property group value at some reference plant pressure usually taken to be 6.894 MPa. The discussion in the previous section indicated that the property group ratio will indeed be close to a constant but will be different from the ratio computed above if the whole pressure transient is to be simulated or if the simulation is shifted to the initiation of two-phase in the reference.

Figure 7 shows power curves calculated for the SRI facility using a number of different assumptions. The top curve results from the assumption of properties at 0.6894 MPa ratioed to 6.894 MPa. The middle curve is that resulting from the property group ratio calculated assuming that the pressure transient is matched starting from the initiation of two-phase flow in the reference. The bottom curve was computed with property ratios computed assuming that the full pressure transient is matched.

The power curves in Figure 7 show two important points. First, the discontinuity between single- and two-phase in how the power should be scaled independent of what assumptions are effected. Secondly, there is a significant difference in the calculated scaled power depending on the

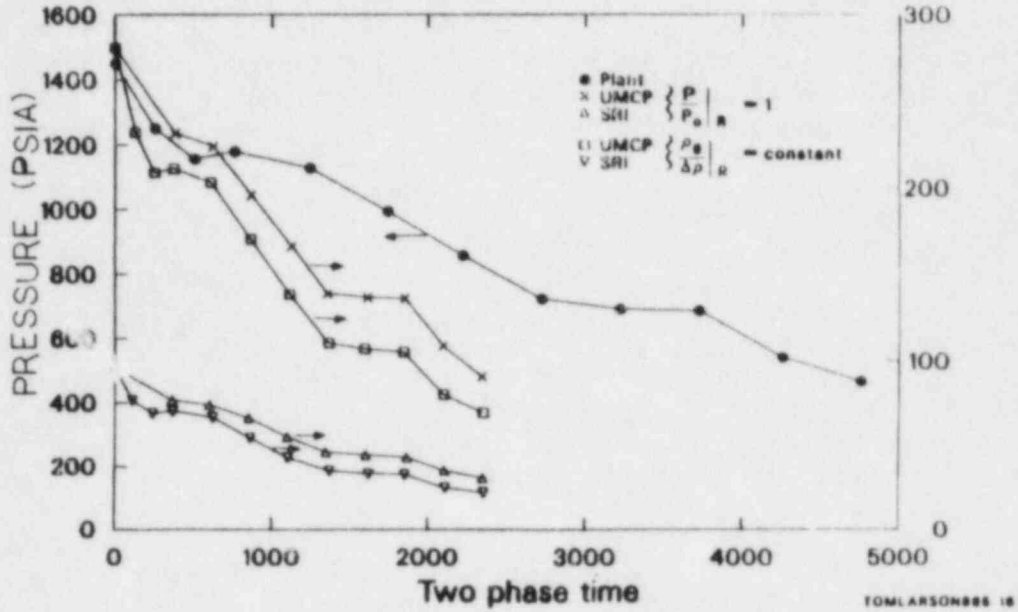


Figure 5. Facility Pressure Transients Required to Simulate TRAC Calculated  $P/P_0$  for Plant Shifted to Initiation of Two Phase (1430 psia) and to Maintain  $\rho_g/\Delta p_R = 1$ .

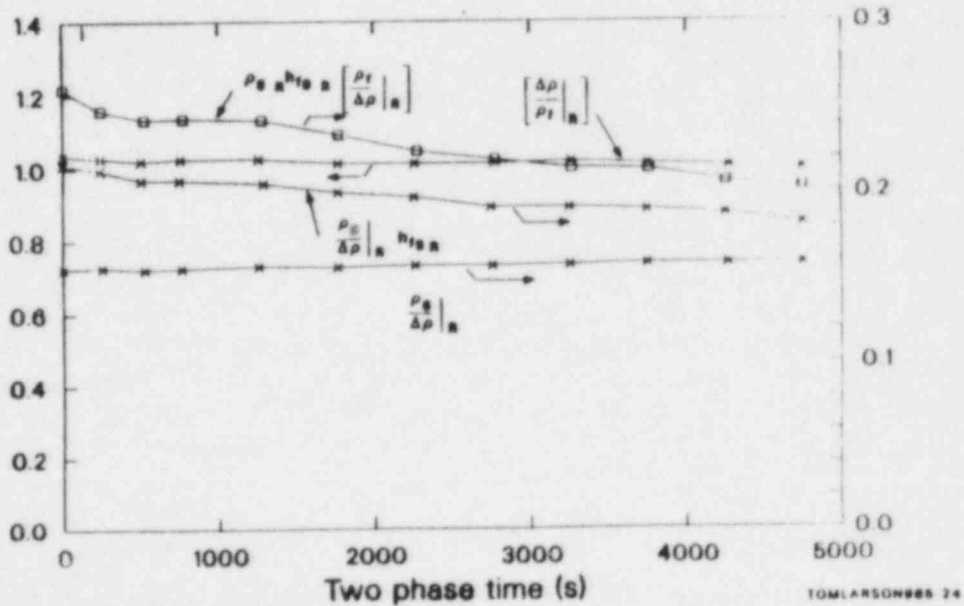


Figure 6. Scale Equation Multipliers for UMCP for Simulation of  $P/P_0$  Required to Force Constant  $\rho_g/\Delta p_R$ .

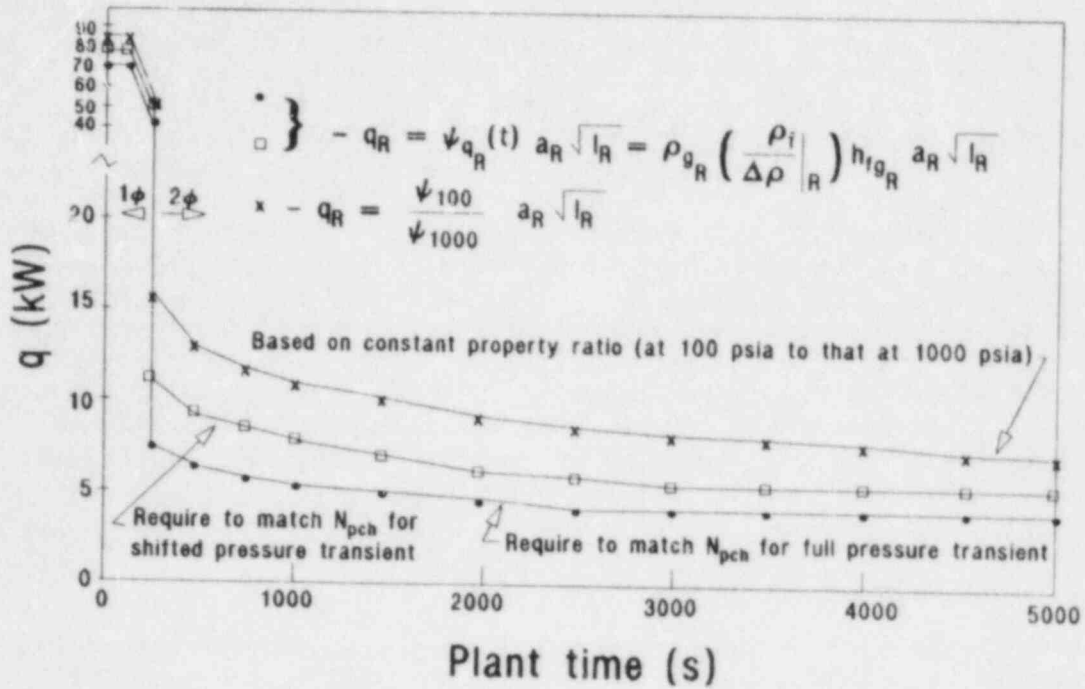
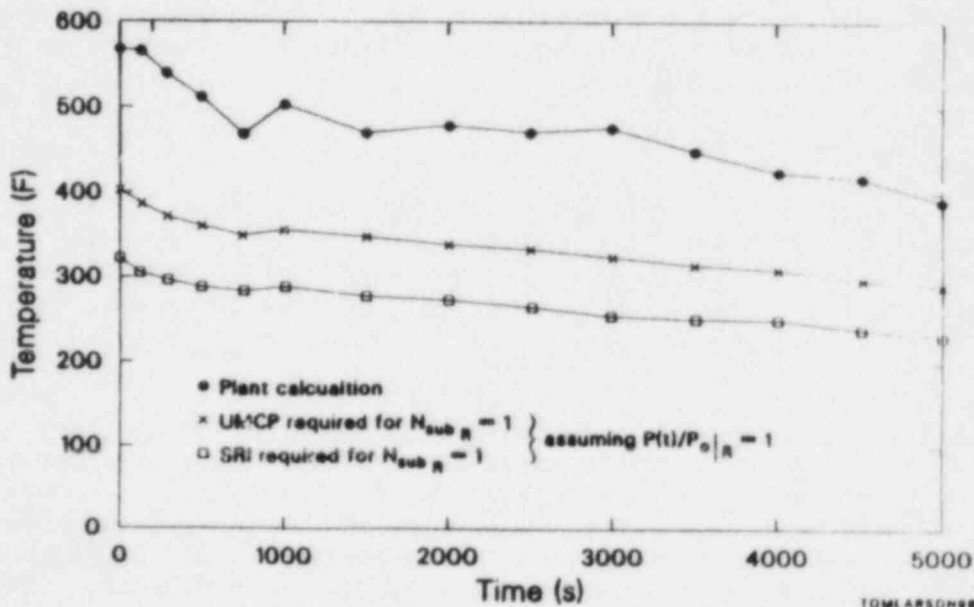


Figure 7. Scaled Core Power for SRI Assuming Full  $P/P_0$  Pressure Transient Matched from Plant Calculation.

TKL0005-98



TOML ARSON 27

Figure 8. Cold Leg Temperatures.



assumptions made with respect to the property group ratio computation. As stated previously, the discontinuity in scaled power required is a consequence of reduced pressure operation. Also note that the initial power(s) shown in Figure 7 are those scaled to ~5% power in the reference plant and represent the maximum power available in the SRI facility.

The implications of the information presented in Figure 7 are severalfold. First, an actual experiment conducted with a step change in power as shown could be a significant perturbation to the system behavior. For example, a sudden power decrease could result in void collapse, vapor generation rate change, etc. Secondly, one will not know precisely when the model system will become two-phase so to effect such a power change may require on-line control. Third, it appears that simply by changing the power it may be possible to force model results to look like a different reference pressure in the plant if the plant power is at a relatively constant value.

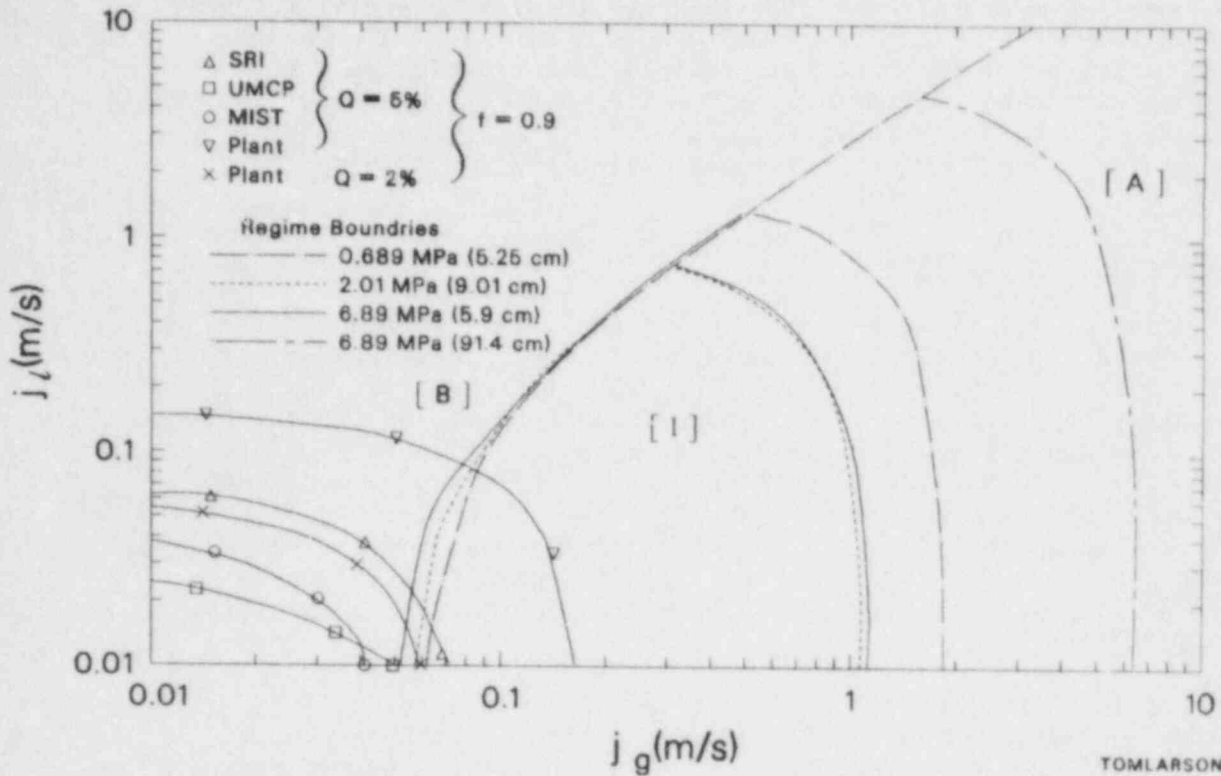
### Subcooling and Cold Leg Temperatures

Using the subcooling number shown in Figure 1 and assuming that  $P(t)/P_0|_R = 1$  for a full pressure transient simulation, the model cold leg temperatures required to force  $N_{SUB,R} = 1$  can be computed through use of the property group values shown in Figures 3 and 4. Figure 8 shows the result of such calculations for the UMCP and SRI facilities and the plant reference calculation as well. Note that as was the case with the scaling of the power, a different temperature transient would be prescribed if the property group ratio for the subcooling had been defined differently. Note also that in order for the temperatures shown in Figure 8 to ever occur in the model facilities, HPI mixing, steam generator control, etc. must be as they are in the reference system. The information in Figure 8 therefore represents an ideal case where the subcooling is scaled exactly and the normalized pressure transient in the model simulates the full normalized pressure transient in the reference.

### Hot Leg Flow Regime Transition

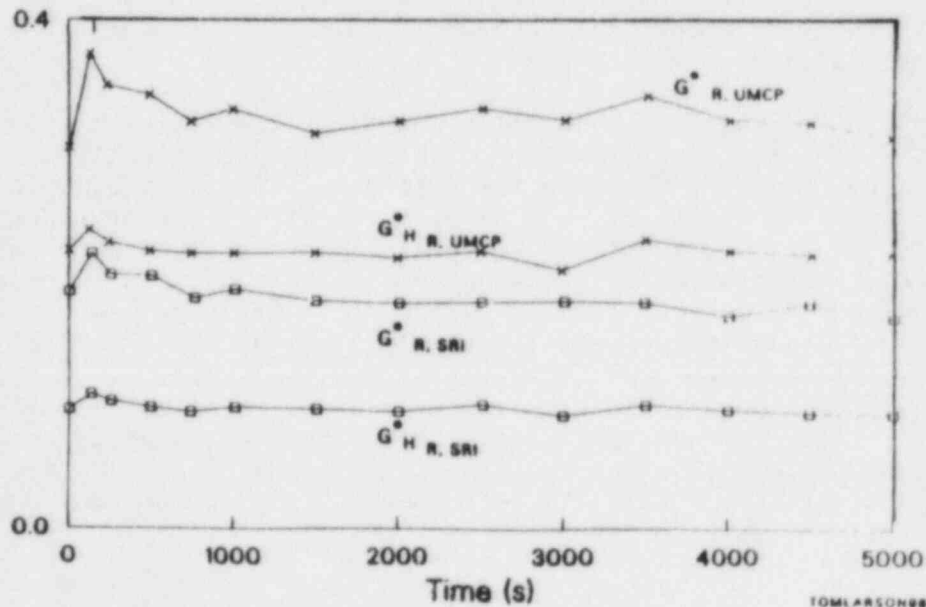
One of the unique features of the B&W NSSS (and therefore the IST facilities) is the long vertical hot leg. It is expected that the behavior in the hot leg can be a significant influence on the overall system response during a transient. It is therefore, useful to examine the effects of pressure, diameter, power scaling, etc. on the hot leg flow regime.

A steady-state energy balance on the core in conjunction with assumptions about the core inlet subcooling and the amount of vapor that passes through the vent valves allows one to compute a locus of superficial gas and liquid velocities expected in the hot leg. Figure 9 shows such a plot for core power and inlet subcooling representative of two-phase natural circulation conditions for the SRI-2, UMCP, and MIST facilities and for a B&W plant. MIST and the plant are assumed to be at 6.894 MPa while SRI-2 and UMCP are assumed to be at 0.6894 and 2 MPa, respectively. In this figure, 90% of the vapor generated by core decay heat was assumed to



TOMLARSON985-17

Figure 9. Superficial Velocity Loci for Natural Circulation in SRI, UMCP, MIST, and Plant on Taitel-Dukler Vertical Flow Regime Map.



TOMLARSON985-23

Figure 10. Ratio of Break Mass and Energy Flux in UMCP and SRI Facilities to Plant Assuming Simulation of  $P/P_0$  and  $N_{SUB}$  for Full Pressure Transient in Plant.

pass through the vent valves. Also shown on the figure are flow regime transition boundaries (vertical pipe) proposed by Taitel and Dukler.<sup>13</sup> The significant point to be made is that for the expected natural circulation operating conditions (core power, system pressure etc.), bubbly flow is expected to dominate in the plant and in all three scaled facilities even though there are significant differences in operating pressure.

### Critical Mass Flux Scaling

In order to size the leak in a scaled facility that represents the leak in the reference system, the effects of reduced pressure on the critical mass flux must be examined. For the reference case under consideration here, observation of the calculation results indicated that the leak flow was subcooled for the majority of the transient. The procedure used here to examine critical mass flux to employ modified Burnell model with the pressures shown in Figure 2 and the cold leg fluid temperatures shown in Figure 8. In effect then the assumption was made that  $N_{SUB,R} = 1$  and  $P(t)/P_0|_R = 1$  and critical mass flux ( $G^*$ ) as a function of time was calculated for the reference system and each of the scaled facilities.

Figure 10 shows the ratios of critical mass flux and critical mass flux times enthalpy in the scaled systems to those in the reference calculation plotted versus reference time in the plant. As was the case for the property ratio multipliers, it is seen that the critical mass and energy flux ratios are relatively constant values. If it is assumed that the pressure simulation starts at the initiation of two-phase in the plant the ratios are still constant but different numerically than those shown in Figure 10. This of course indicates that a different break size depending on the desired pressure transient simulation will be required in the scaled facilities in order to effect the assumed pressure transient. Note that in a system capable of simulating full pressure, the  $G^*$  and  $G^*h$  ratios would be unity assuming that break size or geometry did not influence the critical mass flux.

It should be noted that the enthalpies and fluid temperatures (from Figure 8) utilized in the construction of Figure 10 are effectively mixed mean temperatures that are based on the reference TRAC plant calculation. As such, the overall effects of vent valve flow, HPI injection and mixing, and loop flow (if any) on the fluid temperature, are accounted for within the framework of the TRAC calculation. One question that can be posed is "assuming that the fluid temperatures represented in Figure 8 are mixed mean (or approximately "hot stream") what might be the effect of cold leg temperature stratification during periods of stalled loop flow on the critical flow?" Although the assumption of stalled cold leg flow may not be realistic for any extended period of time, mixing calculations conducted under this assumption give a bound on the fluid temperature stratification and hence allow one to evaluate the influence of this temperature gradient on critical mass and energy flux.

Mixing calculations for the SRI, UMCP, and MIST facilities and for the plant were conducted using the model developed by Iyer and Theofanous.<sup>14</sup> The HPI flow rate was scaled for all of these calculations using the two-phase criteria posed by Ishii (i.e.  $Q_R = u_{R2} a_R = \sqrt{g_R} a_R$ ). Results are shown in Figure 11 where the hot stream temperature and cold stream temperatures as a function of HPI temperature are plotted against the cold stream depth normalized to cold leg diameter. Results similar to those shown in Figure 11 were calculated at several points in time for each of the facilities under consideration and critical mass and energy fluxes were calculated using both the hot and cold stream temperatures. Results of these calculations for the same HPI temperature (289 K) indicate that in the low pressure facilities, the leak critical mass flux is significantly more sensitive to fluid temperature than is the critical mass flux for the reference plant conditions. The implication of this is that if stalled flow should occur and cold leg fluid temperature stratification develop, the  $G^*$  ratios shown in Figure 10 would no longer remain constant. This could ultimately cause a perturbation to the system pressure and hence result in a deviation from the desired  $P/P_0$  value. One possible method of reducing this sensitivity in the low pressure facilities is to heat the HPI water in order to reduce the magnitude of the stratification (see Figure 11). Heating the HPI water has additional advantages as will be discussed later.

### Break Area Scaling

The information in Figure 10 clearly shows that neither the mass or energy flux in a low pressure facility can be maintained relative to the full pressure case. This simply means that if a leak area is sized to preserve mass inventory then the energy inventory will not be correct relative to the reference or vice versa. In the example shown here, it will be assumed that one desires to preserve mass inventory in the scaled facility (in its own time scale) relative to the reference case. Hence, it is desired that

$$\left. \frac{dM}{dt} \right|_R = 1 \approx \frac{\rho_f R V_R}{t_R}$$

where  $M$  is mass,  $\rho_f$  is liquid density,  $V$  is volume, and  $t$  is time. Substituting expressions for the volume and time ratios gives

$$\left. \frac{dM}{dt} \right|_R = \frac{\rho_f R a_R l_R}{\sqrt{l_R}} = \rho_f R a_R \sqrt{l_R}$$

For simplicity, it is assumed that the leak is the only source of mass depletion. The time rate of change of system mass is then equal to the break mass flux times the break area or solving for the break area,

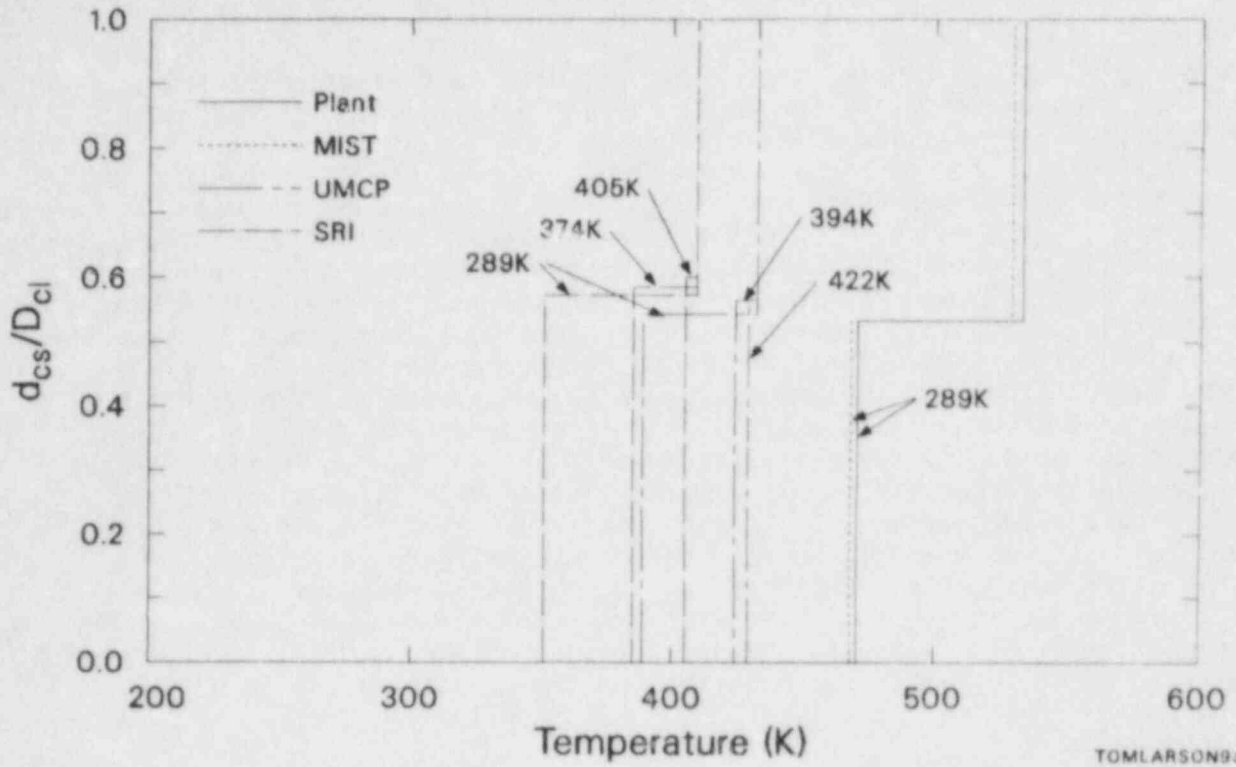


Figure 11. Calculated Cold Leg Stratification

TOMLARSON935-21

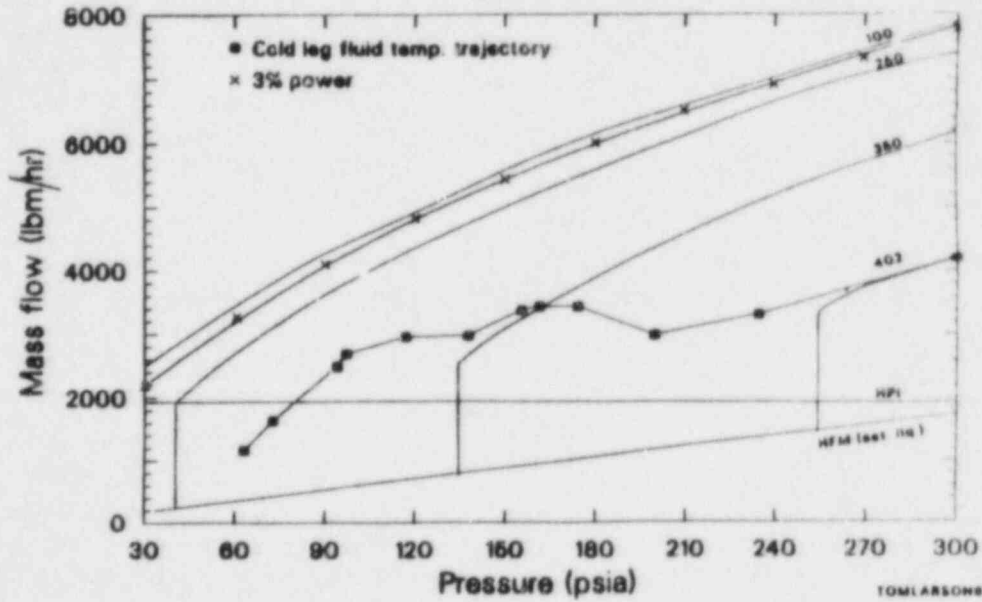


Figure 12. UMCP Equilibrium Curve for  $dM/dt$  Scaled Break ( $A_b = 1.6533E-4 \text{ ft}^2$ ).

TOMLARSON886 B

$$A_{B,R} = \frac{\rho_{fR} a_R \sqrt{g_R}}{G_R^*}$$

Substituting values from Figures 5, 6, and 12 yields the following areas for a leak representing a 10 cm<sup>2</sup> leak in plant scale:

$$A_{B,UMCP} = 0.154 \text{ cm}^2 (1.6653 \text{ E-4 ft}^2)$$

$$A_{B,SRI} = 0.109 \text{ cm}^2 (1.1703 \text{ E-4 ft}^2)$$

These areas correspond to diameters of 44 mm (0.174 in.) and 37 mm (0.146 in.) for the two facilities, respectively.

Several different local scaling effects have been examined. It has been shown that while there are some adverse aspects of operation at reduced pressure relative to typical plant pressures in terms of discontinuities between 1  $\phi$  and 2  $\phi$ , the property group ratio multipliers on the scale equations will be essentially constant if the model pressure transient is such that  $P/P_0|_R = 1$ . For transient experiments, the model

system should be depressurized to a pressure such that  $\psi_{1,R}|_{t=0} \sim \psi_{1,R}|_{t_{final}}$

where  $\psi_1$  are the property group ratios. In effect, it appears that pressure can be scaled through the property group ratios. If the  $\psi_1$  can be maintained, then power scaling can be easily accomplished although there will be a discontinuity between 1  $\phi$  and 2  $\phi$  for reduced pressure operation. Core inlet subcooling may be difficult to scale over the duration of a transient even if the property group ratios are constant. This is due to the fact that  $N_{SUB}$  in the reference may change considerably as a result of break characteristics, HPI mixing, etc. Examination of hot leg flow regimes in the three IST facilities and in the plant for typical natural circulation conditions indicates that bubbly flow is the dominant flow regime. Hence, no adverse consequences of low pressure operation are expected. If  $N_{SUB}$ ,  $P/P_0$ , and mixing are scaled in the model facilities,  $G_R^*$  is expected to be nearly constant for the reference transient examined. If room temperature HPI water is used in the low pressure facilities, it is expected that cold leg fluid temperature stratification during periods of stalled loop flow will have a considerably greater effect on the critical flow than it will in MIST or in a plant. It may therefore be desirable to heat the HPI water in the low pressure facilities to match scaled subcooling in the reference case.

#### METHODOLOGY FOR COMPARISON

It is obviously desirable to be able to compare the results of the low pressure operation facilities to each other and to MIST or to expected plant operation. It is recognized that in the past, large thermal-hydraulic computer codes have been the primary means whereby small scale facility results are extrapolated to larger scale and ultimately to

full scale. Undoubtedly, this philosophy will also be ultimately and eventually be applied in the final analysis of data obtained from the IST program. It must be recognized that funding levels for analysis activities will likely be decreasing in the future and as such, it seems beneficial if any small-scale facility can be operated in a fashion that minimizes the activities necessary to draw inferences to plant space. Possible methods of doing this are discussed below.

### Local Basis

The premise of the scaling criteria presented in Table 2 is that matching phase change and subcooling and with correct geometric similitude, the core outlet quality-density ratio product should be equal to that in the plant reference i.e.

$$\begin{aligned} X \frac{\Delta p}{\rho_g} &= \frac{\Delta p}{\rho_g} \frac{\dot{m}_g}{m} = \frac{\Delta p}{\rho_g} \frac{\rho_g A_g u_g}{\rho_g A_g u_g + \rho_l A_l u_l} = \frac{\Delta p}{\rho_g (\rho_g \alpha u_g + \rho_l (1 - \alpha) u_l)} \\ &= \frac{\Delta p}{\rho_g} \frac{\frac{\rho_g}{\rho_l} j_g}{\frac{\rho_g}{\rho_l} j_g + j_l} \end{aligned}$$

In the low operating pressure facilities, the vapor to liquid density ratio is very small <0.01 and if  $j_g$  and  $j_l$  are of approximately the same order, the expression simply becomes

$$X \frac{\Delta p}{\rho_g} = \frac{j_g}{j_l}$$

and therefore

$$X \frac{\Delta p}{\rho_g} \Big|_{\text{plant}} = \frac{j_g}{j_l} \Big|_{\text{model}}$$

If measurements or estimates of the superficial velocities can be made from the model experiments then the conditions can be transformed to other pressures (i.e., to reference plant conditions) using the scale equations for quality, void, velocity, time, friction, etc. It may be difficult to get good estimates of  $j_g$  and  $j_l$  in the model facilities, however, and thermal-hydraulic computer codes may be necessary to eventually infer these parameters so that transformation of model results to plant space (or any

other space) can be achieved. If this can be reliably done then the following scales will apply:

$$\chi \left. \frac{\Delta p}{\rho_g} \right| = \chi \left. \frac{\Delta p}{\rho_g} \right|_{\text{model}} = \sim \left. \frac{j_g}{j_{g,c}} \right|_{\text{model}}$$

$$\alpha \left. \frac{\Delta p}{\rho_f} \right| = \alpha \left. \frac{\Delta p}{\rho_f} \right|_{\text{model}}$$

$$u = u_{\text{model}} / \sqrt{L_R}$$

$$t = t_{\text{model}} / \sqrt{L_R}$$

$$\Delta P = \Delta P_{\text{model}} / (\rho_R L_R)$$

Therefore local conditions can be transformed to other conditions using these scale equations and the relations for power and subcooling etc.

### Global Basis

The information presented in the previous sections can be used in conjunction with the concept of an equilibrium plot to demonstrate how the scaled facility results may ultimately be related to the reference plant case. Figures 12 and 13 show equilibrium plots for the UMCP and SRI facilities. The equilibrium plots consists of the HPI flow rate and leak flow rates as a function of pressure. A family of curves results for the leak flow since this parameter is also a function of fluid temperature.

If it is assumed that the fluid discharged from the break is heated from the HPI temperature to the leak fluid temperature, then the product of the break flow and this temperature rise at a given pressure and leak temperature defines the amount of power that can be removed by HPI-leak cooling. On Figure 12, this power removal rate curve is depicted by the x and represents 3% scaled power. No allowance has been made for inequalities between the break and HPI flow rates. The assumption has been made that HPI flow is sufficient to sustain leak flow. Also shown on Figures 12 and 13 are cold leg fluid temperature trajectories as determined from  $N_{\text{SUB},R} = 1$  (i.e., from Figure 8).

The interpretation of Figures 12 and 13 is as follows. First, it is noted that with the given fluid temperature trajectory, the operating points all lie far to the right of the 3% power line indicating that the break has the potential to remove in excess of scaled decay heat. Secondly, note that in both cases, the temperature trajectory is such that the expected break flow does not cross over the HPI flow line until very late in the transient. This simply implies that system refill would not commence until near the end of the assumed pressure transient for these cases. Also note that for this break area, core power induced system



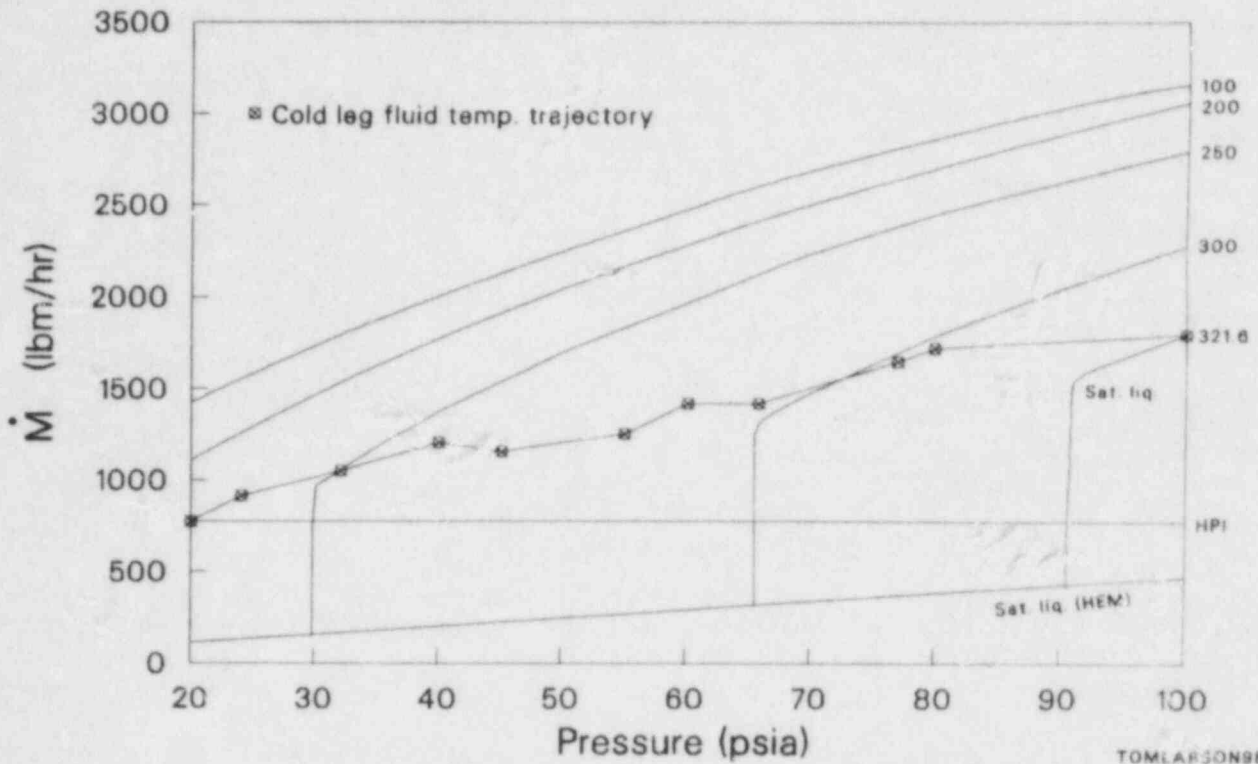


Figure 13. SRI Equilibrium Curve for  $dM/dt$  Scaled Break ( $A_B = 1.1703E-4 \text{ ft}^2$ ).

TOMLARSON885-9

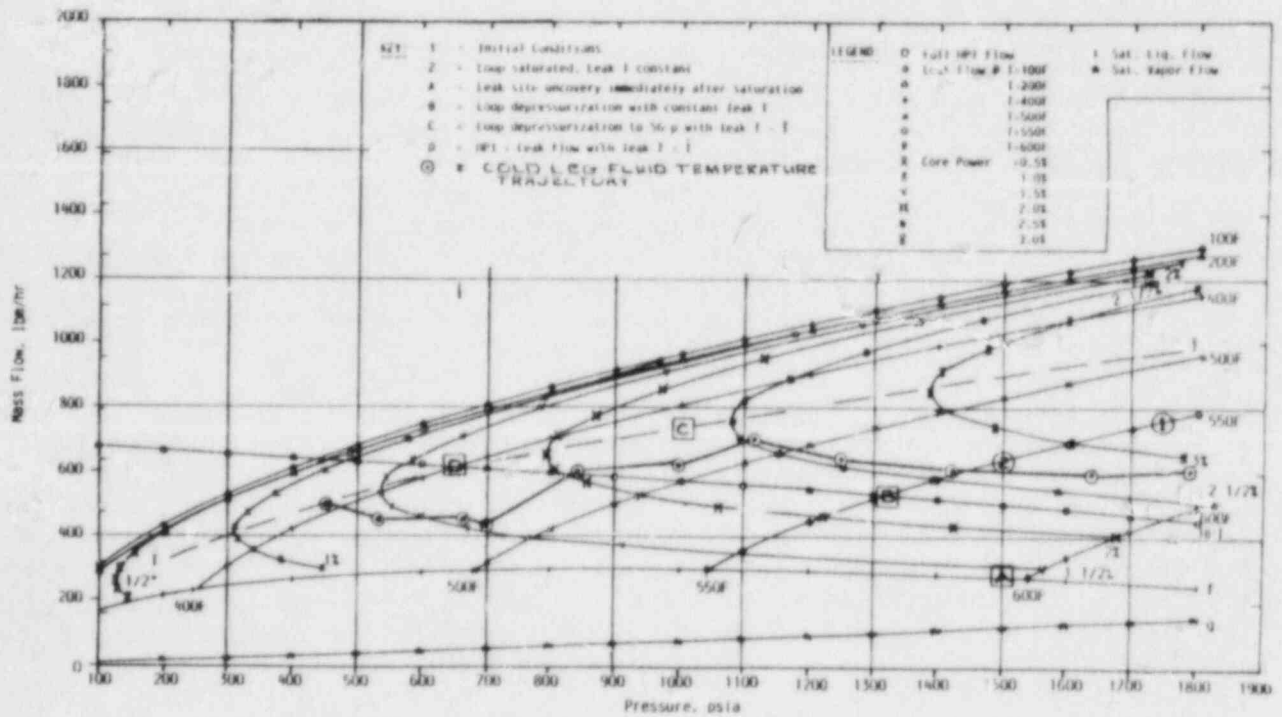


Figure 14. MIST Equilibrium Curve for Nominal Transient -  $10 \text{ cm}^2$  Break and Full HPI (Modified Burnell Model Assuming 90 F HPI and No Heat Loss).

repressurization would not occur since the system conditions are such that energy in excess of the scaled decay heat value can be removed.

Figure 14 is an equilibrium plot drawn for the MIST facility. (An equilibrium plot for the plant case would be the same except for a scale change on the mass flow.) Notice that while the HPI and leak flow lines are similar to those shown on Figures 12 and 13, there are numerous parabolic shaped curves on Figure 14. These parabolic curves define the power which may be removed by HPI-leak cooling. These HPI-leak cooling rates have been converted to scaled full power and plotted for several selected power levels, viz. 0.5, 1.0, 1.5, 2.0, 2.5, and 3.0% of scaled full power. These parabolic shapes indicate that a particular amount of HPI-leak cooling can be obtained for two sets of leak fluid conditions, at a single primary system pressure. This is due to the two ingredient variables, HPI-to-leak temperature rise and leak flow rate. At a single system pressure, the lower leak mass flow rate point on a particular power curve corresponds to a relatively high leak fluid temperature, while the point at the higher leak mass flow rate is obtained at a relatively low leak fluid temperature. For example, at 6.894 MPa, HPI-leak cooling can relieve 2% of scaled full power at a leak flow rate of either 232 or 400 kg/hr. The lower flow rate is achieved at a leak fluid temperature of 541 K; the heatup from (306 K) HPI to this leak temperature is then 235 K, and the product of leak flow rate and fluid heatup is  $232 \times 235 = 64$  kW. At the higher leak flow rate the leak fluid temperature is 444 K, the heatup is 138 K, and again the product of leak flow rate (400 kg/hr) and heatup is 64 kW.

The cold leg fluid temperature trajectory from Figure 8 for the plant is shown on Figure 14. While there are a number of significant points to make about the information in Figure 14, for the present purpose it is important to note that the trajectory crosses over the HPI line at a pressure between 5.5 and 6.2 MPa. This is considerably different from that noted in Figures 12 and 13, i.e., the plant would be expected to start refill at a  $P/P_0$  between 0.4 and 0.5 where the model facilities would, under the assumed circumstances, be expected to start refill at a  $P/P_0$  between 0.2 and 0.25.

A second important point to make about Figures 12 through 14 is that the parabolic HPI-leak cooling curves do not exist for the low pressure operating facilities. Clearly, this is due to the fact that the two-phase power requirement is very low (see Figure 7) and only a small temperature increase (from HPI temperature to leak temperature) is required to remove the core power input. This is significant since one could envision from Figure 14 that if the break were to saturate early in the transient (near point A in Figure 14) then, although the HPI rate exceeds the leak flow, only 1-1/2% of core power could be removed. If loop flow interrupts during this time (hence interruption of primary-to-secondary heat transfer) repressurization could be expected. If the same scenario, i.e., break saturation early in the transient, were to occur in the lower pressure facilities, it appears that repressurization would not necessarily occur since HPI-leak cooling easily can remove in excess of 3% scaled two-phase power. This result suggests that it may be necessary to heat the HPI water

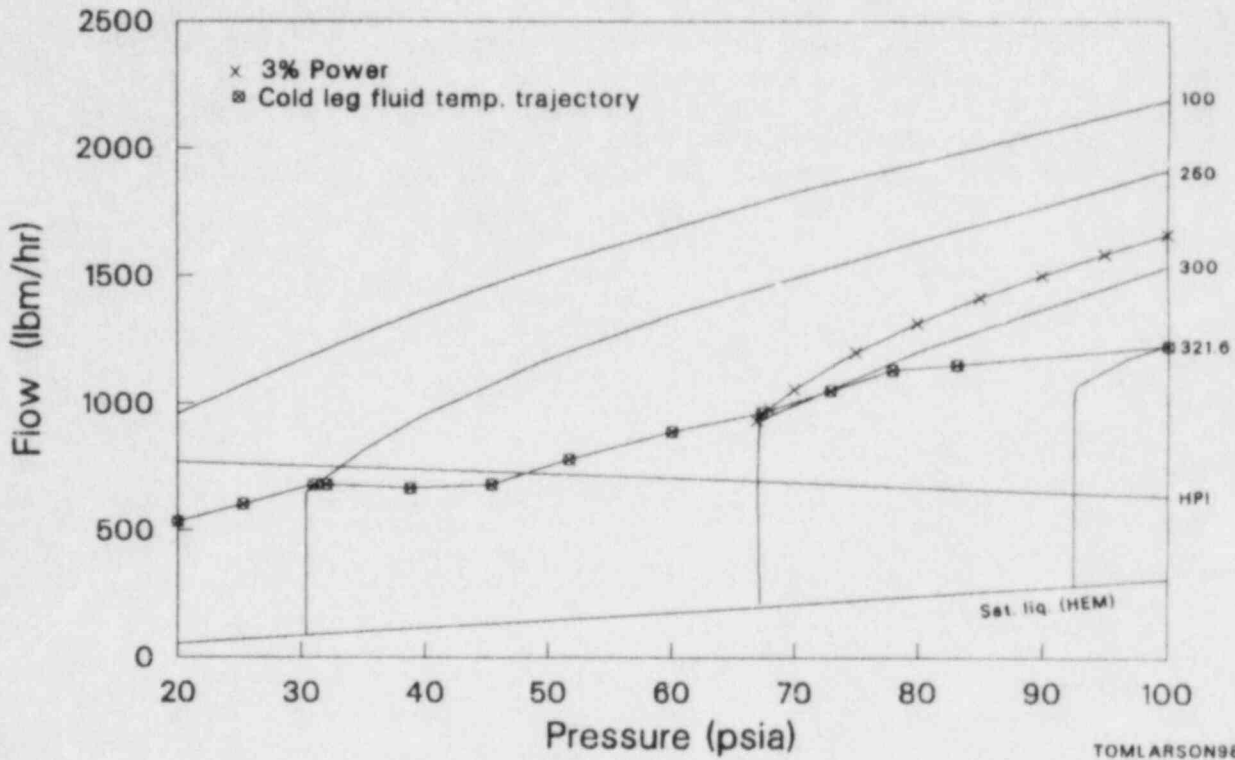
temperature in the low pressure facilities in order to produce parabolic power curves.

The above discussion of behavior in regard to the equilibrium plots is hypothetical since it was assumed that the  $dM/dt|_R = 1$  scaling of the break would more or less force the pressure transient in the model systems to satisfy  $P(t)/P_o|_R = 1$  and  $N_{SUB,R} = 1$ . It is, of course, not known a priori whether such will be the case or not. It is relatively easy to reconstruct the equilibrium plots with a different break area to show that a break area can be found that causes the scaled facility behavior under the assumed circumstances to appear more like the reference plant calculation. Figure 15 shows such a plot for the SRI facility where the break area was scaled so that  $m_{HPI}/(G \cdot A_B)|_R = 1$  at initial conditions. With the given assumptions of  $P(t)/P_o|_R = 1$  and  $N_{SUB,R} = 1$ , Figure 15 shows that the recovery would be expected at a  $P/P_o$  of about 0.48. However, as stated before, there is no more assurance that this break area will force  $P/P_o|_R = 1$  than there was with the  $dM/dt|_R = 1$  scaled break.

It was also noted that the leak-HPI cooling curves were significantly different for the low pressure facilities relative to the reference plant case. This is primarily due to the low values of power required to satisfy the phase change number similarity at low pressure and the assumed room temperature HPI water. Obviously, one could increase the power input to the model facility and eventually cause parabolic shaped curves to appear. Such would of course distort the desired similarity parameters and hence distort the void-quality relationships. As was shown previously, the core power can be "scaled" in a number of different ways and should be parametrically investigated. Another way to cause the appearance of the parabolic shaped power curves to appear is to increase the HPI fluid temperature in the low pressure facilities. If it is assumed that the subcooling in the model HPI fluid is matched relative to the plant at the initiation of HPI, i.e., if

$$\Delta h_{SUB}|_R = \Psi_{SUB}|_R$$

then HPI fluid temperatures for both low pressure facilities can be calculated. Based on the results shown in Figure 8, the property ratio  $\Psi$  from Figures 3 and 4 and an assumed 306 K HPI temperature in the reference plant, required HPI temperatures of 405 K and 422 K are calculated for the SRI and UMCP systems, respectively. It is immediately noted that these temperatures are very near to the cold leg fluid temperatures expected near the end of the postulated transient which could ultimately be a problem unless HPI temperature is changed during the transient. One can also scale the HPI temperature to the ~~reference~~ based on conditions near the end of the transient. Doing so results in calculated HPI temperatures of about 373 K and 394 K for the SRI and UMCP facilities, respectively. Although more typical power removal curves can be produced with these HPI temperatures (373 and 394 K), the nose of the curves lies far to the left of these generated using the warmer HPI fluid. This simply indicates that with the cold HPI fluid, the leak has the ability to remove decay heat in excess of that being input to the system. As stated previously, this can



TOMLARSON985-10

Figure 15. SRI Equilibrium Plot for  $m_{HPI}/(G A_B) \Big|_R = 1$  ( $A_B = 8.066E-5 \text{ ft}^2$ ).

become important during situations where the primary and secondary are decoupled and reference system repressurization results from core energy addition--leak-HPI cooling mismatch.

Figure 15 shows the 3% power curve for the SRI-2 facility (with 405 K HPI temperature). Note that unlike the curves shown in Figure 14 for the high pressure facility, there is no realistic lower solution (at least not in the subcooled regime).

The above discussion shows that the potential for comparison of low pressure scaled facility results to plant behavior via the concept of an equilibrium plot. The ease with which this can be accomplished depends on combinations of local phenomena which influence the ability in the model facility to satisfy the similarity criteria. It was shown that "correct" sizing of the break will most likely be an iterative process. Also, it was shown that it may be necessary to heat the HPI fluid in the low pressure facilities to produce a more typical response on an equilibrium plot.

## CONCLUSIONS

The following conclusions have been drawn:

- o All three of the facilities contributing to the IST program are reasonably well scaled, although neither SRI-2 or UMCP have scaled cores. The steam generators in UMCP are not scaled.
- o Although each facility was designed according to somewhat different criteria and constraints, they are related from a scaling basis by the general similarity laws.
- o In the low pressure facilities the minimum pressure to which the model is depressurized should be such that the property multiplier ratio is approximately equal to the property multiplier ratio at initial conditions. This is equivalent to saying that pressure can be scaled through the property ratio multipliers.
- o If the pressure endpoints are matched but  $P(t)/P_0|_R$  is not approximately unity between the end points, then the property multipliers will not be constant in time.
- o Power scaled using property ratios evaluated at constant pressure results in power larger than ideally scaled power for transient experiments.
- o Since both the phase change number and subcooling number are time dependent variables, it may be difficult to simulate both in a transient since property ratios can change and the reference subcooling can change.
- o If  $N_{SUB,R} = 1$  and  $P(t)/P_0|_R = 1$ , then for subcooled flow (modified Burnell model),

$$\begin{aligned}G^*_R &= 0.38 \\(G^*h)_R &= 0.218\end{aligned}$$

for UMCP and for SRI-2,

$$\begin{aligned}G^*_R &= 0.18 \\(G^*h)_R &= 0.1\end{aligned}$$

- o If model system superficial velocities can be inferred (hot leg for example),  $N_{PCH}$  and  $N_{SUB}$  are properly scaled, and property ratios are known, then model local conditions can be transferred using the scale equations for velocity, time, friction, etc.
- o Because of low pressure considerations, scaling the break to require  $dM/dt|_R = 1$  will probably not produce an equilibrium plot similar to that in MIST or the reference plant.

- o Parametric experiments will be necessary to determine break area, and sensitivity of results to the subcooling and phase change number.
- o It may be necessary to heat the HPI fluid in the low pressure facilities in order to produce equilibrium plots (and preserve phenomena) more typical of those generated for the reference system.
- o Direct inference of results to plant behavior may be difficult without use of code calculations because of the above complications.

## REFERENCES

1. IST Contract Modification No. 5, Contract Among the Babcock & Wilcox Company and Electric Power Research Institute and the U.S. Nuclear Regulatory Commission, Contract No. NRC-04-83-168, RP 2399-1, December 1984.
2. Multiloop Integral Systems Test (MIST) Facility Specification, Babcock & Wilcox Company Document, RDD:84:4091-01-01:01, October 1983.
3. R. L. Kiang and J. P. Sursock, The EPRI Facility at SRI: Description and Connection with IST Program, presentation given at IST Program Coordination Meeting No. 2, Bethesda, Maryland, April 3-4, 1985.
4. D. W. Sallet et al., Final Design Report for the UMCP 2x4 B&W Simulation Loop, Department of Chemical and Nuclear Engineering, Nuclear Engineering Program, College of Engineering, University of Maryland, College Park, Maryland, August 1984.
5. A. N. Nahavandi et al., "Scaling Laws for Modeling Nuclear Reactor Systems," Nuclear Science and Engineering, Vol. 72, November 1982, pp. 75-83.
6. L. J. Ybarrondo et al., "Examination of LOFT Scaling," ASME Winter Annual Meeting, Paper No. 74-WA/HT53, New York, New York, November 1984.
7. T. K. Larson et al., "Scaling Criteria and an Assessment of Semiscale Mod-3 Scaling for Small Break Loss-of-Coolant Transients," NRC/ANS Meeting on Basic Thermal Hydraulic Mechanisms in LWR Analysis, EGG-M-21082, September 14-15, 1982.
8. L. E. Hochreiter et al., Scaling Considerations for Flecht-SEASET, NUREG/CR-2401, February 1983.
9. M. Ishii and I. Kataoka, Similarity Analysis and Scaling Criteria for LWRs under Single- and Two-Phase Natural Circulation, ANL-83-32, NUREG/CR-3267, March 1983.
10. G. Kocamustafaogullari and M. Ishii, Scaling Criteria for Two-Phase Flow Natural and Forced Convection Loop and Their Application to Conceptual 2x4 Simulation Loop Design, ANL-83-61, NUREG/CR-3420, May 1983.
11. R. L. Kiang, "Scaling Criteria for Nuclear Reactor Thermal Hydraulics," 1984 National Heat Transfer Conference, Taipei, Taiwan, October 1984.
12. T. D. Knight (LANL) ltr to T. K. Larson (INEL), "TRAC Plant Calculations," Q-9-85-L-480, July 25, 1985.



13. Y. Taitel and A. E. Dukler, "Modeling Flow Pattern Transitions for Steady Upward Gas-Liquid Flow in Vertical Tubes," AICHE Journal, 2, 3, May 1980.
14. K. Iyer and T. G. Theofanous, "Flooding Limited Thermal Mixing: The Case of High- $F_r$  Injection," to be presented at the Third International Topical Meeting on Reactor Thermal Hydraulics, October 15-18, Newport, Rhode Island, 1985.

CONTINUING INTEGRAL TESTING CAPABILITY-SCALING  
STUDY APPROACH AND PRELIMINARY RESULTS

K. G. Condie, C. B. Davis, T. K. Larson, J. S.  
Martinell, and G. E. McCreery\*

Idaho National Engineering Laboratory  
EG&G Idaho, Inc.

\* University of California, Santa Barbara

ABSTRACT

The United States Nuclear Regulatory Commission (NRC) in assessing their future research needs for both separate effects and integral experiments has requested EG&G Idaho, Inc. to conduct a review to identify and technically evaluate potential concepts that will maintain future capability to conduct integral thermal-hydraulic facility experiments of interest to reactor safety. In the following paper, reactor transients and thermal-hydraulic phenomena of importance (based on probabilistic risk assessment and the International Code Assessment Program) to reactor safety are examined and identified. Transients identified included decrease in reactor coolant inventory (large and small break loss-of-coolant transient), increase in heat removal (steam line breaks), decrease in heat removal (loss-of-heat-sink), and reactivity transients (anticipated transients without scram). Commonly used established methodologies for the scaling and design of small integral thermal-hydraulic testing facilities are identified and examined to ascertain advantages and disadvantages of each method and to identify potential concepts for scaling evaluations. Concepts selected included; full height, full pressure with water as the working fluid (such as the existing MIST and Semiscale facilities); reduced height, full pressure with water as the working fluid; reduced height, reduced pressure with water as the working fluid (such as the existing SRI-2 and University of Maryland facilities), and reduced height, full scaled pressure with Freon as the working fluid. Analysis is conducted to examine the scaling of various phenomena in each of the selected concepts. Analysis performed to date included examination of natural circulation, two-phase flow in pumps, critical flow, flow regimes, pressure drop, flooding behavior, void-quality relationships, and heat transfer in the core and steam generator. Results generally suggest that a facility capable of operating at typical reactor operating conditions will scale most phenomena reasonably well. Although many phenomena in facilities using Freon or water at nontypical pressure will scale reasonably well, those phenomena that are heavily dependent on quality (heat transfer or critical flow for example) can be distorted. Furthermore, relation of data produced in facilities operating with nontypical fluids or at nontypical pressures to large plants will be a difficult and time consuming process.

## INTRODUCTION

The United States Nuclear Regulatory Commission (NRC) is currently assessing their future research needs, including both separate effects and integral experiments, as part of an overall effort to examine the need for continuing experimental capability. EG&G Idaho, Inc. has been requested by the NRC to conduct a review to identify and technically evaluate potential concepts that will allow NRC ability in the future to conduct integral thermal-hydraulic facility experiments of interest to reactor safety. The study has been requested in recognition of the fact that existing NRC experimental research programs will be completed in the near future and the facilities associated with these programs will be shutdown. The evaluation has the following objectives:

1. Identification of the reactor transients of major importance to safety issues.
2. Identification of phenomena within these selected transients that can be of significant importance or influence.
3. Identification and review of existing and commonly used scaling methodologies and criteria employed in the design of small scale integral facilities for the purpose of evaluating advantages and disadvantages of each method.
4. Based on the results of Item 3), identify viable concepts for meeting NRC needs for a continuing experimental capability.
5. Perform a technical evaluation of the "concepts" identified in 4) to evaluate their ability to preserve the phenomena identified in 2) and conduct transients of the type identified in 1).
6. Provide background, technical information, cost/benefit analyses, and recommendations to assist NRC in making decisions on continuing experimental capability.

One of the general rules of the present study was that major use of any facility concept will be for the simulation of plant transients and that minimization of problems associated with drawing inferences about plant behavior from scaled facility behavior is desirable. It is recognized that in the past, large thermal-hydraulic computer codes have been the primary means whereby small scale facility results are extrapolated to larger scale and ultimately to full scale. Undoubtedly, this philosophy will also ultimately and eventually be applied in the final analysis of data obtained from any facility concept adopted by NRC to fulfill their continuing experimental capability needs. It must be recognized that funding levels for analysis activities will likely be decreasing in the future and as such, it seems beneficial if any small-scale facility concept can be designed and operated in a fashion that minimizes the activities necessary to draw inferences to plant space. Furthermore, a potential intended use of a continuing experimental capability concept is for providing data to help in the decision making processes that may be necessary during operating plant transients. Here again, minimization of considerations in drawing inferences to plant space is desirable.

The remainder of this report presents details of work completed to date in the conduct of the subject study. Although the study is not yet complete, the attached information represents the strategy to be employed in the overall evaluation. The initial emphasis of the study was concentrated on transients and phenomena pursuant to the Westinghouse and Babcock & Wilcox reactor designs and the following information represents such. Work related to the Combustion Engineering and General Electric designs will be performed in FY-86.

The remainder of this report contains the following information. First, the logic and methods used in the identification of significant transients and thermal-hydraulic phenomena are given. Also included, is a discussion of the selection of a base plant for the Westinghouse and Babcock & Wilcox designs so that geometric parameters are available for use in generating scaled facility concepts. Second, existing documented methods and criteria for scaling integral facilities are presented. These methods are reviewed to ascertain advantages and disadvantages and to help identify plausible concepts of designing scaled integral thermal-hydraulic facilities. The concept of minimum dimensions for scaled facilities is discussed and tabular geometric data for possible scaled integral facility concepts are given. Third, local scaling analysis methods used in the evaluation of the concepts presented are discussed and results given. Conclusions are drawn from this analysis about the scaleability of the concepts evaluated and the ultimate significance of this scaleability.

## DATA BASE SELECTION AND PHENOMENA IDENTIFICATION

Four distinct tasks were performed in the selection of the data base and identification of the important thermal-hydraulic phenomena for Westinghouse and Babcock and Wilcox (B&W) reactors. First, the thermal-hydraulic transients that the experiment facility should be able to simulate were identified. Second, the data base of thermal-hydraulic calculations for each potential base plant was reviewed. (The base plant is the reference reactor to which the facility will be scaled.) The thermal-hydraulic data base consisted of thermal-hydraulic transient calculations using advanced computer codes. The computer calculations may be the best representation of plant behavior during many transients. Thus, the code calculations could serve as plant "data" to evaluate the different scaling concepts. Third, the base plants were selected based on considerations of plant typicality and the available thermal-hydraulic data base. Fourth, the important phenomena occurring in the selected thermal-hydraulic transients were identified. The ability of the scale models to reproduce the important phenomena is a major factor in the ultimate selection of a scaling concept. The four tasks are described in detail in subsequent sections.

### Transient Selection

Five transients were identified that the experiment facility should be able to simulate. These transients were identified based on potential significance relative to reactor safety and the production of a wide range of thermal-hydraulic phenomena. The thermal-hydraulic transients of potential significance to reactor safety were obtained from two sources: safety analysis reports (SARs)<sup>1</sup> and probability and risk assessments (PRAs).<sup>2,3</sup>

The reviews of both the SAR events and the risk-dominant events yielded similar lists of significant thermal-hydraulic transients. These transients included LOCA, which is a subset of decrease in reactor coolant inventory, ATWS, and total loss of heat sink, which is a subset of decrease in heat removal by the secondary system. Transients initiated by an increase in heat transfer to the secondary system, such as a steam line break, are also of potential interest. These significant transients are summarized in Table 1. Two LOCA transients, a small-break LOCA (SBLOCA) and a large-break LOCA (LBLOCA), are listed in Table 1. While the SBLOCA is more significant relative to risk, the LBLOCA was included because of unique thermal-hydraulic phenomena produced in such a transient.

### Thermal-Hydraulic Data Base

The data base of thermal-hydraulic calculations for Westinghouse, Babcock and Wilcox (B&W), Combustion Engineering, and General Electric were reviewed. The calculations may be the best representation of the plant behavior during certain transients. The calculations were used in the identification of the important thermal-hydraulic phenomena, to be discussed later, that occur in the significant transients. Furthermore, the thermal-hydraulic calculations may be useful to evaluate different scaling rationals. Thus, the availability of thermal-hydraulic calculations is one of the criteria used in the selection of the base plants.

A survey of the thermal-hydraulic plant calculations performed by Argonne National Laboratory, Brookhaven National Laboratory, Idaho National Engineering Laboratory, Los Alamos National Laboratory and Sandia National Laboratories was conducted. Only calculations performed with advanced computer codes, such as RELAP5<sup>4</sup> or TRAC<sup>5</sup> were considered. References 6 through 11 were the primary data sources for determining the available plant thermal-hydraulic calculations.

The results of the survey of the thermal-hydraulic calculations for Westinghouse and B&W reactors indicated that the following plants were potential base plants: H. B. Robinson Unit 2, Zion Unit 1, and Seabrook Unit 1 (Westinghouse) and Oconee-Unit 1, Three Mile Island (TMI) Units 1 and 2, and Bellefonte Unit 1 (B&W). Table 2 lists the potential base plants, the significant thermal-hydraulic transients, the availability of corresponding thermal-hydraulic calculations, and a reference for the available calculations. For Westinghouse, the thermal-hydraulic data base was judged adequate for H. B. Robinson, Zion, and Seabrook. The Zion data base was the most extensive. For B&W, the thermal-hydraulic data base was judged adequate for Oconee and TMI and poor for Bellefonte. A slight preference for the base plant was given to Oconee over TMI because Oconee was selected for analysis by the Pressurized Thermal Shock program. Consequently, the Oconee results were generally more recent, and the Oconee models were quality assured.

#### Base Plant Selection

Paper models of potential experiment facilities will be used to evaluate different scaling rationals. A base plant is the reference reactor to which the paper models are scaled. Two criteria were used in the selection of the base plants: 1) the data base of the thermal-hydraulic calculations and 2) plant typicality. The thermal-hydraulic data base for the potential base plants was described in the previous section. The criterion of plant typicality was based on the idea that the experiment facility should be able to address safety issues as they arise and will probably be related to actual plant transients which are more likely to occur in the most common types of plants. Thus, any new facility should be scaled to a typical plant.

A survey of plants with an operating license, plants near operation including those with a low power license or in power ascension, and plants under construction in the United States was conducted. Plants that had been cancelled were not considered. The survey was based on information presented in References 26 through 28. Based on the survey results and the available plant calculations Seabrook Unit 1 was selected for the Westinghouse base plant and Oconee for the B&W base plant.

#### Phenomena Identification

The important thermal-hydraulic phenomena were identified in the significant transients relative to reactor safety to determine the phenomena that are important to scale in the experiment facility. The important thermal-hydraulic phenomena in the significant transients are summarized in Table 3 for Westinghouse and Table 4 for B&W. The thermal-hydraulic phenomena were based on code assessment matrices proposed

TABLE 1 SIGNIFICANT THERMAL-HYDRAULIC TRANSIENTS

Transient Category	Transient
Decrease in reactor coolant inventory	SBLOCA LBLOCA
ATWS	Loss of feedwater with failure to scram
Decrease in heat removal by the secondary system (total loss of heat sink)	Station blackout
Increase in heat removal by the secondary system	Steam line break

TABLE 2 SUMMARY OF THERMAL-HYDRAULIC DATA BASE

<u>Transient Category</u>	<u>Calculations Available?</u>					
	<u>Westinghouse</u>			<u>B&amp;W</u>		
	<u>H. B. Robinson</u>	<u>Zion</u>	<u>Seabrook</u>	<u>Oconee</u>	<u>TMI</u>	<u>Bellefonte</u>
Decrease in Reactor Coolant Inventory						
SBLOCA	Yes <sup>12</sup>	Yes <sup>13</sup>	Yes <sup>18</sup>	Yes <sup>21</sup>	Yes <sup>23</sup>	No
LBLOCA	No	Yes <sup>14</sup>	Yes <sup>19</sup>	No	No	No
Decrease in Heat Removal By The Secondary System/Total Loss Of Heat Sink	Yes <sup>12</sup>	Yes <sup>15</sup>	Yes <sup>20</sup>	Yes <sup>22</sup>	Yes <sup>22</sup>	Yes <sup>25</sup>
Increase in Heat Removal By The Secondary System/ Steam Line Break	Yes <sup>12</sup>	Yes <sup>16</sup>	No	Yes <sup>21</sup>	Yes <sup>24</sup>	No
ATWS	No	Yes <sup>17</sup>	No	No	No	No







by the Committee on Safety of Nuclear Installations. The transients listed in the tables were previously judged significant to reactor safety. The phenomena not identified as high or medium importance were judged to be unimportant. The importance of the thermal-hydraulic phenomena was evaluated subjectively based partly on a review of the thermal-hydraulic calculations described previously and partly based on knowledge of related calculations, experiments, and topics of research and is affected by the assumed sequence of the transient. For example, pump behavior was listed as of low importance during a small-break LOCA because the reactor coolant pumps would normally be tripped early in the transient. The pump behavior would become highly important if the pumps were not tripped.

## SCALING METHODOLOGIES AND FACILITY CONCEPTS

This section summarizes the scaling relationships which were used to develop the several facility concepts investigated during this study. The ground rules of this study dictated the use of those scaling methodologies which have been published and currently understood, therefore, the development of these methodologies are not presented in this documentation. Advantages and disadvantages of the various concepts are briefly discussed as they apply on a systems basis. Tabular data which describe possible scaled integral facilities are presented for comparison.

### Generalized Scaling Relationships

The work of Ishii et al.,<sup>29,30,31</sup> has provided the development of the scaling relationships which were used in this study. Ishii has developed these scaling relationships for single and two-phase flow for both natural and forced circulation. It can be shown that the so-called "linear scaling" laws of Carbiener and Cudnik<sup>32</sup> and Nahavandi<sup>33</sup> and the "time preserving volume scaling" laws of Nahavandi<sup>33</sup> are logical subsets of the more general Ishii relationships.

Table 5 presents a summary of the scaling relationships developed by Ishii for single-phase forced convection and two-phase natural circulation. The subscript R denotes the ratio between the model and plant and the subscript o denotes a reference component, generally selected to be the core.

There are certain assumptions and limitations which are inherent in the relationships shown in Table 5. For the single-phase forced circulation relationships, these include:

1. One-dimensional flow with negligible turbulent components.
2. The fluid is noncompressible.
3. Buoyancy forces are negligible.
4. The plant rod diameter and pitch are preserved in the model.

TABLE 5. PARAMETER RATIOS FOR SINGLE-PHASE FORCED AND TWO-PHASE NATURAL CIRCULATION.

Parameter	Symbol	Parameter Ratios	
		1 $\phi$ Forced Circulation	2 $\phi$ Natural Circulation
Length	$L_0 R$	$L_{0R}$ Defined	$L_{0R}$ Defined
Diameter	$D_0 R$	$D_{0R}$ Defined	$D_{0R}$ Defined
Area	$A_0 R$	$D_{0R}^2$	$D_{0R}^2$
Volume	$V_0 R$	$D_{0R}^2 L_{0R} = A_{0R} L_{0R}$	$D_{0R}^2 L_{0R} = A_{0R} L_{0R}$
Core $\Delta T$	$\Delta T_0 R$	$\Delta T_{0R}$ Defined	$(\rho_g/\rho_{lg})_R \left(\frac{\rho}{\rho_g}\right)_R n_{lg} R / C_p R$
Velocity	$U_0 R$	$\sqrt{L_{0R}}$	$\sqrt{L_{0R}}$
Time	$t R$	$\sqrt{L_{0R}}$	$\sqrt{L_{0R}}$
Gravity	$g R$	1	1
Power/Volume	$\dot{q}_0 R$	$1 / \sqrt{L_{0R}} \Delta T_{0R} \rho_{0R} C_{pR}$	$1 / \sqrt{L_{0R}} (\rho_g/\rho_{lg})_R \rho_R n_{lg} R$
Heat Flux	$\dot{q}_0 R$	$1 / \sqrt{L_{0R}} \Delta T_{0R} \rho_{0R} C_{pR}$	$1 / \sqrt{L_{0R}} (\rho_g/\rho_{lg})_R \rho_R n_{lg} R$
Core Power	$\dot{Q}_0 R$	$A_{0R} \sqrt{L_{0R}} \Delta T_{0R} \rho_{0R} C_{pR}$	$A_{0R} \sqrt{L_{0R}} (\rho_g/\rho_{lg})_R \rho_R n_{lg} R$
Rod Diameter	$RD R$	1	1
Number Rods	$NR R$	$A_{0R}$	$A_{0R}$
Flow Rate	$\dot{M}_0 R$	$A_{0R} \sqrt{L_{0R}} \rho_{0R}$	$A_{0R} \sqrt{L_{0R}} \rho_{0R}$
$\Delta H$ Subcooling	$\Delta H_{sub} R$	—	$(\rho_g/\rho_{lg})_R n_{lg} R$
$\Delta T$ Subcooling	$\Delta T_{sub} R$	$\Delta T_{0R}$	—
Pump Head	$\Delta H_d R$	$L_{0R}$	—
Friction No.	$F_1 R$	1	1

200 7000-00

5. Geometric scaling is maintained between each component and the reference component, i.e.,  $\left(\frac{\epsilon_i}{\epsilon_0}\right)_R = 1$  where  $\epsilon$  is some geometric parameter and subscripts  $i$  and  $0$  refer to the individual and reference component, respectively.

The parameter ratios presented in Table 5 include both geometry ratio terms and property ratio terms. The property ratio terms provide the scaling basis for using different fluids and/or operating conditions between the model and the plant. Note that if all the property ratios are unity, i.e., if the same fluid and operating conditions are used in the plant and model, then the single-phase and two-phase relationships are identical. In these general relationships, note that both velocity and time are distorted by the square root of the length ratio. Note also that the core  $\Delta T_{OR}$  can be specified independent of geometry scaling where dissimilar fluids or operating conditions are used. Since the core power ratio is directly proportional to the core  $\Delta T_{OR}$ , the facility power requirements may be reduced by using dissimilar fluids and/or operating conditions.

#### Full Height Volume and Linear Scaling Concepts

As mentioned earlier, the scaling concepts sometimes referred to as "full height-volume scaled" and "linear scaled" are subsets of the general Ishii scaling. Table 6 presents the parameter ratio relationships for these two concepts assuming the use of the same fluid and operating conditions between the plant and model.

For the first case shown in Table 6, the  $L_{OR}$  is unity and the other ratios are presented in terms of  $L_{OR}$ . This full height volume scaled concept has been widely used as the scaling basis for thermal-hydraulic experiment facilities including Semiscale, MIST, and ROSA-IV. The reference to volume scaling for this concept comes from the fact that the core power scales as the volume scale.

Many of the advantages of this concept are obvious which include:

1. 1:1 velocity scaling.
2. Real time scaling.
3. 1:1 heat flux scaling.
4. 1:1 power to volume scaling.

However, it is generally not possible to satisfy the Friction No. ratio requirement of unity and still maintain the area ratio,  $\left(\frac{A_i}{A_0}\right)_R$ , at unity.

The friction No. is defined as  $F_i = \frac{f_i L_i}{D_i} + K_i$ .

TABLE 6. PARAMETER RATIOS FOR FULL HEIGHT AND LINEAR SCALING.

Parameter	Symbol	Parameter Ratios	
		Full Height	Linear
Length	$L_{OR}$	1	$L_{OR}$ Defined
Diameter	$D_{OR}$	$D_{OR}$ Defined	$L_{OR}$
Area	$A_{OR}$	$D_{OR}^2$	$L_{OR}^2$
Volume	$V_{OR}$	$D_{OR}^2 (1) = A_{OR} = V_{OR}$	$L_{OR}^3$
Core $\Delta T$	$\Delta T_{OR}$	1	1
Velocity	$U_{OR}$	1	$\sqrt{L_{OR}}$
Time	$t_{OR}$	1	$\sqrt{L_{OR}}$
Gravity	$g_{OR}$	1	1
Power/Volume	$\dot{q}_{OR}$	1	$1 / \sqrt{L_{OR}}$
Heat Flux	$\dot{q}_{OR}$	1	$1 / \sqrt{L_{OR}}$
Core Power	$\dot{Q}_{OR}$	$V_{OR}$	$L_{OR}^{3/2}$
Rod Diameter	$RD_{OR}$	1	1
Number Rods	$NR_{OR}$	$V_{OR}$	$L_{OR}^3$
Flow Rate	$\dot{M}_{OR}$	$V_{OR}$	$L_{OR}^{3/2}$
$\Delta H$ Subcooling	$\Delta H_{sub OR}$	1	1
$\Delta T$ Subcooling	$\Delta T_{sub OR}$	1	1
Pump Head	$\Delta H_G_{OR}$	1	$L_{OR}$
Friction No.	$F_{f OR}$	1	1

222222-100

For the piping, the  $(L_i/D_i)_R$  cannot be maintained at unity for this concept resulting in excessive pressure losses in the piping sections of the model. In existing experimental facilities based on the full height concept, the piping diameters have generally been increased from the ideal scaled value to minimize the pressure drop distortion. This compromise on pipe diameter causes distortions in the local velocity and volume scaling which must be accounted for.

For this study, we define "linear scaling" for the case when  $L_{OR}/D_{OR} = 1$  indicating a "xerox" copy of the plant. Other references to linear scaling have also required the velocity ratio,  $U_{OR}$ , to be unity also, but we have not required this restriction. The second case shown in Table 6 applies to the linear scaled concept. By setting the  $D_{OR} = L_{OR}$  the earlier limitation to one-dimensional flow is removed.

This concept has some potential impracticalities which can best be illustrated by looking at a model of a 3000 Mwt LPWR with a 12 ft long core and approximately 50,000 fuel rods. If we arbitrarily select a length scale,  $L_{OR}$ , of 0.1 then the ideal model would result in the following:

Heater rod length	14.4 in.
Number of heated rods	500
Core power	9.5 MW
Heat flux ratio	3.2
Velocity ratio	0.32

Obviously, the later two items would result in core boiling at conditions even approaching full power. The high heat flux ratio is a direct result of the small length ratio.

The high power requirements required for this scaling concept could be considerably reduced by considering a system of low pressure water or perhaps a fluid other than water and/or using a core  $\Delta T_0$  ratio less than unity. The large number of heater rods required results from the area ratio. If one chose to not directly scale the core and to consider only the net power requirements, the number of rods could also be reduced. The affect of these distortions on local phenomena would then have to be considered.

#### Fluid Property Ratios

The motivation to use different fluids or operating conditions in the model than in the plant comes from the desire to operate at lower pressure which may reduce facility costs and increase safety. Freon and low pressure water have both been used as a working fluid for thermal-hydraulic experiments. Freon has a much lower critical pressure than water and is usually scaled on the basis of the critical pressure ratio  $P/P_c$ . The scaling of low pressure water to high pressure water is not as straight forward, but can be scaled on the basis of the initial ratio of the model

to the plant. The initial model pressure can be selected to provide the most constant property ratios over the plant pressure range of interest. For the system scaling the property groups of interest are given in Table 5 and include:

Saturated liquid density ratio  $(\rho_f)_R$

Ratio of saturated liquid density to density difference ratio  $(\rho_f/\rho_{fg})_R$

Heat capacity ratio  $(C_p)_R$

Heat of vaporization ratio  $(h_{fg})_R$

Additional ratios of other properties such as viscosity and surface tension are also important when investigating local phenomena. Figure 1 shows the above property ratios for Freon 11 as a function of the critical pressure ratio. Figure 2 shows the same ratios for water over the pressure range of interest for PWR transients using a pressure ratio of

$$\frac{P_m}{P_p} = \frac{435}{2170} = .200$$

The Freon-11 property ratios shown are fairly independent of the critical pressure ratio whereas the low pressure water ratios, especially  $(\rho_g/\rho_{fg})_R$  vary considerably with pressure.

#### Selected Scaling Concepts

To provide a basis for the evaluation of the local phenomena scaling, four scaling concepts were used to develop ideal facility configurations for models based on both the B&W Oconee plant and the Westinghouse Seabrook plant. The four concepts agreed upon by NRC were as follows:

- A. Full Height Full Pressure Water (FHFPW)
- B. Reduced Height Reduced Pressure Water (RHRPW)
- C. Reduced Height Full Pressure Water (RHFPW)
- D. Reduced Height Full Scaled Pressure Freon (RHFPH)

Concept A (FHFPW) was selected for evaluation because of the numerous facilities which have been built using this concept. No new configurations were developed for this concept using instead the MIST facility for the B&W plant and Semiscale for the Westinghouse plant.

Concept B (RHRPW) was also motivated by existing facilities, specifically the facilities at University of Maryland and at SRI. The lower pressure and size also offers potential for reduced cost of construction and operation.



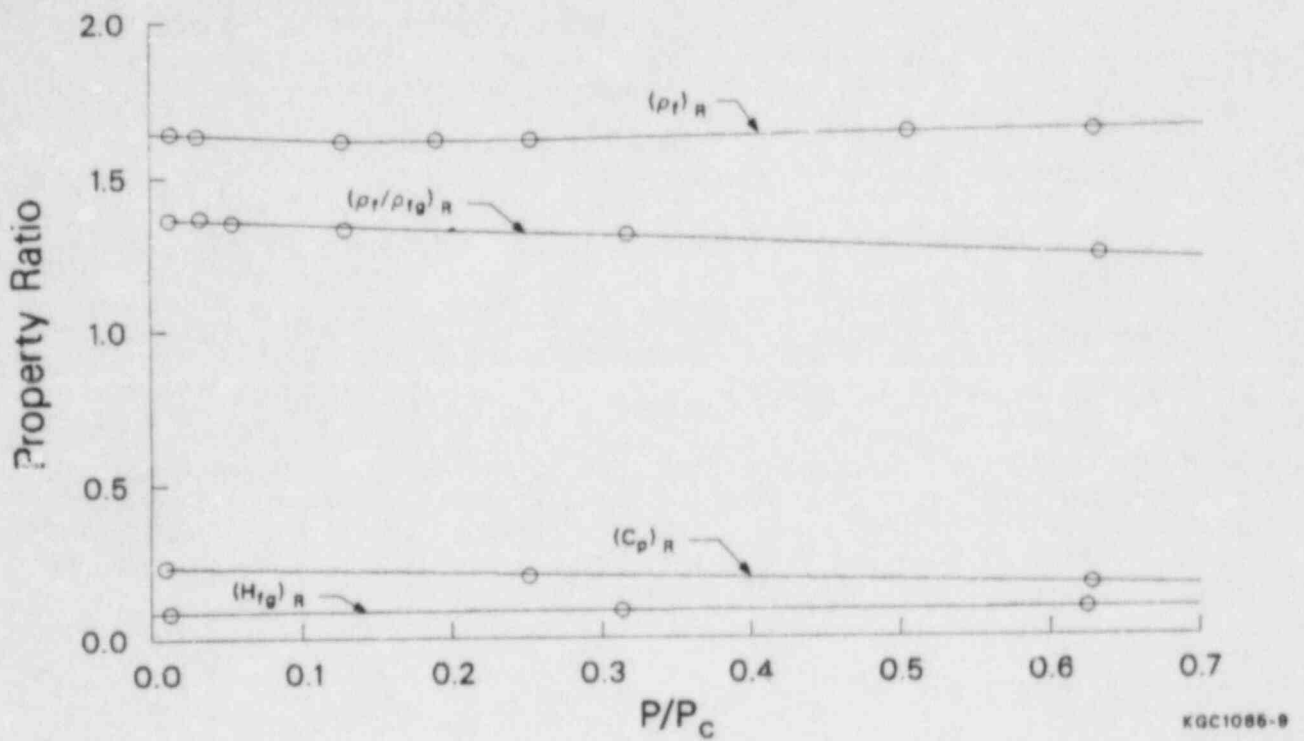


Figure 1. Property ratios for FREON-11 and water.

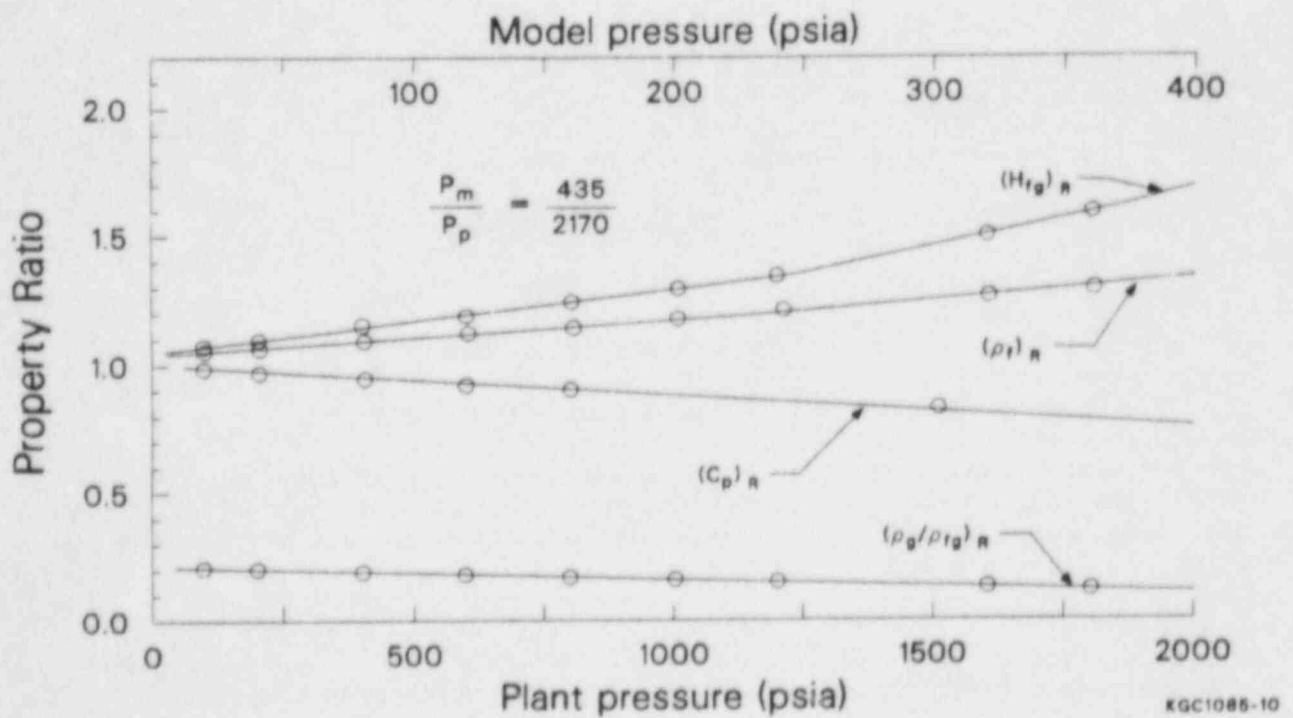


Figure 2. Property ratios for low and high pressure water.

Concept C (RHFPW) was considered as a possibility to reduce the problems introduced by unlike fluid and operating conditions, to potentially lower costs by reducing height and volume, and to provide a closer to ideal pressure drop distribution in the primary system piping.

Concept D (RHFPF) was selected to allow the evaluation of phenomena associated with using a nonwater medium. The use of Freon allows for the use of the smallest system investigated, potentially lowering construction costs. However, these costs may be offset by expense of specialized Freon handling systems.

Under the ground rules of this study, any Continued Experiment Capability would be required to address the full range of postulated plant transients and consequently would be required to scale the full power steady state operating conditions in the plant, thus the single-phase forced circulation relationships are utilized in the development of possible model configurations.

Under the assumption that the smaller the facility the lower would be the construction costs, it was desirable to provide some criteria for selection of minimum model dimension above which most important local phenomena would be preserved in the model. The flooding criteria in the vertical pipe section was used for selection of minimum diameter ratio because of the importance of the flooding in the B&W hot leg. Figure 3 shows a plot of critical superficial velocity  $j_{g,crit}$  as a function of diameter for water and

Freon at various pressures. For small diameters, the critical velocity is shown to be a function of diameter as indicated by the Wallis flooding criteria. Above some minimum diameter the critical velocity is constant with respect to diameter as described by the Kutateladze correlation. The transition point between these two curves is approximately described by a Bond number criteria of 40, where

$$N_{Bond} = \left[ D \frac{\rho_f g}{\sigma g_c} \right]^{1/2}$$

Setting  $N_{Bond} = 40$  and solving for  $D$  gives a criteria for minimum pipe size. Based on this criteria the required minimum diameter gets larger for a lower pressure.

Table 7 provides a summary of the characteristics of a potential ideal model for each of the four scaling concepts discussed, based on the B&W Oconee plant. The MIST Facility is used for the FHFPW concept. Table 8 presents a similar summary based on the Westinghouse Seabrook plant. The Semiscale facility is used for the FHFPW concept.

This discussion has shown the almost endless possibilities for a new facility configuration. There is obviously no one configuration which will provide simulation of controlling phenomena for all important transients. Using the largest possible system with the same fluid and operating conditions as the plant would provide data requiring the least amount of analysis to relate to plant phenomena and would provide the largest range

Concept C (RHFPW) was considered as a possibility to reduce the problems introduced by unlike fluid and operating conditions, to potentially lower costs by reducing height and volume, and to provide a closer to ideal pressure drop distribution in the primary system piping.

Concept D (RHFPF) was selected to allow the evaluation of phenomena associated with using a nonwater medium. The use of Freon allows for the use of the smallest system investigated, potentially lowering construction costs. However, these costs may be offset by expense of specialized Freon handling systems.

Under the ground rules of this study, any Continued Experiment Capability would be required to address the full range of postulated plant transients and consequently would be required to scale the full power steady state operating conditions in the plant, thus the single-phase forced circulation relationships are utilized in the development of possible model configurations.

Under the assumption that the smaller the facility the lower would be the construction costs, it was desirable to provide some criteria for selection of minimum model dimension above which most important local phenomena would be preserved in the model. The flooding criteria in the vertical pipe section was used for selection of minimum diameter ratio because of the importance of the flooding in the B&W hot leg. Figure 3 shows a plot of critical superficial velocity  $j_{g,crit}$  as a function of diameter for water and

Freon at various pressures. For small diameters, the critical velocity is shown to be a function of diameter as indicated by the Wallis flooding criteria. Above some minimum diameter the critical velocity is constant with respect to diameter as described by the Kutateladze correlation. The transition point between these two curves is approximately described by a Bond number criteria of 40, where Setting  $N_{Bond} = 40$  and solving for  $D$

$$N_{Bond} = D \left[ \frac{\rho_{fg} g}{\sigma g_c} \right]^{1/2}$$

gives a criteria for minimum pipe size. Based on this criteria the required minimum diameter gets larger for a lower pressure.

Table 7 provides a summary of the characteristics of a potential ideal model for each of the four scaling concepts discussed, based on the B&W Oconee plant. The MIST Facility is used for the FHFPW concept. Table 8 presents a similar summary based on the Westinghouse Seabrook plant. The Semiscale facility is used for the FHFPW concept.

This discussion has shown the almost endless possibilities for a new facility configuration. There is obviously no one configuration which will provide simulation of controlling phenomena for all important transients. Using the largest possible system with the same fluid and operating conditions as the plant would provide data requiring the least amount of analysis to relate to plant phenomena and would provide the largest range

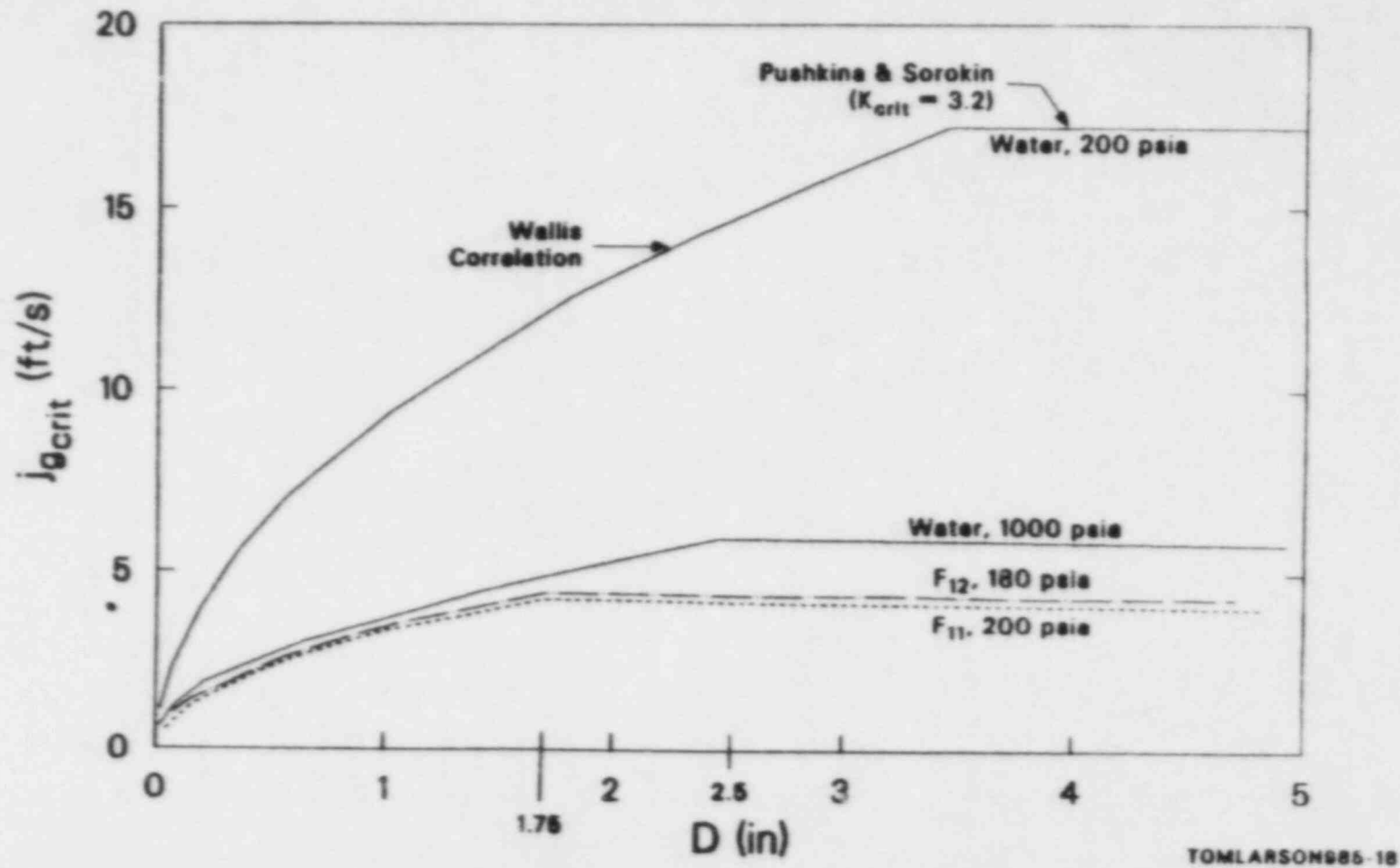


Figure 3. Onset of Flooding (Water and Freon-11) in a Vertical Pipe.

TABLE 7. CONCEPTUAL MODEL PARAMETERS BASED ON B&W LPWR.

Parameter	OCONEE	FHFPW Mini Ideal	RHRPW	RHFPW	RHFPF
Length Ratio	1	1	.375	.342	.375
Diameter Ratio	1	1/28.6	1/10	1/15.35	1/20
Area Ratio	1	1/818	1/100	1/235.65	1/400
Volume Ratio	1	1/818	1/266.67	1/689.04	1/1066.7
Core ΔT Ratio	1	1	.35	1	1
Time Ratio	1	1	.6124	.5848	.6124
Primary Pressure Psia	2170	2170	435	2170	432.5
Primary Flow Rate lbm/hr x10 <sup>-4</sup>	131.3	.161	.937	.326	.329
Primary System Volume ft <sup>3</sup>	11396	13.93	42.7	16.5	10.7
Hot Leg Diameter in.	36	1.26	3.6	2.34	1.80
Number Heater Rods	36816	45	368	156	92
Heater Rod Length in.	144	144	54.0	49.25	54.0
Power/Volume Kw/ft <sup>3</sup>	225.3	225.3	118.37	385.26	109.6
Core Power MW	2568	3.2	5.06	6.37	1.17
Ave Heat Flux Btu/hr-ft <sup>2</sup> x10 <sup>-4</sup>	1.715	1.715	.901	2.93	.834
Secondary Pressure Psia	924.5	924.5	185.3	924.5	184.2

TABLE 8. CONCEPTUAL MODEL PARAMETERS BASED ON WESTINGHOUSE LPWR.

Parameter	Seabrook	FHFPW Semi-ideal	RHRPW	RHFPW	RHFPF
Length Ratio	1	1	.375	.375	.375
Diameter Ratio	1	1/41.3	1/11.81	1/13.89	1/16.67
Area Ratio	1	1/1705	1/139.4	1/193	1/284.6
Volume Ratio	1	1/1705	1/371.8	1/514.7	1/758.8
Core ΔT Ratio	1	1	.35	1	1
Time Ratio	1	1	.6124	.6124	.6124
Primary Pressure Psia	2250	2250	435	2250	448.5
Primary Flow Rate lbm/hr x10 <sup>-4</sup>	140.3	.0823	.718	.445	.494
Primary System Volume ft <sup>3</sup>	11524	6.76	30.99	22.39	15.19
Hot Leg Diameter in.	29	.702	2.456	2.086	1.719
Number Heater Rods	50952	30	365	264	179
Heater Rod Length in.	143.7	143.7	53.89	53.89	53.89
Power/Volume Kw/ft <sup>3</sup>	296	296	155.5	483.4	143.9
Core Power MW	3411	2.00	4.82	10.82	2.185
Ave Heat Flux Btu/hr-ft <sup>2</sup> x10 <sup>-4</sup>	1.898	1.898	.997	3.099	.9229
Secondary Pressure Psia	1000	1000	193.3	1000	199.3

SI-MNL-12

of plant phenomena to be simulated in any single facility. The initial facility expense will, however, be large. As the model moves farther and farther away from the plant in either size, fluid, or operating conditions the capital costs may be reduced significantly but the analysis efforts and costs required to reduce the data and especially to relate the data to operating plant transients will likely increase and the range of phenomena which can be simulated accurately in a given facility could be reduced.

#### PHENOMENA SCALING

Several phenomena have been investigated in a scaled facility and compared with that in a prototype. The calculations performed to date have addressed primarily the small break loss-of-coolant-accident conditions and include the following phenomena:

1. Natural circulation
2. Two phase pump flow
3. Critical flow
4. Flow regimes; horizontal and vertical
5. Pressure change
6. Flooding
7. Void fraction--quality relationships
8. Heat transfer.

The scaled systems considered are based on the relationships given in Table 9 using various length ratios and include

1. Full pressure steam-water
2. Reduced pressure steam-water
3. Freon-11.

Because of space limitations in this paper only limited calculations for the phenomena are presented but the general approach for each phenomena is given along with the conclusions reached relative to each system for the phenomena considered. Calculation details are presented in the detailed scaling report<sup>34</sup> to be published at the completion of the study.

#### Natural Circulation Scaling

Natural circulation phenomena was divided into three modes for the scaling calculations:

1. Single-phase natural circulation
2. Two-phase natural circulation with subcooled liquid at the core inlet

### 3. Fully established two-phase flow with two-phase core inlet.

Scaling ratios were developed for velocity, time constant (i.e., the characteristic time for the primary flow to change from one steady state condition to within  $1/e$  of another due to a step change in primary-to-secondary temperature difference), and core temperature difference for three modes of natural circulation indicated above. The following conclusions were made concerning the scaling of natural circulation phenomena:

The three modes of natural circulation examined (single-phase liquid natural circulation, two-phase natural circulation with core inlet subcooling, and fully established two-phase natural circulation) scale differently if model operation is at nontypical (relative to the reference) operating conditions or with a nontypical fluid.

Using Ishii scaling criteria for full pressure steam-water systems, the scaling ratios for velocity, time constant, and core temperature rise are the same for all three modes.

Due to fluid property differences, the scaling ratio for single phase natural circulation velocity in a 200 psia Freon-11 system (1000 psia full pressure steam-water scaled conditions) is approximately the same as the ratio for two-phase natural circulation with core inlet subcooling. This conclusion is independent of length scale.

The single-phase natural circulation velocity ratio in a reduced pressure steam-water system with  $L_R = 0.5$  (with 300 psia system pressure corresponding to 2250 psia in a full pressure system) is one-half the ratio for two-phase natural circulation.

Core temperature rise for a Freon-11 system is typically between 67 and 69% of that in a full pressure steam-water system for small break LOCA conditions. This conclusion is independent of length scale.

Core temperature rise in a 300 psia reduced pressure steam-water system is 17% of that in a full pressure steam-water system. Measurement accuracy of core temperature rise will therefore be lower in a reduced pressure system.

#### Two-Phase Pump Flow

A pump operated under two-phase flow conditions is unable to maintain the same head ( $\Delta H = \Delta P/\rho$ ) as for single-phase conditions. The pump

head degradation ( $\frac{\Delta H_{2\phi}}{\Delta H_{1\phi}}$ ) becomes significant after voiding is larger than

a critical value, which varies from 5% to 45%,<sup>35</sup> and depends on pump design (radial, mixed, or axial flow), specific speed =  $N Q^{1/2} / (\Delta H)^{3/4}$ , where  $N$  = Angular velocity and  $Q$  = volumetric flow rate, fluid properties, and the line pressure.<sup>36</sup>

The pump should be scaled to deliver the proper single-phase flow rate ratio  $\rho_{0R} A_R \sqrt{L_R}$  at the scaled head ratio

$$\Delta H_R = \frac{\Delta P}{\rho} \Big|_R = \left( \sum_i (N_{f_i} + N_{o_i}) \frac{U_o^2}{2} \right) \Big|_R \quad i \neq i_{\text{pump}}$$

In addition, the normalized head versus void fraction (head degradation) curve should be matched. This is difficult since the head degradation curve for a prototype pump can only be speculated and there is no completely comprehensive analytical model for a condensible fluid. However, the best chance at proper two-phase scaling will be achieved if the pump type, specific speed and fluid properties are matched. The following conclusions for pump scaling for reduced pressure steam-water and from systems were reached.

For a reduced pressure steam-water system the pump head will exhibit considerably more degradation than a full pressure system. Accurate scaling is, therefore, probably impossible.

For a Freon system operated at the same ratio of critical pressure, as a steam-water system the effects of fluid properties on head degradation are not known. No experiments are known to have been performed. This deficiency should be remedied before a large commitment to a Freon system is made.

#### Critical Flow Scaling

Critical mass flow rates are calculated for Freon-11 and reduced pressure steam-water systems for both subcooled and two-phase saturated conditions and are compared with full pressure steam-water calculations.

For proper scaling of a blowdown transient, with subcooled through high quality two-phase flow, the critical mass flux ratio

$$\frac{W}{W_o} \Big/ \frac{W_{2250}}{W_{o2250}} \quad \text{as a function of } P/P_o$$



where

$W$  = mass flux

$W_0$  = initial (subcooled) mass flux at time = 0

$W_{2250}$  = mass flux for full pressure ( $P_0 = 2250$  psia)  
steam-water

should equal 1.0 throughout the transient. A break area may then be found such that the scaled mass flow rate (or scaled depressurization rate) is satisfied.

The critical mass flux ratio, as defined above, was calculated for a reduced pressure steam-water system using the homogeneous equilibrium model (HEM) as tabulated in Reference 37 for LOFT small break experiment L3-7<sup>38</sup> (Figure 4). Two initial pressures, 300 psia and 600 psia were chosen. The initial pressures in the scaled systems correspond to 2250 psia in the prototype system.

Since the critical mass flux ratio is considerably less than 1.0 for the scaled system throughout the majority of the transient, the depressurization rate for two-phase flow will be considerably less than the scaled value  $(dP/dt)_R = t_R = L_R$  if the subcooled value is matched.

No HEM (or other model) tables exist for Freon although the ATHENA code<sup>39</sup> which is used for this analysis predicts results for saturated two-phase flow of Freon that are close to the HEM model. However, before accepting outright the results of the code calculation, an initial evaluation of the scaling may be made by evaluating two extremes--subcooled liquid flow and high quality dispersed mist flow.

Consider the subcooled liquid an incompressible and frictionless fluid with  $P/P_{crit} = 0.32$ , (1000 psia/2250 psia for  $H_2O$ ) and a throat pressure ( $P_t$ ) of atmospheric. Then from the Bernoulli equation,

$$W_x = \left[ 2g \rho_x P_0 (1 - P_t/P_0) \right]^{1/2}$$

where

$P_t$  = throat pressure

$P_0$  = upstream pressure

$W_x$  = liquid mass flux.

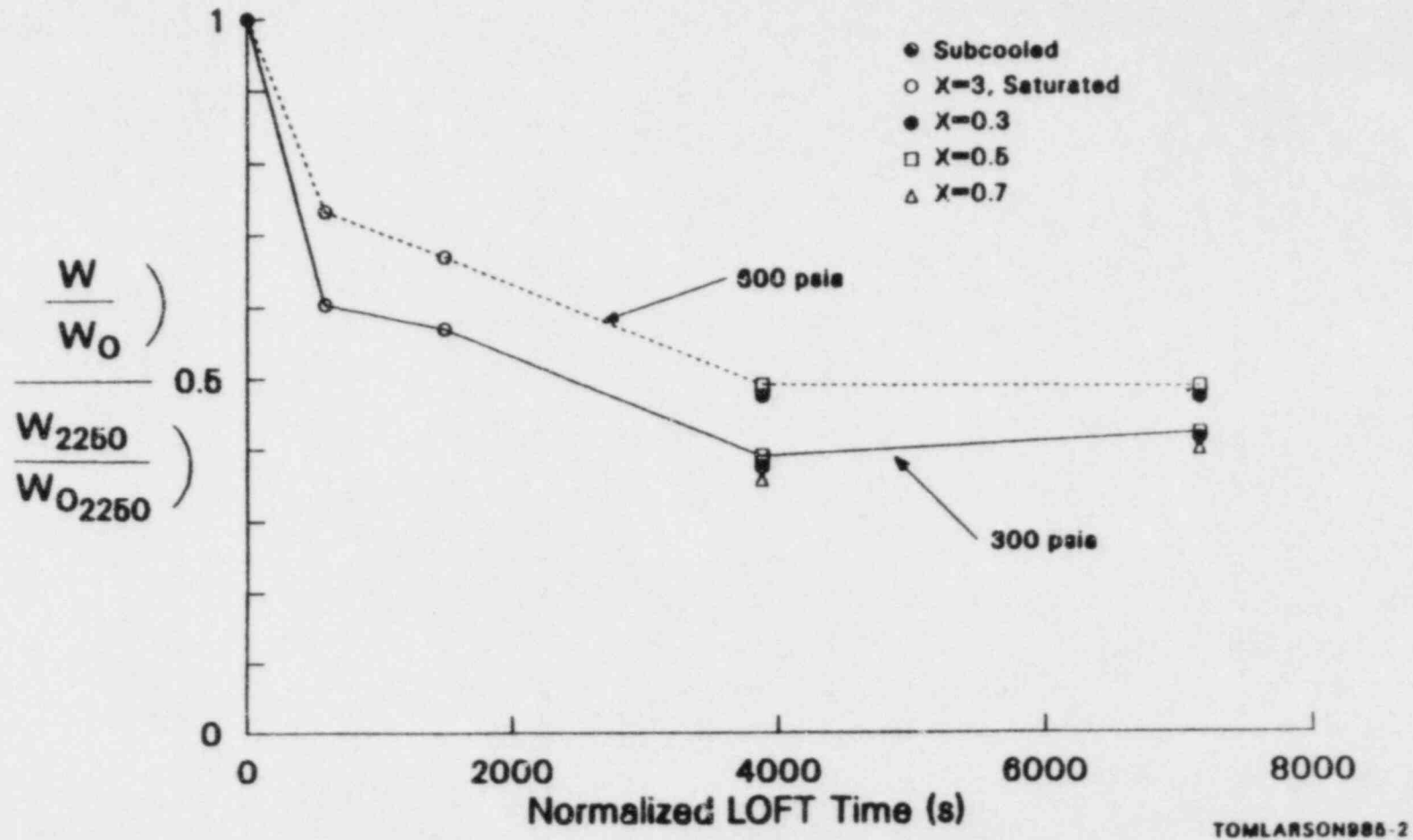


Figure 4. Critical mass flux ( $w$ ) ratio; reduced pressure (300 psia and 600 psia)  $H_2O$  system compared with full pressure (2250 psia) LOFT system for L3-7 transient.

The ratio is then

$$\frac{W_{F11}}{W_{H_2O \text{ sub.}}} = 0.55$$

For high quality dispersed flow, Young<sup>40</sup> shows that the flow becomes choked when the vapor phase velocity attains the frozen speed ( $a_f$ ) of sound for high frequency waves moving through the system, i.e.

$$a_f = (k_f P/\rho_g)^{1/2}$$

where  $k_f$  is the isentropic exponent of the vapor phase alone. then,

$$\frac{W_{F11}}{W_{H_2O} \times \sim 1.0} = \left[ \frac{(k P/\rho_g)_{F11}}{(k P/\rho_g)_{H_2O}} \right]^{1/2}$$

This ratio versus  $P/P_C$  is shown in Figure 5 and varies from 0.64 at  $P/P_C = 0.2$  to 0.625 at  $P/P_C = 0.63$ , which is 15% more than the subcooled value. If the ratio is similar for lower quality saturated flow, critical flow in a Freon-11 system should scale well to high pressure steam-water.

The following conclusions for critical flow scaling are presented.

Critical flow in a reduced pressure steam-water system does not scale well. It is impossible to scale both subcooled liquid mass flow and saturated fluid mass flow with one break size.

Critical flow in a Freon-11 system may be properly scaled to a high pressure steam-water prototype system for both subcooled liquid and saturated two-phase flow. ATHENA code calculations show that Freon temperature should be less than that calculated from Ishii scaled core inlet fluid subcooling (approximately 13°F less) for optimum critical flow scaling.

Subatmospheric containment pressure is necessary to prevent unchoking for modeling blowdowns with steam-water prototype pressure decreasing below approximately 160 psia ( $T_{sat} = 354^\circ\text{F}$ ).

#### Flow Regimes

A number of flow regime maps are available for horizontal flow,<sup>41</sup> such as Baker (1954), Mandhane et al. (1974), Taitel & Dukler (1976), and Weisman et al. (1978).<sup>42</sup> The map of Weisman et al. is chosen for this study because of its inclusion of Freon data, its consideration of diameter effects, and its use of superficial velocities as co-ordinates.

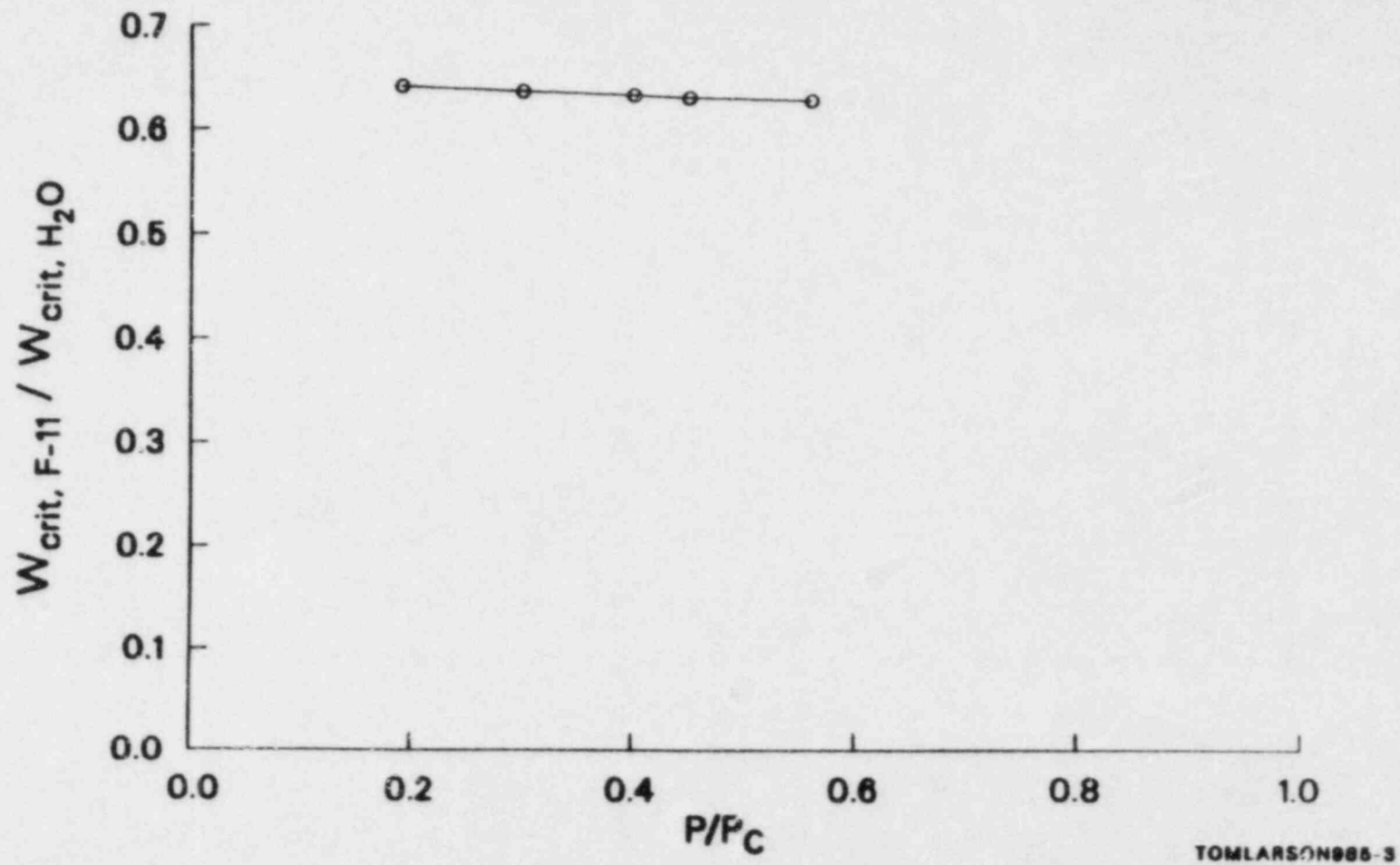


Figure 5. Critical flow rate ratio for high quality, dispersed-mist flow.

The flow regime transition of most concern in natural circulation is the stratified (or stratified-wavy)-intermittent transition. Two-phase natural circulation can only be maintained in a Westinghouse type reactor with intermittent flow regimes in the hot leg. Cessation of liquid carry-over in the steam generator is accompanied by stratification in the hot leg (but intermediate flow regime flow does not necessarily insure liquid carry-over). Taitel and Dukler<sup>43</sup> describe this transition in terms of a classical Kelvin-Helmholtz instability. They specify the transition value as a function of nondimensional liquid height and modified Froude number. If the ratio of densities is approximately constant, as is the case for Freon-11 and H<sub>2</sub>O at the same critical pressure ratio, then the transition is a function only of gas velocity, liquid height, and pipe diameter. If superficial velocity co-ordinates are used, then the transition is a function of superficial velocity and diameter. Figure 6 shows the transition for 1 in. and 3 in. diameter pipes.

The vertical flow regime map of Bennett (1965) may be used in the form given by Zetzmann (1976). Zetzmann modified the abscissa to include the effect of critical pressure ratio, and compared the map with Freon data (Figure 7).

The horizontal flow regime map (Figure 6) shows that the stratified-intermittent transition is essentially the same for Freon, reduced pressure steam water and full pressure steam-water, and is dependent primarily on superficial liquid velocity ( $V_s = (1 - \alpha) <V_f >$ ) and secondarily on pipe diameter and superficial gas velocity ( $V_{s_g} = \alpha <V_f >$ ). With reduced velocity in a scaled system, the

transition from two-phase natural circulation (intermittent-flow) to reflux condensation will therefore occur at a lower void fraction than in the prototype, unless the pipe diameter is reduced considerably to compensate. But, this would conflict with other requirements (pressure loss and flooding criteria).

Other flow regime transitions (stratified-wavy, wavy and intermittent annular, and intermittent-dispersed) occur at lower velocity in a Freon system than full-pressure steam water. A velocity ratio of approximately 1/1.5 in a Freon system (which corresponds to a length ratio of 1/2.25) preserves the flow regime transition scaling, that is, the transitions would occur at the same void fraction.

For vertical upward flow in a scaled Freon system, the churn-annular transition will occur at approximately the same quality (or void fraction) if  $M_f = M_{H_2O}$ . For a 1,000 psia steam-water scaled pressure, the higher

Freon-11 density requires a velocity scale of 1/1.67 or a length scale of approximately 1/2.7. The bubble-churn transition is a function primarily of quality, and this transition will, therefore, be scaled properly.

For horizontal flow in a reduced pressure steam-water system the stratified (or stratified-wavy)-intermediate transition will occur at approximately the same superficial liquid velocity, and other transitions

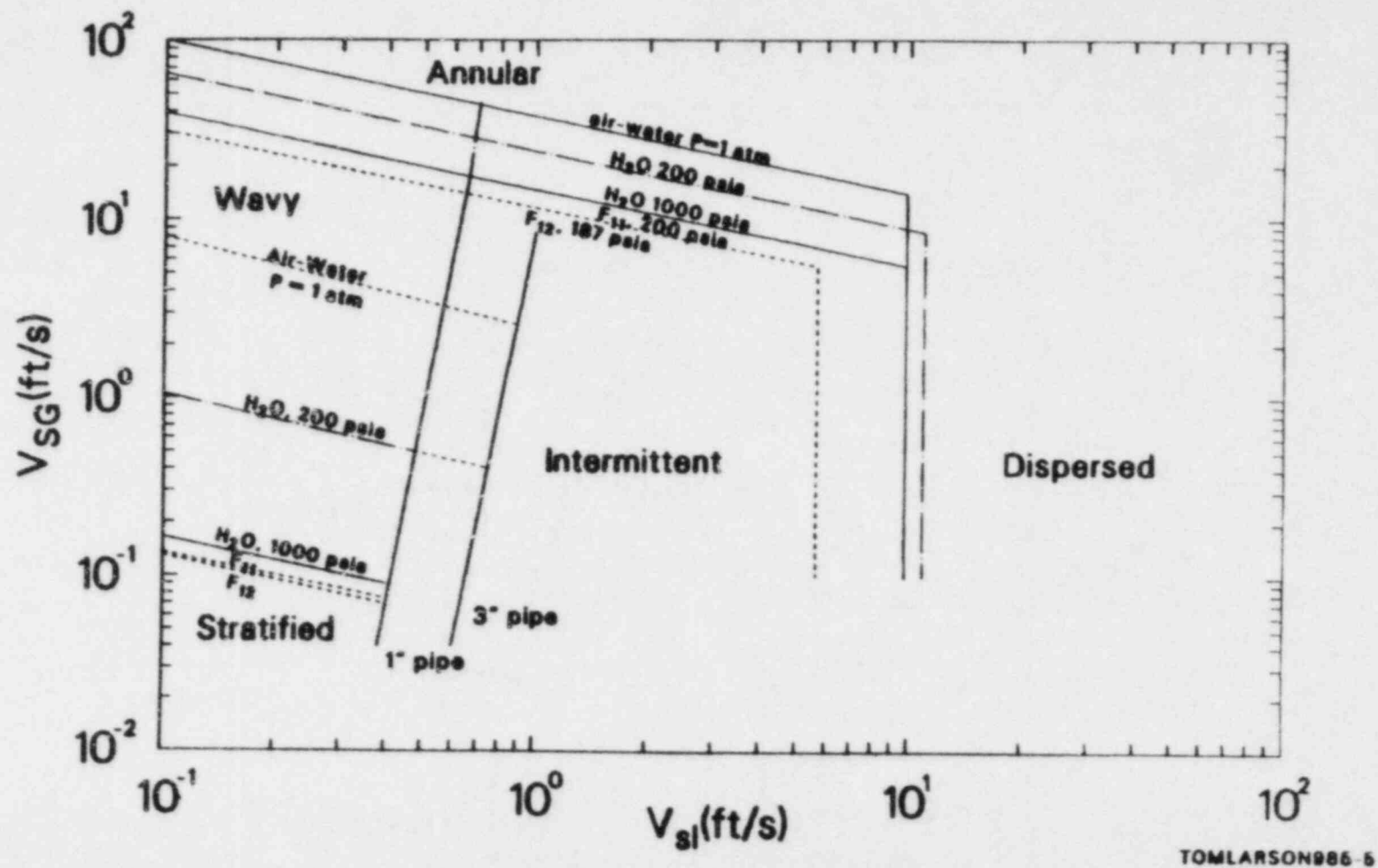


Figure 6. Horizontal flow regime map, 1" diameter pipe method of Weisman et al., 1979.

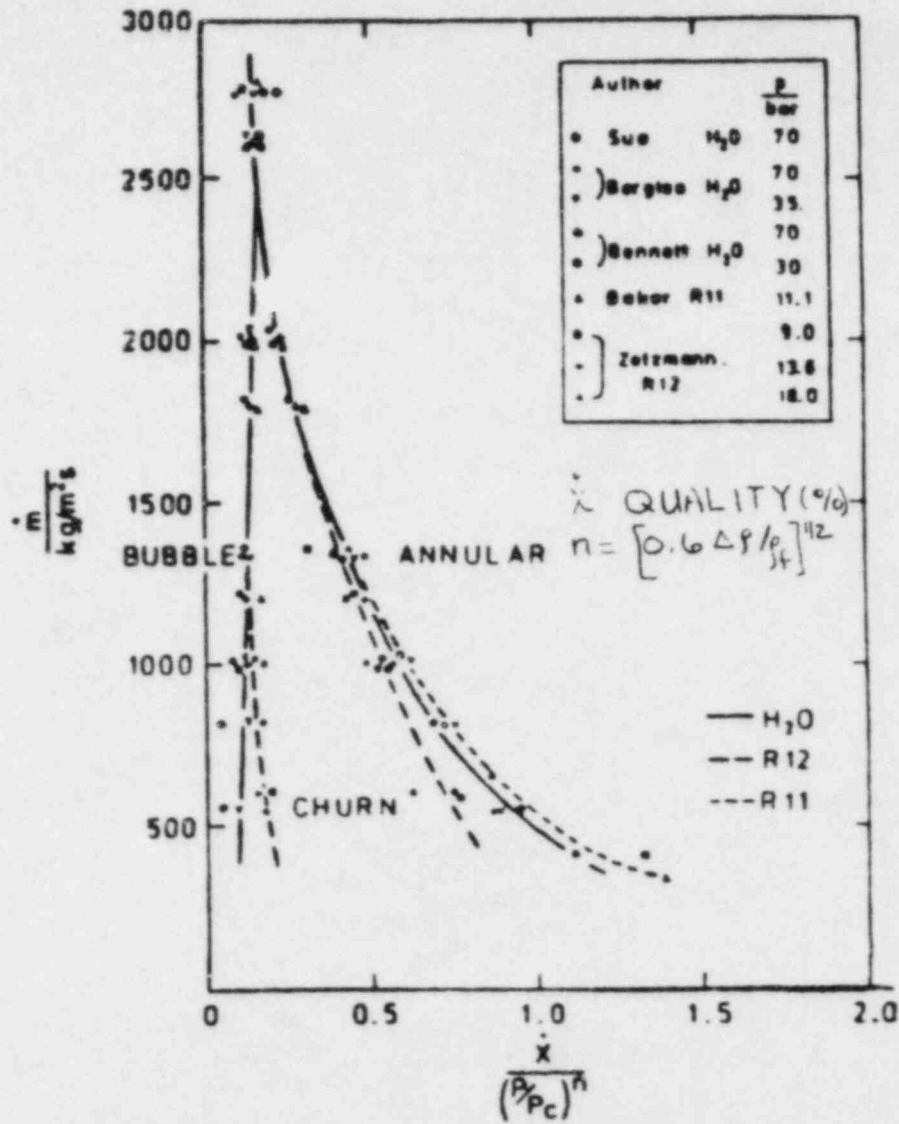


Figure 7. Bennett's flow pattern map, modified according to Zetzmann (1970).

For horizontal flow in a reduced pressure steam-water system the stratified (or stratified-wavy)-intermediate transition will occur at approximately the same superficial liquid velocity, and other transitions will occur at higher superficial velocities than for full pressure steam-water. Since velocities in the scaled system are lower, the transitions are not well scaled i.e. do not occur at the same void fractions. As an example, consider the wavy-annular transition for water at 200 psia vs water at 1000 psia. The ratio of the superficial gas velocities for transition is

$$j_{g, w-A} \Big|_R = \frac{6.4}{3.8} = 1.68 \quad .$$

If in the low pressure system  $X_{\Delta p/\rho_g}$  has been maintained via phase change and subcooling number scaling then the void fraction ratio is approximately unity, the gas and liquid superficial velocities should scale by  $\sqrt{L_R}$ . For the reduced height, reduced pressure system typically considered in this study,  $L_R \sim 0.375$  so that

$$j_{gR} = 0.612 \quad .$$

Ideally, the transition in the model would take place at the same (scaled) superficial velocity as in the reference. For this particular transition, however, it is seen that a distortion (actual/ideal) of

$$f_w = \frac{1.68}{0.612} = 2.7$$

exists. Likewise for Freon as the working fluid,

$$f_F = \frac{0.79}{0.612} = 1.3 \quad .$$

Simply put, these distortion factors mean that in the low pressure water system, wavy to annular transition would not occur until velocities three times the ideal scaled transition value were reached in the model relative to the plant. Similarly for Freon as the working fluid, wavy to annular transition would not occur until velocities 30% larger than the ideal scaled transition value were reached in the model. Similar conclusions are reached with respect to the intermittent to dispersed transition. The stratified to stratified wavy boundary is even more distorted for low pressure water relative to high pressure water. The following flow regime conclusions reached as a result of this study.

Both horizontal and vertical flow regime transitions scale reasonably well in a reduced height system ( $l_R \sim 0.375$ ) using Freon as a working fluid and operated at the same critical pressure ratio as expected in a plant.



Certain flow regime boundaries for both horizontal and vertical flows are strong functions of pressure. A scaled facility operating with water at reduced pressures relative to the reference can have significant distortions in flow regime transition. These distortions become more pronounced as the length ratio decreases.

Under certain operating circumstances, distortions in flow regime transitions in reduced pressure water systems may be of no consequence since the expected operation of the reference plant and the scaled facilities does not result in flow regime boundary crossing.

### Pressure Change Scaling

Pressure change across a component is composed of the irreversible pressure drop plus the gravitational pressure change plus the acceleration pressure change. In forced circulation, the loop pressure change (drop) dictates the pumping requirement, and in natural-circulation the pressure drop is coupled with the circulation rate. The irreversible losses are of primary concern for scaling (a reversible pressure change in one component is recovered in other components), although the reversible components are important if local pressures, or pressure gradients, such as that in the core, are to be scaled.

Ishii scaling dictates that the friction number ratio,  $Nf_R$ , and the orifice number ratio,  $No_R$ , be maintained at 1.0. Also, the area ratio  $A_{iR}$  should equal 1.0. This implies that  $f(L/D)_i$  and  $k_i$  are equal in the model and prototype for single-phase flow.

Two-phase multipliers ( $\phi^2$ ) are given in Figure 8 for steam-water at 1,000 and 133 psia, and for Freon-11 at 200 psia. Two-phase frictional pressure losses ( $\Delta P_f$ ) are then calculated as

$$\Delta P_f = \phi_{\rho 0}^2 f \frac{L}{D} \frac{W^2}{2g \rho_f}$$

Several correlations for  $\phi_{\rho 0}^2$  are available,<sup>41</sup> e.g. Martinelli-Nelson (1948), Baroczy (1963), homogeneous, Friedel (1979), and Chisholm (1973). For low flow rates ( $\Delta < 100 \frac{\text{kg}}{\text{M}^2 \cdot \text{s}}$ ) the Martinelli-Nelson correlation is

applicable, and for flow rates on the order of  $1,000 \frac{\text{kg}}{\text{M}^2 \cdot \text{s}}$ , such as

encountered in low quality natural circulation, the Baroczy correlation or Chisholm's correlation of Baroczy's data is reasonably accurate.<sup>44</sup> (Chisholm's form of the Baroczy correlation is used in these calculations.)

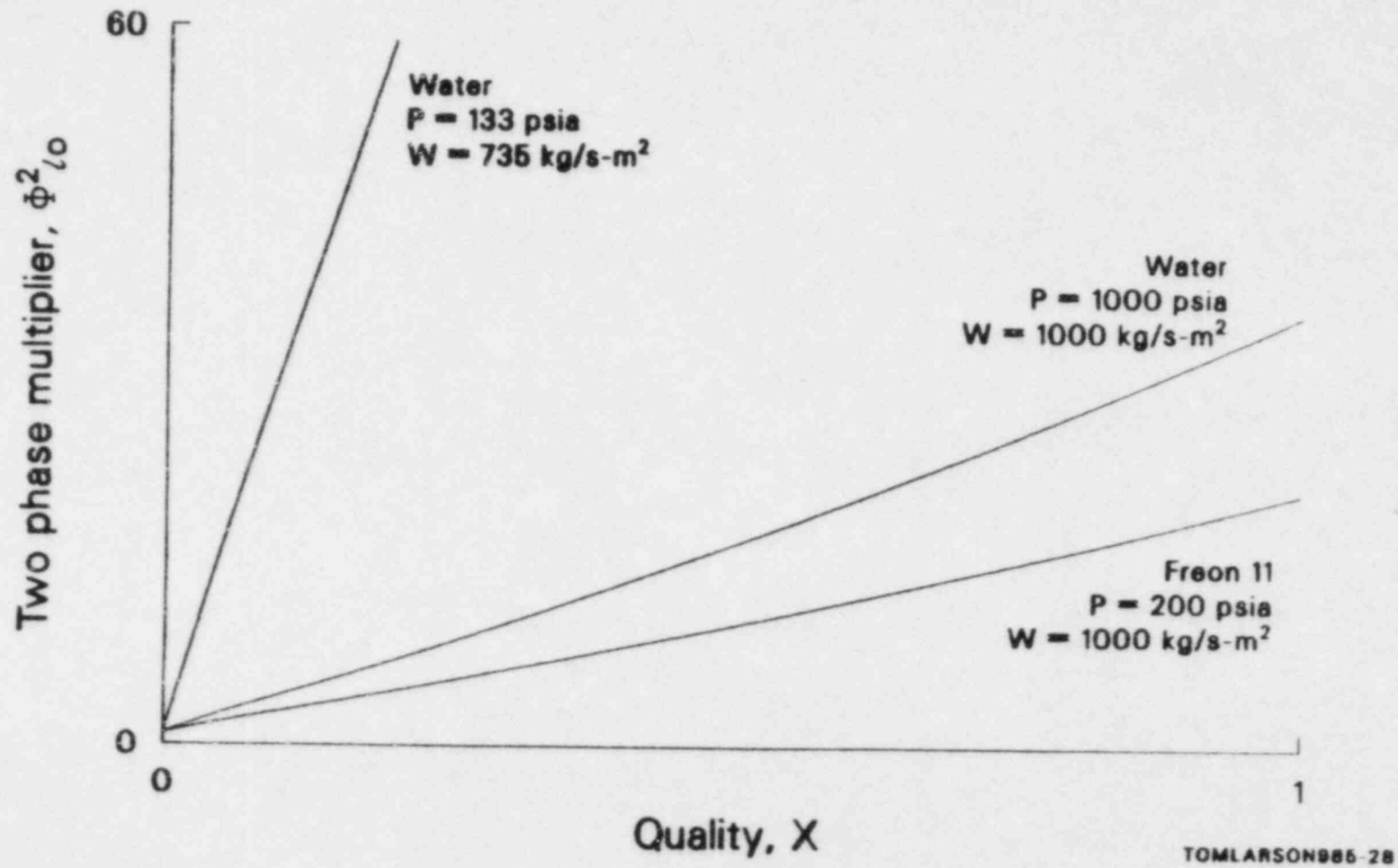


Figure 8. Two-phase friction loss multiplier from Baroczy correlation.

For very high flow rates of  $3,500 \frac{\text{kg}}{\text{M}^2 \cdot \text{s}}$  or above, such as that established

in pump forced circulation, the homogeneous model is applicable.<sup>41</sup>  
 For a properly scaled system, with the same fluid properties, and with  
 $N_{OR} = 1$ ,  $N_{FR} = 1$ , and  $A_i|_R = 1$ , then

$$\Delta P_i|_m = \Delta P_i|_p \frac{W_m^2}{W_p^2} = \Delta P_i|_p L_R$$

Using a different fluid with equal quality, density ratio  $(\rho_f - \rho_g)/\rho_g$   
 and viscosity ratio  $\frac{\mu_f - \mu_g}{\mu_g}$ , then  $N_{OR} = 1$  and  $N_{FR} = 1$ , and with the

assumption that the homogeneous two-phase friction multiplier is applicable  
 (as is assumed in Ishii scaling), then

$$\Delta P_i|_m = \Delta P_i|_p \frac{W_m^2}{W_p^2} \frac{\rho_f}{\rho_{fm}} = \Delta P_i L_R \rho_{FR}$$

The ideal pressure loss relationships become distorted in two-phase  
 flow due to:

1. Different fluid properties and property ratios
2. Different flow quality in the component
3. Differing two-phase friction multipliers
4. Differing characteristics of friction losses compared with component type losses at increasing quality.

Component type pressure losses are calculated by

$$\Delta P_k = K \frac{W^2}{2g \rho_h}$$

where

$$\rho_h = \text{Homogeneous density} = \frac{\rho_f \rho_g}{x \rho_f + (1-x) \rho_g}$$

K = Single phase loss coefficient.

This simple expression is shown by Lahey and Mooney,<sup>45</sup> and others to give reasonable accuracy for component type pressure losses.

The following conclusions were reached:

Wall friction pressure losses are reasonably well scaled in reduced height Freon-11 and reduced pressure water models under two-phase flow conditions. Friction loss ratios during two-phase flow are within 20% of the single-phase ratios.

Component pressure losses are ideally scaled for both Freon-11 and reduced pressure water models during two-phase flow.

The gravitational pressure ratios are well scaled for both Freon-11 and reduced pressure water models during two-phase flow. Ishii scaling caused the gravity pressure change ratios to remain constant. The constant was a weak function of pressure with reduced pressure water.

The total pressure gradient during two-phase flow does not scale as well as the individual components of the pressure gradient. The ratio of model to prototype pressure gradients can vary by a factor of three depending on whether gravity or friction is the major component of the pressure gradient.

#### Flooding and Reflux Transitions

Flooding behavior in the steam generator tubes, in the steam generator inlet plenum, and in the hot legs plays an important role in determining the transition from 2<sub>φ</sub> natural circulation to reflux condensation (or boiler condenser mode in the B&W system). Flooding was examined using the Wallis correlation<sup>46</sup>

$$j_g^* 1/2 + m j_f^* 1/2 = c$$

for small vertical tubes or the Kutateladze correlation<sup>47</sup>

$$\frac{j_g \sqrt{\rho g}}{(\sigma g \Delta \rho)^{1/4}} = C_K$$

for large diameter pipes. A correlation proposed by Wallis and Dobson<sup>48</sup>

$$j_g^* = 0.5 \alpha^{1/2}$$

was used for horizontal pipes.

The two-phase natural circulation reflux transition will occur with approximately the same  $j_g$  and  $j_f$  in a scaled Freon system as in a full pressure steam water system. Since two-phase natural circulation velocity is reduced by a factor of  $\sqrt{L_R}$ , the transition to reflux occurs earlier

in a transient (at a lower void fraction) if the same diameter steam generator tube is used in a reduced height system. If the diameter is reduced by  $L_R^{1/4}$  or the number of tubes reduced by  $\sqrt{L_R}$ ; then  $j^*g$

and  $j^*f$  will be approximately the same as for a PWR. In both cases the heat transfer area will be reduced. Steam generator tube diameter should also be reduced by the same factor in a full pressure steam-water scale system if  $L_R < 1$  to preserve this transition.

The superficial gas velocity for the onset of flooding ( $j_{gcrit}$ ) in a vertical pipe is formulated as a function of tube diameter by employing the Wallis correlation (with  $c = 0.8$ ) for small diameter tubes, and the Kutateladze correlation (with the Pushkina and Sorokin<sup>49</sup> value of  $c_k = 3.2$ ) for large diameter tubes (Figure 9). The tube diameter where the two correlations intersect defines the maximum diameter tube where a change in diameter affects  $j_{gcrit}$ . The onset of flooding line for flooding initiation at the hot leg to steam generator inlet plenum for a U-tube type steam generator is also shown Figure 9.

In a Westinghouse type reactor, hot leg steam velocity is approximately 5.5 times that in steam generator tubes due to smaller flow area. The plenum inlet will therefore flood before the steam generator tubes, with increasing gas superficial velocity. Flooding criteria in a Westinghouse type reactor is shown in Figure 10, and flooding criteria for a B&W plant is shown in Figure 11.

Flooding in a B&W type hot leg will be determined primarily by the long vertical component. In order to preserve the Kutateladze type flooding criteria, the diameter should be greater than about 2.5 inch in a full pressure steam-water system, greater than 1.75 inch in a Freon-11 system, and greater than 3.5 inch in a reduced pressure steam-water system. For smaller diameter pipes with a Wallis type flooding criteria, length increasingly affects the flooding of the falling film and is not easily quantified (or scaled). The following conclusions were reached.

Steam generator tube diameter in a Westinghouse type scale facility should be reduced by  $L_R^{1/4}$  if it is desired to maintain the two-phase natural circulation-reflux transition.

Hot leg diameter in a B&W type reactor scaled facility should be greater than 2.5 inch in a full pressure steam-water facility, greater than 1.75 inch in a Freon system, and greater than 3.5 inch in a reduced pressure steam-water system if it is desired to preserve the Kutateladze type flooding criteria.

#### Void Fraction--Quality Relationship

In the two-fluid model, if quality,  $x$ , and slip ratio,  $S = V_g / V_f$ , are known, then void fraction may be calculated by

$$\alpha = \frac{1}{1 + S \left( \frac{1-x}{x} \right) \frac{\rho_g}{\rho_f}}$$

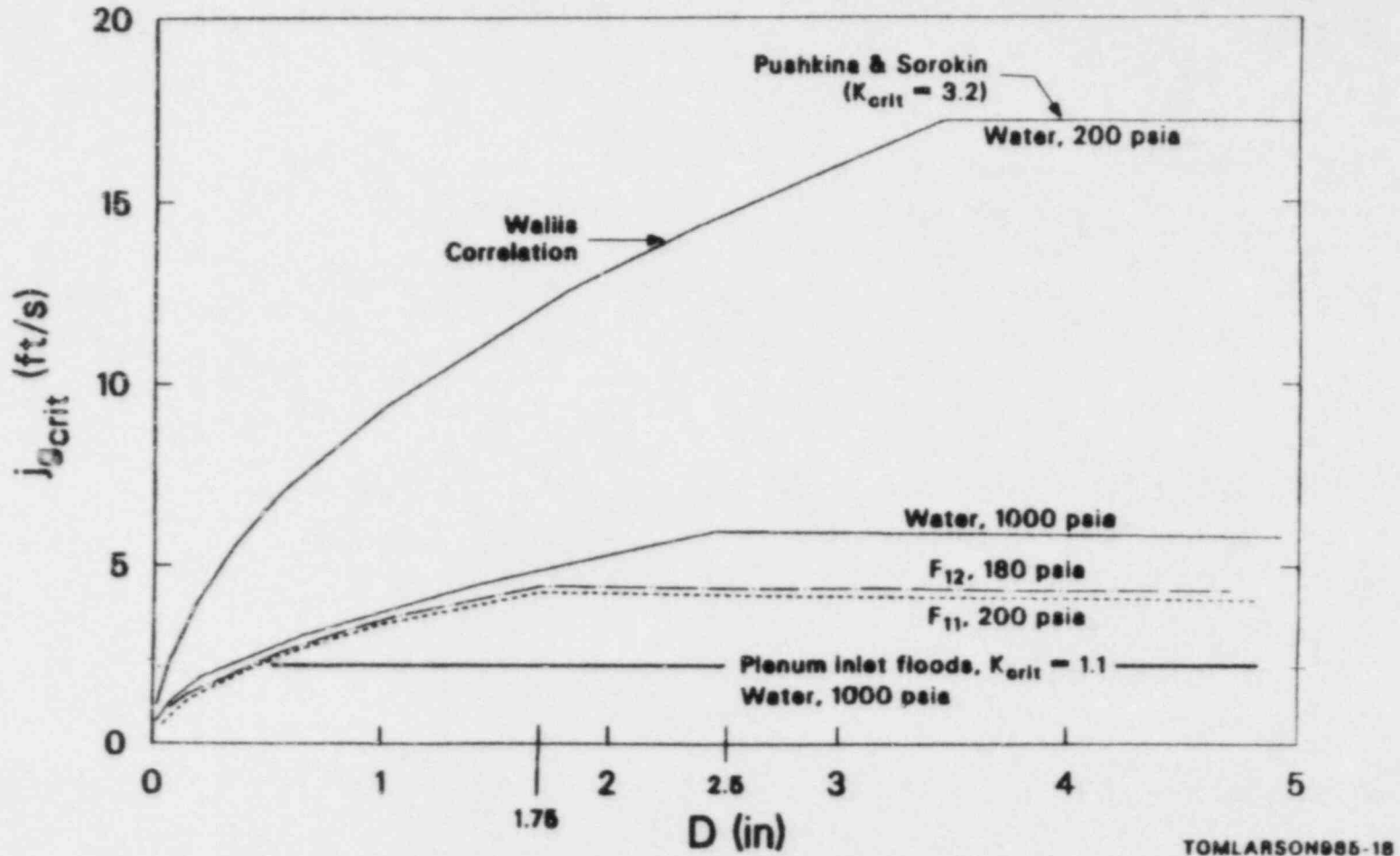


Figure 9. Onset of flooding, water and Freon in vertical pipe.

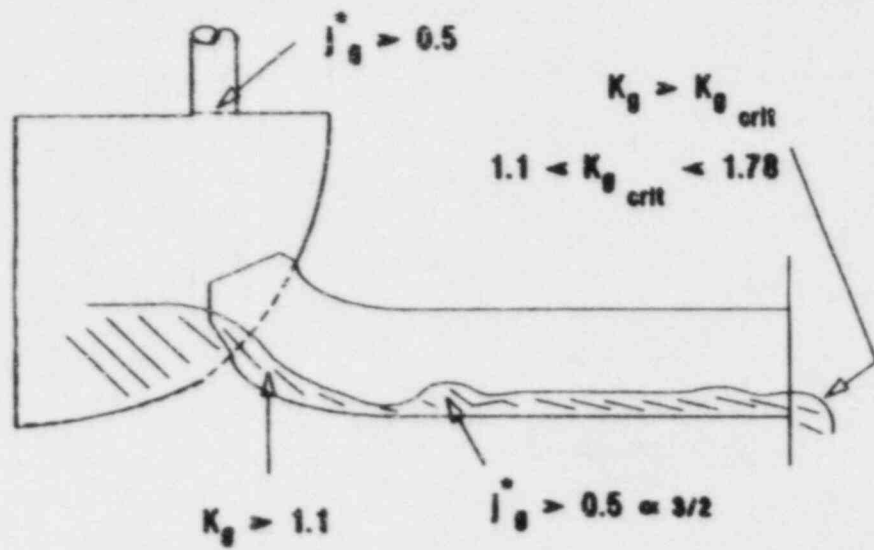


Figure 10. Flooding criteria in W type reactor.

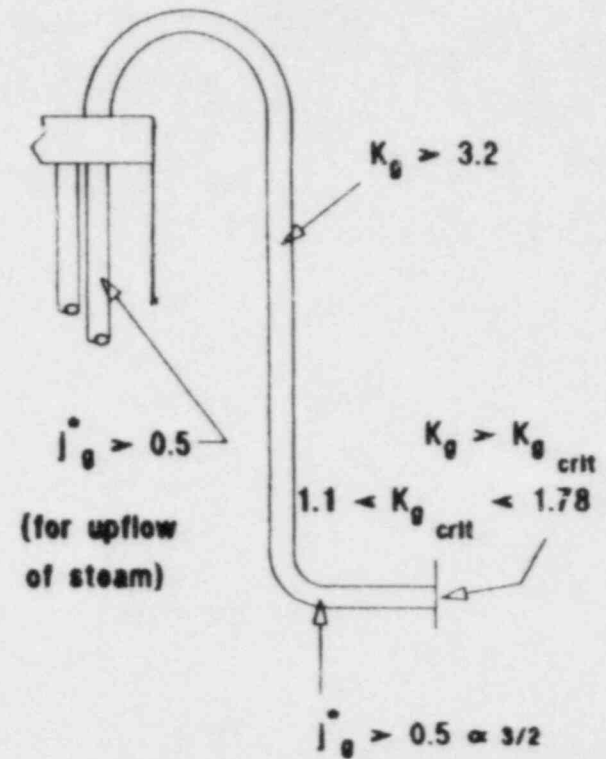


Figure 11. Flooding criteria in B&W type reactor.

The direct dependence of void fraction on the density  $\frac{\rho_g}{\rho_f}$  ratio in this equation.

For a Freon system the density ratio is close to that of full pressure steam water, and if the interphase slip is similar, it is expected that the void fraction quality relationship will be similar. This is confirmed experimentally by Mayinger.<sup>50</sup>

For a low pressure steam-water system the void fraction-quality relationship will not be the same as for the high pressure steam-water system at the same quality. Recall, however, that in the basic similarity criteria it is postulated that the parameter  $x\Delta\rho/\rho_g$  is maintained if the phase change and subcooling numbers are scaled properly. The equation above can be recast in a form containing the parameter  $x\Delta\rho/\rho_g$  as

$$a = \frac{x(1 + \frac{\Delta\rho}{\rho_g})}{x(1 + \frac{\Delta\rho}{\rho_g}) + S(1 - x)}$$

For assumed reference conditions (i.e. quality, pressure, and slip ratio) void fraction can be computed as a function of  $x\Delta\rho/\rho_g$ . Quality and void fraction at any other pressure can be then computed from the postulation that

$$x \left( \frac{\Delta\rho}{\rho_g} \right)_R = 1.$$

Figure 12 shows results for two pressures (100 and 300 psia) with a reference condition of 1000 psi. The slip ratio was assumed to be unity and void fraction and quality ratio are plotted as a function of  $x\Delta\rho/\rho_g$ . As shown, the void fraction is nearly preserved (i.e.  $\alpha_R \approx 1$ ) although quality is not (i.e.  $x_R \neq 1$ ). It should be noted that the ratio  $x\Delta\rho/\rho_g$  is preserved exactly. Figure 13 shows the relationship between reference quality at 1000 psi and reduced pressure system quality at 300 psi and 100 psi, that results if  $x\Delta\rho/\rho_g$  is equal in the reference and reduced pressure systems. Figure 14 shows the relationship between reference void fraction and reduced system pressure void fraction for an assumed slip ratio of 2. As shown, the void fraction is reasonably closely preserved.

The figures presented have shown that the void-quality relationship for Freon-11 relative to water is closely preserved at equal quality. This is a consequence of the fact that  $\Delta\rho/\rho_g$  for Freon-11 is nearly the same as that for water over equivalent reduced pressure ranges. For a low pressure steam-water condition, the void-quality relation is not the same as for a high pressure condition. However, it is shown that if the parameter  $x\Delta\rho/\rho_g$  is maintained between a low pressure and high pressure condition, the void fraction is nearly preserved (for equal slip ratios) even though the quality is not. The implications of this result are that phenomena heavily dependent on void fraction can be preserved in a



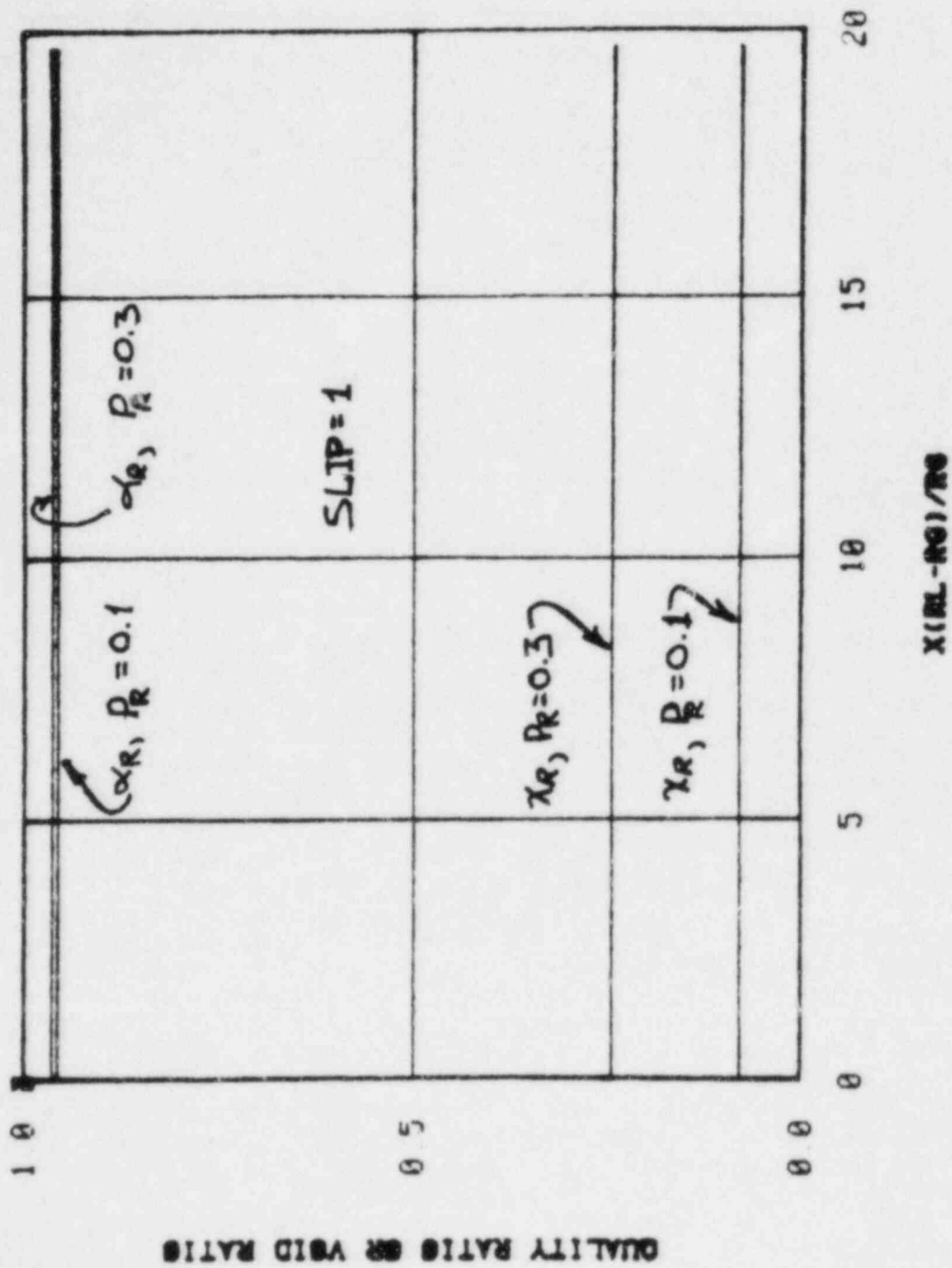


Figure 12. Quality or void ratio vs.  $x(\frac{\Delta \rho}{\rho_g})$

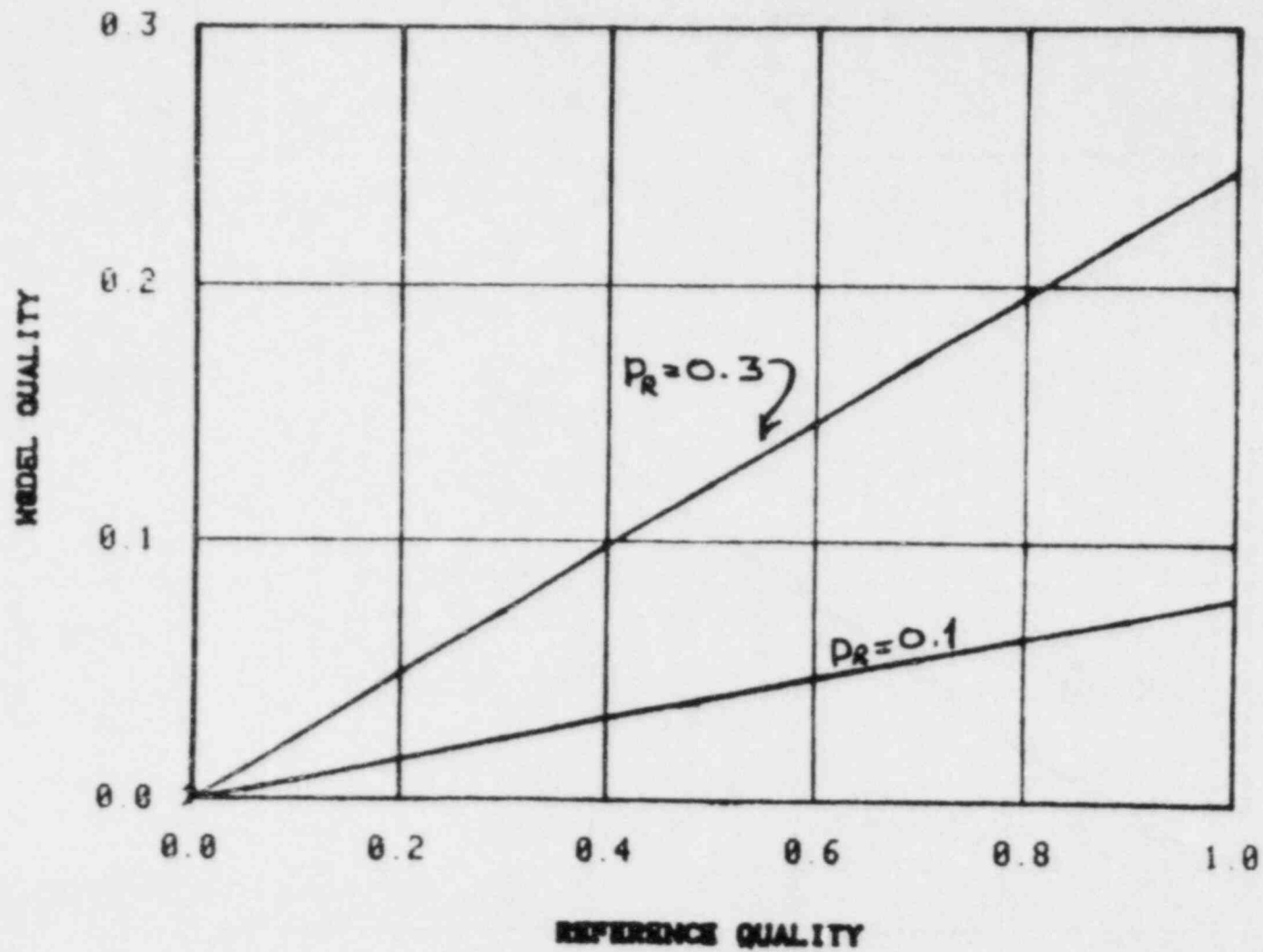


Figure 13. Model quality vs. plant quality for  $X\left(\frac{\Delta P}{A_g}\right)_R = 1$

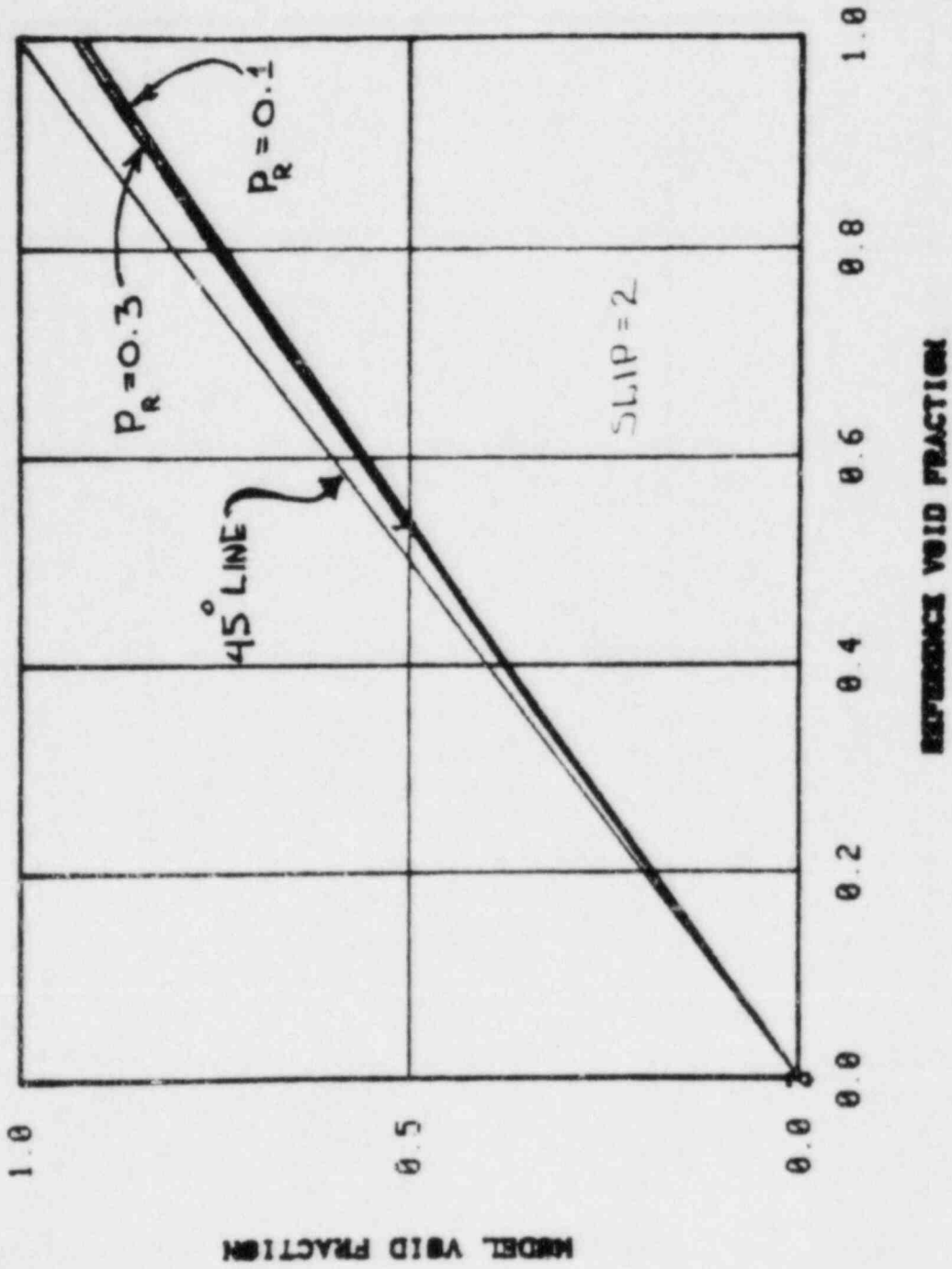


Figure 14. Reference void vs. model void for  $X(\frac{\Delta P}{P_g})|_R = 1$

low pressure steam-water system relative to a high pressure steam water system. Phenomena with a significant quality dependence could be distorted since  $x\Delta\rho/\rho_g$  is preserved rather than quality.

This analysis has led to the following conclusions.

The void fraction-quality relationship for Freon and water is similar assuming the slip ratio is equal.

The void fraction-quality relationship for low pressure water and high pressure water is not the same assuming equal quality and slip ratio.

If the parameter  $x\Delta\rho/\rho_g$  is maintained equal between a low pressure and a high pressure water system, the void fraction will be approximately the same if the slip ratios are similar.

In a low pressure water system, phenomena with a strong dependence on quality may be distorted relative to a high pressure water system since quality will not be preserved.

### Heat Transfer

Local heat transfer phenomena were evaluated in the core and steam generator for four scale models as a function of pressure. The four scale models included full height full pressure water (FHFPW), reduced height full pressure water (RHFPW), and reduced height full pressure Freon-11 (RHFPF). The particular phenomena investigated included critical heat flux (CHF) and dryout in the core and condensation heat transfer in the steam generator.

The general procedure to evaluate local heat transfer phenomena is described below. First, a correlation or relationship to describe the phenomena of interest was determined. Second, the appropriate input parameters for the correlation or relationship were scaled according to the Ishii criteria. For example, the velocity ratio,  $U_R$ , and heat flux ratio,  $q_R$ , were scaled as

$$U_R = L_R \text{ and } q_R = \left(\frac{\rho_f}{\rho_{fg}}\right)_R \rho_{gR} h_{fgR} (L_R)^{-1/2}$$

Finally, the phenomena of interest were evaluated for the four scale models over a range of pressure conditions. Details of the evaluation of the heat transfer phenomena follow.

Three different CHF regimes were evaluated. The correlations and regimes included modified Zuber<sup>51</sup> for pool boiling, Katto<sup>52</sup> for low to intermediate flow, and Biasi<sup>53</sup> for high flow. Typical results are illustrated in Figure 15 which presents ratios of heat flux to CHF ( $q_R/q_{CHF}$ ) for the pool boiling regime. CHF was ideally scaled with the FHFPW model as  $q_R/q_{CHF}$  was identically one. CHF was well scaled with the RHFPW model because  $q_R/q_{CHF}$  was a constant. CHF would occur more readily or earlier in the RHFPF model than in the plant because

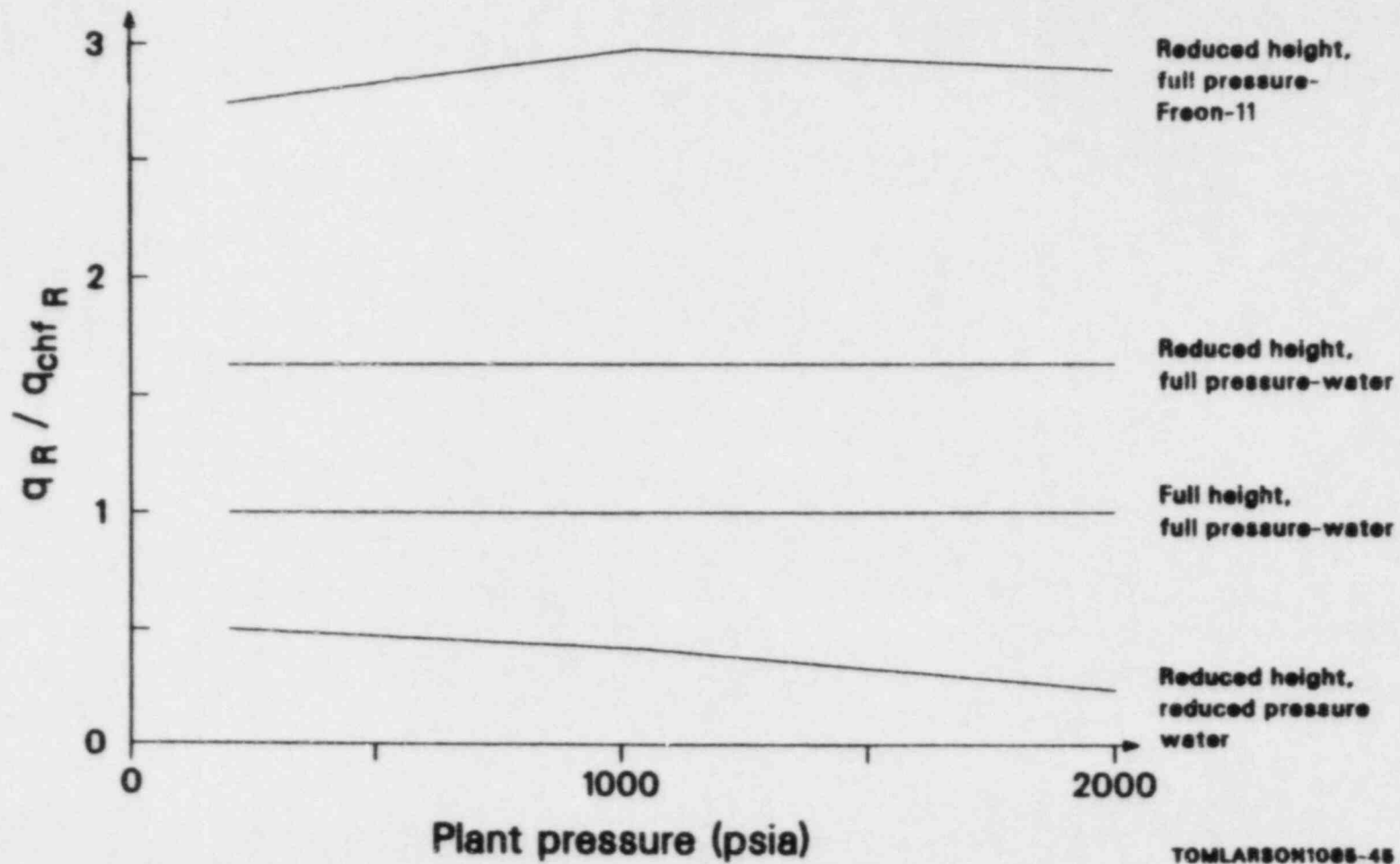


Figure 15. Ratio of heat flux to CHF ratios for pool boiling.

$q_R/q_{CHF}$  was greater than unity. However, the distortion with the RHFPP model was nearly a constant factor of 2.3 over the pressure range investigated. CHF was poorly scaled with the RHRPW model as  $q_R/q_{CHF}$  was much less than one and the ratio varied significantly with pressure. The results indicated that it might be difficult to exceed CHF with the RHRPW mode. Thus, this model would not be appropriate to investigate core dryout and post-CHF heat transfer. Results were similar for the other CHF regimes.

Core dryout was also evaluated at conditions typical of a small-break loss-of-coolant accident. The method of Sun et al<sup>54</sup> was used to evaluate the ratio of collapsed liquid level in the core to the two-phase mixture level and the core dryout rate. The evaluation showed that core dryout would begin near the correct collapsed liquid level with all four models. The ratio of collapsed liquid level to mixture level was well scaled in all four models. The core dryout rate, as determined by the rate of decrease in the two-phase mixture level, was ideally scaled with the FHFPW model. The core dryout rate was fairly well scaled with the RHFPP and RHFPP models. The dryout rates were within 30% of the ideal (plant) dryout rate for the RHFPP and RHFPP models. However, the dryout rate was poorly scaled and with the RHRPW model as the dryout rate was a factor of fourteen too low. This result was consistent with the CHF results described previously.

Primary to secondary heat transfer phenomena were evaluated by assuming that the heat transfer was due to condensation on the primary side, heat conduction through the steam generator tubes, and nucleate boiling on the secondary side. Nusselt's laminar film condensation equation<sup>55</sup> was applied to the primary side, and Chen's nucleate boiling correlation<sup>56</sup> was applied to the secondary side. The total temperature difference between the primary and secondary sides was calculated for nominal decay heat as a function of pressure. The evaluation showed that condensation heat transfer was ideally scaled with the FHFPW model and well scaled with the RHFPP model. Condensation heat transfer was less well scaled with the RHRPW and RHFPP models. The primary to secondary temperature difference was less than half of the ideal difference for the RHRPW model and more than twice the ideal difference for the RHFPP model.

## CONCLUSIONS

The following conclusions have been drawn from the work completed to date on the Continuing Integral Testing Capability.

### Thermal-Hydraulic Data Base and Phenomena Identification

Based on examination of probabilistic risk assessment studies, plant operating history, international code assessment program results, available best estimated advanced computer code calculation, and plant safety analyses, the following transients were selected as the most important to reactor safety studies;

- o Small Break Loss-of-Coolant
- o Loss of Heat Sink
- o Anticipated Transient Without Scram
- o Steam Line Break
- o Large Break Loss-of-Coolant

Review of calculations for existing calculations indicates that Seabrook (W) and Oconee (B&W) are logical choices for reference plants.

Rating of phenomena of importance to simulate in an integral facility is as shown in Table 3 for the W design and Table 4 for the B&W design plant.

### Scaling Methodology

Based on a review of the existing scaling methodologies, the following conclusions have been drawn;

- o Specific scaling criteria such as volume scaling and linear scaling are subsets of the general relationships derived by Ishii.
- o Numerous possibilities are available for facility configuration
- o Local phenomena scaling will determine the applicability of specific concepts to selected transients.
- o Freon or low pressure water, as a working fluid can be scaled to high pressure water reasonably well through property group ratios.
- o Reduced height, dissimilar fluid, and lower pressure in a scaled facility offer potential construction and operating cost savings but will increase required analysis and data interpretation and complicate definition of specific reactor transients to be simulated at the model facility.

## Local Scaling Analysis

Based on the local scaling analysis, the following conclusions have been reached

- o Many reactor related phenomena scale well with Freon as a working fluid
- o Quality dependent phenomena will be distorted in a reduced pressure water system
- o Any new facility considered must allow for multidimensional effects in
  - plenums
  - downcomer
  - number of loops
- o The desire for simulation of multidimensional phenomena in a scaled integral facility dictates a reduced height system
- o Cost/Benefit analyses of new facility concepts will heavily influence decisions
- o Code assessment/development needs must be factored into any new integral facility considered.



## REFERENCES

1. U. S. Nuclear Regulatory Commission, Office of Standards Development, Standard Format and Content of Safety analysis Reports for Nuclear Power Plants LWR Edition, Regulatory Guide 1.7, Revision 3, November 1978.
2. N. G. Cathey et. al., Catalog of PRA Dominant Accident Sequence Information (draft), NUREG/CR-3301 EGG-2259, August 1984.
3. A. M. Kolaczowski et. al., Interim Report on Accident Sequence Likelihood Reassessment (Accident Sequence Evaluation Program), Sandia National Laboratories, August 1983.
4. V. H. Ransom et. al., RELAP5/MOD-2 Code Manual, Volumes 1 and 2 EGG-SAAM-6377 (draft), September 1983.
5. Safety Code Development Group, TRAC-PF1/MOD-1, An Advanced Best Estimate Computer Program for Pressurized Water Reactor Thermal-Hydraulic Analysis, Los Alamos National Laboratory (draft) February 1984.
6. INEL Plant Transient Analysis, EG&G Idaho letter from T. R. Charlton to F. L. Sims, TRC-48-84, May 16, 1984.
7. Sandia National Laboratories letter from L. D. Buxton to B. W. Sheron, April 20, 1984.
8. Argonne National Laboratory letter from L. W. Deitrich to B. W. Sheron, May 2, 1984.
9. List of Transient and Accident Analyses Performed Using TRAC, Los Alamos National Laboratory letter from J. W. Spore to H. S. Tovmassian, June 12, 1984.
10. Brookhaven National Laboratory letter from D. J. Diamond to B. W. Sheron, April 26, 1984.
11. Brookhaven National Laboratory letter from P. Saha to F. Odar, April 4, 1984.
12. C. D. Fletcher et. al., RELAP5 Thermal-Hydraulic Analyses of Pressurized Thermal Shock Sequences for the H. B. Robinson Unit 2 Pressurized Water Reactor, NUREG/CR-3977 EGG-2341, April 1985.
13. J. Koenig, Effects of the Reactor Coolant Pumps Following a Small Break in a Westinghouse PWR, LA-9784-MS NUREG/CR-3312, October 1983.
14. P. D. Wheatly et. al., TRAC-PIA Calculations for a 200%, 0.25 m-diameter, and 0.10 m-diameter Cold Leg Break in a Pressurized Water Reactor, EGG-CAAP-5190, June 1980.
15. B. Boyack, Loss-of-Offsite Power Transient for the Zion-1 PWR, LA-UR-83-1714, June 1983.

16. J. Lime, G. Willcutt, TRAC-PD2 Calculations for a Main-Steam-Line Break in a Westinghouse Pressurized Water Reactor with and without Reactor Coolant Pump Trip, LA-UR-82-3237, November 1982.
17. M. S. Lu et. al., Analysis of Loss-of-Feedwater Transients Without SCRAM for a Westinghouse PWR, BNL-NUREG-33673, July 1983.
18. J. Blakely and J. Cuzzuol, Best Estimate Analysis of a Small Break LOCA in a RESAR-3S Pressurized Water Reactor, EGG-NTAP-6032, September 1982.
19. C. A. Dobbe, Best Estimate Analysis of a Large Break LOCA in a RESAR-3S Pressurized Water Reactor, EGG-NTAP-6030, September 1982.
20. P. D. Bayless and R. Chambers, Analysis of a Station Blackout Transient at the Seabrook Nuclear Power Plant, EGG-NTP-6700, September 1984.
21. C. D. Fletcher et. al., RELAP5 Thermal-Hydraulic Analyses of Pressurized Thermal Shock Sequences for the Oconee-1 Pressurized Water Reactor, NUREG/CR-3761 EGG-2310, June 1984.
22. R. Henninger and N. Demuth, Loss-of-Offsite Power Initiated Loss-of-Feedwater Transients for B&W Plants, LA-UR-83-3001, October 1983.
23. J. Ireland et. al., Preliminary Calculations Related to the Accident at Three Mile Island, NUREG/CR-1353 LA-8273MS, March 1980.
24. G. Willcutt, TRAC-PD2 Calculations of Design-Basis and Severe Overcooling Transients in a Babcock and Wilcox Lowered-Loop Plant, LA-SBT-A-TN-81-6, February 1982.
25. C. A. Dobbe, Analysis of a Station Blackout Transient for the Bellefonte Pressurized Water Reactor, Draft Preliminary Report for Comment, EG&G Idaho, April, 1984.
26. EG&G Idaho internal letter from W. C. Phoenix to B. F. Saffell, Categorization of PWR and BWR Plants for SASA Work, WCP-19-80, August 22, 1980.
27. NUS Corporation, Commercial Nuclear Power Plants Edition 16, February 1984.
28. Nuclear Safety, Volume 26-1, January-February 1985.
29. M. Ishii and I. Kataoka, "Scaling Criteria for LWR's Under Single-Phase and Two-Phase Natural Circulation," Argonne National Laboratory Report ANL-83-32, NUREG/CR-3267, March (1983).
30. G. Kocamustafaogullari and M. Ishii, "Scaling Criteria for Two-Phase Flow natural and Forced Convection Loop and Their Application to Conceptual 2 x 4 Simulation Loop Design", NUREG/CR-3420, ANL-83-61, May 1983.

31. M. Ishii, "Description of the Planned ANL Simulation and Phenomenological Study for Hot Leg U-Bend Flow," Argonne National Laboratory (to be published).
32. A. Carbiener and R. A. Chudnik, "Similitude Considerations for Modeling Nuclear Reactor Blowdowns," Trans. Am. Nucl. Soc., Vol. 12, p. 361 (1969).
33. A. N. Nahavandi, F. C. Castellana, and E. N. Moradkhanian, "Scaling Laws for Modeling Nuclear Reactor Systems," Nucl. Sci. & Eng., Vol. 72, p. 374 (1982)
34. T. K. Larson et. al/. "Results of Continuing Integral Testing Capability Study, NUREG to be published.
35. G. E. McCreery, J. H. Linebarger, and J. E. Koske, Primary Pump Power as a Measure of Fluid Density During Bubbly Two-Phase Flow, Proceedings of Second International Topical Meeting on Nuclear Reactor Thermal-Hydraulics, Santa Barbara, CA, January 1983.
36. D. Furuya, An Analytical Model for Prediction of Two-Phase (noncondensable) Flow Pump Performance, Journal of Fluids Engineering, March 1985, Volume 107/139.
37. D. G. Hall and L. S. Czapary, Tables of Homogeneous Equilibrium Critical Flow Parameters for Water in SI Units, EGG-2056, 1980.
38. W. H. Grush and G. E. McCreery, Posttest Analysis of Loss-of-Fluid Tests L3-2 and L3-7, EGG-LOFT-5632, October 1981.
39. P. A. Roth and H. Chow, Analysis of a Liquid Metal Cooled Blanket Transient Using ATHENA, Fusion Technology, Volume 8, No. 1, Part 2A, Page 581.
40. J. B. Young, Critical Conditions and the Choking Mass Flow Rate in Nonequilibrium Wet Steam Flows, Transfer of the ASME J. Fluids Engineer, December 1984, Volume 106, Page 452.
41. G. Hetsroni, Editor, Handbook of Multiphase systems, Hemisphere, 1982.
42. J. Weisman, et al., "Effects of Fluid Properties and Pipe Diameter on Two-Phase Flow Patterns in Horizontal Lines," I. J. Multiphase Flow, Volume 5, Pages 437-462, 1979.
43. Y. Taitel and A. E. Dukler, "Modeling Flow Pattern Transitions for Steady Upward Gas-Liquid Flow in Vertical Tubes," AICHE Journal, Vol. 2, No. 3, May 1980.
44. A. E. Bergles, et al., Two-Phase Flow and Heat Transfer in the Power and Process Industries, Hemisphere, 1981.
45. R. T. Lahey Jr. and F. J. Moody, The Thermal-Hydraulics of a Boiling Water Nuclear Reactor, ANS, 1979.

46. G. B. Wallis, One-Dimensional Two-Phase Flow, McGraw-Hill, 1969.
47. S. S. Kutateladze, "Elements of Hydrodynamics of Gas-Liquid Systems," Fluid-Mechanics-Soviet Research, 1, 29-50, 1972.
48. G. B. Wallis and J. E. Dobson, "The Onset of Slugging in Horizontal Stratified Air-Water Flow," Int. J. Multiphase Flow, 1, 173, 1973.
49. O. L. Pushkina and Y. L. Sorokin, "Breakdown of Liquid Film Motion in Vertical Tubes," Heat Transfer-Soviet Research, 1, 56, 1969.
50. F. Mayinger "Scaling and Modelling Laws in two-phase Flow and Boiling Heat Transfer, Chapter 14 of Two-Phase Flow and Heat Transfer in the Power and Process Industries, Hemisphere, 1981.
51. W. P. Rohsenow and J. P. Hartnett, Handbooks of Heat Transfer, McGraw-Hill, 1973, P. 13-34.
52. M. Ishii and I. Kataska, Similarity Analysis and Scaling Criteria for Two-Phase Natural Circulation, NUREG/CR-3267, ANL-83-82, March 1983, P. 24.
53. J. G. Collier, Convective Boiling and Condensation, McGraw-Hill, 1972, P. 255.
54. K. H. Sun et al, "The Prediction of Two-Phase Mixture level and Hydro-dynamically-Controlled Dryout Under Low Flow Conditions," Int. J. Multiphase Flow, Vol. 7, No. 5., Pages 521-543, 1985.
55. Collier, P. 317.
56. Collier, PP. 211-212

## Results of CCTF Tests

Yoshio MURAO, Tadashi IGUCHI, Jun SUGIMOTO,  
Hajime AKIMOTO, Tsutomu OKUBO, Tsuneyuki HOJO

Japan Atomic Energy Research Institute

### 1. Introduction

A reflood test program<sup>(1)</sup> for a large-break Loss-Of Coolant Accident (LOCA) of Pressurized Water Reactor (PWR) has been conducted at Japan Atomic Energy Research Institute (JAERI), by using large scale test facilities, which are the Cylindrical Core Test Facility (CCTF)<sup>(2)</sup> and the Slab Core Test Facility (SCTF)<sup>(3)</sup>. This program has been in a part of 2D/3D project which is performed by USNRC, BMTF and JAERI.

The CCTF is an experimental facility designed to model a four-loop 1100 MWe class PWR<sup>(4)</sup> with the flow area scaling ratio of 1/21.4 and to simulate the thermo-hydraulic behavior in the primary system during the refill and the reflood phases of a PWR-LOCA. The CCTF has a full-height scaled pressure vessel with a cylindrical core of about 2000 electrically-heated rods and four loops with passive and active components.

The main purpose of the CCTF tests is to investigate the integral system behavior as well as the core thermo-hydraulic behavior during the refill and reflood phases of a PWR-LOCA.

Since 1979, JAERI has performed 56 CCTF tests. They can be classified into 5 categories.

---

The work was performed under contract with the Atomic Energy Bureau of Science and Technology Agency of Japan.

- (1) Cold-leg-injection simulation tests under evaluation model (EM) condition.
- (2) Cold-leg-injection simulation tests for parametric effect study.
- (3) Cold-leg-injection tests to verify that the CCTF simulates a PWR properly.
- (4) Alternative ECC simulation tests, such as upper plenum injection, downcomer injection and combined injection (cold legs and hot legs).
- (5) Refill simulation tests to investigate the thermal hydraulics in the primary system during the end-of-blowdown to reflood initiation.

The experimental work of JAERI for CCTF has completed in March, 1985. Currently, the analytical work is in progress. The major findings upto the last year for the cold leg injection simulation tests are :

- (1) The thermo-hydraulics in the primary system are nearly the same as the current EM models assumed in the safety evaluation analysis.
- (2) The core cooling is much better than that predicted with the current EM model.

It can be concluded that the current EM model is reasonable and that it conservatively predicts the clad temperature during the reflood phase.

The JAERI's activity is mainly focused on alternative ECC simulation tests and refill simulation tests for this year. In this presentation, the following topics are explained ;

- (1) Refill test,
- (2) Upper plenum injection test and
- (3) Combined injection test.

## 2. CCTF Facility

The CCTF is designed to provide the capability to reasonably simulate the flow conditions in the primary system of a PWR during the refill and reflood phases of a large-break LOCA, and models a four-loop 1100 MWe class PWR with the flow area scaling ratio of 1/21.4. It has a scaled pressure vessel with a full height core and four loops with passive and active component simulators, eg. active steam generators, pump simulators and containment tank, as shown in Fig. 1.

The core has about 2000 electrically heated rods arranged in cylindrical configuration, as shown in Fig. 2. Each heated rod is a full-size 15 X 15 - array fuel rod simulator. It consists of a spiral heater element, insulator, and inconel clad. The diameter and the heated length of the rod are 10.7 mm and 3.66 m, respectively. Each rod has an axial power distribution with a peaking factor of 1.4. The core can be subdivided into three regions to achieve a desired radial power profile, as indicated by A, B and C regions in Fig. 2. An annulus downcomer with a gap of 61.5 mm is surrounding the core.

The CCTF simulates a 200 % cold leg break and can be operated at the pressure less than 0.6 MPa. The various ECC simulations (cold leg injection, downcomer injection, upper plenum injection and combined injection) are equipped.

The broken hot and cold legs have cold-leg-break-simulation valves to simulate the end-of-blowdown by quickly opening the valves which function as pressure boundaries.

### 3. Refill test with core reversal steam flow

#### 3.1 Objective

A part of generated steam due to flashing in the upper head is expected to flow through the core to the lower plenum at the end-of-blowdown phase of a cold leg large break LOCA. The objective of this refill test is to investigate the effect of this core reversal steam flow on the thermo-hydraulic behavior during the end-of-blowdown to reflood initiation. In the test, the steam is injected into upper plenum to simulate the steam generation due to flashing in the upper head.

#### 3.2 Test procedure and evaluation method

Figure 3 shows the test procedures of this refill test. The pressure vessel was pressurized up to 0.6 MPa and the lower plenum was filled with saturated water to the specified level before test start (Fig. 3(1)) for the pre-conditioning of the test. By opening the cold-leg-break-simulation valves, the depressurization of the vessel was initiated (Fig. 3(2)) and subsequently ECC water was injected into cold legs. At the same time, the steam injection into upper plenum was initiated to simulate the steam generation due to flashing in the upper head (Fig. 3(3)). At 20 s after initiation of steam injection, steam injection was terminated (Fig. 3(4)). The power was determined based on the following equation, referring 30 s after scram.

$$1.02 \times (\text{ANS} \times 1.2 + \text{Actinide} \times 1.1) \times \text{Fex}$$

Fex is an experimental margin ( $\approx 1.07$ ) used in CCTF tests to attain a conservative experimental condition.

The test results was compared with the previous refill test with no steam injection that is, no steam injection refill test<sup>(5)</sup> in order to investigate the effect of steam injection.

#### 3.3 Results

Figure 4 shows the comparison of the water inventory in lower plenum between the steam injection refill test and no steam injection refill test, which has been performed for a reference.

In no steam injection refill test, the refill initiated at 3~4 s after the start of Accumulator (Acc) injection. On the other hand, the refill initiated at 10 s after the start of Acc injection in the steam injection refill test. It is considered that the delayed refill initiation of the steam injection refill test was caused by the core reversal steam



flow.

In the steam injection refill test, the increasing of water inventory in lower plenum is very low in steam injection period, in order words, in depressurization period. It is considered that the ascending steam (or two phase) flow in downcomer restrains the complete penetration of ECC water into lower plenum in this period.

At the termination of steam injection (nearly equal to the termination of the depressurization), the lower plenum is rapidly filled with water due to the fall back of the water held in the downcomer. Eventually the reflood initiates at 3.1 s after the start of the depressurization. In steam injection period, the upper and central portions of the core were cooled due to core reversal steam flow. The steam became high temperature due to this heat transfer in upper core, and lower portion of core is slightly heated by the high temperature steam flow.

#### 3.4 Summary

The test results showed the followings.

- (1) A part of the steam injected into upper plenum flowed downward in the core and delayed the end of bypass.
- (2) In the period of the depressurization, the downcomer CCFL continued and the lower plenum filling was restrained. In this period, the core cooling due to core reversal steam flow was observed.
- (3) At the termination of the depressurization, the lower plenum was rapidly filled with the water held in the downcomer due to the fall back, and eventually the reflood initiated.

#### 4. Upper plenum injection test under single failure condition of LPCI pump

##### 4.1 objectives

In several two-loop PWRs, the ECC water is injected directly into the upper plenum with a Upper Plenum Injection (UPI) system as a Low Pressure Coolant Injection (LPCI). For UPI system, the ECC water is injected through two injection nozzles located diagonally on the side wall of the upper plenum. If assuming no failure of LPCI pumps, the ECC water is injected relatively symmetrically through two injection nozzles. On one hand, if assuming single LPCI pump failure, the ECC water is injected only through one injection nozzle and the UPI rate becomes half of one at no LPCI pump failure. In this case, the distribution of UPI water becomes asymmetrical and the core cooling might be degraded in a localized region.

An asymmetric UPI test with simulating single LPCI pump failure has been performed with CCTF. The objectives of the test are to investigate the effect of asymmetric UPI on reflood phenomena and to confirm the effective core cooling under asymmetric UPI simulating single LPCI pump failure.

##### 4.2 Test procedure and evaluation method

Figure 5 shows the test procedure and the location of the ECC injection, respectively. The ECC water simulating Acc and High Pressure Coolant Injection is injected into cold legs after short injection into lower plenum. The ECC water simulating LPCI is injected asymmetrically into upper plenum. The rate is determined based on single LPCI pump failure.

The pressure at break point was set at 0.2 MPa. The power was set at the same value as in the refill test. In order to examine the effect of asymmetrical injection, a reference test named symmetrical injection test<sup>(6)</sup> was performed for comparison with the same test condition except for injection manner where two nozzles were used but total flow rate was preserved as the asymmetric injection test and ratio of flow rates to two nozzles were 1 : 1.6.

##### 4.3 Result

Figure 6 shows the representative clad temperature in horizontally different position at the core midplane (1.83 m elevation) where the maximum clad temperature was observed. The clad temperature is higher with the higher power density. However, it is little variant except for the clad temperature with top-quenching as far as the power density is equal. This indicates that the localized degradation of core cooling is hardly observed

under asymmetric UPI condition at the elevation.

Figure 6 shows also the representative clad temperature at 2.44 m elevation. The clad temperature is rather variant at the elevation than the midplane. However, the heat transfer coefficient on the rod, where the core cooling is the poorest in each power zone, is higher in asymmetric UPI test than symmetric UPI test, as shown in Fig. 7. Since then, even in the upper part of the core, it is considered that the degradation of the core cooling due to the asymmetric UPI does not occur. This enhancement of the heat transfer coefficient under asymmetric UPI condition is considered to be due to two dimensional flow in upper core as well as upper plenum, which is promoted by asymmetric UPI. The significant two dimensional flow under asymmetric UPI condition is suggested by the measured axial differential pressure distribution in upper core and the measured steam up-flow distribution with turbine meters located at end box.

Figure 8 shows the quench time for asymmetric UPI test and symmetric UPI test. The variance of the quench time at each elevation is shown with a horizontal bar. Earlier quench than the quench at lower elevation is considered to be quench from top of core, that is, top-quench. Asymmetric injection shows more influence on top quenching than symmetric injection. This indicates that the asymmetric UPI promotes the top quenching occurrence. The promotion of top quenching must be due to the significant two dimensional flow mentioned above. On the contrary, the quench time in the region of bottom quenching is nearly the same with each other for both tests.

#### 4.3 Summary

The test results showed the followings.

- (a) The effective core cooling was observed even under the conditions of the single failure assumption of LPCI pumps.
- (b) The asymmetric upper plenum injection gave rather good core cooling as the symmetric upper plenum injection.
- (c) Asymmetrical injection showed more influence on top-quenching than symmetrical injection and weak influence on bottom-quenching.

## 5. Combined injection tests

### 5.1 Objectives

The objectives of the tests are to investigate the thermo-hydraulics during the refill and reflood phases of a LOCA in combined injection type PWRs like German PWR in which the ECC water is injected into cold legs and hot legs simultaneously and to confirm the effective core cooling under combined injection condition.

According to the safety evaluation in Germany, a single failure of active component and a repairment of passive component are assumed. The most severe case is predicted to be the combination of a LPCI pump failure and a failure of a block valve at ECC injection line to a hot leg. For an evaluation model (EM) condition, this combination can be assumed. On one hand, for a best estimation (BE) condition, no failure of LPCI pumps and no repairment of block valves are assumed.

With CCTF, the thermo-hydraulics under EM condition and BE condition have been investigated. In addition, the effect of the ECC flow rate into hot legs is investigated.

### 5.2 Test condition

The purpose and the major test conditions for three combined injection tests are as follows:

Test No (Test ID)	Purpose	Major test conditions
Run 79 (EM test)	Thermal hydraulics under EM condition	5/8 ECC (2HL + 3CL) Steep radial power profile
Run 80 (BE test)	Thermal hydraulics under BM condition	7/8 ECC (4HL + 3CL) Flat radial power profile
Run 81 (Hi-ECC EM test)	Effect of ECC flow rate into hot legs	7/8 ECC (4HL + 3CL) Steep radial power profile

Figure 9 shows the test procedure for EM test.

The ECC flow rate for BE test was nearly equal to that for high-ECC EM test and is twice of that for EM test. The radial power profile was flat

for BE test and steep for both EM test and high-ECC EM test. For the combined injection type PWR the ECC water from hot leg injection port is predicted to come in an upper plenum at the refill initiation. So that, the above combined injection tests with CCTF simulates the hydraulics from 0.6 MPa of the pressure, which is predicted to be pressure at end-of-blowdown.

### 5.3 Results

Figure 10 shows the axial differential pressure in upper plenum for EM test. Up to 20 s after ECC injection initiation, mass calculated from the differential pressure is equal to the integrated mass of the water injected into hot legs. This indicates that the counter current flow limitation (CCFL) occurs at tie plate due to steam up-flow generated by flashing in lower plenum and the water in upper plenum is prevented from falling-down.

The differential pressure decreases rapidly during about 20 ~ 30 s, when the depressurization terminates. This indicates that CCFL breaks occurred at that time and much amount of water in upper plenum, fell back into the core due to decrease of the steam up-flow.

Figure 11 shows the typical clad temperature transients in peripheral and central regions in the core for EM test. It was found excellent core cooling in this test. A rod in the peripheral region shows that the early quenching occurs simultaneously from the top to the bottom during 20 ~ 30 s, when the break through occurs. On the other hand, a rod in the center region shows the gradial quenching from the bottom.

Figure 12 shows the map of location of the early quenching due to the break through for EM test. The early quenching is localized in the region near a hot leg, where the ECC water is injected, suggesting that the break through is localized. The core thermo-hydraulic behavior in bottom quench region was similar as that for cold leg injection type ECCS.

Figure 13 shows the distribution of the fluid temperature in upper plenum for EM test. At the elevation of the hot legs, the fluid temperature is low in the region near hot legs where the ECC water is injected. However the region of high-subcooled fluid more concentrates at lower elevation. This indicates that the fluid mixing in upper plenum is not so good and there exists a three dimensional flow towards the break through region.

Figure 14 shows the measured differential pressure at each location in loops for EM test. The differential pressure across steam generator

(SG) is nearly zero for intact loops, indicating no fluid flow through intact loops. Accordingly, most ECC water injected into hot legs is considered to flow into upper plenum and then into the core. The differential pressure from loop seal bottom to pump outlet shows a rapid increase at 20 s after ECC injection, indicating the water filling of loop seal in intact loops. Both the differential pressure across SG inlet plenum including the hot leg riser part and the differential pressure from loop seal bottom to pump outlet is oscillatory from 50 s to 100 s in broken loop. Since both oscillation is out of phase with each other, it is considered that the oscillation is caused by the increase of water level in SG U tubes, the increase of the generated steam, the increase of the pressure loss at pump simulator, and resultant pushing back of water level in SG U tubes.

According to the observation of the fluid behavior, the solid water with including few tiny bubbles stagnated in hot legs this observation result and no intact loop mass flow suggest that the steam is condensed completely in upper plenum, due to the subcool energy of water injected into hot legs. Therefore it is concluded that the system behavior was completely different from that for cold leg injection type ECCS as shown in Fig. 15.

The localized CCFL break-through at end box, the significant horizontal ununiformity of core cooling and upper plenum thermal hydraulics and fluid oscillation in broken loop were commonly observed even in BE test and high-ECC EM test. In addition, most ECC water injected into hot legs flew into core via upper plenum and steam generated in core was completely condensed in upper plenum due to subcooled ECC water injection into hot legs for both two tests. The core was also cooled effectively in BE test and high-ECC EM test.

#### 5.4 Summary

The test results showed the followings.

- (a) The following three characteristic thermal hydraulics were observed:
  - (i) localized CCFL break-through at end box
  - (ii) significant horizontal ununiformity of core cooling and upper plenum thermal hydraulics
  - (iii) fluid oscillation in broken loop
- (b) The effective core cooling was observed both under EM condition and best estimate condition.

- (c) Most ECC water injection into hot legs flew into upper plenum and then into core.
- (d) Steam generated in core was completely condensed in upper plenum due to subcooled ECC water injected into hot legs.
- (e) System behavior was completely different from that for cold leg injection type ECCS, however core thermo-hydraulic behavior in bottom quench region was almost the same.

#### 6. Concluding remarks

We have completed CCTF tests for refill and reflood phases in PWRs with various ECCS. We appreciate contribution of US and FRG on polishing up of design, experimental plan and interpretation of test results. Analysis by TRAC code and data from US-provided advanced instrumentation provided much information for analysis.

Analyses are still in progress and will be summarized in near future. In this process, data from UPTF are expected to provide much information on scaling problems.

#### 7. Reference

- (1) Hirano, K. and Murao, Y. : Large scale reflood test, J. At. Energy Soc. Japan, (in Japanese), 22 [10], 681 (1980).
- (2) Okubo, T. et al. : Evaluation report on CCTF Core-II reflood test C2-4 (Run62), JAERI-M 85-026, (1985).
- (3) Adachi, H. et al. : Design of slab core test facility (SCTF) in large scale reflood test program, Part 1 : Core-I, JAERI-M 83-080, (1983)
- (4) Trojan nuclear plant, Final safety analysis report volume 1~9, DOCKET-50344-38 46, (1973).
- (5) Murao, Y. et al. : Status of CCTF/SCTF test programs, 12th WRSR information meeting, Maryland, USA (1984).
- (6) Murao, Y. et al. : Results of CCTF upper plenum injection tests, 12th WRSR information meeting, Maryland, USA (1984).

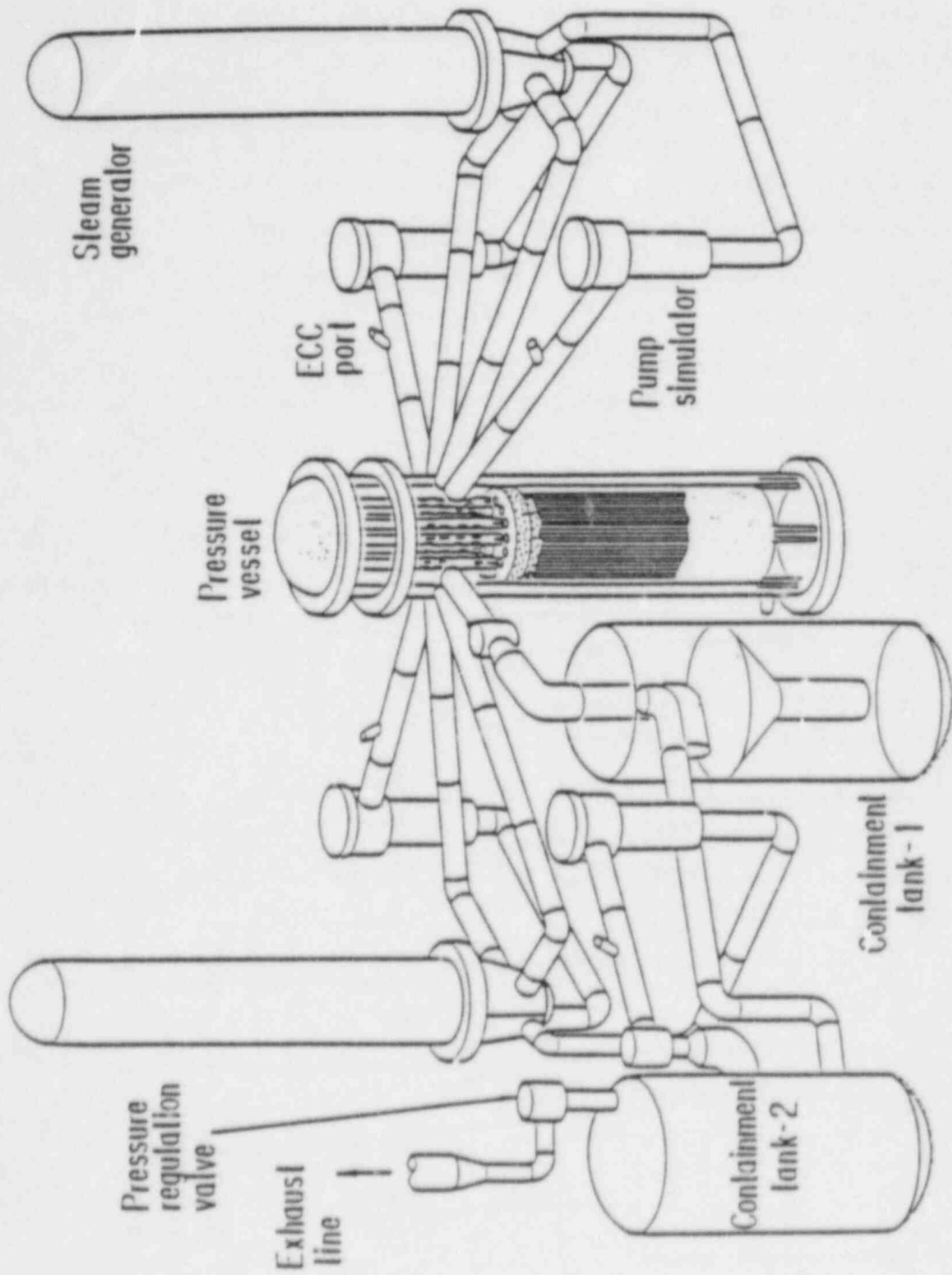
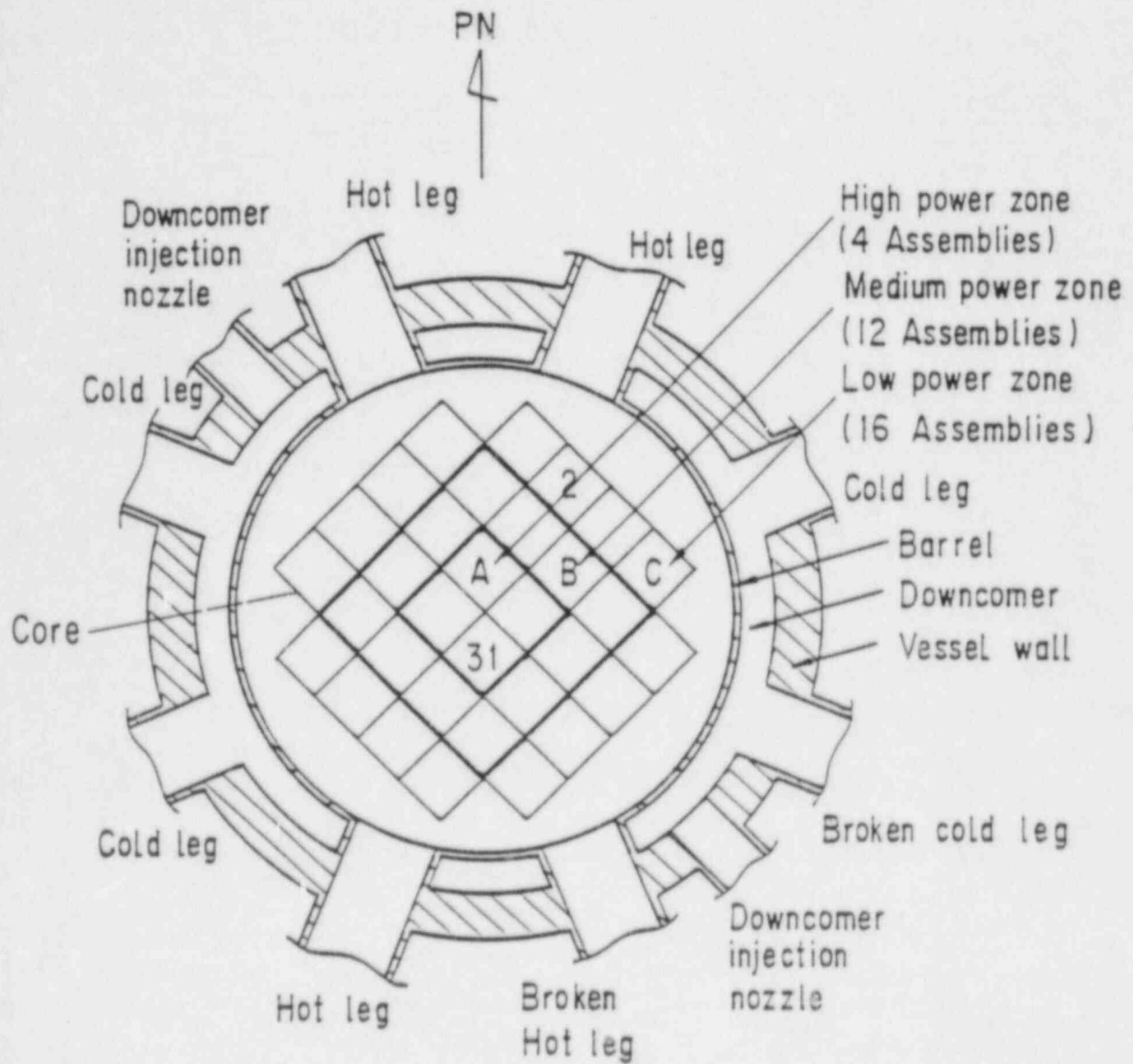


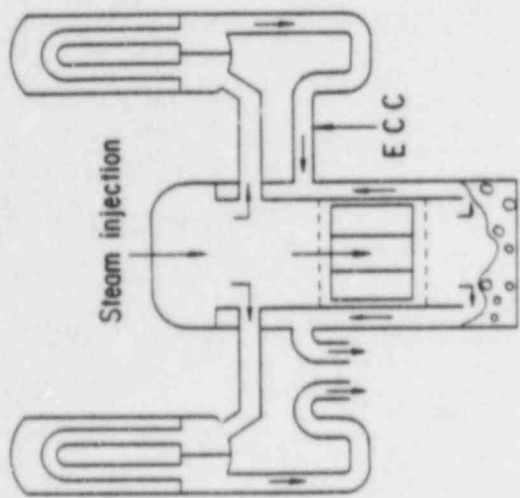
Fig. 1 Bld's-eye view of CCTF



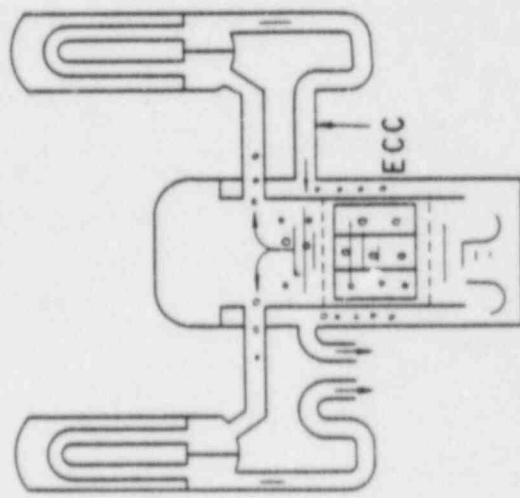


( Number in core shows bundle number referred in this paper )

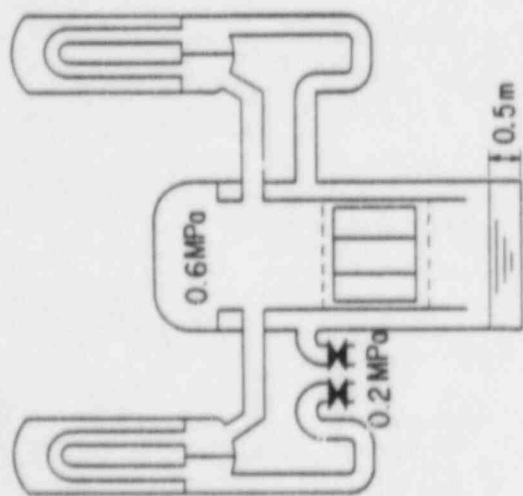
Fig.2 Cross section of CCTE Core-II



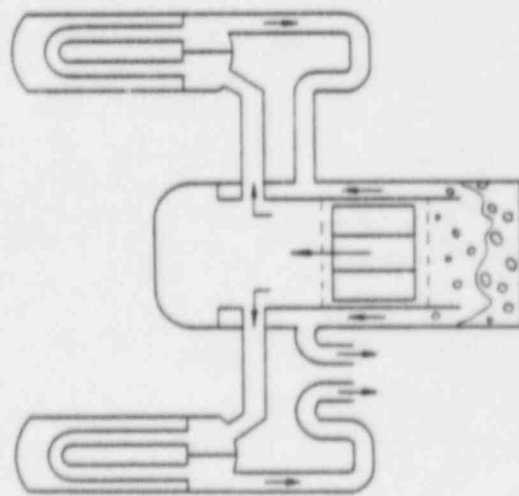
(3) During steam injection



(4) After termination of steam injection



(1) Before test start



(2) After initiation of depressurization

Fig.3 Test procedure for the refill test

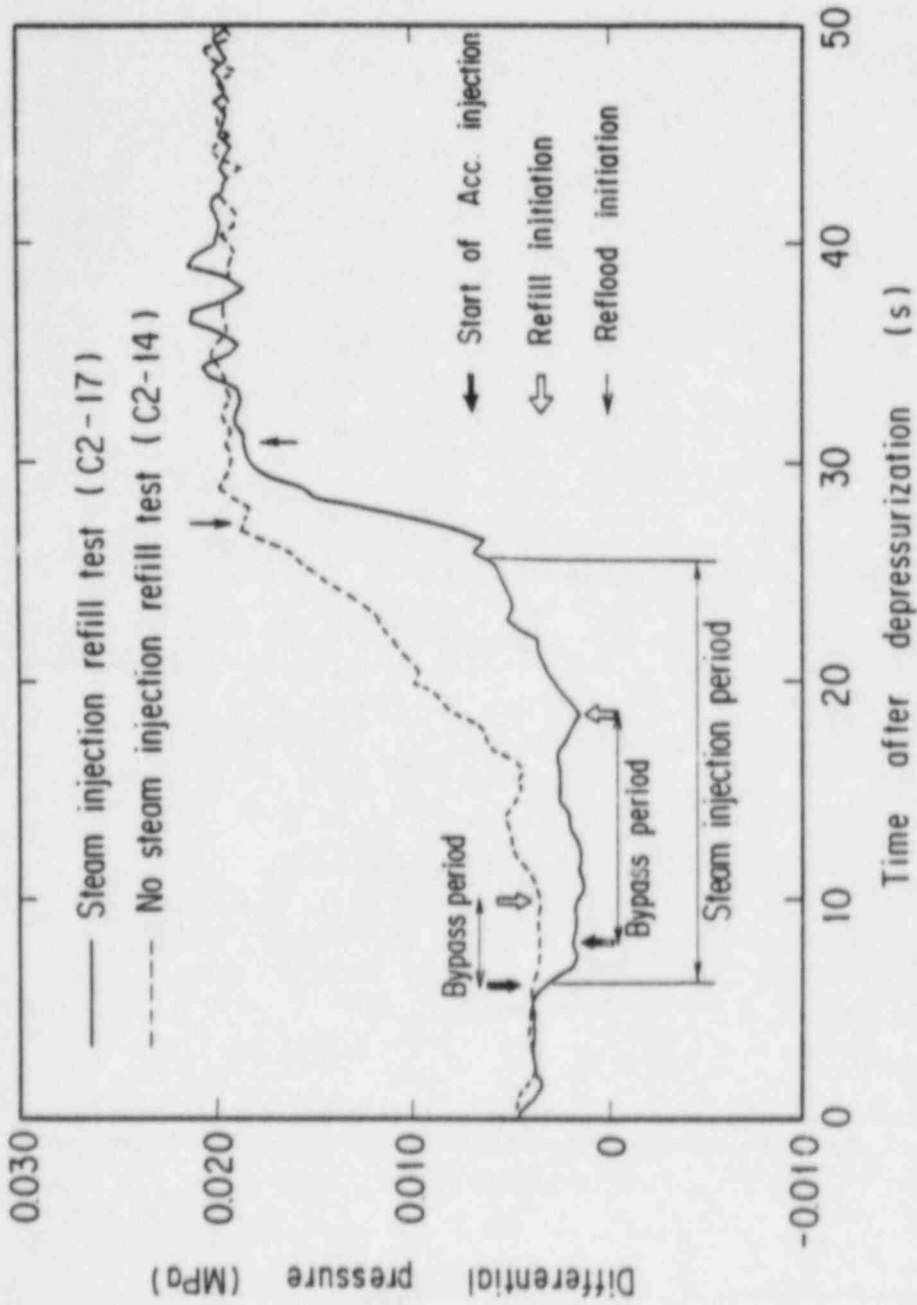


Fig.4 Effect of steam injection on water inventory in lower plenum

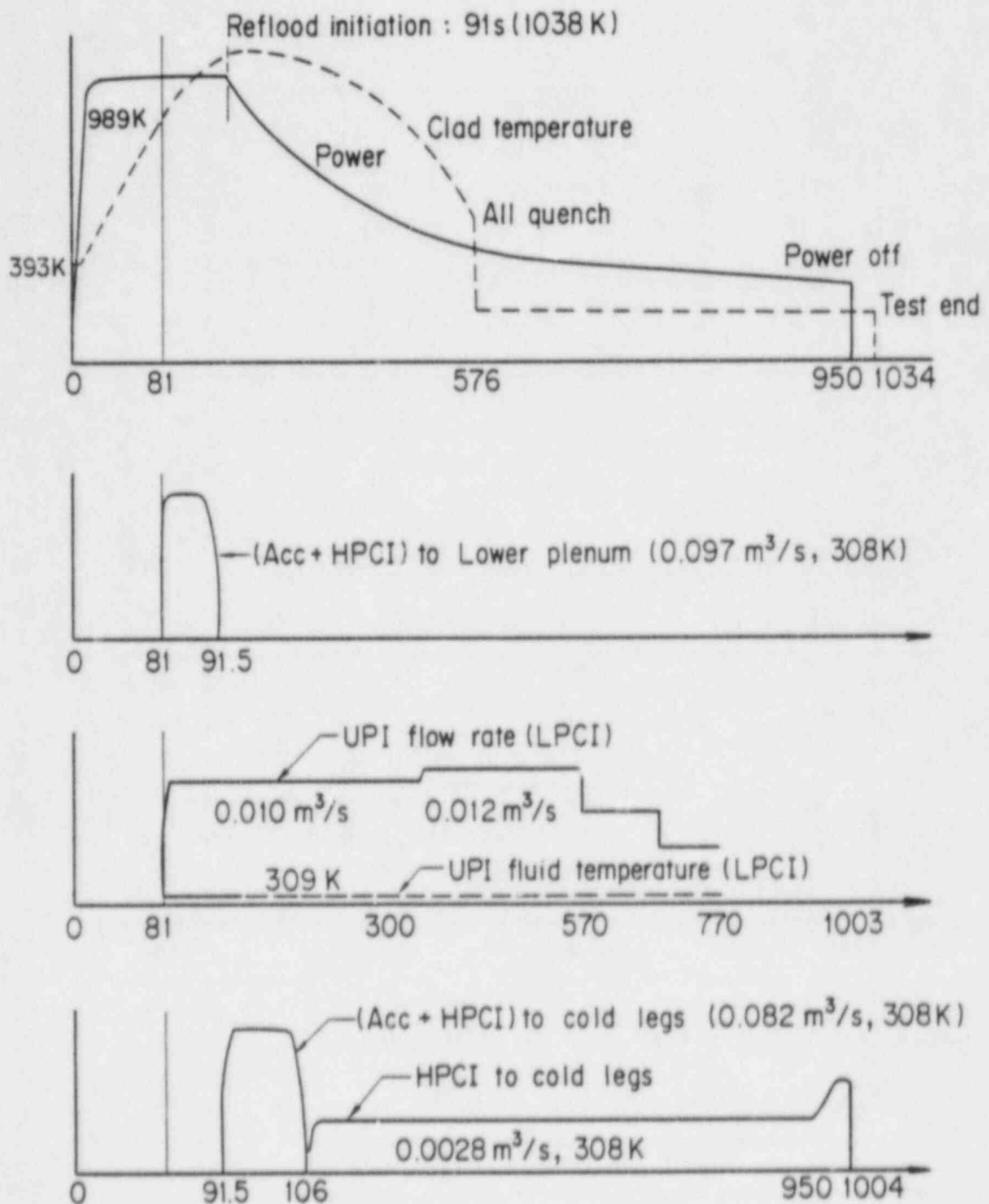


Fig. 5 Test sequence of UPI test

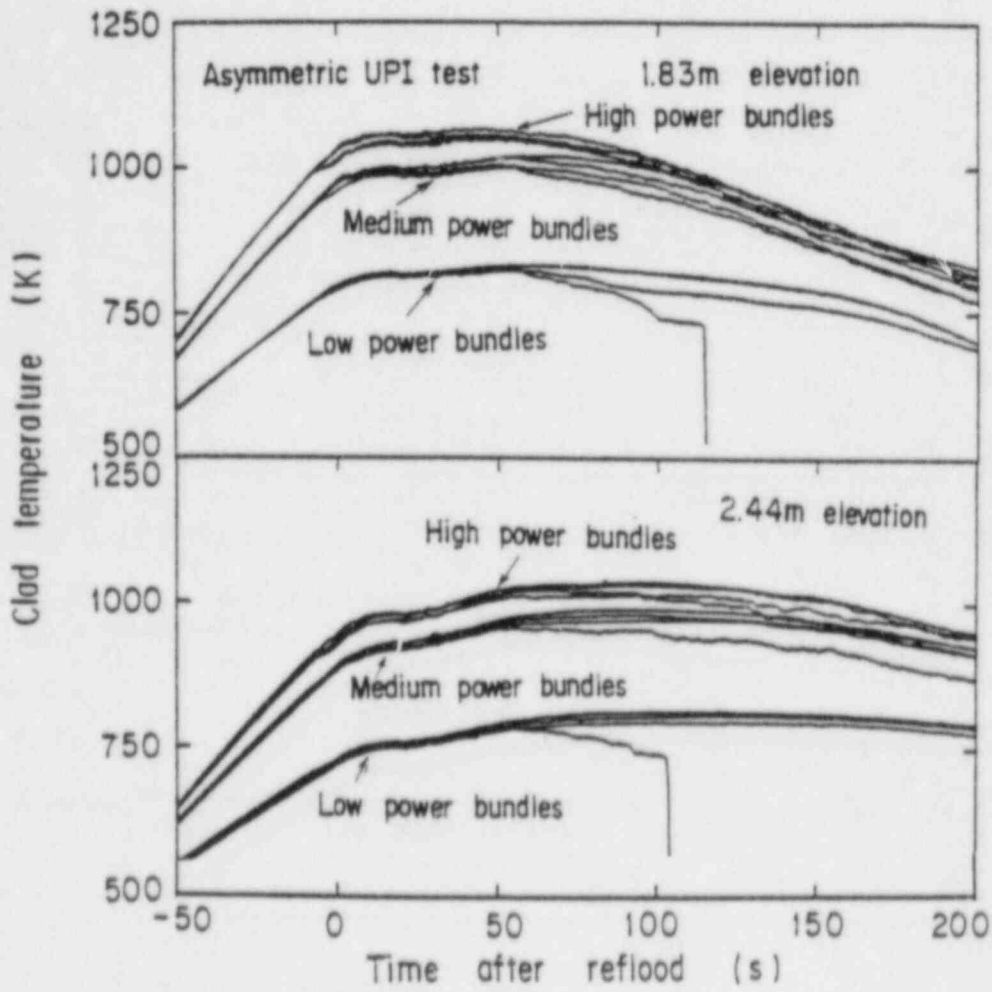


Fig.6 Radial uniformity of clad temperature

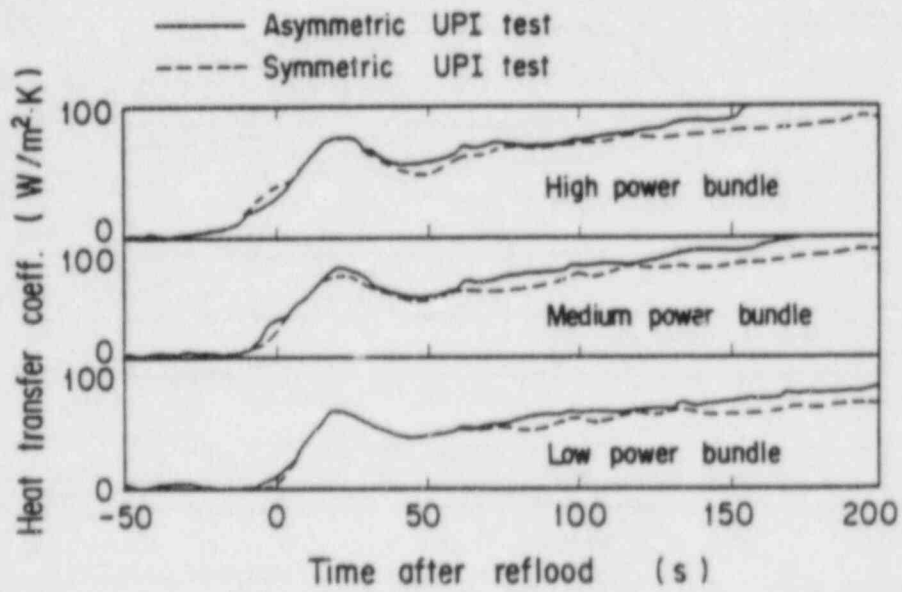


Fig.7 Comparison of heat transfer coefficient (244m elevation)

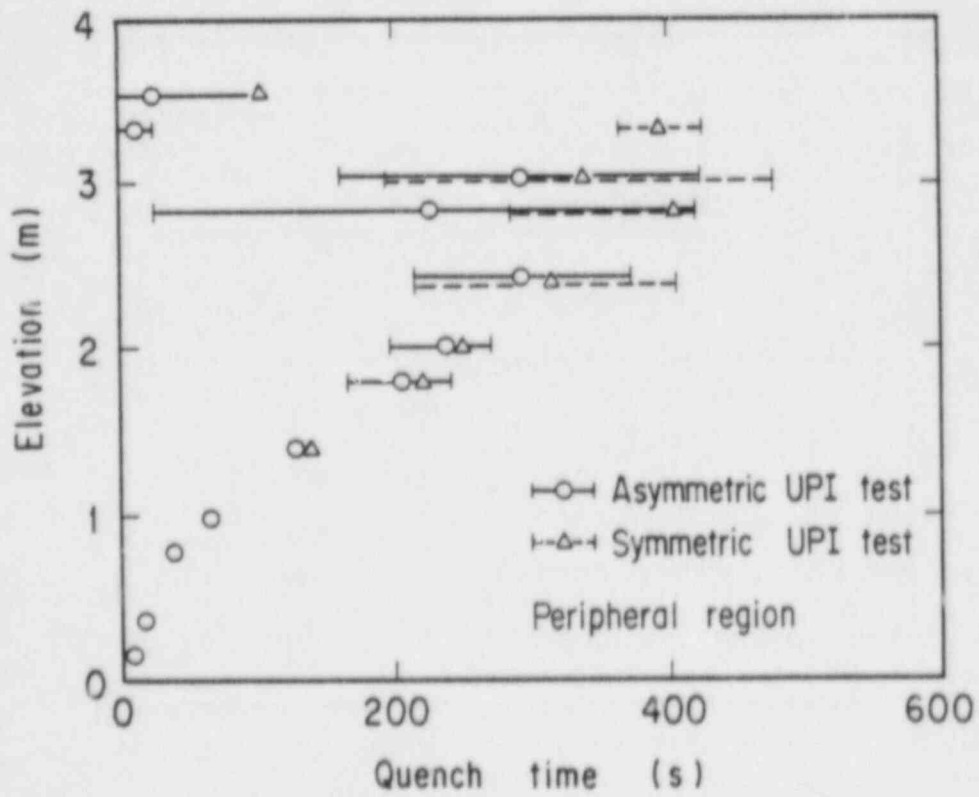
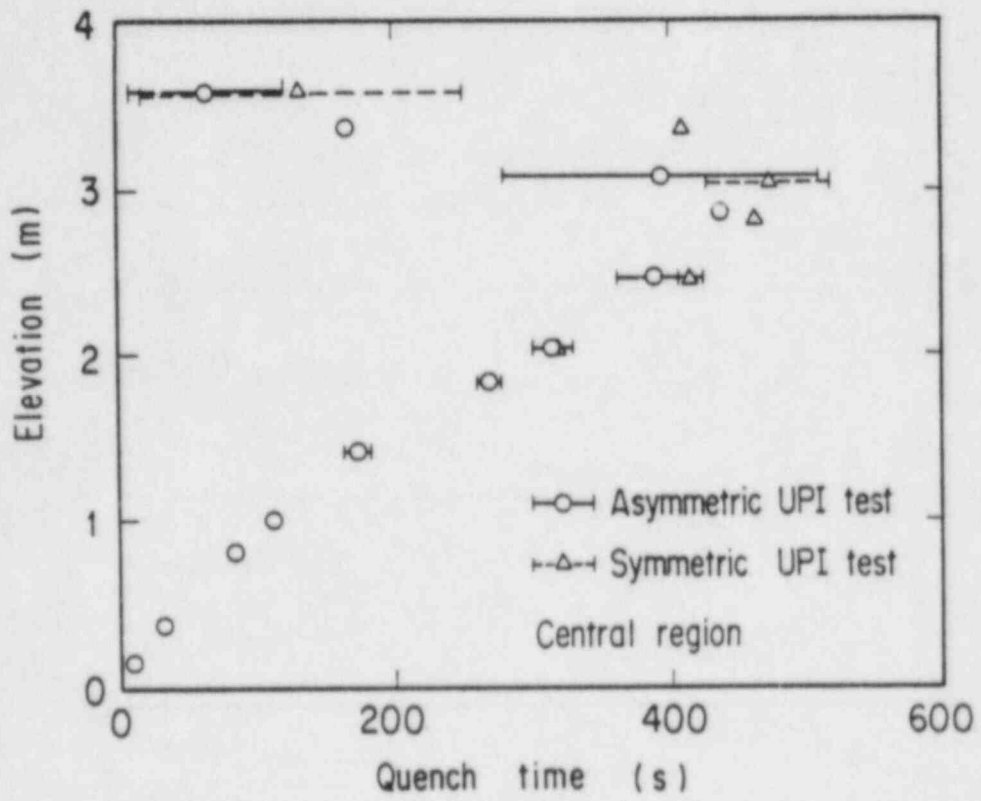


Fig. 8 Comparison of quench time

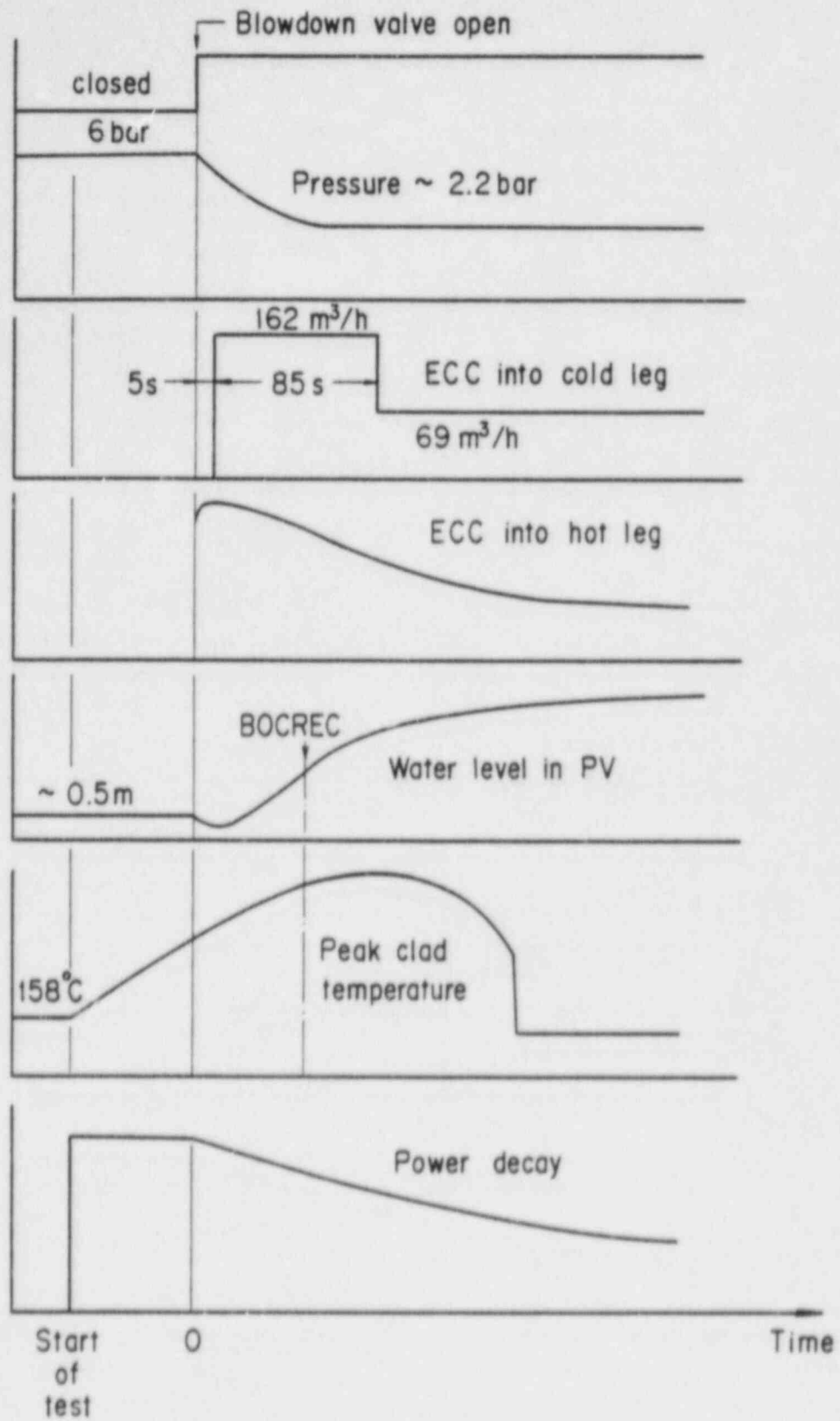


Fig.9 Test sequence of combined injection test (Run 79)



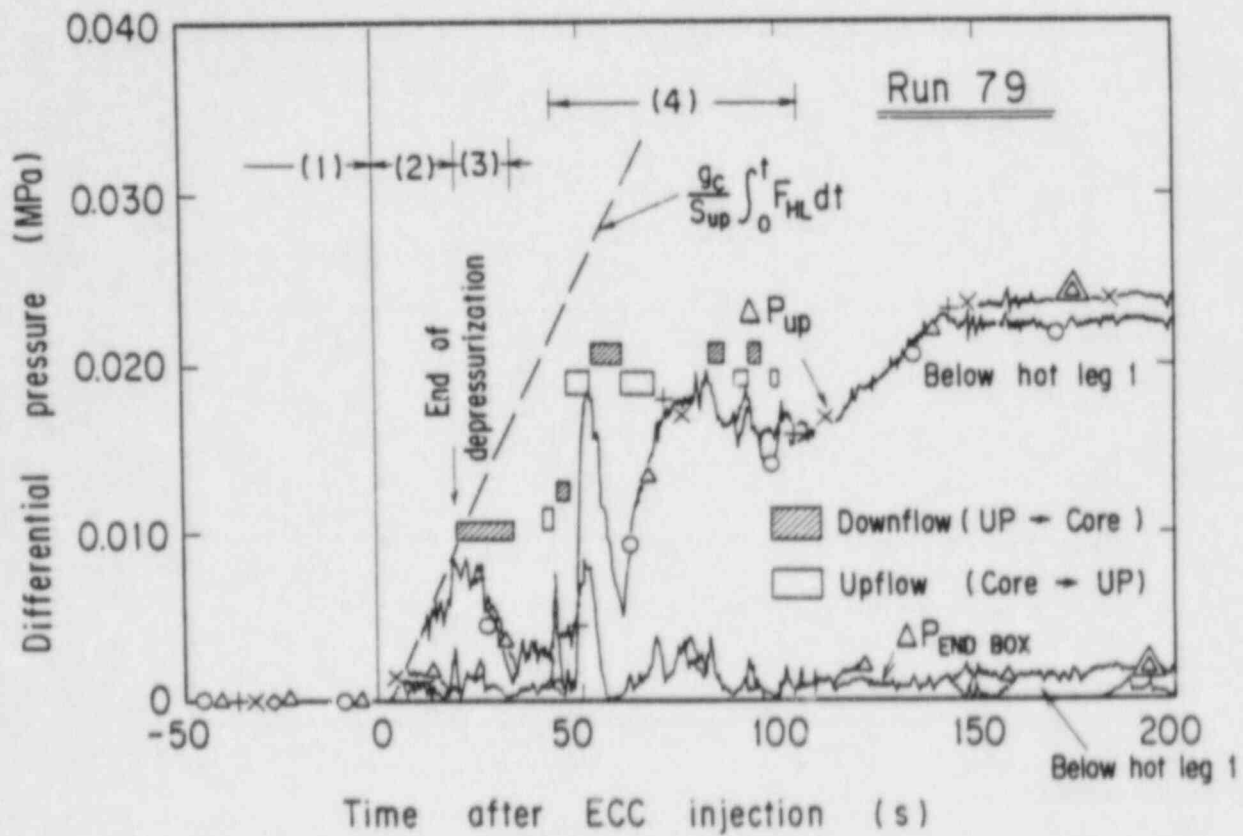


Fig.10 Differential pressure of upper plenum and end box

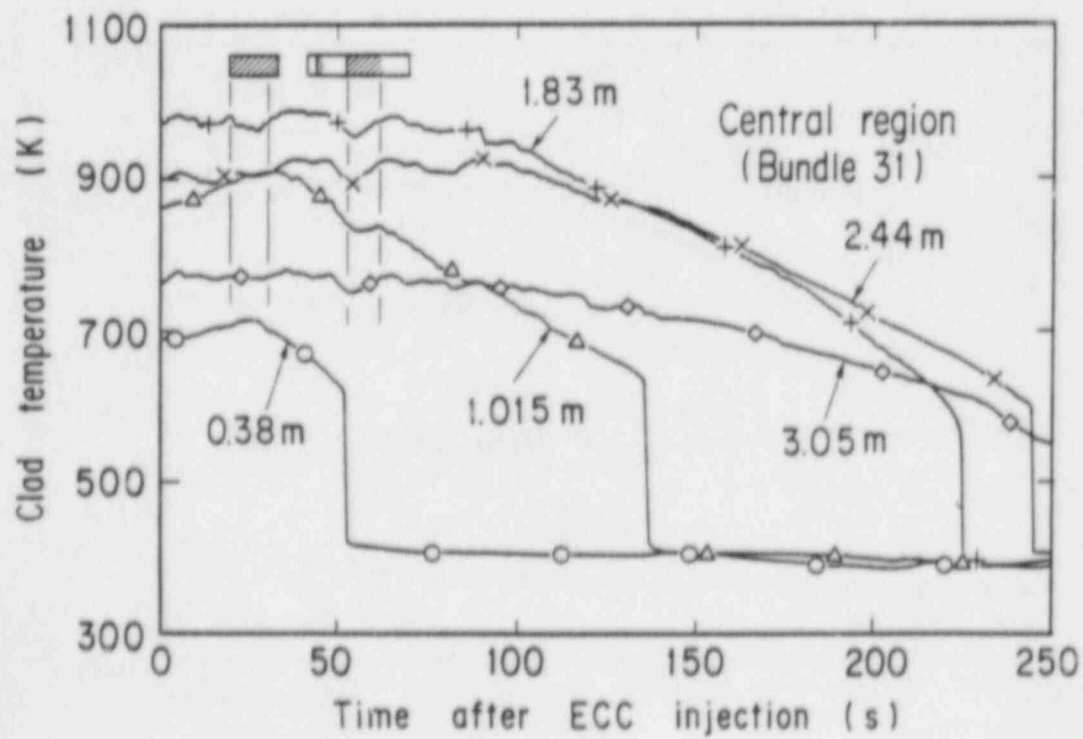
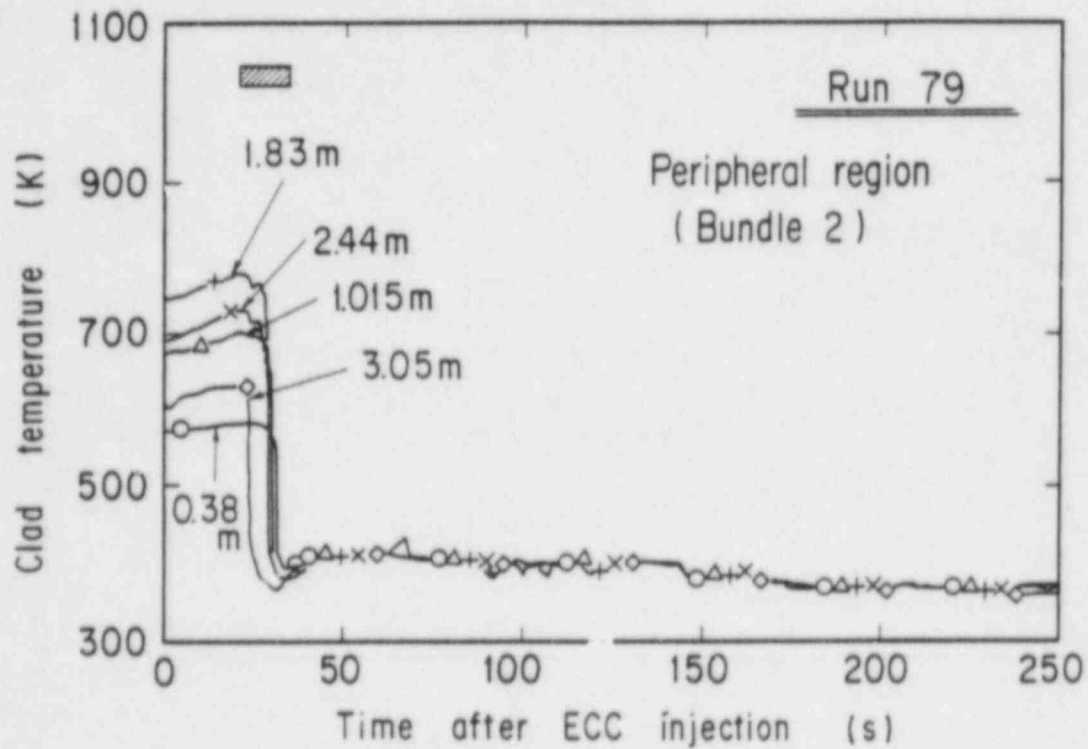


Fig.11 Clad temperature

Run 79 (EM - Case)

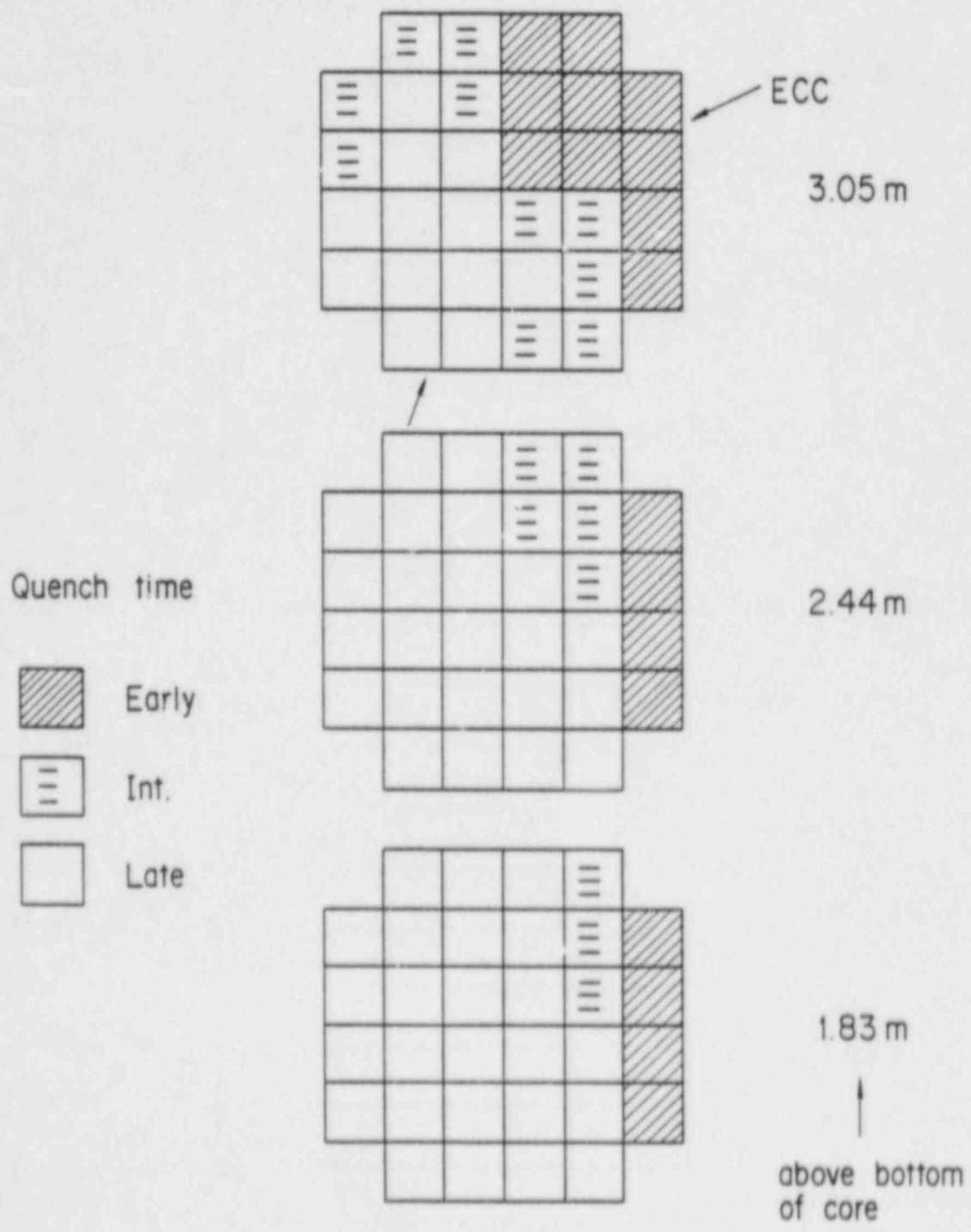
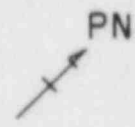
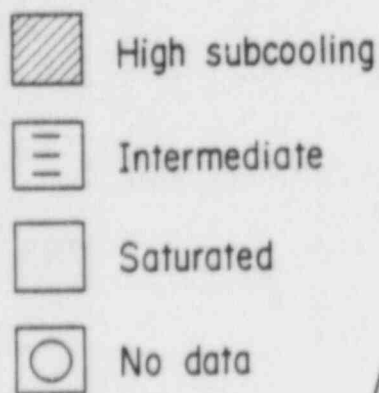


Fig.12 Characteristic of core cooling in the upper part of core

Run 79  
(EM - Case)



$20 < t < 30$

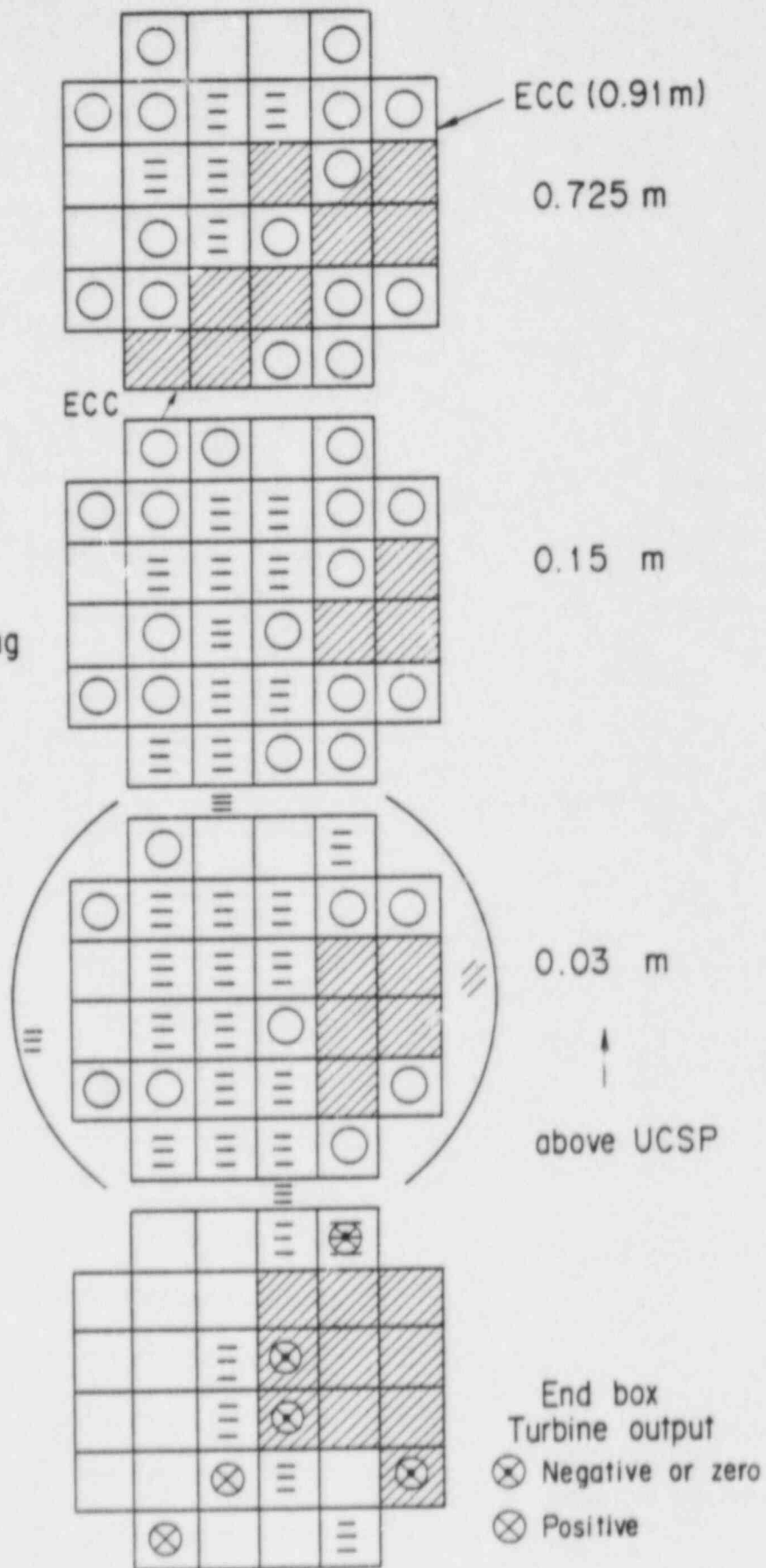


Fig.13 Fluid temperature distribution in upper plenum

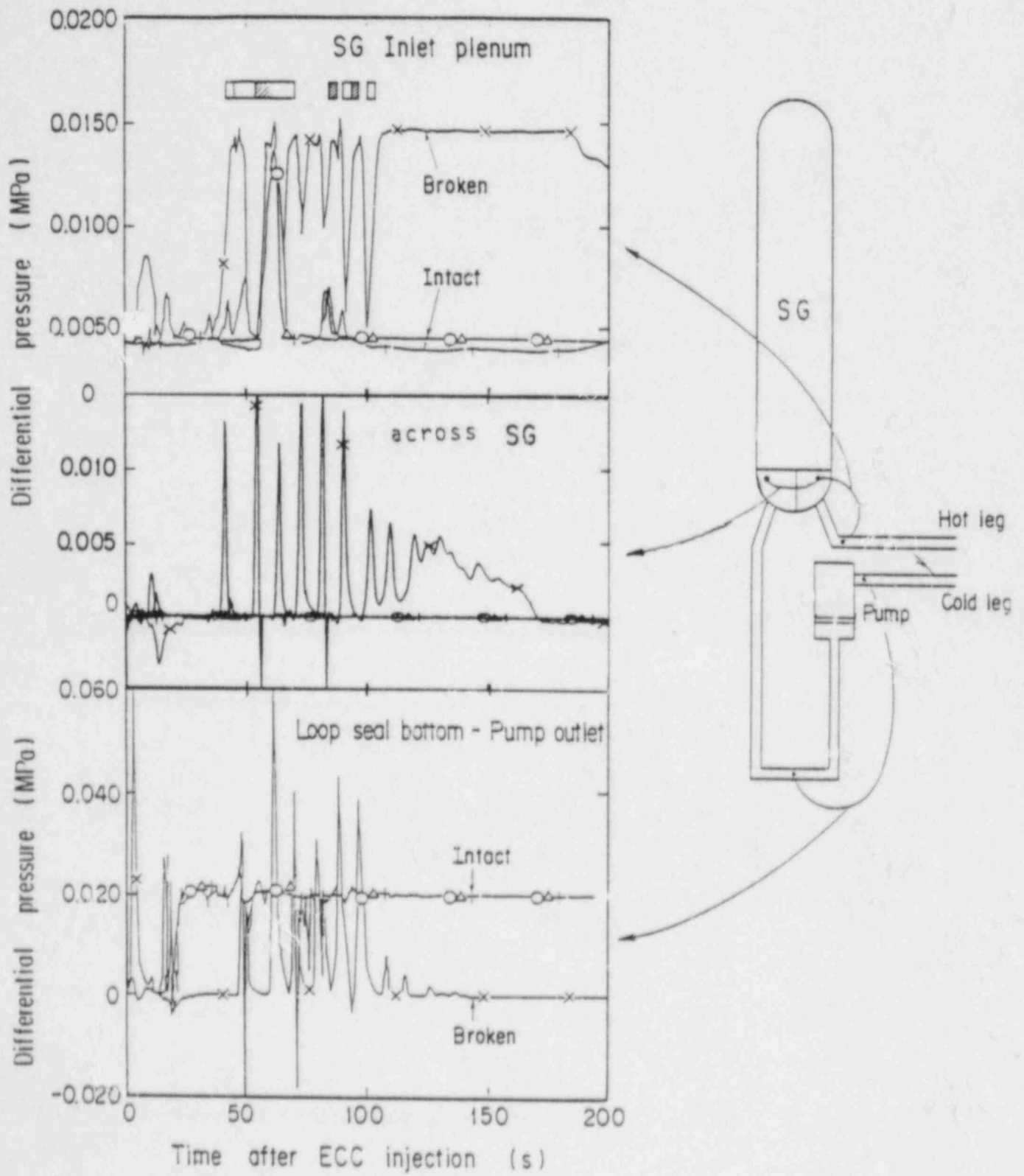
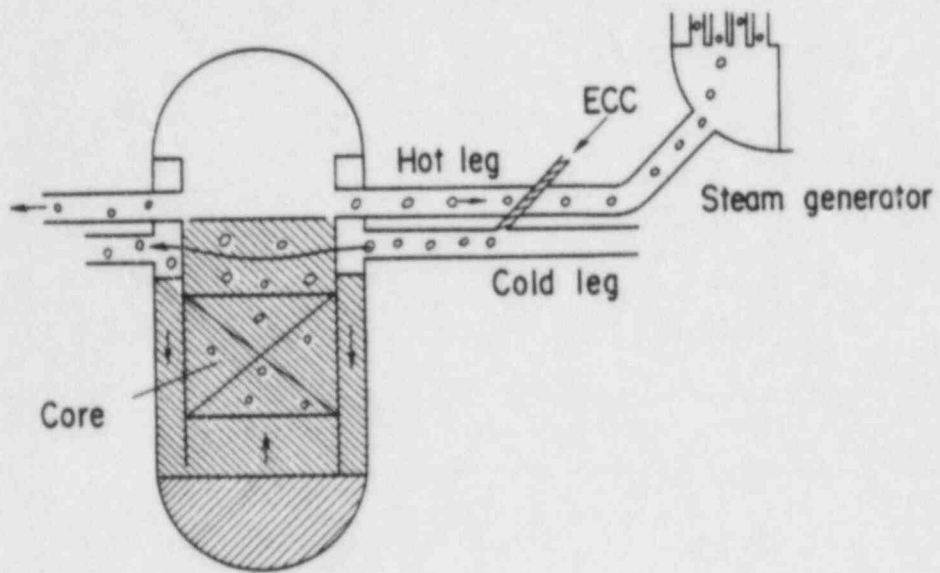
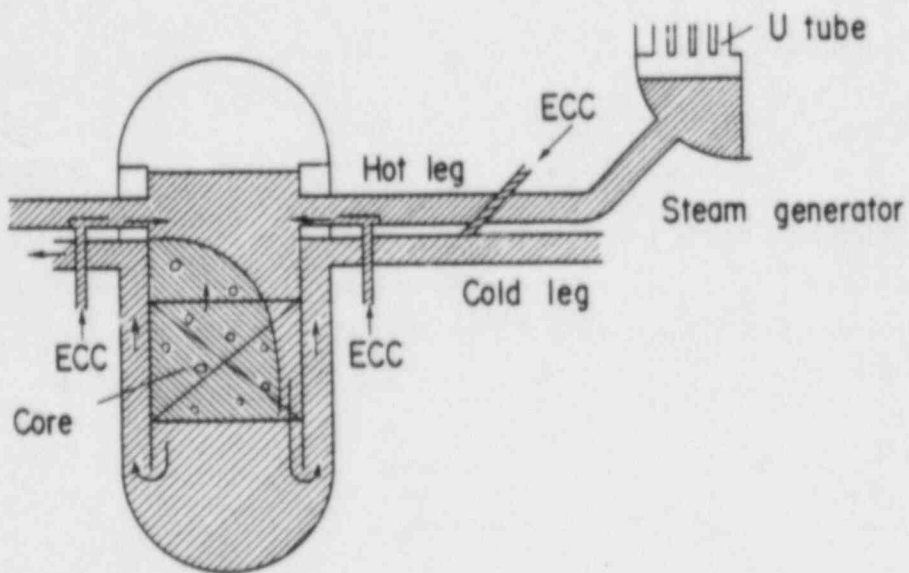


Fig.14 Water accumulation in SG inlet plenum and loop seal



Reflow phenomena for cold leg injection type ECCS



Reflow phenomena for combined injection type ECCS

Fig.15 Illustrated hydraulic behavior during reflow phase for cold leg injection and combined injection type ECCSs

## RESULTS OF SCTF REFLOOD TESTS

Takamichi IWAMURA, Makoto SOBAJIMA, Hiromichi ADACHI,  
Akira OHNUKI, Tsutomu OKUBO, Yutaka ABE and Yoshio MURAO

Japan Atomic Energy Research Institute

### Abstracts

Two-dimensional effects on the core cooling behavior during the reflood phase of a PWR-LOCA were experimentally studied by using the Slab Core Test Facility (SCTF). Heat transfer was enhanced for the high power bundles and degraded for the peripheral low power bundles due to the effect of radial power distribution. In addition the quench propagation in the bundles corresponding to the peripheral bundles of a PWR core was suppressed by the non-uniform water accumulation in the upper plenum. It was found that the radial temperature distribution which was induced by the radial power distribution was the dominant factor of the two-dimensional thermal-hydraulic behavior in the core.

#### 1. Introduction

The Slab Core Test Facility (SCTF) test program<sup>(1),(2),(3)</sup> is a part of the large scale reflood test program together with the Cylindrical Core Test Facility (CCTF) test program. These programs are involved in the 2D/3D project which is performed by JAERI, USNRC and BMFT of West Germany. The major objective of the SCTF program is to investigate two-dimensional thermal-hydraulic behavior in the core during the reflood phase of a loss-of-coolant accident (LOCA) of a pressurized water reactor (PWR). In order to meet this objective, SCTF simulates a full radial slab section of a PWR.

In the present paper, the effects of radial power distribution and non-uniform water accumulation in the upper plenum on the core cooling characteristics are experimentally studied based on the SCTF test results. Also the effect of radial power distribution itself and the effect of radial temperature distribution induced by the radial power distribution are evaluated separately by performing tests with various combinations of radial power and temperature distributions.

#### 2. Facility

The pressure vessel of SCTF is shown in Fig. 1. The pressure vessel includes a simulated core, an upper plenum with internals, a lower plenum, a core baffle and a downcomer. The SCTF pressure vessel simulates a full radius slab section with full height of a 1,100 MWe PWR.

---

The work was performed under contract with the Atomic Energy Bureau of Science and Technology Agency of Japan.

The simulated core consists of 8 bundles arranged in a row with full radial width. Bundle 1 corresponds to the center bundle and Bundle 8 corresponds to the peripheral bundle of a PWR. Each bundle consists of 234 heater rods and 22 non-heated rods arranged in 16 X 16 array. The axial peaking factor is 1.4. In order to investigate the effects of radial core power and temperature distributions, the heating power for each bundle can be independently controlled.

As schematically shown in Fig. 2, the primary coolant loops of SCTF consist of a hot leg equivalent to four actual hot legs, a steam/water separator corresponding to four actual steam generators, an intact cold leg equivalent to three intact cold legs, a broken cold leg on the pressure vessel side, and a broken cold leg on the steam/water separator side. These two broken cold legs are connected to two containment tanks which are connected with each other by a pressure equalizing pipe.

The flow area scaling ratio is 1/21 of a 1,100 MWe PWR, whereas the heights of each component are preserved.

### 3. Test Results and Discussions

#### 3.1 Two-Dimensional Effects under Gravity Feed Condition

The tests referred to are steep radial power distribution test (S2-06) and flat radial power distribution test (S2-SH2) which were performed under gravity feed condition. Major test conditions for these two tests are listed in Table 1. The accumulator water was injected into the lower plenum and then the injection port was switched to the intact cold leg for the low pressure coolant injection (LPCI). The test conditions except the radial power distribution were selected to reasonably represent the situation of the reflood phase of a PWR-LOCA. The accumulator injection rate was reduced from the scaled injection rate to prevent significant U-tube oscillation observed in the scaled accumulator injection rate test and the accumulator injection period was extended instead. The LPCI flow rate was also reduced from the scaled value in these two tests to realize proper core reflooding rate during the LPCI period. The normalized power ratio in Test S2-06 is 1.0 (Bundles 1 & 2), 1.2 (Bundles 3 & 4), 1.0 (Bundles 5 & 6), and 0.8 (Bundles 7 & 8).

The two-dimensional effects observed in these two gravity feed tests are classified into the following two individual effects.

##### (1) Effect of radial core power/temperature distribution

As shown in Fig. 3, the heat transfer above the quench front is enhanced in the high power bundle (Bundle 4) and degraded in the low power bundle (Bundle 8) in the test with steep radial power distribution (S2-06), while the difference between bundles is small in the test with flat radial power distribution (S2-SH2). In order to quantitatively evaluate the effect of radial power distribution on the cladding temperature, hypothetical temperature transients were calculated by applying the experimentally obtained heat transfer coefficients from Tests S2-SH2 and S2-06 to the conditions with the same initial temperature and power transients given in Test S2-06. Figure 4 compares these two temperature transients of Bundle 5 which is the average power bundle adjacent to the high power bundle. As shown in this figure, the decrease of turnaround temperature due to the radial power distribution is estimated to be



approximately 90 K at 2.76 m from the bottom of heated part in Bundle 5.

## (2) Effect of non-uniform water accumulation in the upper plenum

The collapsed water level in the upper plenum becomes gradually higher in the hot leg side on the periphery than in the radial center side as shown in Fig. 5. The quench in the upper half of the core was delayed in the peripheral bundles as shown in Fig. 6. This is considered to be caused by the flow stagnation trend in those bundles because the pressure in the outer bundles became higher with time than the pressure in the inner bundles due to the non-uniform water accumulation in the upper plenum and resultantly the flow tended to be concentrated in the Bundle 1 side. The variation of radial power distribution has little effect on the non-uniform water accumulation behavior in the upper plenum. Since this effect dominated after the turnaround of the cladding temperature, the turnaround temperature was not much affected by this effect in the present SCTF tests.

## 3.2 Separate Evaluation of the Effects of Radial Temperature Distribution and Radial Power Distribution

As discussed before, the radial core power distribution has more significant effect on the reduction of peak cladding temperature than the non-uniform water accumulation in the upper plenum in the SCTF Core-II gravity feed tests. When the radial core power distribution was given, the radial rod temperature distribution was also induced in the previous tests and therefore the effects of core power and rod temperature distributions could not be distinguished from each other. In order to separately evaluate these two effects, four tests were performed with various combinations of core power and rod temperature distributions as follows :

Test number	S2-12	S2-14	S2-15	S2-21
Core heating power distribution	Steep*	Flat	Steep*	Flat
Initial rod temperature distribution	Steep	Flat	Flat**	Steep

\* Normalized power ratio : 1.0 (Bundles 1 & 2), 1.2 (Bundles 3 & 4),  
1.0 (Bundles 5 & 6), and 0.8 (Bundles 7 & 8)

\*\* Nearly flat. That is, the temperature in Bundles 3 & 4 was slightly higher and the temperature in Bundles 7 & 8 was slightly lower than the average temperature.

These tests were performed under the forced flooding condition to make the core inlet flow rate the same. In these tests, the downcomer was isolated from the lower plenum and emergency core cooling (ECC) water was directly injected into the lower plenum. By comparing counterpart tests under the forced feed and the gravity feed, it was concluded that the ECC injection mode has little effect on the two-dimensional thermal-hydraulic behavior in the core<sup>(4)</sup>. The water in the upper plenum was extracted in these tests so as to avoid the effect of non-uniform water accumulation in the upper plenum. Major test conditions for these tests are listed in Table 2.

The radial temperature distribution at 0, 50, 100 and 200 s from the beginning of reflood are compared in Figs. 7(a) and 7(b). The difference in the temperatures among bundles in Test S2-15 is much smaller than in Test S2-12 while it is slightly larger than in Test S2-14. The radial temperature distribution in Test S2-15 becomes similar to that in Test S2-

12 at the later period due to the steep radial power distribution. On the other hand, the initial temperature distribution in Test S2-21 agrees well with that in Test S2-12. However, the temperature distribution in Test S2-21 is flattened with time and approaches that in flat power and temperature Test S2-14.

Figure 8 compares the horizontal differential pressures between Bundles 4 and 8 at the middle elevation of the core. As shown in this figure, the pressure in Bundle 4 is higher than the pressure in Bundle 8 in Test S2-12, while the pressure difference between bundles is negligibly small in Test S2-14. The horizontal differential pressure in Test S2-15 is close to that in Test S2-14 during the initial 80 s and thereafter approaches that in Test S2-12. On the contrary, the horizontal differential pressure in Test S2-21 is close to that in Test S2-12 during the initial 40 s and thereafter approaches that in Test S2-14. In order to compare the overall pressure distributions in the core, the isobar lines for these four tests at 50 and 200 s are compared in Figs. 9(a) and 9(b), respectively, together with the radial distributions of bottom quench front. At 50 s, the pressure above the quench front except at the top of the core in the Bundle 8 side is lower than that in the Bundle 1 side in Tests S2-12 and S2-21, while approximately flat distribution is observed in Tests S2-14 and S2-15 as well as the quench front distribution. In Tests S2-12 and S2-21, the quench front is lower in Bundles 3 and 4 and higher in Bundles 7 and 8 in accordance with the initial radial temperature distribution. As shown in Fig. 9(b), both the radial pressure and quench front distribution in Tests S2-15 and S2-21 are similar to those in Tests S2-12 and S2-14, respectively. This is corresponding to the fact that the radial temperature distribution is similar to the radial power distribution at 200 s. It is suggested from the above-mentioned behaviors of horizontal differential pressure and isobar lines that the two-dimensional hydraulic behavior above the quench front is not so much affected by the radial power distribution itself but is affected mainly by the radial temperature distribution which is induced by the radial power distribution.

The heat fluxes at 2.33 m in Bundle 4 are compared in Fig. 10. During the initial 40 s, the heat flux in Test S2-21 agrees well with that in Test S2-12 and thereafter the heat flux in Test S2-21 approaches that in Test S2-14. The heat flux in Test S2-15 also approaches that in Test S2-12 at the later period. However, the heat flux in Test S2-15 is significantly lower than those in the other three tests during the initial 100 s. This peculiarity is explained by the fact that additional stored heat was released from the non-heated rods and the side walls in Test S2-15 and the steam in the core was superheated due to the longer time at adiabatic high temperature before the beginning of reflood in this particular test.

Figure 11 compares the average heat transfer coefficients vs. time in Bundles 4 and 8 at 2.33 m. In order to clarify the two-dimensional heat transfer characteristics, these heat transfer coefficients were re-plotted against the distance from the bottom quench front in Fig. 12. As known from these figures, the heat transfer is enhanced in the high power bundle (Bundle 4) and degraded in the low power bundle (Bundle 8) in Test S2-12, whereas no significant difference between bundles is observed in Test S2-14 as in the comparison of the gravity feed Tests S2-06 and S2-SH2 shown in Fig. 3. In Test S2-15, the difference between the heat transfer coefficients for Bundles 4 and 8 is initially small. As the quench front approaches the 2.33 m elevation, the difference increases due to the development of the radial temperature distribution in this test. In Test S2-21, on the contrary, the difference between the heat transfer

coefficients for Bundles 4 and 8 is initially large and then decreases as the quench front approaches this elevation corresponding to the fact that the radial temperature distribution becomes flat with time as shown in Fig. 7(b).

Below the quench front, only the effect of radial power distribution exists because the cladding surface temperature is approximately equal to the saturation temperature independent of the radial power distribution. During the initial period, the steam generation rate below the quench front was much smaller than the total steam generation rate because the heating length was shorter and the heating power was lower below the quench front. Therefore, the radial power distribution below the quench front had little effect on the two-dimensional heat transfer behavior above the quench front during the initial period.

#### 4. Conclusions

- 1) Two-dimensional flow in the core was induced radial power distribution in the core and the non-uniform water accumulation in the upper plenum.
- 2) Heat transfer was enhanced for the high and average power/temperature bundles and degraded for the peripheral low power/temperature bundles and resultantly the peak cladding temperature was reduced due to the effect of radial power distribution. The ECC injection mode has little effect on the two-dimensionality.
- 3) The non-uniform water accumulation in the upper plenum suppressed the quench propagation in the upper half of the core in the bundles corresponding to the peripheral bundles of a PWR core.
- 4) The radial temperature distribution which accompanied the radial power distribution was the dominant factor of the heat transfer enhancement in high power bundles during the initial period of the reflood phase. However, it should be taken into account that the radial power distribution below the quench front had little effect on the two-dimensional heat transfer behavior above the quench front during the initial period.

#### References

- (1) H. Adachi, et al., 10 th WRSR Information Meeting, (1982).
- (2) H. Adachi, et al., 11 th WRSR Information Meeting, (1983).
- (3) Y. Murao, et al., 12 th WRSR Information Meeting, (1984).
- (4) A. Ohnuki, et al., JAERI-M to be published.

Table 1 Test Conditions for Tests S2-SH2 and S2-06

Common conditions

Injection mode	:	Gravity feed
System pressure	:	0.2 MPa
Maximum Acc injection rate	:	19 kg/s
Acc injection period	:	55 s
LPCI injection rate	:	5.4 kg/s

Different conditions

Test No.	S2-SH2	S2-06
Radial power distribution	Flat	Steep*
Initial temperature distribution	Flat	Steep
Bundles 1 & 2	1012 K	1060 K
" 3 & 4	1022 K	1163 K
" 5 & 6	1040 K	1072 K
" 7 & 8	1035 K	955 K

- \* Normalized power ratio: 1.0 (Bundles 1 & 2), 1.2 (Bundles 3 & 4),  
1.0 (Bundles 5 & 6), and 0.8 (Bundles 7 & 8)

Table 2 Test conditions for Tests S2-12, S2-14,  
S2-15 and S2-21

Common conditions

Injection mode	:	Forced feed
System pressure	:	0.2 MPa
Maximum Acc injection rate	:	26 kg/s
Acc injection period	:	36 s
LPCI injection rate	:	4.7 kg/s

Different conditions

Test No.	S2-12	S2-14	S2-15	S2-21
Radial power distribution	Steep*	Flat	Steep*	Flat
Initial temperature distribution	Steep	Flat	Flat	Steep
Bundles 1 & 2	940 K	907 K	922 K	934 K
" 3 & 4	1046 K	927 K	931 K	1045 K
" 5 & 6	961 K	921 K	892 K	969 K
" 7 & 8	857 K	935 K	895 K	865 K

- \* Normalized power ratio: 1.0 (Bundles 1 & 2), 1.2 (Bundles 3 & 4),  
1.0 (Bundles 5 & 6) and 0.8 (Bundles 7 & 8)

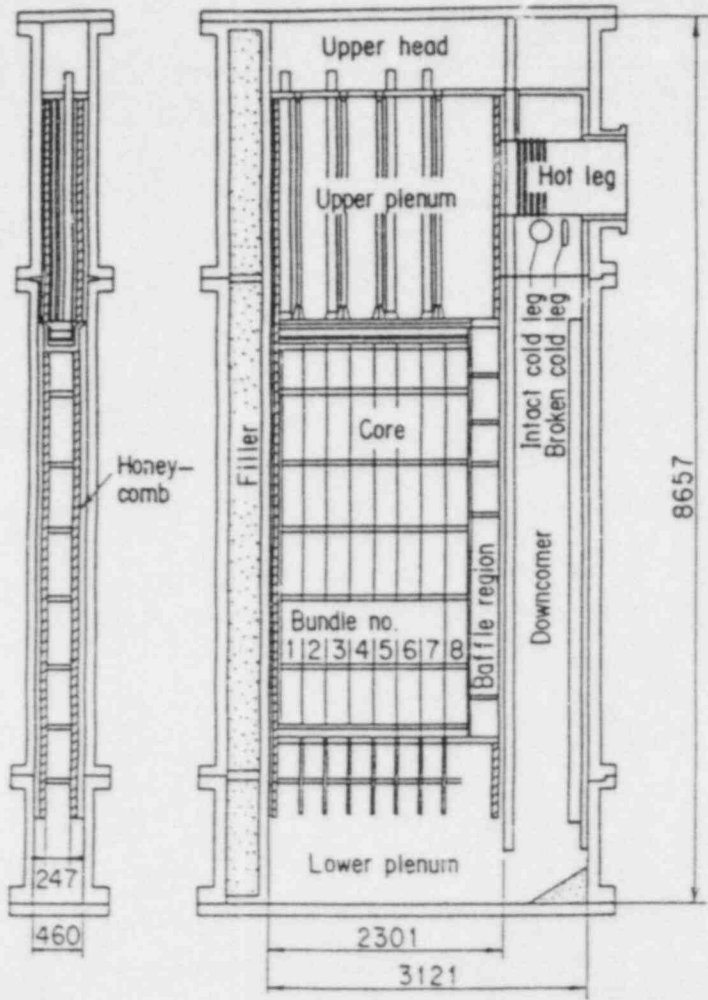
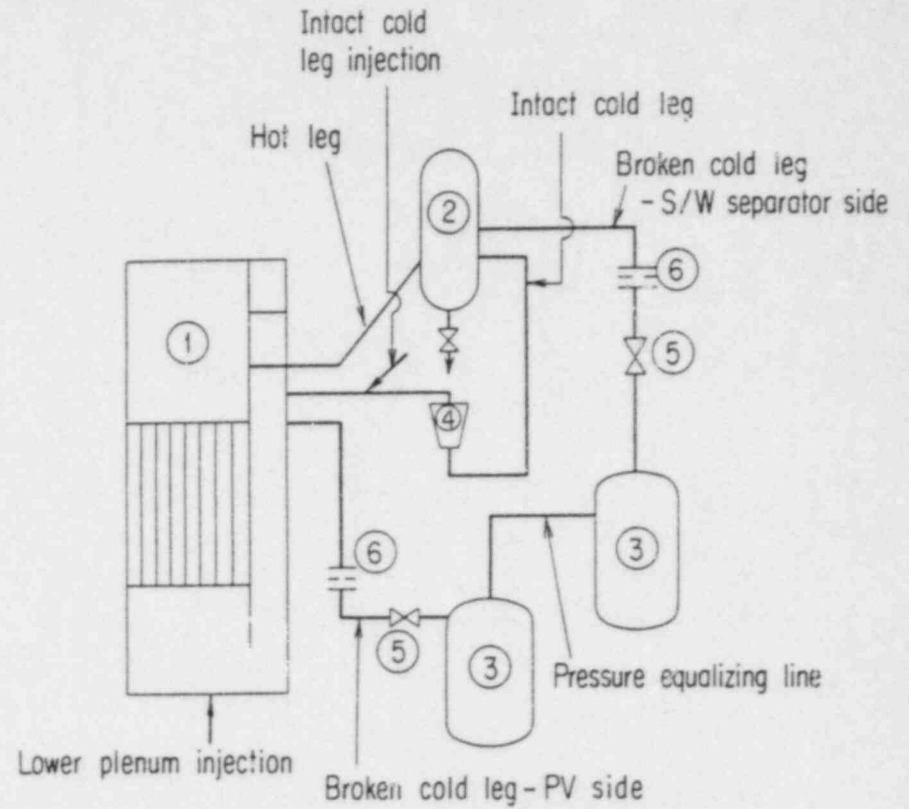


Fig. 1 Pressure vessel of Slab Core Test Facility



- ① Pressure vessel
- ② Steam/water separator
- ③ Containment tanks
- ④ Pump simulator
- ⑤ Break valves
- ⑥ Flow resistance simulators

Fig. 2 Schematic diagram of Slab Core Test Facility

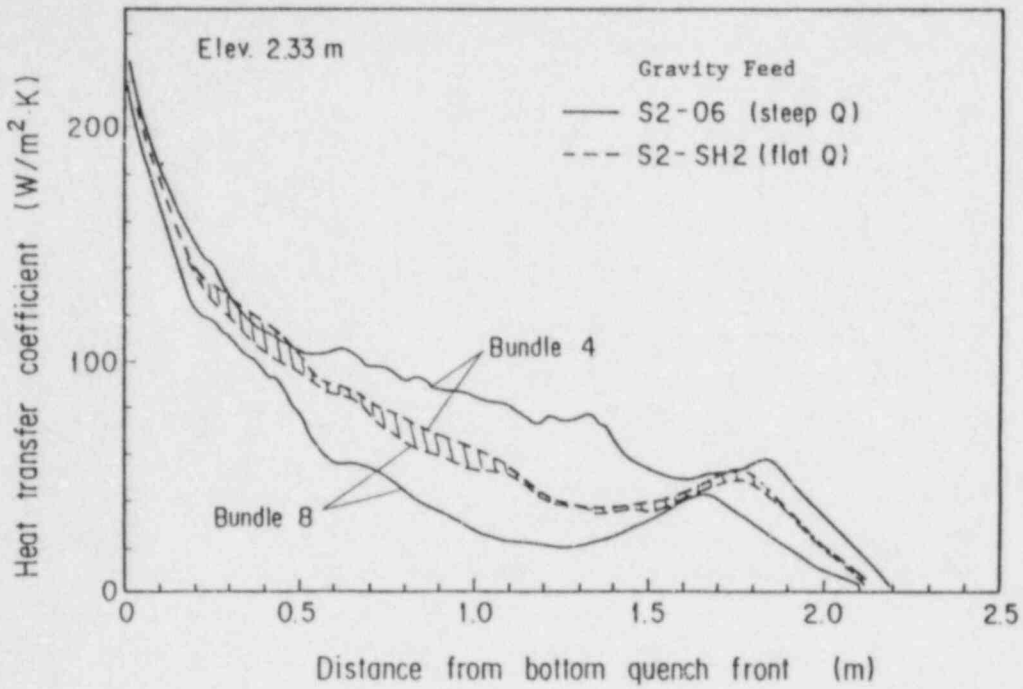


Fig. 3 Heat transfer coefficient vs. distance from bottom quench front

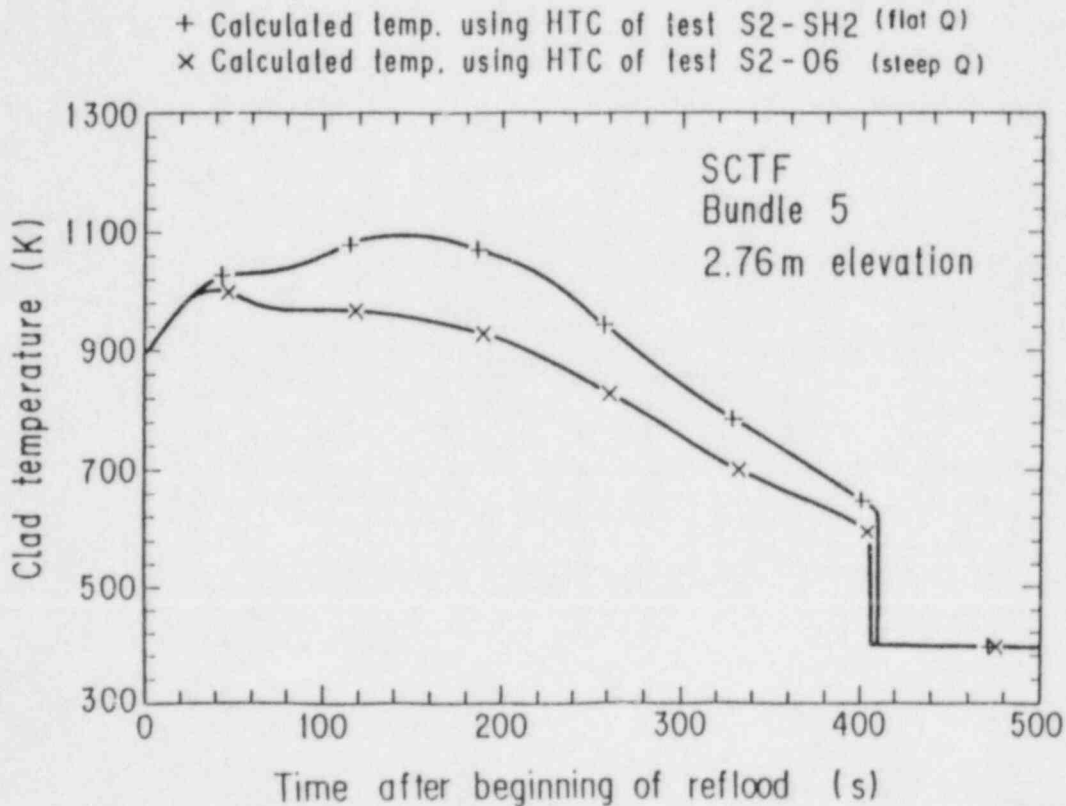


Fig. 4 Effect of radial core power distribution on cladding surface temperature

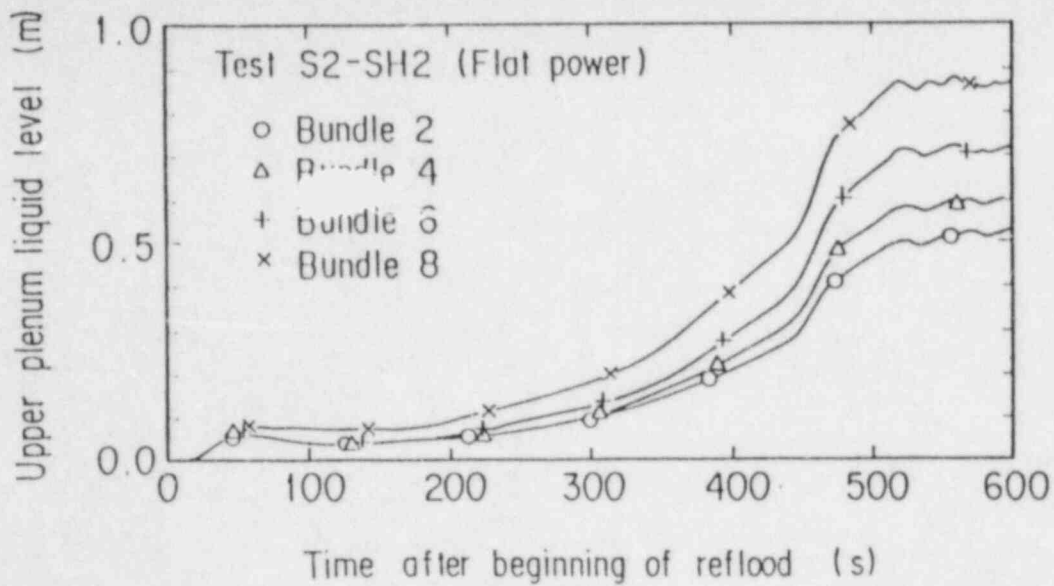


Fig. 5 Liquid level distribution in upper plenum

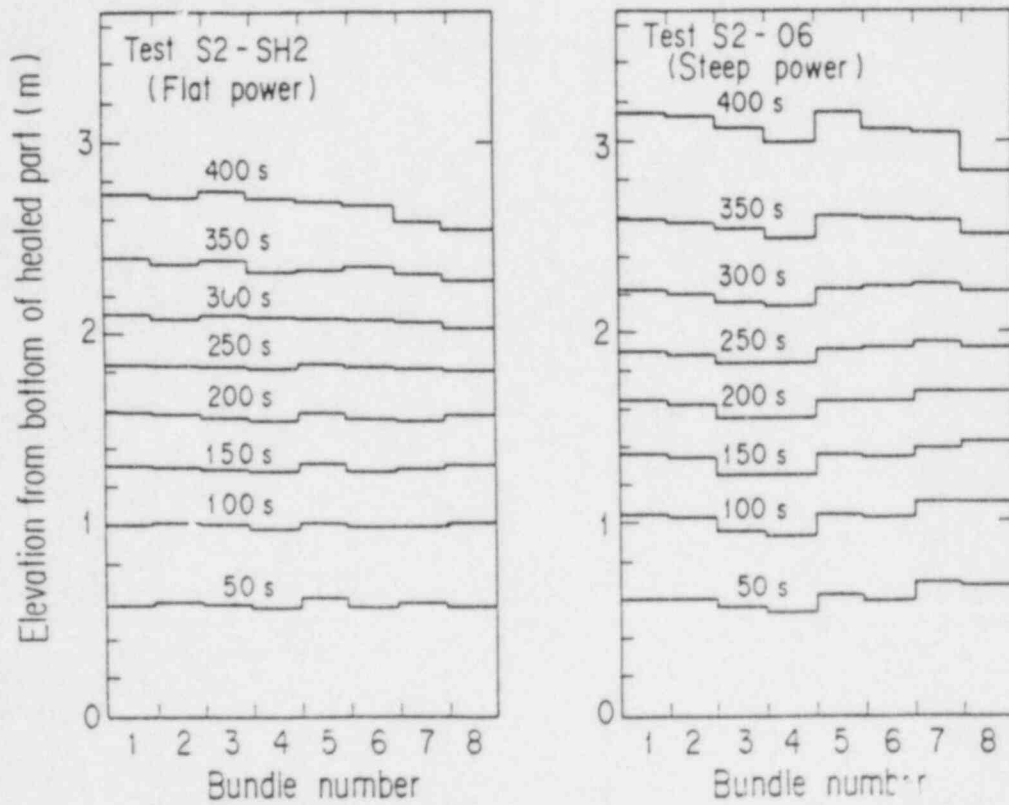


Fig. 6 Quench front distributions

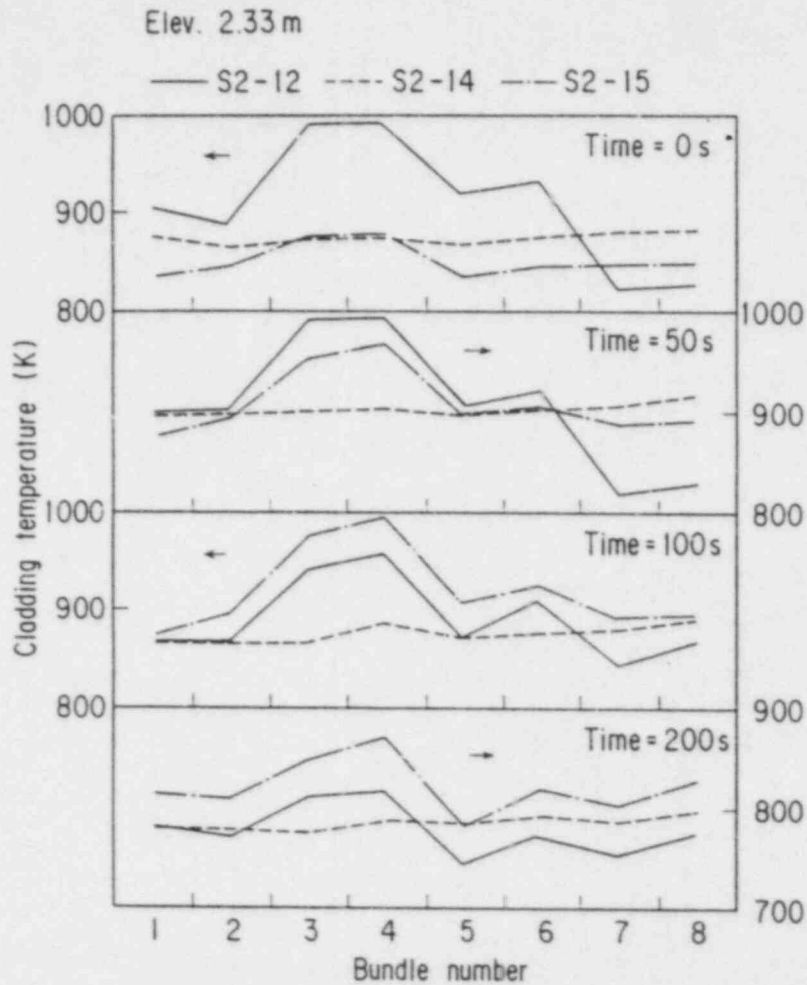


Fig. 7(a) Comparison of radial temperature distributions among Tests S2-12, S2-14 and S2-15

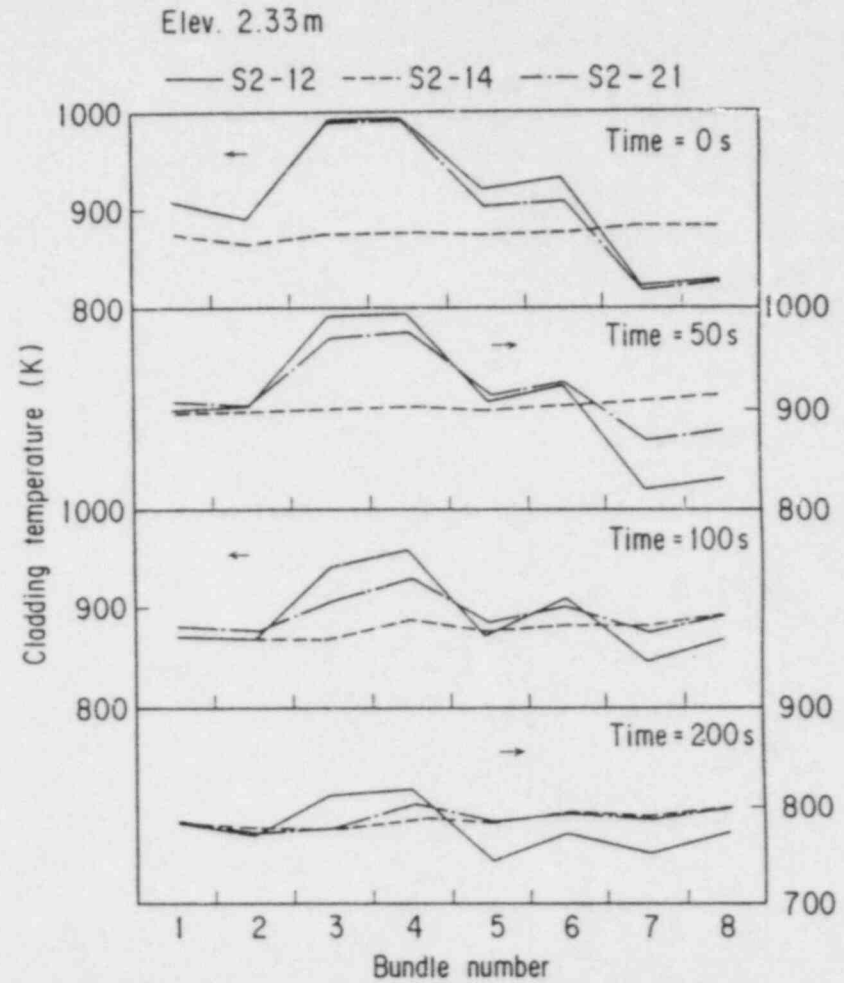


Fig. 7(b) Comparison of radial temperature distributions among Tests S2-12, S2-14 and S2-21



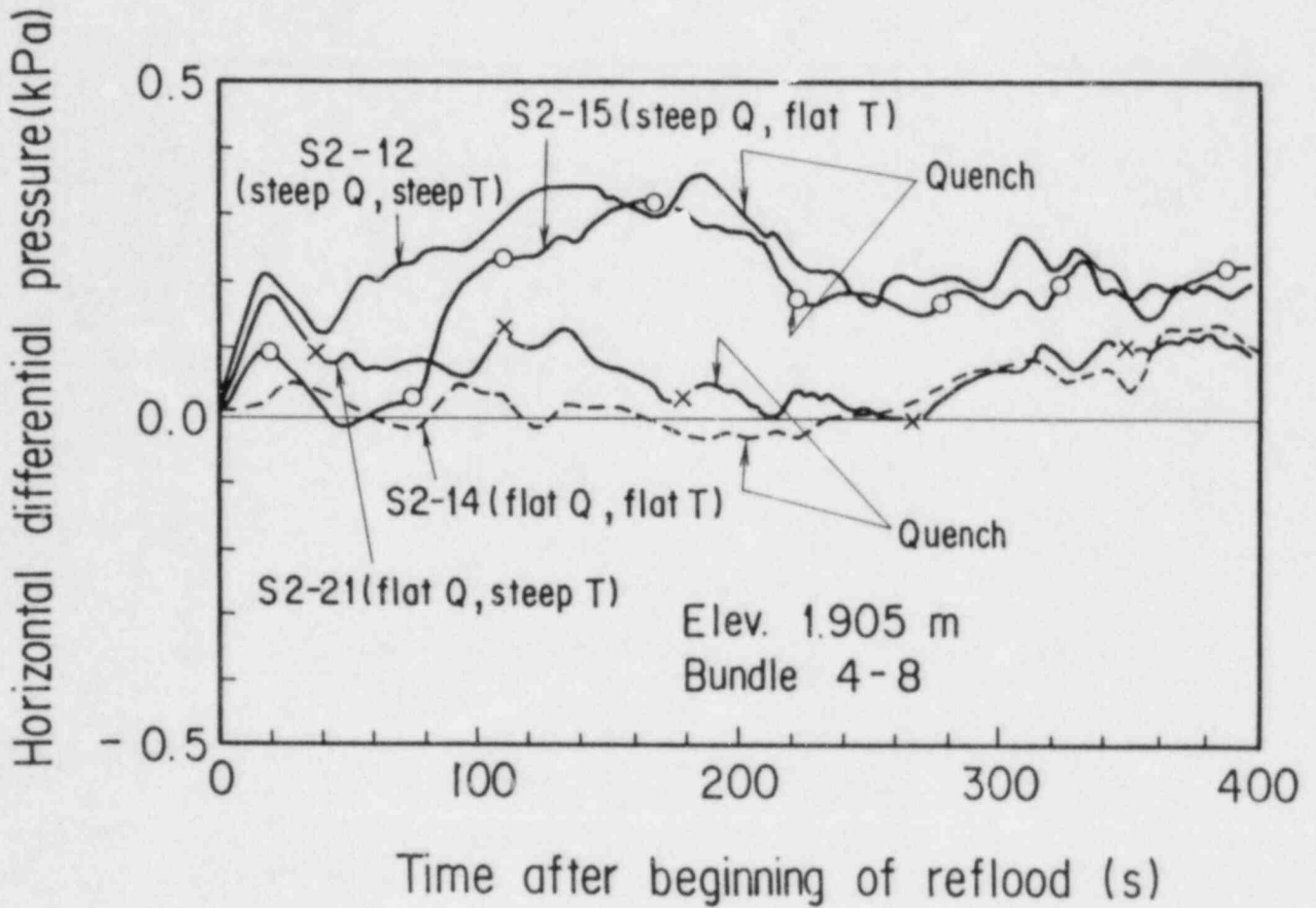


Fig. 8 Comparison of horizontal differential pressures between Bundles 4 and 8 at 1.905 m

Time = 50 s

--x-- Bottom quench front

Line interval = 0.5 kPa

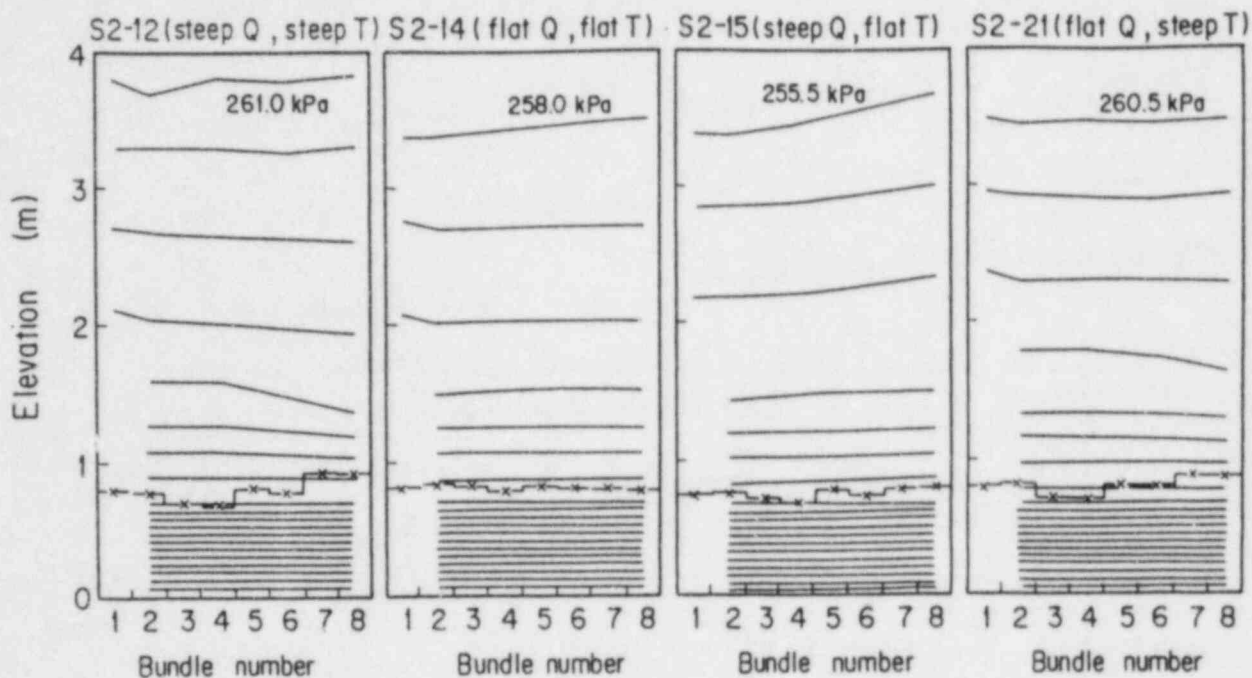


Fig. 9(a) Isobar lines in core at 50 s

Time = 200 s

--x-- Bottom quench front

Line interval = 0.5 kPa

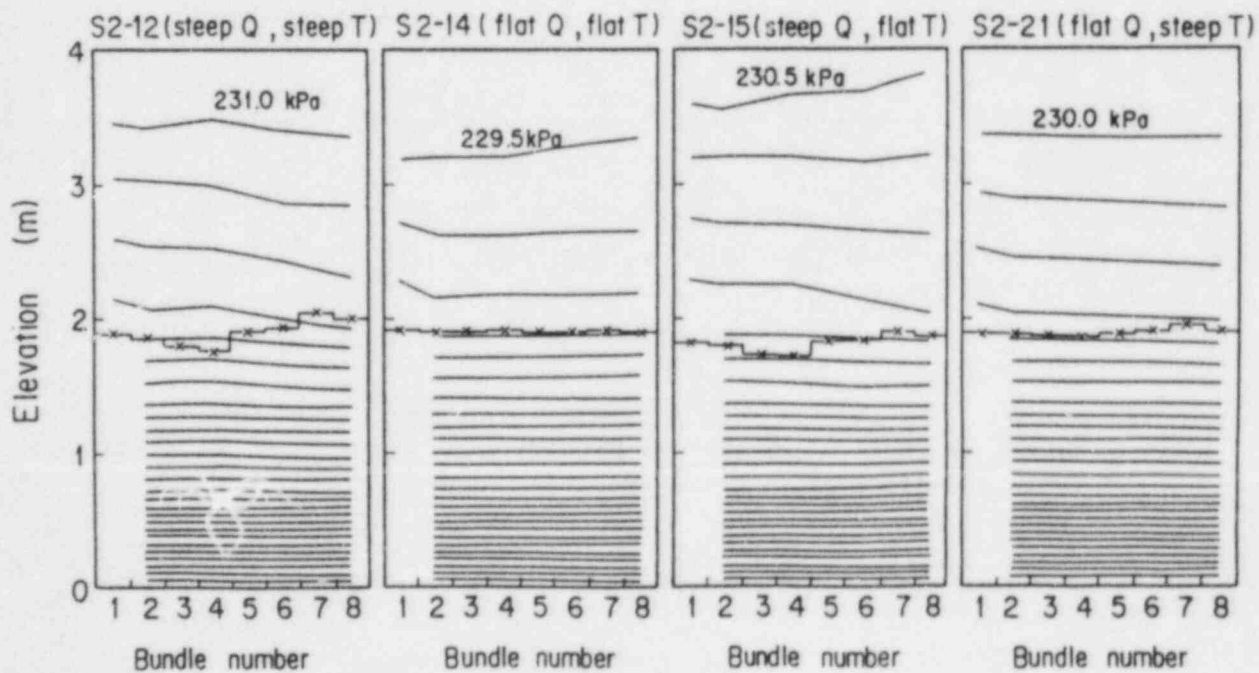


Fig. 9(b) Isobar lines in core at 200 s

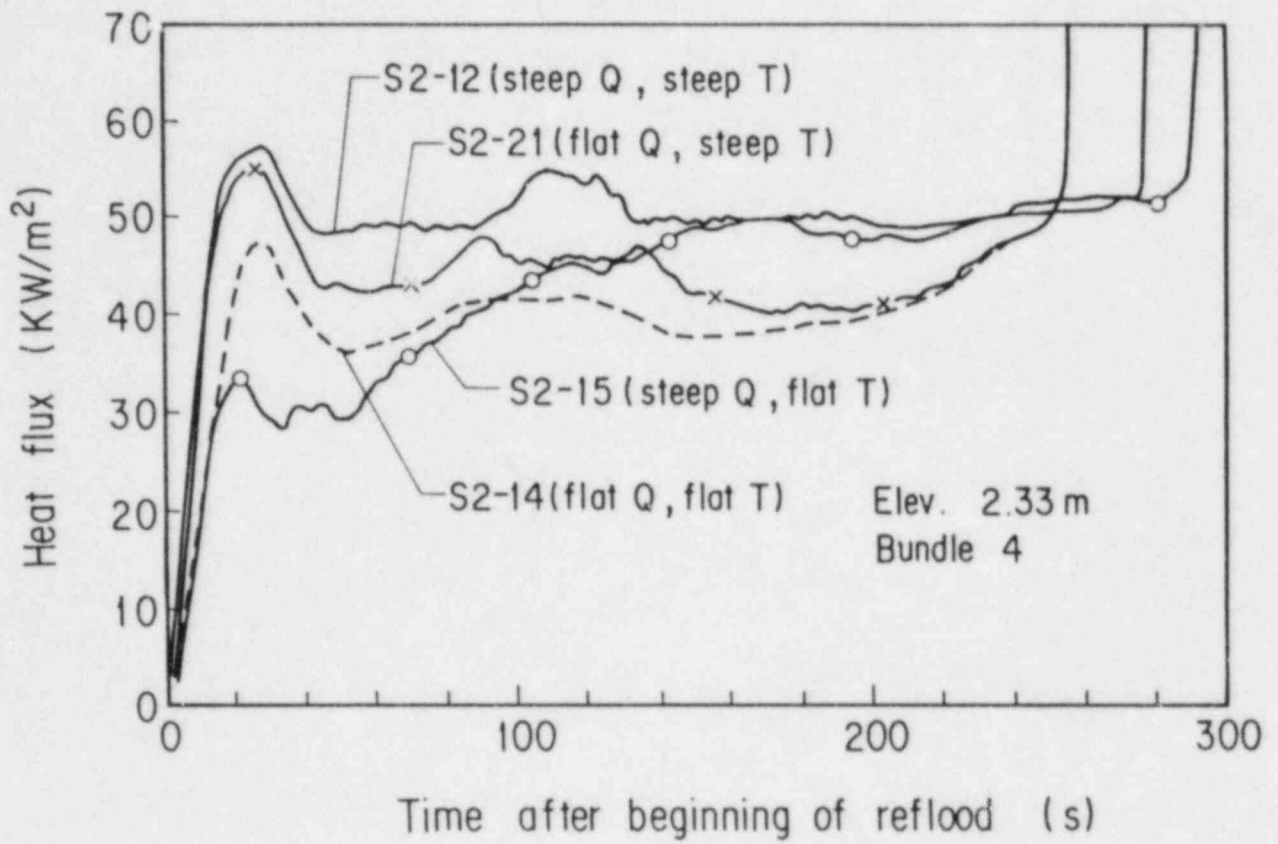


Fig. 10 Comparison of average heat fluxes at 2.33 m in Bundle 4

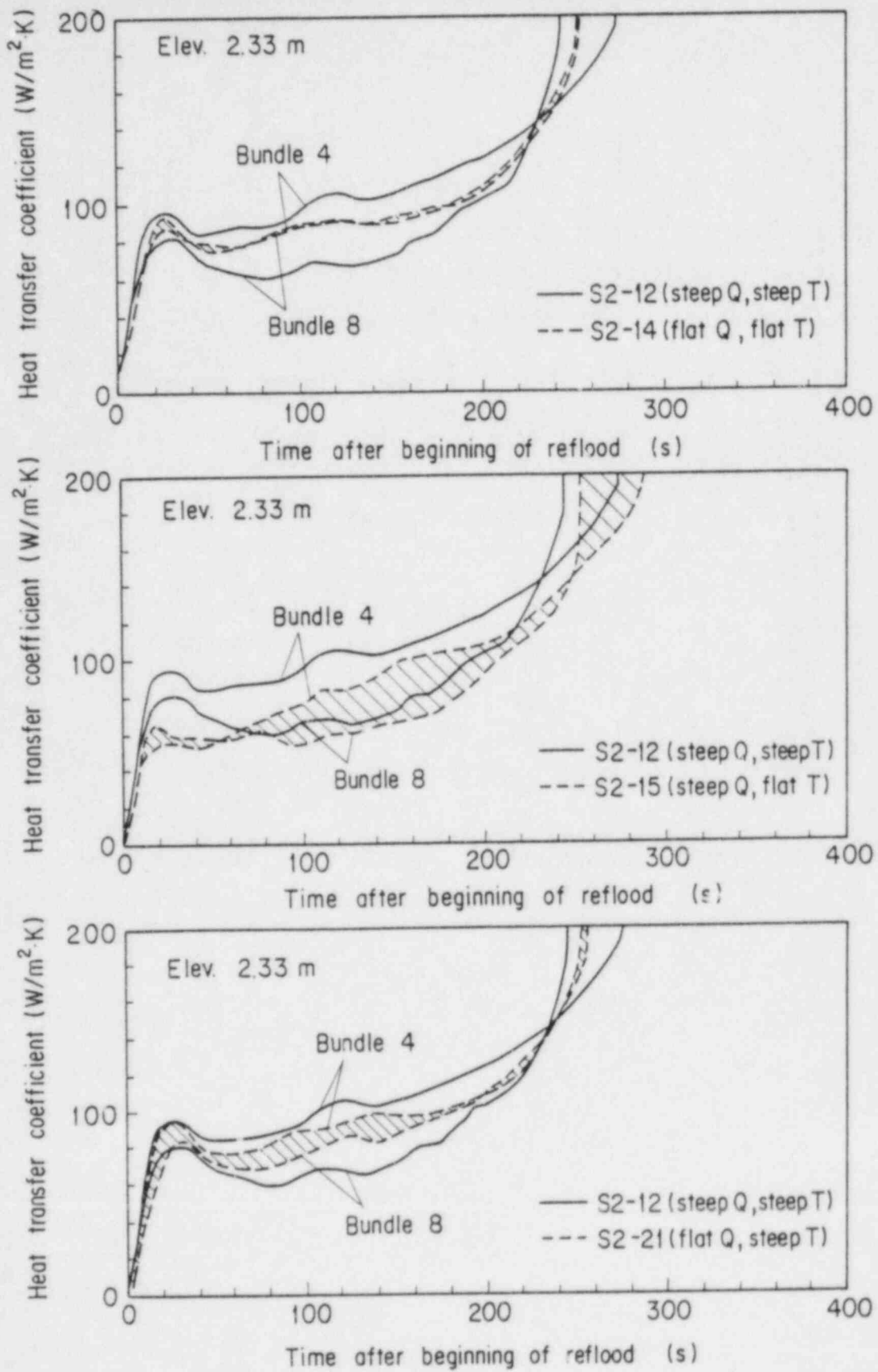


Fig. 11 Heat transfer coefficient vs. time  
(Effect of radial power and temperature distribution)

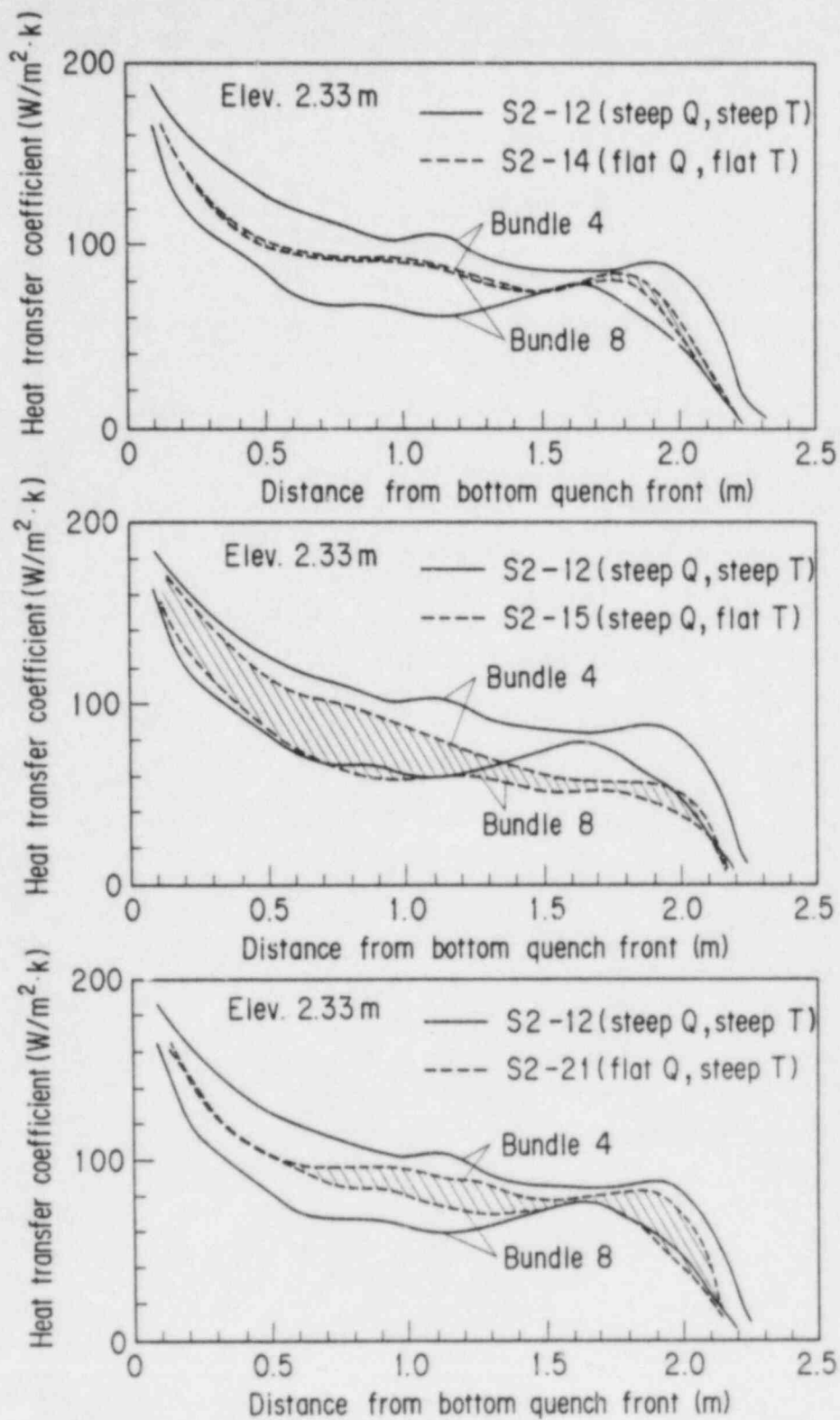


Fig. 12 Heat transfer coefficient vs. distance from bottom quench front  
(Effect of radial power and temperature distribution)

## Status of the German UPTF Program

K. R. Hofmann

Gesellschaft fuer Reaktorsicherheit

### Abstract

The objective of the 2D/3D project, performed within international cooperation between Japan (JAERI), USA (USNRC) and the Federal Republic of Germany (BMFT) is the experimental and analytical investigation of the multidimensional flow behavior in the primary cooling system of a PWR during a loss of coolant accident (LOCA). The effectiveness of emergency core cooling systems (ECCS) will be studied considering multidimensional flow effects in the reactor core, in the upper plenum and in the downcomer during the end of blowdown, refill and reflood phases of the LOCA. Experimental data of the large scale test facilities CCTF (Cylindrical Core Test Facility) and SCTF (Slab Core Test Facility) in Japan and UPTF (Upper Plenum Test Facility) in Germany are being used to assess the TRAC computer code developed by the USNRC. The overall aim of the project is to provide computer code capability for best estimate LOCA analyses and to quantify the existing margins in safety analyses.

The UPTF, the German contribution to the 2D/3D project, will provide experimental 1 : 1 scale data of the flow behavior in the upper plenum in the loops and in the downcomer. The core behavior is simulated by controlled steam and water injection. The construction of the facility has been completed in June 1985. Following up the current commissioning program, 30 experiments will be performed starting in April 1986.

### Objectives of the UPTF

The UPTF sponsored by the Ministry for Research and Technology (BMFT) is the German contribution to the trilateral 2D/3D project (Fig. 1). The objective of the UPTF is to investigate the three dimensional flow behavior in the upper plenum and in the downcomer during the end-of-blowdown, refill and reflood phases of the LOCA. The flow conditions at the core boundaries are simulated by a controlled steam and water injection into the core region of the UPTF according to the thermodynamic phenomena studied in the Japanese SCTF and by TRAC system analyses. The UPTF experiments aim at the investigation of phenomena in the upper plenum and in the downcomer, including the connected loops, which occur during ECC injection and strongly affect the core cooling process. The various experiments will consider different ECC concepts, as cold leg injection, combined cold and hot leg injection and downcomer injection with vent valves between the upper plenum and the downcomer. The major phenomena to be studied include penetration of ECC water into the upper plenum and into the downcomer, condensation and mixing processes at the injection locations as well as in the downcomer and the upper plenum, coolant and flow distribution in the downcomer and upper plenum, and the interaction at the core/upper plenum interface as the boundary between the UPTF and SCTF experiments. Entrainment and deentrainment phenomena occurring in the flow path from the core exit through the upper plenum

and the hot legs into the steam generator will also be investigated. In order to obtain data for the computer model development and assessment the major part of the UPTF test matrix consists of separate effects tests which allow to study specific phenomena by parametric variations. The effectiveness of various ECC concepts and configurations will be investigated by integral tests which provide information for overall code assessment.

### Description of the Test Facility

The UPTF simulates the primary cooling system of a KWU 1300 MW PWR. Fig. 2 gives an overview of the features of the test facility, Fig. 3 shows the overall flow diagram and Fig. 4 the side view of the test building with the facility inside. The upper plenum, including internals, the downcomer and the four connected loops are represented in 1 : 1 scale (Fig. 5).

The core is simulated by a controlled injection of steam and water supplied from external sources. In Fig. 6 the arrangement of the core simulator injection nozzles with the fuel element dummies and the end boxes for a 3 x 3 bundle injection zone is shown. The cross section of the core simulator, in the upper part consisting of 193 fuel element dummies, is subdivided into 17 injection zones where the injection and mixing of steam and water can be controlled independently (Fig. 7). A total of 1500 kg/s water and 360 kg/s saturated steam is available for injection into the core simulator. TRAC analyses and data of SCTF are used to specify the boundary conditions in order to create the required flow conditions at the core/upper plenum interface.

The three intact loops are equipped with flow restrictors simulating the reactor coolant pumps, and with steam/water separators (Fig. 8) representing the steam generators. The hot and cold legs of the broken loop lead through steam/water separators and break valves into the containment simulator. Breaks of variable sizes can be simulated in the hot and in the cold leg respectively.

The containment simulator, with a volume of 1500 m<sup>3</sup>, is designed as pressure suppression system with steam injection capability in order to keep the back-pressure level according to realistic containment conditions (Fig. 9). To maintain the mass balance in the UPTF system, appropriate drainage devices are installed.

The ECC system simulating accumulator and low pressure injection consists of four pressurized storage tanks, and is designed to inject into the cold and hot legs of the loops and into the downcomer in any configuration according to the various reactor designs. Vent valves for the B&W/BBR reactor simulation can be activated. The capability for nitrogen injection is also available.

Large amounts of steam and water needed to operate the UPTF are provided by a power plant and stored in supply tanks before the experiment is started.

Nearly 1200 measurement channels are being used to record the data from various kinds of instruments during the test. An extensive number of advanced instruments to measure two phase flow phenomena have been developed and provided by USNRC (Fig. 10) including the data acquisition system.

## Current Status and Plans

The construction of the facility which began in 1981 was completed in June 1985. An extensive commissioning program is currently underway. Up to now all cold system checks, i. e. pressurization of vessels and volume measurements have been successfully completed. The first hot system checks have been performed which began with the commissioning of the steam supply system (steam line, steam cooler). Further steps will include system checks of the steam generator simulators (separators), the containment simulator and the core simulator, and the experimental determination of all control valve characteristics (ECCS, core simulator, break valves). Instrument checks and measurements of loss coefficients are also part of the ongoing activities.

A final acceptance test planned for April 1986 will conclude the commissioning program followed by the first experiment.

A total of 30 experiments is planned including integral and separate effects tests. Approximately one half of the experiments will be specified to investigate the phenomena occurring during cold leg injection and the resulting downcomer behavior, the other half will focus on the effects during combined hot and cold leg injection and the resulting upper plenum behavior.

Up to now the first eight experiments have been specified (Fig. 11). The six separate effects tests concern fluid/fluid mixing, tie plate and downcomer counter-current flow phenomena, flow patterns in the loops and counter-current flow in the hot leg pipe under small break LOCA conditions. The two integral tests will be a cold leg and a combined cold and hot leg injection case respectively. Further tests will be specified in cooperation with JAERI and USNRC when the first experimental data are available.

## Calibration of the Tie Plate Instruments

Within the German 2D/3D program the calibration of the UPTF tie plate instruments provided by USNRC has been performed. These measurements basically consisting of tie plate dragbodies, flow turbines and break through detectors play an important role to determine and control the boundary conditions at the core/upper plenum interface. A single bundle test loop was used to calibrate the instruments for the various single and two-phase flow conditions. Appropriate algorithms for data evaluation and interpretation have been developed and tested.

Fig. 12 shows a cross-section of the UPTF end box with the integrated tie plate drag body and the associated transducer. The vertical positions of the thermocouples are also marked. These thermocouples are used to determine the fluid temperature profile above the tie plate, as well as for thermal compensation of the transducers.

The top view of tie plate area (Fig. 13) shows the positions of the instruments attached to the UPTF end box. The drag body is part of the tie plate itself while the break through detector is mounted below and the turbine flow meter is mounted above the tie plate.

The flow modules have been calibrated at various pressures in the flow regimes shown in Fig. 14. The physical relationships found for cocurrent upflow, cocurrent downflow, simultaneous steam up and water downflow and single phase wa-



ter downflow are indicated also. A sophisticated logic has been developed to apply the adequate algorithms according to the existing flow conditions.

### Analyses

To define the initial and boundary conditions for the experiments, evaluation of TRAC analyses for the reference reactor and the UPTF system are required. These analyses as well as the later test calculations and the final assessment work are partly performed by LANL and the German contractors of BMFT.

- JAERI (Japan):
- Cylindrical Core Test Facility (CCTF)  
Integral system behaviour (1:25 scale)
  - Slab Core Test Facility (SCTF)  
2 D-flow behaviour in core (8 bundles),  
coupling with UPTF
- BMFT (Germany):
- Upper Plenum Test Facility (UPTF)  
3 D-flow behavior in upper plenum and  
downcomer, steam injection for core  
simulation,  
coupling with SCTF
- USNRC (USA):
- TRAC code development and test  
analyses
  - Development and supply of advanced  
instrumentation



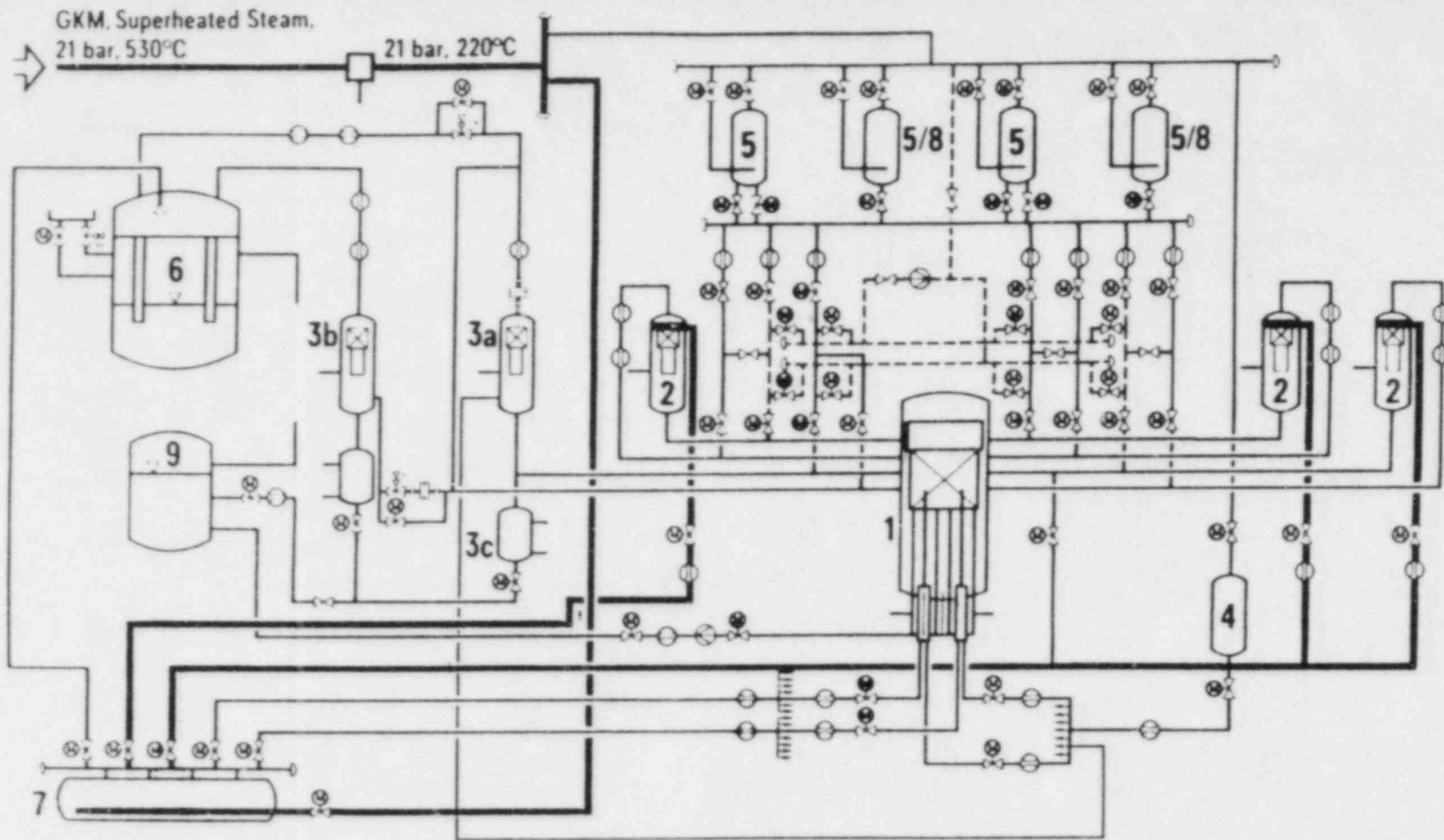
- Full size reactor pressure vessel including upper plenum and downcomer (pressure 22 bars)
- Core simulation by controlled steam/water injection, 17 independent injection zones (1500 kg/s water, 360 kg/s steam)
- 3 full size intact loops, 1 broken loop with break valves
- Steam generators simulated by separators
- Pumps simulated by flow restrictors
- Containment simulation with pressure suppression system (1500 m<sup>3</sup>)
- ECC-system: 4 pressurized storage tanks to simulate accumulator and low pressure injection system (750 kg/s/ injection point), nitrogen injection capability, hot and/or cold leg, downcomer injection, vent valves

1621K

## FEATURES OF UPTF



FIG. 2



337

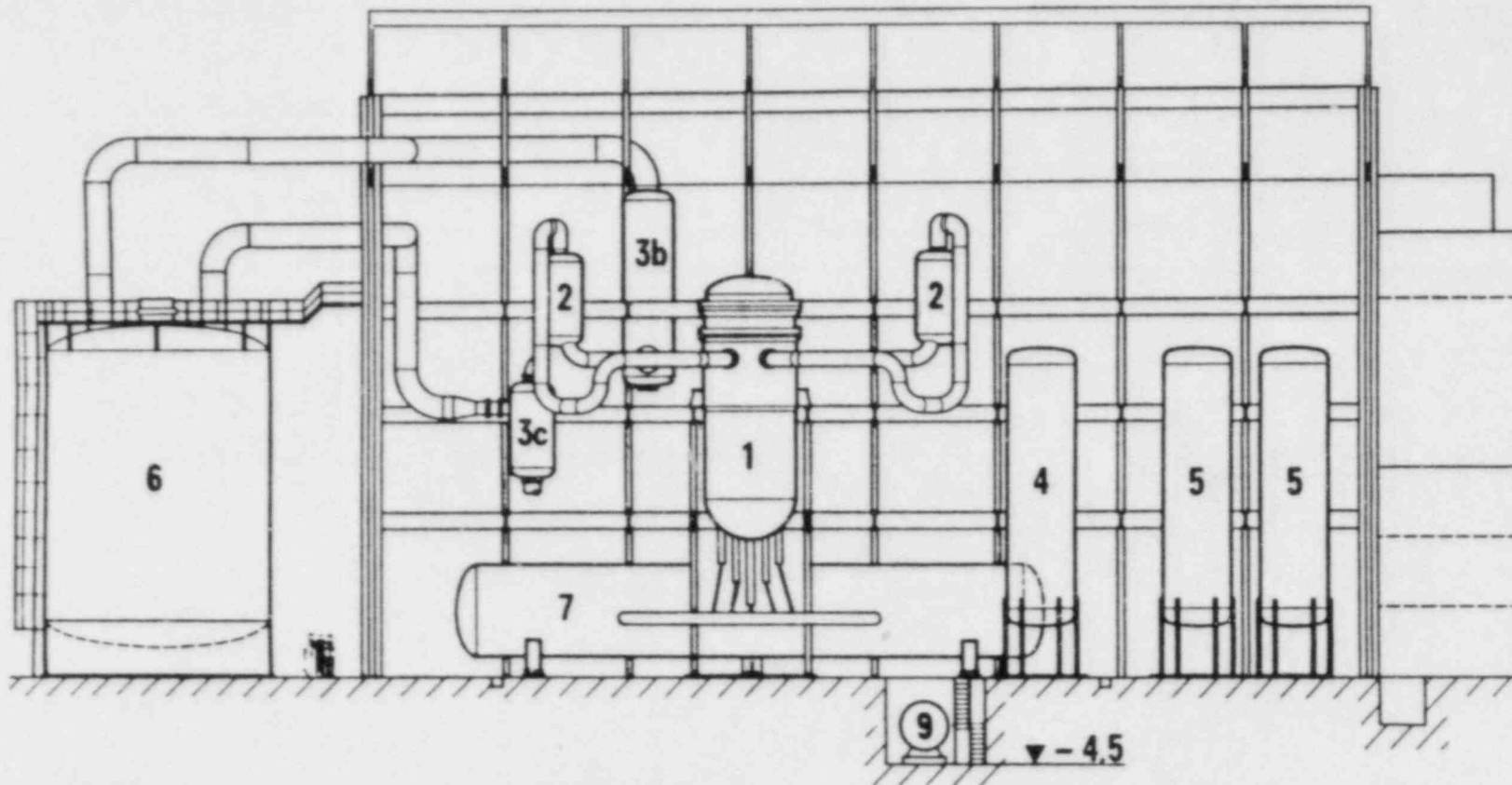
- |     |  |     |  |   |                       |
|-----|--|-----|--|---|-----------------------|
| 1   | Test Vessel                                | 3 b | Water Separator<br>(Broken Loop, Cold Leg) | 5 | Accumulator           |
| 2   | Steam Generator Simulator<br>(Intact Loop) | 3 c | Drainage Vessel<br>for Hot Leg Break       | 6 | Containment Simulator |
| 3 a | Water Separator<br>(Broken Loop, Hot Leg)  | 4   | Hot Water Storage Tank                     | 7 | Steam Storage Tank    |
|     |  |     |  | 8 | N <sub>2</sub> - Tank |
|     |  |     |  | 9 | Water Collecting Tank |

Status Feb.'85

FIG. 3

### UPTF-Flow Diagram

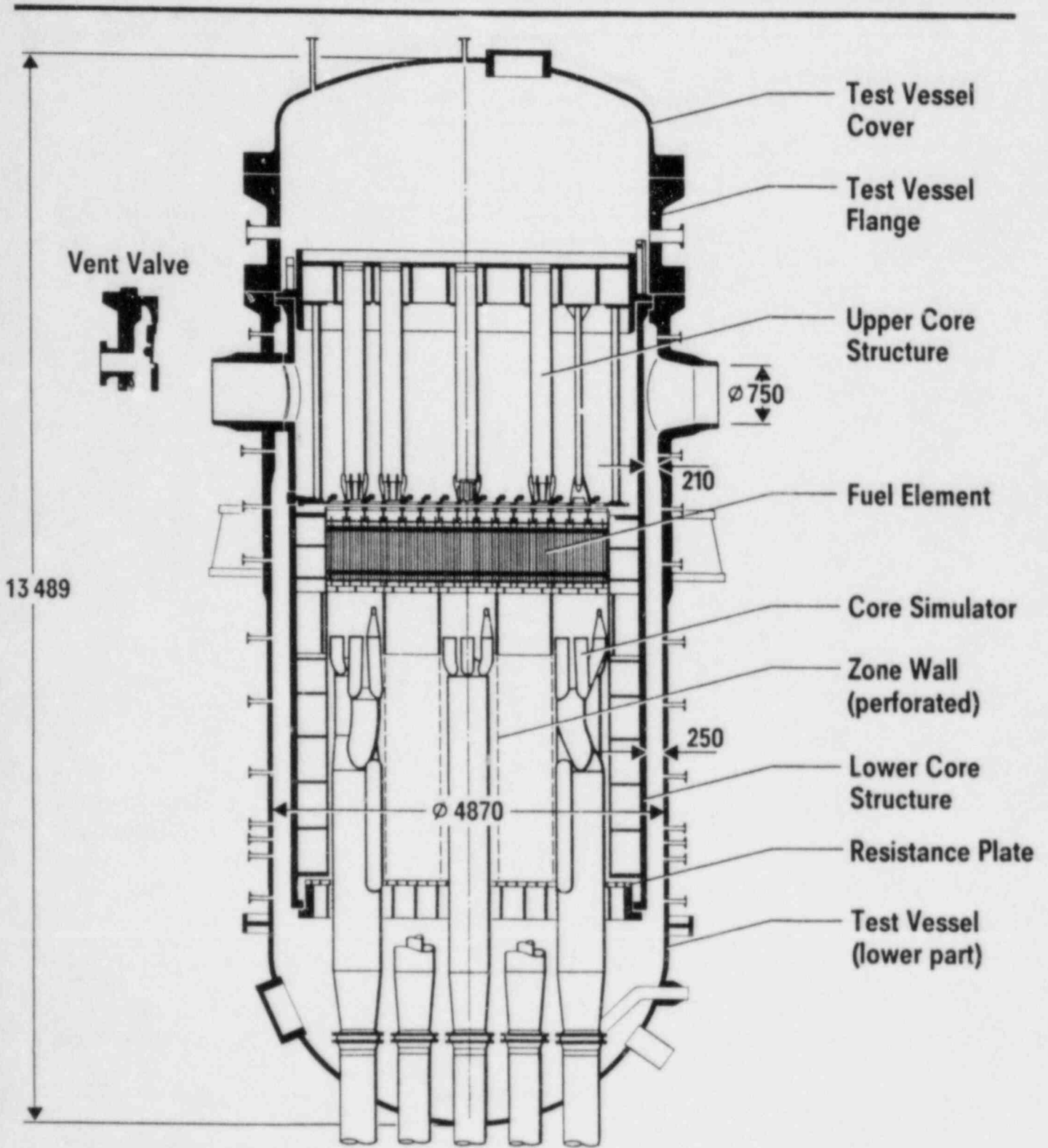
Saturated Steam Version with Preheated ECC Water



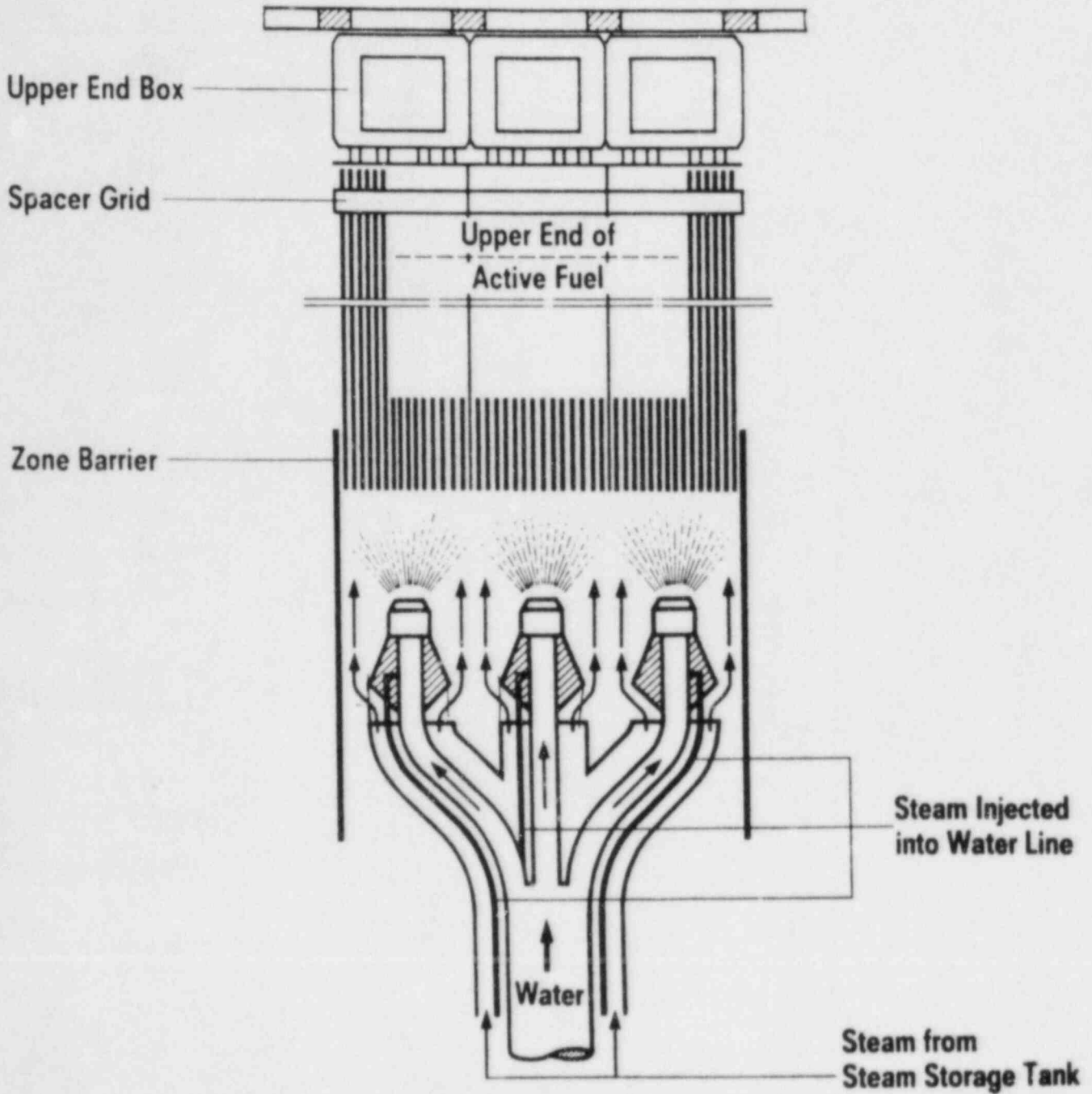
- |   |   |                      |
|---|---|----------------------|
| 1 Test Vessel                                 | 3c Drainage Vessel<br>for Hot Leg Break | 7 Steam Storage Tank |
| 2 Steam Generator Simulator,<br>(Intakt Loop) | 4 Hot Water Storage Tank                | 9 Drain Storage Tank |
| 3b Water Separator<br>(Broken Loop, Cold Leg) | 5 Accumulators                          |                      |
| 6 Containment Simulator                       |   |                      |

FIG. 4

**UPTF - Layout  
Front View**

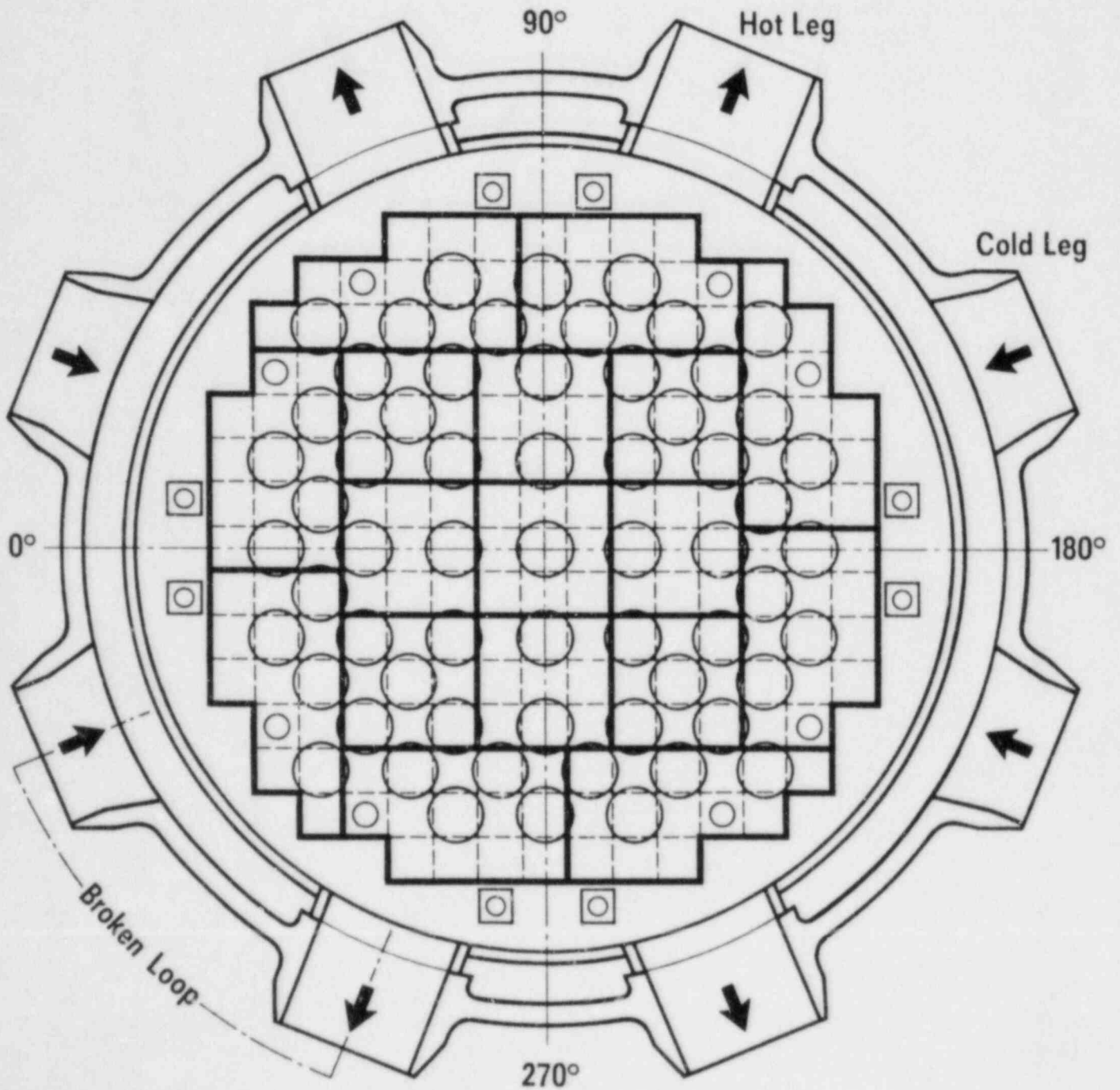


UPTF - Test Vessel  
and Test Vessel Internals



**Core Injection Zone (UPTF)  
Nozzle Concept, Preliminary Design**

**FIG. 6**

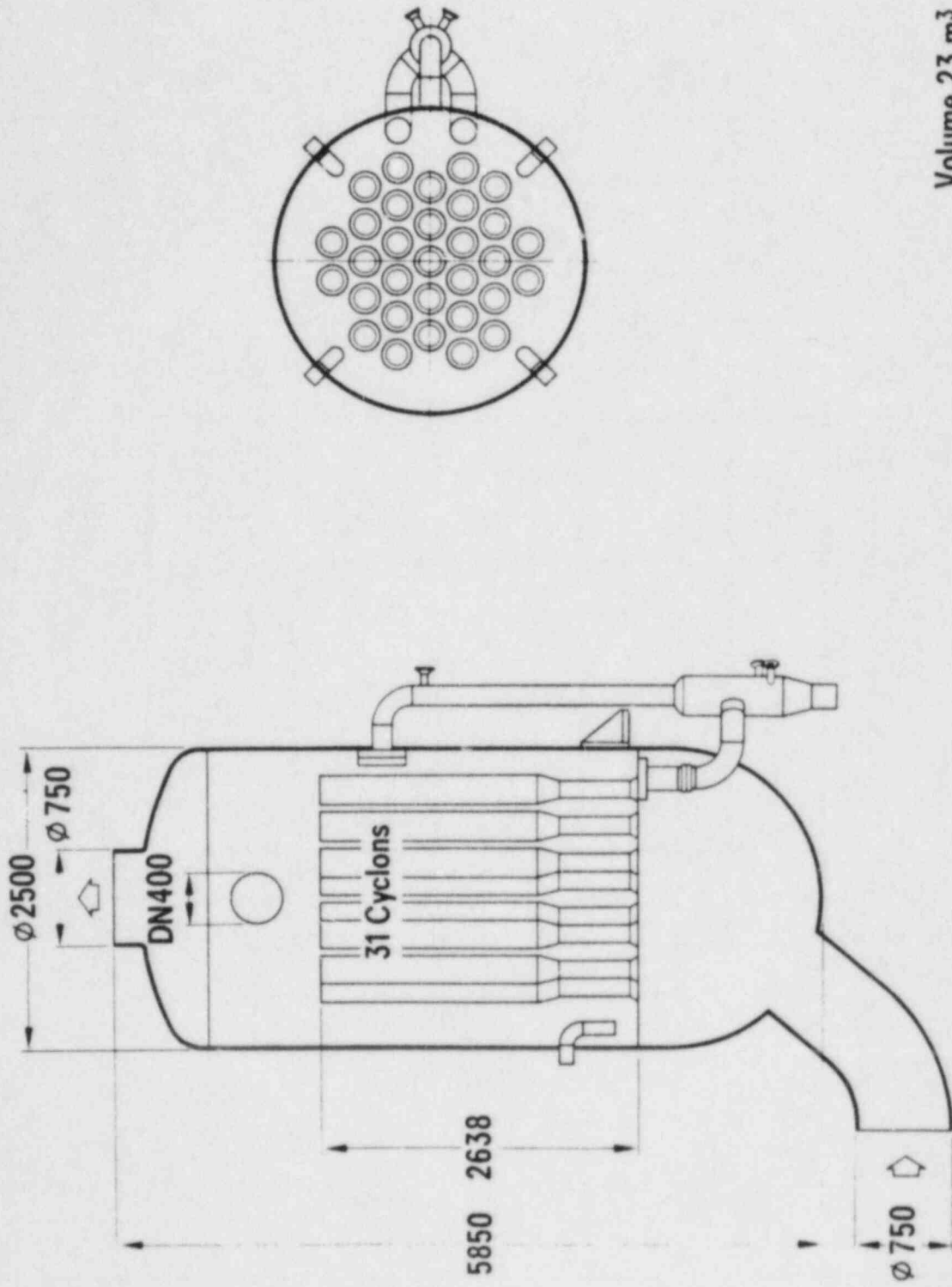


**17 Injection Zones, (UPTF)**

9 Injection Zones, 9 Fuel Elements

8 Injection Zones, 14 Fuel Elements

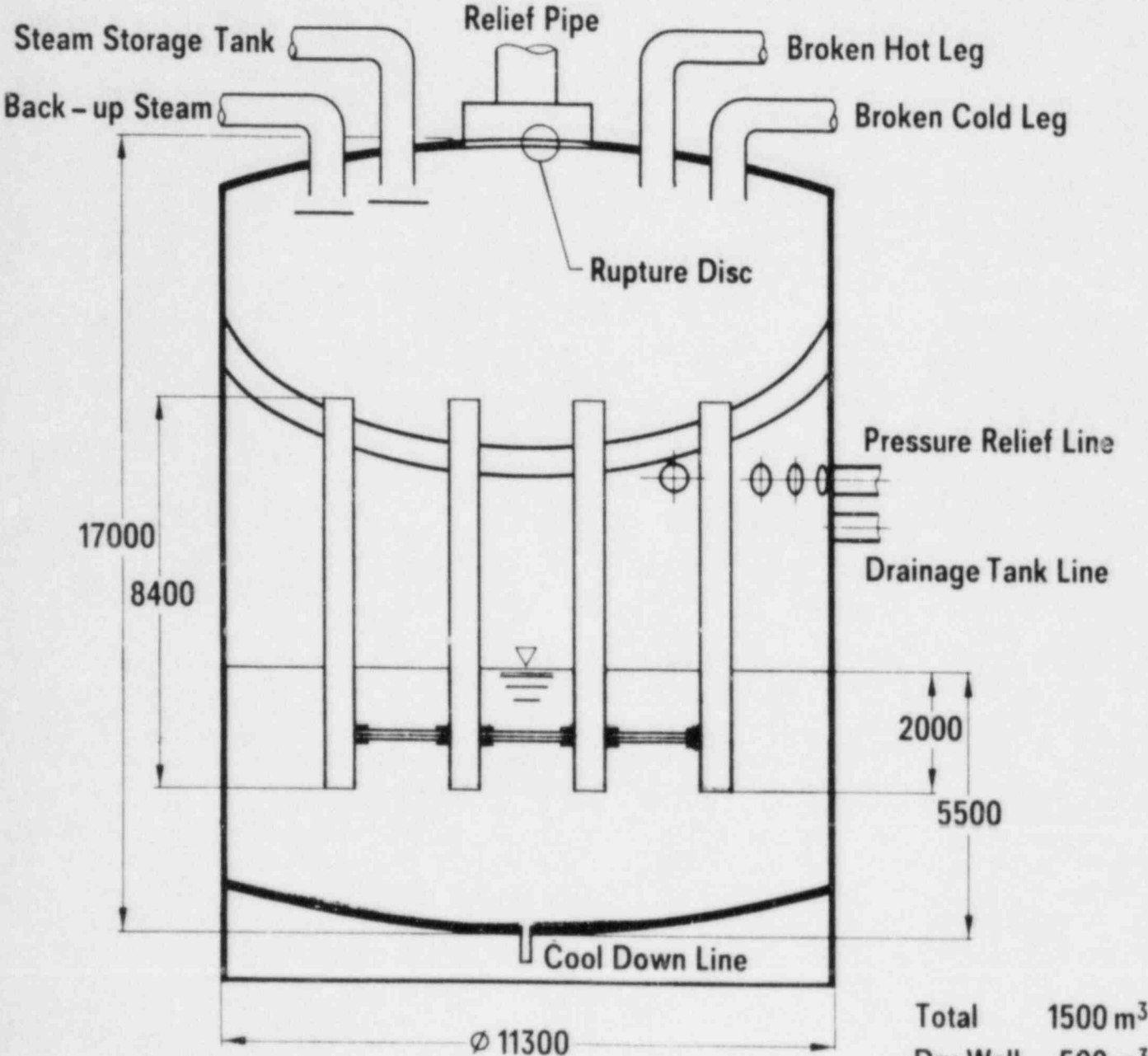




Volume 23 m<sup>3</sup>

**UPTF – Steam Generator Simulator  
Intact Loop**

FIG. 8



Total	1500 m <sup>3</sup>
Dry Well	500 m <sup>3</sup>
Wet Well	1000 m <sup>3</sup>
Water	500 m <sup>3</sup>

**Containment Simulator (UPTF)**

**FIG. 9**

ADVANCED INSTRUMENTATION FOR THE UPPER PLENUM TEST FACILITY

QUANTITY

I. UPPER PLENUM

1.	LOCAL FLOW PATTERNS	VIDEO OPTICAL PROBE	3
2.	LOCAL FLUID VELOCITY	TURBINE METERS (4V, 2H)	6
3.	POOL FORMATION	LLD	8 x 19
4.	VENT FLOW	TURBINE METER	5
		DP	5
5.	POOL FORMATION	FLUID DISTRIBUTION GRID	45 x 7

II. CORE - UPPER PLENUM INTERFACE

1.	UPWARD FLOW VELOCITY	TURBINE METER	36
2.	FLUID LEVEL IN END BOX	FLUID DISTRIBUTION GRID	INCLUDED IN I.5
3.	MASS FLOW	DRAG BODIES	36
		NARROW DP	9
		WIDE DP	36
		BREAKTHROUGH DETECTORS	94
4.	CROSS FLOW BETWEEN END BOXES	TURBINE METER	6

III. CORE

1.	LIQUID LEVEL	LLD	2 x 19
----	--------------	-----	--------

IV. HOT LEG

1.	DENSITY, $\alpha$	MULTI-BEAM GAMMA DENSITOMETER	4
2.	VELOCITY (MOMENTUM)	DRAG RAKE (BIDIRECTIONAL)	4

V. COLD LEG

1.	DENSITY	MULTI-BEAM GAMMA DENSITOMETER	1
2.	VELOCITY (MOMENTUM)	DRAG RAKE (BIDIRECTIONAL)	1
3.	FLUID TEMPERATURE	T/C'S FOR RAKES IN CL No 2	24

VI. LOWER PLENUM

1.	LIQUID LEVEL	LLD	EXT. OF III.1
----	--------------	-----	---------------

VII. DOWNCOMER

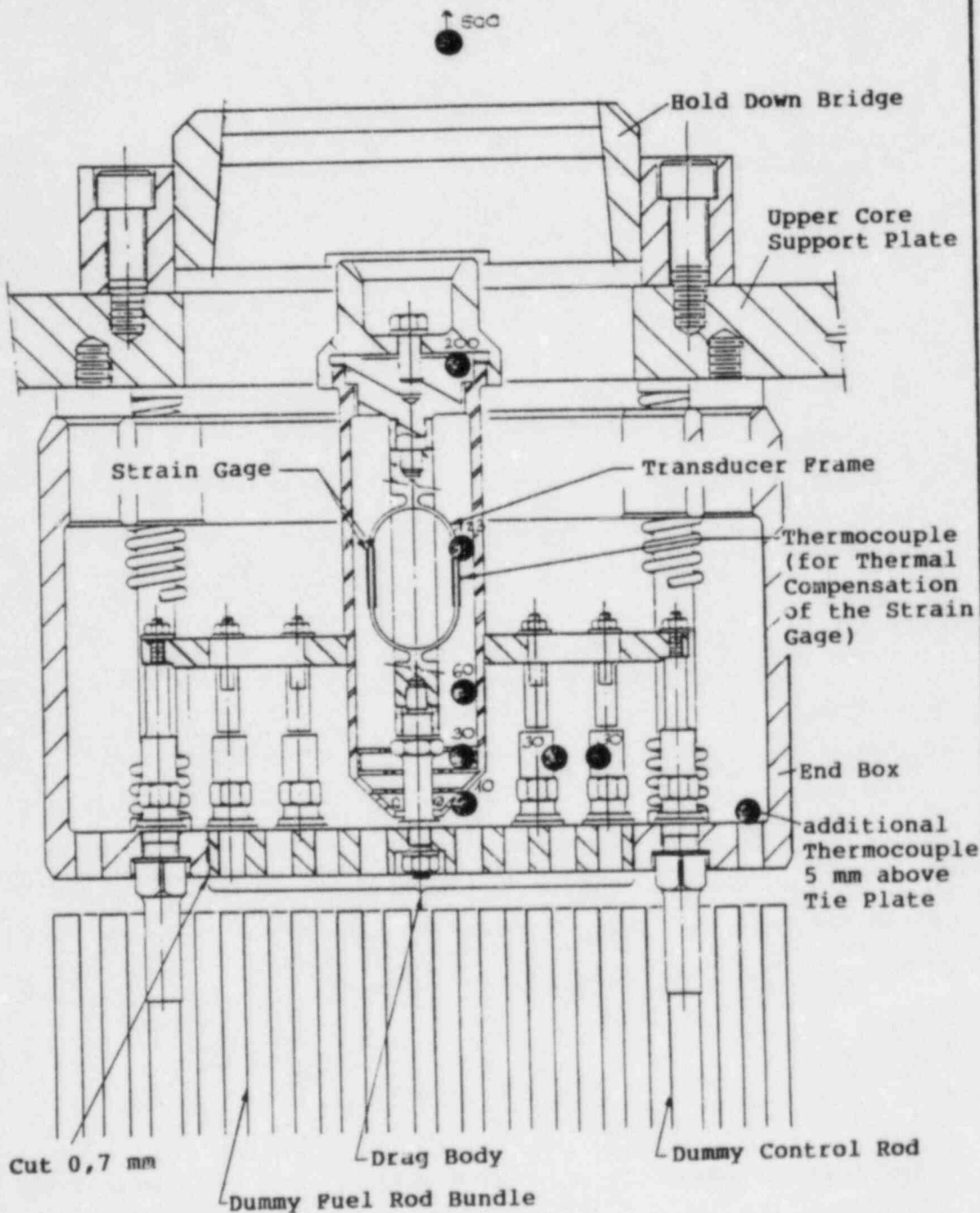
1.	FLOW PATTERNS	FLUID DISTRIBUTION GRID	50 x 3 + 50 x 1
2.	LOCAL FLUID VELOCITY	TURBINE METER	8

FIG. 10

## FIRST EIGHT UPTF EXPERIMENTS

- 1 FLUID/FLUID MIXING
- 2 DOWNCOMER CCF - BASE CASE
- 3 TIE PLATE CCF, SATURATED ECC
- 4 HOT AND COLD LEG FLOW PATTERN
- 5 HOT LEG CCF, SBLOCA
- 6 INTEGRAL TEST, 200 % CL BREAK, 5/8 COMBINED INJECTION
- 7 TIE PLATE CCF, SUBCOOLED ECC
- 8 INTEGRAL TEST, 200 % CL BREAK, COLD LEG INJECTION

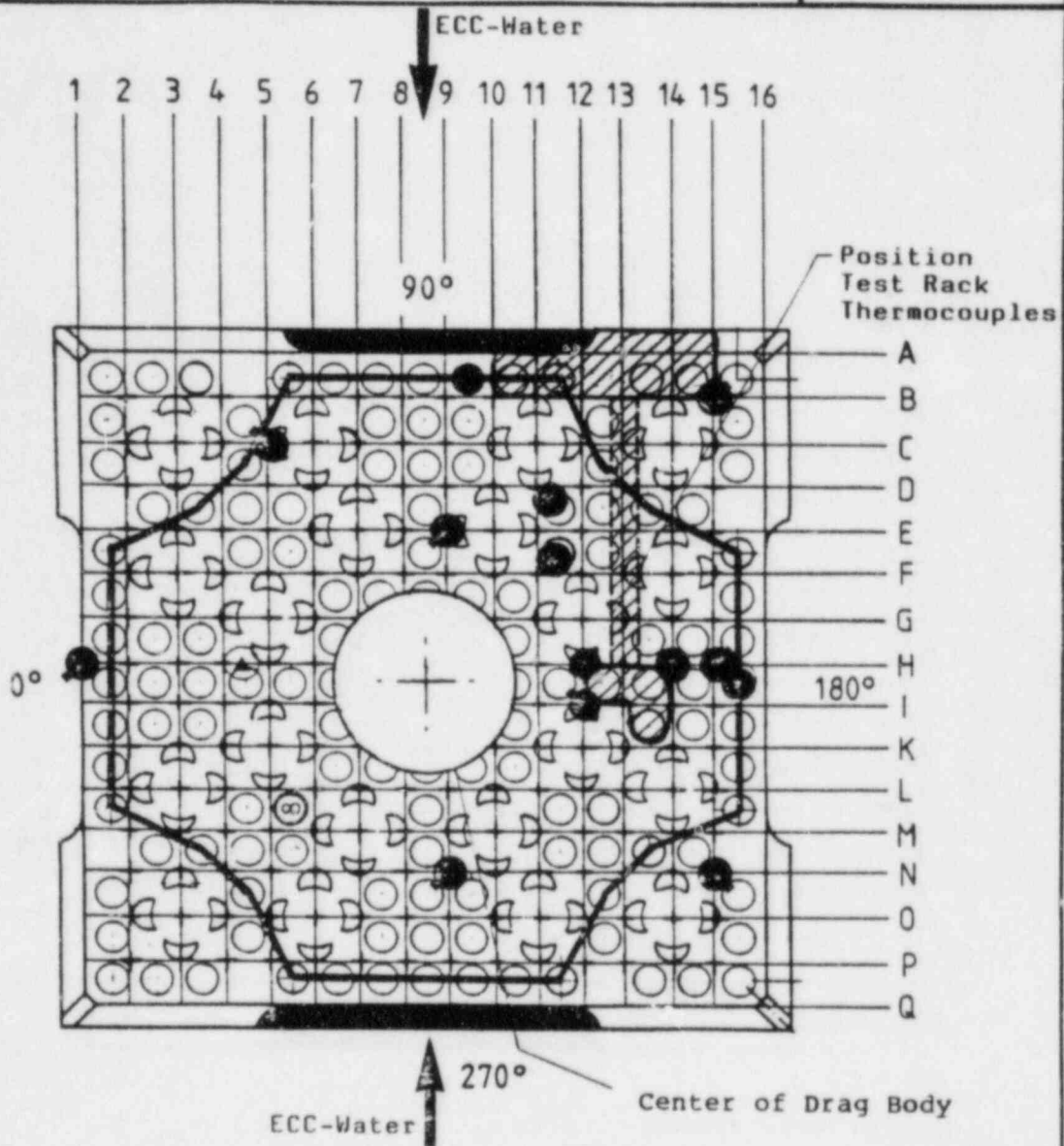
FIG. 11



10 ← Distance above Tie Plate in mm;  
 ● Position of Thermocouples in the Test Rack

View into the End Box with Axial Measurement Positions of the Thermocouple Test Rack

FIG. 12

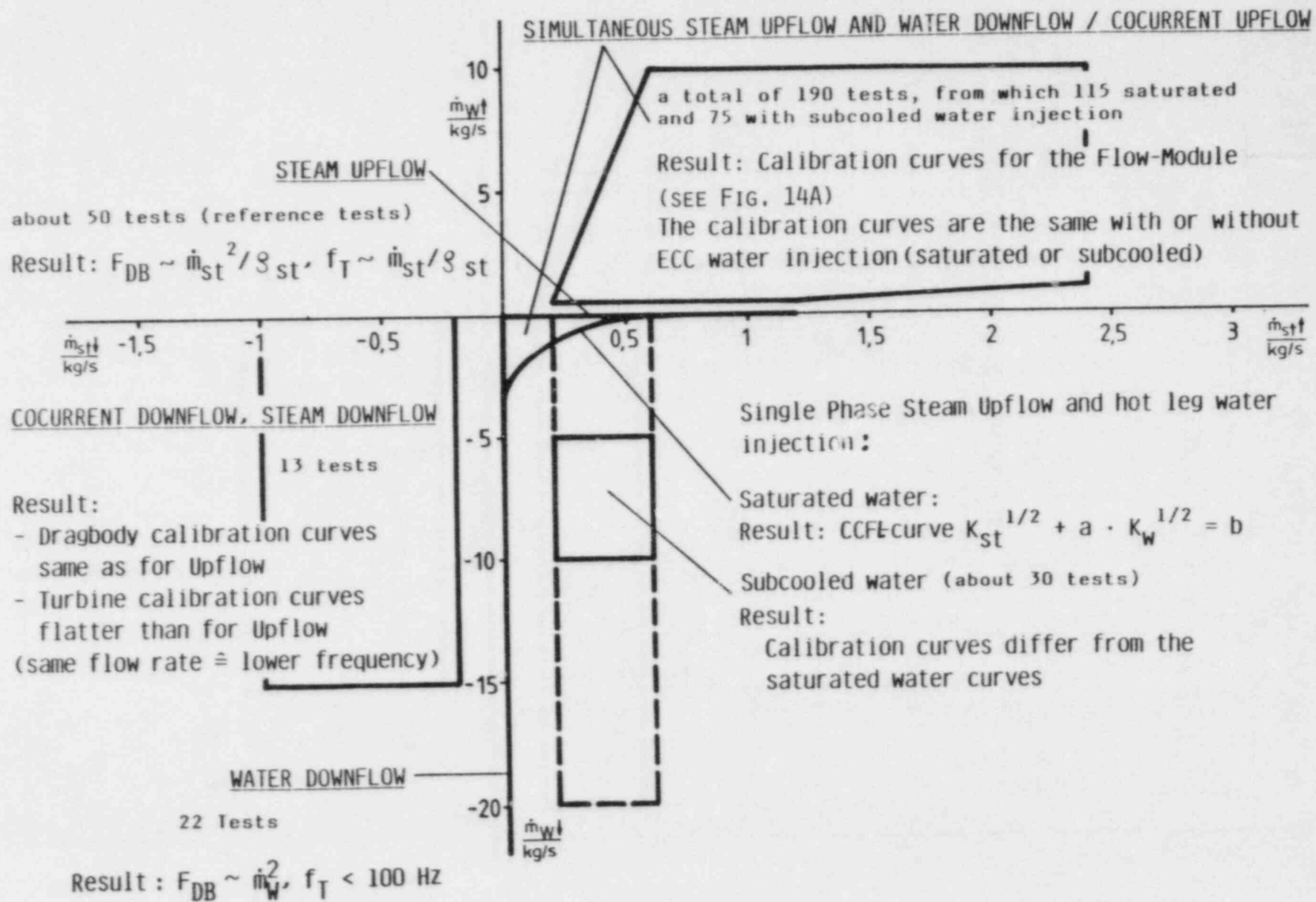


- ▲ Position of UPTF-Thermocouples
- ⊙ Location of the Turbine Meter
- ⌚ Location of the Break Through Detector
- Thermocouple Positions of the Bundle
- Thermocouple Positions 30 mm above Tie Plate

Tie Plate Level Instrumentation in the Subcooled Water Tests:  
Positions of the Thermocouples and of the Break-Through-Detector

FIG. 13

UPTF-Calibration Tests: Tested Flow Regimes and Results



348

FIG. 14

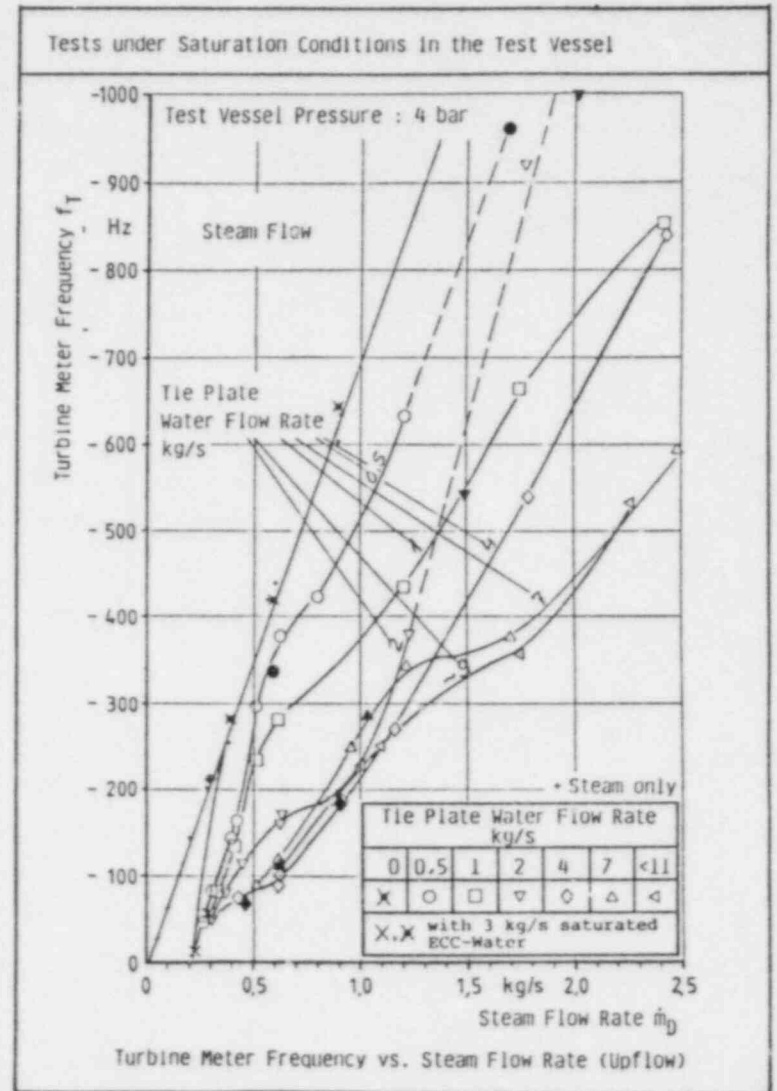
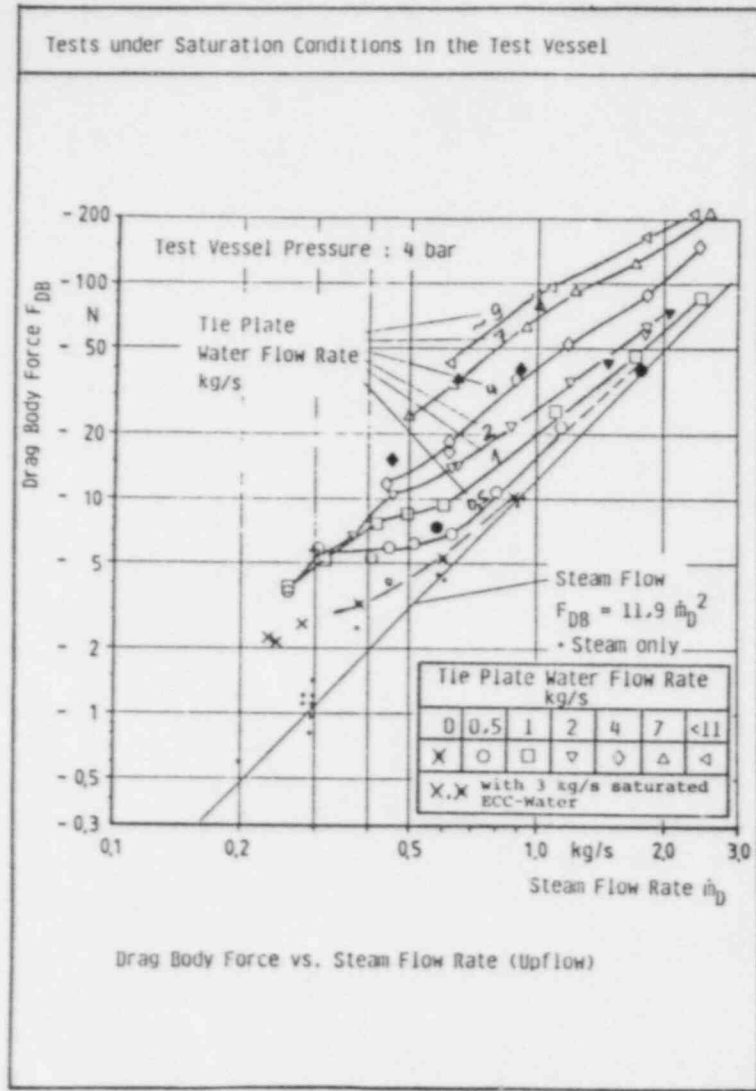


FIG. 14A



TRAC ANALYSES FOR CCTF AND SCTF TESTS  
AND UPTF DESIGN/OPERATION\*

by

Jay W. Spore  
Michael W. Cappiello  
Paul J. Dotson  
Joel S. Gilbert  
Victor Martinez  
Henry J. Stumpf  
Code Development Group  
Energy Division  
Los Alamos National Laboratory  
Los Alamos, New Mexico 87545

ABSTRACT

The analytical support in 1985 for Cylindrical Core Test Facility (CCTF), Slab Core Test Facility (SCTF), and Upper Plenum Test Facility (UPTF) tests involves the posttest analysis of 16 tests that have already been run in the CCTF and the SCTF and the pretest analysis of 3 tests to be performed in the UPTF. Posttest analysis is used to provide insight into the detailed thermal-hydraulic phenomena occurring during the refill and reflood tests performed in CCTF and SCTF. Pretest analysis is used to ensure that the test facility is operated in a manner consistent with the expected behavior of an operating full-scale plant during an accident. To obtain expected behavior of a plant during an accident, two plant loss-of-coolant-accident (LOCA) calculations were performed: a 200% cold-leg-break LOCA calculation for a 2772 MW<sub>t</sub> Babcock and Wilcox plant and a 200% cold-leg-break LOCA calculation for a 3315 MW<sub>t</sub> Westinghouse plant. Detailed results will be presented for several CCTF UPI tests and the Westinghouse plant analysis.

---

\*Work performed under the auspices of the US Nuclear Regulatory Commission

## INTRODUCTION

The 2D/3D Program is a multinational (Germany, Japan, and the United States) experimental and analytical nuclear reactor safety research program. Its main purpose is the investigation of multidimensional thermal-hydraulic behavior in large-scale experimental test facilities having hardware prototypical of pressurized water reactors (PWRs). The Japanese are operating two large-scale test facilities as part of this program: the Cylindrical Core Test Facility (CCTF), which completed its testing program this year, and the Slab Core Test Facility (SCTF), which will begin its third phase of testing in 1986. The CCTF is a 2000-electrically heated-rod, cylindrical-core, four-loop facility with active steam generators primarily used for investigating integral system reflood behavior. The SCTF is a 2000-electrically-heated-rod, slab-core (one fuel assembly wide, eight across, and full height), separate-effects reflood facility. Both facilities have prototypical power-to-volume ratios preserving full-scale elevations, and both are much larger than any existing facilities in the United States. The German contribution to the program is the Upper Plenum Test Facility (UPTF) in Mannheim, West Germany, a full-scale facility with vessel, four loops, and a steam-water core simulator. All these facilities have more instruments than any other existing facilities: each has more than 1500 conventional instrumentation data channels, alone. As its contribution to the program, the United States is providing advanced two-phase flow instrumentation and analytical support.

The Los Alamos National Laboratory is the prime contractor to the US Nuclear Regulatory Commission (NRC) in the latter activity. The main analytical tool in this program is the Transient Reactor Analysis Code (TRAC), a best-estimate, multidimensional, nonequilibrium, thermal-hydraulics computer code developed for the US NRC at Los Alamos. Through code predictions of experimental results and calculations of PWR transients, TRAC provides analytical coupling among the facilities and extends the results to predict actual PWR behavior.

During FY 1985, TRAC-PF1/MOD1 analyses were completed for seven CCTF-II experiments. Predictions of upper-plenum injection (UPI) tests 57, 72, 76, and 78 demonstrated that TRAC can predict correctly when UPI flows enhance core cooling and when they contribute to steam binding and degraded core cooling. In addition, TRAC was used to analyze nine SCTF experiments: the base case for Core-II (Run 604), the flat power and initial rod temperature profile (Run 605), the steep power and initial rod temperature profile (Run 611), the FLECHT-SET coupling test (Run 613), the best-estimate base case (Run 614), the separate-effects countercurrent flow-limiting (CCFL) tests (Runs 608 and 610), and others. The analyses of these tests demonstrated that in general TRAC-PF1/MOD1 accurately simulates the reflood thermal-hydraulic behavior of the SCTF tests.

In support of the UPTF, three pretest predictions were performed with TRAC-PF1/MOD1: downcomer separate-effects analyses, a German PWR base case analysis, and a hot-leg small-break test analysis. From these analyses, initial and boundary conditions for the tests can be determined to ensure proper operation of the test facility.

A fine-node 200% cold-leg-break loss-of-coolant-accident (LOCA) calculation of a Babcock and Wilcox (B&W) 2772 MW<sub>t</sub> PWR, assuming licensing-type boundary and initial conditions, was completed. This calculation predicted a peak cladding temperature (PCT) of 995 K to occur in the average rod during blowdown.

In addition, a fine-node 200% cold-leg break LOCA calculation of a Westinghouse 3315 MW<sub>t</sub> PWR, assuming licensing-type boundary and initial conditions, was completed. This calculation predicted a PCT of 897 K to occur in the average rod during blowdown.

#### MAJOR PHENOMENA DURING A LARGE BREAK LOCA IN A UPI PLANT

For a Westinghouse two-loop PWR with a 200% cold-leg break, the sequence of events may vary slightly from plant to plant because of geometry differences and operating assumptions; however, a "typical" sequence of events can be specified (Ref. 1) and is given in Table I.

The blowdown transient is typically less than 20 s, because of the large break area to primary-fluid-volume ratio. During the blowdown transient as the core voids, the core heats up significantly. LOFT experiments and TRAC calculations indicate that the heating during blowdown is terminated when choked-flow conditions at the break restrict the outflow and allow the remaining fluid in the intact cold legs and downcomer to reflood the core partially. The extent of this core recovery during blowdown is dependent upon the number of intact loops, whether or not the reactor-coolant system (RCS) pumps are tripped, and upon the subcooling in the lower plenum and upper head.

For the "typical" sequence of events given in Table I, the refill period is between 18 and 28 s. During the refill period, the core will heat up until core recovery begins. The degree of heating during refill is dependent upon the amount of stored energy retained in the core at the end of blowdown, core power level, and core steam-flow rates. Most of the accumulator flow injected into the cold legs bypasses the downcomer and lower plenum and exits the break during blowdown. However, during refill, most of the accumulator flow in the intact loops ends up in the downcomer and lower plenum. For the "typical" sequence of events given in Table I, both accumulators are empty at the end of the refill phase of the transient.

TABLE I  
TYPICAL EVENT SEQUENCE FOR A 200% COLD-LEG BREAK  
IN A WESTINGHOUSE TWO-LOOP PWR

<u>Event</u>	<u>Times(s)</u>
200% cold leg break	0.0
Reactor scram & feedwater trip	0.1-1.0
High-pressure injection	1.0
Accumulator check valves open:	
Loop A (Intact)	6.0-7.0
Loop B (Broken)	3.0
Low-pressure injection	13.0
Pressurizer empty	15.0
End of blowdown	18.0
Accumulators empty:	
Loop A (Intact)	28.0
Loop B (Broken)	25.0
Beginning of reflood	28.0
Core quenched	300.0-500.0

Of most interest in UPI plants is the reflood phase of the transient, when the water level in the lower plenum reaches the bottom of the core. During reflood, the low-pressure injection (LPI) flow is injected into the upper plenum. Typical LPI flow rate assuming single failure, is ~120 kg/s. The high-pressure injection (HPI) flow into the cold leg is at a rate of ~19 kg/s. During the later stages of refill and the early stages of reflood, the UPI water entering the upper plenum forms a pool in the upper plenum. Small-scale experiments<sup>3,4</sup> and large-scale experiments<sup>5</sup> indicate that subcooled CCFL breakdown requires penetration of subcooled water into the core. Once subcooled water penetrates the core, the steam flow upward is reduced because of condensation and more subcooled water is allowed into the core, which results in more condensation. This is the process that initiates the dumping of UPI water from the upper plenum into the core region. The rods below this region of UPI-water dumping begin to quench, producing additional steam. The steam can either flow up and interact with the subcooled water falling back into the core or it can flow radially over and then up. The latter case is illustrated in Fig. 1.

For the case in which the steam flows radially out and then up, the low-power bundles in that region of the core will quench much earlier than the rest of the core, which then allows dumping of the UPI water directly into the pool of water that is quenching the core from the bottom.

If the additional steam produced from quenching bundles directly below UPI nozzles flows up and interacts with the UPI water falling into the core, then dumping in that region of core will be stopped. Once dumping is stopped, then steam production is reduced and subcooled water begins to penetrate again and the cycle repeats. Therefore, the difference between the two cases is that one results in continuous dumping of (ECC) water from the upper plenum into the core, while the other results in intermittent dumping. The continuous-dumping case tends to result in lower PCTs and faster core quenches. Calculations and data tend to support the continuous dumping case, if sufficient subcooling is available in the upper plenum. It should be noted that even if the core radial power profile is flat, dumping in the outer bundles still occurs, since the largest amount of subcooling of the UPI water will still be directly below the UPI nozzles. The UPI water interacts very quickly with the upper plenum structure and tends to fall to the upper core support plate (UCSP) and to form a pool.

The outer bundles directly under the region of the core dumping will quench in 100 to 200 s. The rest of the core will quench in 300 to 500 s depending upon core-stored energy and ECC flows and temperatures.

#### UPI Test (CCTF)

Experimental data from the Japanese Atomic Energy Research Institute (JAERI) CCTF UPI tests listed in Table II and the TRAC analyses of these tests showed the following phenomena to be significant.

1. Pooling in the upper plenum.
2. Subcooling in the upper plenum.
3. Entrainment of water from the upper plenum into the hot legs.
4. Dumping or channeling of water in the low-power region of the core.
5. Condensation in the upper plenum.

In the Run 57 experiment and in the posttest calculation,<sup>6</sup> significant core heating was observed after beginning of core recovery (BOCREC). As this was a high-power, high-stored-energy experiment, this heating was expected. In the calculation, significant amounts of water were entrained into the hot legs

ROD TEMPERATURES  
INDICATE DOWNFLOW  
IN LOW POWER ZONE  
ON HIGH FLOW SIDE

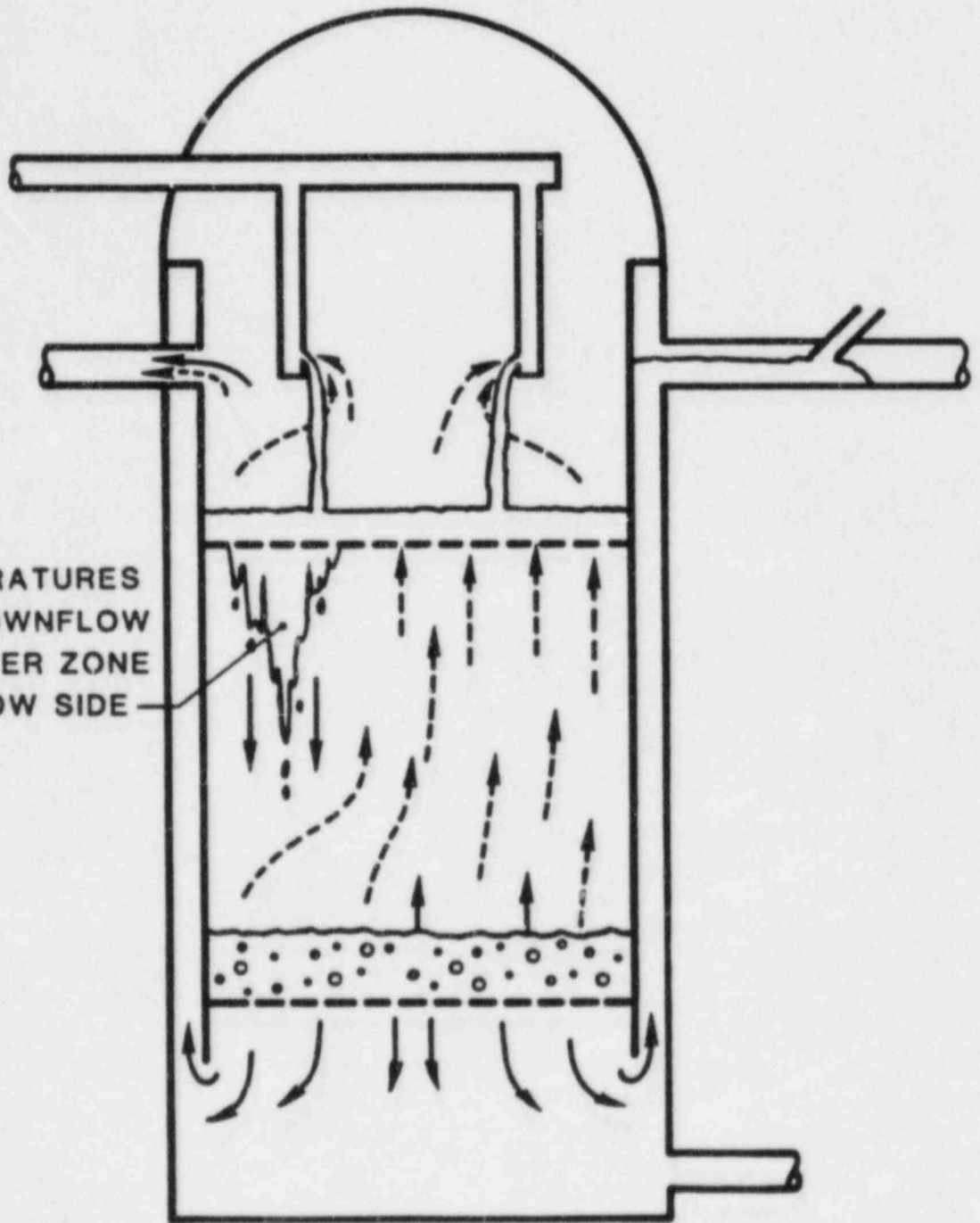


Fig. 1.  
Observed experimental behavior in the CCTF.

TABLE II

## UPI TEST ANALYZED WITH TRAC

Run #	Description and Comments	Power Level	ECC FLOWS				PCT at BOCREC (k)	PCT (K)
			CL	UPI	UPI Flow Split			
57	High Power, High CL ECC Flow, Low UPI Flow, High Stored Energy	(1.2*ANS + Actinides) @ 30 s after scram	3/4 (ACC + 10*HPCI)	3/8 LPCI	1.6/1.0	1085	1242	
59	Single Failure UPI, High Stored Energy	(1.03*ANS + Actinides) @ 30 s after scram	3/4 (ACC + HPCI)	1/2 LPCI	1.6/1.0	1074	1110	
72	No Failure UPI, High Stored Energy	(ANS + Actinides) @ 30 s after scram	3/4 (ACC + HPCI)	Full LPCI	1.0/1.0	1057	1070	
76	Asymmetric Injection High Stored Energy	1.07 * 1.02 * (ANS + 1.1 * Actinides) @ 30 s after scram	3/4 (ACC + HPCI)	1/2 LPCI	0.0/1.0	1073	1100	
78	Refill-BE-Reflood, Low Stored Energy	1.02 (ANS + Actinides) @ 40 s after scram	3/4 (ACC + HPCI)	1/2 LPCI	0.0/1.0	692	722	

LPCI ~15 l/s

HPCI ~3.7 l/s

ACC ~100 l/s

from the upper plenum. As the water flashed in the steam generator tubes, the resulting pressure increase in the steam generator caused the core quench front propagation to slow down. In the experiment, the power in the high power bundles was tripped at 200 s to protect the electrical rods from damage. The calculation at this point was stopped. Both the calculation and the data indicate that UPI water was penetrating into the core. However, in comparison to the data, TRAC predicted too much steam and entrained UPI water flowing into the hot legs. It is anticipated that a higher UPI flow with more condensation in the upper plenum would have reduced the steam flow and entrained UPI water into the hot legs; an earlier turnaround of the rod temperatures would have been the result.

For Run 59 the UPI flow rate was increased and the core power level was decreased compared to Run 57. With the higher UPI flow, more condensation occurred in the upper plenum, resulting in less steam flow and fewer entrained droplets into the hot legs. Both the TRAC calculation<sup>7</sup> and the experimental data indicate lower PCTs for Run 59 as compared to Run 57.

For Run 72, the UPI was increased again, and the power and stored energy were reduced slightly as compared to Run 59. In Run 72, significant channeling was observed in both the experiment and the calculation.<sup>8</sup> This channeling or dumping of ECCS water occurred in the low-power region of the core and was observed to occur on only one side of the core underneath one of the injection nozzles, even though the UPI flow is the same in both UPI nozzles.

Input errors were found in the original TRAC calculation for Run 72; therefore, the calculation is being repeated with the errors corrected. The repeat calculation is in progress and preliminary results are available. In Fig. 2, TRAC results are compared with experimental data for the high-power region of the core. TRAC is overpredicting the PCT by ~70 K because of core heating that was calculated by TRAC to occur from 120 to 200 s. This core heating was not observed in the data. The difference may be caused by TRAC's overestimating the amount of UPI water entrained into the hot legs; however, it is still being investigated at this time. For the rest of the transient, the comparison is quite good and the overall trends are being predicted. As illustrated in Figs. 3 and 4, dumping was correctly predicted by TRAC. Rods 9 and 12 are TRAC-simulated rods in the low-power region of the CCTF core. As illustrated in Fig. 3, neither TRAC nor the data indicate significant dumping in the region around rod 12. In Fig. 4, TRAC and the data both indicate significant dumping in the region around rod 9. It should be noted that the TRAC rod 9 simulates all of the rods in CCTF bundles 5, 6, 7, and 8; therefore, exact comparison with a single measurement is not expected.

For Run 76, the initial stored energy and transient power level were both increased as compared to Run 72. The UPI flow was reduced. In Run 76, only one injection nozzle was used; therefore, asymmetric quenching was expected. Again, both in the data and in the TRAC calculation, channeling and dumping of ECC water were observed. Comparisons to TRAC for Run 76 are illustrated in Figs. 5 and 6. TRAC overpredicted the PCT by ~100 K and calculated heating in the upper portion of the rods that was not observed in the data. Overprediction of the entrainment of UPI water into the hot leg as was mentioned for Run 72 and overprediction of the boiloff of water in the downcomer are two explanations currently being considered.

For the UPI transients, negative core inlet flow is established at or soon after BOCREC. The water flowing out the bottom of the core is saturated liquid or a low void fraction bubbly mixture. This saturated liquid mixes with the cold water in the downcomer and lower plenum, causing a temperature rise. Wall heat transfer from the hot vessel walls also contributes to the heating of the

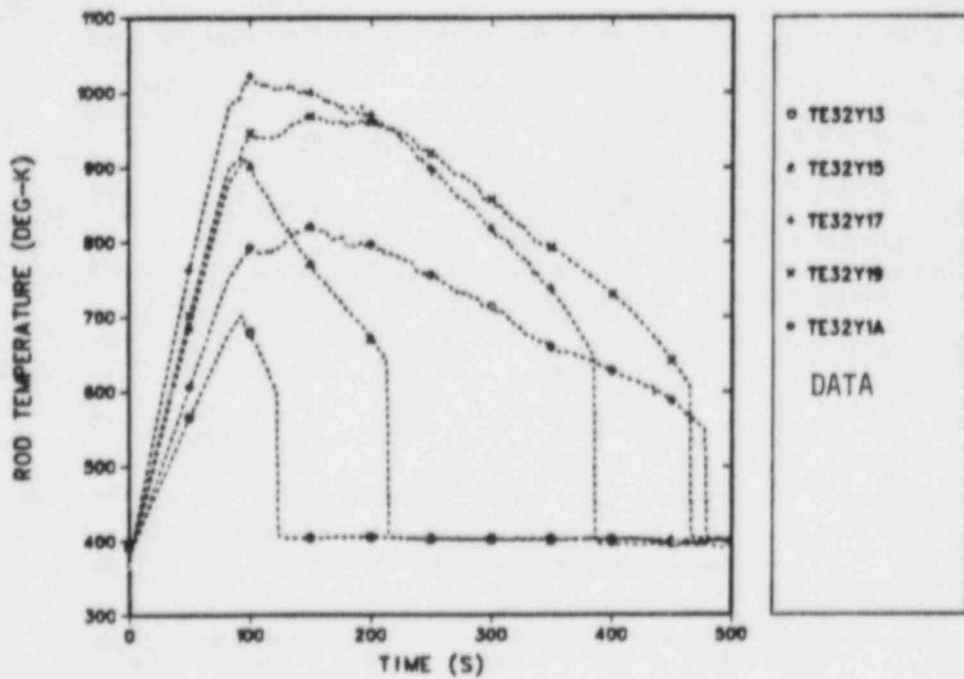
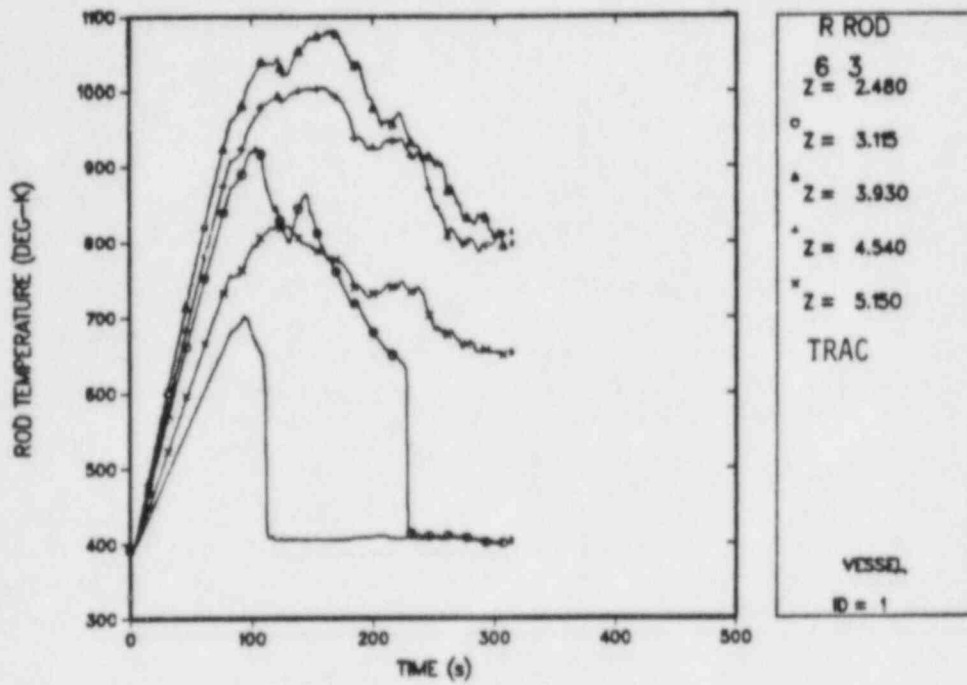


Fig. 2.  
 TRAC comparison to rod temperature data in the high-power region of the core for Run 72.



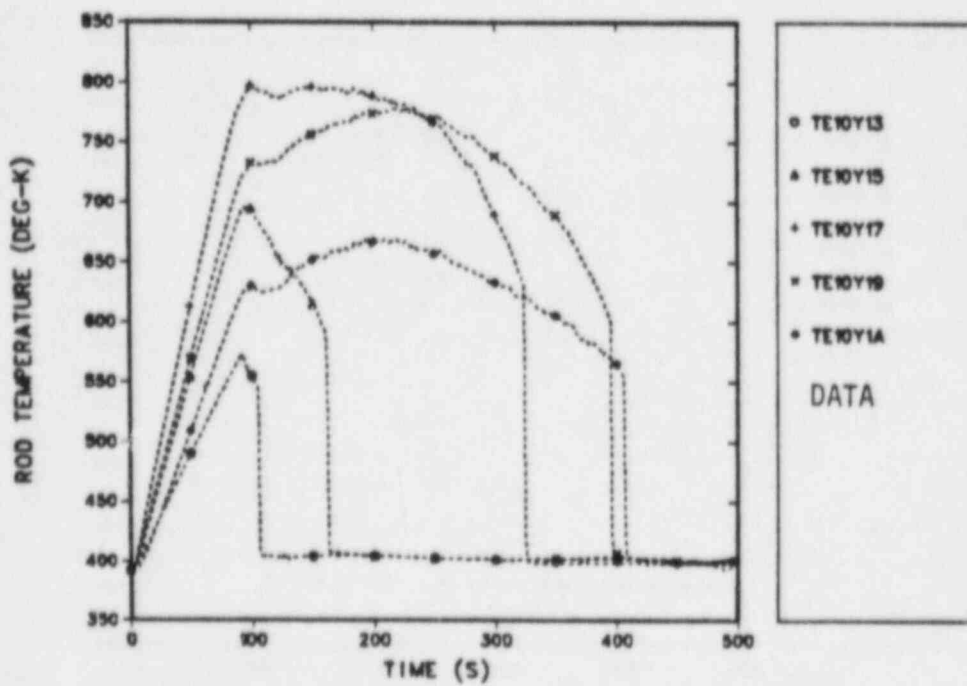
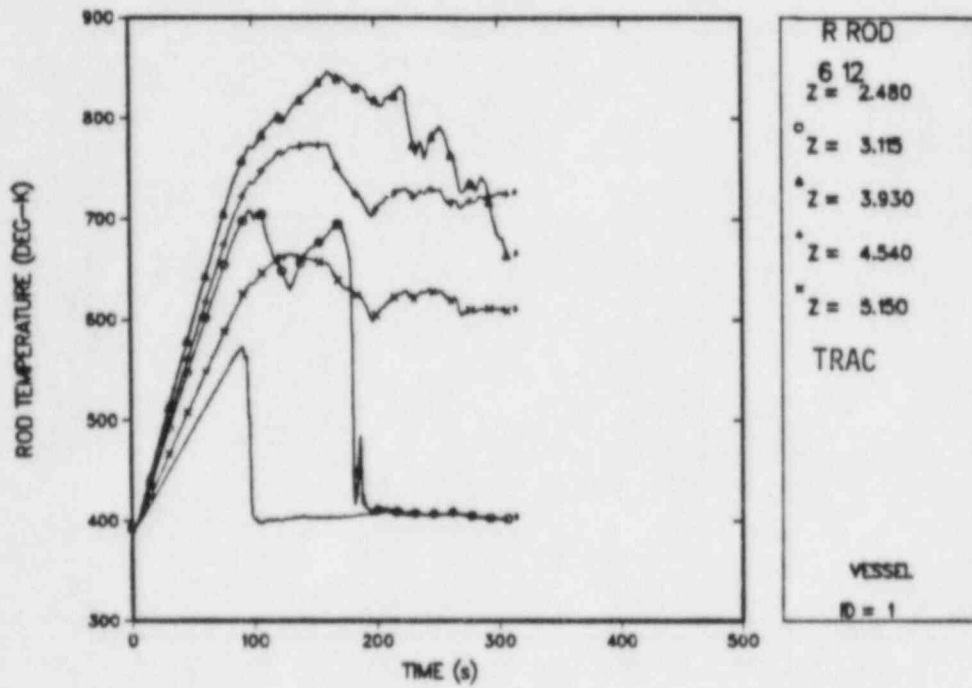


Fig. 3.  
 TRAC comparison to rod temperature data in the low-power region of the core for Run 72.

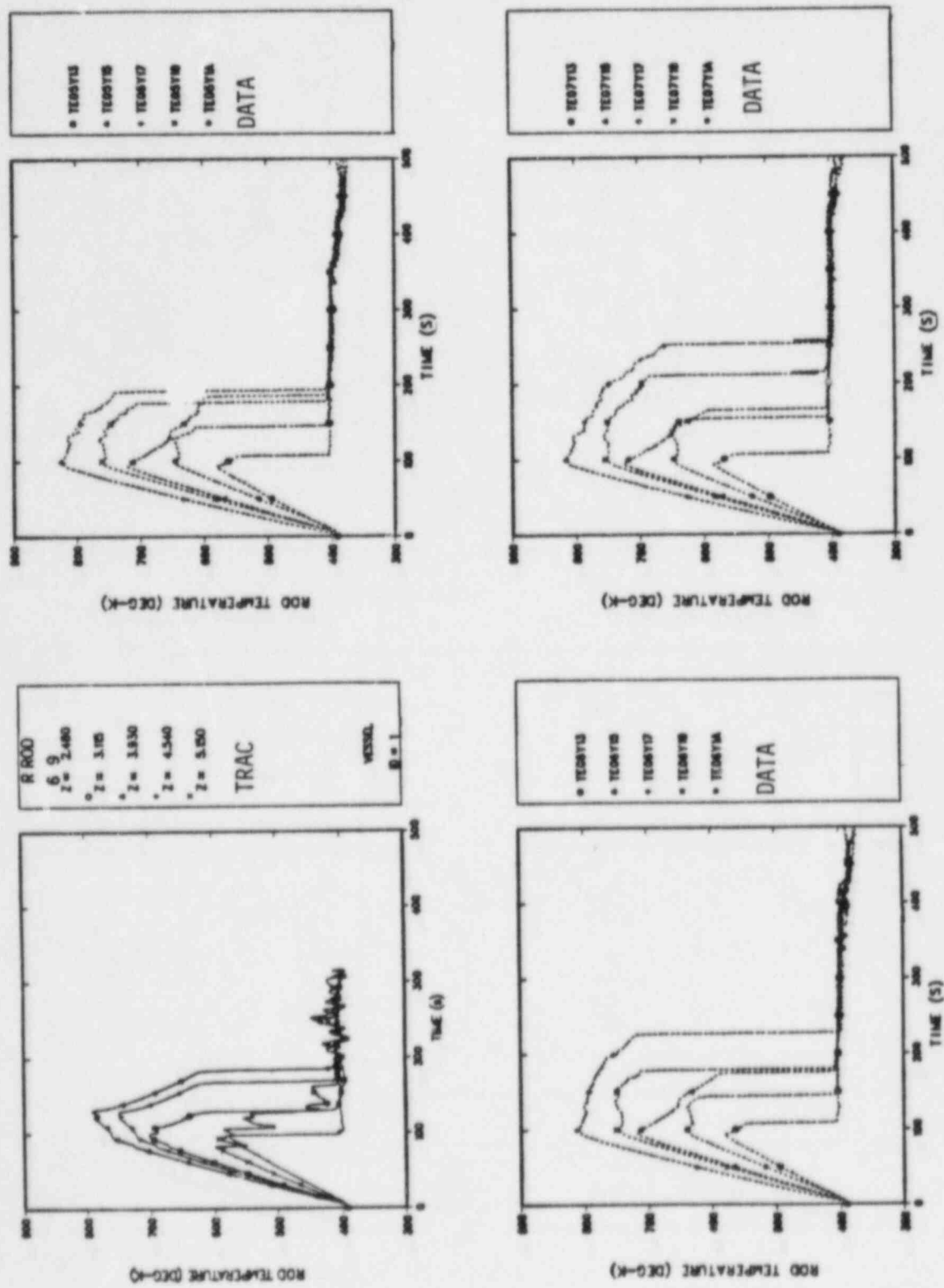


Fig. 4. TRAC comparison to rod temperatures in the low-power region of the core where dumping occurs for Run 72.

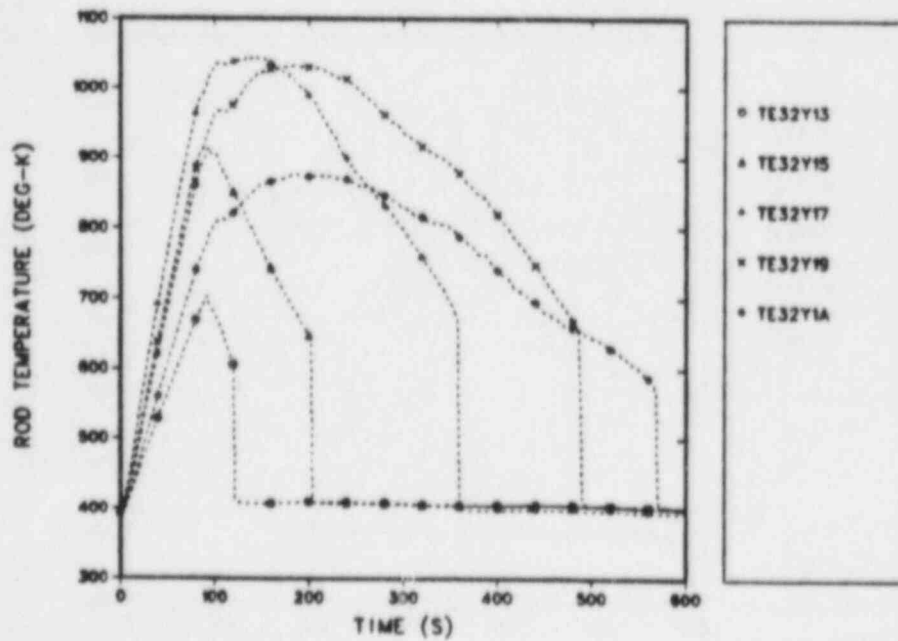
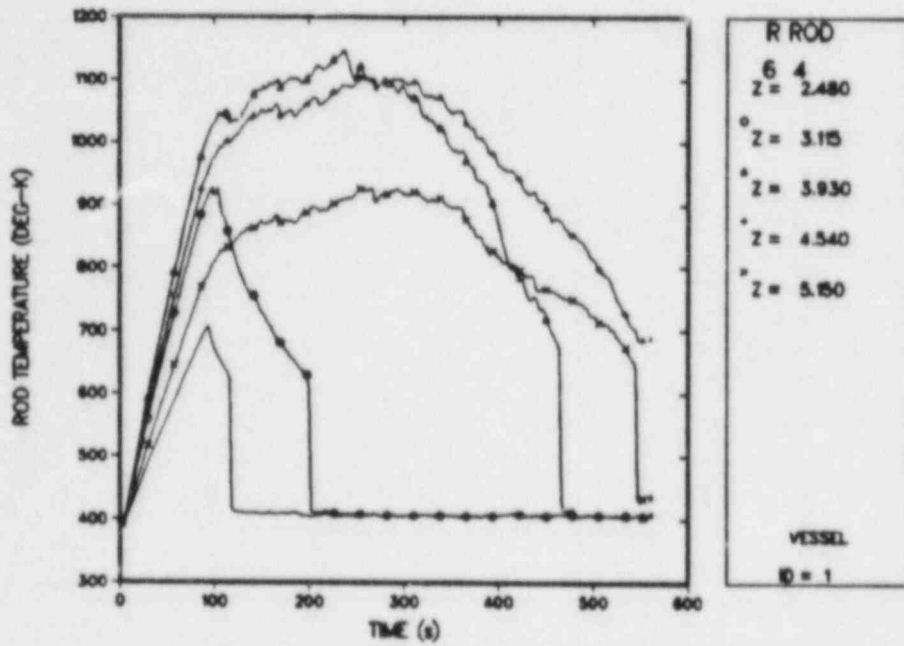


Fig. 5.  
 TRAC comparison to rod temperature data in the high-power region of the core for Run 76.

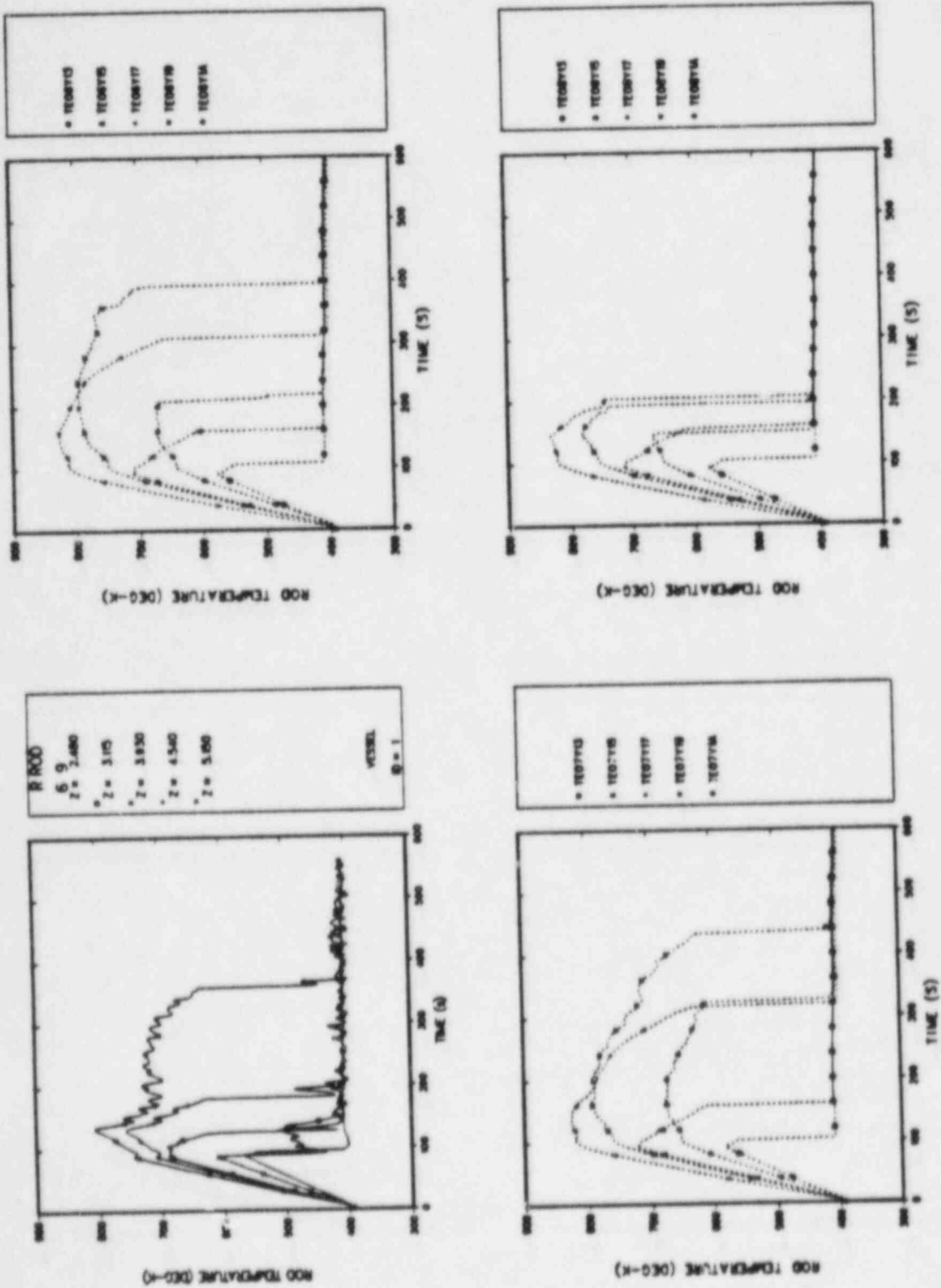


Fig. 6. TRAC comparison to rod temperature data in the low-power region of the core for Run 76.

fluid. TRAC, in all the UPI calculations, tends to overpredict this heating and subsequent boiling of fluid in the downcomer.

Channeling of the UPI flow into the core was observed in both the experiment and the data. As shown in Fig. 6, core assembly 8 experiences a very early quench. This assembly is located very near the injection point. Nearby assemblies 6 and 7 do not exhibit such a strong effect and quench somewhat later. The TRAC calculation for this region shows a somewhat average behavior of the data.

For Run 78, both the power and the core initial stored energy were reduced. In addition, the radial power distribution was flat in Run 78 as opposed to the steep radial power profile in Run 76. However, the UPI rate was the same. Figures 7 and 8 illustrate that TRAC did a good job of predicting the overall PCT and the channeling in the outer bundles, although TRAC-calculated quench occurs too early. This is believed to be caused by TRAC's allowing too much UPI water to fall back into the core. This is consistent with comparison of TRAC to small-scale CCFL data.<sup>9</sup> At low steam-flow rates, TRAC tends to let too much water fall down as compared with the data.

#### Westinghouse 3315 MW<sub>t</sub> Plant Analysis

The TRAC model uses 950 cells to model a Westinghouse 3315 MW<sub>t</sub> plant with 15 × 15 fuel-rod assemblies. All the loop components such as the hot leg, steam generator, loop seal, circulating pump, cold leg, and emergency core-cooling system (ECCS) were modeled as physically complete as possible. A schematic of the vessel component is shown in Fig. 9. The vessel has been subdivided into 17 axial levels, 4 radial rings, and 8 azimuthal sectors for a total of 544 hydrodynamic cells. The core region consists of the two inner radial rings and the five axial levels extending between levels 4 to 9. The barrel baffle region extends from levels 4 to 10 and occupies the third radial ring within these levels. The fourth radial ring represents the downcomer region from levels 3 to 15. At the top of level 15 in the fourth radial ring and in each azimuthal sector are open flow area passages that model the upper head spray nozzles. Flow paths between the upper head and upper plenum were represented at the top of level 15 and in the three inner rings by modeling the appropriate reduced flow area and flow losses to simulate the flow through the control-rod penetrations in the upper support plate.

This PWR analysis simulates a 200% guillotine break of a cold leg between the cold-leg nozzle and the ECC injection port immediately outside of the biological shield. ECC flows were based on the single failure assumptions. Accumulators contained the minimum volume allowed, and the core power was 2% over the design limit. The core-power peaking was based on beginning of life; however, the power-decay curve assumed an infinite operating period.

The maximum average rod temperature is shown in Fig. 10. At the beginning of the blowdown phase the core voids rapidly and the fuel rod cladding heats up quickly. The PCT occurs during this early portion of the blowdown. However, as can be seen from Fig. 11, the core fills to ~75% full within the first 10 s after the first dryout. This is because the core flow turns positive as the three intact loop flows exceed the two-phase choked flow out the broken loop. This positive flow into the core from the lower plenum terminates the early heating of the fuel rod cladding. As the blowdown transients continue, the core dries out again; however, steam flow rates through the core are high enough such that no significant heat up occurs until refill begins at about 25 s.

At the end of blowdown and at the beginning of refill steam flows through the core are insufficient to cool the core; therefore, heating occurs again from about 20 to 40 s. This second period of core heating is terminated by the

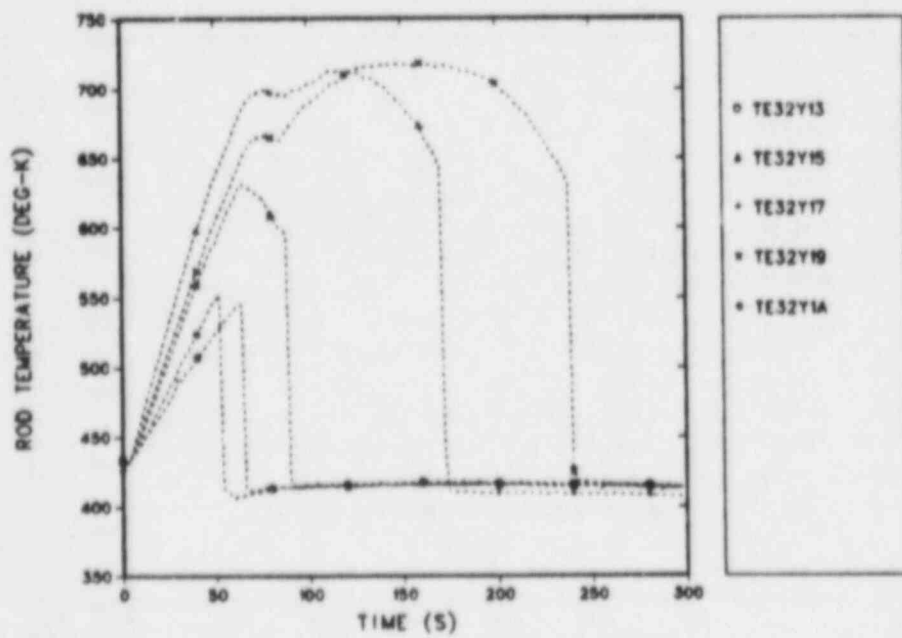
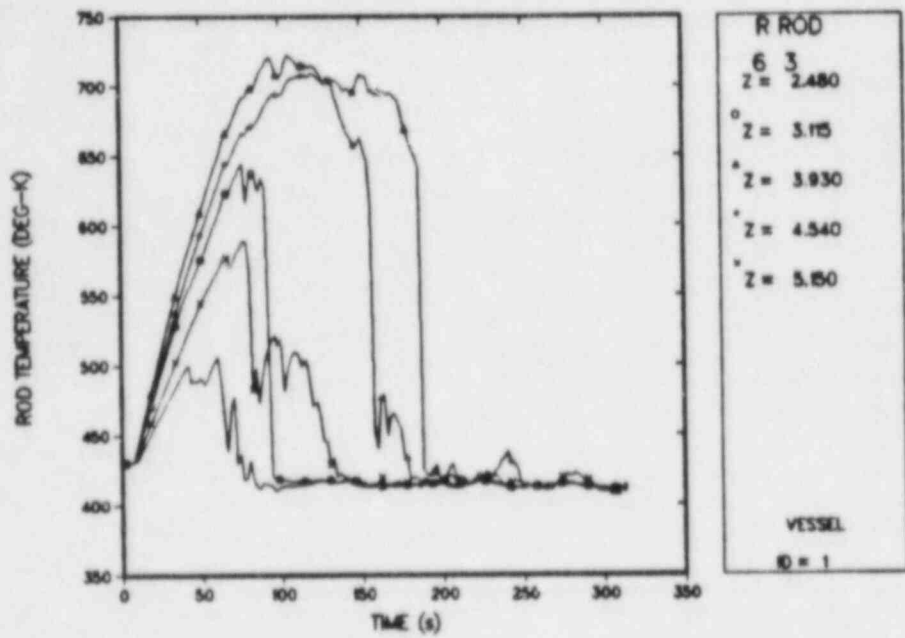


Fig. 7.  
TRAC comparison to rod temperature data in the high-power region of the core for Run 78.

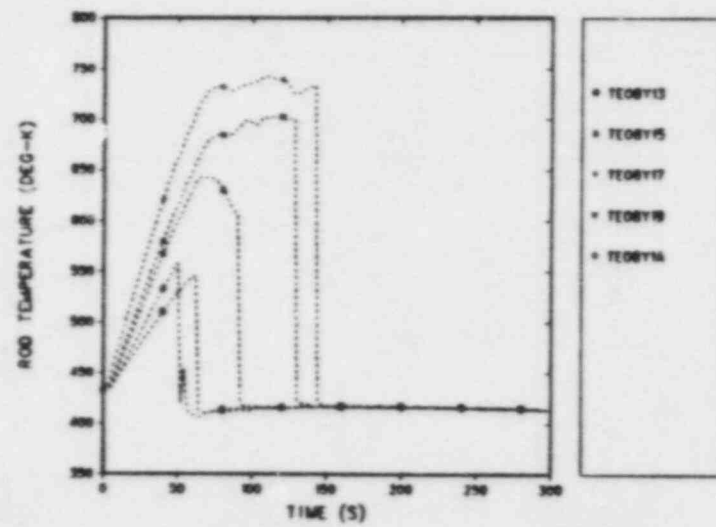
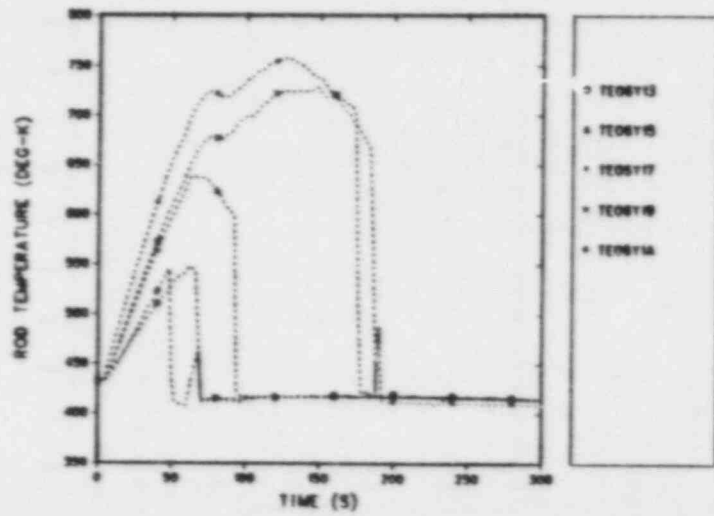
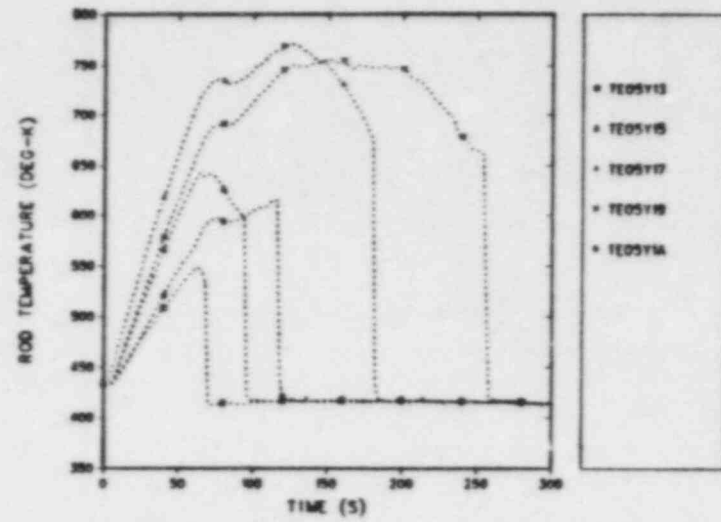
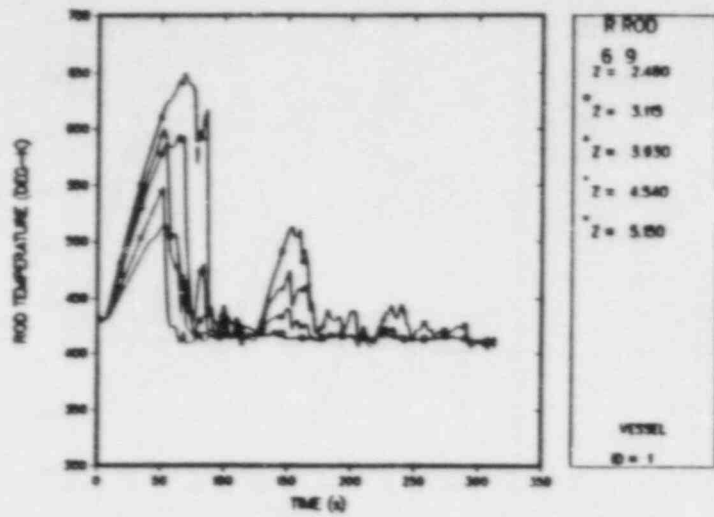


Fig. 8.  
 TRAC comparison in the low-power region of the core for Run 78.

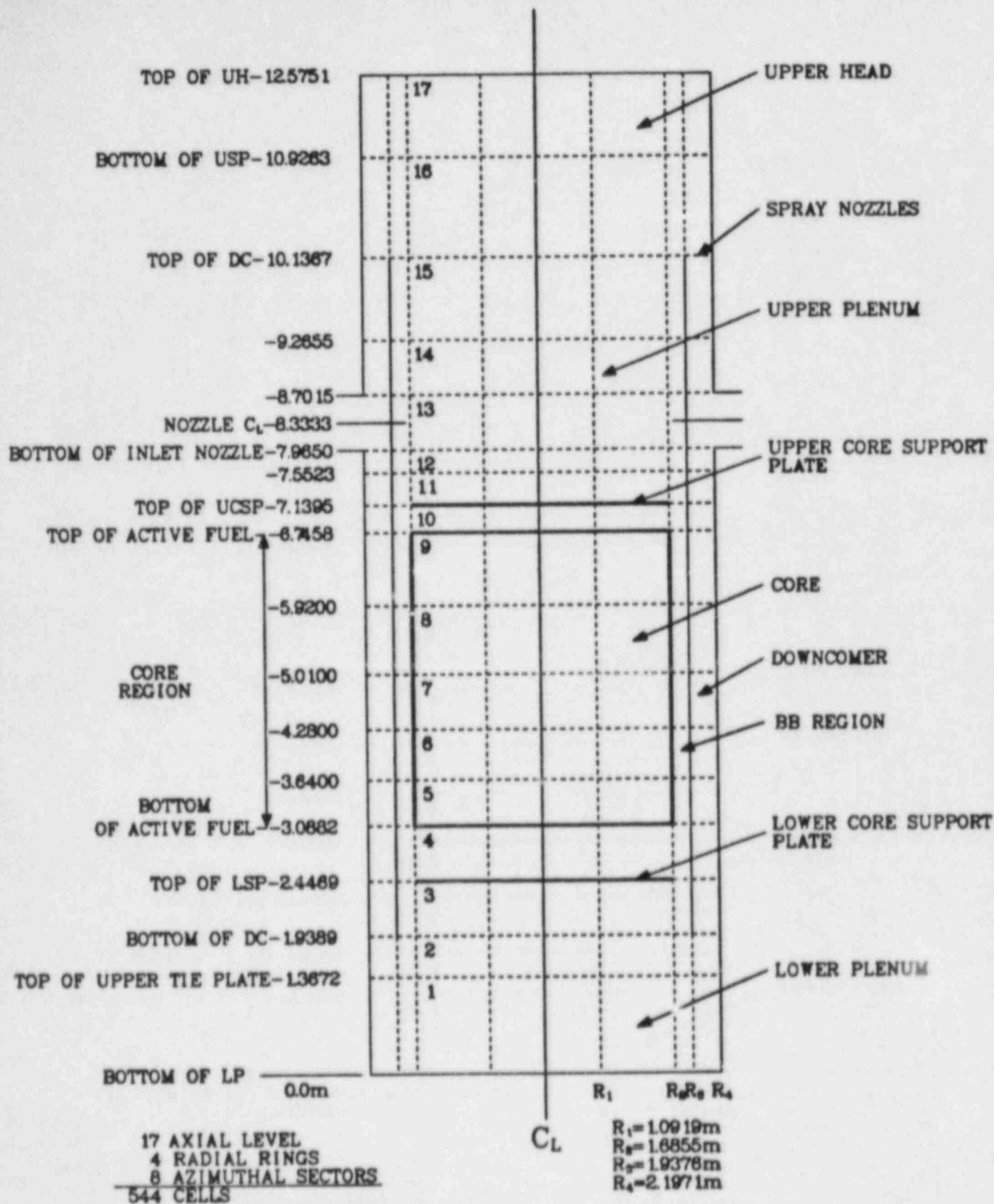


Fig. 9.  
Vessel component for Westinghouse PWR.



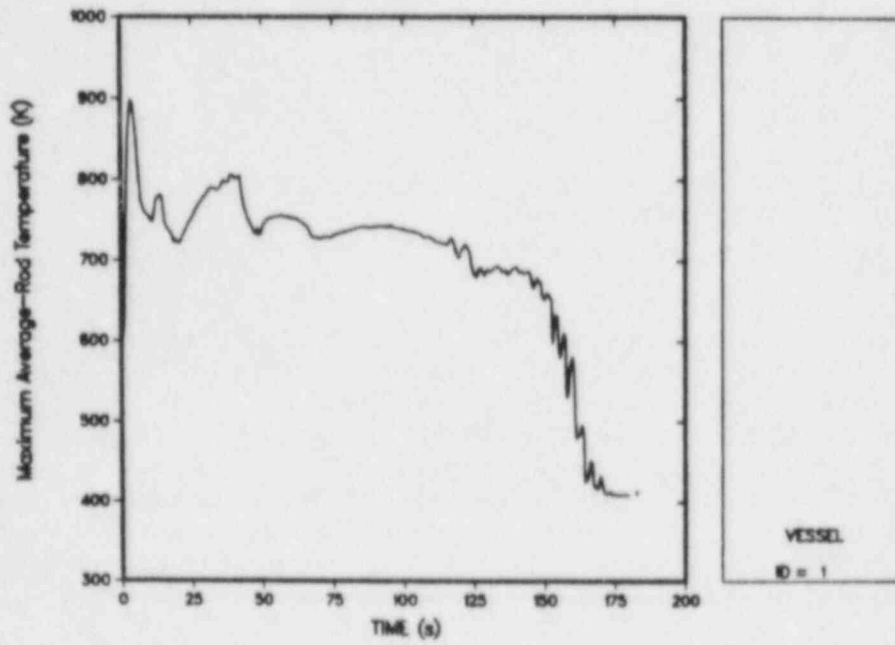


Fig. 10.  
Maximum average rod temperature.

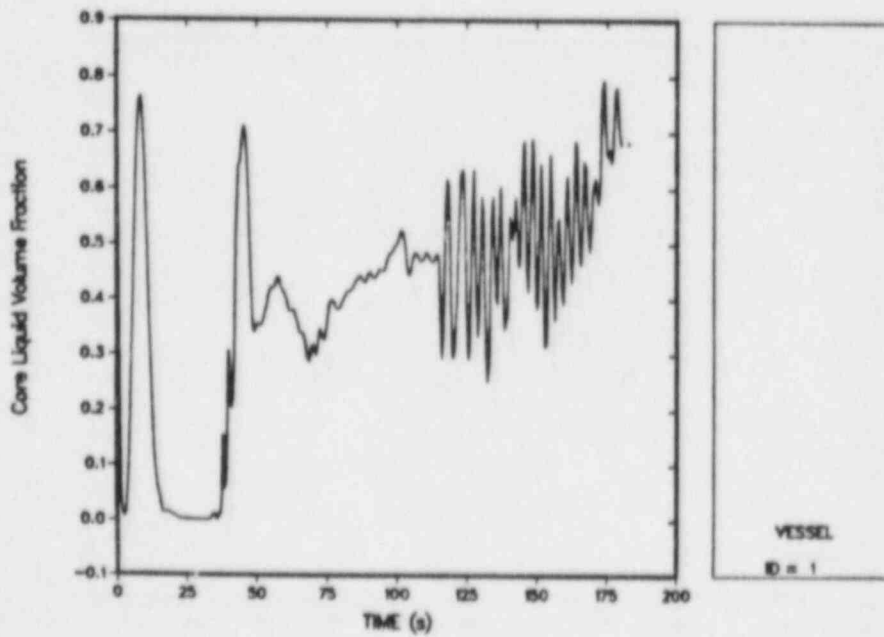


Fig. 11.  
Core liquid volume fraction.

BOCREC that occurs at ~39 s. A very rapid core cooldown occurs from ~45 to ~55 s as the intact accumulators empty and nitrogen gas from the accumulators enters the cold legs and top of the downcomer. This nitrogen gas has the effect of reducing the condensation rate in the intact cold legs and pressurizing the intact cold legs and downcomer. As can be seen from Fig. 11, this results in a core refill to ~70% liquid full just before 50 s.

From ~55 s to ~170 s, the core slowly cools and quenches with no other significant heating in the average rods. Late in the reflood transient, manometer-like oscillations between the downcomer and core occur (Figs. 11-12); however, the core continues to cool.

## CONCLUSIONS

Both the TRAC calculations and the CCTF UPI experimental data indicated channeling of ECC water from the upper plenum into the core. The experimental data indicated asymmetric behavior in the core and upper plenum, even when the power profile was flat or when UPI flows were symmetric; therefore, multidimensional analysis capability was required to simulate the test behavior accurately. TRAC correctly predicted when UPI flows enhance core cooling and when they contribute to steam binding and degraded core cooling. TRAC tended to overpredict the steam binding effect at high power and overpredict the water fallback rate at low power.

The Los Alamos analysis effort is functioning as a vital part of the 2D/3D Program. Results from this program have already addressed, and will continue to address, key licensing issues including scaling, multidimensional effects, downcomer bypass and refill, reflood steam binding, core blockage, alternate ECCS, and code assessment. The CCTF analyses have demonstrated that TRAC-PF1/MOD1 can correctly predict multidimensional, nonequilibrium behavior in large-scale facilities prototypical of actual PWRs. Through these and future TRAC analyses, the experimental findings can be related from facility to facility; more important, the results of this multinational research program can be related directly to licensing concerns affecting actual PWRs.

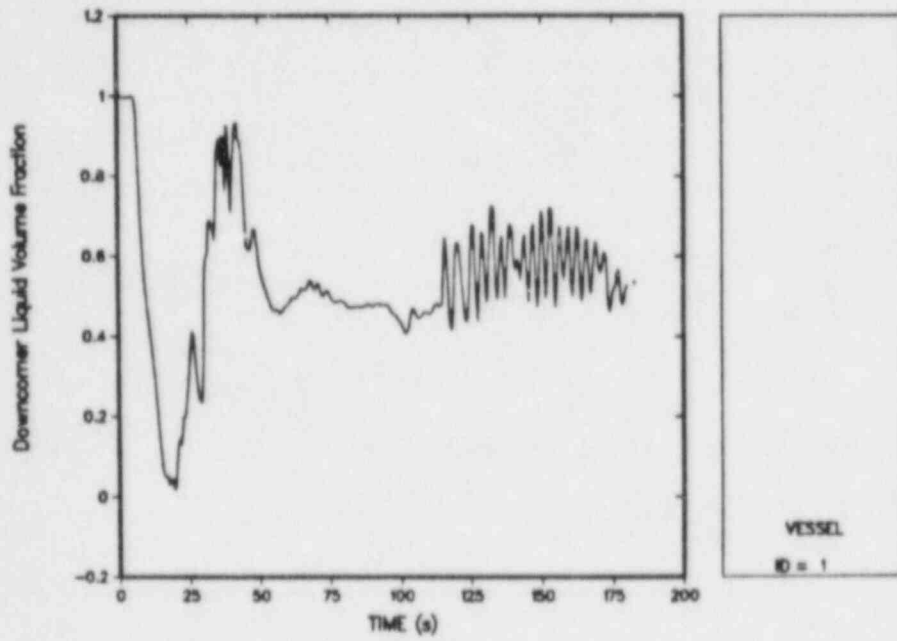


Fig. 12.  
Downcomer liquid volume fraction.

## REFERENCES

1. D. Dobranich and L. D. Buxton, "Large Break LOCA Analyses for Two-Loop PWRs with Upper Plenum Injection," Sandia National Laboratory report SAND84-0040, NUREG/CR-3639, May 1984.
2. T. D. Knight, "TRAC-PD2 Independent Assessment," Los Alamos National Laboratory report LA-10166-MS, NUREG/CR-3866, December 1984.
3. D. D. Jones, "Subcooled Counter-Current Flow Limiting Characteristics of the Upper Region of a BWR Fuel Bundle," General Electric Company report NEDG-NUREG-23549, July 1977.
4. S. G. Bankoff et al., "Countercurrent Flow of Air/Water and Steam/Water Through Horizontal Perforated Plate," *Int. J. Heat Mass Transfer*, Vol. 24, No. 8, pp. 1381-1395, 1981.
5. J. A. Findlay, "BWR<sub>0</sub> Refill-Reflood Program Task 4.4-CCFL/Refill System Effects Tests (30 Sector) Evaluation of Parallel Channel Phenomena," General Electric Company report GEAP-22044, NUREG/CR-2566, November 1982.
6. J. W. Spore et al., "TRAC-PF1/MOD1 Calculation of CCTF Core-II UPI Test Run 57," Los Alamos National Laboratory, Safety Code Development (Q-9) technical note LA-2D/3D-TN-85-11 (to be published).
7. Michael W. Cappiello, "CCTF Run 59 TRAC-PF1/MOD1 Analysis," Los Alamos National Laboratory, Safety Code Development (Q-9) technical note LA-2D/3D-TN-85-1, January 1985.
8. Michael W. Cappiello, "CCTF Run 72 TRAC-PF1/MOD1 Analysis," Los Alamos National Laboratory, Safety Code Development (Q-9) technical note LA-2D/3D-TN-85-12 (to be published).
9. Michael W. Cappiello, "Assessment of the Annular Mist Interface Shear in TRAC-PF1/MOD1 Against Downcomer Bypass and Tie-Plate Flooding Data," ASME, 84-WA/HT-84.

HEAT TRANSFER, CARRYOVER AND FALL BACK  
IN NUCLEAR STEAM GENERATORS DURING  
TRANSIENTS

Lih-Yih Liao  
Former Research Assistant, MIT

Alex Parlos  
Research Assistant, MIT

Peter Griffith  
Professor of Mechanical Engineering  
Massachusetts Institute of Technology  
Cambridge, MA 02139

ABSTRACT

The analysis of steam line breaks, feed line breaks and steam line breaks with tube rupture accidents all involve calculating the heat transfer, carryover and fall back on the secondary side of the steam generator during off-normal conditions. The work reported here has been done to fill this need. A computer program, SIT-SG (Simulator of Transient in Steam Generator), is developed. This is a one-dimensional best-estimate code with the assumption that the vapor and liquid phases are in thermal equilibrium but not homogeneous. The drift flux model is used to describe the relationship between the vapor and the liquid phase velocity. No momentum equation is required for SIT-SG because the detailed pressure distribution in the vessel is not important for the blowdown process.

Based on the comparisons between the code predictions and the data obtained from the experiments conducted at Battelle-Frankfurt and at GE, the best drift flux model constants for various flow regimes are selected. SIT-SG has been used to predict the carryover, fall back and heat transfer for the M.I.T. steam generator blowdown experiments. The results are encouraging.

It is found that the measured dryout front is much higher than the calculated mixture level. If the effective heat transfer area is determined from the mixture level, the primary-to-secondary heat transfer will be substantially underpredicted.

From the result of the liquid hold-up study we would expect to find two mixture levels, one in the bottom of the steam generator and one above the top tube support plate, provided that flooding occurs at all.

## I. INTRODUCTION

Due to the concern over PTS (pressurized thermal shock), the resulting reactivity insertion into the primary system, and the impact on containment design resulting from a steam line break or a feedwater line break, attention has been focused on the processes occurring during blowdown of the secondary side of a steam generator.

As a part of the effort mounted to resolve the pressurized thermal shock issue, this work is directed toward the study of the carryover, fall back and heat transfer on the secondary side of the steam generator which is subjected to either a steam line break or a feed line break. A computer program named SIT-SG (standing for Simulator of Transient in Steam Generator) has been established to model the steam generator during blowdown so that realistic estimates of the steam generator thermal hydraulic behavior can be made and appropriate strategies for handling the transient can be identified. In parallel with the model development, a series of blowdown experiments has been performed to generate data which can be used to verify the analytical model. Additional experiments have been run to establish the effect of tube support plates on the steam generator secondary side liquid distribution during blowdown.

To make a study of the processes in the secondary system easier to handle, the behavior of the secondary side of the affected steam generator is studied without confusing effects of heat transfer and fluid mechanics in both the primary system and the intact secondary system.

Our goal is to predict the heat transfer on the secondary side of the affected steam generator. As long as the tubes are wet on the secondary, the heat transfer is excellent. On the other hand, whenever the tubes are dry the heat transfer is negligible. Therefore, the fraction of wetted area is particularly important. The principal factors that affect the heat transfer include: the amount of carryover and fall back, the mixture level propagation, the temperature on the steam generator secondary side and the period during which a high rate of cooling prevails.

Large heat transfer rates and long heat transfer times are two essential conditions for pressurized thermal shock to occur. Both of these conditions relate closely to the size of break. For a large steam line break, the heat transfer rate is large while the period during which high rate of cooling prevails is short. This is reversed for a small steam line break. Therefore, five break sizes are used to evaluate the effect of break size on the heat transfer.

## II. ANALYTICAL SYSTEM MODELS

### A. Hydrodynamic Model

The basic hydrodynamic model is based on a one-dimensional, two-equation formulation for the two-phase flow. It consists of one mixture mass equation and one mixture energy equation. The momentum

equation is not required because we believe that the detailed pressure distribution in a large vessel is not important during the blowdown process.

The transient two phase flow is assumed to be in thermal equilibrium but not homogeneous. The difference between liquid phase velocity and vapor phase velocity is taken into account by the drift flux model. This model is the simplest one that can adequately describe the important two-phase flow phenomena. In particular, it allows us to track the water level in a physically realistic way.

### 1. Conservation Equations

#### Mixture Mass Equation

$$\frac{\partial(\alpha\rho_v + (1-\alpha)\rho_l)}{\partial t} + \nabla \cdot (\alpha\rho_v \bar{v}_v + (1-\alpha)\rho_l \bar{v}_l) = 0 \quad (1)$$

#### Mixture Energy Equation

$$\begin{aligned} & \frac{\partial(\alpha\rho_v e_v + (1-\alpha)\rho_l e_l)}{\partial t} + \nabla \cdot (\alpha\rho_v e_v \bar{v}_v + (1-\alpha)\rho_l e_l \bar{v}_l) \\ & = -p\nabla \cdot (\alpha\bar{v}_v + (1-\alpha)\bar{v}_l) + \dot{Q}_{wv} + \dot{Q}_{wl} \end{aligned} \quad (2)$$

### 2. Flow Regime and Flow Regime Transition Criteria

The two-phase flow regimes (1) used in the calculations are: (1) the bubbly flow regime, (2) the churn-turbulent flow regime (3) the annular flow regime and (4) the liquid dispersed flow regime. During blowdown the flow is expected to be highly turbulent so that large diameter bubbles do not have a chance to develop before they are destroyed. Therefore, the slug flow regime is not expected to occur in the steam generator blowdown. It is assumed that the flow changes from bubbly flow to churn-turbulent flow directly.

Because the void fraction itself is a good indication of flow regime, the combination of theoretical analysis equation and the void fraction value is used to predict the transition of flow regimes. The criteria for the flow regime determination, based on the flow regime transition, are summarized in Table 1.

### 3. Drift Flux Model

For a two phase flow the velocity of individual phase can be related by the drift flux model proposed by Zuber (2).

$$\langle j_v \rangle = \langle \alpha \rangle (C_0 \langle j \rangle + v_{gj}) \quad (3)$$

where  $\langle \rangle$  indicates an average over the flow cross-section.

Flow regime dependent drift flow model constants are studied and a comparison of all the weighted mean drift velocities is shown in Fig. 1. The legends used in Fig. 1 are given in Table 2. Fig. 1 is obtained by assuming the pressure is 1000 psia, the diameter is 0.34 ft, and  $C_0$  is 1.0 in the Wilson correlation. Large variations have been found for the various drift flux model constants.

As far as the mixture level is concerned, the drift flux constants in the churn-turbulent flow regime are most important. The following drift flux constants in the churn-turbulent flow regime are recommended. The flow and void fraction distribution parameter  $C_0$  is selected from Ishii's correlation and its value as function of pressure and void fraction is shown in Fig. 2. The weighted mean drift velocity being selected is originated from the equation proposed by Zuber with the coefficient given by Bertodano (3).

$$\bar{v}_{gj} = 0.33(\sigma g(\Delta\rho)/\rho_g^2)^{0.25} \quad (4)$$

This correlation is used in conjunction with the upper limitations provided by the slug flow regime correlation

$$\bar{v}_{gj} = 0.35 (gD(\Delta\rho)/\rho_f)^{0.5} \quad (5)$$

and a constant value of 3 ft/sec (4), which is the maximum drift velocity having been observed. The weighted mean drift velocity so obtained is plotted, in terms of pressure and vessel diameter, in Fig. 3. The recommended drift flux constants for the other flow regimes include. (i)  $V_{gj}$  and  $C_0$  from Wallis correlation (5) for bubbly flow regime (ii)  $V_{gj}$  and  $C_0$  from Ishii correlation (6) for annular flow regime. The correlations used for the various flow regimes are connected with a smoothing scheme.

#### 4. Break Flow Model

The break flow model contains both a critical flow model and a subcritical flow model. According to Fauske (7), if the break flow path has L/D ratio greater than 12, the pressure at the throat is about 0.55 times of the vessel pressure. Therefore, a vessel pressure of 26.73 psia, which equals 14.7 psia divided by 0.55, is chosen as the criterion for the transition between the critical flow model and the subcritical flow model.

Many two-phase critical flow models have been proposed over the years. For steam generator blowdown, the flow quality at the entrance is high, suggesting that the slip equilibrium model is adequate for the steam generator blowdown. Among the familiar slip equilibrium models, the Henry-Fauske model (8) has been selected in our code because it is simple and takes into account the L/D effect explicitly. It has been proven to be a good choice. The subcritical flow happens when blowdown is ending and the break quality should be very high by then. Therefore, the flow through the break is assumed to be pure vapor. With the standard pressure loss equation the mass flux through the break can be obtained.



## B. Heat Transfer Model

As far as the stored heat is concerned, two models are used for the calculation of hot metal temperature. If the conductivity of the metal is low, a finite difference heat conduction model is adopted to calculate the temperature distribution in the metal. If the conductivity of the metal is very large, the temperature distribution is no longer important and a lumped parameter method is chosen to calculate the metal temperature.

As far as the heat transfer coefficient is concerned, whether the tubes are wet or dry is very important. If the tubes are wet, the heat transfer is excellent. On the contrary, whenever the tubes are dry, the heat transfer is negligible. The accuracy of the secondary side heat transfer coefficient for the wet surface is not important because the wall conduction, the primary heat transfer coefficient and the fouling factor are the real limits. In our model, a constant value of 8000 Btu/hr ft<sup>2</sup> °f, which is the value of the secondary side heat transfer coefficient in the steady state, is assumed to be the value during the transient.

## C. Water Level Model

In the literature there are two kinds of water levels, namely, the collapsed water level and the mixture water level. The collapsed water level represents the total amount of water inventory while the mixture water level represents the actual liquid distribution. As far as the heat transfer is concerned, the mixture water level is the one which is important and requires careful modeling. In the following context, the mixture water level will be abbreviated as the water level. A water level propagation model is used to decide where the water level is and in which node the water level currently resides. If the water level disappears, a water level reappearance criterion is applied to determine when the water level will reappear. Once the water level reappears, the motion of the water level is once again traced by the water level propagation model.

### 1. Water Level Propagation Model

Two kinds of water level propagation methods are used in the water level propagation model. The first method (9) is derived from the continuity of matter. If one is attached to the water level front and assuming the mass transformation between the liquid phase and the vapor phase at the interface can be neglected, then from the continuity of the vapor phase and the liquid phase it can be shown that the water level propagation velocity is

$$v_w = \frac{(\alpha^+ C_o^+ - \alpha^- C_o^-)j + (\alpha^+ v_{gj}^+ - \alpha^- v_{gj}^-)}{\alpha^+ - \alpha^-} \quad (6)$$

This model is very good for describing the phenomena involving a continuous water level change such as pool swelling under intermediate transient. Therefore it is used to simulate the pool swelling before the water level has disappeared.

The second method is a kind of interpretation. As we know, the void fraction below the mixture level front is quite different from the void fraction above the mixture level front. If we average the void fraction below and above the mixture level front in control volume  $i$  and call them  $\alpha_{bot}$ ,  $\alpha_{top}$  respectively, the balance of the void fraction in control volume  $i$  requires

$$(ELEV)_i \alpha_i = (MIXL)_i \alpha_{bot} + (ELEV - MIXL)_i \alpha_{top} \quad (7)$$

where  $MIXL_i$  = mixture level in control volume  $i$   
 $ELEV_i$  = elevation of control volume  $i$

If the void fraction  $\alpha_{bot}$ ,  $\alpha_{top}$  are assumed to be equal to the void fraction  $\alpha_{i-1}$ ,  $\alpha_{i+1}$  respectively, the mixture level is obtained

$$(MIXL)_i = \left( \frac{\alpha_i - \alpha_{i+1}}{\alpha_{i-1} - \alpha_{i+1}} \right) (ELEV)_i \quad (8)$$

Therefore, given a control volume which contains the mixture level front, the value of mixture level can be calculated from the void fraction distribution. If the mixture level is smaller than 1% of the elevation height of the control volume, the mixture level front is assumed to cross the lower boundary and appears in the lower control volume.

## 2. Water Level Reappearance Criterion

The water level will reappear after it disappears. With some physical insight, a simple approximate criterion for the water level reappearance from the top can be established.

When the water reappears from the top, the void fraction in the top control volume probably will be quite high. Most likely, the flow regime in the top control volume will be annular flow regime. Now, if the liquid film is running down the wall, a water level will reappear from the top. Therefore, the water level reappearance criterion for the top node is:

$$\alpha_{top\ node} > 0.8 \text{ and } j_g < 0.0 \quad (9)$$

## E. Pool Entrainment Model

Entrainment of liquid drops from a continuous liquid phase interface often occurs in various conditions involving heat and mass transfer. The mechanism of entrainment is different for each condition. For an annular dispersed flow in a pipe, the liquid drops are entrained from liquid film to the central region by the gas flow.

In contrast to the above mentioned phenomena, the continuous liquid phase may be located below the vapor phase. This can occur when liquid drops are entrained by vapor bubbling through a liquid pool. This is

called pool entrainment.

In our simple model, there is no distinction between dispersed liquid phase and continuous liquid phase in the annular dispersed flow regime. Therefore, only the pool entrainment phenomena are modeled. Ishii's model (10) is adopted to calculate the pool entrainment phenomena.

### III. METHODS OF SOLUTION

With the boundary conditions provided by the break flow model and under the assumption that thermal equilibrium exists between vapor phase and liquid phase, the flow distribution inside the secondary side of the steam generator can be established without a momentum equation. This is done by a two-step scheme. First, the whole pressure vessel is considered as a single component. The pressure of this component is solved with boundary conditions provided from the calculation of the break flow model. This single component system is referred to as the global vessel system. After the pressure is obtained, the local void fraction and flow distribution can be determined using the drift flux model under the assumption of thermal equilibrium. This is referred to as the local control volume system. For a local control volume system the flow path is divided into many control volumes, and each control volume is stacked on top of another control volume.

A finite difference scheme is used to solve the integrated conservation equations.

#### 1. Hydrodynamic Modeling

##### a. Global Vessel System

The conservation equations for the global vessel system can be obtained by summing up the conservation equations for individual control volumes,

$$\frac{M_G^{n+1} - M_G^n}{\Delta t} = ((j_v \rho_v + j_l \rho_l)^{n+\frac{1}{2}} A)_{in} - ((j_v \rho_v + j_l \rho_l)^{n+\frac{1}{2}} A)_{out} \quad (10)$$

$$\begin{aligned} \frac{H_G^{n+1} - H_G^n}{\Delta t} = & \frac{(P^{n+1} - P^n) V_G}{\Delta t} + ((j_v \rho_v h_v + j_l \rho_l h_l)^{n+\frac{1}{2}} A)_{in} \\ & - ((j_v \rho_v h_v + j_l \rho_l h_l)^{n+\frac{1}{2}} A)_{out} + \dot{Q}_G^n \end{aligned} \quad (11)$$

To close these equations, a state equation is required:

$$P^{n+1} = f(\rho_G^{n+1}, h_G^{n+1}) = f\left(\frac{M_G^{n+1}}{V_G}, \frac{H_G^{n+1}}{V_G}\right) \quad (12)$$

For a given  $\Delta t$  and boundary conditions, the three unknowns  $M_G^{n+1}$ ,  $H_G^{n+1}$ ,  $p^{n+1}$  can be solved from Eqs. (10) through (12). The boundary conditions are provided by the mass and energy flow rate of the feed water flow and the break flow. In this model, the feed water flow condition is assumed to be given. If there is no feed water flow, such as the case in our experiments, this value becomes zero. The break flow is determined by the break flow model.

As mentioned above, the sets of equations can be solved by a given  $\Delta t$  and calculating  $p^{n+1}$ ,  $M_G^{n+1}$ ,  $H_G^{n+1}$ . In this code, however, the equations are solved by giving the new pressure,  $p^{n+1}$ , and calculating  $\Delta t$ ,  $M_G^{n+1}$ ,  $H_G^{n+1}$ . There are two advantages in doing it this way: (i) If  $\Delta t$  is given, we need to solve  $p^{n+1} = f(e_G^{n+1}, h_G^{n+1})$  which requires initial guess and iteration of pressure. If the new pressure,  $p^{n+1}$ , is given we now solve  $e_G^{n+1} = f(p^{n+1}, h_G^{n+1})$  which usually does not require iteration. (ii) The time step is automatically adjusted. For a given constant "pressure step", the corresponding time step size is not constant. If the transient is more severe, the depressurization rate is larger and the corresponding time step size becomes smaller.

Under saturation conditions with a zero feed water flow,  $t$  can be obtained.

$$\Delta t = \frac{-\rho_{fg}^{n+1} (H_G^n + (P^{n+1} - P^n) V_G - \rho_f^{n+1} h_f^{n+1} V_G) + (\rho_f h_f - \rho_g h_g)^{n+1} (M_G^n - \rho_f^{n+1} V_G)}{-\rho_{fg}^{n+1} ((GhA)_{out}^n - \dot{Q}_G^n) + (\rho_f h_f - \rho_g h_g)^{n+1} (GA)_{out}^n} \quad (13)$$

where  $(h^n)_{out}$  is the flow averaged enthalpy at the break junction defined as

$$h_{out}^n = \left( \frac{j_v \rho_v h_v + j_l \rho_l h_l}{j_v \rho_v + j_l \rho_l} \right)_{out}^n \quad (14)$$

#### b. Local Control Volume System

Assuming saturation condition prevails, the conservation equations for the local control volume system can be expressed in the following form.

$$(\rho_f(1-\alpha) + (\rho_g \alpha))_i^{n+1} V_i - M_i^n = ((j_v^{n+1} \rho_g^n + j_l^{n+1} \rho_f^n) A)_{j-1} \Delta t - ((j_v^{n+1} \rho_g^n + j_l^{n+1} \rho_f^n) A)_j \Delta t \quad (15)$$

$$\begin{aligned}
 & (\rho_f h_f (1-\alpha) + \rho_g h_g \alpha)_i^{n+1} V_i - H_i^n = \\
 & (p^{n+1} - p^n) V_i + ((j_v^{n+1} \rho_g h_g^n + j_l^{n+1} \rho_f h_f^n) A)_{j-1} \Delta t \\
 & - ((j_v^{n+1} \rho_g h_g^n + j_l^{n+1} \rho_f h_f^n) A)_j \Delta t + \dot{Q}_i^n \Delta t
 \end{aligned} \tag{16}$$

Here, we use the old state thermal dynamic properties to represent the intermediate state thermal dynamic properties.  
To close the equations, we need the drift flux model

$$(j_v)_j^{n+1/2} = \alpha (C_o j + v_{gj})_j^{n+1/2} \tag{17}$$

It is of great interest to find out that the solution of Eqs. (15), (16) and (17) can be expressed in an explicit form.

$$j_j^{n+1/2} = \text{ABOVE/BELOW} \tag{18}$$

where

$$\begin{aligned}
 \text{ABOVE} = & -(\rho_f \rho_g h_{fg})^{n+1} V_i - M_i^n (\rho_f h_f - \rho_g h_g)^{n+1} + H_i^n \rho_{fg}^{n+1} \\
 & - (GA)_{j-1}^{n+1/2} \Delta t (\rho_f h_f - \rho_g h_g)^{n+1} + ((GhA)_{j-1}^{n+1/2} \Delta t + \dot{Q}_i^n \Delta t \\
 & + (p^{n+1} - p^n) V_i) \rho_{fg}^{n+1} - (\text{COEF}) A_j \Delta t \alpha_i^n v_{gj}^n
 \end{aligned} \tag{19}$$

$$\text{BELOW} = (-\rho_f^n (\rho_f h_f - \rho_g h_g)^{n+1} + (\rho_f h_f)^n \rho_{fg}^{n+1} + (\text{COEF}) \alpha_i^n C_o^n) A_j \Delta t \tag{20}$$

and

$$\text{COEF} \equiv (\rho_{fg}^n (\rho_f h_f - \rho_g h_g)^{n+1} - \rho_{fg}^{n+1} (\rho_f h_f - \rho_g h_g)^n) \tag{21}$$

If the control volume  $i$  happens to be the control volume where water level resides, the volume flow rate of liquid at the junction located between control volume  $i$  and  $i+1$  is neglected. In other words, we can substitute  $\alpha_i^{n+1} = 1.0$ ,  $C_{o,j}^n = 1.0$ ,  $(v_{gj})_j^n = 0.0$  into Eqs. (18), (19) and (20).

### B. Time Step Control

To obtain a reasonably accurate result and to avoid possible numerical difficulties, a small time step is required for a fast transient. This requirement can be relaxed as the transient becomes slower and the rate of change of system parameters also becomes slower. In order to save computational time, the largest possible time step size is always desirable. Unfortunately, the transients usually do not proceed with the same speed and a code user can not foresee the appropriate time step sizes

for a given transient.

As has already been described, the 'pressure step' concept can automatically handle this difficulty. In SIT-SG, the time step size is mainly determined by the given pressure step size. The time step size so obtained is then subject to an upper limitation specified by the computer code user. The user specified maximum time step size should not be greater than (1) the maximum time step size required by the stability of the heat conduction equation, and (2) the Courant condition which requires that the time step size be smaller than the node size divided by the flow velocity.

#### C. Determination of Void Fraction Distribution in a Control Volume

For a given control volume and a given volume averaged void fraction, the void can distribute in various ways in the control volume. How the void fraction ends up in its current configuration depends on the history of the development process as well as the value of the void fraction and the flow rate. In an attempt to differentiate these various possibilities, the following selection logic is established:

1. From the previous state information, the control volume where the water level resides is identified.
2. If the water level resides in the given control volume, the flow regime below the mixture level is determined from the average void fraction below the mixture level and the vapor velocity. The average void fraction below the mixture level is assumed to be the same as the average void fraction of the control volume right below the given control volume. A vapor velocity, given in Table 1, proposed by Ishii (13), which determines the transition from the churn-turbulent flow regime to the annular flow regime, is used to determine whether the annular flow regime exists.
3. If the mixture level does not reside in the given control volume, the average void fraction of this control volume and the vapor velocity are used to determine the void fraction distribution.

#### IV. VERIFICATION OF MODEL

SIT-SG has been used to calculate the pressure and the mixture level for the Battelle-Frankfurt blowdown experiment (11, 12), the G.E. small vessel (13, 14), and the G.E. large vessel blowdown test (13). From a comparison of the calculated results and the experiments, the best drift flux model coefficients are selected. With these coefficients, SIT-SG has been used to calculate our steam generator blowdown tests.

##### 1. Test Facility

The experimental facility, which represents the secondary side of the steam generator, is shown in Fig. 4. The vessel of the simulator is made from stainless steel pipe, 3.826 inches in inside diameter, and 9.0 ft in

height. An external downcomer, 1.5 inches in inside diameter and 6 feet in height, is connected to the steam generator vessel so that downcomer effects can also be studied. Three heaters are used to bring the system pressure and temperature to the normal U-tube steam generator operating conditions, namely, 1055 psi and 550 °F respectively. The blowdown section consists of a 10 feet long, 1 inch stainless steel pipe, positioned parallel to the vessel and ended into the suppression pool (as shown in Fig. 4). The blowdown section is divided by two flanges, between which the simulated breaks are placed. These breaks are built from various sizes of tubing. The lengths of tubing are chosen so that the L/D is constant at 20. To cover the range of break sizes of interest, five break diameters are selected: 1/2, 3/8, 1/4, 1/8 and 1/16 of an inch. The 3/8 inch diameter is selected in order to make the break flow area to vessel flow area ratio in the experiment the same as that of the typical U-tube steam generator. In this way, a realistic range of superficial velocities can be achieved in the experiment. The other four sizes are used to show the effect of the break sizes to the transient.

The suppression pool consists of a 30 gallon tank, which is counterbalanced by another 30 gallon tank through an "I" beam. The blowdown pipe discharges the liquid and vapor into one of the tanks. At the opposite end of this suppression tank the "I" beam is fastened to the floor through two sections of chain jointed by a rod which has a strain gage mounted on it. The strain gage is used to measure the mass added to the suppression tank. With this information the total amount of expelled fluid (which is also called carryover in the following context) at any instant can be obtained. For the large breaks, the first few seconds, discharge measurement is flawed by the sloshing in the pool.

## 2. Empty Vessel Test

Empty vessel tests were performed first before the installation of the rod bundle. The predicted and the measured pressure and carryover are shown in Figs. 5a and 5b. Good agreement has been obtained. Fig. 6 shows the predicted break flow rate with and without the pool entrainment model. As we learn from the Ishii pool entrainment model, it is only the period when the mixture water level is close to but not high enough to reach the break that pool entrainment has a sensible effect on the break flow rate. The fact that this period is short implies that the pool entrainment model has insignificant effect on the total carryover. The time integration of heat transfer from the wall for five break sizes is calculated and shown in Fig. 7. The results show that the largest heat transfer does not necessarily occur with the largest break size. This result was anticipated and the calculation demonstrates that it does, in fact, occur.

## 3. Test with Rod Bundles

The comparison between the predicted mixture level and the measured dryout front is shown in Fig 8. Large discrepancies exist between the predicted mixture level and the measured dryout front. The high dryout front indicates that a large wet area is sustained between the mixture level and the dryout front. It is found that dryout occurs when when

blowdown is almost over. By then the mixture water level is already very small. Therefore, the amount of heat transfer will be greatly underestimated if the mixture level is used to calculate the effective heat transfer area.

## V. LIQUID HOLD-UP EXPERIMENT

When the flow goes through the tube support plate in a steam generator, a much higher velocity is obtained because the flow area is greatly reduced by the tube support plates. As a result, flooding occurs easily once countercurrent flow is established. When the flooding occurs, there is a maximum amount of liquid which is allowed to penetrate down through the tube support plate for a given upward vapor flow rate. This limitation on downward liquid flow rate may result in excess liquid accumulating above the tube support plate and deficient liquid below the tube support plate. The excess liquid accumulated above the tube support plate is the liquid hold-up. When there is more than one plate, it is important to find out whether the liquid hold-up phenomena will occur above each plate and result in the establishment of multi-liquid levels. If the multi-level hold-up occurs, the effective heat transfer area is going to increase a lot and the heat transfer from the primary side will increase proportionally. Therefore, in order to find out whether the multi-level phenomena will actually occur, an air-water apparatus is set up to run experiments at atmosphere pressure.

### 1. Facility Description

The test section for the multi-level test is a pipe, 4 inches in diameter and 4 ft in height. The pipe is made of plexiglass so that visual observation is possible. A schematic diagram of the test section is shown in Fig. 9. The air enters the test section from the bottom while the water enters from the top so that a countercurrent flow can be established. Three plates of the same type are installed in the vessel to simulate the tube support plates. Monometers are provided to measure the collapsed liquid level above each plate (see Fig. 9).

### 2. Countercurrent Flow Experiment

The purpose of this experiment is to study the effect of the plate geometry on the onset of flooding. The countercurrent flow is established by supplying a constant air and water flow rate to the test section from bottom and top of the test section respectively.

#### a. Result of Countercurrent Flow Experiment

Observation of the experiments show a strong tendency of liquid hold-up above the top plate. In fact, we find out that the one plate (top plate) flooding phenomenon is more likely to occur than multi-level flooding. This can be explained by the pressure drop along the flow path. Because of the pressure drop, the pressure faced by the bottom plate is higher than that by the top plate. For a given liquid flow rate, the required gas velocity for flooding varies with gas density:



$$(j_g)_{\text{flooding}} \propto (\rho_g)^{-0.5} \quad (22)$$

with other parameters not very sensitive to the pressure. For a steady state flow, the mass conservation requires

$$(\rho_g j_g A) = \text{Constant} \quad (23)$$

$$(j_g) \propto (\rho_g)^{-1} \quad (24)$$

Therefore,

$$\frac{j_g}{(j_g)_{\text{flooding}}} \propto (\rho_g)^{-0.5} \quad (25)$$

For a plate at a higher location, the pressure is lower, the gas density is smaller and, therefore, the potential for flooding, i.e.  $(j_g)/(j_g)_{\text{flooding}}$  is larger. This also implies that the drainage capability is smaller for a plate at a higher location. For a given intermediate plate, the amount of drain from the next higher plate is less than the amount of drain from the plate in question. With less input and more output, liquid is not very likely to accumulate above an intermediate plate.

#### b. Conclusion of Countercurrent Flow Experiment

For a steam generator blowdown, the tendency of top plate flooding is further enhanced by heat transfer from the hot surface and flashing. The steam velocity increases with the elevation due to the generation of steam from the heat transfer, flashing, and the expansion resulting from the pressure dropping. Consequently, we would only expect to find a pool of liquid in the bottom of the steam generator or on top of the tube bundle, provided that flooding occurs.

#### VI. SUMMARY AND CONCLUSION

A computer program, called SIT-SG, has been developed to predict the heat transfer on the secondary side of a steam generator, the pressure, the carryover, the mixture water level, the flow rate distribution, and the void fraction distribution during the steam generator blowdown. This computer program is developed for best estimate predictions with a fast running capability.

Flow regime dependent drift flow model constants are used to take into account the difference between the liquid velocity and the vapor velocity. A large discrepancy has been found for current available drift flux model constants. These discrepancies have a large effect on the water level prediction. Based on the comparisons between the code predictions and experimental data the best drift flux constants have been selected. The correlations used for the various flow regimes are connected with a

smoothing scheme.

From the computer code calculations, the key parameters in the transient can be identified and a better understanding of the transient process has been obtained. With respect to the transient process and the computer code modeling, the following conclusions can be drawn.

- . The pool entrainment phenomenon has a small effect on both the total amount of outgoing fluid and the transient water level response.
- . In general, the thermal hydraulic properties in a control volume can be considered as homogeneous. However, special attention should be focused on the modeling of the node which contains the sharp water-vapor interface. Interpretation of node average quantities can be misleading under many circumstances. For example, using the node average void fraction to determine flow regime can result in significant error. In addition to void fraction, the knowledge of flow developing history and velocity level are also important for determining the flow regime in a control volume.

SIT-SG has been used to perform the pressure and the mixture level calculation for the Babcock-Frankfurt blowdown experiment, the G.E. small vessel and the G.E. large vessel blowdown test. SIT-SG has also been used to predict the pressure, the water level, the carryover, the pool temperature and the heat transfer from the hot wall for the MIT steam generator simulator. The comparisons between the code prediction and the experimental data give rise to the following conclusions:

- . Good agreement is observed between the code prediction and experimental data for the pressure, the total amount of outgoing fluid and the suppression pool temperature response. These results justify our assumption in the code: (i) The pressure distribution is not important inside the secondary vessel and no momentum equation is required. (ii) The behavior of the fluid in the vessel is basically one-dimensional and a one-dimensional equation is capable of describing the system response. (iii) The drift flux model is an adequate model for predicting the two-phase flow under blowdown conditions. (iv) Thermal equilibrium exists between vapor and liquid phases.
- . The slip equilibrium critical flow model proposed by Fauske is selected for the calculation of two-phase critical flow rate. Good agreement has been achieved by comparing the predicted pressure response with the experimental data measured in the GE large vessel blowdown test, the MIT empty vessel test and MIT tests with internals. Therefore, this model is good for the blowdown pipe with  $L/D$  equals 20. Short  $L/D$  nozzles were not tested.
- . The measured dryout front is much higher than the predicted mixture water level. Consequently, the calculated effective heat transfer area is much smaller than the measured effective heat transfer area.

The heat transfer rate from the steam generator primary side to the secondary side and the duration of effective heat transfer will be underpredicted if the dryout front is regarded as the mixture level. However, it should be pointed out that in our experiment, the heat flux is quite low which leads to a reduced evaporation rate of liquid film and consequently results in a larger difference between dryout front and mixture level. Further study on the relation between dryout front and mixture level as a function of entrainment rate and deposition rate, evaporation rate is recommended.

- . From the liquid hold-up experiment, we find that flooding can occur at the tube support plates, where the flow area is minimal. The potential for the liquid hold-up due to flooding is largest for the top tube support plate. When this is applied to the blowdown in the steam generator secondary side, we would expect to find two mixture levels, one in the bottom of the steam generator and one above the top tube support plate, provided that flooding occurs.

Several areas require further investigation are described as he follows:

- . In SIT-SG, the effect of the separator to the blowdown is ignored. During a steam line break or a combined steam line break plus tube rupture, the behavior of the separator is unknown at present. It is expected that as the flashing occurs, the water level swells and the flow direction in the drain line of the separator may reverse. The exact conditions which lead to flow reversal in the drain line have not been delineated. It is also expected that the separator may have large effects on the amount of radioactive material released in the combined steam line break plus tube rupture. Therefore, a study of the performance of separator during blowdown is recommended.
- . The calculation results show that large discrepancies exist between the calculated mixture level and the measured dryout front. It is suspected that the large discrepancy is a result of the low heat flux on the rod bundle surface. In a real steam generator, the difference may be smaller due to the higher surface heat flux in which a little bit of spray will not be able to keep the tube wet. It is recommended to study the effect of heat flux on the discrepancies between the predicted mixture level and the measured dryout front.

## REFERENCES

1. Collier, J.G., Convective Boiling and Condensation, McGraw-Hill Book Co., England, 1980.
2. Zuber, N. and Findlay, J.A., "Average Volumetric Concentration in Two-Phase Flow Systems", Trans. ASME, J. of Heat Transfer, pp. 453-468, November 1965.
3. Bertodano, M.A.L.D., "Fast Computational Methods for Two Phase Flow Situations in Pressurized Water Reactors", Nuclear Engineer Thesis at MIT, January 1983.
4. Styrikovich, M.A., and Vinokour, J.G., "Experimental Data on Hydrodynamics of Two-Phase Mixture", Teploenergetika, Vol.8, no. 9, p. 56, 1961.
7. Fauske, H.K., "The Discharge of Saturated Water Through Tubes", Chem. Eng. Prog. Ser. 61,59, 210-216, 1965.
8. Fauske, H.K., "Contribution to the Theory of Two-Phase, One-Component Critical Flow", ANL-6633, Argonne National Lab, October 1962.
9. Wulff, W., "The Kinematics of Moving Flow Regime Interface in Two-Phase Flow", Proceeding of the Third CSNI Specialist Meeting, Hemisphere Publishing Corporation, 1983.
10. Kataoka, I. and Ishii, M., "Mechanistic Modeling and Correlations for Pool Entrainment Phenomena", NUREG/CR-3304, ANL-83-37, April 1983.
11. Holzer, B., et al., "Specification of OECD Standard Problem No.6 : Determination of Water Level and Phase Separation Effects During the Initial Blowdown Phase", Battelle-Institute of Frankfurt (Main) Report, February 1977.
12. Saha, P., et al., "Independent Assessment of TRAC-PD2 and RELAP5/MOD1 Codes at BNL in FY 1981", NUREG/CR-3148, BNL-NUREG-51645, December 1982.
13. Findlay, J.A., "BWR Refill-Reflood Program Task 4.8-Model Qualification Task Plan", NUREG/CR-1899, EPRI NP-1527, GEAP-24898, August 1981.
14. Slifer, B.C., "Loss of Coolant and Emergency Core Cooling Models for General Electric Boiling Water Reactors", NEC-10329, Class 1, General Electric Company, April 1971.

TABLE 1  
CRITERIA FOR FLOW REGIME DETERMINATION

Bubbly Flow	$j_g > 2.34 - 1.07 \frac{[g\Delta\rho\sigma]}{\rho_f^{1/2}}$ and $\alpha < 0.1$
Churn-turbulent	$ j_v  < \left(\frac{\Delta\rho g D}{\rho_g}\right)^{0.5} \cdot \left(\frac{1}{C_*} - 0.1\right)$ and $\alpha < 0.8$
Annular	$ j_v  > \left(\frac{\Delta\rho g D}{\rho_g}\right)^{0.5} \cdot \left(\frac{1}{C_*} - 0.1\right)$ or $\alpha > 0.8$

TABLE 2  
DRIFT FLUX MODEL CONSTANT  $v_{gj}$  USED IN FIGURE 1

Key	Name of Model	Applicable Regime
2	Wallis Model	Bubbly Flow
3	Ishii Model	Churn-Turbulent
4	Zuber Model	Churn-Turbulent
5	Zuber Model <sup>a</sup>	Churn-Turbulent
6	Ishii Model	Annular Flow
7	Ishii Model	Liquid Dispersed
8	Wilson Model	Low and High Void Fraction
9		Slug Flow
10	Wallis Model	Annular Flow

a : The coefficient is given by Bertodano

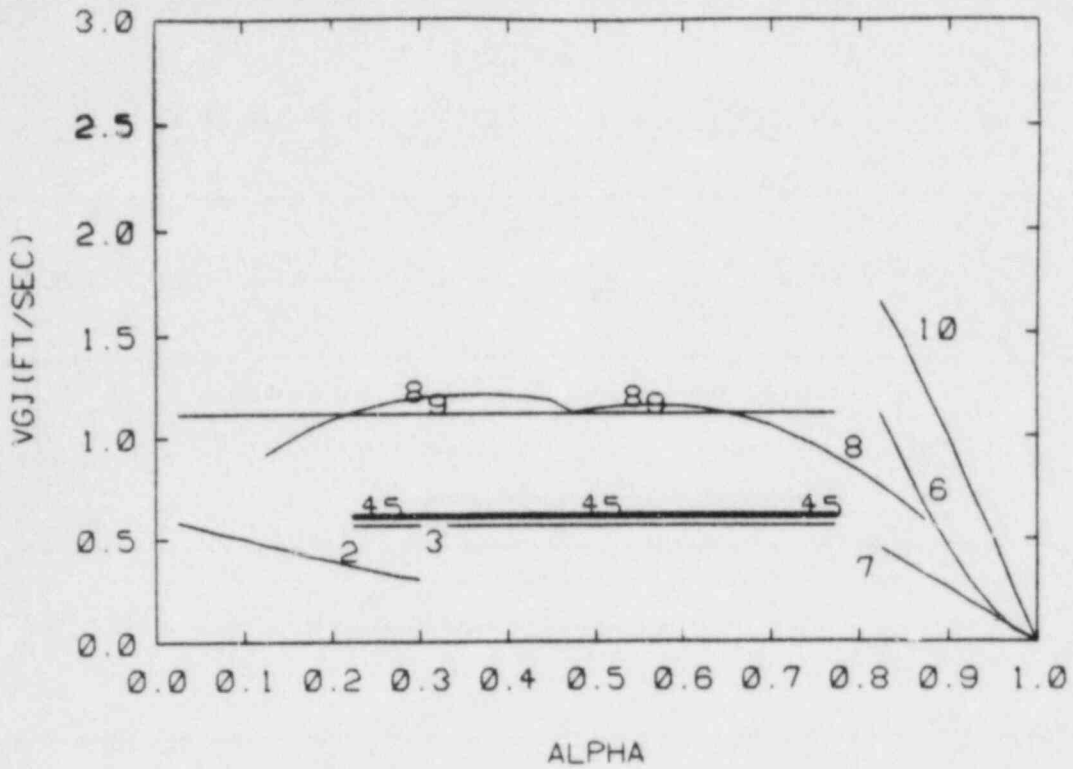


Figure 1. Comparison of Various Weighted Mean Drift Velocities as Function of Void Fraction at a Pressure of 1000 psi

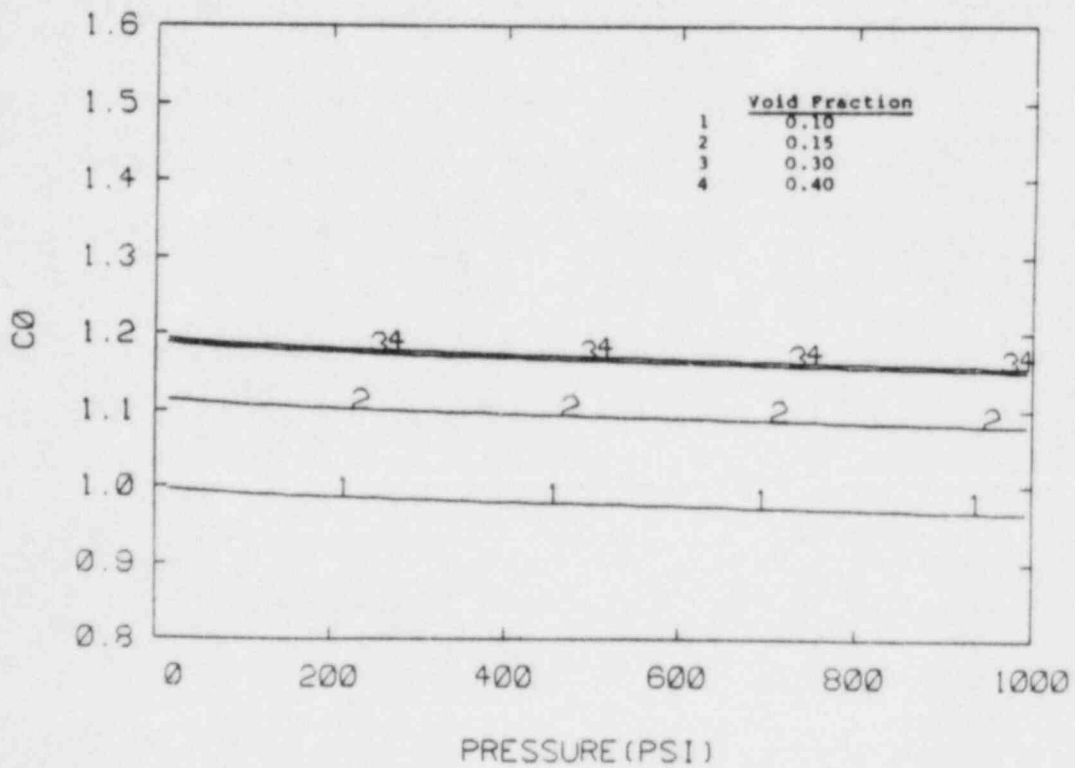


Figure 2. Recommended Drift Flux Model Constant  $C_0$ , Churn-Turbulent Flow Regime

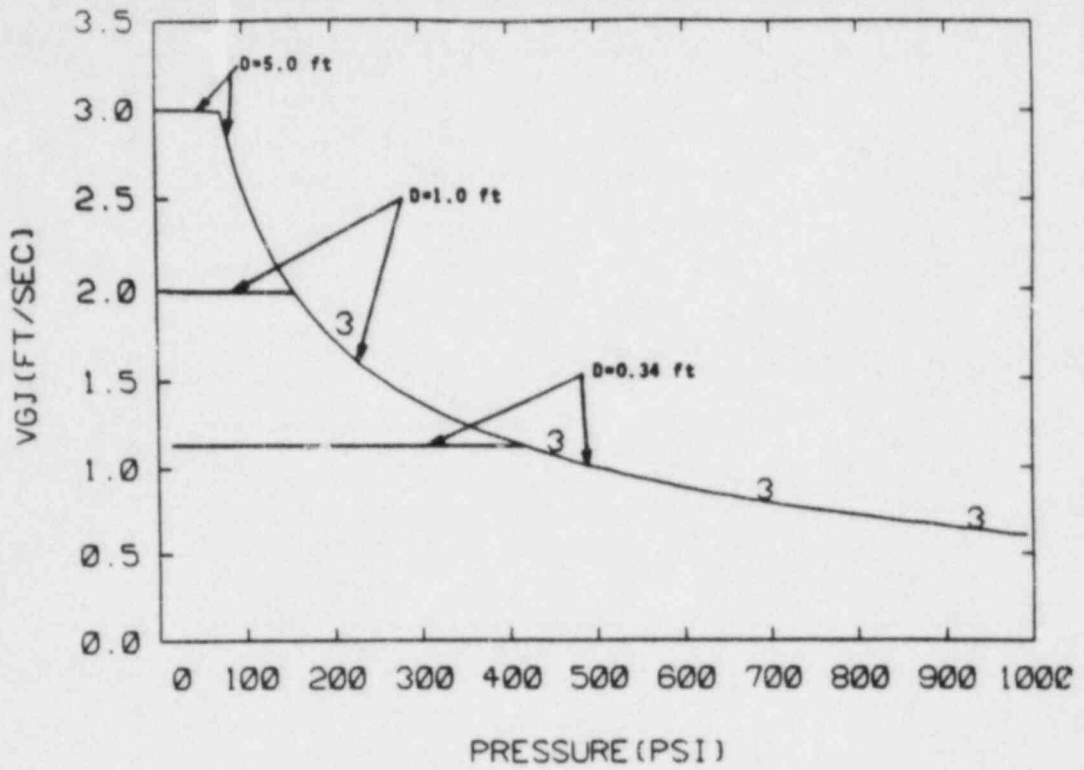


Figure 3. Recommended Drift Flux Model Constant  $V_{gj}'$ , Churn-Turbulent Flow Regime

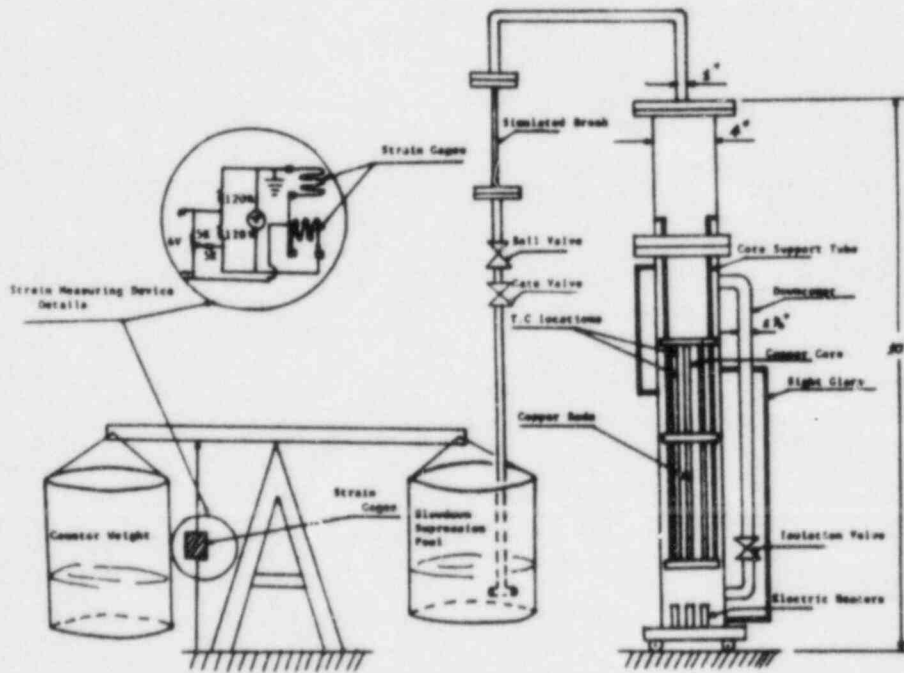


Figure 4. Schematic of Steam Generator Simulator Test Facility

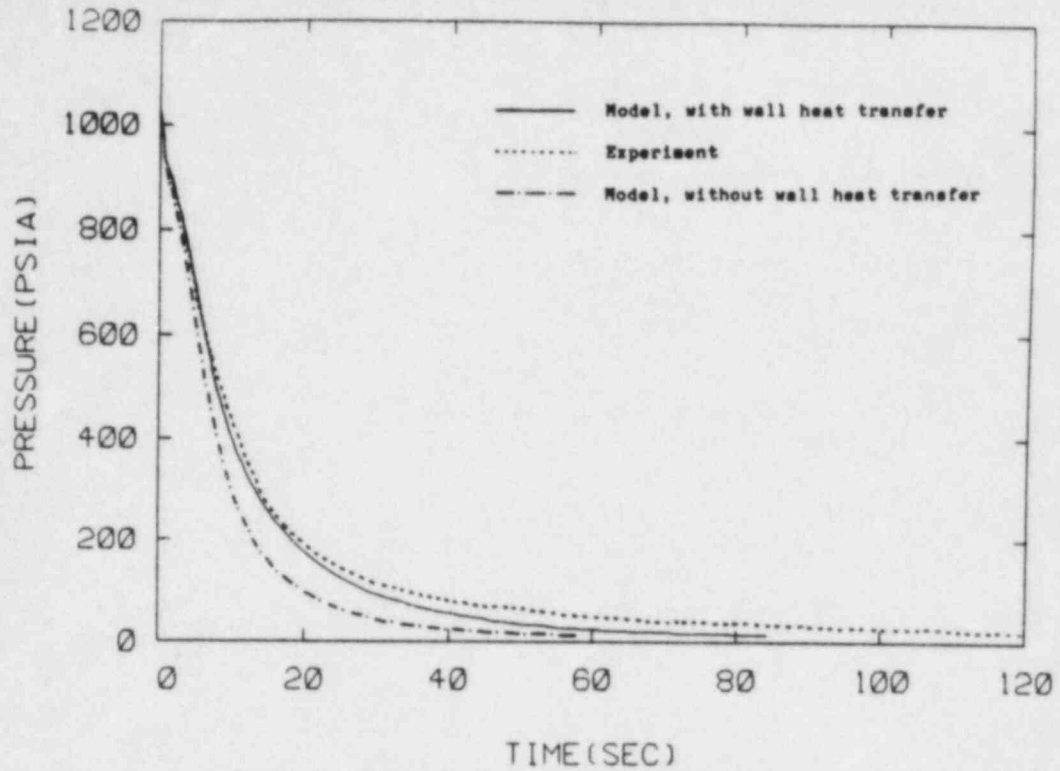


Figure 5a. Comparison Between the Measured and Predicted Pressure for MIT Test Run 9, 1/4" break

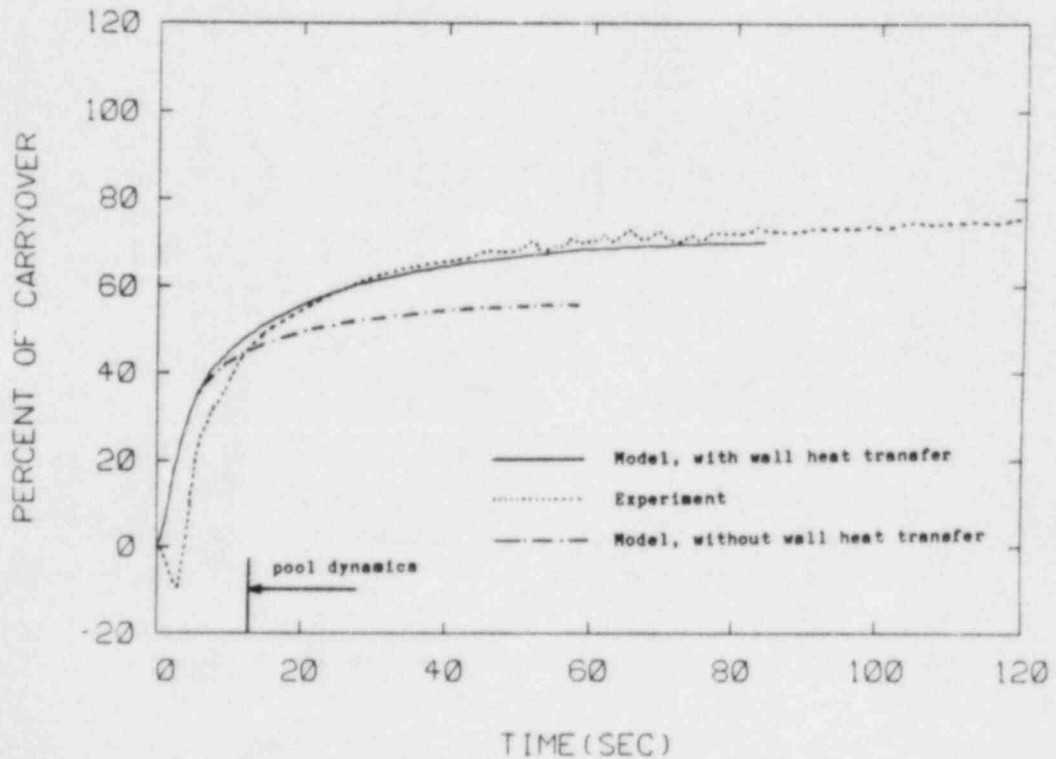


Figure 5b. Comparison Between the Measured and Predicted Carryover for MIT Test Run 9, 1/4" break



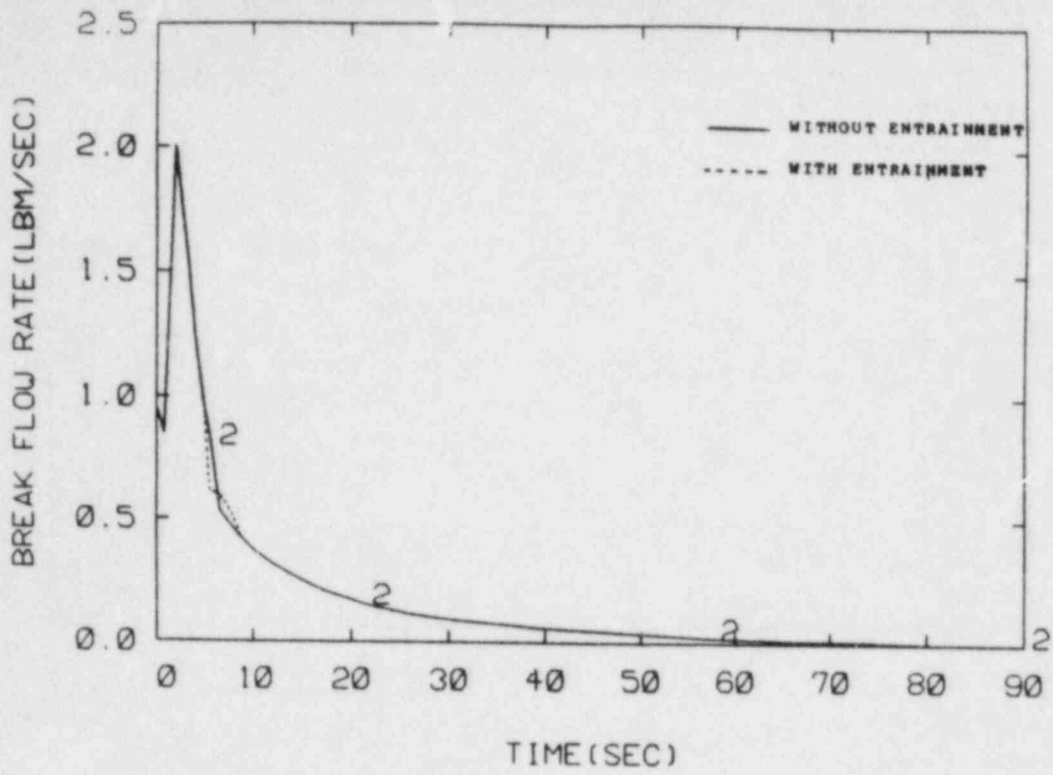


Figure 6. Predicted Break Flow Rate for MIT Test Run 9, 1/4" Break

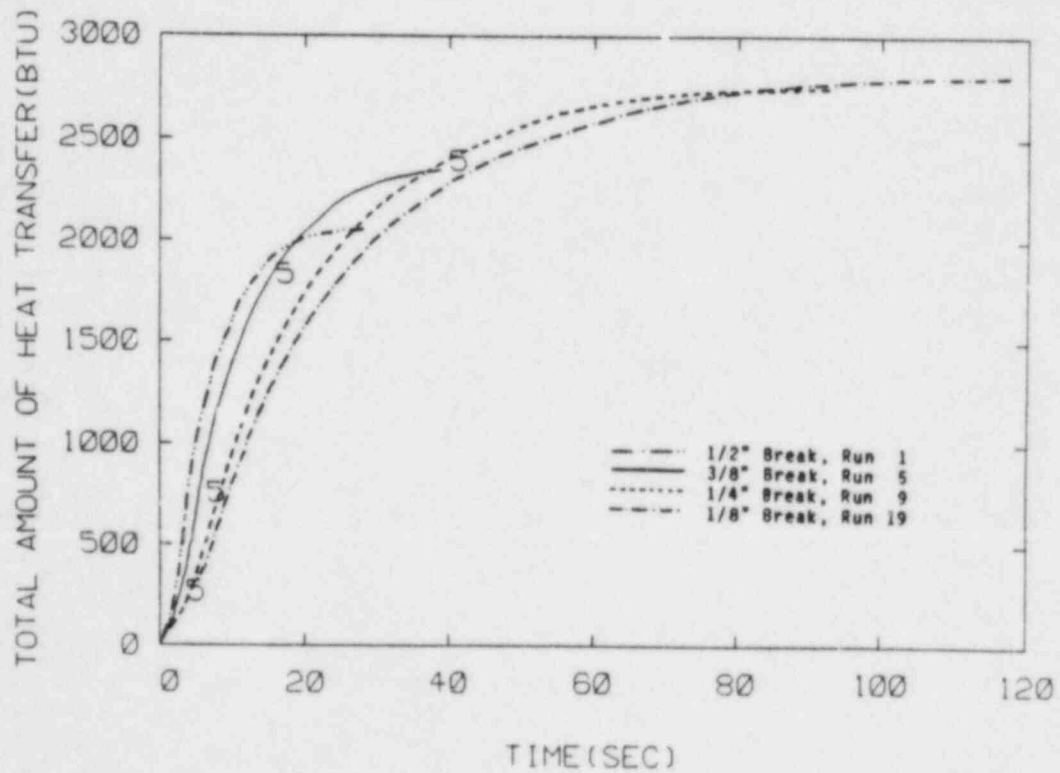


Figure 7. Predicted Time Integration of Heat Transfer for MIT Test Run 1,5,9,19

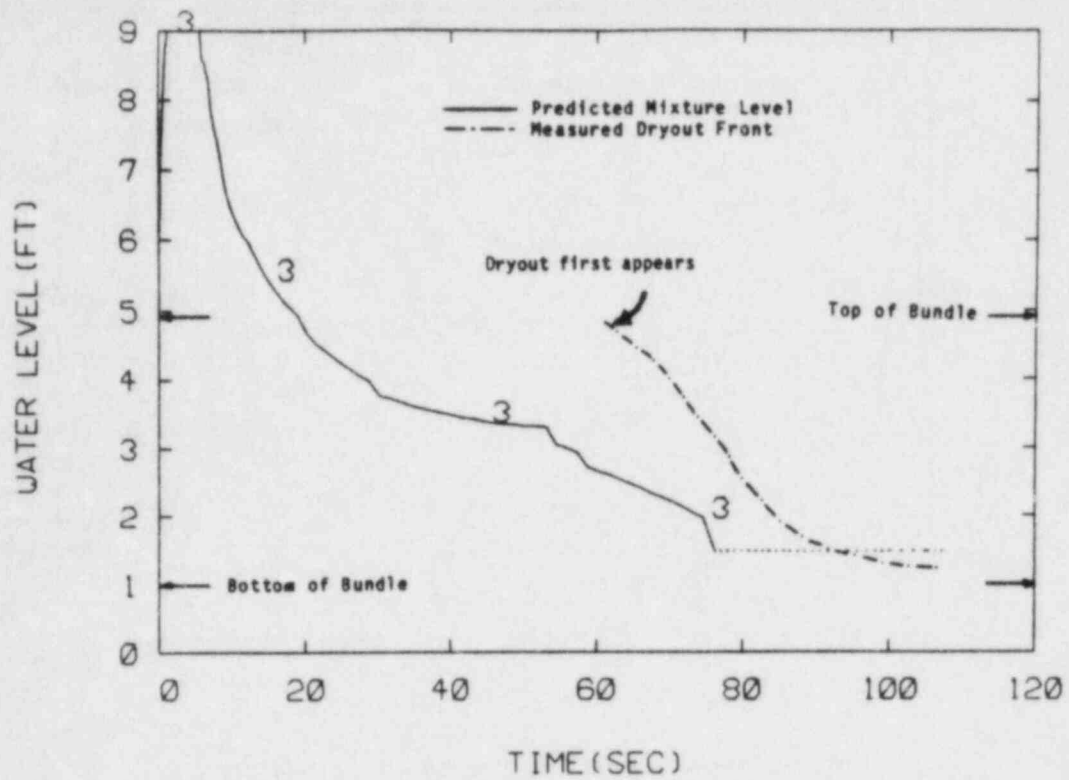


Figure 8. Comparison Between the Predicted Mixture Level and the Measured Dryout Front for MIT Test Run 49, 1/4" Break

## STEAM SEPARATOR MODULE DESCRIPTION

C. Y. Paik, Research Assistant  
Peter Griffith, Professor of Mechanical Engineering  
Massachusetts Institute of Technology

Abstract - This is a progress report on the MIT program on separator modeling. Though both high vapor and liquid flow rates or high water levels can cause a separator to fail, the most important factor is high water level. Appreciable carry-over from the separator section of a system generator occurs when the drain lines from the three stages of separation (the centrifugal, gravity and secondary) are unable to carry off the liquid flow. A module showing the needed inputs and the outputs from the proposed separator model is shown.

### Introduction

The steam-water separation used in a PWR steam generator is accomplished in three stages; centrifugal separation, gravitational separation and secondary (impingement) separation. Within the design envelope, the combined efficiency of the two separators in series is practically 100%. However, a tube rupture or a steam line break may give high flow rates and high downcomer water levels that are outside of the design envelope. How the separator will perform under these circumstances is very important because the separator can substantially alter water inventory in the system.

A combined steam line break plus tube rupture provides a direct leakage path through and out of the secondary system for radioactive materials contained in the primary fluid. Under these conditions, where all the radiation that is released is in the form of iodine, the separator efficiency over the entire range of operation may be important. The most important flow parameters affecting the efficiency of separators are  $j_g$  (superficial vapor velocity) and  $j_f$  (superficial liquid<sup>g</sup> velocity) in the riser, the water level, and the system pressure. How the separator will fail during a transient such as a steam line break can be summarized from observations made on the M.I.T. air-water experiment. (See Figure 1.)

## Failure Mechanism

When the downcomer water level rises above the design value, the hydrostatic head for the drain line from the centrifugal separator is reduced. This reduces down the flow rate out the drain, causing more water to collect on the deck plate. As the carry-over from the centrifugal separator increases, the flow rate through the deck drain line tends to increase due to the increase in the hydrostatic head. At some point, however, so much water is carried over that it starts to accumulate on the deck plate and forms a pool. Until the pool reaches the top of the outlet of the centrifugal separator, the amount of carry-over from the system is still negligible. This is true because both the gravity separator and the secondary separator are still effective in removing any liquid entrainment.

When the water level is further increased, the effectiveness of the centrifugal separator is diminished because the pool on the deck plate completely covers the top of the centrifugal separator outlet. In this case, the amount of water carried into the secondary separator increases significantly. It is also possible that the two-phase mixture level at the deck plate could reach the inlet of the secondary separator. When this happens, the flow rate in the secondary separator drain line increases such that the hydrostatic head required to drain is larger than that available. As a result, the bottom of the secondary separator floods and the carry-over from the system increases rapidly. Ultimately, water flows in excess of the capacity of the drain lines will be carried over. In every stage of separation, the downcomer water level is the most important parameter affecting the carry-over. The effects of the  $j_g$  and  $j_f$  on carry-over are minor compared to that of the downcomer water level.

A simple and physically based separator model that is suitable for a system code such as TRAC or RELAP-5 will be developed to predict the separator efficiency in the tube rupture and steam line break accidents. The model will consist of three stages of separation; centrifugal separation, gravity separation and secondary separation. It will stress the importance of the total separation efficiency rather than that of each individual separation stage. The model will include the geometric effects so that it will be able to predict the performance for the different geometry type separators.

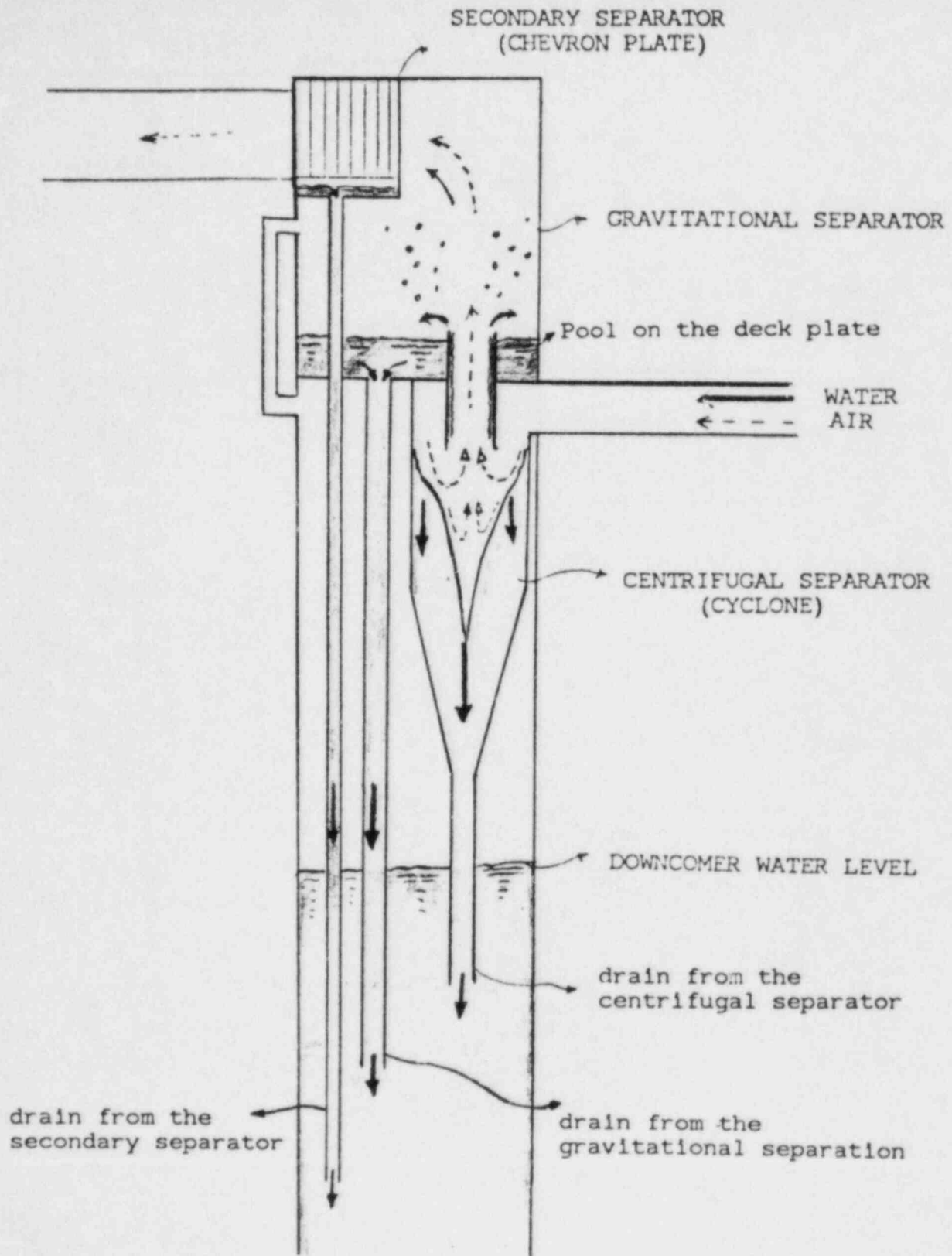
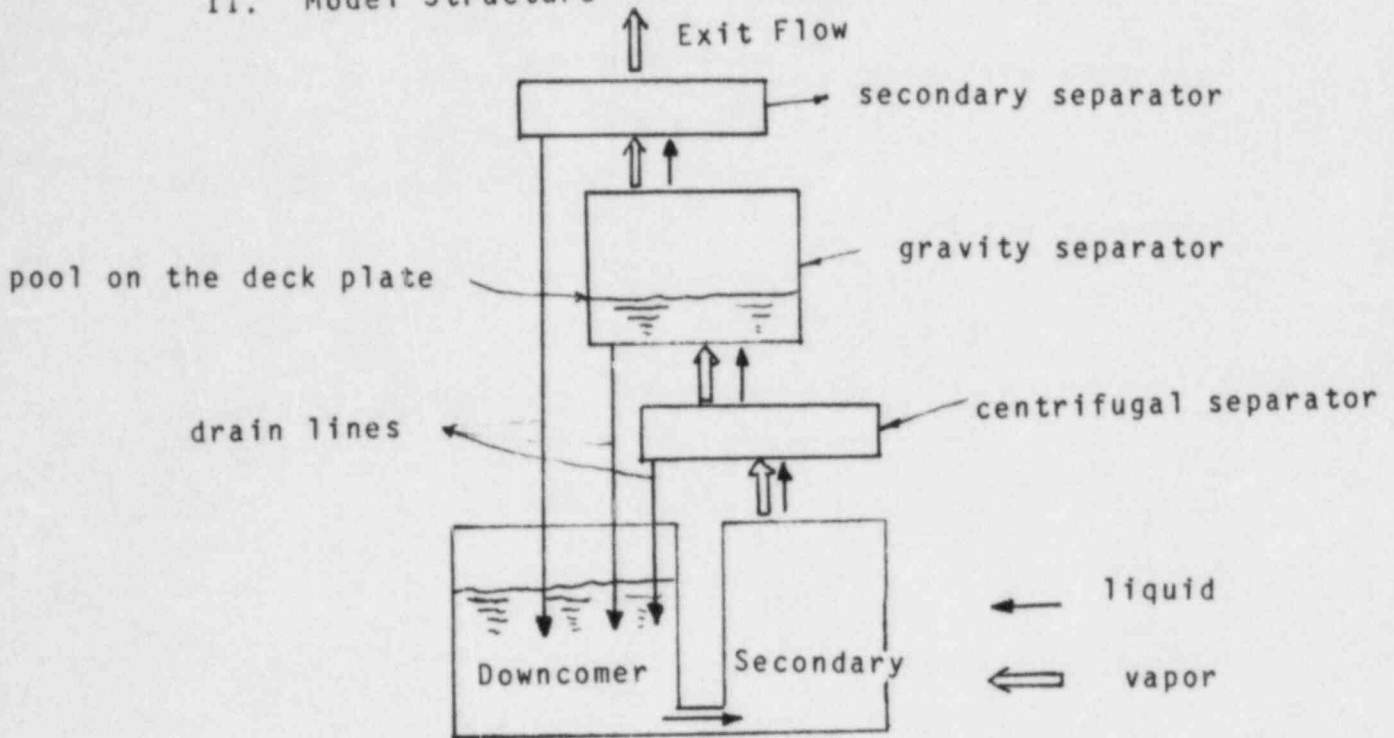


FIGURE I. M.I.T. AIR - WATER SEPARATOR SYSTEM

## II. Model Structure



Steam Generator Model

1. Required Boundary Conditions:
    - $j_g, j_f$  at the riser
    - system pressure
    - downcomer two-phase mixture level and void reaction
  2. Model
    - centrifugal separator
    - gravitational separator
    - secondary separator
- \* The pool level on the deck plate is the only time-dependent calculated variable.

Critical Flow Through a Small Break on a Large Pipe  
with Stratified Flow

V. E. Schrock, S. T. Revankar, R. Mannheimer,  
C-H Wang and D. Jia

Department of Nuclear Engineering  
University of California, Berkeley  
Berkeley, California

Abstract

The analysis of small break loss of coolant accidents is an essential part of light water reactor safety assessment. In these analyses the discharge of primary coolant must be calculated accurately in order to track the primary coolant inventory. In the case of a small break situated on a large horizontal pipe carrying stratified two-phase flow, the effective stagnation state driving the critical discharge depends upon the proximity of the interface in the upstream region to the entrance of the break channel. Vapor pull through and liquid entrainment will determine the inlet quality and hence have a major effect upon the critical flow out the break. This paper reports the results of an experimental investigation of steam-water discharge from a stratified upstream region through small diameter break channels oriented at the bottom, top and side of the main channel. The main pipe was 102mm in diameter and the break tubes were 4, 6 and 10mm in diameter and 123mm in length. Both air-water and steam-water were used at pressures up to 1.07 MPa.

The results for incipient vapor pull through and the onset of entrainment are correlated in terms of Froude number for the break flow. Some difference between air-water and steam-water was observed and it is suggested that surface tension differences may be the cause. The results for liquid entrainment are the same for steam-water and air-water. Comparisons are made with the recent work at KfK (Kern forschungszentrum Karlsruhe) on air-water and INEL (Idaho National Engineering Laboratory) on steam-water, both in larger scale.

Quality of the mixture entering the break can be represented as a function of  $h/h_b$  for the range of system pressure and break size as suggested in the KfK work, with some modification. This requires a reliable correlation for the incipient level  $h_b$  for steam-water as presented here. The critical discharge may then be evaluated applying an appropriate model to the break channel.

## Background

The small break critical flow problem was brought to the fore by the LOFT L3-5 [1,2] test, for which the measured break flow was quite different from predictions using codes such as RELAP-5 and TRAC. It was recognized that stratification in the upstream pipe is a complicating factor not handled by the codes. Zuber [3] presented a survey of the available literature on draining of tanks, pump suctions and the like in relation to the potential for gas pull through and liquid entrainment in small break accidents. This showed the importance of the upstream hydrodynamics in determining the stagnation state driving the critical flow. Crowley and Roth [4] performed a visualization study using air-water in a 67mm horizontal pipe with a 6.3mm I.D. orifice break oriented for down, side and up flow. Subsequently a more comprehensive air-water study was initiated by Reimann [5,6,7] using a 206mm mainline pipe with break tubes of 6, 12 and 20mm I.D., orificed at the end. Earlier work on vortex induced, Dagget and Keulegan [8], and vortex free or Bernoulli induced, Lubin and Hurwitz [9], gas pull through as well as early work on liquid entrainment by Rouse [10], Craya [11] and Gariel [12] was all concerned mainly with the identification of the levels with respect to the break for incipience. The KfK work [5,6,7] recognized the importance of obtaining the quality of the mixture entering the break as the level was modified following incipient two-phase flow.

Correlations for liquid entrainment have been developed in the form

$$Fr \left( \frac{\rho_l g}{\Delta \rho} \right)^{0.5} = A \left( \frac{h_b}{d} \right)^n \quad (1)$$

The coefficients A and n depend on the geometry of the space above the interface. A has been reported to range from 0.4 to 5.7 while n is reportedly in the range of 2.0 to 2.5.

The correlations for incipient vapor pull through at submerged drains or pump suctions have been presented in the form

$$Fr \left( \frac{\rho_l g}{\Delta \rho} \right)^{0.5} = B \left( \frac{h_b}{d} \right)^c \quad (2)$$

in which various authors find B and C to depend upon the intake geometry. Reimann and Khan [5] also have noted that the coefficients depend upon the presence of liquid velocity in the direction perpendicular to the break. Without the flow across the break they observed vortex flow and with the cross flow the vortex was suppressed. Values of B have been reported ranging from 0.2 to 3.2 while values of C ranging from 1.5 to 2.5 have been used to fit particular data sets.

Recently Smoglie of the KfK group presented dimensional analysis and potential flow theory in support of the general correlation form and for the effect of transverse flow. She suggested the results be applied to LWR calculations for steam and water by assuming that flashing does not modify



the incipient data and using the homogeneous equilibrium model to predict the critical flow in the break channel. Implicitly she assumes there is no other difference between the steam-water and air-water systems.

Concurrent with Berkeley experiments, Anderson [13] has conducted experiments at INEL using steam-water in a 28.4 cm I.D. horizontal pipe for down and side orientations and pressure up to 6.2 MPa. The 16mm break was the geometrically complicated hardware that had been used in the LOFT L3-5 test. Incipient pull through data have not been directly observed but inferred by the onset of noise in  $\Delta p$  readings. The few points presented tend to agree with KfK and Berkeley air-water data.

#### Description of the Experiment

The test facility is illustrated in Figure 1 together with the legend in Table 1. It consists of pressure vessel constructed of 12 inch IPS Schedule 5 stainless steel pipe with welded end caps, 3m in height, which serves as a reservoir and a steam generator, a horizontal test pipe, a tee break section and a recirculation loop. The reservoir is heated using three adjustable 4kW immersion heaters during steam-water tests. By maintaining the reservoir pressure 15 to 35 kPa above the desired test section pressure the steam, taken off the top and liquid flow taken off the bottom provided independently controlled flows to the test section. For air-water tests the reservoir was pressurized by the laboratory compressed air supply for pressures up to 650 kPa and using cylinders of compressed nitrogen for pressures up to 1065 kPa. The test pipe was equipped with a calming grid at the inlet. Viewing windows were placed at the break section and in the pipe just upstream and downstream of the break to allow observation visually and photographically, of the two-phase interface. The liquid passing the break was pumped back to the entrance in the recirculation loop. The steam passing the break was directed through a flow meter to a quench tank. The break flow went to a weigh tank. For air-water tests a separator and air meter were also installed. In steam-water tests the steam in the discharged water was quenched in the weigh tank. Sufficient pressure and temperature measurements were provided to allow complete mass and energy balances to be performed. The data were recorded using an Auto Data Eight digital data acquisition system. Construction of the break channel is illustrated in Figure 2.

Data for incipient pull through and onset of entrainment were obtained visually for each break orientation and each fluid while simultaneously recording the system pressure and flowrates. Break flow was found from weigh tank measurements and also from level measurements in the reservoir and mass balance. Following incipient two-phase flow entering the break, the quality entering the break was deduced from mass flow measurements and the energy balance for steam-water. In the air-water tests water and air discharge rates were individually measured.

## Results

Mass flux out the break is shown in Figure 3 for single phase entrance to the break as a function of stagnation pressure. The cold water (air-water tests) data are subcritical flow whereas saturated water entering the break produced choked flow when the stagnation pressure was above about 150 kPa. Differences in channel L/D cause some differences in these mass flowrates. Single phase entrance data are of course independent of the break orientation.

Figure 4 shows the data for down oriented breaks for both air-water and steam-water. The heights at incipient and continuous pull through thresholds are shown for each fluid system. As can be seen, the height for steam-water is about 30% higher than for air water at the same Froude number. Vortex flow was observed at incipience in our tests. The steam-water incipient pull through data are represented by

$$\text{Fr} \left( \frac{\rho_l}{\Delta\rho} \right)^{0.5} = 0.78 \left( \frac{h_b}{d} \right)^{2.0} \quad (3)$$

and the air-water data by

$$\text{Fr} \left( \frac{\rho_l}{\Delta\rho} \right)^{0.5} = 1.47 \left( \frac{h_b}{d} \right)^{2.0} \quad (4)$$

The air-water data are close to those of Reimann and Khan for vortex free flow, which were correlated by

$$\text{Fr} \left( \frac{\rho_l}{\Delta\rho} \right)^{0.5} = 0.94 \left( \frac{h_b}{d} \right)^{2.5} \quad (5)$$

For comparison the INEL data for steam water are shown in Figure 4 and can be seen to be closer to our air-water data than to our steam water data. Thus the INEL data, obtained in an indirect way, do not confirm the air-water/steam-water difference seen in the present results. The correlation lines of the present investigation are also compared with Reimann and Khan in Figure 5. In an attempt to explain the difference between fluid systems the role of surface tension was considered. The shape of the liquid-vapor interface at the incipient pull-through is considered to depend upon surface tension. Then a Bond number

$$\text{Bo} = d \sqrt{\frac{g\Delta\rho}{\sigma}} \quad (6)$$

should play a role. As seen in Figure 6 the data sets can be brought together by multiplying the Froude number by

$$\left( \frac{\text{Bo}_{\text{steam}}}{\text{Bo}_{\text{air}}} \right)^4$$

It should be noted that both density difference and surface tension are

different in these fluid systems because of the temperature difference.

Dependence of gas and liquid mass fluxes in the break upon the liquid level after inceptions of pull through is shown in Fig. 7 for the air-water case and Fig. 8 for steam water. In Fig. 9 we show break entrance quality as a function of submergence expressed as  $h/d$  or  $h/D$ . As expected the quality increases with increasing system pressure for the same  $h/d$ . In Fig. 10 the quality is correlated with  $h/h_b$  which gives a single curve for all pressures. In this figure we show the present data together with the INEL reduced using the Berkeley correlation for  $h_b$ . The data in this form agree well and produce a single steam-water correlation

$$x = (0.006)^{h/h_b} \left[ 1 - \frac{1}{2} \frac{h}{h_b} \left( 1 + \frac{h}{h_b} \right) \right]. \quad (7)$$

This is similar to the KfK correlation [7] for air-water.

The vapor-pull through for side breaks is similar to that for down flow. Fig. 11 shows the difference between air-water and steam-water incipient data. Fig. 12 again shows that the same Bond number ratio brings the data together. Steam-water incipience is described by

$$\text{Fr} \left( \frac{\rho_l}{\Delta\rho} \right)^{1/2} = 1.19 \left( \frac{h_b}{d} \right)^2. \quad (8)$$

As for downflow, the INEL data are closer to the Berkeley air-water data. Liquid entrainment onset for side orientation is shown in Fig. 13. For upflow no difference between steam-water and air-water entrainment was observed. In side flow, only air-water entrainment could be clearly observed but, based on the upflow case, no difference is expected. The INEL entrainment onset agree with the present data as shown in Fig. 13. The present data are correlated by

$$\text{Fr} \left( \frac{\rho_g}{\Delta\rho} \right)^{0.5} = 3.25 \left( \frac{h_b}{d} \right)^{2.5}. \quad (9)$$

Figure 13 also compares the KfK entrainment onset results with those from Berkeley and INEL for side orientation. Quality vs  $h/h_b$  is shown in Fig. 14 where both Berkeley and INEL steam-water data are shown. The INEL data for vapor pull through were reduced using the Berkeley correlation for  $h_b$  (Equation 8). The quality correlation is represented by

$$x = x_o (1+h/h_b)^{0.7} \left[ 1 - \frac{c}{2} \frac{h}{h_b} \left( 1 + \frac{h}{h_b} \right) \right] \quad (10)$$

where  $x_o = 0.06$

$$c = \begin{cases} 1 & \text{for } \frac{h}{h_b} \leq 0 & \text{(Liquid Entrainment)} \\ 0 & \text{for } \frac{h}{h_b} > 0 & \text{(Vapor Pull-Through).} \end{cases}$$

For the up orientation of the break, the entrainment onset is shown in Fig. 15. This figure also shows the KfK correlation which is higher. The present data are correlated for both air-water and steam-water by

$$Fr \left( \frac{\rho_g}{\Delta\rho} \right)^{0.5} = 0.395 \left( \frac{h_b}{d} \right)^{2.5} \quad (11)$$

Break entrance quality vs  $h/h_b$  is shown in Fig. 16 where it is seen that the Berkeley and KfK results compliment one another. INEL did no up flow tests. The combined data have been fit by the equation

$$x = \left( \frac{h}{h_b} \right)^{3.25} (1-h/h_b)^2 \quad (12)$$

### Critical Flow Results

In the present experiments most of the break flows were choked. Although it was not the objective of the program to develop new models for the calculation of the critical discharge, given the stagnation state of the fluid entering the break channel, the existence of choked flow was considered desirable in that it ensured that the range of Froude number covered by the experiments corresponded to that for which the discharge flows would be expected to be choked. A difference between the two fluid systems is the fact that the flow is always unchoked at single phase entrance states for the air-water system, while for saturated liquid entering the break (the case of the steam-water system with  $h > h_b$ ) the flow is choked due to flashing unless the stagnation pressure is very low (about twice the atmospheric pressure). Figure 17 illustrates the pressure profiles in the break channel when the fluid entering was saturated liquid. Figure 18 illustrates the profiles when the entrance condition is two-phase. The results are qualitatively similar but as expected the pressure gradients in the pipe are greater for the higher qualities associated with the two-phase entrance condition. Homogeneous equilibrium (HEM) calculations were performed for the experimental conditions assuming isentropic entrance flow and Fanno type flow in the straight pipe. The measured flow rates were 50 to 150 percent higher than predicted by HEM. The critical flow data from the present tests are not included here but will be documented in a future NUREG report.

The break geometry in both the KfK and INEL experiments was different from that of the present experiment, as noted previously. Thus models for prediction of critical flow in each should reflect the difference in geometry of the break channel. The same is true for any application to reactor plant calculations. The recommended procedure is therefore to use the present steam-water correlations for incipient entrainment, i.e., Equation 3 for down oriented breaks, Equation 8 for vapor pull through in side breaks, Equation 9 for liquid entrainment in side breaks, and Equation

11 for top breaks. These correlations establish the reference values  $h_b$  for use in the associated quality correlations, Equations 7, 10 and 12.<sup>b</sup>

The problem in the application to plants will generally be posed as: given break channel geometry and upstream stratified flow pattern (liquid depth) and pressure, find the critical discharge. To utilize Equation 3, 8, 9 or 11 it is first necessary to apply the best available critical flow model for the break channel geometry of the hypothetical problem to calculate the break flow for single-phase fluid (either saturated liquid or saturated vapor depending upon break location in relation to the liquid-vapor interface) entering the break. The appropriate entrainment correlation is then used to obtain  $h_b$ , which is in turn used via the appropriate quality correlation, to obtain the break entrance quality. The critical flow model is then used with this entrance quality to predict the break flowrate. Smoglie (7) recommends using the IHEM for the break flow prediction, which ignores the effect of pipe friction. We have seen that HEM with pipe friction greatly under predicts the measured results for our break channels. Models that account for thermal nonequilibrium would be more appropriate.

#### Concluding Remarks

Critical flow through small breaks on horizontal pipes carrying stratified two-phase fluid depends strongly upon the quality of fluid entering the break channel and therefore upon the phenomena of vapor pull-through and liquid entrainment. The present study using steam-water compliments the results of the air-water experiments at KfK and the steam tests at INEL. The KfK study showed that the interface level for incipient entrainment of the second phase has some dependence upon channel conditions, whether the break is fed from both sides, is near a dead end in the pipe or has stratified flow passing the break. The first two involved vortex flow entering the break at incipience, while the third, which is most relevant to the reactor application, was vortex free. In the present tests, both steam-water and air-water incipience involved a vortex flow which subsequently underwent transition to vortex free flow as the liquid level was reduced. In the present study, the steam-water level for incipient vapor pull-through was higher than that for air-water in both bottom and side breaks. The air-water data are close to the KfK data with cross flow despite the difference in the character of the flow. The present work resulted in correlations for incipient pull-through that are recommended for use in reactor safety applications. Unfortunately INEL made no direct observations of incipient pull-through and the few points presented from indirect evidence are closer to the air-water data than to the steam-water data. However, using the Berkeley incipience correlation to normalize the INEL data produces quality in good agreement with the Berkeley quality measurements in the same generalized correlation form as proposed by the KfK group.

In the case of liquid entrainment at top breaks the present results showed no difference between air-water and steam-water while the data are a little higher in level at the same Froude number than the KfK data. At

the side break only air-water data could be successfully obtained and are assumed to represent steam-water as well because of the top break results. Three points from the INEL study agree with our data while the KfK data show somewhat higher levels. From the results of the three studies a correlation for quality during liquid entrainment was developed and is recommended for use in reactor safety calculations.

The difference between steam-water and air-water may be due in part to difference in physical properties. We have shown that surface tension and density differences (Bond number) may serve to unify the data, however this difference is not considered to be satisfactorily resolved and will receive further study.

Finally, the application of the recommended correlations to the reactor safety calculation has been discussed.

## References

1. Doa, L. T. C. and Carpenter, J. M., "Experiment Data Report for LOFT Nuclear Small-Break Experiment L-35/L3-5A," NUREG/CR-1695, EGG-2060, November 1980.
2. Condie, K. G., "LOFT LOCE L3-5/L3-5A Result and Analysis," paper presented at the LOFT Review Group Meeting, Idaho Falls, Idaho, November 6, 1980.
3. Zuber, N., "Problems in Modelling of Small Break LOCA," NUREG-0724, 1981.
4. Crowley, C. J. and Rothe, P. H., "Flow Visualization and Break Mass Flow Measurements in Small Break Separate Effects Experiments," Small Break Loss-of-Coolant Accident Analysis in LWR's, EPRI WS-81-201, August 1981.
5. Reimann, J. and Khan, M., "Flow Through a Small Break at the Bottom of a Large Pipe with Stratified Flow," presented at the 2nd International Topical Meeting on Nuclear Reactor Thermal Hydraulics, Santa Barbara, CA, Jan. 11-14, 1983.
6. Reimann, J. and Smoglie, C., "Flow Through a Small Break at the Top of a Large Pipe with Stratified Flow," presented at the annual meeting of the European Two-phase Flow Group: Zurich, Switzerland, June 14-16, 1983.
7. Smoglie, C., "Two-phase Flow Through Small Branches in a Horizontal Pipe with Stratified Flow," Kernforschungszentrum Karlsruhe, KfK 3861, December 1984.
8. Dagget, L. and Keulegan, G., "Similitude in Free Surface Vortex Formation," J. Hydr. Div. ASCE Vol. 100, p. 1565, 1974.
9. Lubin, B. and Hurwitz, M., "Vapor Pull-Through at a Tank Drain with and without Dielectrophoretic Buffling," Proc. Conf. Long Term Cryopropellant Storage in Space, NASA Marshall Space Centre, Huntsville, AL, p. 173, 1966.
10. Rouse, H., "Seven Exploratory Studies in Hydraulics," Proc. ASCE Vol. 82, 1956.
11. Craja, A., "Theoretical Research in the Flow of Non-Homogeneous Fluids," La Houille Blanche, pp 44-55, Jan-Feb. 1949.
12. Gariel, P., "Experimental Research on the Flow of Non-Homogeneous Fluids," La Houille Blanche, pp 56-64, Jan-Feb. 1949.

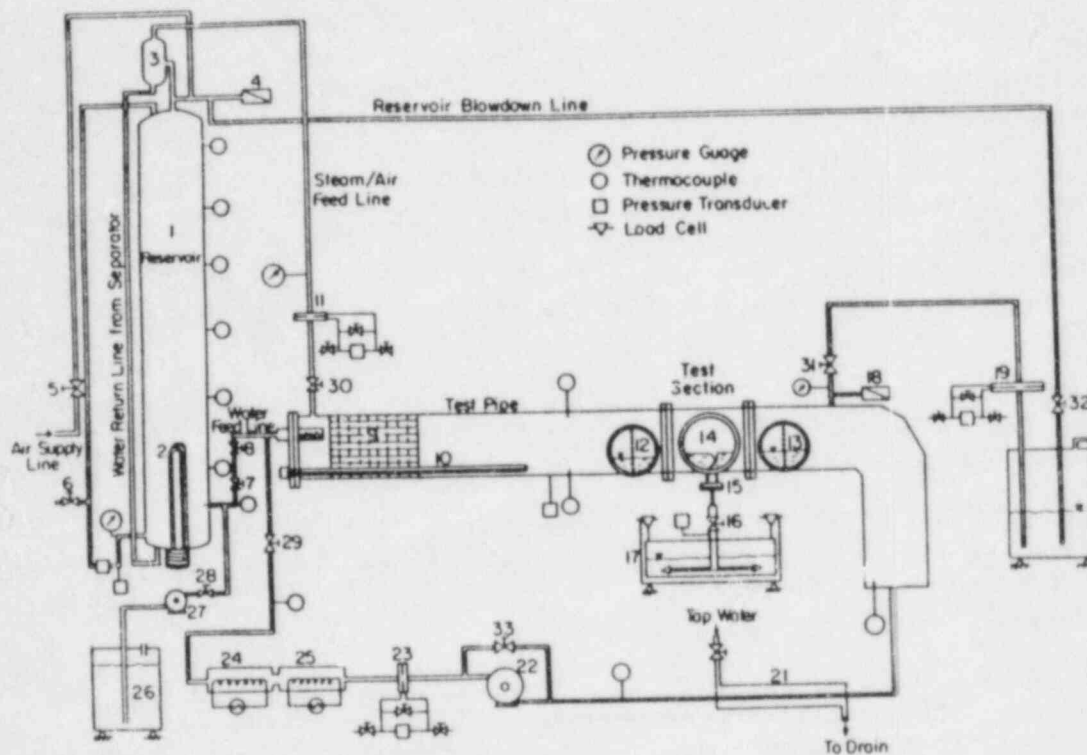


FIG. 1. EXPERIMENTAL SYSTEM SCHEMATIC (REFER TO TABLE 1 FOR COMPONENT DETAILS)

TABLE 1. KEY TO FIGURE 1

Component Number	Description
1	Pressure Vessel Steam Water Reservoir
2	Pressure Vessel Immersion Heaters
3	Steam Separator
4	Reservoir Pressure Relief Valve
5	Air/Nitrogen Supply Shut-Off Valve
6	Vessel Vent Line Valve
7	Water Feed Regulating Valve
8	Water Feed Shut-Off Valve
9	Honeycombed Test Pipe Flow Homogenizer
10	Test Pipe Immersion Heater
11	Gas Entry Orifice Meter
12	Upstream View Window for Liquid Level Indicator
13	Downstream View Window for Liquid Level Indicator
14	Test Section Flow Entry View Window
15	Break Discharge Section
16	Break Discharge Gate Valve
17	Weigh Tank
18	Test Pipe Pressure Relief Valve
19	Gas Exit Orifice Meter
20	Quench Tank
21	Double Pipe Heat Exchanger
22	Water Recirculation Pump
23	Water Recirculation Orifice Meter
24	Water Recirculation Reheater
25	Water Recirculation Reheater
26	Distilled Water Storage Tank
27	Reservoir Fill Pump
28	Reservoir Fill Line Regulating Valve
29	Recirculation Rate Regulating Valve
30	Gas Entry Regulating Valve
31	Gas Exit Regulating Valve
32	Reservoir Blowdown Regulating Valve
33	Pump Bypass Line Regulating Valve
34	Heat Exchanger Cold Water Feed Regulating Valve



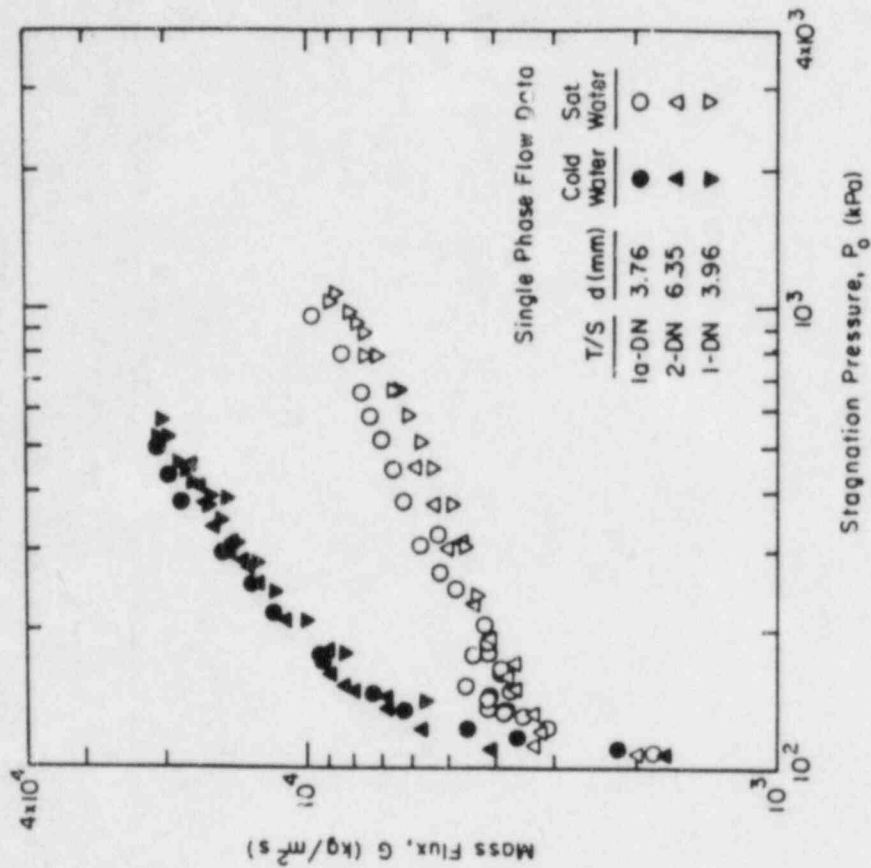


FIG. 3. SINGLE PHASE MASS FLUX DATA

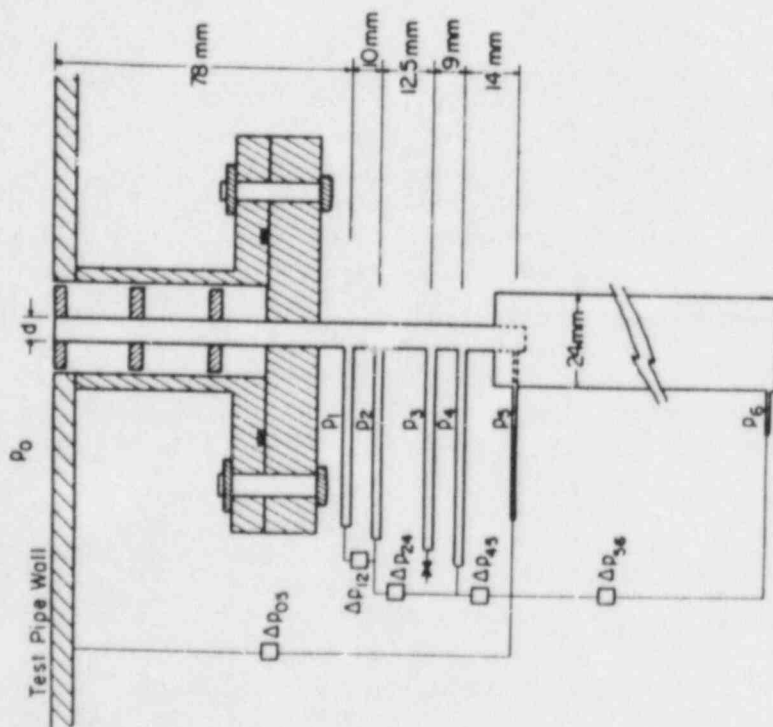


FIG. 2. BREAK TUBE SECTION AND TEST SECTION MOUNTING

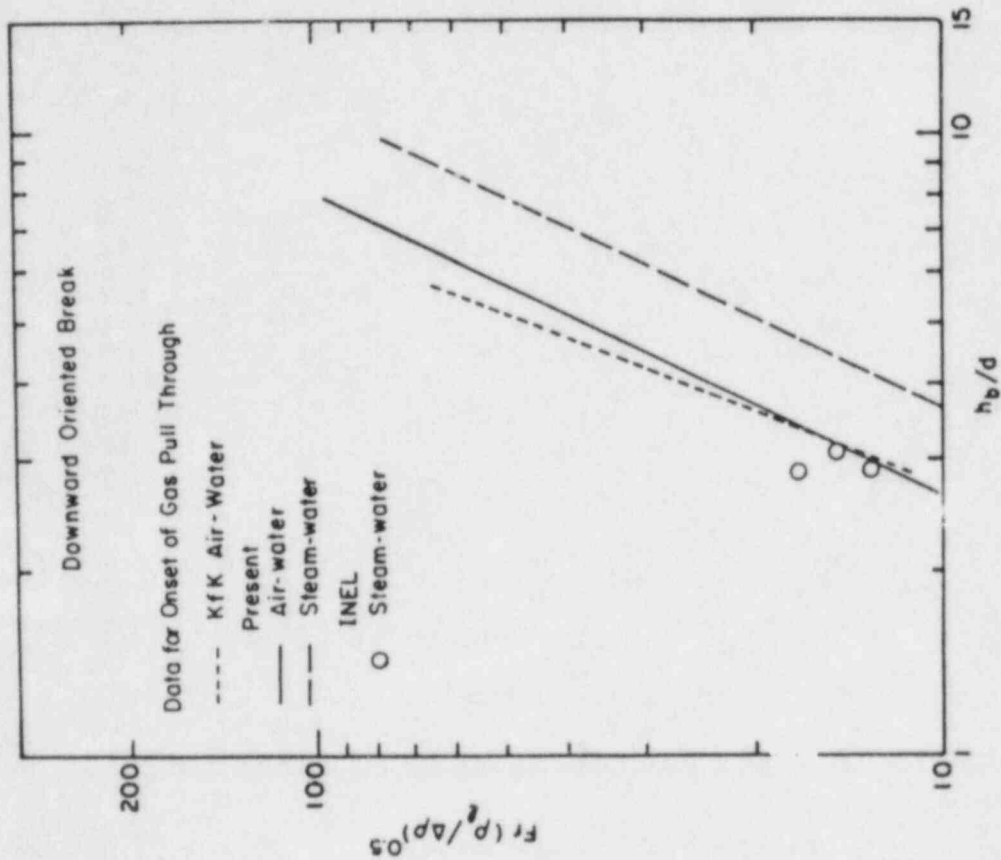


FIG. 5. COMPARISON OF VAPOR FULL-THROUGH INCEPTION WITH INEL AND KfK RESULTS, DOWNWARD BREAK

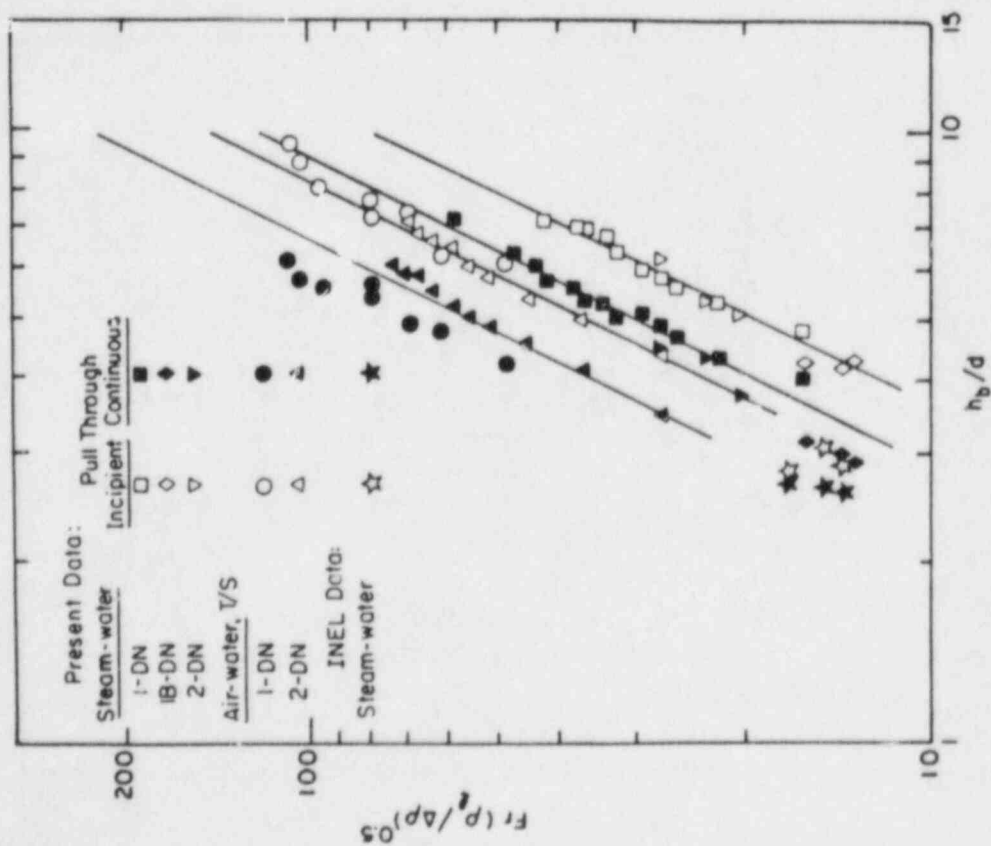


FIG. 4. INCIPENT VAPOR FULL-THROUGH FOR DOWNWARD ORIENTED BREAK

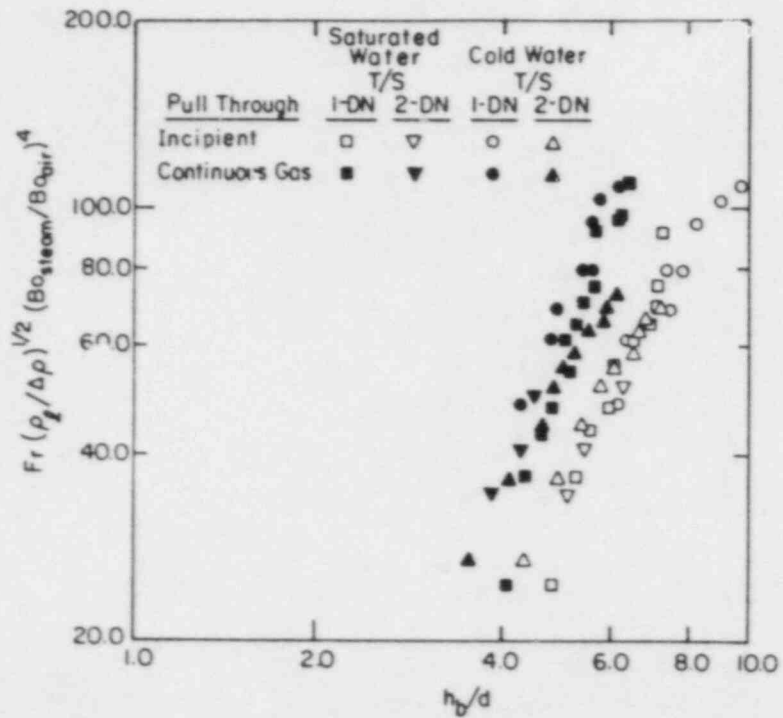


FIG. 6. VAPOR PULL-THROUGH INCEPTION USING BOND NUMBER CORRECTION FOR DOWNWARD ORIENTED BREAK

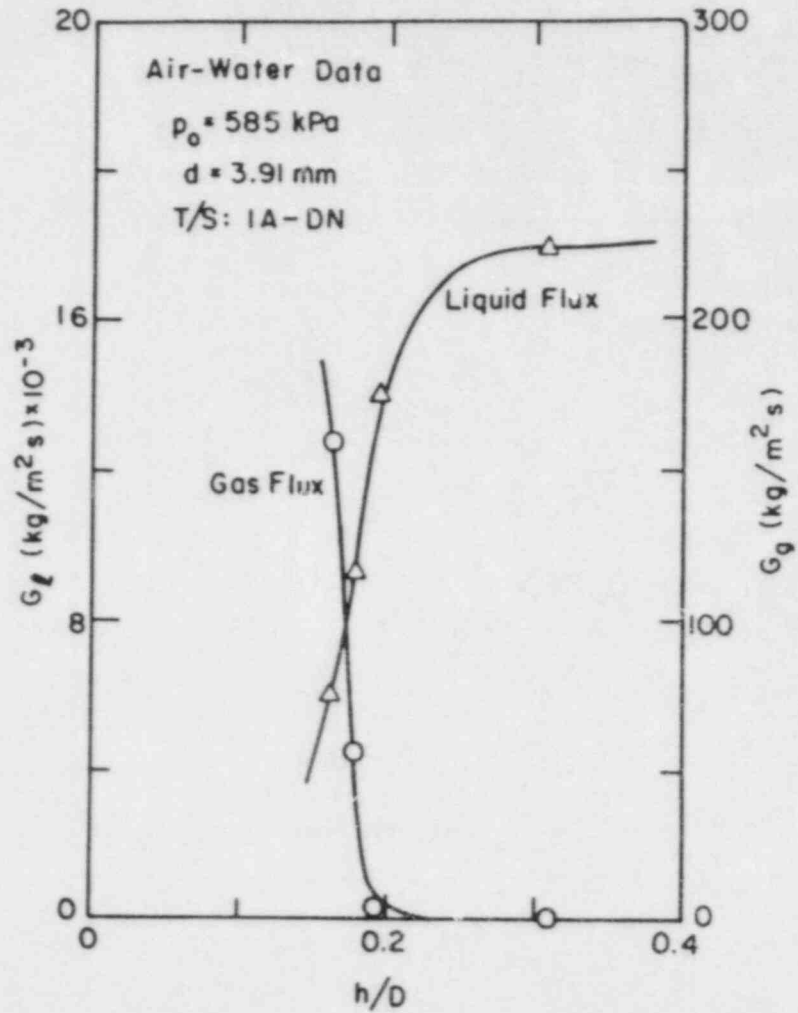


FIG. 7. LIQUID AND GAS MASS FLUX FOR DOWNWARD ORIENTED BREAK  
 $P_o = 585 \text{ kPa}$ , AIR-WATER DATA

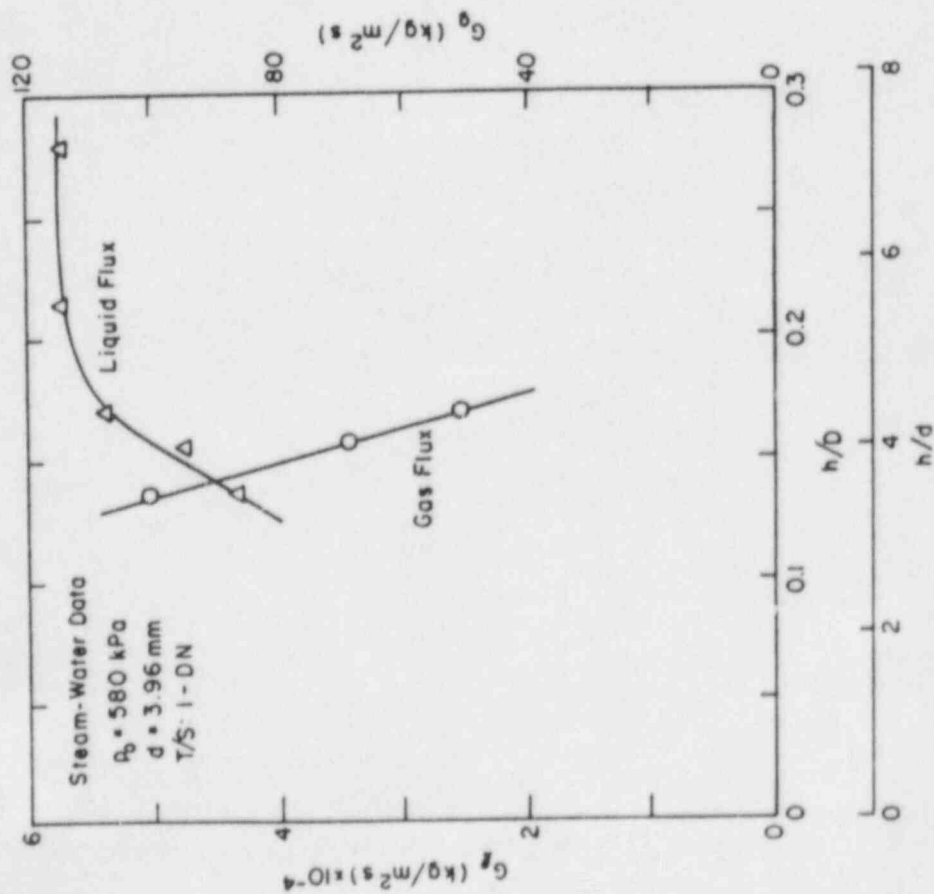


FIG. 8. LIQUID AND GAS MASS FLUX FOR DOWNWARD ORIENTED BREAK  
 $P_0 = 580$  kPa, STEAM-WATER DATA

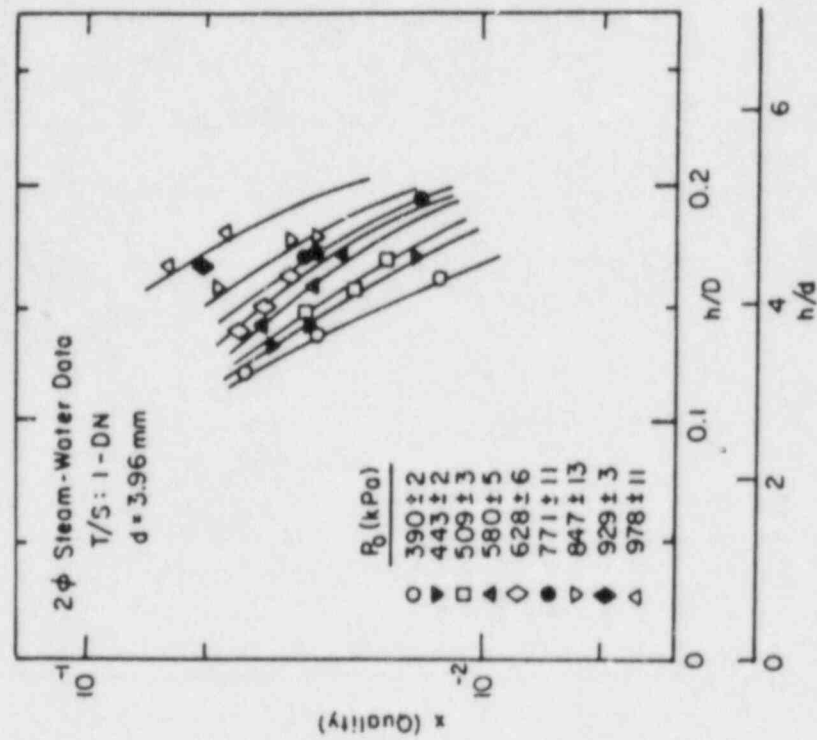


FIG. 9. BREAK ENTRANCE QUALITY AS FUNCTION OF  $h_0/d$  FOR DIFFERENT STAGNATION PRESSURE FOR DOWNWARD ORIENTED BREAK

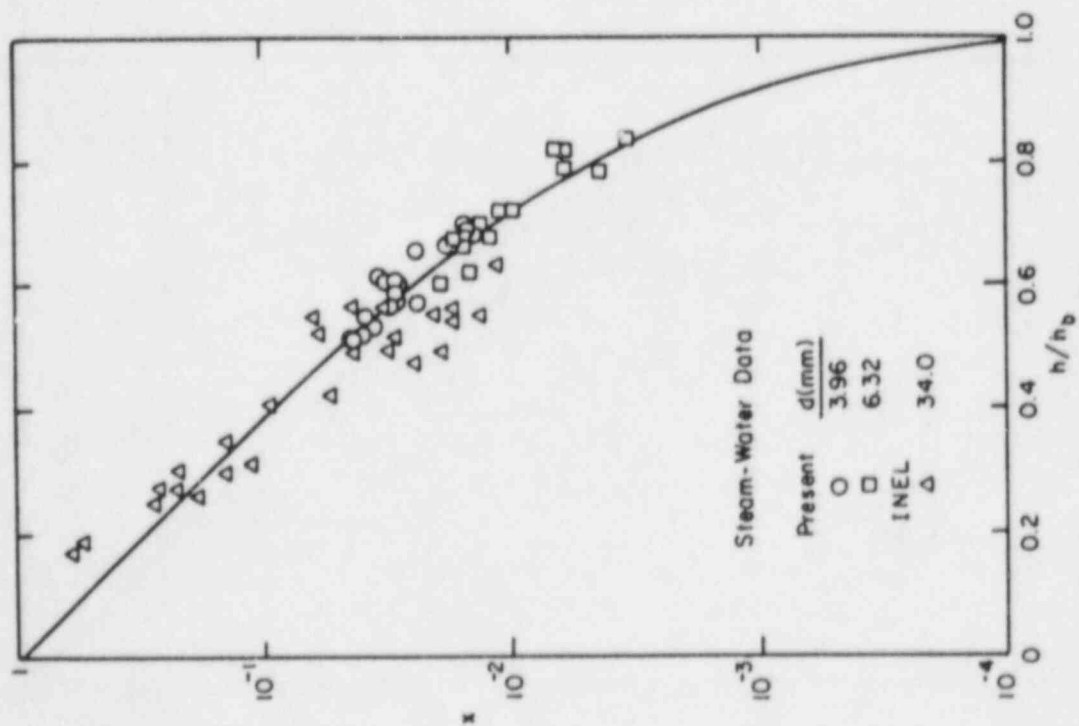


FIG. 10. BREAK ENTRANCE QUALITY AS A FUNCTION OF  $h/h_b$  FOR DOWNWARD ORIENTED BREAK

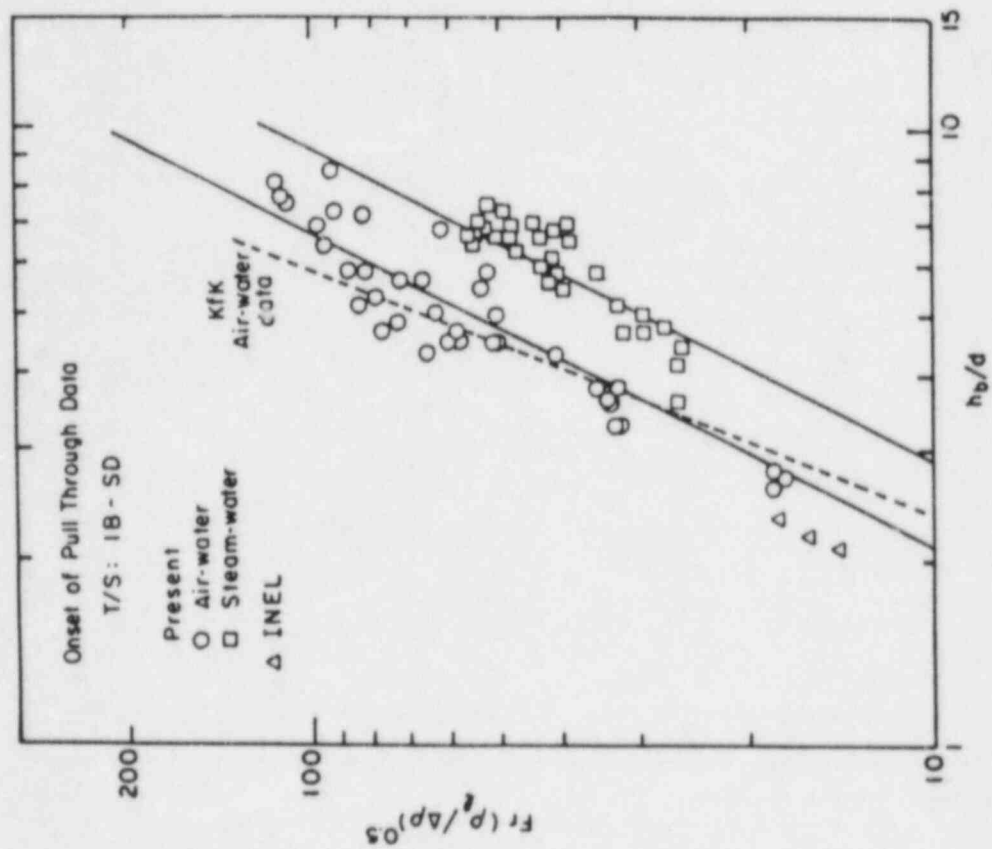


FIG. 11. VAPOR PULL-THROUGH INCEPTION FOR SIDE ORIENTED BREAK

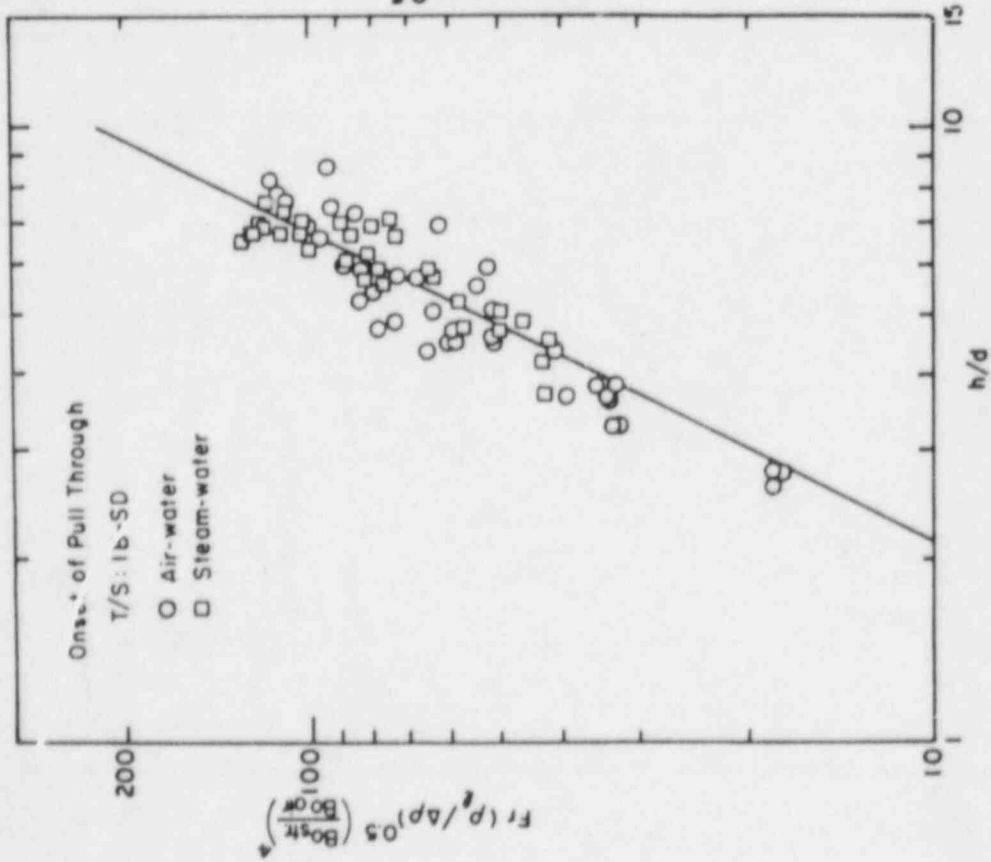
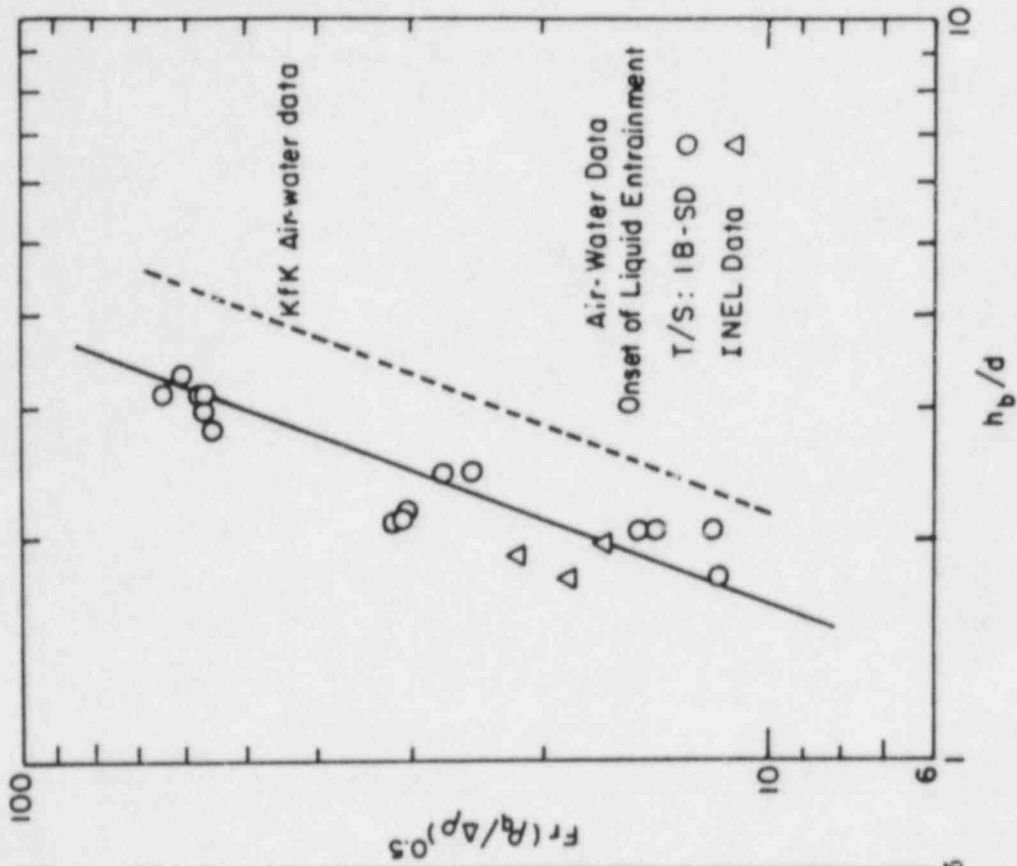


FIG. 12. VAPOR PULL-THROUGH INCEPTION USING BOND NUMBER CORRECTION FOR SIDE ORIENTED BREAK

FIG. 13. ONSET OF LIQUID ENTRAINMENT RESULTS FOR SIDE ORIENTED BREAK

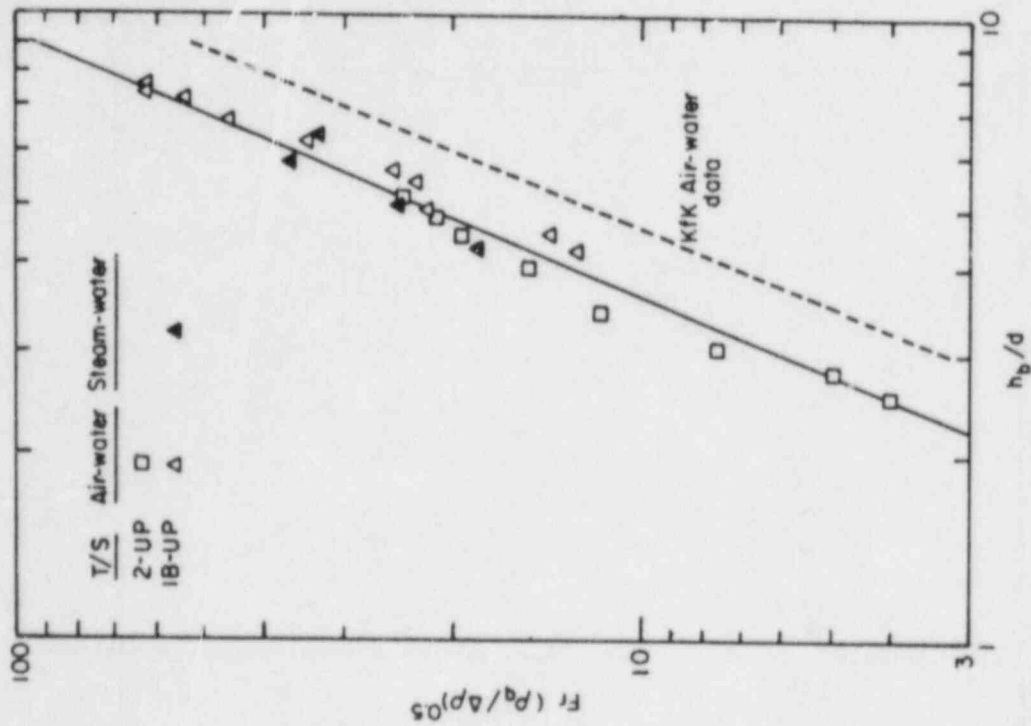


FIG. 15. ONSET OF LIQUID ENTRAINMENT RESULTS FOR TOP ORIENTED BREAK

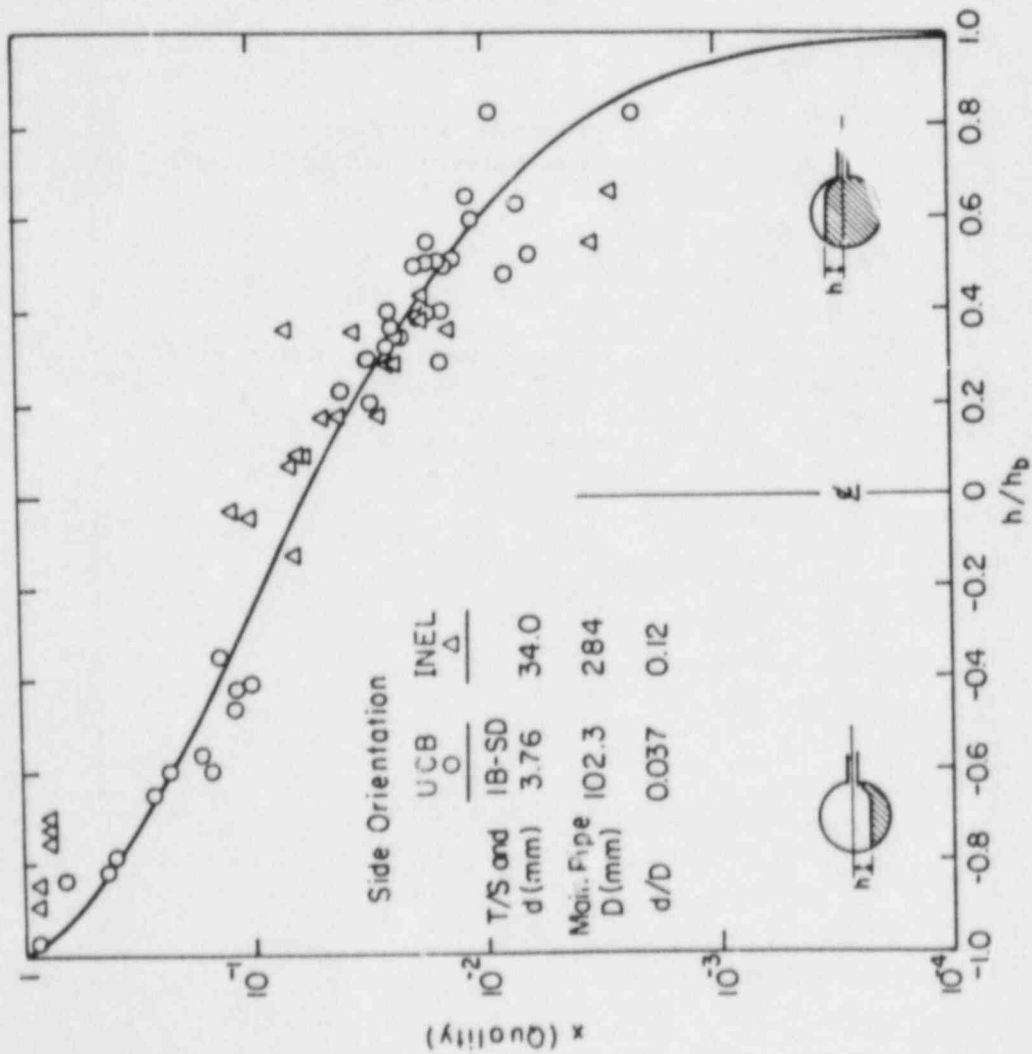


FIG. 14. BREAK ENTRANCE QUALITY AS FUNCTION OF  $h/h_b$  FOR SIDE ORIENTED BREAK

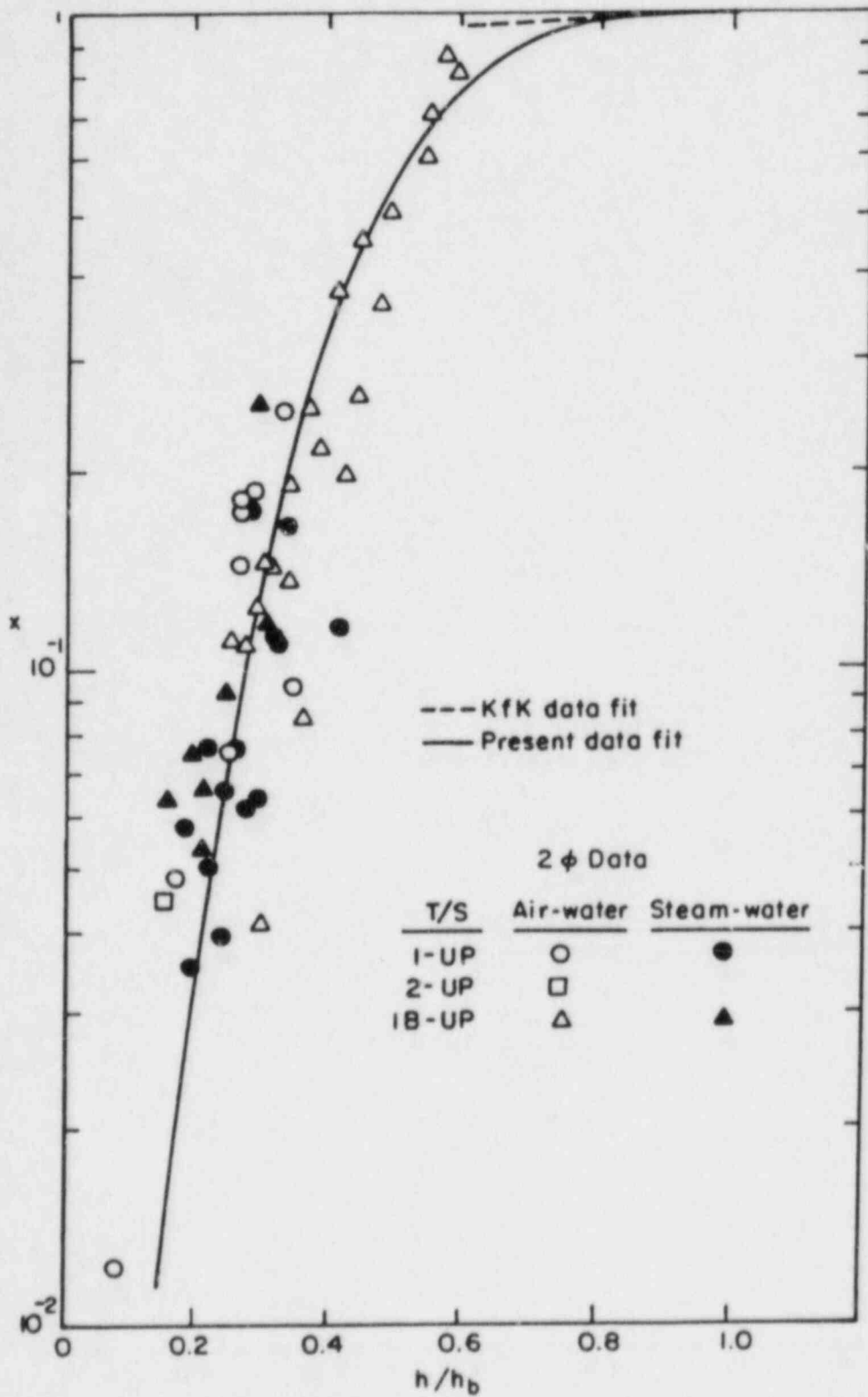


FIG. 16. BREAK ENTRANCE QUALITY AS FUNCTION OF  $h/h_b$  FOR TOP ORIENTED BREAK



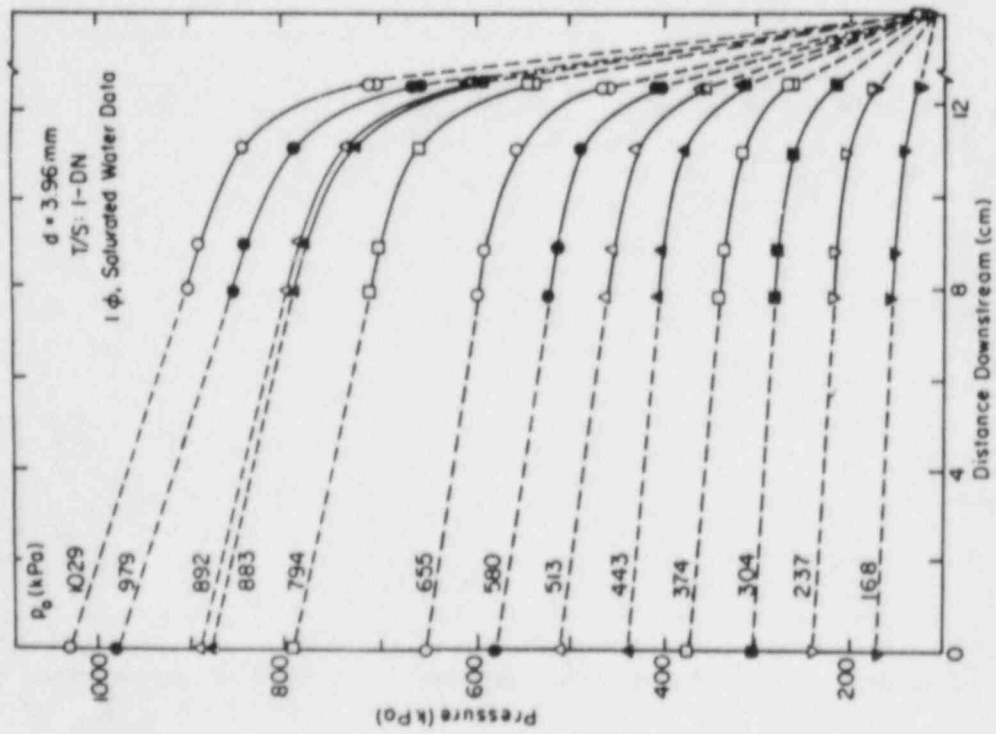


FIG. 17. PRESSURE PROFILES FOR SINGLE PHASE, SATURATED WATER ENTRANCE CONDITIONS

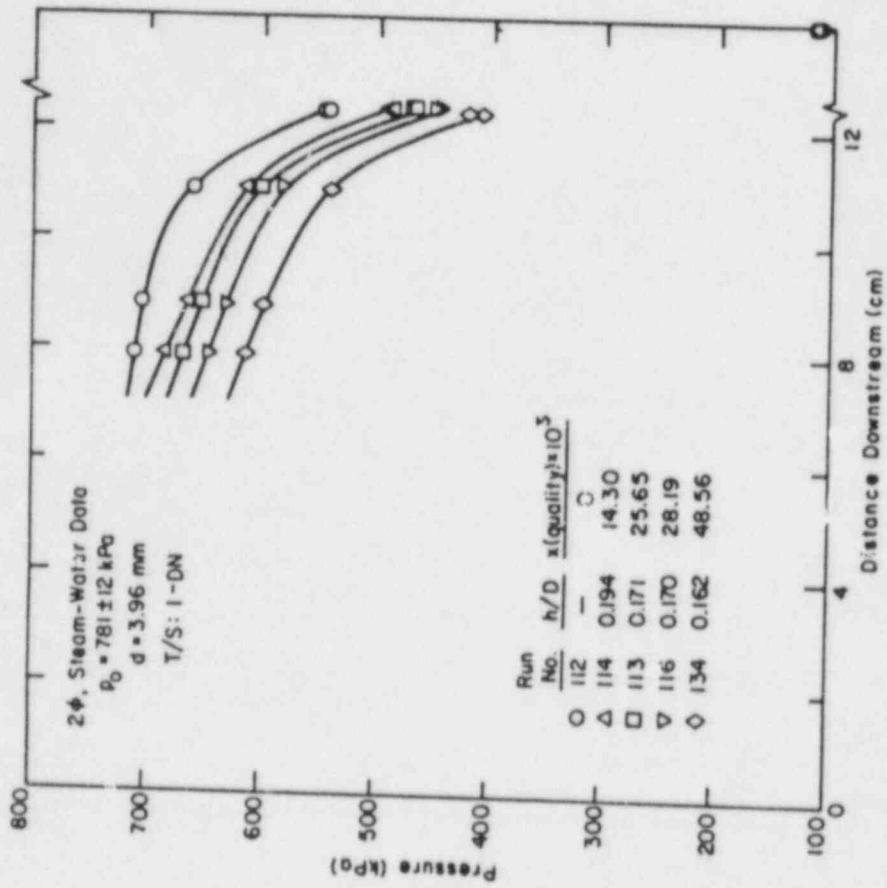


FIG. 18. PRESSURE PROFILES FOR TWO-PHASE STEAM-WATER ENTRANCE CONDITIONS

## CRITICAL FLOW THROUGH IGSCC IN PIPES

V. E. Schrock, S. T. Revankar, and S. Y. Lee  
Department of Nuclear Engineering & Lawrence Berkeley Laboratory  
University of California, Berkeley

### Abstract

The presence of intergranular stress corrosion cracks (IGSCC) in thermal stressed zones in stainless steel piping and associated components is of much concern in reactor safety. The prediction of leak rates through the cracks is important in assessing the plant reliability. An analytical model has been developed to predict flow rates of initially subcooled or saturated water through these cracks. The model assumes the flow in the crack to be homogeneous and in thermal equilibrium. The crack geometry was idealized as a convergent straight slit of constant gap thickness. The fluid is assumed to enter the crack without separation. The one dimensional model accounts for the changing cross sectional area in the flow direction. The effects of wall friction, expansions/contractions and tortuosity of the actual flow path are lumped into an equivalent friction. The numerical scheme developed for the model solution has been programmed into a Fortran computer code called SOURCE. A companion subroutine STEAM provides the saturated fluid properties. Inputs to SOURCE are the upstream stagnation pressure and temperature, the crack geometry specification, and the equivalent friction factor.

SOURCE has been assessed against the experimental data obtained in the Battelle Columbus Laboratories (BCL) study using actual crack specimens. From a parametric study of those results using SOURCE, a procedure for estimating the equivalent friction factor was identified and a subcooling correction factor developed to modify SOURCE predictions. SOURCE with the subcooling correction is recommended for use in estimating the leak rate through IGSCC cracks.

### Background

The presence of intergranular stress corrosion cracks (IGSCC's) in weld heat affected zones of types 304 and 316 stainless steel piping and associated components of commercial boiling water reactors and steam generator tubes in pressured water reactors has attracted a considerable amount of attention over the past several years [1,2]. Because of economic and safety considerations, it is highly desirable to determine if the failure of the piping system will occur in a leak-before-break mode. Leak-before break is demonstrated by establishing that postulated cracks in a pipe will be detected by leak detection methods before such cracks reach a critical size to cause unstable fracture. The ability to predict the leak rates through cracks is vital to demonstrate the leak-before-break approach to reactor safety.

Most reports on critical two-phase flow are related to flow in pipes, nozzles and orifices and there is little literature on two-phase flow in tight cracks. Agostinelli et al. [3] studied flows of flashing water and steam

through a smooth annular passages of constant area and with hydraulic diameters in the range of 0.15 to 0.43 mm. Test data were obtained with stagnation conditions of pressure from 3.50 to 20.51 MPa and subcooling from 9.3 to 67 C. Hendricks et al. [4] made a qualitative study of radially inward flow of liquid nitrogen through a 0.076 mm gap between parallel glass plates. Flashing was seen to occur near the end of the 0.72 cm radial flow passage. Simoneau [5] carried out an experimental study of two-phase nitrogen flow through a rectangular slit. The test section was 2.54 cm in length and width, with a gap of 0.292 mm. He concluded that a uniform two-phase flow pattern existed in most of the test runs and that flashing started at or near the exit plane. Amos and Schrock [6] carried out experiments on rectangular slits 20 mm in width, gaps of 0.127 to 0.318 mm and L/D ratios from 83 to 400. Their data for subcooled water at pressures from 4.1 to 16.2 were intended to simulate crack leakage at LWR conditions. The results showed that friction is a dominant factor in such channels and although the pressure profiles were not well predicted by the homogeneous equilibrium model, compensating effects result in the measured critical mass flux being less than 20% greater than the HEM prediction.

More recently, an experimental program was carried out at BCL by Collier et al. [7]. The experiments were done in two phases. In the first, simulated cracks were used while in the second actual IGSCC cracks were used. Partially cracked pipes were machined on the outer surface to remove a portion of the uncracked wall material thus creating a through-crack which served as the test flow channel. The test sections produced in this way are illustrated in Figure 1. Five different crack channels were tested. BCL [8] developed an analytical model by extending Henry's [9] non-equilibrium homogeneous model to account for flow area change and bends in the flow path. Further modifications were made to this model by Abdollahian and Chexal [10] to improve its agreement with the data. Both versions of this model, coded into programs LEAK and LEAK 01 respectively, assumed that flashing always begins at an L/D of 12 and that the quality varies linearly with distance along the flow path. Quality was evaluated assuming an isentropic process in LEAK and an isenthalpic process in LEAK 01. The calculations were done by separately calculating channel pressure drop due to momentum and friction based upon length averaged conditions rather than solving the equations in a marching method to obtain the distribution of pressure and quality along the crack length.

Work done at General Electric Co. [11] gives some indication of the global features of IGSCC geometry. The crack cross sectional area, A, can be related to the surface crack length,  $\ell$ , as

$$A = \frac{\sigma}{2E} \ell^2 \pi F\left(\frac{\sigma}{\sigma_y}\right) \quad (1)$$

Here the function  $F$  is of order unity. For a typical stress  $\sigma = 8 \times 10^3$  psi and  $E = 26 \times 10^6$  psi, the area is given as

$$A = 5 \times 10^{-4} \ell^2 \quad (2)$$

Thus the equivalent gap would be

$$t = 5 \times 10^{-4} \ell \quad (3)$$

These relations apply to cracks that penetrate through the pipe to produce the circumferential length  $\ell$ . As such, they may be different than the cracks of the BCL experiments. However these relations were used to choose the gap range of interest in Amos's experiment [6]. In figure 2 photomicrographs of typical IGSCC in weld sensitized type 304 stainless steel are shown. These pictures reveal the tortuous and irregular nature of the channel with many expansion and contractions along the passage.

#### Modelling

Based upon the results of Amos's experiment [6], we do not believe that flow entering crack separates giving the type of phenomenon that Henry sought to represent by his model. Furthermore, the assumption of linear quality variation with length is not consistent with Fanno flashing flow in straight pipes and is probably not valid for crack flow. In view of the need to have a model that adds little to the running time costs of large code into which it is incorporated and also from the experience of Amos's calculations it appeared that the HEM is a good choice for the crack problem. Thus we have developed a computer code based upon the steady state form of the homogeneous equilibrium model. The geometry for the problem is depicted in Figures 3 and 4. The governing equations are:

Continuity:

$$\frac{d}{dz} (\rho AV) = 0 \quad (4)$$

Momentum:

$$-\frac{dp}{dz} = \rho V \frac{dV}{dz} + \tau_w \frac{P}{A} \quad (5)$$

Energy:

$$\frac{d}{dz} \left( h + \frac{V^2}{2} \right) = 0 \quad (6)$$

State

(1) Two-Phase

$$v = (1 - x)v_f(p) + x v_g(p) = v_f(p) + x[v_g(p) - v_f(p)] \quad (7)$$

$$h = (1 - x)h_f(p) + x h_g(p) = h_f(p) + x [h_g(p) - h_f(p)] \quad (8)$$

(2) Single Phase Liquid

$$v_\ell \sim \text{constant} = v_f(T_o) \quad (9)$$

$$h_\ell \sim h_f(T_o) \quad (10)$$

Critical Flow Criterion

$$v_a = v_e = \left\{ \left( \frac{\partial p}{\partial \rho} \right)_e \right\}^{1/2} \quad (11)$$

$$v_c = v_a = v \left[ - \left\{ (1-x) \frac{\partial v_f}{\partial p} + x \frac{\partial v_g}{\partial p} + (v_g - v_f) \left( \frac{\partial x}{\partial p} \right)_s \right\} \right]^{1/2} \quad (12)$$

where

$$\left( \frac{\partial x}{\partial p} \right)_s = \frac{\left( \frac{\partial s_f}{\partial p} \right) (1-x) + x \left( \frac{\partial s_g}{\partial p} \right)}{(s_g - s_f)}$$

The wall sheer term in Equation 5 was represented by an equivalent friction factor in the usual form

$$\left( \frac{dp}{dz} \right)_f = \frac{f_e}{D} \frac{\rho v^2}{2} \quad (13)$$

and

$$f_e = f + D \sum_i n_i K_i \quad (14)$$

where  $f$  is the rough pipe friction, the  $K_i$  represent the loss factors for specific effects such as bends, contractions, expansion, and tortuosity, and the  $n_i$  represent the number per unit length in the flow direction of the type  $i$ . A properties subroutine was developed using the equations for water given by Ishimoto et al. [12]. This is a very efficient and accurate package for saturation property evaluation.

These equations were put into finite difference form and a Fortran code called SOURCE was developed. The calculation is initiated by assuming the mass flowrate and then the calculation marches downstream to obtain the fluid conditions in the channel. If choking is encountered before reaching the end of the channel the calculation is stopped and the mass flowrate is

reduced for the next pass. If the calculation reaches the end of the channel with the flow still subcritical the flowrate is increased for the next pass. The procedure is continued until the mass flowrate is found that corresponds to choking at the outlet. Details of the coding will be presented elsewhere. The code has been found to be very fast running and can complete a typical evaluation in about 3 seconds of CPU time on an IBM 3081.

### Results

The SOURCE code was used to conduct a parametric study of the BCL data in order to determine the best fit equivalent friction factor for each of the five crack geometries. Of the 83 runs reported by BCL 22 were disqualified for this purpose because they showed major discrepancies with the general trends of data dependence upon stagnation pressure and subcooling. For each of the remaining 61 tests, SOURCE was used with a minimum of three trial values of the equivalent friction factor. Each computation produced a predicted mass flowrate which was compared to the measured value. In this way an optimum equivalent friction factor was found that best fit all the data for each test section. This involved a graphical interpolation procedure. Once the optimum equivalent friction factor was obtained it was used to again run SOURCE for each test condition. When these results were compared it was apparent that a systematic deviation existed between the prediction and the data that was dependent upon the stagnation subcooling. A correction factor was therefore developed as shown in Figure 5. The predicted value then becomes the SOURCE result multiplied by the correction factor. The correction factor is given by

$$\begin{aligned}
 C &= 1.3015 - 5.3075 \times 10^{-3} \Delta T_{\text{sub}} \quad \text{for } \Delta T_{\text{sub}} < 60\text{C} \\
 &= 1.0 \quad \text{for } \Delta T_{\text{sub}} > 60\text{C}
 \end{aligned}
 \tag{15}$$

Applying the correction factor to all of SOURCE predictions then gave the comparison between the final prediction and the experimental data shown in Figure 6. Considering the evident lack of coherence in the basic BCL data, this final comparison is remarkably good. Consequently it is felt that predictive method developed here offers excellent capability to predict crack flows if the geometry is known. The greatest uncertainty in the use of the method will result from the rather uncertain details of the crack geometry. It should be noted that the optimum friction factor found for one of the test sections was exceptionally high. The low measured mass flowrates for this test section were pointed out by the BCL group who suggested that the crack may have plugged by fine particulate material swept by the flow. This is another uncertainty regarding crack geometry. The SOURCE model could be modified to include changing gap thickness in the flow direction but such a complication does not seem warranted when the crack geometry is so uncertain.

Figures 7, 9, and 11 and Figures 8, 10 and 12 show quality and pressure profiles respectively predicted by SOURCE for three levels of stagnation subcooling. The most striking feature of these predictions is the extreme nonlinearity and the very strong gradient near the channel exit plane.

#### Concluding Remarks

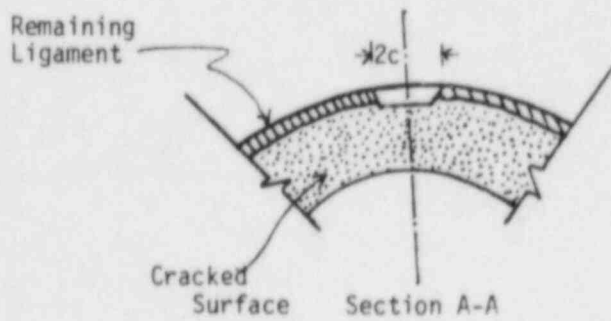
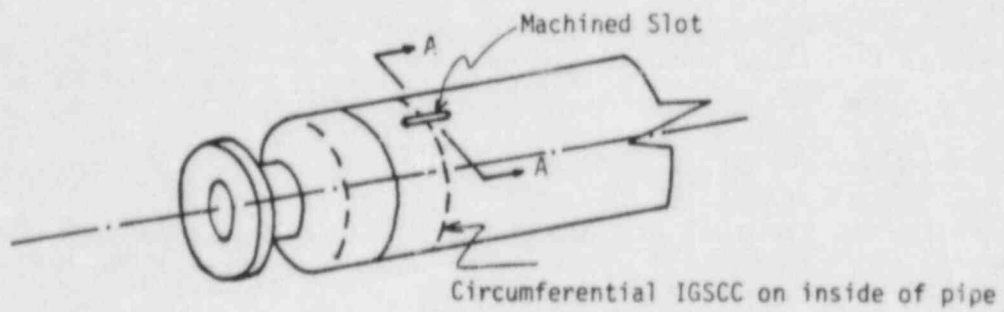
A computer code has been developed based upon the homogeneous equilibrium model and an equivalent friction factor that represents the physical features of IGSCC cracks. The code was used in a parametric study of the BCL experiment data from which optimum equivalent factors were determined for each crack. These factors lead to the development of a subcooling correction factor which applied to predictions brings them into close agreement with the data. In addition the optimum friction factors were used to improve the method of their estimation from the known physical features of IGSCC cracks. The code SOURCE is very fast running and should be adaptable to large systems codes without significant sacrifice in cost. The method developed is recommended for use in estimating leakage through IGSCC cracks.

#### References

1. Walker, W.L. and Higgins, J.P., "Performance of 304 Stainless Steel Structural Components in General Electric Company Boiling Water Reactor," Paper No. 103, NACE Corrosion Conference. Anaheim, CA, 1973.
2. Klepfer, H.H., et al., "Investigation of Cause of Cracking in Austenitic Stainless Steel Piping," General Electric Report NEDO- 21,000, July 1975
3. Agostinelli, A., Salemann, V. and Harrison, N.J., "Predictions of Flashing Water Flow Through Fine Annular Clearances," ASME Transactions, Vol. 80, 1958, pp. 1138-1142.
4. Hendricks, R.C., Simoneau, R.J. and Usu, Y.Y., "A Visual Study of Radial Inward Flow of Subcooled Nitrogen," in: Advanced in Cryogenic Engineering, Vol. 20, K.D. Timmehaus, ed., Plenum Press, New York, p. 370, 1975.
5. Simoneau, R.J., "Two-Phase Choked Flow of Subcooled Nitrogen Through a Slit," NASA Lewis Research Center, NASA TM-71516, 1974.
6. Amos, C.N. and Schrock, V.E., "Critical Discharge of Initially Subcooled Water Through Slits," NUREG/CR-3475, LBL-16363, 1983.
7. Collier, R.P., Stulen, F.B., Mayfield, M.E., Pope, D.B. and Scott, P.M., "Two-Phase Flow Through Intergranular Stress Corrosion Cracks and Resulting Acoustic Emission," EPRI Final Report NP-3540-LD, RP-T118-2, 1980.
8. Mayfield, M.E., et al., "Cold Leg Integrity Evaluation - Final Report," NUREG/CR-1319, Battelle Columbus Laboratories, 1980.

9. Henry, R.E., "The Two-Phase Critical Discharge of Initially Saturated or Subcooled Liquid," Nuclear Science and Engineering Vol. 41, op. 336, 1970.
10. Abdollahian, D. and Chexal, D., "Calculation of Leak Rates Through Cracks in Pipes and Tubes," EPRI Final Report NP-3395 RP-1757-19, December 1983.
11. General Electric Report NEDC-24750-4.
12. Ishimoto, S., Uematsu, M., Tanishita, I., "New Equations for the Thermodynamic Properties of Saturated Water and Steam". Bulletin of the JSME Vol. 15, No. 88, p. 1278, 1972.





1 a.

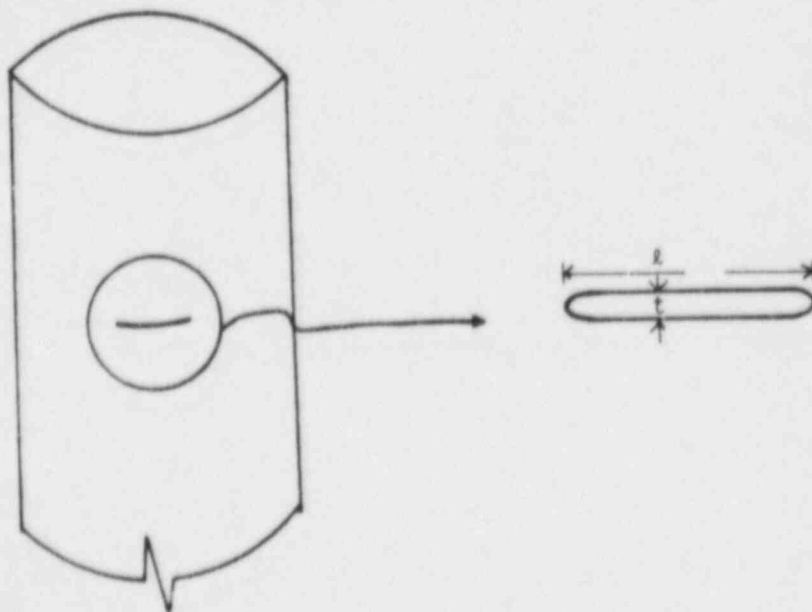
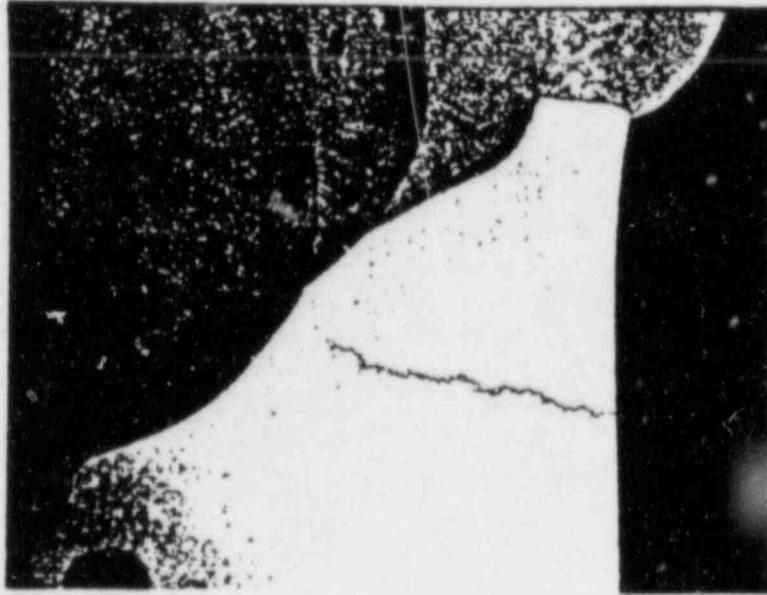
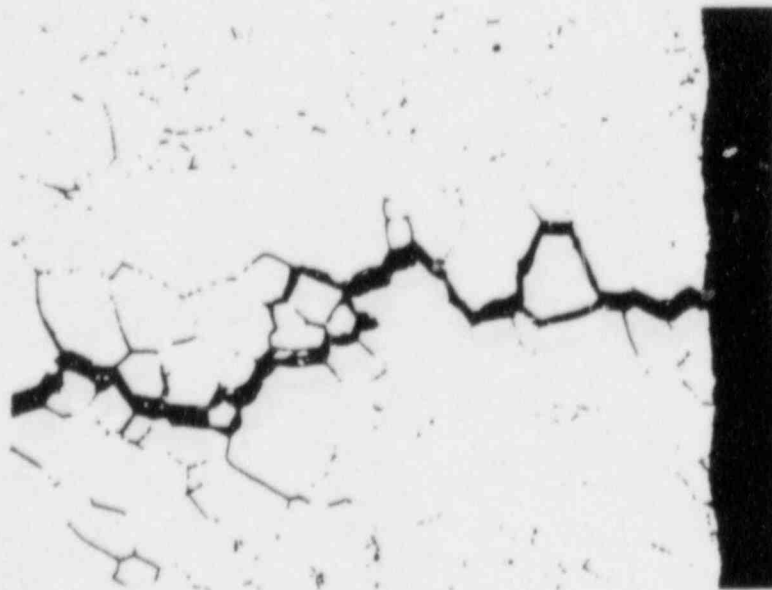


FIG. 1. SKETCH OF CRACK DETAIL



IGSCC IN WELD HEAT AFFECTED ZONE - 8X



HIGHER MAGNIFICATION - 125X

FIG. 2. PHOTOMICROGRAPHS OF TYPICAL IGSCC IN WELD SENSITIZED TYPE 304 STAINLESS STEEL



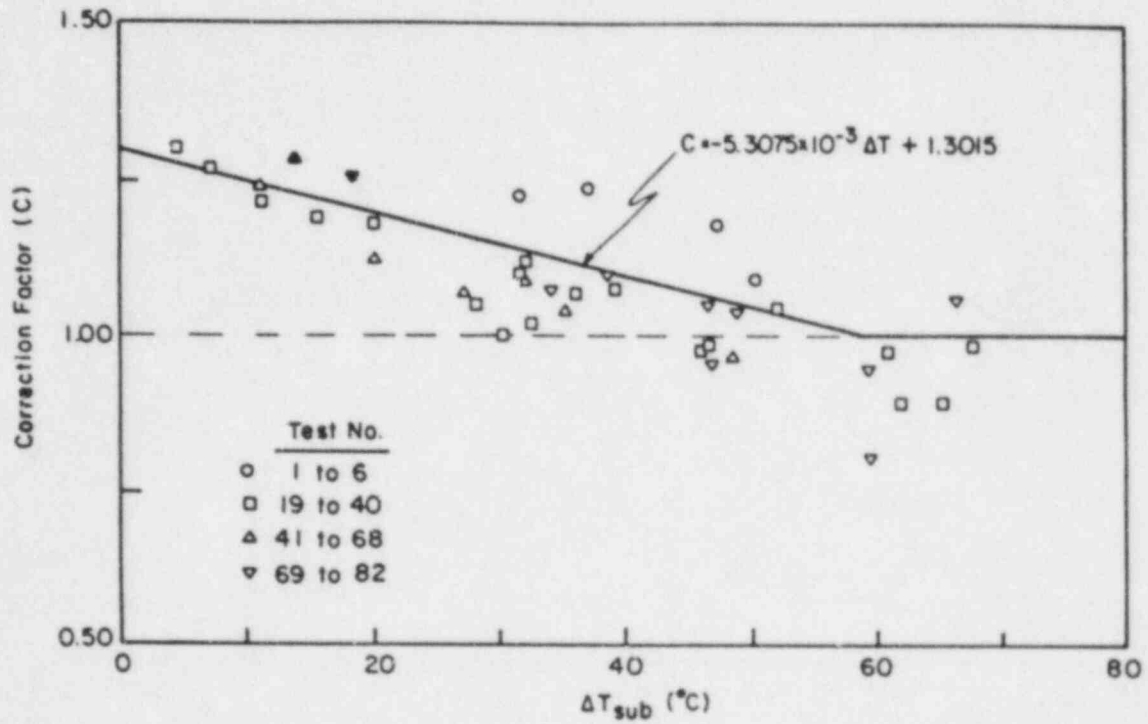


FIG. 5. SUBCOOLING CORRECTION FOR 'SOURCE'

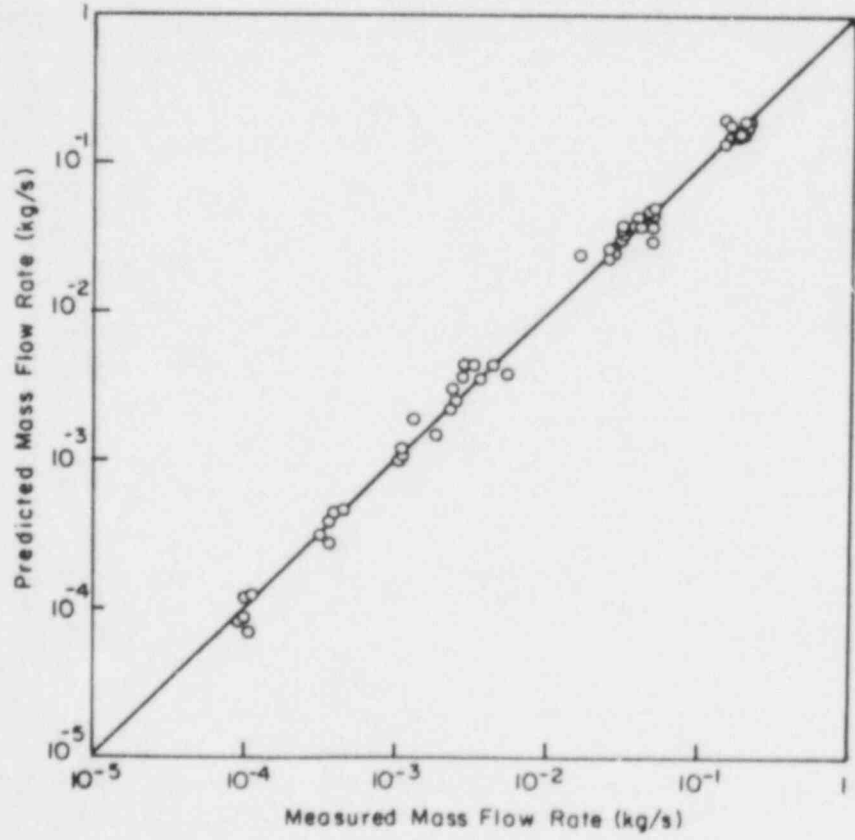


FIG. 6. CORRECTED SOURCE PREDICTIONS COMPARED WITH BCL DATA

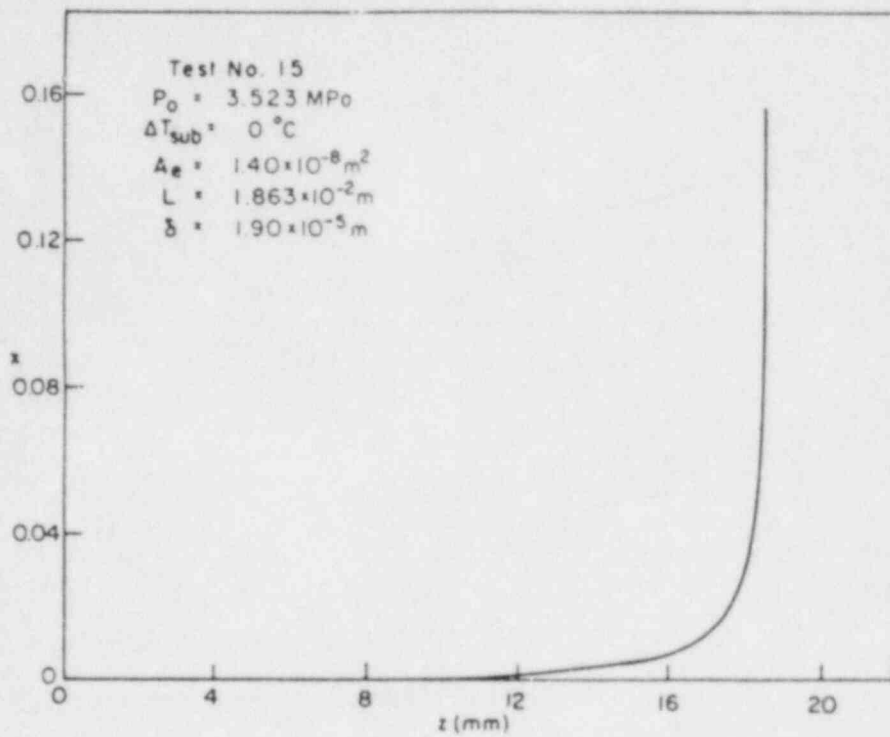


FIG. 7. PREDICTED QUALITY PROFILE FOR BCL TEST NO. 15 CONDITIONS (ZERO SUBCOOLING)

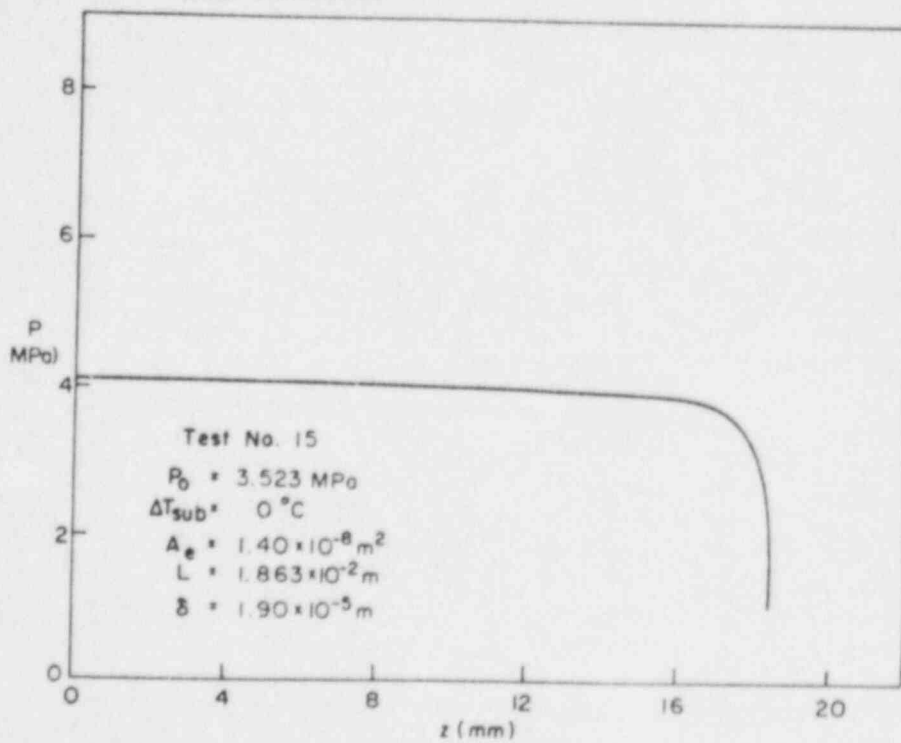


FIG. 8. PREDICTED PRESSURE PROFILE FOR BCL TEST NO. 15 CONDITIONS (ZERO SUBCOOLING)

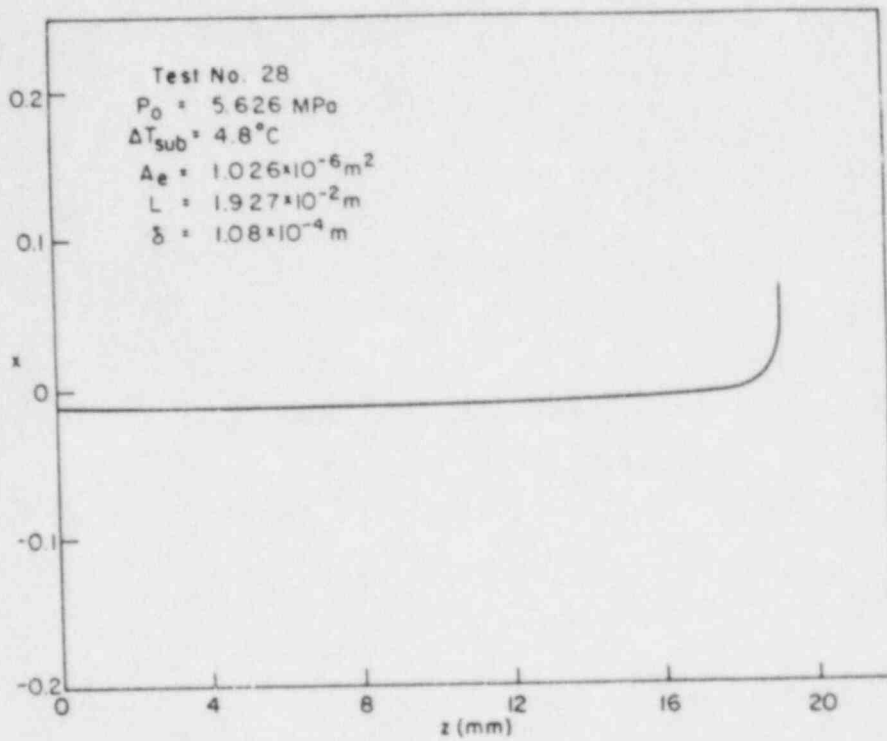


FIG. 9. PREDICTED QUALITY PROFILE FOR BCL TEST NO. 28 CONDITIONS (LOW SUBCOOLING)

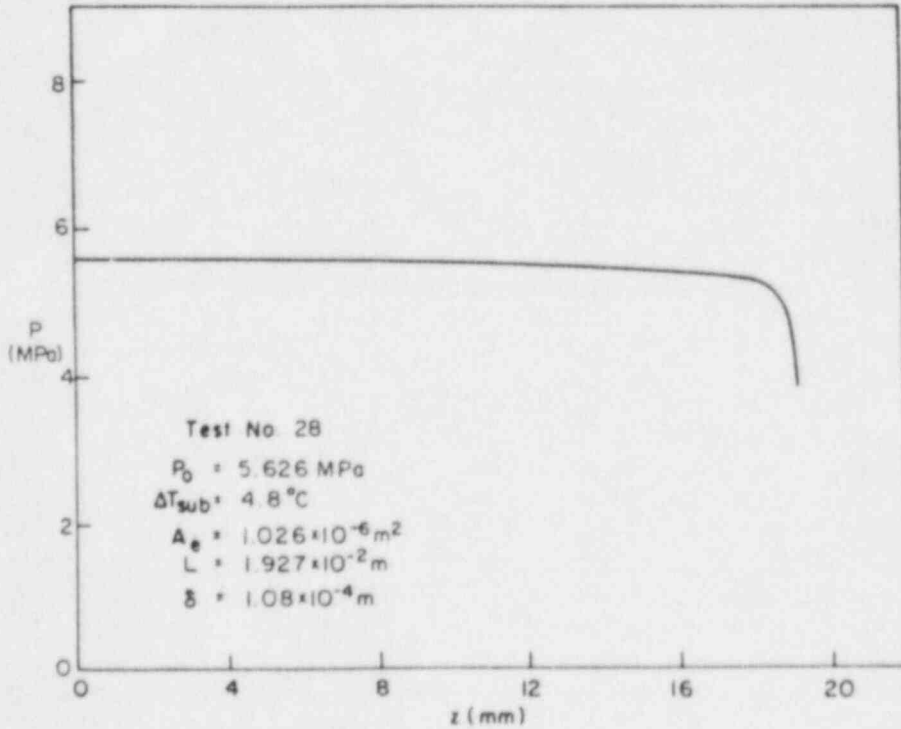


FIG. 10. PREDICTED PRESSURE PROFILE FOR BCL TEST NO. 28 CONDITIONS (LOW SUBCOOLING)

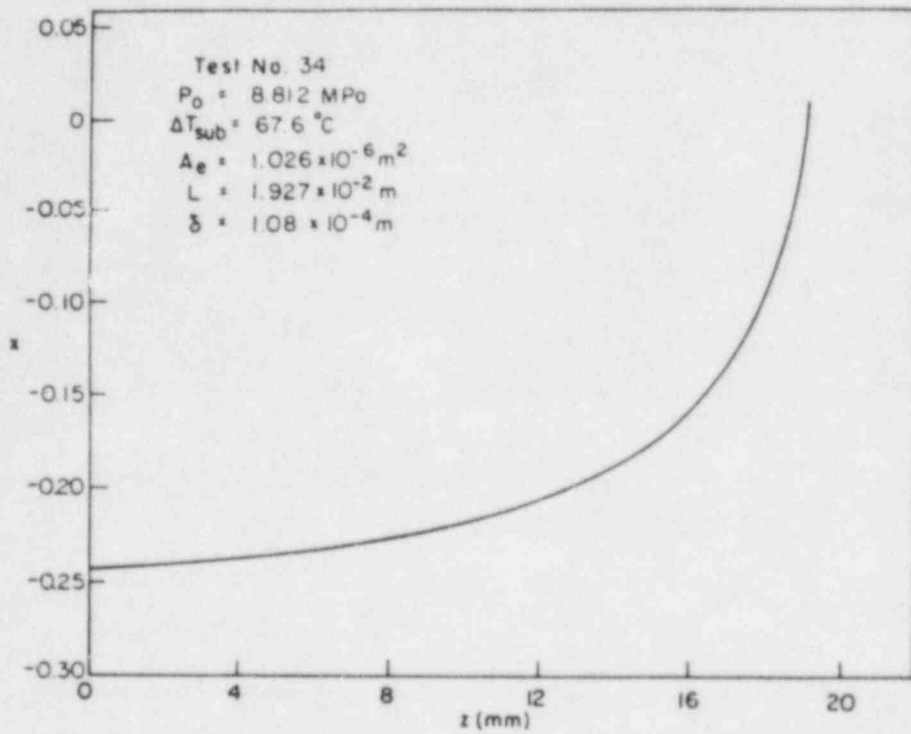


FIG. 11. PREDICTED QUALITY PROFILE FOR BCL TEST NO. 34 CONDITIONS (HIGH SUBCOOLING)

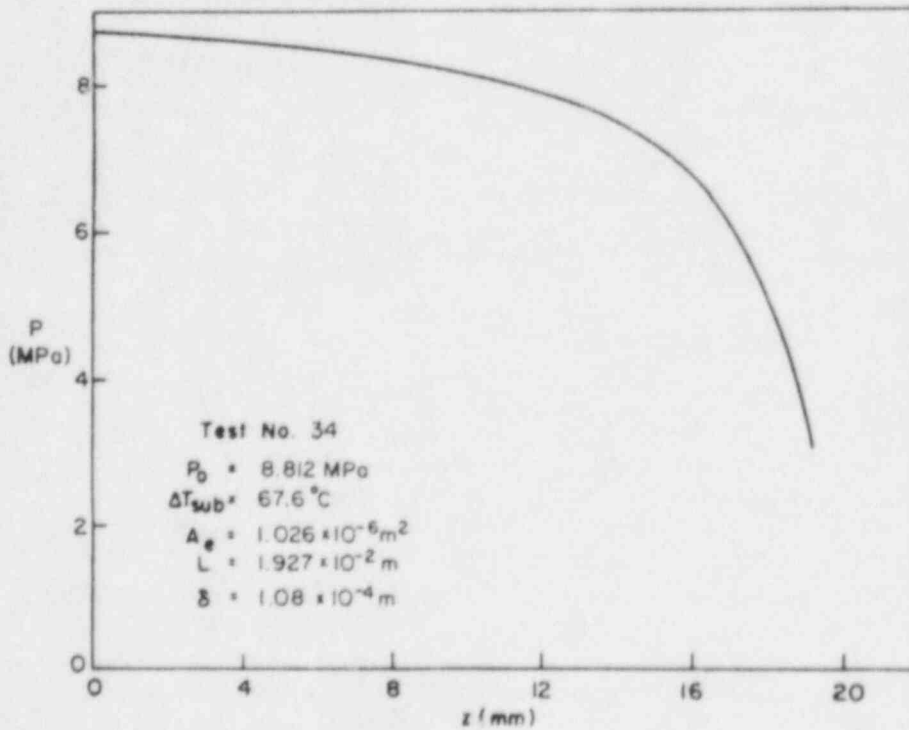


FIG. 12. PREDICTED PRESSURE PROFILE FOR BCL TEST NO. 34 CONDITIONS (HIGH SUBCOOLING)

A FINAL REPORT ON THERMAL MIXING FOR PTS ANALYSES

T.G. Theofanous\*  
School of Nuclear Engineering  
Purdue University  
W. Lafayette, IN 47906

This presentation brings together recent results of PTS-oriented thermal mixing work for the purpose of providing the evidence necessary to consider this problem closed.

From a detailed consideration of the multitude of PTS scenarios [1,2,3] and the quantitative, system-wide, thermal-hydraulic response of representative sets of such scenarios [4,5,6,7] a rather effective focusing of the thermal-mixing aspects of the problem has emerged.

(a) All-loop Natural Circulation. This condition pertains to the vast majority of cases. Natural circulation flows are typically 10 to 20 times HPI flows and good mixing within the cold leg can be expected [8]. Stratification is absent and system's code results are directly applicable.

(b) Asymmetric Loop Operation. This condition has been identified to result from reverse heat transfer in the isolated steam generator(s) leading to loop flow stagnation. The remaining steam generators continue to promote natural circulation within their respective primary coolant loops. A couple of different analytical approaches [9,10] have shown that under such conditions the circulating loops dominate the downcomer response, which, therefore, for practical purposes may be treated as well mixed. System's code results are directly applicable to this case also, provided that spurious, strong oscillations in the stagnated loop(s) are absent.

---

\*Present Address: Chemical and Nuclear Engineering  
University of California, Santa Barbara, CA 93106



(c) Complete and Persistent Stagnation. This condition was found to arise from LOCA events where coolant loss could not be fully compensated by the high pressure emergency injection system. With a sufficient amount of coolant loss all natural circulation paths are interrupted by steam bubbles and complete stagnation can be obtained. However, only a small subset of such LOCAs, those with intermediate size breaks, can maintain the high primary system pressures of interest for potential PTS. Both TRAC and RELAP-5 results indicate that under such conditions a quasi-equilibrium between coolant loss and HPI may be achieved with system pressures decaying slowly, within the 1100 to 700 psi range over a period of several hours. Inability of these codes to handle the stratified regime has prevented a clear elucidation of the detailed physics of the stagnation phenomena, and of subsequent system response, particularly with regards to rates of depressurization and/or reestablishment of natural circulation. The resulting focus of thermal mixing work in this area is, therefore, to quantify stratification under complete and unlimited, in time, stagnation.

High pressure, and makeup, injection in a fully stagnated reactor coolant loop gives rise to a transient cooldown process. The cooldown is driven by the cold injection water and it is moderated by the quantities of hot primary fluid that can participate in the mixing process and by the associated structural heat. All primary system fluid that can reach the HPI location by a series of horizontal or vertical displacements is available to participate. This includes cold leg, downcomer, and major portions of the lower plenum, pumps, and loop seals [11,12]. As mentioned, earlier system's code results

are not reliable, in this regime, for indicating net flow throughputs and directions. It is generally agreed, however, that it is adequate (and conservative) to consider that all net flow throughput is into the reactor core. The task is to quantify stratification and associated cooldown transients, particularly within the downcomer region, for specific reactor geometrics and injection conditions.

Clearly, integral experimental simulations had to satisfy geometric and Froude number similarity. At small scales this leads to large distortions in momentum fluxes and Reynolds numbers. This is further aggravated at low pressure thermal simulations because of the small  $\Delta\rho/\rho$  values attainable. Uncertainties associated with such effects, and the need for highly reliable results, led to a whole array of experimental facilities spanning a range of scales (see Figure 1), both thermal and salt induced bouyancy, and a variety of measurement techniques [13]. Through the use of the Regional Mixing Models (RMM) [8,11,12] and the associated computer programs REMIX and NEWMIX [14] it has been possible to quantitatively interpret and thus unify the complete database thus generated.

The overall process conforms to the basic concept of the RMM, namely, that of quasi-steady decay of cold streams within a slowly varying "ambient." Three cold leg and a single downcomer mixing regimes have been identified, as shown in Figure 2. The low Froude number downwards injection regime is typical of Westinghouse and Combustion Engineering plants. A well-defined nearly vertical plume travels the height of the hot stream before it becomes submerged into the cold stream. The amount of entrainment depends upon the injection Froude number and extent of exposure (L/D) to the hot stream [11,12]. It may also be expressed in the form of Figure 3, where  $Q$  is the

entrainment rate normalized by the HPI flow rate,  $A^*$  is the area of the cold stream normalized by the cold leg flow area,  $D_r$  is the cold leg diameter normalized by the injector diameter, and  $Fr_{HPI,CL}$  is the Froude number based on HPI flow rate and cold leg dimensions.\* On the other hand the counter-current flow limitation at the cold leg exit [11,12]

$$F_{cs}^2 + F_{hs}^2 = 1$$

may also be expressed in terms of  $Q^*$ ,  $A^*$ ,  $Fr_{HPI,CL}$ , and  $\phi^* = \rho_{hs} / \rho_{HPI}$  as shown in Figure 4 [16]. According to the RMM procedure, for any particular value of  $Fr_{HPI,CL}$ , the solution is obtained by intersection of the corresponding lines in Figures 3 and 4. The high Froude number regime is typical of Babcock & Wilcox reactors and is characterized by a forceful jet of sufficient momentum to impact the opposite wall, and splash creating a convoluted, highly chaotic flow pattern. Entrainment of hot stream fluid under such conditions should proceed at the maximum possible rate allowed by the counter-current flow criteria. This corresponds to the maxima of Figure 4 [16]; that is, for any particular  $\phi^*$  and  $Fr_{HPI,CL}$ , the rate of entrainment and the height of the cold stream may be read directly off Figure 4. Clearly, this mixing regime should be largely independent of the orientation of injection. The low Froude number upwards, or horizontal, injection regime was examined in connection with a proposed thermal mixing test at the full-scale UPTF facility in Germany. Scoping tests at Purdue's 1/2-scale facility revealed a quiet flow pattern and very low mixing and led to the recommendation

\*Effects of backflow in the injection line and associated mixing have also been discussed [15].

that the design be changed to yield either one of the other two regimes mentioned above [20]. Finally, downcomer behavior entails the decay of the planar plumes created by the cold stream exiting the cold legs. Initial conditions for such plumes were established with the help of Purdue's 1/2-scale tests [8,15,17]. The planar plume is taken to form within a distance of two cold leg diameters below the cold leg centerline and to be fed in equal volumetric flow rates by the cold stream and the surrounding hot fluid. Below this point the decay is approximated to that of a planar plume of initial width equal to  $D_{CL}$  and  $FR_I = 1.0$ .

Representative comparisons to the CREARE 1/5-scale data have been presented in [12]. Documentation of the full set is given in [18]. The Purdue 1/2-scale data and associated interpretation may be found in [8,9,15,16,17,18,19]. A representative interpretation of the CREARE 1/2-scale experiments may be found in [13]. A full documentation is given in [18]. Similarly consistent interpretations were possible with the first round of the CREARE 1/2-scale data obtained under the interference of a spurious heat source in the lower plenum, provided the reported magnitude of this effect was taken into account. As these data have not been officially released said comparisons have not been documented. Except for a single CREARE 1/5-scale test and a single Purdue 1/2-scale test which fell in the high Froude number regime, all above tests belong in the low Froude number regime. Additional interpretations in the high Froude number regime have been made with reference to the IVO (Finish) tests. As these data are proprietary, the comparisons have not been documented. The IVO facility is presently utilized in a joint USNRC/IVO program to

investigate multiloop effects in the downcomer. The preliminary review of these data indicated that asymmetric loop operation yields a well mixed downcomer, confirming the analyses mentioned above, while multiple downcomer plumes under stagnant loop conditions exhibit better mixing (shorter plumes) as compared to single loop operation. Finally, successful pretest predictions of the initial round of the full-scale HDR data (Germany) have been documented [13,18]. Predictions of the subsequent sets have also been made but have not been released as yet. The work will culminate with the interpretation of the UPTF thermal mixing data expected in the next 3 to 6 months.

Reactor predictions of the REMIX/NEWMIX have also been documented [6,7,16,17]. For the high Froude number regime and conditions typical of B&W reactors maximum cold leg stratification of  $\sim 40^{\circ}\text{C}$  has been obtained. With the additional mixing in the downcomer entrance region a peak downcomer stratification of less than  $20^{\circ}\text{C}$  can be expected [16]. For the low Froude number regime conditions typical of Westinghouse and Combustion Engineering plants, a maximum cold leg stratification of  $60$  to  $80^{\circ}\text{C}$  was predicted, yielding an expected downcomer stratification of  $30$  to  $40^{\circ}\text{C}$  [17]. Furthermore, as illustrated in Figures 5 and 6 the cooldown transient is relatively slow yielding modest temperature gradients within the reactor vessel wall.

#### REFERENCES

1. Burns, T.J., et al., "Preliminary Development of an Integrated Approach to the Evaluation of Pressurized Thermal Shock Risk as Applied to the Oconee Unit 1 Nuclear Power Plant," NUREG/CR-3770 (ORNL/TM-9176), November 1985.
2. Selby, D.L., et al., "Pressurized Thermal Shock Evaluation of the Calvert Cliffs Unit 1 Nuclear Power Plant," NUREG/CR-4022 (ORNL/TM-9408), September 1985.

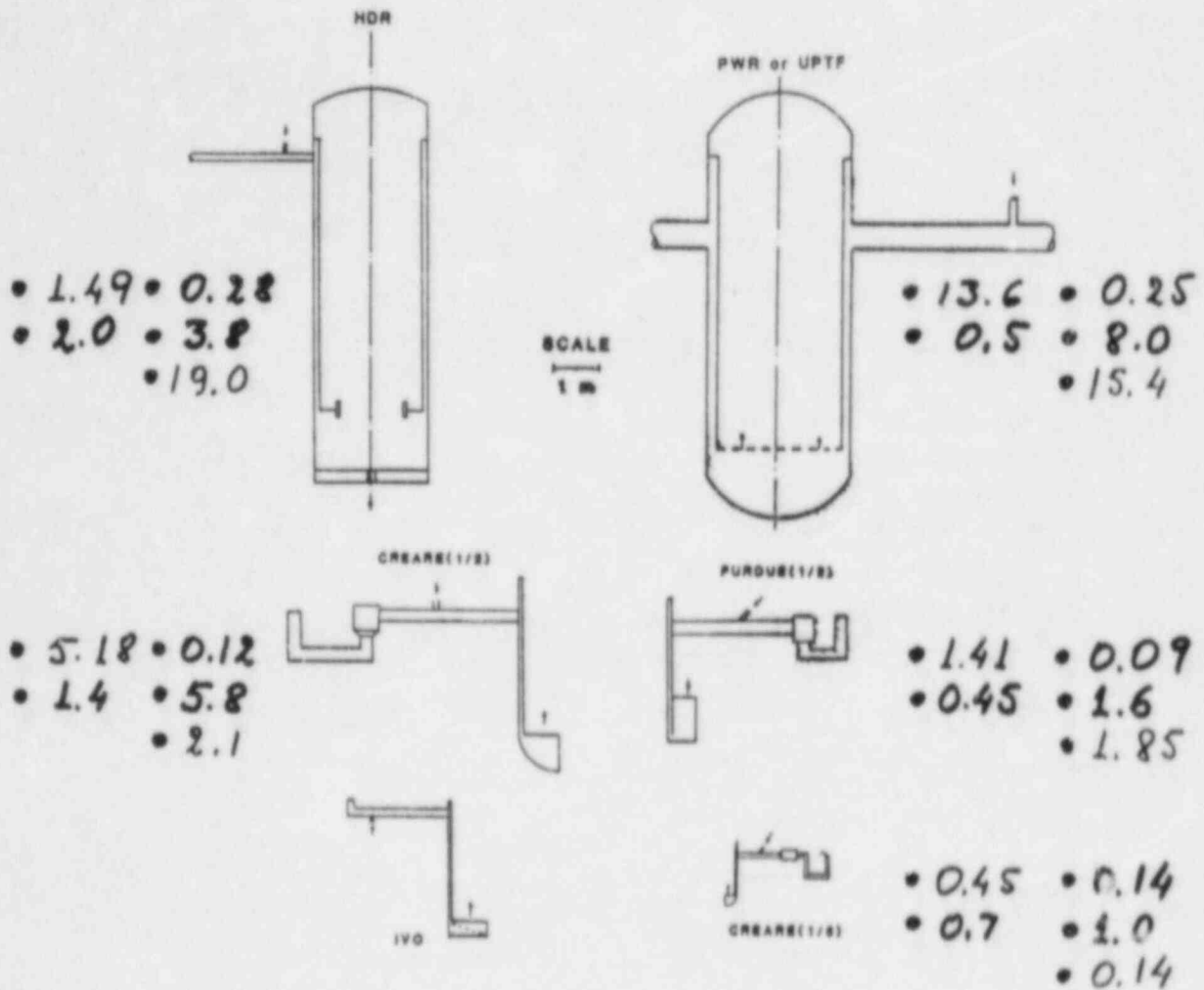
3. Selby, D.L., et al., "Pressurized Thermal Shock Evaluation of H.B. Robinson Unit 2 Nuclear Power Plant," NUREG/CR-4183 (ORNL/TM-9567), September 1985.
4. Ireland, J.R., et al., "TRAC Analyses of Severe Overcooling Transients for the Oconee-1 PWR," NUREG/CR-3706 (LA-10055-MS) May 1985.
5. Fletcher, C.D., et al., "RELAP-5 Thermal-Hydraulic Analyses of Pressurized Thermal Shock Sequences for the Oconee-1 Pressurized Water Reactor," NUREG/CR-3761 (EGG-2310), June 1984.
6. Spriggs, G.D., et al., "TRAC-PF1 Analyses of Potential Pressurized Thermal Shock Transients at Calvert Cliffs/Unit 1," NUREG/CR-4109 (LA-10321-MS), February 1985.
7. Fletcher, C.D., et al., "RELAP-5 Thermal-Hydraulic Analyses of Pressurized Thermal Shock Sequences for the H.B. Robinson Unit 2 Pressurized Water Reactor," NUREG/CR-3977 (EGG-2341), April 1985.
8. Theofanous, T.G., H.P. Nourbakhsh, P. Gherson and K. Iyer, "Decay of Buoyancy Driven Stratified Layers with Applications to Pressurized Thermal Shock," NUREG/CR-3700, May 1984.
9. Iyer, K., H.P. Nourbakhsh and T.G. Theofanous, "REMIX - A Computer Program for Temperature Transients Due to HPI at Stagnated Loop Flow," NUREG/CR-3701 (in press).
10. Daly, B.T., "Three-Dimensional Calculations of Transient Fluid-Thermal Mixing in the Downcomer of Calvert Cliffs-1 Plant Using SOLA-PTS," NUREG/CR-3704, April 1984.
11. Theofanous, T.G. and H.P. Nourbakhsh, "PWR Downcomer Fluid Temperature Transients Due to High Pressure Injection at Stagnated Loop Flow," Proceedings of Joint NRC/ANS Meeting on Basic Thermal Hydraulic Mechanisms in LWR Analysis, September 14-15, 1982, Bethesda, MD, NUREG/CP-0043, pp. 583-613.
12. Nourbakhsh, H.P. and T.G. Theofanous, "Decay of Buoyancy Driven Stratified Layers with Applications to PTS Part I: The Regional Mixing Model," Nuclear Engineering and Design (in press).
13. Theofanous, T.G. and K. Iyer, "Mixing Phenomena of Interest to SBLOCAs," Invited paper for the "Specialists Meeting on Small Break LOCA Analyses in LWRs," Pisa, Italy, June 23-27, 1985.
14. Theofanous, T.G., K. Iyer, P. Gherson, and H.P. Nourbakhsh, "Buoyancy Effects on Overcooling Transients Calculated for the NRC-PTS Study," NUREG/CR-3702 (in press).
15. Theofanous, T.G., P. Gherson, H.P. Nourbakhsh and K. Iyer, "Decay of Buoyancy Driven Stratified Layers with Applications to PTS Part II: Purdue's 1/2-Scale Experiments," Nuclear Engineering and Design (in press).

16. Iyer, K. and T.G. Theofanous, "Flooding Limited Thermal Mixing - The Case of High-Fr Injection," Proceedings of the Third International Topical Meeting on Reactor Thermal Hydraulics held at Newport, Rhode Island, October 15-18, 1985.
17. Iyer, K. and T.G. Theofanous, "Decay of Buoyancy Driven Stratified Layers with Applications to PTS: Reactor Predictions," ANS Proceedings of the 1985 National Heat Transfer Conference in Denver, Colorado, August 6-9, 1985.
18. Iyer, K. "Thermal Hydraulic Mixing in the Primary System of a Pressurized Water Reactor During High Pressure Safety Injection Under Stagnated Loop Conditions," PhD Thesis, Purdue University December 1985.
19. Iyer, K., P. Gherson, and T.G. Theofanous, "Purdue's One-Half Scale HPI Mixing Test Program," Second Proceedings of Nuclear Thermal-Hydraulics, Annual Meeting of the American Nuclear Society, New Orleans, LA, June 3-7, 1984, pp. 165-171.
20. Theofanous, T.G., "Mixing with Horizontal Low Froude Number Injections - Recommendations for UPTF," Presented at the 2D/3D Review Meeting, Manheim, Germany, June 1985.]

#### ACKNOWLEDGEMENTS

Financial support by the Nuclear Regulatory Commission under Grant No. NRC-03-003 is gratefully acknowledged. We also wish to extend our appreciation to Mr. J. Reyes and Dr. N. Zuber of the USNRC for their cooperation and encouragement.

# INTEGRAL HPI-MIXING FACILITIES

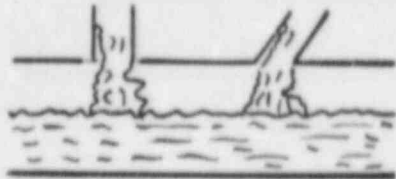


$$\begin{aligned}
 & \bullet \dot{m} \left( \frac{kg}{s} \right) \bullet \Delta p / \rho_{HPI} \\
 & \bullet Fr_{HPI} \bullet Re_{HPI} \times 10^{-4} \\
 & \bullet V_T \times 10^{-6} \text{ (cm}^3\text{)}
 \end{aligned}$$

Fig. 1 Scaled representation of integral HPI-mixing facilities in comparison to a PWR. In addition shown are HPI injection rates ( $\dot{m}$ ) peak buoyancy potentials ( $\Delta p / \rho$ ), Froude numbers at the injection nozzle ( $Fr_{HPI}$ ), Reynolds numbers at the injection nozzle, and system volume ( $V_T$ ).



Fig 2. INJECTION GEOMETRIES..... MIXING REGIMES  
..... CALCULATIONAL TOOLS



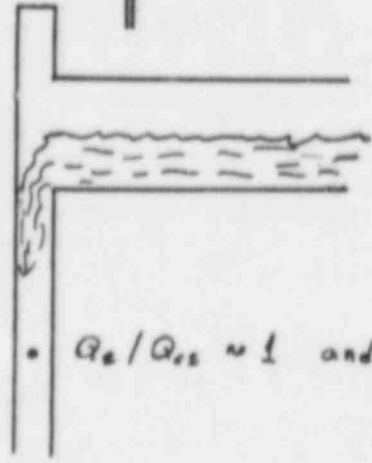
$Fr_2 \sim 0.2 \text{ to } 1 \quad Q_e / Q_{HPZ} \sim 4$   
REMIX:  $\frac{Q_e}{Q_{HPZ}} = f(Fr, l/h_{in})$   
 $Fr_{cl}^2 + Fr_{cs}^2 = 1.$



$Fr_2 \sim 1 \quad Q_e / Q_{HPZ} \sim 1$



$Fr_2 > 10 \quad Q_e / Q_{HPZ} \sim 4 \text{ to } 6$   
NEWMIX:  $Fr_{cl}^2 + Fr_{cs}^2 = 1.$



$Fr_{cs} \sim 0.6$

•  $Q_e / Q_{cs} \sim 1 \text{ and } Fr_{cs} = 1 \Rightarrow T^* = f(L/D_{cl})$

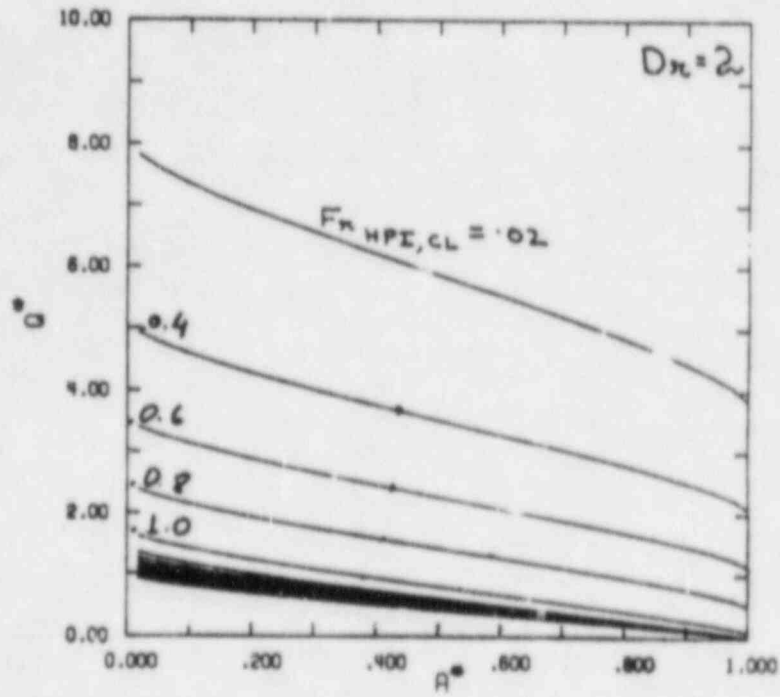


Fig. 3 Dimensionless representation of injection plume entrainment rate.

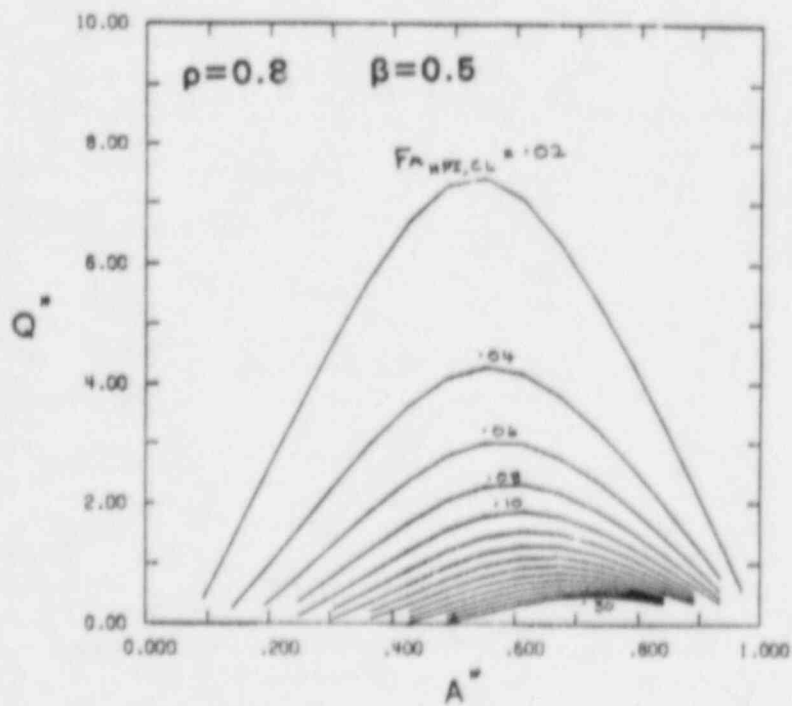


Fig. 4 Dimensionless representation of the counter-current flow limitation on entrainment rates.

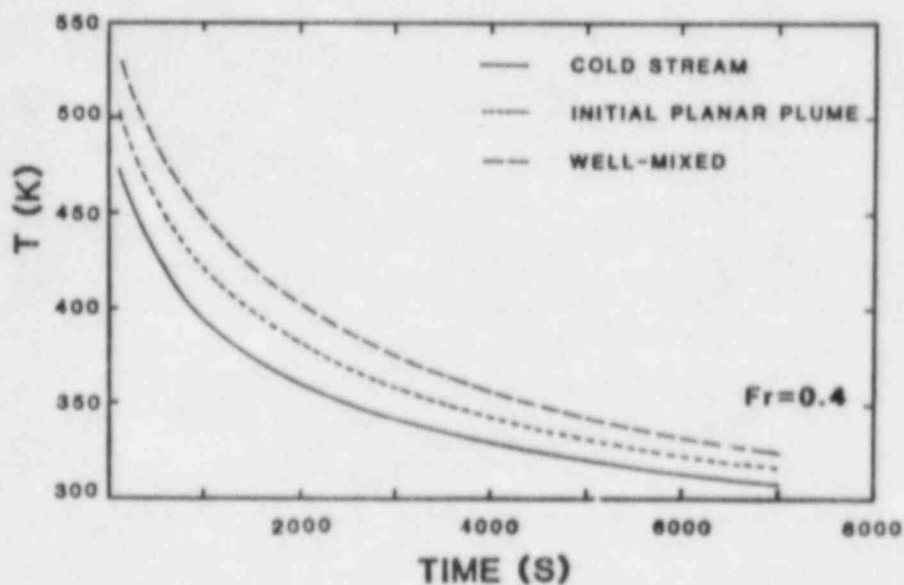


Fig. 5 Transient cooldown in H.B. Robinson for injection Froude number of 0.4.

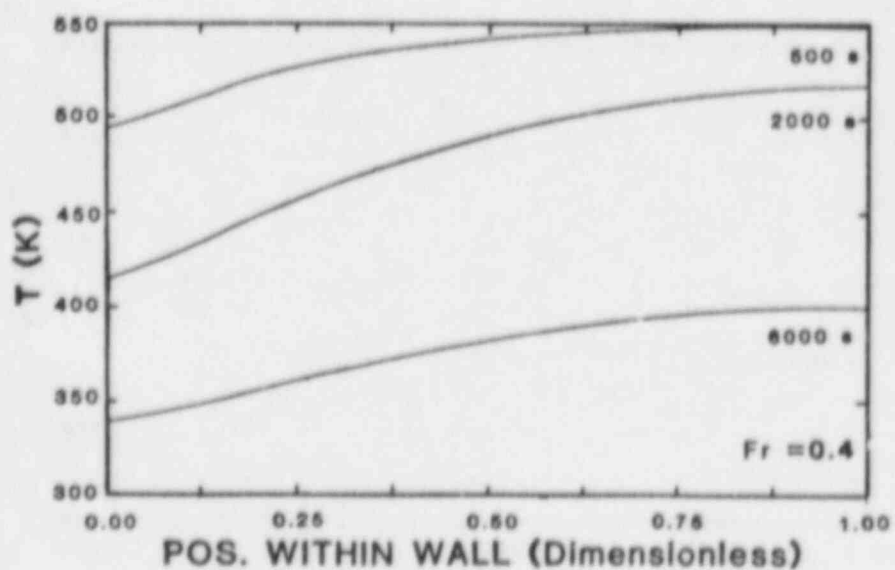


Fig. 6 Temperature gradients within the reactor vessel wall for the cooldown of Figure 5.

STEAM EXPLOSIONS: ENERGY CONVERSION EFFICIENCIES OF STEAM EXPLOSIONS  
FROM TWO MAJOR ACCIDENTS IN THE PULP AND PAPER INDUSTRY

T. M. Grace (The Institute of Paper Chemistry)  
R. R. Robinson (IIT Research Institute)  
J. Hopenfeld (U.S. Nuclear Regulatory Commission)

ABSTRACT

The objective was to determine the overall energy conversion efficiency (thermal to mechanical) of steam explosions by analysis of smelt-water explosions that have occurred in kraft paper pulp mill recovery boilers. Analyses were carried out for two major accidents, one in each of the two types of recovery boilers currently in use.

The energy conversion efficiency was calculated as the ratio of the deformation energy in the furnace structure to the energy content of the molten smelt in the unit. The mechanical deformation energy was determined by developing models of the furnace structure and calculating the deformation energy consistent with the observed damage. Estimates were made of the amount of smelt present within the unit, smelt temperature, and the amount of water which entered the unit. Only the sensible heat in the molten smelt above the freezing point and the heat of fusion were included in calculating the energy available for the explosion. The best estimates for the energy conversion efficiency were 0.25% for one case and 0.55% in the other. Despite the uncertainties involved, it is extremely unlikely that the energy conversion efficiency exceeds 1% in either case. These efficiencies are the first step in assessing the effects of scale or system constraints on steam explosions.

INTRODUCTION

The question of how to scale data on steam explosions from laboratory tests has been raised in the course of several risk assessment studies of severe nuclear reactor accidents. Information on damage to kraft paper pulp mill recovery boilers may provide some answers in this regard because the scale of structures involved and the volumes of water and smelt (fuel) are roughly on the same order as those encountered in nuclear reactors.

In spite of the fact that there have been more than 80 steam explosions in recovery boilers, there has been no published information on the analysis of the structural damage sustained. The ultimate purpose of the present task is to utilize this damage data, together with laboratory observations, to provide some insight on the effect of scale and containment on the energy release from steam explosions.

The present paper is a first step toward this goal. It provides energy conversion efficiencies from two steam explosions. One explosion occurred in a Babcock & Wilcox (B&W) boiler in Oct. 24, 1982. The second occurred in a Combustion Engineering (CE) boiler on July 11, 1973.

## BRIEF DESCRIPTION OF ACCIDENTS

### Case 1: B&W Unit

This unit was started up in December 1977. It is of membrane wall design (individual waterwall tubes are welded to a connecting membrane). Prior to the explosion, the boiler was operating at about 125% of the rated solids capacity and 98% of the rated steam capacity. The steam rating is 248,300 lb/hr at 825°F and 900 psig.

Two rapid explosions occurred approximately 25 minutes after a furnace roof tube ruptured. They were described as large bangs, 3 to 5 seconds apart. An Emergency Shutdown Procedure (ESP) was initiated about 5 minutes after the tube ruptured. (The ESP immediately shuts off all fuel and shuts off forced air to the furnace, and opens motorized valves to rapid-drain the boiler. The I.D. fan remains operating to maintain a balanced draft.) Damage from the explosion was severe enough that all 4 waterwalls and the furnace floor were replaced.

The roof tube which failed was the second from the wall on the north side. The failure point was about 15 feet from the front wall. The rupture had a "fish mouth" appearance and was about 8" in length. The ceiling tube ruptured because of erosive thinning by a water/steam stream from a nearby wall tube. The stream originated from a slot in the wall tube. This slot in turn was cut by an impinging jet from a pinhole leak in an adjacent tube weld of yet a second wall tube. The location of the rupture on the roof tube would direct the water vertically downward in the furnace.

A diagram of the unit showing the location of the ruptured tube is given in Fig. 1.

### Case 2: CE Unit

This unit was placed in operation in March 1967. It is of membrane wall design (individual waterwall tubes are welded together to form a gas-tight wall surface). At the time of the explosion the unit was off the line, with no black liquor or auxiliary fuel being fired. There was molten smelt in the unit. The steam rating is 320,500 lb/hr at 830°F and 850 psig.

Prior to the incident the boiler was operating normally on black liquor. One sootblower appeared to be malfunctioning, and they began substituting load carrying oil burners for liquor to permit inspection and work on the malfunctioning sootblower and to clean partially plugged gas passages. As this substitution was carried out, the liquor was cut off individually at the liquor guns, and the steam valves at each gun were opened to clean them out. The liquor guns were left in place with steam going through them. Substituting oil for black liquor burned out the char bed, but left a pool of smelt in the bottom of the unit. (The CE design has a flat hearth with the smelt spouts located about 11 inches above the floor. The smelt is decanted out of the unit.)

At 9:30, it was learned that the paper machine would be shut down at 11:00 for one to two hours. Since this would reduce the demand for steam, it was decided to take the recovery boiler off-line at 11:00 to permit a more thorough cleaning of the boiler gas passages. Plans were also made to take advantage

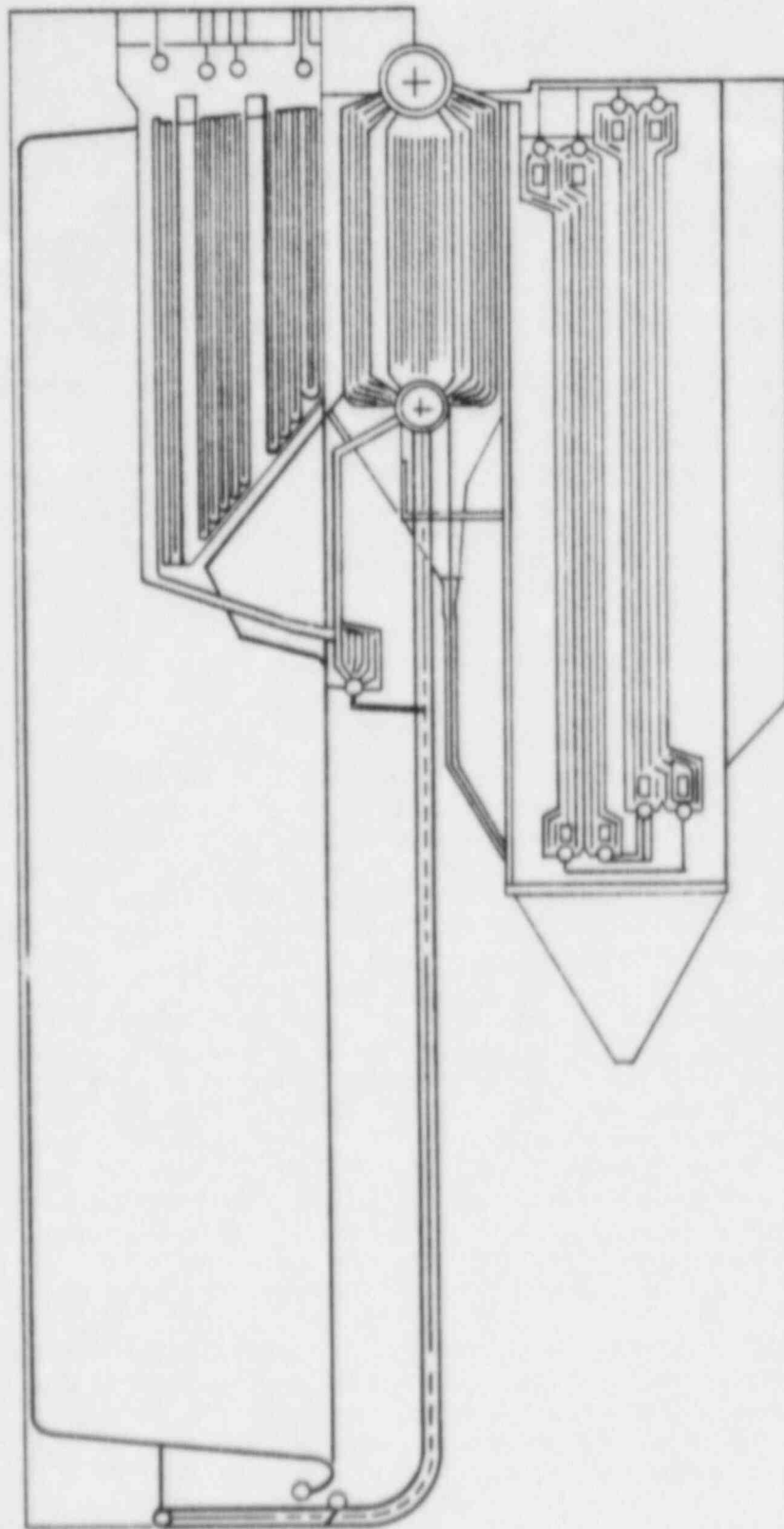


Figure 1. Diagram of B&W furnace.

of the boiler outage to clean the cascade evaporator, which until then had been kept full of heavy liquor ready to resume firing liquor. (The cascade evaporator is a device for concentrating black liquor by direct contact with flue gas.)

At 9:45 they began dumping liquor from the cascade. At 10:30 they started cleaning the cascade and liquor header by filling the cascade with water and circulating it through the furnace liquor header. At 11:00 the oil fire was removed to take the boiler off the line. By this time the char bed had burned completely out, leaving in the furnace only the pool of molten smelt about 8 inches deep, contained by the decanting bottom. The explosion occurred at 11:35 as a rapid series of 3 blasts.

Inspections made after the explosion revealed that of the six liquor guns in firing position at the time of the explosion, one did not have its liquor valve closed and steam valve open as had been believed. It is thought that this gun may have been plugged with liquor solids prior to and during the period the furnace was fired on oil, and may have been cleaned out by the wash water circulating through the liquor header. In any event, wash water entered the furnace through the open liquor gun and sprayed onto the smelt in the bottom of the furnace.

#### STRUCTURAL DAMAGE

##### Case 1: B&W Unit

The floor beams and the furnace area just above the tertiary air belt sustained the greatest damage. The maximum retained deflection from centerline in floor beams and sidewall buckstays was approximately one foot (1 ft).

Buckstays sheared off at several corners. The three floor beams sheared off on the south (right) side. Tables 1 and 2 show deflection patterns. Table 3 has additional notes of the damage on each floor level.

The floor beam deflection pattern indicated that the greatest force was released along the south (right) wall. The explosive force concentrated especially toward the east (rear) of the furnace. At the firing deck level, the south (right) side sustained the greatest force. Slightly above the tertiary air belt (194 ft, 6 inches) to just above the fourth floor (215 ft, 3 inches) the deflection pattern was more uniform. Buckstays began shearing at the tertiary air level. The deflection pattern concentrated on the west (front) side in the furnace nose region, above 226 ft 0 inch. The southwest (SW) corner at 237 ft 3 inches had a very large deformity next to the wall. Once above the nose, the north (left) and south (right) sides had the greatest deflections.

Boiler casing and insulation were damaged extensively above the fifth floor. The north (left) and south (right) sides just past the steam drum/mud drum region from floors 7 and 9 had extensive openings. Table 3 gives the details. The west (front) side of the penthouse remained intact. The wall tubes on the north (left) side did separate four to five inches from the ceiling tube sheet toward the west (front) side of the furnace. Some tube tearing was evident. The east (rear) side of the penthouse at the tenth floor level blew completely open. This area plus those mentioned above on the north (left) and south (right) sides were the major escape points for the gases. Although some

Table 1. Center line deflection in buckstays, inches.

Floor No. <sup>a</sup>	Elevation	West (Front)	North (Left)	East (Rear)	South (Right)	
10	273 ft 8 inches	(No buckstays measured at this level).				
9	264 ft 8 inches	2	3 3/4	0 <sup>b</sup>	3 3/4	
8	355 ft 8 inches	2 1/2	4	0 <sup>b</sup>	2	
(7)	249 ft 0 inch	5	3 1/2	0 <sup>b</sup>	d	
(6)	237 ft 3 inches	8 1/4	2 3/4	0 <sup>c</sup>	5	NW & SW corners sheared. Off-center deflections.
(5)	226 ft 0 inch	8 1/2	0	0 <sup>c</sup>	3	SW & NW corners sheared.
(4)	215 ft 3 inches	8 3/4	9 1/2	6	8	NE corner sheared.
(3)	204 ft 6 inches	(Could not be measured)				NE, NW, & SW corners sheared.
(3)	194 ft 6 inches	10-12	10-12	12	12	NE & SE corners sheared.
2	181 ft 6 inches	3 3/4	5 3/4	3 3/4	7 1/2	No shearing at corners.
1	162 ft 6 inches	(No buckstays measured at this level)				Casing cracked in center over doghouse. No damage seen around smelt spouts.

<sup>a</sup>Numbers in parentheses, floor from which buckstays were inspected.

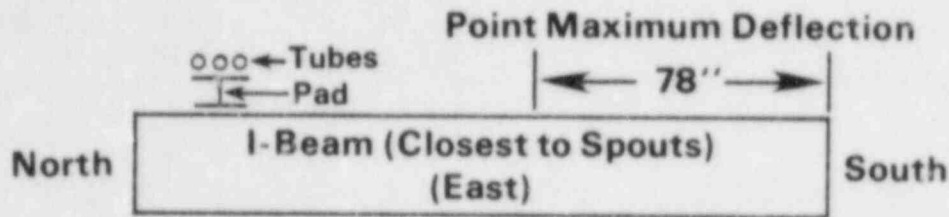
<sup>b</sup>East side of economizer.

<sup>c</sup>Behind furnace nose.

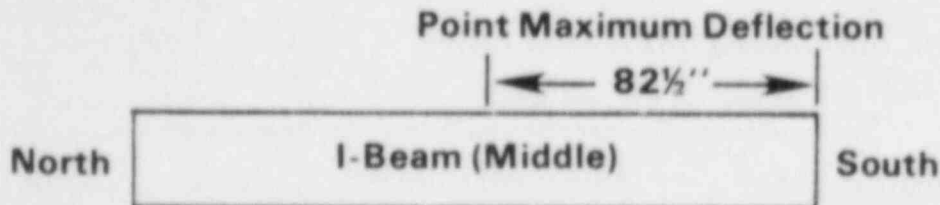
<sup>d</sup>Not recorded.



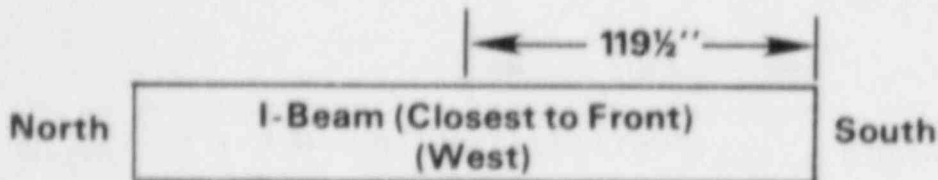
Table 2. Floor beam deflections.



11-12 inch vertical deflection down.  
10 inch horizontal twist toward east.  
1 of 7 floor pads remaining.  
South side sheared clear of wall support.  
North side still attached to wall support.



5-6 inch vertical deflection down.  
Only a very slight twist.  
1 of 7 floor pads remaining.  
South side sheared clear of wall support.  
North side still attached to wall support.



4 inch vertical deflection down.  
No evident twist.  
South side sheared clear of wall support.  
North side still attached to wall support.

Note: \* Directly below a number of floor pads the I-beam would have sharp depressions. The maximum depressions would be close to the point of maximum deflection noted above.

\* I-beam length approximately 20 foot 6 inch.

Table 3. Additional notes on damaged areas.

Floor No.	West (Front)	North (Left)	East (Rear)	South (Right)
10	FS slight bulging ES no bulging	FS bulging 6-8 inch No char/ $\text{Na}_2\text{SO}_4$	FS penthouse casing off	FS casing split toward rear ES casing intact all around
9	Not much bulge in tubes after buckstays removed	Tube wall out about 5 inches. Viewed ruptured tube. Char	ES minimal damage. Bent out but sprang back	FS casing blown out 7 inches
8		ES buckstay showed 6-6 1/2 inches deflection	Minimal damage	Tubes deflected apart. Casing split. Char present
7		All casing blown off near ES. 18 ft opening	Economizer internal baffle blown down	ES casing blown off 4 x 12 ft. Tubes still in line
6	ES 4-1/2 inch deflection. FS SW corner ballooned	ES extensive casing loss	ES slight bulge. FS no damage	ES 7 inch deflection
5	Ash hopper lines moved toward furnace 3-4 inches Major force	Casing out. No deflection on buckstay	Minimal damage	Casing intact slight bow. Furnace opened at SW corner
4	ES slight bow	ES slight bow	ES slight bow	ES casing bowed
3	SW corner had maximum separa- tion of buckstays 2-3 ft apart		Tertiary air ports bulging out	NE & SE furnace wall corners opened up slightly
2	Char and salt cake over floor area. No casing blown off. See slight bow.			
1	Glass on air ports intact. Could not see much damage at this level. Char present in all parts/doors. Char sprayed on boiler house wall.			

NOTES: FS Furnace side.  
ES Economizer side.

bulging was evident near the exit of the economizer and entrance to the precipitator, extensive damage was not evident in these areas.

The extensive damage described above required replacement of all water walls and floor tubes. The casing, buckstays, and floor beams were all replaced in the furnace area. No damage was evident in the steam and mud drums, or in superheater, boiler, and economizer tubes.

#### Case 2: CE Unit

The major damage sustained is summarized below. Sketches of the furnace bottom contours and the floor beam deflections are shown in Fig. 2 and 3.

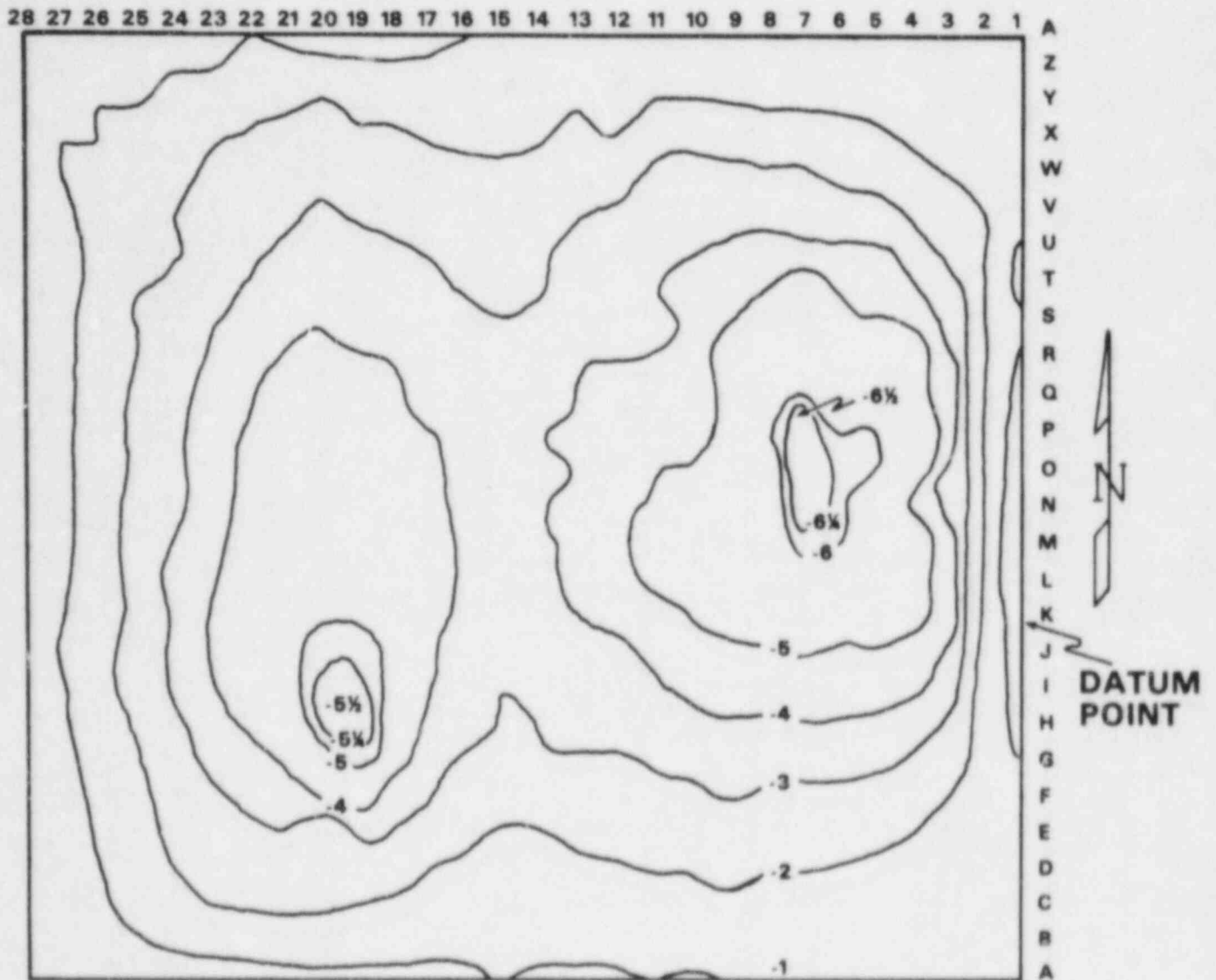
- (1) The furnace walls, bottom, and floor beams were sufficiently deformed as to require replacement. The walls were bulged up to about 20 inches, and the floor had two separate depressions about 5-1/2 to 6 inches deep. The heavy floorbeams were also noticeably deformed.

The contours of the bottom show that there were two separate and distinct depressions in the floor about 6 inches deep, which indicate at least two separate locations for explosions.

- (2) The load-carrying burners and sootblowers were all damaged.
- (3) The nose baffle was pushed down and two outside tubes were pulled in two.
- (4) The mud drum was moved to the rear (4-6 inches).
- (5) The economizer back wall was pushed out and the lower economizer header moved back about 8 inches.
- (6) The inspection doors were blown open and off, pulling attachments welded to the tubes with them and tearing out tube metal.
- (7) The screen tube header was bowed 8-10 inches.
- (8) The F.D. ductwork was bulged all the way from the furnace back through the air heater to the outlet of the F.D. fan.
- (9) The ductwork to the cascade evaporator was ruptured, and the ductwork from the cascade to the I.D. fan bulged.
- (10) Pieces of aluminum siding were blown off all four sides of the boilerhouse, including some from one wall which is separated from the recovery boiler by the power boiler which occupies the same building.

#### ANALYSIS

The analysis focuses on an energy balance between the available thermal energy and the mechanical deformation energy. The information needed to construct such a balance is not measured in operating recovery boilers, so many assumptions had to be made in the course of the analysis. In general, methods were chosen which would yield conservative results (upper limits) regarding the energy conversion efficiencies. Because of these assumptions the results are presented as a range instead of a single value.

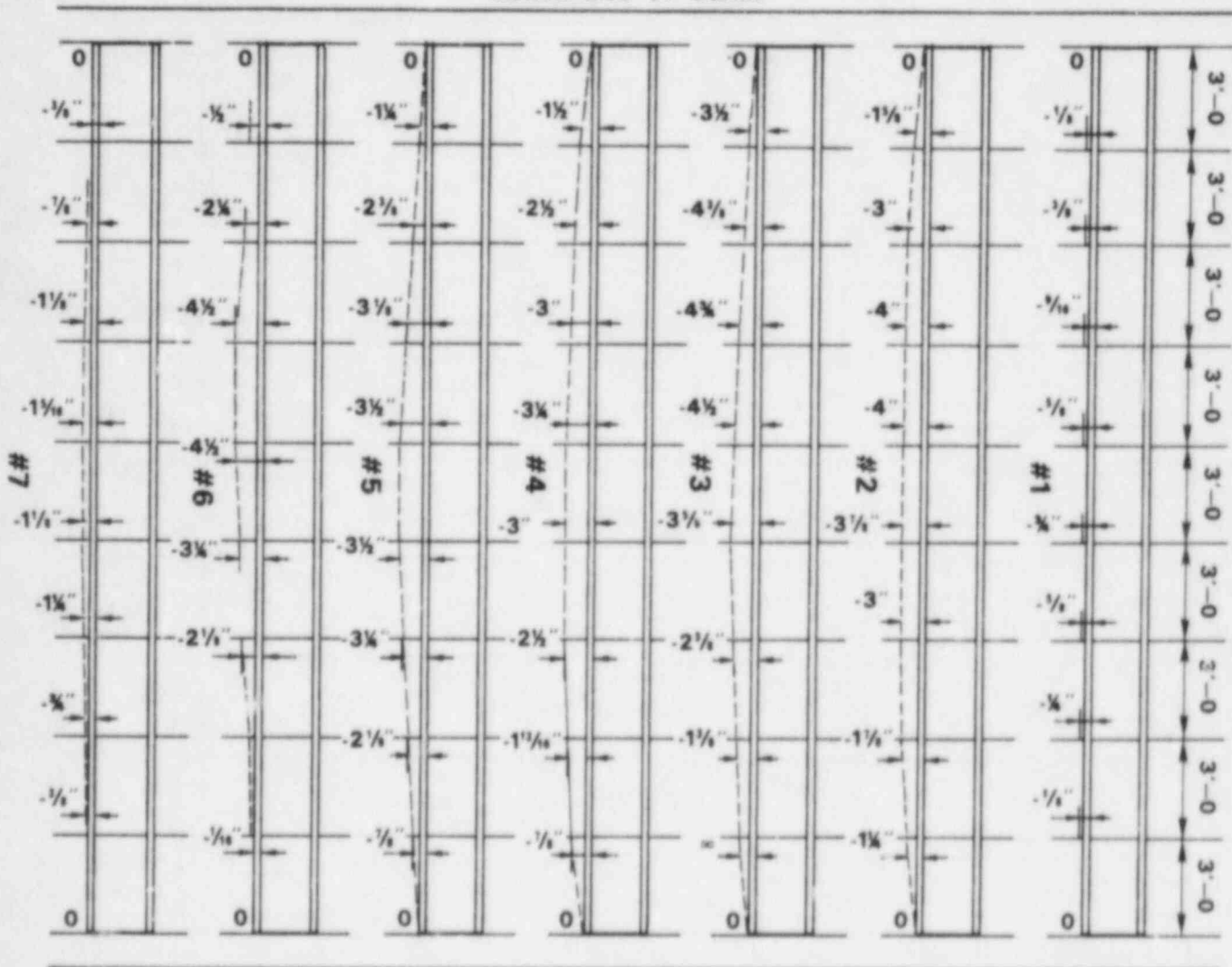


**GENERAL NOTES**

1. ALL CONTOURS ARE NEGATIVE IN INCHES RELATIVE TO LOCATION (K-1)
2. LOWEST POINT IS LOCATED AT (P-7)
3. GRID INTERVALS ARE ONE FOOT

Figure 2. Furnace floor contours.

NORTH END OF BEAM



SOUTH END OF BEAM

Figure 3. Floor beam bottom deformations.

## Energy Available

The energy available is assumed to be stored as a latent plus sensible heat in the molten smelt. The most difficult task is to estimate the amount of smelt which actually was involved in the interaction plus its initial and final temperatures.

The black liquor fired into a kraft recovery boiler contains about 20% sodium and 4 to 5% sulfur (wt.% on a dry solids basis). Combustion converts these elements into sodium carbonate and sodium sulfide along with a small amount of sodium sulfate. These leave the furnace as a mixture of molten salts called smelt. The total amount of smelt produced is usually about 40 to 50% (by weight) of the solids fired.

A substantial part of the burning takes place on the hearth in the so-called char bed. Black liquor burns in 2 stages. In the first stage, the organic content pyrolyzes and combustible gases are generated which burn. The second stage occurs after pyrolysis is complete. The residual char, containing about 25% carbon and 75% inorganic, burns on the char bed. During char burning, the carbon is burned out and the inorganics melt and form smelt. The char bed is very heterogeneous, containing frozen smelt, molten smelt, and char of varying carbon content. There are pronounced temperature variations within the bed, due to exothermic reactions occurring below the bed surface.

### Case 1: B&W Unit

Because of certain design and operating features, char beds in B&W units tend to be rather large and dense. The floor of the unit is slanted about 5° from front to back. The spouts for smelt discharge are located on the back wall and are flush with the floor. Primary air ports are located in all 4 walls, about 3 ft above the floor. Secondary air ports are located in all 4 walls, a nominal 8 ft above the hearth. Much of the liquor is sprayed on the walls, where it dries and falls to the hearth as rather large chunks. Primary air pushes this material away from the wall toward the center of the furnace.

The bed normally is slightly below the secondary air level. It tends to rise steeply along the sides, and may also be depressed in the center (because relatively little material reaches the center of the bed). A typical B&W bed is sketched in Fig. 2. The most intense burning takes place along the sides of the bed, where the primary air impinges on the bed. The smelt formed here collects in troughs that are formed naturally around the perimeter of the bed and flows to the spouts. Some smelt may also permeate the bed and form channels underneath the bed. A large part of the bed is an inactive core consisting of a porous structure of solidified smelt and char. It has a density ranging from 50 to 120 lb/ft<sup>3</sup>.

Very little is known in detail about the amount and location of molten smelt in an operating B&W unit. The only published information bearing on smelt inventory is some data on smelt residence time distribution.<sup>1</sup> This can be used to estimate smelt inventory when other data is lacking.

The Case 1 boiler was operating at a firing rate of 78,100 lb solids/hr, producing 35,000 lb smelt/hr. The bed was relatively low. One report said 2

ft (above primary air level), another said 6 ft (above floor) and a third said below secondary air ports. These are qualitative judgments, not measured values. The bed was close to the walls (4 to 6 inches from primary air ports).

The best estimate of molten smelt inventory is obtained by estimating residence time. Tracer experiments in a 400 TPD B&W furnace showed a first order time constant of 25 minutes. If the bed is treated as a stirred tank reactor, this is directly related to smelt inventory. Since the Case I boiler is larger (nominal 500 TPD), it appears reasonable to assume a residence time of 30 minutes. This gives a smelt inventory of

$$35,000 \frac{\text{lb smelt}}{\text{hr}} \times \frac{30 \text{ min}}{60 \text{ min/hr}} = 17,500 \text{ lb molten smelt}$$

(This would correspond to a layer about 3 inches thick distributed uniformly over the hearth.)

The heat content of the molten smelt is also difficult to estimate because of the pronounced variation in smelt temperature that exists. Bed surface temperatures can range up to 2000°F. Smelt discharge temperatures run between 1400 to 1550°F. Melting temperatures depend on composition, but typically run about 1400°F. None of these is routinely measured. The average smelt temperature is perhaps 200°F above its melting point.

Sensible heat in molten smelt:

$$17,500 \text{ lb} \times 0.3 \frac{\text{Btu}}{\text{lb}^\circ\text{F}} \times 200^\circ\text{F} = 1,050,000 \text{ Btu}$$

Heat to freeze molten smelt:

$$17,500 \text{ lb} \times 60 \text{ Btu/lb} = 1,050,000 \text{ Btu}$$

Total heat in molten smelt:

(relative to b.p. water)

$$17,500 \text{ lb} \times 500 \text{ Btu/lb} = 8,750,000 \text{ Btu}$$

The heat content of the molten smelt is only a small fraction of the total heat in the bed. The total mass of the bed can be estimated as follows.

$$\begin{array}{ccccccc} 524 \text{ ft}^2 & \times & 6 \text{ ft} & \times & 80 \text{ lb/ft}^3 & = & 252,000 \text{ lb} \\ \text{(plan area)} & & \text{(bed height)} & & \text{(bed density)} & & \end{array}$$

Total heat in bed:

$$252,000 \text{ lb} \times 500 \text{ Btu/lb} = 126 \times 10^6 \text{ Btu}$$

Case 2: CE Unit

The floor of a CE unit is flat. Smelt is drained from the unit through spouts (water cooled troughs) which are located in the walls about 11 inches above

the floor. Small units have spouts in only one wall, while large units have spouts in two opposite walls. The smelt builds up in a pool in the bottom of the unit until it overflows out of the spouts. A frozen smelt layer exists along the floor, which protects the floor tubes from erosion and corrosion, and helps to seal against smelt leaks through the floor. The char bed rests on the frozen smelt, with the bottom part of the bed saturated with molten smelt. Small char beds may float on the molten smelt pool. The smelt-char bed in a CE unit is shown in Fig. 4.

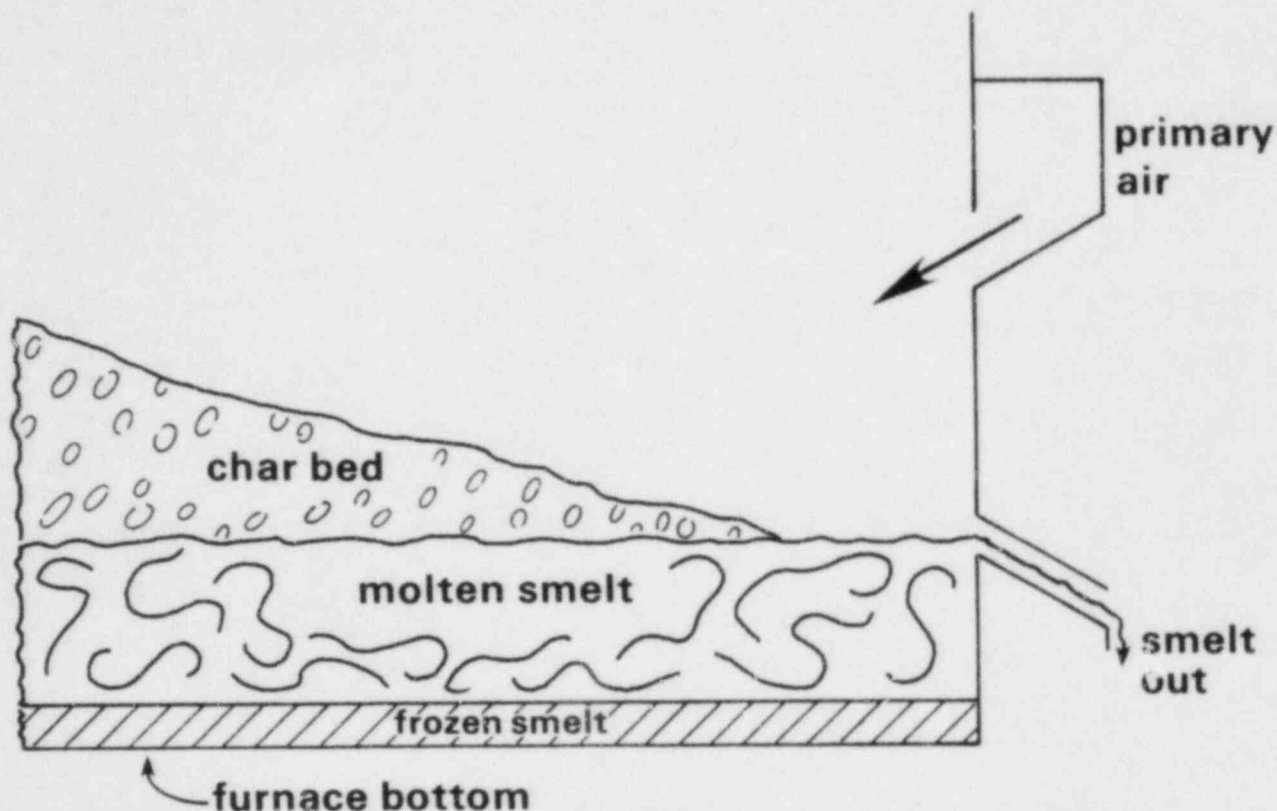


Figure 4. Bottom of a CE furnace.

Prior to the explosion, liquor firing had been terminated and auxiliary fuel (oil) substituted to maintain steam production. During this time the char bed was burned out so that only the molten smelt pool and the frozen smelt layer next to the floor tubes remained. Thirty-five minutes before the explosion, the auxiliary fuel firing was stopped and the unit was taken off-line. It was estimated that the pool of molten smelt was 8 inches deep at the time of termination of oil firing. No specific observations or measurements were made of the smelt pool, as there was no reason to do so.

Once the oil firing was stopped, the smelt pool would begin to cool by radiation to the surrounding furnace walls. Thus there are two problems which must be dealt with in estimating the amount of smelt in the unit and its heat content at the time of the explosion.

1. What is the depth and temperature of the smelt in the furnace at the time that oil firing ceased?



2. How much cooling and freezing took place in the 35 minutes between stopping the oil firing and the explosion?

The best estimate of the depth of molten smelt at the time of termination of oil firing is 8 inches. The furnace cross section is 27 ft x 26.5 ft or 716 ft<sup>2</sup>. Thus the initial amount of molten smelt in the unit is 716 ft<sup>2</sup> x 8/12 ft x 120 lb/ft<sup>3</sup> = 57,300 lb. The uncertainty in this value is due to the uncertainty in the thickness of the frozen layer over the floor tubes. This is determined by heat transfer considerations for removal of the net heat flux coming to the pool from the oil fire. A minimum pool depth under these circumstances would seem to be 6", and the maximum is, of course, 11" since that is fixed by the location of the spouts. Thus, for the initial amount of smelt the most probable value is about 57,000 lb with an upper bound of about 75,000 lb and a lower bound of about 43,000 lb.

The smelt temperature is not normally measured. As was discussed earlier the smelt typically runs out of the unit at temperatures between 1400 and 1550°F. The melting temperature is usually around 1400°F. In a situation with the bed burned out and a load carrying oil fire going, the smelt temperature is likely to be somewhat higher than it is for black liquor firing. For our purposes we assume an initial smelt temperature of 1700°F and a melting point of 1400°F.

The sensible heat in the molten smelt is

$$57,000 \text{ lb} \times 0.3 \frac{\text{Btu}}{\text{lb}^\circ\text{F}} \times (1700-1400)^\circ\text{F} = 5.13 \text{ million Btu}$$

The heat to freeze the molten smelt is

$$57,000 \text{ lb} \times 60 \frac{\text{Btu}}{\text{lb}} = 3.42 \text{ million Btu}$$

The total heat in the molten smelt (relative to the boiling point of water) is

$$57,000 \text{ lb} \times 500 \text{ Btu/lb} = 28.5 \text{ million Btu}$$

Once the oil fire is cut off, the smelt pool will begin to cool by radiation to the furnace walls and bullnose. Assuming a smelt emissivity of 0.8 and a view factor of one, and neglecting back-radiation from the walls, the radiant heat flux is about 30,000 Btu/hr ft<sup>2</sup> at 1700°F and 16,400 Btu/hr ft<sup>2</sup> at 1400°F. Even at 1400°F, radiant cooling could remove

$$16,400 \frac{\text{Btu}}{\text{hr ft}^2} \times 716 \text{ ft}^2 \times \frac{35}{60} \text{ hr} = 6.8 \text{ million Btu's in 35 minutes}$$

This is more than enough to remove the sensible heat in the smelt pool and initiate freezing of the surface.

In actual fact the pool will not cool as quickly. At the time of stopping the oil fire, the furnace walls would be covered with slag that could have a surface temperature as high as the smelt melting temperature. The resulting

back-radiation would retard the cooling rate until the slag on the walls had cooled. Despite this, it is not unreasonable to assume that the sensible heat in the molten smelt was rapidly lost in this case, and that some freezing of the surface had begun. (Smelt, cooled from the top, freezes like water, from the top down.)

Once the smelt pool surface begins to freeze, cooling slows down because of the conductive resistance in the frozen layer. The thermal conductivity of frozen smelt is about 0.5 Btu/hr ft°F. Thus a layer of smelt 1 inch in thickness with a 500°F temperature across it would have a heat flux of

$$0.5 \frac{\text{Btu}}{\text{hr ft}^2} \times \frac{500^\circ\text{F}}{1/12 \text{ ft}} = 3000 \frac{\text{Btu}}{\text{hr ft}^2}$$

This would about match the radiant flux from a surface 500°F below the melting temperature of 1400°F. If the cooling flux is 3000 Btu/hr ft<sup>2</sup>, the freezing rate is

$$\frac{3000 \text{ Btu/hr ft}^2}{60 \frac{\text{Btu}}{\text{lb}} \times 120 \text{ lb/ft}^3} = 0.417 \frac{\text{ft}}{\text{hr}} = 5 \text{ inches/hr}$$

which is still fairly fast. The freezing rate would be about one-half that value if the frozen smelt were 2 inches thick. Taking these numbers into consideration, it is not unreasonable to assume that the smelt could cool to the freezing point and freeze out a surface shell of an inch or so thickness in 35 minutes. The smelt layer at the bottom would also increase, possibly by as much as an inch.

Thus, the best estimate of the smelt configuration at the time of the explosion is a 6-inches-thick pool at a temperature of 1400°F (the melting point) with a 4-inches-thick frozen layer below it and a 1-inch-thick layer of frozen smelt on its surface.

If, as in Case I, we assume that only the heat available while the smelt is in the liquid state is accessible to the explosion, the heat available is

$$43,000 \text{ lb} \times 60 \frac{\text{Btu}}{\text{lb}} = 2.58 \text{ million Btu}$$

This would be a conservative estimate. An upper bound could be obtained by assuming all of the heat in the molten smelt down to the boiling point of water is accessible. This value is  $43,000 \text{ lb} \times 500 \frac{\text{Btu}}{\text{lb}} = 21.5 \text{ million Btu}$ .

#### MECHANICAL DEFORMATION ENERGY

Analysis of the damage sustained in the explosion was done under subcontract by IIT Research Institute. Reports covering each case are available<sup>2,3</sup>.

Case 1: B&W Unit

The most significant deformations from the standpoint of the energy involved are:

1. buckstay bending
2. floor beam bending
3. waterwall tube deformations between buckstays (and concrete floors)

The deformation energy of the buckstay corner tie failures is small relative to other deformation energies, and can be neglected. In addition, the floor tube displacement energy is neglected, since the floor tube loaded area is small relative to the waterwall area.

Both buckstay bending deformations and floor beam bending deformations were measured and documented during the post-explosion investigation. Waterwall deformations between buckstays were not. When the importance of this latter type of deformation to energetics became known, it was decided to calculate the term for a range of deformations, while trying to ascertain from the mill involved the extent of deformation actually encountered.

A summary of the deformed structure energy is as follows:

	<u>U (in-lb)</u>	<u>U (Btu)</u>
Buckstay deformation energy	10,400,000	1,110
Floor beam deformation energy	1,050,000	110
Wall tube deformation 2 inches	30,800,000	3,300
1 inch	16,800,000	1,800
0.5 inch	8,980,000	960

Two features are immediately evident in these data:

1. The structural deformation energies are quite small (a few thousand Btu's).
2. Wall tube deformation energies are large relative to the other terms. Thus the deformations which were not measured or documented have a dominant influence.

Subsequent discussions with the mill provided the information that all four waterwalls were ultimately constrained by concrete floors that were located between buckstays, and deformations were up to 2 inches beyond the concrete floor. Some crushing of the concrete floors and of the tubes at the point of impact also occurred. In view of this the 2-inch wall tube deformation appears to be the most realistic one to use, and it may be somewhat conservative.

At the present time our best estimate of the structural deformation energy is 5000 Btu. The lower bound is about 3000 Btu and the upper bound about 8000 Btu. The biggest source of uncertainty is the wall deformations. The most promising method of overcoming this difficulty is to carry out a nondynamic

response analysis of a model in which the walls and buckstays deform together and the wall deformation is taken as that which is consistent with the buckstay deformations.

Case 2: CE Unit

Six types of deformations were modeled for energy calculations. These are:

1. floor beam bending
2. buckstay bending
3. waterwall tube bending between buckstays (and concrete floors)
4. waterwall tube extensional strain energy
5. floor tube flattening over floor beams
6. waterwall tube flattening at concrete floors.

In this explosion the buckstays did not open up at the corners, so there is no contribution from buckstay corner tie failures. Floor tube deformations (other than crush at the floor beams) were neglected because the floor area is small compared to the waterwall area. Other reported damage such as a 4- to 6-inch horizontal movement of the mud drum, bowing of the screen tube header, a small amount of metal tearing at welds, and bulging of ductwork was not subjected to analysis.

A summary of the deformed structure energy is given in Table 4. A brief discussion of how these numbers were arrived at follows.

Table 4. Deformed structure energy.

	<u>U (in-lb)</u>	<u>U (Btu)</u>
Floor beam bending	$2.6 \times 10^6$	280
Buckstay bending	$19.1 \times 10^6$	2050
Waterwall tube bending	$50.6 \times 10^6$	5420
Waterwall tube extension	$28.8 \times 10^6$	3080
Floor tube flattening	$14.6 \times 10^6$	1560
Waterwall tube flattening	$14.7 \times 10^6$	1570
	<hr/> $130.4 \times 10^6$	<hr/> 13,960

Detailed data were available on the floor beam deflections, so the deformation energies were calculated for each floor beam and then added together.

Buckstay deflections are not known with precision. The various reports which we have indicate general bowing of all buckstays (all were replaced). Values for the deformations include "up to about 20 inches," "bowed out 2 ft to 3 ft at all levels above the operating floor," and "maximum measured buckstay deformation - 21 inches." Deformation energies were calculated parametrically for a representative buckstay made up of four beams pinned at the corners and assuming each beam has the same permanent deflection at its midpoint. The value given in Table 4 is based on a permanent deflection of 21 inches.

Waterwall tube bending is the outward bowing of the waterwall beyond the constraints exerted by the buckstays and concrete floors surrounding the unit.

The deformation energy is calculated parametrically as a function of the span and permanent deflection for a single waterwall tube. The total deformation energy is then obtained by adding together that for all such deformations on the four walls. In this case there are eleven sets of buckstays and seven concrete floors constraining the waterwalls. The value of the deformation energy in Table 4 is based on a 4-inch deflection of the walls in the span between the concrete floors and a 2-inch deflection of the walls in the span over the buckstays. Further details are given in Appendix II of Ref. 4.

Waterwall tube extensional deformation energy is the energy associated with the stretching that the tubes undergo as they deform. This was calculated parametrically as a function of span and deflection for a waterwall tube fixed at the span ends. The total extensional deformation was estimated by superposing the extensions for a single 20-inch deflection over the 120-ft height of the furnace and those corresponding to the 4-inch deflections over the 15-ft spans between concrete floors. The value for the deformation energy given in Table 4 is for a single 120-inch span with a deflection (34.2 inches) giving the same total extensional deformation as that calculated by superposition. A factor of 0.8 was applied to allow for the fact that the tubes near the corner were not as extensively bowed. Details of this calculation are given in Appendix II of Ref. 4.

Floor tube flattening deformation energy is the strain energy of bending as the cross-section of the floor tube distorts as it contacts the top flange of the floor beams. The model describing this is given in Appendix D of Ref. 3. The value given in Table 4 is based on a flattening parameter of 0.25, which means that the vertical diameter of the tube is reduced by 25%.

Wall tube flattening deformation energy is that associated with crushing of the wall tubes where they contacted the concrete floors of the building. This calculation used the same model as for floor tube flattening. The value in Table I assumes a flattening parameter of 0.15. Details are given in Appendix II of Ref. 4.

As is evident from the above discussion, there is a degree of arbitrariness in the choice of parameters used in the deformation energy calculations, and consequently a range of uncertainty in the estimate of the energy. As a general rule, where there was a need to estimate a deflection, we tried to pick what we felt was a maximum reasonable value. Thus, the value of about 14,000 Btu for the deformed structure energy is more likely to be high than to be low. This should compensate for the energy associated with the miscellaneous damage items which were not included in the analysis.

At this time our best estimate of the structural deformation energy for Case II is 14,000 Btu. The upper bound is considered to be about 18,000 Btu and the lower bound about 8,000 Btu.

## RESULTS

A summary of the results of the analysis for the two cases is given in Table 5. These results indicate that the efficiency is considerably less than 1%.

Table 5. Summary of results.

Unit	B&W	CE
Smelt inventory, lb		
Molten form	17,500	57,000
Range	10,000-25,000	43,000-75,000
Water inventory, lb		
Lower limit	8,500	1,000
Upper limit	21,000	5,000
Best estimate	Not the limiting factor	3000 (not limiting)
Energy available, Btu		
Lower limit	$1 \times 10^6$	$2 \times 10^6$
Upper limit	$4 \times 10^6$	$4 \times 10^6$
Best estimate	$2 \times 10^6$	$2.6 \times 10^6$
Deformation energy, Btu		
Lower limit	3,000	8,000
Upper limit	8,000	18,000
Best estimate	5,000	14,000
Efficiency, %		
Range	0.075-0.8	0.2-0.9
Best estimate	0.25	0.55

#### DISCUSSION

Case II (CE Unit) was a more energetic explosion than Case I (B&W Unit). The best estimate of the structural deformation energy was 14,000 Btu for Case II as compared to 5,000 Btu for Case I. This is not really surprising because the recovery boiler was larger in Case II, there was more smelt in the unit, and there was no char bed to interfere with smelt-water contact.

The best estimate of the energy conversion efficiency was 0.25% for Case I and 0.55% for Case II. Although there is a wide range of uncertainty in the efficiency values, it is considered extremely unlikely that the energy conversion efficiency exceeds 1% in either case.

Both of these smelt-water explosions can be characterized as inefficient, low-energy events occurring in weak structures. Since these were two of the more destructive explosions which have been experienced, and no smelt-water explosion is known that clearly resulted in an order-of-magnitude more damage, it is quite possible that low energy conversion efficiencies are characteristic of large-scale smelt-water explosions. If this is the case, it suggests that physical explosions of this type (especially with liquids having the properties of smelt and water) are inherently inefficient.

The difference in energy conversion efficiencies between Case I and Case II may not be as great as it appears. The damage analysis for Case I did not include all the deformation modes that were considered in Case II. In particular, waterwall tube extensional deformation and flattening of floor and wall tubes were not included in the Case I analysis. Thus the estimated deformed structure energy for Case I may be low. It is appropriate to examine the extent to which this is true.

The magnitudes of wall deformations were much smaller in Case I. Maximum buckstay deflections were only 12 inches compared to 21 inches in Case II. Since the extensional deformation strain energy is such a nonlinear function of deflection, it seems unlikely that extensional deformation energy is an important factor in Case I. We estimate it to be about 2 million in.-lb or about 210 Btu. The walls were ultimately constrained by concrete floors, and deformations were up to 2 inches beyond the concrete floor. Some crushing of the concrete floors and of the tubes at the point of impact also occurred. We estimate the energy in wall tube flattening to be 5 million in.-lb or about 530 Btu. Some floor tube flattening also undoubtedly occurred. It may not be too great, since there were only three floor beams and they sheared from their wall supports on one side. We estimate the energy in floor tube flattening at 2 million in.-lb or 210 Btu. Thus these three terms would add about 920 Btu to the structural deformation energy. The actual accountable structural deformation energy in Case I was 4,520 Btu. Thus adding 920 Btu gives 5,440 Btu as the energy for Case I. This is still not appreciably different from the original estimate of 5,000 Btu.

#### REFERENCES

1. Kelly, P.; Frederick, W. J.; Grace, T. M., Tappi 64(10):85-7(Oct., 1981).
2. Robinson, R. R. Structural analysis of case I/B&W boiler smelt water explosion. First Interim Report, IITRI Project H06100, IIT Research Institute (Feb. 7, 1985).
3. Robinson, R. R. Structural analysis of case 2/CE boiling smelt water explosion. Second Interim Report, IITRI Project H06100, IIT Research Institute (Aug., 9, 1985).
4. Grace, T. M. Energetics of smelt/water explosion. Second Interim Report, IPC Project 3575, Grant No. NRC-G-04-84-009, The Institute of Paper Chemistry (Aug. 29, 1985).

NRC FORM 335 (2-84) NRCM 1102, 3201, 3202		U.S. NUCLEAR REGULATORY COMMISSION		1. REPORT NUMBER (Assigned by TIDC, add Vol. No., if any)  NUREG/CP-0072 Vol.	
SEE INSTRUCTIONS ON THE REVERSE					
2. TITLE AND SUBTITLE  Proceedings of the Thirteenth Water Reactor Safety Research Information Meeting				3. LEAVE BLANK	
5. AUTHOR(S)  Compiled by Allen J. Weiss, BNL				4. DATE REPORT COMPLETED MONTH   YEAR January   1986	
7. PERFORMING ORGANIZATION NAME AND MAILING ADDRESS (Include Zip Code)  Office of Nuclear Regulatory Research U. S. Nuclear Regulatory Commission Washington, D. C. 20555				6. DATE REPORT ISSUED MONTH   YEAR February   1986	
10. SPONSORING ORGANIZATION NAME AND MAILING ADDRESS (Include Zip Code)  Same as Item 7 above				8. PROJECT/TASK WORK UNIT NUMBER  A-3283	
12. SUPPLEMENTARY NOTES  Proceedings prepared by Brookhaven National Laboratory				9. FUND OR GRANT NUMBER  A-3283	
13. ABSTRACT (200 words or less)  <p>This six-volume report contains 111 papers out of the 178 that were presented at the Thirteenth Water Reactor Safety Research Information Meeting held at the National Bureau of Standards, Gaithersburg, Maryland, during the week of October 22-25, 1985. The papers are printed in the order of their presentation in each session and describe progress and results of programs in nuclear safety research conducted in this country and abroad. Foreign participation in the meeting included thirty-one papers presented by researchers from Japan, Canada and eight European countries. The titles of the papers and the names of the authors have been updated and may differ from those that appeared in the final program of the meeting.</p>				11a. TYPE OF REPORT Proceedings of conference <u>on safety research</u> b. PERIOD COVERED (Inclusive dates) October 22-25, 1985	
14. DOCUMENT ANALYSIS - a. KEYWORDS/DESCRIPTORS  reactor safety research nuclear safety research  b. IDENTIFIERS/OPEN-ENDED TERMS				15. AVAILABILITY STATEMENT  Unlimited	
				16. SECURITY CLASSIFICATION (This page) Unclassified (This report) Unclassified	
				17. NUMBER OF PAGES	
				18. PRICE	



UNITED STATES  
NUCLEAR REGULATORY COMMISSION  
WASHINGTON, D.C. 20555

OFFICIAL BUSINESS  
PENALTY FOR PRIVATE USE, \$300

SPECIAL FOURTH CLASS RATE  
POSTAGE & FEES PAID  
USNRC  
WASH D.C.  
PERMIT No. G-67

120555078877 1 1AN1R21R4  
US NRC  
ADM-DIV OF TIDC  
POLICY & PUB MGT BR-PDR NUREG  
W-501  
WASHINGTON DC 20555